**Title**
High-Resolution Photoelectron Imaging and Infrared Photodissociation Spectroscopy of Cold Negative Ions



**Author**
DeVine, Jessalyn Anna

**Publication Date**
2019

Peer reviewed|Thesis/dissertation

# High-Resolution Photoelectron Imaging and Infrared Photodissociation Spectroscopy of Cold Negative Ions

by

Jessalyn A. DeVine

A dissertation submitted in partial satisfaction of the

requirements for the degree of

Doctor of Philosophy

in

Chemistry

in the

Graduate Division

of the

University of California, Berkeley

Committee in charge:

Professor Daniel M. Neumark, Chair
Professor Richard J. Saykally
Professor Hartmut Häffner

Fall 2019

High-Resolution Photoelectron Imaging and Infrared Photodissociation Spectroscopy of Cold Negative Ions

## Abstract

High-Resolution Photoelectron Imaging and Infrared Photodissociation Spectroscopy of Cold Negative Ions

by

Jessalyn A. DeVine

Doctor of Philosophy in Chemistry

University of California, Berkeley

Professor Daniel M. Neumark, Chair

Slow electron velocity-map imaging of cryogenically-cooled anions (cryo-SEVI) is a versatile spectroscopic technique that provides high-resolution detachment spectra of molecular ions, yielding insight into the vibrational and electronic properties of neutral species. This method provides orders-of-magnitude improvement in resolution over earlier measurements, and invariably reveals new subtleties in the resultant spectra. The cryo-SEVI apparatus has multiple ion-generation and photodetachment modes of operation which enable application to a vast range of molecular species, including organic radicals, reactive intermediates, and metal-oxide clusters.

While free radicals are generally highly reactive and difficult to isolate in a laboratory experiment, their corresponding anions are closed-shell, and thus cryo-SEVI is particularly well-suited for characterization of the vibronic structure of neutral radicals with relevance to combustion and atmospheric chemistry. In this thesis, several free radicals were probed by photodetachment of the corresponding anions. The cryo-SEVI spectrum of the *tert*-butyl peroxide anion showed detachment to two electronic states of the corresponding peroxy radical, giving a number of vibrational and electronic quantities regarding this atmospherically-relevant species. In addition to the peroxy radical, the heterocyclic aromatic radicals derived from hydrogen abstraction from furan and pyridine have been studied. These isomer-specific spectra showed interesting isomeric trends in their photoelectron angular distributions, providing insight into the charge distribution resulting from deprotonation of the parent heterocycle.

In a similar vein, the vinylidene anion ($H_2CC^-$) is used to obtain spectroscopic access to neutral vinylidene, a high-energy isomer of acetylene. The isomerization of vinylidene to acetylene on the neutral ground state surface has a remarkably low barrier, resulting in the potential for coupling between vinylidene vibrational states and highly excited levels of acetylene. The extent to which this coupling occurs, and the resultant lifetime of neutral vinylidene, has been the subject of some debate in the physical chemistry community. By performing cryo-SEVI experiments on the vinylidene anion and relating these results to a

highly accurate *ab initio* potential energy surface, the state-specificity of coupling to acetylene was clearly established. The detachment spectra of vinylidene anions also showed other interesting spectroscopic effects, such as vibronic coupling between excited neutral states as well as resonant autodetachment from vibrationally excited anions.

Finally, cryo-SEVI has also been used to investigate gas-phase clusters which serve as models for the defect sites that constitute reactive centers on catalytic surfaces. These defect sites have geometries, stoichiometries, and charge distributions which differ from that of the rest of the surface, and can be challenging to probe in bulk experiments. Gas-phase metal oxide cluster anions thus provide model systems whose properties can be monitored as a function of cluster size and stoichiometry. To this end, two bare aluminum oxide clusters, $Al_2O_2^-$ and $Al_3O_3^-$, have been characterized using cryo-SEVI. This work revealed electronically-mediated autodetachment from $Al_2O_2^-$, and established the energy ordering of the close-lying $Al_3O_3^-$ isomers.

Following characterization of the bare cluster anions, it is of interest to characterize the products formed by reaction of metal oxide clusters with molecules of interest to catalysis, providing spectroscopic access to other parts of the potential energy surfaces of model catalytic reactions. To this end, cryo-SEVI was used to interrogate the product formed by reaction of $TiO_2^-$ with a single $H_2O$ molecule, and comparison of these results to the cryo-SEVI spectra of bare $TiO_2^-$ showed a similar energetic dependence of charge state as is observed for bulk water splitting on titania surfaces.

While cryo-SEVI provides invaluable information regarding neutral species via photodetachment of the corresponding anion, infrared photodissociation (IRPD) experiments may be used to structurally characterize the anions themselves, which can be particularly useful in cases where multiple low-lying isomers are expected. In an IRPD experiment, an ion of interest is complexed with a weakly interacting tagging species (such as Ar or $D_2$) in a cryogenic ion trap, and the resultant cluster is irradiated with tunable infrared light. When the incident light is resonant with a vibrational transition of the ion, the tagging molecule is lost, and so monitoring the mass spectrum following irradiation provides a measurement of the vibrational spectrum of the bare ion. In this thesis, IRPD is used to observe the loss of a $D_2$ tag from microhydrated acetate anions, $CH_3CO_2^-(H_2O)_n{\cdot}D_2$, to determine the first steps in the structural evolution of the first solvation shell for this carboxylate anion.

To my parents,
Kevin and Larene.

What a long, strange trip it's been.

# Contents

# List of Figures

# List of Tables

# Acknowledgments

As with all scientific endeavors, the progress I've made in graduate school was only possible due to a wonderful community of friends, family, peers, and advisors. (And my cat, Clyde.)

First and foremost, I must thank my thesis advisor, Prof. Daniel Neumark. I truly believe I could not have found a better advisor for my PhD work. Through all the bumps in the road, he has been incredibly helpful and supportive of my growth as a scientist, and my work in his group has given me the confidence to continue to work in this field. I will sincerely miss him and his group, and will keep the conceptual toolbox I've learned from him close to me for the rest of my career.

I also owe quite a bit to Marissa Weichman, a scientific superstar who taught me all the basics (and then some) of SEVI, and set a strong example for me to aspire to as a scientist and graduate student. And though her departure was absolutely terrifying, I wasn't left alone, and must also thank Mark Babin for helping me come into my own as a senior student. I feel confident leaving the project with him and Marty, and look forward to seeing where it goes in the future.

Beyond guidance and support, an important part of graduate school is sharing in your successes and failures with your peers. For that, I must thank Alice Kunin. From David Chandler's and Bill Miller's classes, to pushing Dan's car up a mountain, to figuring out how to write a post-doc proposal, she has been a wonderful colleague who kept me grounded in a sea of stress and doubt. I'm also grateful to the rest of the Neumark group, who has been like a family to me (as cliché as that sounds) over the past five and a half years.

In addition, the work that is represented in this thesis would have been considerably more difficult to accomplish without the support of several people working in Latimer Hall. Michelle Haskins' unending patience and hard work was necessary to keep everything up and running, and I know I speak for all of the Neumark group when I say that we are blessed to have her around. I also have to thank the guys in the machine shop - particularly Eric and Clint - for helping me whenever I needed something fixed or built.

Thanks also to the numerous people outside of Latimer Hall who helped me keep myself from becoming fully lost in my work. The original Pathfinder squad – Xantheus (a.k.a. Will), Nyl (a.k.a. Brett), Lox/Lex (a.k.a. Alex), and of course our GM Brad – gave me a weekly escape that I will greatly miss as we all scatter to whatever is next. I am also forever grateful for the love of my friends from back east – Olivia, Jen, George, and Alex Davis – who always help me remember who I am. And of course I must acknowledge Laura McCaslin, who started off as a great conference buddy and has grown into a wonderful forever-friend.

And finally, I would literally not be here, in Berkeley, were it not for my family. My parents and my brother are the best family someone like me could ask for. Though it has been painful to be far from them for so long (and I'm not exactly going to be any closer to New Jersey while I'm living in Germany), just knowing that they are there and rooting for me has always been an important part of my mental security.

I will always treasure my years at Berkeley; no matter how stressful things were, regardless of the level of imposter syndrome, I leave here knowing that I was in the exact right place.

# Part I

# Background and Methods

Hofstadter's Law: It always takes longer than you expect, even when you take into account Hofstadter's Law.

---

Douglas Hofstadter
*Gödel, Escher, Bach: an Eternal Golden Braid.*

# Chapter 1

# Introduction

## 1.1 Anion Photoelectron Spectroscopy

Anion photoelectron spectroscopy (PES) is a highly versatile spectroscopic technique wherein a laser with frequency $\nu$ interacts with a gas phase anion ($A^-$) leading to ejection of a photoelectron,

$$A^- + h\nu \rightarrow A + e^-. \tag{1.1}$$

The resultant electron kinetic energies (eKEs) are determined by the electron binding energies (eBEs) of the neutral molecule by eKE = $h\nu$ − eBE. This is illustrated in Figure 1.1, showing detachment to various vibrational levels of two neutral electronic states, where each discrete eKE corresponds to a different final vibronic state of the neutral. Measurement of the eKE distribution resulting from anion photodetachment can thus be used to extract

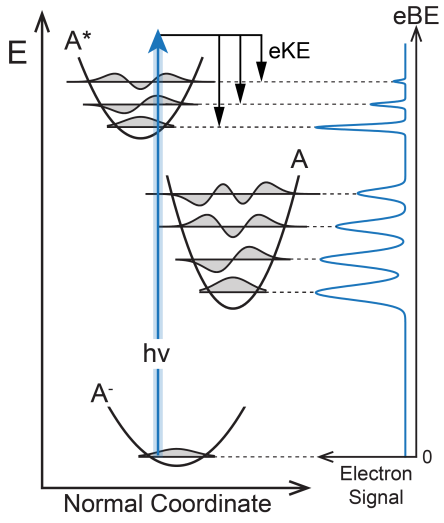


**Figure 1.1:** Energy diagram of an anion PES experiment.

quantities such as adiabatic electron affinities, electronic term energies, and vibrational frequencies of neutral molecules.

Initial iterations of anion PES employed methods which were largely borrowed from photoionization experiments, where the high energies of neutral-to-cation transitions usually require high-frequency light sources, such as vacuum ultraviolet discharge lamps or synchrotrons, that can be difficult to incorporate into the average laboratory experiment.[1] While gas-phase ion sources typically produce lower number densities than those afforded by experiments on neutral molecules, the electron affinities of neutrals are often lower than their ionization energies, enabling the use of table-top laser systems whose high power output can compensate for the loss of signal.

Anion PES experiments were first carried out using a continuous wave laser for photodetachment, and the eKE distributions were measured using a hemispherical energy analyzer.[2] This technique could give spectra with resolution as high as 5 meV (40 $cm^{-1}$).[3–6] While this method has been widely successful in determining the electron affinities of small molecules,[7] it is limited to ions that can be generated continuously, and that have detachment energies below $\approx$ 3.5 eV. The development of pulsed ion sources led to methods centered around pulsed photodetachment, where the eKE distributions are measured using a time-of-flight (TOF) electron detection scheme based on a field-free or magnetic bottle TOF spectrometer. These experiments did not substantially improve the achievable resolution in anion PES, but did allow for its application to a wider range of molecular systems.[8–10]

The development of velocity-map imaging (VMI) by Eppink and Parker[11] and the photofragment and photoelectron imaging studies carried out by Chandler[12] and Helm[13] enabled the next important advance in anion PES, where a velocity-map imaging spectrometer is used to measure the eKE distribution.[14,15] In addition to improving energy resolution and the detection efficiency for low-eKE electrons, this method has the benefit of providing simultaneous measurement of the photoelectron angular distribution (PAD) without any modification to the experiment and is thus a powerful technique for elucidating the electronic structure of gas-phase molecules.[16] These imaging experiments formed the foundation for the primary experimental method used in this thesis: slow electron velocity-map imaging (SEVI).

### 1.1.1 SEVI and Cryo-SEVI

SEVI is a variant of the photoelectron imaging experiments carried out in the early 2000's.[14,15] The VMI method, discussed in more detail in Section 2.5, has a roughly constant resolving power $\Delta v$ within a single image. Thus, as eKE is quadratic in velocity, the eKE spread is roughly given by $v\Delta v$ and so better resolution is obtained for slower electrons. The SEVI technique aims to exploit this property by using a tunable detachment laser to selectively collect multiple high-resolution windows of the overall spectrum, which are then concatenated to yield a full photodetachment spectrum.[17]

A typical SEVI experiment, illustrated in the energy diagram of Figure 1.2, starts with obtaining an overview scan at a relatively high photon energy such that multiple peaks are observed in the resultant spectrum (blue trace). The detachment energy is then tuned to

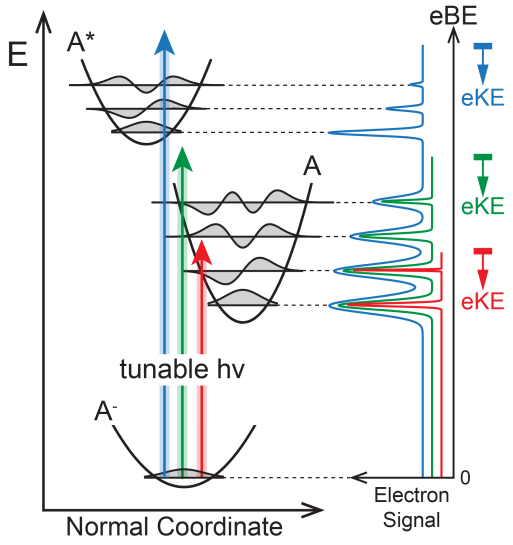


**Figure 1.2:** Energy diagram of a cryo-SEVI experiment.

within <100 $cm^{-1}$ of each region of interest (red and green traces), giving enhanced resolution over narrow windows of eBE. These high-resolution windows are then scaled to match relative intensities observed in the overview spectrum and spliced together, yielding a full photoelectron spectrum with excellent resolution. With the new VMI design described in the thesis of Marissa Weichman,[18] peaks as narrow as 1.2 $cm^{-1}$ full-width at half-maximum (fwhm) can be obtained for detachment from atomic anions, providing a substantial improvement over the $\approx$ 40 $cm^{-1}$ resolution attainable with non-imaging PES techniques.

For molecular anions, the rotational degrees of freedom result in intrinsically broadened linewidths for a photodetachment experiment which lacks sub-$B$ resolution, where $B$ is the smallest rotational constant of the molecule in question. Peak widths in SEVI spectra are thus limited by the underlying rotational contour, which is in turn governed by the anion temperature. Anion temperature can also have an impact on spectral clarity, as detachment from vibrationally excited anions introduces hot bands, leading to congested spectra that can be difficult to interpret. To further improve the resolution of the SEVI experiment as well as expand its applicability to more complex ions, a cryogenic ion trap was built in 2012 to trap and cool the ions prior to mass selection.[19] In these SEVI experiments performed on cryogenically-cooled anions (cryo-SEVI), ions are first confined in a radiofrequency octupole trap filled with a 5 K buffer gas, most commonly a 20% mixture of $H_2$ in He. This substantially reduces the average internal energy of the anions through collisions with the buffer gas, leading to narrower features and clearer spectra.

With this high resolution, cryo-SEVI is a powerful method that provides intimate vibronic details regarding neutral molecules (and, in some cases, their corresponding anions). In the work described in this thesis, three primary categories of species were studied using cryo-SEVI: free radicals, reactive intermediates, and metal oxide clusters. While many of

these systems have been studied before using anion PES, cryo-SEVI invariably provides new information – both quantitative and qualitative – regarding each neutral molecule. The following sections provide a summary of the fundamental concepts used to extract the information contained in these cryo-SEVI results and document several causes of deviation from these considerations that arise in the following chapters.

## 1.2 Fundamentals of Anion PES

### 1.2.1 Selection Rules

The selection rules for anion photoelectron spectroscopy can be derived from Fermi's Golden Rule, which states that the rate of a transition from an initial state $|\Psi'\rangle$ to a final state $|\Psi\rangle$ induced by absorption of a photon with energy $\hbar\omega$ is given by

$$\text{Rate} \propto |\langle\Psi'|\hat{\mu}|\Psi\rangle|^2 \cdot \rho \cdot \delta(\Delta E - \hbar\omega), \tag{1.2}$$

where $\rho$ is the density of final states and $\Delta E = E - E'$. In the case of anion photoelectron spectroscopy, $|\Psi'\rangle$ corresponds to the initial anion state, $|\Psi\rangle$ consists of the final neutral state plus the detached electron, and $\Delta E = \text{eKE} + \text{eBE}$ due to conservation of energy. For the transition from $|\Psi'\rangle$ to $|\Psi\rangle$ to be 'allowed,' the rate must be nonzero, which gives rise to two key requirements; $\Delta E$ must be equal to the photon energy, and the dipole moment matrix element

$$M = \langle\Psi'|\hat{\mu}|\Psi\rangle \tag{1.3}$$

must be nonzero. As the free electron eigenfunctions form a continuum, the first condition can always be satisfied so long as the photon energy exceeds the electron affinity of the neutral molecule. The selection rules governing the accessible levels of the neutral $|\Psi\rangle$ with eBE$< \hbar\omega$ are derived by considering the conditions under which $M \neq 0$.

To simplify the derivation of the selection rules, we will apply the Born-Oppenheimer approximation, which reasons that, as nuclei are so much more massive than electrons, their motions occur on a substantially longer timescale. As a consequence, the neutral $|\Psi\rangle$ and anion $|\Psi'\rangle$ wavefunctions can be expressed as

$$|\Psi'\rangle = |\psi'_{elec}\rangle|\phi'_{nuc}\rangle \quad \text{and} \quad |\Psi\rangle = |\psi_{elec}\rangle|\phi_{nuc}\rangle\,,$$

where the nuclear and electronic degrees of freedom have been separated. This expression can be further simplified by expressing the electronic wavefunction as a product of spin and orbital components, $|\psi_{elec}\rangle = |\psi_e\rangle|s\rangle$.

As is typical when considering electronic motion within a Born-Oppenheimer framework, we will impose the Condon approximation (sometimes also referred to as the sudden approximation), so that the detachment transitions described in this section are assumed to occur without any change in nuclear coordinates. As a result, the electronic and nuclear contributions to the dipole moment operator $\hat{\mu}$ can be separated,

$$\hat{\mu}(\mathbf{r}, \mathbf{q}) = \hat{\mu}_e(\mathbf{r}) + \hat{\mu}_{nuc}(\mathbf{q}),$$

where $\hat{\mu}_e$ and $\hat{\mu}_{nuc}$ only involve the electronic ($\mathbf{r}$) and nuclear ($\mathbf{q}$) degrees of freedom, respectively. The $M \neq 0$ selection rule then implies that

$$\langle\psi'_e|\,\hat{\mu}_e\,|\psi_e\rangle\,\langle s'|s\rangle\,\langle\phi'_{nuc}|\phi_{nuc}\rangle + \langle\psi'_e|\psi_e\rangle\,\langle s'|s\rangle\,\langle\phi'_{nuc}|\,\hat{\mu}_{nuc}\,|\phi_{nuc}\rangle \neq 0.$$

As the initial and final electronic states are nondegenerate eigenstates of the same $N$-electron Hamiltonian, they are orthogonal, and the second term is zero. Considering the first term, we note that given the separability of rotational and vibrational motion,[20] the nuclear component may be expressed as $|\phi_{nuc}\rangle = |\phi_{rot}\rangle\,|\phi_{vib}\rangle$; typically, individual rotational lines are not resolved in cryo-SEVI spectra, as molecular rotational constants are usually on the order of $\lesssim 1$ cm$^{-1}$. We therefore neglect the rotational contributions to $|\phi_{nuc}\rangle$ and the selection rule becomes

$$\langle\psi'_e|\,\hat{\mu}_e\,|\psi_e\rangle\,\langle s'|s\rangle\,\langle\phi'_{vib}|\phi_{vib}\rangle \neq 0. \tag{1.4}$$

This can be simplified further by applying the frozen-core approximation, wherein the detachment transition is described as sudden ejection of an electron from a single-electron molecular orbital (MO) on the anion, $|\psi_{MO}\rangle$, and the remaining occupied molecular orbitals of the anion and neutral are assumed to be identical. The electronic wavefunction of the anion may then be expressed in terms of the remaining core MOs, described by the $(N-1)$-electron state $|\psi_{core}\rangle$, as $|\psi'_e\rangle = |\psi_{core}\rangle\,|\psi_{MO}\rangle$. Furthermore, the outgoing electron is assumed to move away from the molecular frame rapidly enough such that the neutral states are not perturbed by its presence; as a consequence, the electronic degrees of freedom corresponding to the neutral molecule and the departing electron can be separated, so that the electronic contribution to the final (neutral + electron) state may be expressed as $|\psi_e\rangle = |\psi_{core}\rangle\,|\psi_k\rangle$, where $|\psi_k\rangle$ is the wavefunction of the outgoing electron which has momentum $k = \sqrt{2m(\mathrm{eKE})}$. After integrating over the $(N-1)$ core electronic coordinates, Equation 1.4 becomes

$$\langle\psi_k|\,\hat{\mu}_e\,|\psi_{MO}\rangle\,\langle s'|s\rangle\,\langle\phi'_{vib}|\phi_{vib}\rangle \neq 0, \tag{1.5}$$

from which the electronic and vibrational selection rules of anion PES can be inferred.

The spin and electronic factors in Equation 1.5 govern the symmetry and multiplicity of neutral states that can be probed experimentally. As a single electron is detached, the spin of the neutral electronic state is limited to $S = S' \pm \frac{1}{2}$; therefore, single-photon detachment from a singlet anion state can only form a doublet neutral, detachment from a doublet anion can form either a singlet or triplet neutral, and so on. The symmetry of the final neutral state is dictated by the molecular orbitals of the species in question. In general, electronic transitions are always allowed, as the outgoing electron can carry away any amount of angular momentum to satisfy the conservation law; however, within the frozen-core approximation, only neutral states that differ in the occupation of a single molecular orbital can be accessed.

For example, in the case of vinylidene ($H_2CC^-$), the $\tilde{X}\ ^2B_2$ anion has an electron configuration of $...(1b_1)^2(5a_1)^2(2b_2)^1$. Removal of the unpaired electron from the $2b_2$ orbital forms the neutral $\tilde{X}\ ^1A_1$ ground state, and removal of an electron from the $5a_1$ orbital forms the $\tilde{a}\ ^3B_2$ excited state. These are single-electron transitions, and thus these states

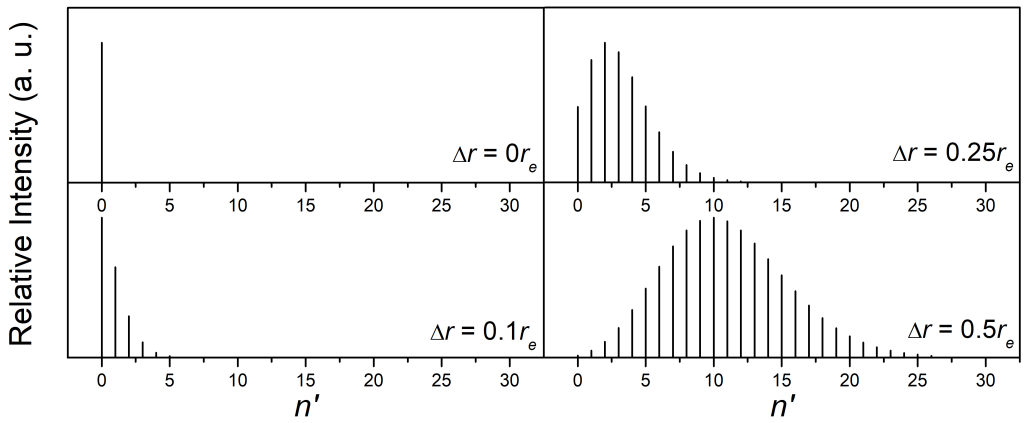


**Figure 1.3:** Example FC profiles for detachment from a homonuclear diatomic anion (bond length $r_e$) to form a neutral with equilibrium bond length $r_e + \Delta r$, showing the relative intensities for detachment to a state with $n'$ quanta of excitation along the bond-stretching mode. The vibrational frequencies were taken to be identical for anion and neutral.

are accessible via photodetachment. In contrast, photodetachment of $H_2CC^-$ to a neutral state with electron configuration $...(1b_1)^1(5a_1)^1(2b_2)^2$ is not allowed within the frozen-core approximation.

The third factor in Equation 1.5, $\langle \phi'_{vib} | \phi_{vib} \rangle$, is referred to as the Franck-Condon (FC) factor and dictates the allowed final vibrational states of the neutral following detachment. In cryo-SEVI experiments, the anions are taken to be in their ground vibrational state, and so the FC factor can only be nonzero if the neutral's vibrational wavefunction is totally symmetric within the appropriate molecular point group. In the case of vinylidene, which has $C_{2v}$ symmetry, this can be achieved if the final neutral state has any number of quanta along an $a_1$-symmetric vibrational mode, or an even number of quanta along $a_2$, $b_1$, or $b_2$-symmetric modes.

For a given electronic band, the relative intensities of the different vibrational transitions are given by $|\langle \phi'_{vib} | \phi_{vib} \rangle|^2$, which is in turn connected to the difference between the anion and neutral equilibrium geometry. To illustrate this, Figure 1.3 shows example FC profiles for photodetachment of a diatomic anion to various neutral vibrational levels, where the equilibrium bond length of the neutral varies by 0%, 10%, 25%, and 50% relative to $r_e$ of the anion ground state. As the displacement along the normal mode between the anion and neutral equilibrium structures is increased, higher-quanta vibrational levels in the neutral are populated, and the intensity peak shifts away from the vibrational origin. Thus, a larger change in equilibrium geometry between anion and neutral generally allows for detachment to a larger number of neutral vibrational levels, though the geometries must still be similar enough for the FC factors to be nonzero.

For more complex systems, this relationship between geometry displacement and the FC profile typically holds, provided the individual normal modes of the molecule are (a) similar for the anion and neutral and (b) well-described as independent harmonic oscillators. In

this case, the most FC activity is observed for vibrational modes along which there is a relatively large displacement between anion and neutral geometries. Therefore, transitions to neutral states with even quanta of excitation along non-totally-symmetric modes, though FC-allowed, are usually not observed (unless there is a substantial difference in harmonic frequency between anion and neutral), as displacement along such modes would imply that either the anion or neutral breaks symmetry.

### 1.2.2 Photodetachment Cross Sections and Angular Distributions

#### Energetic Effects on Detachment Cross Sections

The energy-dependence of the cross section for detachment of low-eKE electrons is of vital importance to cryo-SEVI, where eKEs typical of high-resolution spectra do not far exceed $\sim$100 cm$^{-1}$. The treatment of ejection of low-eKE electrons from anions has been addressed by Wigner,[21] who found that the detachment cross section scales with the outgoing electron's angular momentum $\ell$ as

$$\sigma \propto (\text{eKE})^{\ell+1/2}. \tag{1.6}$$

This equation is derived by considering the interaction between the outgoing electron and the neutral molecule. Assuming that the molecule does not have a particularly large permanent dipole moment, the dominant Coulombic interaction between the detached electron and the neutral is an attractive charge-induced dipole relation that scales as $V_{Coul} \propto -r^{-4}$. The total interaction potential includes a centrifugal term, so that the effective interaction potential is given by

$$V_{eff} = V_{Coul} + \frac{\hbar^2}{2\mu}\frac{\ell(\ell+1)}{r^2}, \tag{1.7}$$

where $\mu$ is the reduced mass of the system. For $\ell > 0$, this results in a centrifugal barrier at low $r$ with a height that increases with increasing $\ell$, as illustrated in Figure 1.4a. If the eKE

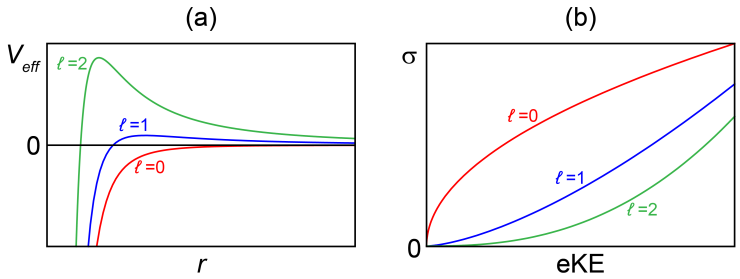


**Figure 1.4:** **(a)** Illustration of the potential presented in Eq. 2.7, describing the interaction between a neutral molecule and an outgoing electron with angular momentum $\ell$ following photodetachment of an anion. **(b)** Scaling of the detachment cross section as given by the Wigner threshold law.

is not sufficient to overcome this barrier, then the detached electron will only be observed (i.e., will not recombine with the neutral) if it manages to tunnel through. Calculation of the tunneling probability using Wentzel-Kramers-Brillouin (WKB) theory gives rise to Eq. 1.6.

For cryo-SEVI, the Wigner threshold law can affect the ultimate achievable resolution for a given detachment transition. Transitions which result in outgoing $s$-wave ($\ell = 0$) electrons are most favorable, as these maintain sufficient intensity near-threshold to be acquired in high resolution. For transitions where no $s$-wave detachment is available, the near-threshold attenuation of the detachment cross section prevents as close an approach to the experimental feature. This is illustrated in Figure 1.4b. Additionally, as the threshold behavior is directly related to the electronic symmetry of the detachment transition, features with different electronic character can sometimes be distinguished by their differing near-threshold signal attenuation (see Chapter 10).

### Photoelectron Angular Distributions

Photoelectron imaging experiments provide simultaneous measurement of the photoelectron spectrum and the photoelectron angular distribution. For single-photon photodetachment with linearly polarized light, PADs have the form

$$I(\theta) = \frac{\sigma_{tot}}{4\pi}\left[1 + \beta P_2(\cos\theta)\right], \tag{1.8}$$

where $\sigma_{tot}$ is the total detachment cross section, $P_2(x)$ is the second-order Legendre polynomial, $\theta$ is the angle of the outgoing electron's velocity vector with respect to the laser polarization axis, and $\beta$ is the anisotropy parameter. The angular dependence is entirely determined by $\beta$, which ranges between -1 and +2 and is generally a function of eKE; Figure 1.5 illustrates the angular distributions observed in VMI images for parallel ($\beta > 0$), perpendicular ($\beta < 0$), and isotropic ($\beta = 0$) detachment transitions.

The anisotropy parameter for a particular detachment transition is determined by the angular momentum of the outgoing electron, $\ell$. Operating within the frozen-core approximation, conservation of momentum requires that $\ell = l \pm 1$, where $l$ is the angular momentum

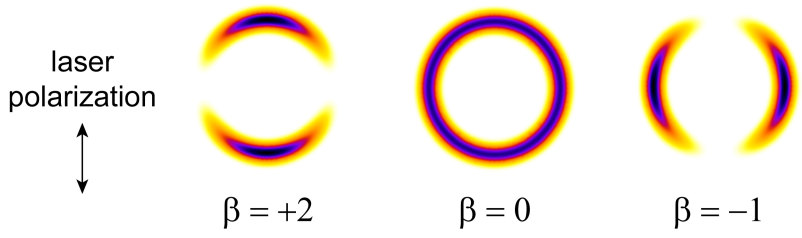


**Figure 1.5:** Illustration of VMI images obtained for transitions which have parallel ($\beta > 0$), isotropic ($\beta = 0$), and perpendicular ($\beta < 0$) angular distributions.

of the anion orbital $|\psi_{MO}\rangle$. From this, a relationship between $\beta$ and $l$ can be derived which implicitly describes the eKE dependence of the anisotropy parameter. This is given by the Cooper-Zare formula,[22]

$$\beta = \frac{l(l-1)\chi_{l,l-1}^2 + (l+1)(l+2)\chi_{l,l+1}^2 - 6l(l+1)\chi_{l,l+1}\chi_{l,l-1}\cos\left(\delta_{l+1,l-1}\right)}{3(2l+1)\left[l\chi_{l,l-1}^2 + (l+1)\chi_{l,l+1}^2\right]}. \tag{1.9}$$

Here, $\delta_{l+1,l-1}$ denotes the phase shift between the outgoing $l \pm 1$ partial waves, and the eKE dependence is encapsulated in the dipole radial matrix elements, $\chi_{l,l\pm1}$.

Hanstorp's central potential formulation[23] builds on the Cooper-Zare derivations, noting that at low eKEs, the Wigner threshold law (Eq. 1.6) describes the relative contributions from the $l \pm 1$ detachment channels. This enables replacement of the dipole matrix elements with terms that explicitly involve the eKE (denoted as $\varepsilon$ in the following equations) as well as a coefficient $A$ which represents the relative scaling of the $l+1$ and $l-1$ detachment channels, giving an alternative expression of $\beta$,

$$\beta = \frac{l(l-1) + (l+1)(l+2)A^2\varepsilon^2 - 6l(l+1)A\varepsilon\cos(\delta_{l+1} - \delta_{l-1})}{(2l+1)\left[l + (l+1)A^2\varepsilon^2\right]}, \tag{1.10}$$

where $\delta_{l\pm1}$ denotes the phase shift in the partial wave components induced by the interaction with the remaining neutral core. Thus, the eKE dependence of the anisotropy parameter is directly linked to the orbital angular momentum of the detached orbital.

For molecular systems, $l$ is not a well-defined quantum number; however, there still exists a connection between the eKE-dependence of $\beta$ and the angular momentum of the detached molecular orbital. One formulation which illustrates this relationship is the mixed-*sp* model developed by Sanov and coworkers,[24–26] which is most applicable for treating detachment from single-centered *sp*-hybridized molecular orbitals (for example, the furanide anions discussed in Chapter 4). This model considers the detached orbital as a superposition of *s*- and *p*-components with fractional *p*-character $\gamma$. As shown in the initial derivation of the model,[24] this greatly simplifies Eq. 1.10, giving

$$\beta = \frac{2Z\varepsilon + 2A\varepsilon^2 - 4\varepsilon\cos(\delta_2 - \delta_0)}{A^{-1} + 2A\varepsilon^2 + Z\varepsilon}, \tag{1.11}$$

where $Z = \frac{1-\gamma}{\gamma}\frac{B}{A}$ and $B$ is a constant similar to the $A$ Hanstorp coefficient representing the relative scaling of the $s \rightarrow p$ and $p \rightarrow s$ detachment channels. The fraction $B/A$ can be derived under particular assumptions (for example, in the case of a $2s2p$ hybrid orbital, $B/A = 8/3$),[27] and thus the mixed-*sp* model gives a relatively straightforward interpretation of experimental PADs in terms of orbital angular momentum. Additional developments have expanded this treatment to consider single-center orbitals of arbitrary angular momentum composition;[28] this generalized framework is used to understand the PADs observed for detachment from the three pyridinide isomers (Chapter 6), where a *d*-component is required to explain the observed angular distributions.

### 1.2.3 Non-Franck Condon and Anharmonic Effects

The selection rules discussed in Section 1.2.1 serve as a starting point for analysis of a cryo-SEVI spectrum. By comparing simulated Franck-Condon profiles and photoelectron angular distributions to experimental spectra, the final electronic and vibrational states of the neutral may be assigned, and the binding energies may be used to calculate useful molecular information. However, in many cases, the most interesting features of the spectra are those that result from a breakdown of the assumptions used to derive these selection rules. This section describes several phenomena which have resulted in such deviations; these effects arise either from a failure of the Born-Oppenheimer approximation (resulting in nuclear-electronic coupling) or from anharmonic effects that result in coupling between vibrational levels in a single electronic state.

#### Herzberg-Teller Coupling

By far the most prevalent effect that results in the appearance of non-Franck-Condon vibrational features in SEVI spectra is Herzberg-Teller coupling (HT), most commonly within the neutral's manifold of vibronic states.[29–38] HT coupling arises due to a breakdown of the Condon approximation, and therefore also of the Born-Oppenheimer approximation, such that the electronic contribution to the dipole moment operator $\hat{\mu}_e$ depends on both the electronic and nuclear coordinates. As a consequence of expanding $\hat{\mu}_e$ as a power series of the nuclear coordinates, an expression for coupling between Born-Oppenheimer states can be derived, which is then simplified using symmetry considerations.[39–41]

Within this framework, two vibronic states $|a\rangle$ and $|b\rangle$, with vibrational and electronic symmetries given by $\Gamma_{vib}^{a,b}$ and $\Gamma_{elec}^{a,b}$, respectively, can couple provided

$$\Gamma_{vib}^{a} \otimes \Gamma_{elec}^{a} \otimes \Gamma_{vib}^{b} \otimes \Gamma_{elec}^{b} \supset \Gamma_{TS}, \tag{1.12}$$

where $\Gamma_{TS}$ is the totally symmetric representation within the relevant molecular point group. This coupling results in mixing between vibronic levels $|a\rangle$ and $|b\rangle$, so that the true states can be expressed as $|\Psi_a\rangle = \alpha_{aa}|a\rangle + \alpha_{ab}|b\rangle$ and $|\Psi_b\rangle = \alpha_{bb}|b\rangle + \alpha_{ba}|a\rangle$. If $|b\rangle$ is nominally FC-forbidden (i.e. $\langle\Psi'|b\rangle = 0$, where $|\Psi'\rangle$ is the initial anion state), then detachment to $|\Psi_b\rangle$ may be observed provided $|a\rangle$ has nonzero FC overlap with the ground state anion. In this case, detachment to the FC-forbidden level will occur near the binding energy associated with state $|b\rangle$, while possessing the electronic character (observable through the threshold behavior and PAD) of state $|a\rangle$.

As an example, consider the detachment spectrum of the $TiO_3H_2^-$ anion, which has a $C_{2v}$ molecular geometry. In the cryo-SEVI spectrum of this anion (Chapter 10), detachment transitions terminating in $b_1$-symmetric vibrational levels of the $\tilde{X}\ ^1A_1$ neutral state gain intensity through HT coupling between the ground electronic state of the neutral and some excited electronic state. In the notation introduced above, the observed FC-forbidden levels correspond to $|b\rangle$, with $\Gamma_{vib}^{b} = b_1$ and $\Gamma_{elec}^{b} = A_1$. For coupling to a vibronic level $|a\rangle$ to result in the appearance of these features, $|a\rangle$ must be FC allowed for detachment from

the vibrationally cold $\tilde{X}\ ^2A_1$ anion ground state, i.e. $\Gamma^a_{vib} = a_1$. Therefore the state $|a\rangle$ which couples to $|b\rangle$ must have $\Gamma^a_{elec} = B_1$. As detailed in Chapter 10, such an assignment is supported by consideration of the threshold behavior and photoelectron angular distributions of FC-allowed versus FC-forbidden peaks; these signatures of the electronic character of different detachment transitions are frequently used to bolster an argument involving HT effects in cryo-SEVI spectra.

**Anharmonic Effects**

This section will consider features which arise in cryo-SEVI spectra through a breakdown of the harmonic oscillator approximation. Within the Born-Oppenheimer approximation, the full molecular Hamiltonian is given by

$$\hat{\mathscr{H}} = \hat{T}_N + \hat{T}_e + \hat{V}_{ee} + \hat{V}_{eN} + \hat{V}_{NN} = \hat{H} + \hat{T}_N + \hat{V}_{NN}, \tag{1.13}$$

where $\hat{H} = \hat{T}_e + \hat{V}_{ee} + \hat{V}_{eN}$ is the electronic Hamiltonian. For a particular electronic state, the nuclear potential energy $\hat{V}_{NN}$ determines the vibrational characteristics. Within the harmonic approximation, and neglecting rotational and translational degrees of freedom, $\hat{V}_{NN}$ is expressed in terms of conveniently-defined normal coordinates $\{q_i\}$ as $\hat{V}^{HO}_{NN} = \frac{1}{2}\sum_i \omega_i q_i^2$. The true nuclear potential energy includes higher-order terms,[20]

$$\hat{V}_{NN} = \hat{V}^{HO}_{NN} + \frac{1}{3!}\sum_{ijk}\eta_{ijk}q_iq_jq_k + \frac{1}{4!}\sum_{ijkl}\eta_{ijkl}q_iq_jq_kq_l + \cdots \tag{1.14}$$

The typical Franck-Condon simulations used to analyze a cryo-SEVI spectrum are based on a treatment of the molecular normal modes as independent harmonic oscillators, neglecting higher-order contributions to the nuclear potential energy. However, if the higher-order force constants are non-negligible, then the true vibrational wavefunctions are better described as linear combinations of the harmonic oscillator eigenfunctions. This results in coupling between the zeroth-order vibrational levels, particularly in cases of near-degeneracies. The first-order mixing coefficient describing the contribution to $\psi_a(\mathbf{q})$ from a zeroth-order level $\psi_b^{(0)}(\mathbf{q})$ induced by the inclusion of higher-order terms in is then given by[42]

$$c^{(1)}_{ab} = \frac{\int d\mathbf{q}\,\psi_b^{(0)*}(\hat{V}_{NN} - \hat{V}^{HO}_{NN})\psi_a^{(0)}}{E_a^{(0)} - E_b^{(0)}}, \tag{1.15}$$

where the integration is performed over all the normal modes of the molecule. If this mixing coefficient is large enough, then it is possible for a state $\psi_a^{(0)}$ which (at zeroth-order) has no FC overlap with the anion ground state to obtain a non-zero Franck-Condon factor through coupling to a state $\psi_b^{(0)}$ that possesses more FC intensity.

As an example, consider the electronic ground state of the *p*-pyridyl radical, which is probed in the cryo-SEVI spectra presented in Chapter 6. The detachment spectrum of the *p*-pyridinide anion showed that transitions identified as terminating in vibrational levels

involving 3 quanta of excitation along a particular totally-symmetric mode ($\nu_9$) were split by around 10 cm$^{-1}$, indicating the existence of some vibrational state of the neutral which lies $\approx 10$ cm$^{-1}$ below the $3\nu_9$ level. As this anomalous feature does not appear to have different electronic character than FC-allowed transitions, it is assumed to be a totally-symmetric vibrational level of the neutral radical, rather than a FC-forbidden, HT-allowed level. A harmonic analysis shows that the $1\nu_8 + 2\nu_{16}$ combination band is energetically close enough to the $3\nu_9$ level to be a candidate for the unexplained spectral features; this would involve a fifth-order term in the Hamiltonian. A similar phenomenon was also observed in the detachment spectrum of the 1-anthracenyl anion.[43]

**Autodetachment**

The considerations above have assumed that the only process contributing to the production of photoelectrons is direct detachment, defined by Eq. 1.1. An alternative process that can lead to emission of an electron is autodetachment. This can occur when the incident photon is resonant with a particular anion excitation; if this excited anion state is higher in energy than the neutral, it can then spontaneously detach through a non-radiative process,[44,45]

$$\mathrm{A}^- + h\nu \rightarrow (\mathrm{A}^-)^* \rightarrow \mathrm{A} + e^-. \tag{1.16}$$

Eq. 1.16 can only occur provided there is some degree of coupling between the anion and neutral states, and thus the observation of autodetachment in cryo-SEVI experiments provides valuable information regarding the anion and neutral potential energy surfaces. Regardless of the mechanism of this coupling, the key signature of autodetachment in a photoelectron spectrum is the observation of features which only appear when specific ranges of detachment energies are used, or whose intensities exhibit dependences on photon energies which otherwise deviate from the expectations set forth by the Wigner threshold law. Thus this effect is particularly striking in cases where Eq. 1.16 provides access to neutral states which are FC-forbidden for detachment from the anion ground state, as illustrated in Figure 1.6a.

The first case of autodetachment described in this work is vibrationally-mediated autodetachment from the vinylidene anion ($H_2CC^-$), wherein vibrational excitation in the anion is converted to electronic motion of the outgoing electron.[46,47] Excitation of the anion using infrared light was found to result in two separate autodetachment mechanisms, leading to the observation of both constant-eBE features (Fig. 1.6b) and constant-eKE features over separate ranges of photon energies. Closer inspection of the highly accurate *ab initio* potential energy surface previously considered by Guo and coworkers[37,48,49] revealed an intersection of the anion and neutral ground state surfaces, which results in strong coupling between particular anion vibrational levels and neutral states lying near the zero-point energy of $H_2CC$. This provides observation of transitions which are best described as terminating in states involving an intermediate well along the vinylidene-acetylene isomerization coordinate, supporting the multi-well picture of this isomerization set forth in Reference [49].

While the constant-eBE intermediate-well autodetachment features are well described by the mechanism shown in Figure 1.6a, the constant-eKE features were, at first, puzzling, as

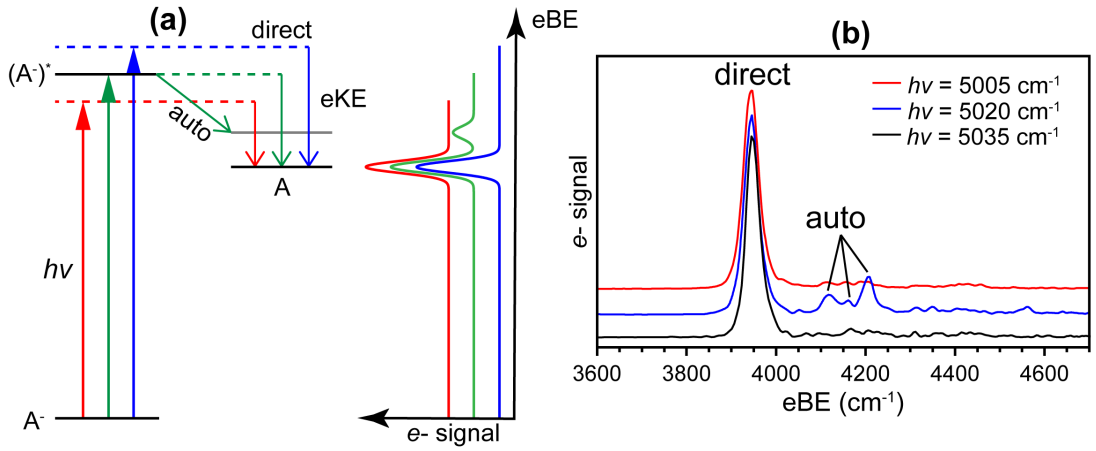


**Figure 1.6:** **(a)** Illustration of direct detachment and autodetachment for a system where an excited state of the anion couples to a FC-forbidden neutral state (gray line). The spectra that would result from these processes happening simultaneously are also illustrated. **(b)** Autodetachment behavior for the vinylidene anion, revealing the intermediate-well states near eBEs of 4200 $cm^{-1}$.

such behavior typically requires a dense near-continuum manifold of states that can disperse energy such that the eKE release is the same regardless of the anion excited state. An example of this type of autodetachment is thermionic emission, where statistical redistribution of energy in the anion results in autoemission of low-eKE electrons over a wide range of photon energies.[14] As discussed in Section 9.2.3, it was determined that in the case of $H_2CC^-$, the constant-eKE transitions arise through $\Delta K = \Delta J = 0$ transitions between different rotational levels of the excited anion and neutral ground state, yielding photon-dependent enhancement of the various underlying rotational bands constituting the rotational contour of the vibrational origin. Thus both classes of autodetachment observed for the vinylidene anion are vibrationally-mediated, illustrating that this type of autodetachment can lead to the observation of both constant-eKE and constant-eBE features in photoelectron spectra.

Signatures of autodetachment were also observed in the cryo-SEVI experiments probing the $Al_2O_2^-$ anion discussed in Chapter 11. In contrast to the vibrationally-mediated autodetachment observed for vinylidene anions, consideration of the electronic structure of anionic and neutral $Al_2O_2$ led to the conclusion that $Al_2O_2^-$ autodetaches through a purely electronic mechanism involving a two-electron transition. While this phenomenon has not been noted in previous cryo-SEVI studies, it is well-known to occur for specific systems, such as $Ba^-$ or $N_2$.[50,51] In these types of electronically-mediated autodetachment transitions, ejection of an electron occurs simultaneously with relaxation of an electron in a higher-lying orbital, releasing the loss in internal electronic energy through the eKE of the detached electron. The transitions discussed in Chapter 11 thus represent a valence-orbital version of the Auger effect; rather than relaxing to fill a hole in the core-electron orbitals, electron emission is accompanied by a relaxation within the anion's higher-energy valence molecular orbitals.

## 1.3 Theoretical Methods

The high resolution of the cryo-SEVI experiment lends itself to combining theory and experiment to obtain an improved understanding of the molecular physics of a range systems. In Sections 1.3.1 and 1.3.2, the methods used to calculate Franck-Condon profiles and photoelectron angular distributions are discussed. Before such calculations can be performed, the geometries and normal modes of the anion ground state and neutral states of interest must be determined.

In general, the problem electronic structure theories try to solve is the diagonalization of the electronic Hamiltonian, which is typically performed iteratively until self-consistency is achieved to yield a ground-state wavefunction for the system in question. The main difficulty that arises in these calculations is in the treatment of electron-electron interactions in many-electron systems. Exact treatment of these interactions comes with prohibitive computational cost, and thus there is a wide range of methods used to treat molecular systems in an approximate manner. One approach that has been remarkably successful in cutting back on the computational expense required to obtain reliable ground state molecular properties is density functional theory (DFT),[52] and this formalism is the dominant one used to analyze the cryo-SEVI spectra presented in this thesis.

In the formulation of DFT, the wavefunction is replaced by the electron density, $\rho(\mathbf{r})$, which has the same spatial charge distribution of the $N$-electron wavefunction while being a function of a single electronic coordinate. The Born-Oppenheimer electronic energy is then expressed as a functional of $\rho(\mathbf{r})$,

$$E[\rho(\mathbf{r})] = T_e[\rho(\mathbf{r})] + V_{eN}[\rho(\mathbf{r})] + V_{ee}[\rho(\mathbf{r})] + E_{XC}[\rho(\mathbf{r})]. \tag{1.17}$$

The $V_{eN}$ and $V_{ee}$ contributions to the electronic energy, given by

$$V_{eN}[\rho(\mathbf{r})] = -\sum_{\alpha} \int \frac{Z_\alpha}{|\mathbf{r} - \mathbf{R}_\alpha|} \rho(\mathbf{r}) d\mathbf{r} \quad \text{and} \quad V_{ee}[\rho(\mathbf{r})] = \frac{1}{2} \int \int \frac{\rho(\mathbf{r}_1)\rho(\mathbf{r_2})}{r_{12}} d\mathbf{r}_1 d\mathbf{r}_2, \tag{1.18}$$

are known and can be solved exactly. In general, the other two contributions to Eq. 1.17 – the electronic kinetic energy $\hat{T}_e[\rho(\mathbf{r})]$ and the quantum mechanical exchange-correlation term $E_{XC}[\rho(\mathbf{r})]$ – cannot be exactly solved in terms of $\rho(\mathbf{r})$. A massive collection of density functionals have been developed over the past several decades to approximate these terms using a range of approaches that vary in computational complexity and chemical accuracy; a somewhat recent review of the differences in these functionals as well as their relative successes can be found in Reference [52].

While some cases require more in-depth computational work, DFT is sufficient in many cases for describing the experimental spectra presented in this thesis. In cases where outside assistance was not required, the electronic structure calculations described in the following chapters use either Gaussian[53,54] or Q-Chem[55] to obtain optimized equilibrium geometries, electronic energies, and harmonic frequencies for all electronic states involved in the experimental spectra. For systems where excited state calculations are desired, the excited state

geometry is determined by performing maximum-overlap method (MOM) calculations in Q-Chem,[56] though this method is ill-suited for application to multi-reference systems. Other methods that can be used to calculate excited state geometries include coupled-cluster calculations, though these generally require a closed-shell reference state, and thus are unsuited to the calculation of open-shell excited states of a molecule with an open-shell ground state.

### 1.3.1 Simulating Photoelectron Spectra

As discussed in Section 1.2.1, the relative intensities of individual vibrational transitions within a given electronic band in a cryo-SEVI spectrum are in part governed by the Franck-Condon overlap between the anion ground state $\phi_0^A = \langle q|\phi_{vib}\rangle$ and the various vibrationally excited levels of the neutral. These Franck-Condon profiles are calculated using the equilibrium geometries, harmonic frequencies, and normal mode displacements as input for either the ezSpectrum[57] or PESCAL[58] software package. For each vibrationally excited neutral level $\phi_{\mathbf{n}}^N = \langle q|\phi'_{vib}\rangle$ specified by $\mathbf{n} = (n_1, n_2, ..., n_M)$ where $M$ is the total number of vibrational modes, these programs compute the $2M$-dimensional integrals

$$\int\int \phi_0^A(\mathbf{q}_A)^* \phi_{\mathbf{n}}^N(\mathbf{q}_N)\; d\mathbf{q}_N\; d\mathbf{q}_A, \tag{1.19}$$

where $\mathbf{q}_N$ and $\mathbf{q}_A$ refers to the normal coordinates of the neutral and anion, respectively.

Evaluation of these integrals requires a transformation between the anion and neutral normal coordinates. The simplest is the parallel approximation, which assumes that the normal modes of the anion are identical to those of the neutral. More generally, we may define a linear transformation between the two sets of coordinates,[59]

$$\mathbf{Q}' = \mathbf{J}\mathbf{Q} + \mathbf{K}', \tag{1.20}$$

where $\mathbf{Q}$ and $\mathbf{Q}'$ define the neutral and anion normal coordinates, respectively. The matrix $\mathbf{J}$ is the Duschinsky rotation matrix, and $\mathbf{K}'$ gives the geometry difference between anion and neutral in terms of the anion normal coordinates. The Duschinsky matrix is block-diagonal, such that only modes of the same symmetry can be mixed by this transformation.

It should be noted that a discrepancy between the calculated FC profile and cryo-SEVI spectra does not necessarily imply that one of the effects discussed in Section 1.2.3 is impacting the spectrum. The FC profiles are highly sensitive to the displacement between the anion and neutral geometries used in the calculation, and small changes such as rotation of a methyl group can have a significant impact on the predicted activity of particular vibrational modes. For example, it was found that slightly altering the geometries used to calculate the FC profile for detachment from *tert*-butyl peroxide resulted in the appearance or disappearance of peaks from the theoretical spectrum, and these small displacements were sufficient to describe the observed vibrational structure without invoking more complex effects.[60] This is discussed in detail in Section 5.7.1.

### 1.3.2 Calculating Photoelectron Angular Distributions

As discussed in Section 1.2.2, the photoelectron angular distributions obtained from the cryo-SEVI technique reflect the electronic character of individual detachment transitions. Thus calculation of these PADs from first principles can be useful for developing a qualitative understanding of the electronic structure of the neutral molecule(s) in question, as well as for confirming assignments involving vibronic coupling.

The discussions of the photoelectron angular distributions that have been presented above have made a common assumption; namely, that the wavefunction describing the detached electron immediately prior to detachment can be identified as a molecular orbital of the initial anion. A more correct representation of the soon-to-be-detached electron is the Dyson orbital, which for anion PES is a one-electron wavefunction defined by the overlap between the ground state $N$-electron anion wavefunction $\psi'_e(r_1, r_2, ..., r_N)$ and the final $(N-1)$-electron state of the neutral molecule $\psi_e(r_1, r_2, ..., r_{N-1})$,

$$\phi^d(r) = \int \psi'^*_e(r_1, ..., r_N)\psi_e(r_1, ..., r_{N-1})\, dr_1\, dr_1 \cdots dr_{N-1}. \tag{1.21}$$

The Dyson orbital can be calculated using equation-of-motion coupled-cluster (EOM-CC) calculations,[61,62] the output of which is provided to the ezDyson software package for calculation of the PAD.[63]

To calculate the PAD for a particular Dyson orbital, ezDyson calculates the matrix elements $\langle\phi^d|\hat{r}|\psi_k\rangle$ where $|\psi_k\rangle$ describes the wavefunction of the outgoing electron with momentum $k$. To do so, $|\psi_k\rangle$ is treated as a plane wave and subsequently expressed as a superposition of spherical waves. From this description of the outgoing electron and calculated Dyson orbital, the differential cross section, total cross section, and anisotropy parameter may be calculated for particular eKEs. Additionally, from the plane wave expansion, partial-wave characters $C_{k\ell m}$ may be defined, which can be used to determine the contributions of different angular momenta to the outgoing electron. This can often be related to threshold behavior of different vibronic transitions, as discussed in Chapters 5 and 10.

The calculation of a Dyson orbital has two main limitations for our purposes. First, the computational expense associated with a coupled-cluster calculation can be debilitating for larger molecules. Second, EOM-CC methods typically require a closed-shell reference, and thus cannot be performed for systems where both the anion and neutral states in question are open shell. In cases such as these, the frozen-core picture is typically applied (i.e. $\psi_e = \psi_{core}$), and the code of Liu and Ning may be used to calculate the expected PAD for detachment from a specified molecular orbital obtained using standard DFT techniques.[64] This uses a similar analysis as the ezDyson software, without requiring computationally expensive coupled-cluster calculations. The key failure of the DFT-based approach relative to a Dyson orbital treatment is that it is restricted to systems which reasonably obey the frozen-core approximation; however, in most cases, the Dyson orbital strongly resembles a molecular orbital on the anion, and the two methods give comparable results.

## 1.4 Systems of Interest

### 1.4.1 Free Radicals

Free radicals are an important class of chemical species defined by having an unpaired electron, which greatly impacts chemical behavior.[65–67] While some stable radical species have been produced due to their potential for application in magnetic materials and data storage,[68–70] radicals are typically associated with high reactivity and short lifetimes. Free radicals play vital roles in organic and polymer synthesis,[71–75] biological processes,[76] atmospheric reactions,[77,78] and combustion chemistry.[79] While reactivity studies can provide a great deal of insight into the dynamics of such reactions, the static properties of free radicals can be difficult to measure. In contrast, the corresponding anions are closed-shell and generally easy to form in standard gas-phase ion sources, and thus anion PES is an ideal technique for probing such transient molecules. The radicals studied in this work fall into two categories: deprotonated aromatic heterocycles and alkyl peroxy radicals.

#### Aromatic Heterocyclic Radicals

Extended ring systems based on aromatic heterocycles such as furan or pyridine are common structural components of coal and other high-energy-density materials.[80–82] Thermal decomposition of these parent molecules typically results in loss of an H-atom to form a radical, which can then participate in radical chain reactions with implications for formation of soot and volatile organic compounds in the atmosphere.[83,84] Additionally, various forms of polycyclic aromatic hydrocarbons (PAHs) and their heterocyclic cousins have been suggested as contributors to various astronomical measurements,[85–88] and careful determination of their gas-phase properties could help to confirm or refute these assignments.

These radicals are also of considerable interest from a fundamental perspective.[89] In common with PAHs, the aromatic stabilization present in such systems results in a relatively stable radical when compared to non-aromatic radical systems. However, in contrast with PAHs, the heteroatoms often introduce lone pairs that can interact with the radical electron, resulting in interesting electronic effects that can vary between isomeric forms.[90] Anion PES is a desirable method for probing such electronic effects, and the PADs provided by cryo-SEVI can provide insight into the effects of heteroatom proximity on the hybridization of the molecular orbitals of deprotonated aromatic species.[91] To this end, isomer-specific cryo-SEVI spectra have been obtained for the furanyl (Chapter 4) and pyridyl (Chapter 6) radical systems.

#### Alkyl Peroxy Radicals

Alkyl peroxy radicals (ROO·) form in the atmosphere when alkyl radicals combine with molecular oxygen.[92–96] These species are important reactive intermediates in a wide range of atmospheric processes, and can undergo reaction with NO, $NO_2$, $HO_2$, themselves, or other alkyl peroxy radicals.[97–100] As a result of this chemistry, peroxy radicals play key roles in

formation of atmospheric aerosols, degradation of volatile organic compounds, and formation of tropospheric ozone.[101–107] Many of the reactions underlying these general processes are photochemical in nature, and a wide body of work exists studying the photochemistry and spectroscopy of alkyl peroxy radicals.[108–113] These studies are often assisted by knowledge of the vibrational and/or electronic energies of the radical ground and excited states; this information is easily gleaned from a cryo-SEVI spectrum of the corresponding anion, which can be generated by gas-phase deprotonation of an appropriate hydroperoxide. In this thesis, the *tert*-butyl peroxy radical is probed using cryo-SEVI (Chapter 5), providing a number of quantitative and qualitative insights into its fundamental molecular properties.

### 1.4.2 The Vinylidene-Acetylene Isomerization

The isomerization of vinylidene ($H_2CC$) to acetylene (HCCH) is a fundamental unimolecular chemical transformation that represents the simplest 1,2-hydrogen shift reaction common in organic chemistry.[114] The barrier for isomerization to acetylene is remarkably low on the ground state surface;[48,115–118] in fact, early considerations of this reaction treated vinylidene as a transition state, rather than a reactive intermediate corresponding to a true local minimum.[119] This low barrier has motivated a large body of work aimed at understanding the dynamics underlying the $H_2CC \rightarrow HCCH$ rearrangement.[120–125] While the HCCH configuration is favored for the neutral ground state, the $C_2H_2^-$ anion takes the vinylidene global minimum, providing spectroscopic access to the neutral vinylidene well by photodetachment of the $C_2H_2^-$ anion.

Previous experimental studies concerning photodetachment from vinylidene anions have generated controversy regarding the stability/lifetime of neutral vinylidene formed in this manner. The anion photoelectron spectrum reported by Ervin and coworkers[126] showed that features in the ground state electronic band were anomalously broadened, an effect which was ascribed to detachment to form a short-lived neutral that isomerizes to acetylene on a sub-ps timescale. In contrast, Coulomb explosion imaging experiments found that neutral vinylidene persisted over several microseconds following anion photodetachment.[127]

The cryo-SEVI spectra presented in Chapters 7-9 represent a considerable effort to resolve these discrepancies, as well as to learn more about the vinylidene photoelectron spectrum and the extent to which the low ground-state isomerization barrier plays a role. While signatures of coupling to HCCH are identified in the ground state band, the acetylene-decoupled electronically excited states of vinylidene are found to be interesting in their own right, with a collection of spectral features arising due to a conical intersection between electronic states. In addition to these results, the autodetachment behavior identified previously by Johnson and coworkers[128] has been revisited and explained. This collection of work demonstrates the power of cryo-SEVI as a probe not only of molecular vibronic properties, but also of fundamental chemical reaction dynamics.

### 1.4.3 Metal Oxide Clusters

In many cases, the reactive sites responsible for the catalytic behavior of metal and metal-oxide surfaces correspond to surface defects such as steps, vacancies, or site impurities, where the local structure, stoichiometry, and charge density differs from the bulk surface.[129–133] Experimental probes of the electronic and structural properties of these reactive sites is of fundamental interest for developing an understanding of the chemistry underlying catalytic behavior that is relevant on a societal scale. However, it can be difficult to definitively and selectively probe surface defects, as they only make up a small fraction of the total surface and can be difficult to reproducibly generate.

An alternative approach to understanding the chemistry of reactive sites on catalytic surfaces is through the study of size-selected gas-phase ionic clusters.[134–139] These model systems can be reliably generated and controlled for factors such as size, charge, and stoichiometry, and spectroscopic studies can therefore elucidate how these impact chemical behavior.[140–144] Characterization of such systems by traditional anion PES has typically yielded spectra with little to no vibrational resolution, due to the high-temperatures inherent in the ion sources used to generate these clusters;[145–150] cryo-SEVI has enabled extraction of a wealth of information regarding the vibronic and geometrical structure of such clusters that was previously unresolvable.[34,151–156]

Following characterization of the bare clusters, reactions with molecules of interest can be carried out to study the resultant complexes in an effort to further the use of these clusters as models for catalytic reactions. The ion source described in Chapter 3 was developed to introduce this capability to the cryo-SEVI technique. Whereas spectroscopic studies of bare clusters probe the reactant well for such model reactions (as illustrated in Figure 1.7), the (anion·reactant) complex can provide access to intermediates, transition states, or products for the corresponding neutral reaction, depending on the geometry of the anionic cluster. As discussed in Chapter 10, this new capability shows promise for using cryo-SEVI to obtain a clear picture of how chemical reactivity develops with cluster size.

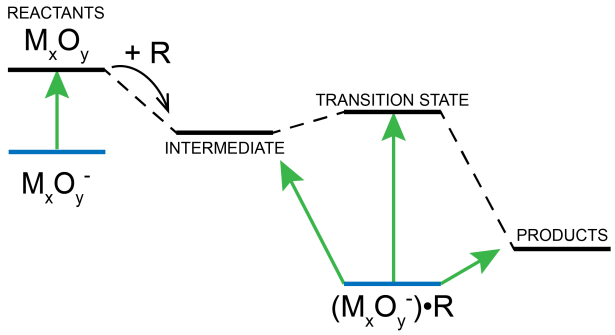


**Figure 1.7:** Illustration of how detachment from metal oxide anions may be used to explore the potential energy surfaces for neutral reactions of the form $M_xO_y$ + R.

# Chapter 2

# Experimental Methods

The cryo-SEVI method and apparatus have been described in detail in previously published papers[17,157,158] as well as the theses of several graduate students.[18,159–163] A diagram of the current incarnation of the machine is shown in Figure 2.1, where the major segments of the experiment are labelled. In this chapter, these segments will be described in detail.

Ions are generated using one of several possible source configurations described in Section 2.1. These ions are directed with two radiofrequency multipoles and deposited into an octupole ion trap, which is held at 5 K and filled with a buffer gas (Section 2.2). The ions are stored in the trap for around 40 ms, after which they are extracted into a Wiley-McLaren time-of-flight (TOF) mass spectrometer (Section 2.3) and focused into the interaction region of a velocity-map imaging (VMI) spectrometer. The ions are detached by a tunable laser (Section 2.4), and the resultant photoelectrons are projected towards a microchannel plate/phosphor screen detector by the VMI lens assembly (Section 2.5). The back of the phosphor screen is photographed by a camera with each laser shot, and these photographs are analyzed for individual electron events which are binned into a grid. After tens of thousands laser shots, an accumulated image is obtained which represents a 2D projection of the 3D velocity distribution; from this, a vertical slice down the centroid of the 3D distribution is extracted using a reconstruction algorithm (Section 2.5.1), providing the photoelectron radial and angular distributions.

The cryo-SEVI apparatus consists of five differentially-pumped regions, labelled 1-5 and signified by the five different color blocks in Fig. 2.1. Each region is pumped by a magnetically-levitated turbomolecular pump backed by a mechanical pump, as described in the thesis of Marissa Weichman.[18] The chamber pressures decrease from regions 1 to 5, such that the lowest pressures are achieved in the region housing the VMI spectrometer. While operating, typical pressures range from $\approx 10^{-5}$ Torr in Region 1 to $\approx 10^{-8}$ Torr in Region 5.

The timings of different components of the experiment are controlled by two eight-channel pulse generators. For each output channel $a$, the reference channel ($b$), delay ($D_a$), and width ($W_a$) can be changed independently to give a transistor-transistor logic (TTL) pulse rising at $D_b + D_a$ and falling at $D_b + D_a + W_a$. The first pulse generator (Q1) is triggered internally at 20 Hz and controls the timings for experimental components relating to ion generation

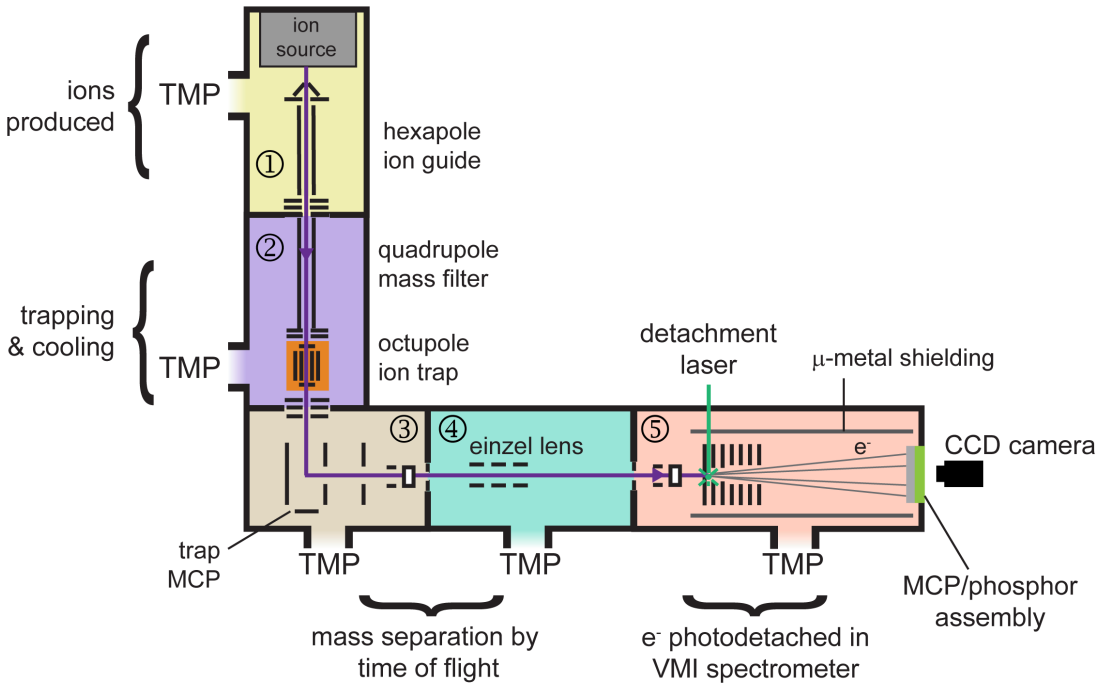


**Figure 2.1:** Schematic of the cryo-SEVI apparatus. Each color represents a separate differentially-pumped region backed by a turbomolecular pump (TMP).

**Table 2.1:** Settings used to control the relative experimental timings. Channels ending in 1 are the outputs on the first box, which is internally triggered ($T_0$); channels ending in 2 are the outputs for Q2, whose "time-zero" is set by Q1.

| Ch. | Ref. | Delay | Width | Component |
|---|---|---|---|---|
| A1 | $T_0$ | 5 ms | 10 μs | Even-Lavie valve |
| B1 | A1 | 100 μs | 1 μs | ionizer anode |
| C1 | A1 | -2.8 ms | 10 μs | trap gas valve |
| D1 | A1 | 37 ms | 1 ms | trap exit electrode |
| E1 | F1 | -300 μs | 10 μs | ablation flashlamps |
| F1 | A1 | 180 μs | 10 μs | ablation Q-switch |
| G1 | A1 | 100 μs | 8 μs | ablation reactant valve |
| H1 | D1 | -1 ms | 10 μs | trigger for Q2 |
| A2 | H2 | 23.2-93.2 μs | 4 μs | first Wiley-McLaren plate |
| B2 | A2 | 230-930 ns | 3 μs | second Wiley-McLaren plate |
| C2 | A2 | var. | 10 μs | detachment Q-switch |
| D2 | C2 | -140-180 μs | 10 μs | detachment flashlamps |
| E2 | A2 | var. | 600 ns | MCP gate |
| F2 | A2 | var. | 500 ms | mass gate |
| G2 | H2 | -300 μs | 100 μs | CCD camera |
| H2 | H1 | 1 ms | 10 μs | re-define $T_0$ for Q2 |

and trapping. Q1 is also used to trigger the second pulse generator (Q2), whose outputs control the mass selection, detachment, and imaging portions of the experiment. Table 2.1 describes the current configuration of Q1 and Q2, as well as typical settings used.

## 2.1 Ion Source

The versatility of the cryo-SEVI method hinges upon our ability to form a wide range of gas phase anions. As the anions generated in the source can later be mass selected, the method used to generate them does not need to be terribly specific; as long as the anions of interest are at least a minor product of the source chemistry, electrostatic fields can be used to ensure that only ions of the correct mass are probed. The current machine can be easily interfaced with three ion source configurations, described below. The most recently developed configuration – the laser ablation reactor – is described in detail in Chapter 3.

### 2.1.1 Filament Ionizer

The first ion source configuration uses a circular filament ionizer coupled to an Even-Lavie (EL) pulsed molecular beam valve.[164] A current of 4 A running through the thoriated tungsten filament results in emission of electrons, and an anode is pulsed to -300 V to direct these electrons inwards onto a pulse of gas from the valve. Most often this electron injection is used to make atomic anions via dissociative electron attachment to a neutral molecular precursor.[165] For example, injection of electrons into a pulse of gas containing trace $NF_3$ results in the formation of $F^-$ ions,[166]

$$NF_3 + e^- \rightarrow F^- + NF_2. \tag{2.1}$$

The resultant fluoride anions may then be used as reactants in subsequent gas-phase chemistry reactions which form the ions of interest. For example, reaction of a hydroperoxide (ROOH) with $F^-$ results in formation of the corresponding peroxide anion,

$$ROOH + F^- \rightarrow ROO^- + HF. \tag{2.2}$$

This technique was used to access the *tert*-butyl peroxy radical described in Chapter 5.

In the case of systems where multiple sites of deprotonation are possible, the above mechanism will either provide an isomeric mix of the resultant anions, or predominantly the most stable isomer. In these cases, isomer-specific spectra can be obtained by exploiting the strength of the F-Si bond and using an appropriate trimethylsilyl (TMS) substituted precursor,[167]

$$R\text{-}Si(CH_3)_3 + F^- \rightarrow R^- + FSi(CH_3)_3. \tag{2.3}$$

Another commonly used atomic anion is $O^-$, which is formed by dissociative electron attachment to $N_2O$,[168]

$$N_2O + e^- \rightarrow O^- + N_2. \tag{2.4}$$

The resultant $O^-$ anions can then be used to form the vinylidene anion by reaction with ethylene gas (Chapters 7-9),

$$C_2H_4 + O^- \rightarrow H_2C{=}C^- + H_2O. \tag{2.5}$$

The molecular precursor used in the gas expansion can be introduced a number of ways. For a gaseous precursor such as ethylene or $NF_3$, the gas is included directly in the source gas cylinder which provides the backing pressure to the EL valve. A volatile liquid, such as methanol or dichloromethane, can also be included in this gas mixture by opening the evacuated cylinder to a glass capillary containing a small liquid sample prior to filling it with the carrier gas. Non-volatile liquids and solids can be loaded into a cartridge attached to the EL valve, so that the gas flows over the precursor prior to being pulsed into vacuum. If necessary, this cartridge can then be thermally controlled, enabling heating of the sample to encourage vaporization of the loaded material.

### 2.1.2 Laser Ablation

The ionizer itself provides great variability in the ions that can be generated, but is limited to those which can be formed by relatively straightforward gas-phase chemistry. Laser ablation ion sources have been widely used in the study of atomic and metal oxide clusters,[169] and such an ion source was developed for the cryo-SEVI experiment as described in the thesis of Jongjin Kim.[163]

In this source configuration, the frequency-doubled output of a neodymium-doped yttrium-aluminum-garnet (Nd:YAG) laser (Continuum NY60B-2) impinges on a rotating and translating target through a narrow channel in an aluminum plate, resulting in plasma formation at the surface of the target. The laser is typically operated with relatively low power (2-3 mJ/pulse), and the rotation/translation stage ensures that a new part of the surface is sampled with each laser shot. The EL valve couples to a channel perpendicular to the laser channel, and a pulse of carrier gas (He, pulse widths of 40-70 μs, backing pressure around 100 psig) intersects with and entrains the plasma. Collisions with the carrier gas in the growth channel following the point of intersection result in cooling of species present in the plasma, which leads to cluster and ion formation. The entrained species then undergo supersonic expansion into the source region through a 30° nozzle.

The laser ablation source is predominantly used for the purposes of studying metal oxide clusters, though use of other solid targets such as carbon and silicon enable formation of non-metallic clusters.[33] As the ablation targets are stored in ambient conditions when not in use, the surface oxide layer proves sufficient to form $M_xO_y^-$ without the addition of an oxidizing agent to the carrier gas. Most metal targets can be purchased commercially, though these can be quite expensive if isotopic purity is required. In these cases, disk targets can be home-made by using a hydraulic press to compress a mixture of the powdered isotope with a binding material, such as bismuth.

### 2.1.3 Laser Ablation Reactor

The pre-existing laser ablation ion source was primarily intended to provide access to bare metal oxide clusters, $M_xO_y^-$. The motivation for the study of gas phase metal oxide clusters is to achieve a detailed understanding of mechanisms involved in catalytic reactions, as described in Section 1.4.3; considering a reaction of the type shown in Figure 1.7, detachment from a bare metal oxide cluster only provides spectroscopic access to the reactant well of a model catalytic reaction.

To probe other parts of the reaction surface, one would need to form the $(M_xO_y\cdot R)^-$ ions, where R is the reactant of interest (e.g. $CO_2$, $H_2O$, or $CH_4$). Such ions may be generated using a Smalley-type fast flow cluster reactor, which involves injection of reactants into the helium-cluster mixture formed in a laser ablation source.[170] In an ideal fast flow reactor, the reactant pulse collides with the plasma entrainment pulse at relatively high speeds, resulting in efficient mixing of the two pulses. This approach has been successfully used by other groups, though the specific designs vary; the design used here is similar to that used in the group of Prof. Caroline Chick-Jarrold, where the clusters are exposed to the reactant prior to expansion into vacuum.[171] A consequence of this configuration is that the cluster/molecule reactions occur with rather high available energy, and thus the product distribution does not generally favor weakly-bound molecularly adsorbed clusters where the reactant molecule remains intact, unless such a geometry constitutes the global minimum on the anion potential energy surface.

The cryo-SEVI fast flow reactor source configuration is almost identical to the pre-existing laser ablation source. The key difference is the geometry of the plate containing the channel where clusters are formed. In the reactor source, a second channel following the initial growth channel is added, and this channel is connected to a pulsed General Valve through which the desired reactant is introduced. A small slit between the growth and reaction channels minimizes back flow of the reactant gas. Following the reaction channel the clusters undergo supersonic expansion into vacuum as in the original ablation source. Further details of the fast flow reactor source design and operating parameters can be found in Chapter 3.

## 2.2 Radiofrequency Ion Optics

Radiofrequency (RF) multipoles are invaluable tools for manipulation of gas-phase ions, and the motion of charged particles in RF fields has been extensively studied by Gerlich and others.[172–174] An ideal multipole of order $n$ consists of $2n$ cylindrical electrodes (radius $\rho$) that are positioned along a cylinder of radius $R_0$, where $\rho = R_0/(n-1)$ is the optimal electrode radius for approximating the ideal multipole potential (see Fig. 2.2a). The resulting electric potential (neglecting effects from the finite length along the $z$-axis) is given in cylindrical coordinates by

$$V(r,\phi,t) = V_0\cos(n\phi)\left(\frac{r}{R_0}\right)^n \sin(\omega t), \tag{2.6}$$

where $V_0$ and $\omega$ are the amplitude and frequency, respectively, of the applied radiofrequency voltage. The equation of motion for a charged particle subjected to this potential is exactly solvable for $n = 2$, leading to well-defined conditions for stable trajectories (i.e. the particle does not collide with one of the electrodes and remains axially confined while passing through the multipole) for transmission of charged particles through a quadrupole.

For $n > 2$, stability conditions are not exactly solvable, and the effective potential approximation is typically applied. This assumes that the trajectory of a trapped particle consists of a rapid oscillatory motion superimposed with a slower drift motion. If the frequency of the radiofrequency driving field is sufficiently faster than the drift motion, then the potential in Eq. 2.6 may be replaced with the time-independent pseudopotential in Eq. 2.7.

$$V_{eff}(\vec{r}) = \frac{q^2 n^2 V_0^2}{4m\omega^2 R_0^2} \left( \frac{r}{R_0} \right)^{2n-2} \tag{2.7}$$

The result of this effective potential is trapping of charged particles (both positive and negative) in a "field-free" region, illustrated in Figure 2.2b for several commonly used configurations. As the order of the multipole is increased, the potential becomes flatter, which is optimal for minimizing RF heating of the ions which results when they encounter regions of non-zero field; however, this comes at the expense of the extent of radial confinement. Thus, while 22-pole traps are often used in applications where cold ions are desired, the cryo-SEVI experiment uses an octupole ($n = 4$) configuration, to balance the effects of RF heating and extraction efficiency.

### 2.2.1 RF Optics in Cryo-SEVI

The first leg of the cryo-SEVI experiment (Regions 1 and 2 in Fig. 2.1) uses several RF ion optics to control the anions generated in the source. The construction of these components is documented in the thesis of Jongjin Kim.[163] A schematic of the optics used to direct ions from the source to the time-of-flight mass spectrometer is illustrated in Figure 2.3, and typical operating voltages are provided in Table 2.2.

Anions formed following supersonic expansion are passed through a skimmer and electrostatic aperture and are transferred to the RF hexapole ion guide, which serves to collimate the ion packet. In addition to the radiofrequency voltage, the entire hexapole is held at a slight bias relative to ground. Three apertures in an einzel lens configuration (one of which constitutes the differential pumping aperture separating regions 1 and 2) couple the hexapole to a RF quadrupole. The quadrupole can be operated at a frequency of either 0.63 Mhz (for masses below 300 amu) or 1.25 MHz (for masses between 300 and 1000 amu), and may be operated in mass-resolving mode by adding a direct current (DC) quadrupole field to the RF field. Like the hexapole, the entire quadrupole may also be held at a bias voltage relative to ground, and this can be used to further tune the mass distribution of ions.

The ions are passed through two more electrostatic apertures, the trap entrance aperture, and are finally deposited into the ion trap, a cross section of which is reproduced in Figure

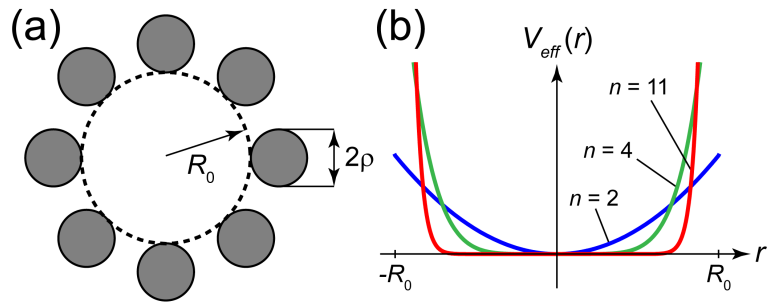


**Figure 2.2:** **(a)** Electrode configuration for an ideal RF multipole with $n = 4$. **(b)** Effective trapping potentials given by Eq. 2.7 for $n = 2$, 4, and 11.

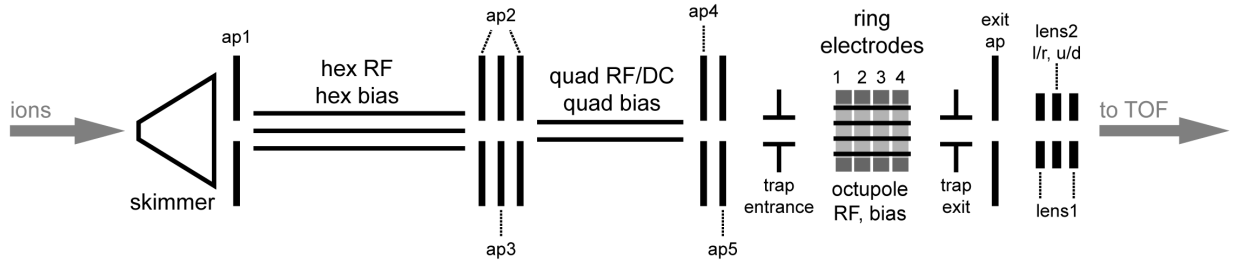


**Figure 2.3:** Schematic of the various ion optics comprising the first leg of the cryo-SEVI experiment (ap = aperture, hex = hexapole, quad = quadrupole).

**Table 2.2:** Typical operating voltages for the components shown in Fig. 2.3.

| Component | Voltage |
|---|---|
| skimmer | -5 to -100 V |
| aperture 1 | -5 to -50 V |
| hexapole | 100-300 Vpp, $f = 3$MHz; -5 to -20 V bias |
| aperture 2 | 20 to 60 V |
| aperture 3 | 60 to 80 V |
| quadrupole | mass-dependent, $f = 0.63$ or 1.25MHz; -10 to 10 V bias |
| aperture 4 | 0 to 20 V |
| aperture 5 | 20 to 60 V |
| trap entrance | -5 to -10 V |
| octupole | 300-600 Vpp, $f = 3$MHz; -1 to 1 V bias |
| ring electrodes 1, 2, 3, 4 | -100 V, -10 V, 10 V, 100 V |
| trap exit | -16 V; pulsed to +16 V for extraction into TOF |
| trap exit aperture | -2 to -15 V |
| lens 1 | 5 to 80 V |
| lens 2 | 50 to 150 V; -10 to 10 V l/r, u/d |

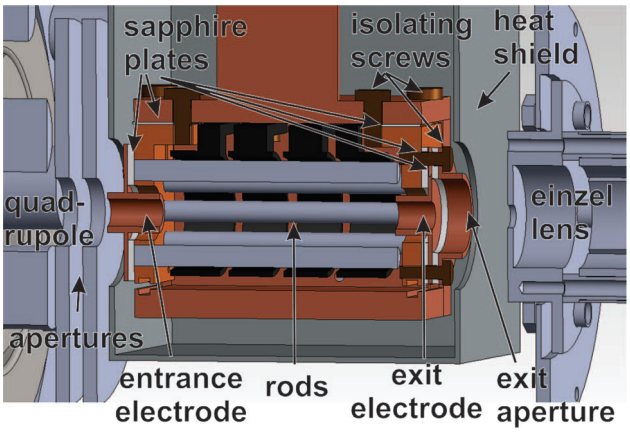


**Figure 2.4:** Cross-sectional view of the octupole ion trap reproduced from Reference [19].

2.4. The ions are stored in the trap for roughly 40 ms, during which collisions with the cold gas remove any internal excitation to cool them to their full ground states.[19] The cryogenic ion trap consists of a linear RF octupole housed in a copper enclosure. The RF octupole field confines the ions radially, while axial confinement is achieved using ring electrodes and an exit electrode. Specifically, four ring electrodes surround the octupole rods, with DC voltages applied to encourage the ions to pool near the exit aperture. The exit electrode is held at a repulsive voltage and then pulsed to extract the ions at the end of the cooling period. A microchannel plate (MCP) is positioned after the trap exit (as shown in Figure 2.1) and can be used to assess whether or not ions are being successfully trapped.

The octupole rods are enclosed in a copper box which is in thermal contact with the second stage of a two-stage helium cryostat (Sumitomo F-70L), which reaches temperatures as low as 4.7 K. Trap temperatures between 4 and 300 K are monitored and maintained using two silicon diodes (Lakeshore DT-670C-ET) mounted on the trap enclosure and interfaced with a cryogenic temperature controller (Stanford Research Systems CTC100). To avoid heating of the trap interior through blackbody radiation emitted by various objects in the lab, the copper enclosure is surrounded by thermal shielding which is in thermal contact with the first stage of the cryostat (∼40 K). The shield temperature is also monitored by a silicon diode connected to the temperature controller.

The ion trap is filled with a pulse of buffer gas prior to ion generation in the source region by a Parker Series 9 General Valve backed by 3 psi of either pure He or 20% $H_2$ in He (pulse widths of 300-500 μs). The trap then gradually loses pressure until the next gas injection, so that the trap is almost entirely evacuated by the time the ions are extracted from the trap. This minimizes the potential for collisions with the buffer gas during extraction, which could lead to warming of the ions. The average pressure inside the trap is estimated to be on the order of 1 mTorr by consideration of the pressure in the surrounding chamber and the conductance of the apertures in the trap enclosure; under these conditions, the ions are expected to undergo between $10^3$ and $10^4$ collisions prior to extraction.[19]

### 2.2.2 Buffer-Gas Cooling and Ion Temperature

The cryogenic cooling component of cryo-SEVI has provided significant gains in terms of spectral clarity and resolution. Removal of populations from excited electronic and vibrational states ensures that the spectra are free of hot bands, resulting in spectral features that primarily reflect the vibronic structure of the neutral. As the linewidths for detachment from molecular anions are rotationally limited, rotational cooling is particularly important for achieving the best spectral resolution. We typically consider the ions to be fully thermalized by the end of their residence time in the trap, meaning that a single temperature can be used to describe the translational (T), vibrational (V), rotational (R), and electronic (E) degrees of freedom.

Use of an atomic buffer gas such as He provides energy-transfer channels which involve conversion of the anions' energy into translational energy of the collision partner. The T→T energy-transfer channel is expected to bring the ions to a translational temperature close to that of the 5K buffer gas in under 100 or so collisions.[175] Due to the small energy level spacings typical of molecular rotational levels, the R→T channel is also fairly effective; however, the V→T is much less efficient, as vibrational degrees of freedom do not couple as effectively to the translational continuum. Vibrational cooling is thus typically the most challenging to achieve, and studies of collisional cooling of vibrationally excited molecules have shown that the V→R,V channels are the most efficient pathways for loss of vibrational excitation.[176] Thus, to enhance the vibrational and rotational cooling of ions in our trap, a mixture of 20% $H_2$ in He is used, which provides the generally more facile V→R,V and R→R energy-loss channels.

The estimation of ion temperature is performed by examination of the anions' detachment spectra. For molecules with relatively large rotational constants, our resolution may be sufficient to partially resolve the rotational substructure underlying a particular vibronic transition. In these cases, a rotational simulation is used to estimate the rotational temperature ($T_{rot}$).[177,178] In other cases, relative peak intensities may be used along with an assumption of a Boltzmann distribution. For example, the relative intensities of different spin-orbit peaks in the cryo-SEVI spectrum of $C_5^-$ were used to extract an approximate spin-orbit temperature ($T_{SO}$) to 10(2) K.[19] A similar process may be used in cases where vibrationally excited anion states are populated, though this is typically not observed.

Estimations of ion temperature based on our cryo-SEVI spectra typically give temperatures on the order of 10-15 K, indicating that the anions are not fully cooled to the 5 K temperature of the ion trap. This is likely due to RF heating of the ions in the trap, as well as warming during and subsequent to extraction from the trap. RF heating effects can be especially detrimental when the trap becomes overloaded with ions, where space-charge effects push the ions closer to the regions of the trap with non-zero average fields.

## 2.3 Time-of-Flight Mass Spectrometer

Following extraction from the octupole trap, ions are steered and focused into the next differentially-pumped region by a combination deflector / einzel lens assembly described in the thesis of Jongjin Kim.[163] This region of the cryo-SEVI apparatus contains a Wiley-McLaren (WM) time-of-flight mass spectrometer, based on the design first reported in 1955.[179] The geometry of a typical WM-TOF mass spectrometer is shown in Figure 2.5, and the parameters used in the cryo-SEVI experiment are provided in Table 2.3.

In the WM-TOF spectrometer, ions are injected along a starting plane (gray dashed line in Figure 2.5). The first WM plate ($V_1$) is pulsed to a repulsive voltage, pushing the ions along the time-of-flight axis; when the ions reach the second acceleration region, the second plate ($V_2$) is pulsed. The ions then reach a field-free region, and as they continue along the TOF axis, the gained kinetic energy and corresponding velocity discrepancies result in separation of the ions based on mass. In this section, the qualitative and practical aspects of the mass spectrometer as they pertain to the cryo-SEVI experiment will be discussed; for a quantitative treatment of the equations of motion involved, see Reference [179].

The focusing conditions provided by the implementation of two acceleration regions enables use of purely electrostatic fields to obtain high-resolution mass spectra, and can be optimized for either spatial focusing or energy focusing of the ions. For the cryo-SEVI experiment, spatial focusing is desired, so that the maximum number of ions are detached in the interaction region of the VMI spectrometer. The spatial resolving power is defined by the maximum mass, $M_s$, such that the time separation between $M_s$ and $M_s + 1$ is larger than the changes in time-separation caused by variation in the initial $\Delta s$ in Figure 2.5. In the limit that $k_0 = (V_1 + V_2)/V_1$ is much greater than 1 and $d/s_0$, $M_s$ is given by Eq. 2.8.

$$M_s \approx 16 k_0 \left(\frac{s_0}{\Delta s}\right)^2 \tag{2.8}$$

Using the values typical of the cryo-SEVI experiment, the $k_0$ qualifier used to approximate Eq. 2.8 does not quite apply ($k_0 \approx 2$, $d/s_0 \approx 0.7$); keeping this in mind, we still use this to estimate $\approx 400$ amu as an upper bound for $M_s$.

The energy resolving power of a WM-TOF spectrometer is defined by a similar maximum mass, $M_\theta$, which is defined analogously to $M_s$ where the effects of $\Delta s$ are replaced by the discrepancies induced by the ions' initial velocity along the TOF axis. Given the geometry of

**Table 2.3:** Parameters used in the cryo-SEVI WM-TOF mass spectrometer.

| Parameter | Value |
|---|---|
| WM 1 voltage | 1.850 kV |
| WM 1 timing | 23.2-103.2 μs (after extraction) |
| WM 2 voltage | 1.720 kV |
| WM 2 timing | 230-1030 ns (after WM 1) |

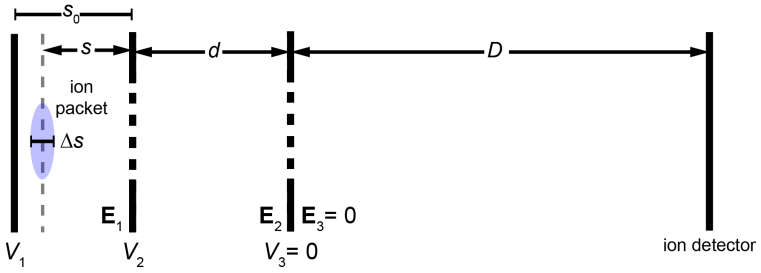


**Figure 2.5:** Schematic of a Wiley-McLaren time-of-flight mass spectrometer. Two acceleration regions are followed by a field-free region ($V_3$=0), and ions are detected at a point along the TOF axis. In the TOF spectrometer currently used in the cryo-SEVI apparatus, $s_0$ = 3.5 cm, $d$ = 2.5 cm, and $D \approx 1$ m, taking the point of ion detection to be the retractable microchannel plate detector.[159] The initial spatial spread is limited by the size of the aperture connecting the trap and TOF regions, so that $\Delta s < 1$ cm.

the cryo-SEVI experiment, this initial velocity should be minimal, as most of an ion's initial velocity is perpendicular to this axis. The ions' velocities are fairly small to begin with, due to the relatively low voltages used to extract them. Thus, we consider the maximum resolvable mass to be given by $M_s$. This can be increased by adjusting the TOF voltages, or by increasing the separation between the extractor plate and the grounding plate ($d$ in Fig. 2.5).

Extraction from the trap occurs such that there is some mass distribution along the starting plane, with lighter ions reaching the center of the TOF spectrometer earlier. As a consequence, the relative timings used for the voltage pulses ($V_1$ relative to trap extraction, $V_2$ relative to $V_1$) vary depending on the target ion in question, where experiments on lighter ions require shorter time delays for these pulses. Incorrect timings can result in a failure to transmit the mass of interest through the remainder of the experiment.

Immediately following the field-free region of the TOF spectrometer is a set of two deflectors, used to steer the ions into the next differentially-pumped region. This region contains an einzel lens (operating voltage of 2.42 kV), which decreases the spatial spread perpendicular to the TOF axis for each ion packet. The ions then pass through a gate valve and another set of deflectors steers the ion packet into the interaction region of the VMI spectrometer. The ion TOFs are measured in the middle of the field-free region of the VMI spectrometer, where a retractable MCP detector can be inserted into the ions' flight path. A circuit diagram of this detector is provided in Ref. [159].

## 2.4 Detachment Laser

The cryo-SEVI technique requires the ability to generate a wide range of photon energies, and thus for a truly universal experiment it is desirable to have a broadly tunable light source ranging from the infrared to the ultraviolet. While multiple commercial optical parametric

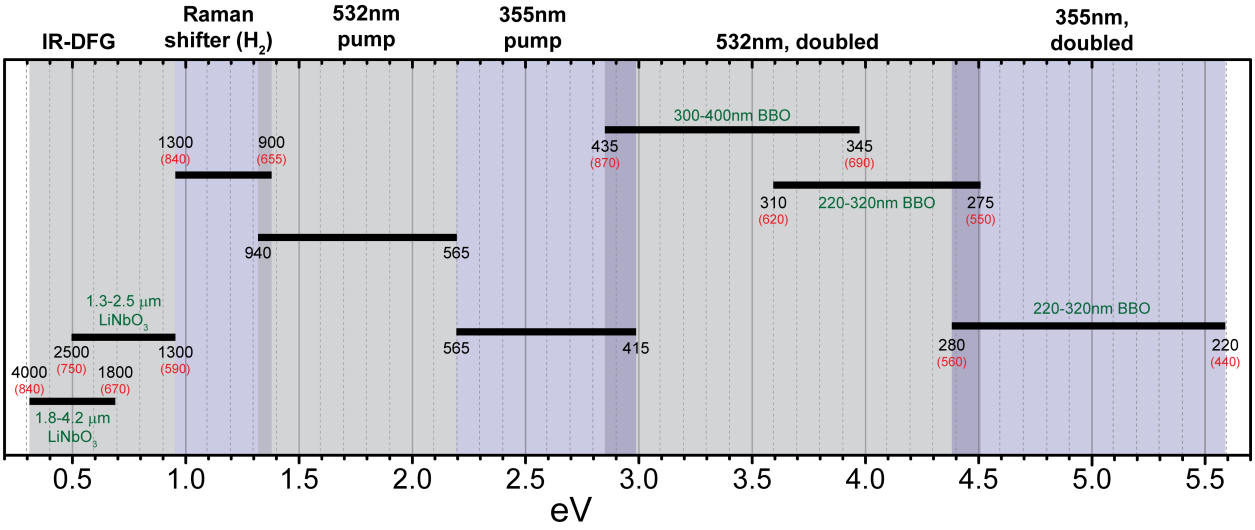


**Figure 2.6:** Summary of the ranges of tunable detachment energy generated using the different optical configurations described in Section 2.4. Red numbers indicate the dye-laser wavelength (in nm) necessary to produce photons with wavelengths given by the black numbers (also in nm) using the indicated technique.

**Table 2.4:** Summary of the energy ranges covered by the different optical configurations used in the cryo-SEVI lab. Together, these provide spectroscopic access to molecular species with electron binding energies ranging from 0.3-4.9 eV. For each energy range, the atomic system used for energy calibration is provided (see Table 2.5). For DFG, calibration is performed using the dye laser output, which is assumed to be collinear with the DFG light.

| pump $\lambda$ | scheme | eV | nm | cal. system |
|---|---|---|---|---|
| 355 nm | doubling (220-320 nm BBO) | 4.42-5.64 | 220-280 | $Cl^-$ |
| 532 nm | doubling (220-320 nm BBO) | 3.59-4.51 | 275-345 | $Cl^-$ |
| 532 nm | doubling (300-400 nm BBO) | 2.85-4.00 | 310-435 | $F^-$ |
| 355 nm | dye laser | 2.19-2.99 | 415-565 | $S^-$ |
| 532 nm | dye laser | 1.32-2.19 | 565-940 | $O^-$ |
| 532 nm | $H_2$ Raman shifter | 0.95-1.38 | 900-1300 | $Ni^-$ or $O^-$ |
| 532 nm | DFG, 1.3-2.5 μm $LiNbO_3$ | 0.50-0.95 | 1300-2500 | $O^{-*}$ |
| 532 nm | DFG, 1.8-4.2 μm $LiNbO_3$ | 0.30-0.69 | 1800-4000 | $O^{-*}$ |

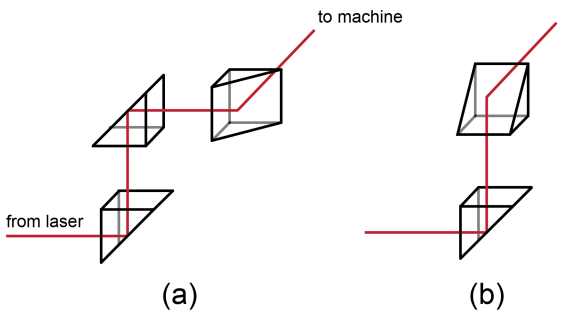


**Figure 2.7:** Prism configurations used to steer the laser beam into the machine and ensure vertical polarization in the interaction region.

amplifiers can cover such a broad range of the electromagnetic spectrum, these typically have linewidths on the order of a few $cm^{-1}$ (particularly in the higher-frequency regime), which would limit the spectral resolution given the excellent resolving power of the VMI lens. Dye lasers give much narrower linewidths (typically $\approx 0.1$ $cm^{-1}$), and the output frequency can be easily tuned by changing the angle of a grating which selects a single wavelength from the broad dye emission. As such, the detachment laser used in the cryo-SEVI experiment is centered around a dye laser pumped by a Nd:YAG laser. The Nd:YAG described in the thesis of Marissa Weichman[18] was replaced in 2016 by a QuantaRay Pro 290-30 (SpectraPhysics), which has been reconfigured for a repetition rate of 20 Hz. By using appropriate pumping frequencies, laser dyes, and nonlinear optical mixing techniques, we are capable of generating the ranges of photon energies summarized in Figure 2.6 and Table 2.4.

The most simple laser configurations directly use the output of the dye laser, which can be pumped by either the second (532 nm, 2.3 eV) or third (355 nm, 3.5 eV) harmonic output of the Nd:YAG laser. Provided the harmonic generator and separator modules of the pump laser are configured appropriately, this results in tunable light with linear polarization that is vertical with respect to the laser table. The prism scheme shown in Figure 2.7a is used to ensure that this vertical polarization is preserved in the interaction region. The commercial dyes used and their emission ranges have been summarized in the thesis of Marissa Weichman;[18] without additional optics, the 532 nm and 355 nm pumping configurations provide access to detachment energies ranging from $\sim 1 - 3$ eV.

Frequency doubling of the dye laser output provides access to photon energies over 3 eV. This is achieved using a β-barium borate (BBO) crystal (220-332 nm or 300-400 nm) which is held in a motorized mount inside the dye laser. The BBO crystal is rotated by the motorized mount to find optimum phase-matching conditions for the desired wavelength, and a compensating crystal is mounted at a complementary angle to ensure the beam path through the machine is independent of the BBO angle. After exiting the dye laser, the doubled and undoubled light are separated using a harmonic separator. As the frequency doubling is a type-I process, the doubled light is horizontally polarized; to ensure vertical polarization in the interaction region, the prism setup shown in Fig. 2.7b is used.

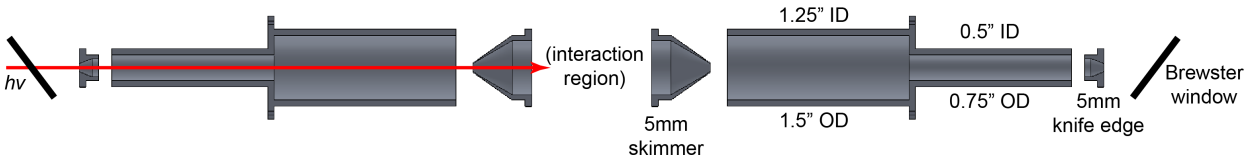


**Figure 2.8:** Schematic of the current baffling scheme used in the detector region of the cryo-SEVI apparatus. Everything between the two Brewster windows is in vacuum. The baffling components are shown in an exploded view and are made of anodized aluminum.

One barrier to using high photon energies in the cryo-SEVI experiment arises when the photon energy exceeds the work function of the stainless steel, so that scattered light can cause electron ejection from surfaces inside the vacuum chamber. This is mediated by using a set of light baffles, pictured in Figure 2.8, to absorb any scattered light before the beam enters the VMI lens. These newly-designed light baffles have substantially reduced the noise arising from the laser beam by about a factor of 10.

### 2.4.1 Difference Frequency Generation

To obtain photon energies below $\sim$ 1 eV, difference frequency generation (DFG) is performed using a lithium niobate crystal to mix the 565-940 nm light from the dye laser with the 1064 nm fundamental of the Nd:YAG pump laser. The cryo-SEVI DFG setup was first described in the thesis of Marissa Weichman[18] and can be used to generate light from 4.2-1.3 μm (0.3-0.95 eV). The second time DFG was used for cryo-SEVI took place after the switch to the QuantaRay Nd:YAG, and so the new setup varies slightly from that described previously.

The primary difference arises from the polarization of the 1064 nm Nd:YAG fundamental, which is elliptically polarized for the type-II doubling crystal used to obtain the 532 nm harmonic. The majority of the fundamental power from the old laser was horizontally polarized, and so several thin film polarizers and a half-wave plate were used to ensure that the 1064 nm light is vertically polarized in the $LiNbO_3$ crystal. With the new laser, the polarization of the 1064 nm beam was found to be predominantly vertical, and so fewer optics were required to prepare and steer this beam.

The setup used with the new laser is shown in Figure 2.9. Following the second-harmonic generation (SHG) unit in the Nd:YAG laser, the (elliptically polarized) 1064 nm fundamental is reflected off of two high-reflecting (HR) mirrors, while the (vertically polarized) 532 nm is transmitted straight into the dye laser. The 1064 nm arm is then reflected off of another HR mirror and onto a thin film polarizer (TFP). The TFP reflects the vertically polarized component of the 1064 nm beam, which was found to constitute the majority of the power; the residual horizontally-polarized component is dumped into a beam dump. The beam reflected from the TFP is then directed through the back of the dye laser and onto the $LiNbO_3$ DFG crystal using a pair of 1064 nm HR mirrors.

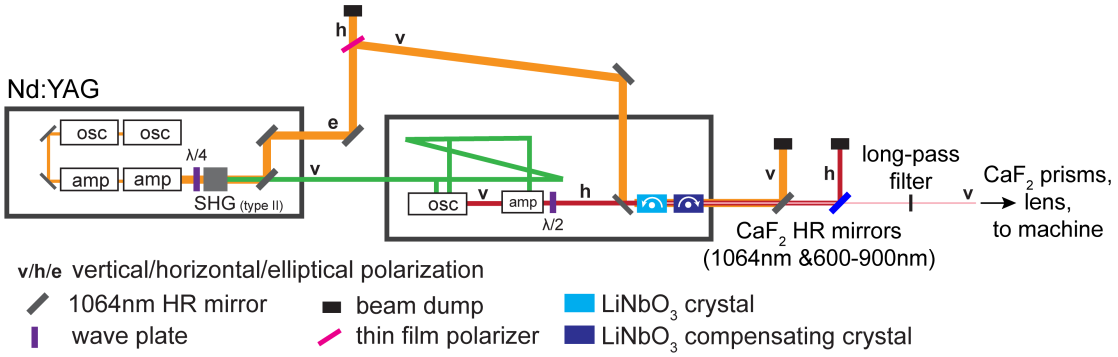


**Figure 2.9:** Difference frequency generation setup used following the installation of the QuantaRay Nd:YAG laser, adapted from the figure in the thesis of Marissa Weichman.[18]

The $LiNbO_3$ crystal used for the DFG process is a type-I nonlinear mixing crystal. In this type of crystal, the two lowest frequency photons ($\omega_1 \leq \omega_2$) are polarized orthogonally to the highest frequency photon ($\omega_3$) involved in the mixing process. For the IR-DFG discussed here, $\omega_2$ corresponds to the 1064 nm Nd:YAG fundamental, and $\omega_1$ is the desired difference frequency signal. Thus to obtain vertically polarized DFG light, the dye light must enter the nonlinear mixing crystal with horizontal polarization. This is achieved by inserting a half wave plate in the beam path immediately following the amplifier cell of the dye laser.

The $LiNbO_3$ crystal is secured on a motorized mount inside the dye laser; as different crystal angles are required to generate tunable light, a compensator is mounted at a complementary angle to ensure that the beam path is independent of the crystal angle. Two crystals are available, covering different ranges of photon energies, as summarized in Table 2.4.

Outside the dye laser, the beam is passed through two $CaF_2$ HR mirrors that separate out the 1064 nm and tunable dye light. Any residual higher-frequency light is then removed by a long-pass filter with a cut-on wavelength of either 900 or 1100 nm, depending on the DFG energies being used. The DFG light is then steered into the machine using $CaF_2$ prisms as shown in Fig. 2.7a, and focused into the interaction region with a 500 mm focal length $CaF_2$ cylindrical lens.

Energy calibration (see Section 2.5.2) of the VMI when using DFG is performed in a slightly different manner than the other optical setups. Making the assumption that the dye light is perfectly collinear with the DFG light, we use the dye output to calibrate with the detachment transitions of $O^-$. To ensure that the resultant calibration is adequate for both the DFG and visible components of the beam, the 600-900 nm $CaF_2$ mirror is replaced with a $CaF_2$ window of identical width, and care is taken to ensure that the 1064 nm and dye laser output are collinear over a relatively long distance. As the long pass filter is mounted at a 90° angle relative to the incident beam, this optic can be removed without disrupting the beam path.

### 2.4.2 Hydrogen Raman Shifter

To bridge the gap in laser tunability between DFG and the simpler laser configurations, a Raman shifter cell containing $H_2$ may be used. The most intense line in the Raman spectrum of $H_2$ is by far the $Q(1)$ feature in the 1-0 vibrational band, which has a Raman shift of 4155.201 $cm^{-1}$.[180] Thus, the frequency of the shifted light obtained by focusing light with frequency $\omega_d$ into the Raman cell is $\omega_s = \omega_d - 4155.201$ $cm^{-1}$, and so dye wavelengths from 840-655 nm are necessary to cover the 1.0-1.4 eV energy range.

This is easily achieved by using the undoubled output of our 532 nm-pumped dye laser. The setup of the Raman cell is shown in Figure 2.10. Two plano-convex lenses with 50 cm focal lengths are used to focus the dye light into a 63 cm-long tube containing $\approx$ 200-400 psi of $H_2$. The unshifted light is separated from the resultant beam using a dichroic mirror (600-900 nm reflectance) and a longpass filter with a cutoff wavelength of either 900 or 1100 nm. The resultant beam has the same diameter as the incident beam, but with frequency red-shifted by 4155.201 $cm^{-1}$.

The Raman-scattered light is not perfectly coherent with the unshifted dye laser light, meaning that the vertical polarization of the dye light is not rigorously preserved. The depolarization ratio, $\rho = I_\perp / I_\parallel$, quantifies the extent to which the Raman-shifted light's polarization differs from the initial beam. The depolarization ratio for $H_2$ has been measured to be 0.01048(4),[181] indicating that only a small portion of the Raman signal is depolarized; this fraction is filtered out by a linear polarizer following the longpass filter, ensuring vertically polarized light in the interaction region of the cryo-SEVI apparatus.

The primary challenge in using a Raman shifter cell for our purposes is the balance of efficiency and linewidth. Grossmann and co-workers[182] reported 15% conversion efficiency for production of 940 nm light in a Raman cell similar to that in Fig. 2.10 with a pressure of 200 psi; in the design implemented here, pressures of around 400 psi are required to get substantial conversion efficiency, with the efficiency decreasing as wavelength is increased.

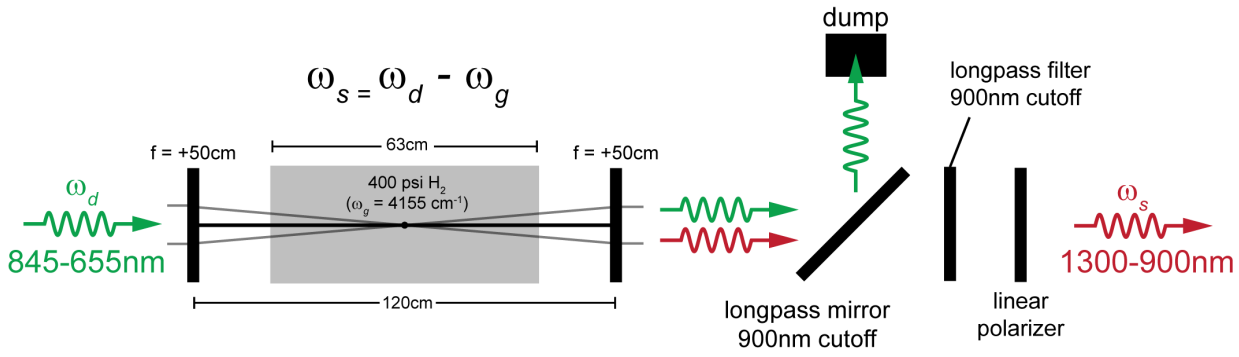


**Figure 2.10:** Schematic of the Raman shifter cell and associated optics. $\omega_d$ is the frequency of the light from the dye laser, $\omega_g$ is the frequency of the $Q(1)$ feature in the Raman spectrum of $H_2$, and $\omega_s$ is the frequency of the Stokes-shifted light.

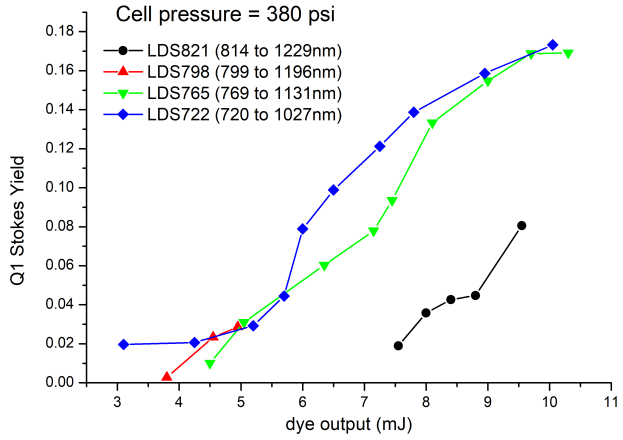


**Figure 2.11:** Characterization of the efficiency of the Raman shifter cell showing the quantum yield of the $Q(1)$ Stokes-shifted light as a function of the energy of the dye laser output.

Figure 2.11 shows the quantum yield (QY) of the $Q(1)$ Stokes-shifted light for a cell pressure of 380 psi, with data taken for several different dyes lasing at their peak emission wavelengths. The QY is given by

$$\text{QY} = \frac{P_s \nu_d}{P_d \nu_s}. \tag{2.9}$$

where $P_s$ and $\nu_s$ are the power and frequency of the shifted light, and $P_d$ and $\nu_d$ are the power and frequency of the dye laser output. As can be seen in Fig. 2.11, the highest efficiency is obtained for higher-energy dyes, and does not exceed $\sim 18\%$. Decreasing the cell pressure was found to result in little to no conversion for the lowest-energy dye used in this exercise (LDS821).

The effects of collisions on the linewidth of the Raman-shifted light can be summarized by a collisional-broadening and collisional-narrowing term, with Grossmann finding that these effects were well-balanced for pressures $< 200$ psi. Thus, the pressures used here likely result in more collisional broadening than is desired. Due to the limited operating range of the spectrometer used to view the energy profile of the dye laser output, a quantitative characterization was unable to be carried out on the Raman-shifted light; however, scans taken using the Raman shifter in the cryo-SEVI spectrum of $TiO_3H_2^-$ (Chapter 10) did not appear broadened relative to those taken using the dye laser output, and so this broadening is expected to be a small enough effect so as to not limit the resultant spectral resolution.

## 2.5 Velocity-Map Imaging Spectrometer

A traditional Eppink-Parker velocity-map imaging spectrometer, illustrated schematically in Figure 2.12a, consists of an electrostatic lens, a field-free region, and an imaging detector. The simplest lens that may be used in such a spectrometer consists of three plate

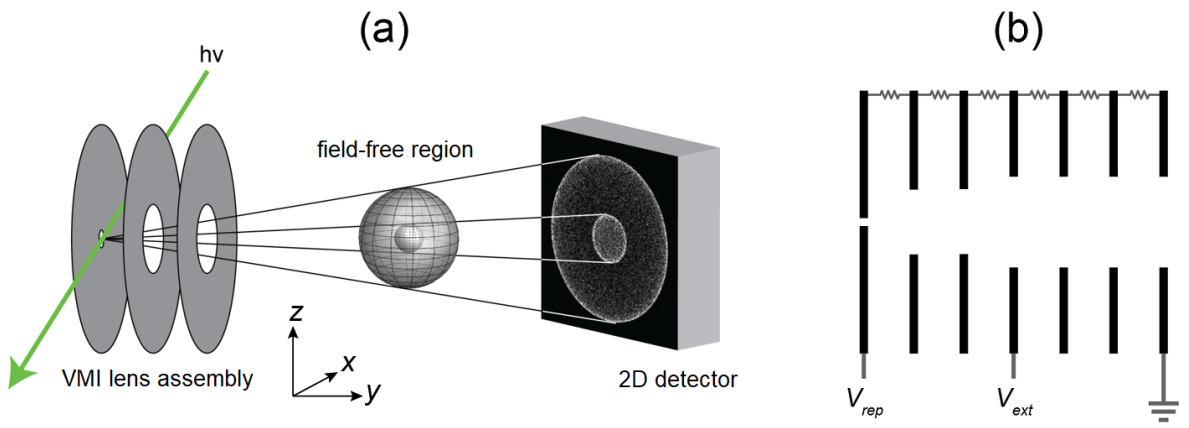


**Figure 2.12:** **(a)** Illustration of an Eppink-Parker VMI spectrometer being used to image photoelectrons following photodetachment of $F^-$. **(b)** Schematic of the seven-plate VMI lens assembly designed by Marissa Weichman and currently in use for the cryo-SEVI experiment.

electrodes – the repeller, the extractor, and a grounding plate – whose voltages create two acceleration regions. In a photoelectron imaging experiment, ions are detached by linearly polarized light within the first region. After exiting the lens assembly, the focusing conditions induced by the relative magnitudes of the extractor and repeller voltages ensure that as they propagate along the time-of-flight axis, electrons detached with the same speed $|\vec{v}|$ lie along the outside of some spherical region with a defined $R$, referred to as a Newton sphere; the distribution of electrons across each Newton sphere is cylindrically symmetric with respect to the laser polarization axis ($z$-axis in Fig. 2.12a). The field-free region of the spectrometer is enclosed in μ-metal shielding to minimize penetration of external fields, so that the focusing conditions and initial electron velocities are the only factors which affect the electron trajectories. As a result, the Newton spheres expand linearly in time so that electrons arising from different detachment transitions become increasingly separated as they propagate along the time-of-flight axis, and are then projected onto the position-sensitive detector.

The velocity-map imaging spectrometer used to obtain cryo-SEVI spectra is similar in operating principle to the Eppink-Parker design. A collinear geometry is used to minimize the effects of Doppler broadening that may arise from an initial spread in the ions' translational velocities. The electrostatic lens, described in detail in the thesis of Marissa Weichman,[18] is shown diagrammatically in Fig. 2.12b, and consists of seven plate electrodes which create two acceleration regions. The addition of intermediate electrodes was performed to decrease the effective size of the interaction region relative to the VMI lens, affording better spectral resolution than was obtained using a three-plate configuration. For high-resolution images, repeller voltages of $V_{rep} \approx -300$ V are used, and the extractor voltage is tuned to minimize the observed radial spread in the resultant images (typically, $V_{ext} \approx 70\%$ of $V_{rep}$). Use of lower repeller voltages was not found to appreciably increase the achievable resolution

for low-eKE transitions, likely due to longer time spent in the (nominally) field-free region during which weak external fields can influence the slow electrons' flight paths. Overview spectra are typically obtained using higher repeller voltages ($V_{rep} \approx -600$ V), resulting in a lesser degree of magnification of the Newton spheres so that a wider range of eKEs may be simultaneously imaged.

After a $\approx 50$ cm flight path in the field-free region, electrons impinge upon a 2D detector comprised of two 75 mm chevron-stacked imaging-quality MCPs that are coupled to a phosphor screen (PHOTONIS, part number 39082). The front of the MCP stack is grounded to maintain zero-field conditions in the flight tube. To ensure that only electrons (rather than the parent ions) are detected and to protect the MCPs from damage, the back of the MCP stack is pulsed from +1 to +2 kV for a $\approx 50$ ns window centered around the electrons' time-of-flight. The phosphor screen is held at +6 kV such that the electron cascade resulting from a photoelectron hitting the MCP stack produces a bright spot on the phosphor screen, the back of which is photographed with a charge-coupled device (CCD) camera positioned outside of the vacuum chamber. In the event that the TOF of the electrons is close to that of some ion of a lower mass than the system of interest, a set of deflectors situated prior to the VMI lens may be pulsed to ensure that only ions within a particular mass window enter the spectrometer.

Data acquisition is performed using a modified version of the NuACQ software developed by Arthur Suits.[183] Each photograph from the CCD camera is analyzed for individual electron events, the centroids of which are calculated and binned in a specified grid. Prior to the implementation of the seven-plate VMI lens assembly, the 1024×1024 binning native to the CCD camera was sufficient; with the improvement in resolution afforded by the updated assembly, this bin size sometimes limits spectral resolution, and so a larger bin is used. Typically, high-resolution images are obtained by using a 2200×2200 grid for this centroiding process.

### 2.5.1 Data Processing

The ultimate goal of VMI measurements is to obtain the velocity-map, $F(z, r)$, which gives rise to the measured image, $D(x, z)$ (see Fig. 2.12 for definition of the Cartesian coordinate system). Extraction of the velocity-map requires reconstruction of the 3D velocity distribution $P$ from the image $D$. For a given distribution $P(x, y, z)$, the corresponding image $A(x, z)$ is the projection onto the $(x, z)$ plane,

$$A(x, z) = \int_{-\infty}^{\infty} P(x, y, z)\, dy. \tag{2.10}$$

Due to the cylindrical symmetry of the VMI experiment, $A(x, z)$ is related to the velocity-map $F$ by the Abel transform,

$$A(x, z) = 2 \int_{x}^{\infty} F(z, r) \frac{r\, dr}{\sqrt{r^2 - x^2}}. \tag{2.11}$$

Thus, given a measured image $D(x,z)$, the corresponding velocity-map may be obtained numerically by performing the inverse-Abel transform,

$$F(z,r) = -\frac{1}{\pi}\int_r^\infty \frac{\partial D}{\partial x}\frac{dx}{\sqrt{x^2-r^2}}. \tag{2.12}$$

However, several problems are associated with numerical inversion in this manner, which have been discussed in previous theses from the cryo-SEVI project.[18,163]

Rather than performing direct numerical inversion of the data $D$, the maximum entropy methods developed by Bernhard Dick[184,185] and used for all cryo-SEVI data in this thesis aim to determine the velocity-map $F$ (corresponding to image $A$ given by Eq. 2.11) that maximizes the quantity

$$\Pr(F|D) = \frac{\Pr(D|F)\Pr(F)}{\Pr(D)}, \tag{2.13}$$

which corresponds to the probability that the map $F$ describes the 3D distribution which gives rise to the data $D$. Noting that $\Pr(D)$, the *a priori* probability of the data set, is a constant for each image, maximizing $\Pr(F|D)$ requires maximizing the conditional probability $\Pr(D|F)$ and the *a priori* probability of the map, $\Pr(F)$.

The conditional probability $\Pr(D|F)$ in Eq. 2.13, describing the likelihood that the data $D$ arises from the velocity-map $F$, is related to the likelihood estimator $L$ by

$$\Pr(D|F) \propto e^{-L}. \tag{2.14}$$

The likelihood estimator quantifies the agreement between the data $D$ and the image $A$ (constructed as a matrix with the same dimensions as $D$) arising from the velocity-map $F$. For an electron imaging experiment, where Poisson statistics are obeyed, the likelihood estimator is given by

$$L_P = \sum_J [A_J - D_J \ln A_J + \ln(D_J!)], \tag{2.15}$$

where the summation over $J$ is performed over each pixel in the data set. Thus, the first step in maximizing Eq. 2.13 is to minimize the likelihood estimator below some threshold value $L_0$.

As the number of parameters in the map and data are comparable, there are generally multiple maps $F$ with likelihood estimators that satisfy $L < L_0$. To find the map $F$ that has the greatest probability, we define the *a priori* probability of the map as

$$\Pr(F) = e^{\alpha S}, \tag{2.16}$$

where $S$ is the entropy function for the map, defined relative to some default map $B$,[a]

$$S = \sum_J F_J \ln\left(\frac{F_J}{e\,B_J}\right). \tag{2.17}$$

[a]The choice of $B$ is, to some extent, arbitrary; the MEVELER algorithm used in this work uses a crude inverse-Abel transform of the image $D$ for this default map. This code also uses $B$ as the initial map $F$, so this choice of $B$ generally results in a more efficient reconstruction.

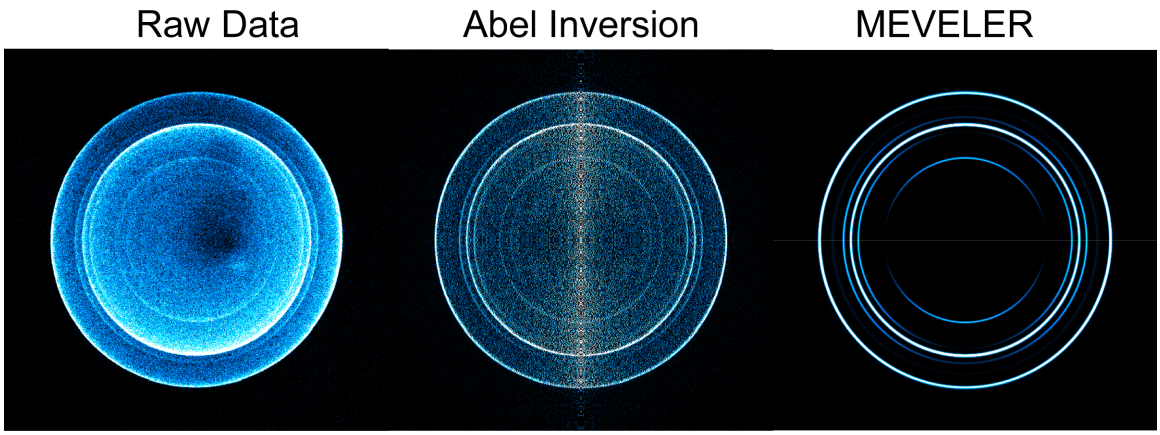


**Figure 2.13:** Comparison of numerical and maximum entropy methods of reconstructing a VMI image, shown for detachment from $Al_2O_2^-$ with a photon energy of 16802 $cm^{-1}$. The dark spot near the center of the raw data is an artifact that arose due to the age of the phosphor screen used in these measurements.

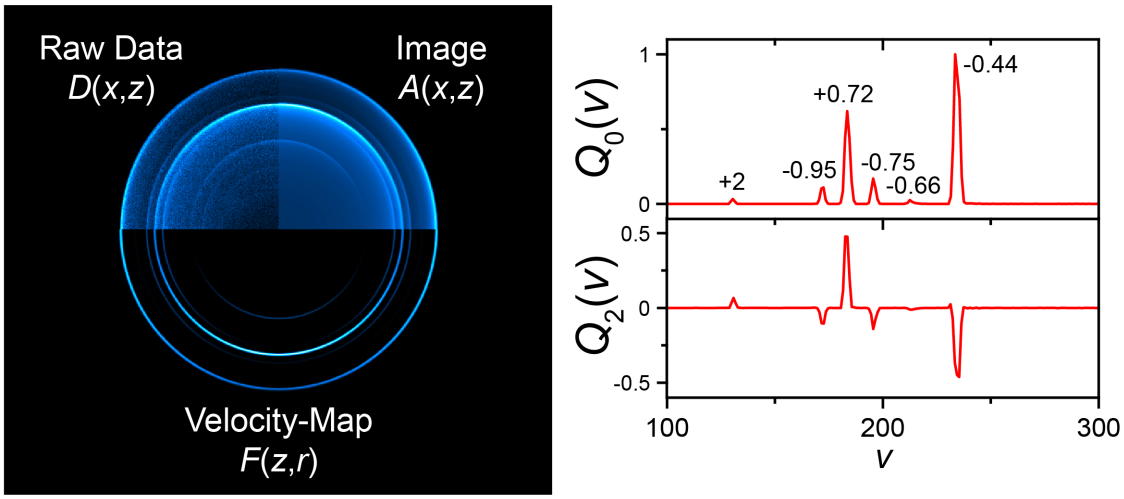


**Figure 2.14:** Illustration of the quantities involved in the MEVELER reconstruction algorithm, using a sample image corresponding to detachment from $Al_2O_2^-$ using a photon energy of 16802 $cm^{-1}$. The left-hand panel shows the raw data, maximum-entropy velocity-map, and image; the right-hand panel shows the corresponding $Q_0(v)$ and $Q_2(v)$ used to calculate photoelectron spectra and anisotropy parameters. The anisotropy parameters are shown above each peak in the $Q_0(v)$ plot.

Thus to select the optimum $F$ from the manifold of $L < L_0$ maps requires maximizing the entropy $S$, which is equivalent to minimizing the information contained in the map; this ensures that the final map does not contain any information that is not in the data set $D$.

Figure 2.13 compares the velocity-map obtained from numerical inversion of the data set to that given by the maximum entropy method most commonly used to analyze cryo-SEVI data, where the numerical inversion was performed using the BASEX algorithm.[186] In addition to removal of the noise about $\theta = 0$ that arises due to singularities in the numerical inversion algorithm, the noise inherent in the raw data is not transformed into the maximum-entropy reconstruction; as a result, when intensity is plotted as a function of radius, the maximum entropy approach gives a much cleaner-looking spectrum, and low-intensity features are easier to distinguish from noise.

### MEVIR and MEVELER

The primary results of the maximum entropy velocity image reconstruction (MEVIR) algorithm is the final map $F$, which is obtained by first minimizing $L$ below some threshold $L_0$ and then maximizing $S$ holding $L = L_0$. The map $F$ obtained in this manner is transformed by Eq. 2.11 to obtain the image $A(x, z)$, which is related to the 3D electron distribution by Eq. 2.10. Thus all information regarding the 3D electron distribution may be extracted from the maximum-entropy map $F$. Figure 2.14 shows an example of the map and image that result from application of a maximum-entropy algorithm to data obtained for detachment from $Al_2O_2^-$. The most important quantities we aim to extract are the photoelectron spectrum - i.e. electron signal as a function of $v$ - and the anisotropy parameters described in Section 1.2.2.

Due to the geometry of the VMI experiment, it is generally more convenient to consider the 3D distribution as a function of spherical coordinates, $P^S(v, \theta, \phi)$. The cylindrical symmetry imposed by the detachment geometry allows us to express this as

$$P^S(v, \theta, \phi) = P^S(v, \theta, 0) = P(v, \theta). \tag{2.18}$$

The distribution $P(v, \theta)$ may then be expressed in terms of the Legendre polynomials, $\mathscr{P}_\ell$,

$$P(v, \theta) = \frac{1}{v^2} \sum_\ell Q_\ell(v) \mathscr{P}_\ell(\cos\theta), \tag{2.19}$$

and due to the orthogonality of the Legendre polynomials,

$$Q_\ell(v) = v^2(2\ell + 1) \int_0^\pi P(v, \theta) \mathscr{P}_\ell(\cos\theta) \sin\theta \, d\theta. \tag{2.20}$$

The $Q_\ell(v)$ functions provide the data that we use to obtain our cryo-SEVI spectra. The factor of $v^2$ in Eq. 2.20 ensures that $Q_0(v)$ simply gives the particle count as a function of $v$;

in other words, $Q_0(v)$ directly gives the photoelectron spectrum. The anisotropy parameters are then defined (for velocities where the spectrum has non-negligible intensity) as

$$\beta^\ell(v) = \frac{Q_\ell(v)}{Q_0(v)}. \tag{2.21}$$

The maximum entropy velocity Legendre reconstruction (MEVELER) algorithm is in much the same spirit as MEVIR, but assumes that the 3D electron distribution is well-described as a linear combination of a small number of Legendre polynomials. The MEVELER algorithm then involves construction of a matrix $\mathbf{Q}$ with elements $Q_{k\ell} = Q_\ell(v_k)$, and uses this directly to perform minimization of $L$ and maximization of $S$; thus, rather than $F$ being the direct result of the MEVELER algorithm, the direct results are the $Q_\ell(v)$ functions. For our experiments, $\ell = 0$ and $\ell = 2$ are the only values which are physically meaningful; these are illustrated in Figure 2.14 for the sample spectrum. The anisotropy parameters of each peak are also provided, and are calculated by integrating $Q_0(v)$ and $Q_2(v)$ over the corresponding peak,

$$\beta = \frac{\int Q_2(v)dv}{\int Q_0(v)dv}. \tag{2.22}$$

### 2.5.2 Energy Calibration

The radii of features in a velocity-map image are roughly proportional to the velocity $v \propto R$, so that in a typical electron imaging experiment, eKE scales with $R^2$. Following introduction of the new VMI lens assembly described in the thesis of Marissa Weichman,[18] the cryo-SEVI spectrometer's energy calibration was found to require addition of an $R^4$ term in order to achieve the desired statistics in the fit. Now, the radii of features in the reconstructed images are related to electron kinetic energy by eKE $= a_2R^2 + a_4R^4$, where $a_2$ and $a_4$ are determined for a particular set of VMI voltages by obtaining images for detachment from atomic anions for which the detachment energies are known to a high degree of precision. These constants are sensitive to the location of the interaction region, and thus calibration must be performed following any change in the detachment laser path. The specific atomic system used for calibration depends on the detachment energies available with the current laser alignment (see Table 2.4). A summary of the atomic anions used for calibration and their detachment transitions is provided in Table 2.5, and example spectra are shown in Figure 2.15. The general calibration procedure is as follows:

1. Determine which repeller voltages are to be used (usually -300 V for high-resolution, low-eKE spectra and -600 V for low-resolution, high-eKE spectra).

2. For each $V_{rep}$, determine the extractor voltage $V_{ext}$ that gives the narrowest features for the target eKE range.

3. For each $(V_{rep}, V_{ext})$ set, obtain detachment images at several photon energies and work up the data to obtain electron intensity as a function of $R$.

**Table 2.5:** Detachment transitions of selected atomic anions and their corresponding molecular precursors used for energy calibration of the VMI spectrometer. Ions indicated with an asterisk are difficult or impossible to form when $H_2$ is present in the trap buffer gas.

| anion | m/z | peak | transition | eBE ($cm^{-1}$) | precursor | Ref. |
|---|---|---|---|---|---|---|
| $Cl^-$ | 35 | a | $^2P_{3/2} \leftarrow {}^1S$ | 29145.47 | $CH_2Cl$ | [187] |
| | | b | $^2P_{1/2} \leftarrow {}^1S$ | 30027.82 | (vapor) | |
| $F^-$ | 19 | a | $^2P_{3/2} \leftarrow {}^1S$ | 27432.45 | $NF_3$ | [188] |
| | | b | $^2P_{1/2} \leftarrow {}^1S$ | 27836.53 | (gas) | |
| $*S^-$ | 32 | a | $^3P_2 \leftarrow {}^2P_{1/2}$ | 16268.65 | $S_2(CH_3)_2$ | [189, 190] |
| | | b | $^3P_1 \leftarrow {}^2P_{1/2}$ | 16664.70 | (liquid) | |
| | | c | $^3P_2 \leftarrow {}^2P_{3/2}$ | 16752.98 | | |
| | | d | $^3P_1 \leftarrow {}^2P_{3/2}$ | 17149.04 | | |
| | | e | $^3P_0 \leftarrow {}^2P_{3/2}$ | 17326.62 | | |
| $*O^-$ | 16 | a | $^3P_2 \leftarrow {}^2P_{1/2}$ | 11607.24 | $N_2O$ | [189, 190] |
| | | b | $^3P_2 \leftarrow {}^2P_{3/2}$ | 11784.68 | (gas) | |
| | | c | $^3P_1 \leftarrow {}^2P_{3/2}$ | 11942.94 | | |
| | | d | $^3P_0 \leftarrow {}^2P_{3/2}$ | 12011.66 | | |
| $*Ni^-$ | 58 | a | $^3D_2 \leftarrow {}^2D_{5/2}$ | 8727.97 | Ni | [191] |
| | | b | $^3F_4 \leftarrow {}^2D_{5/2}$ | 9333.15 | (solid) | |
| | | c | $^3D_3 \leftarrow {}^2D_{5/2}$ | 9537.94 | | |

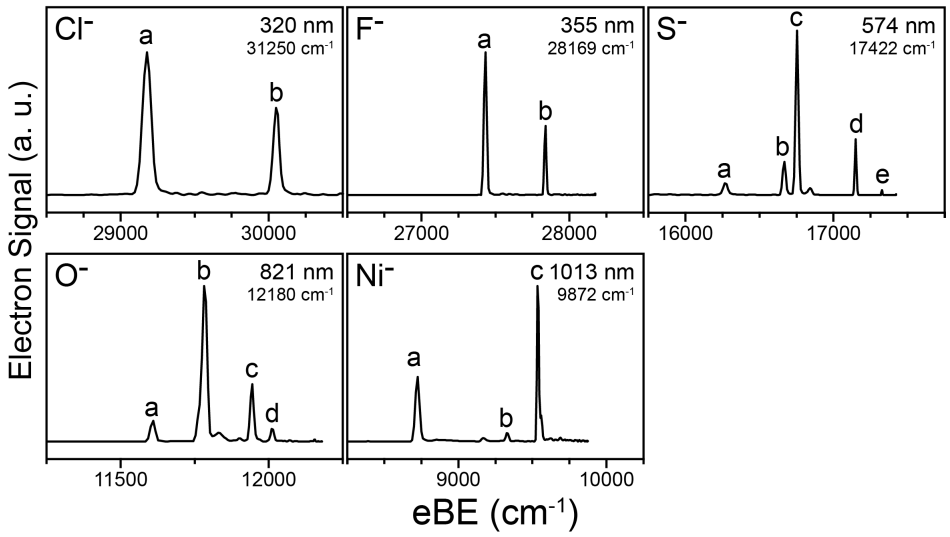


**Figure 2.15:** Photoelectron spectra of the five atomic anions used for energy calibration of the cryo-SEVI spectrometer. The wavelength and photon energy used to acquire each spectrum is provided in the top-right corner of each panel.

4. For each individual scan, plot electron intensity versus $R^2$, identify the transitions $i$ summarized in Table 2.5, and fit each transition to a Gaussian to extract its center $R_i^2$.

5. Using a least-squares fitting procedure such as that implemented in Microsoft Excel, fit $\mathrm{eKE}_i = h\nu - \mathrm{eBE}_i$ as a second-order polynomial in $R_i^2$, setting the zeroth-order term of the polynomial to zero to obtain the coefficients $a_2$ and $a_4$.

6. Continue adding data points until the $\mathrm{R}^2$ of the fit exceeds 0.99999, where

$$\mathrm{R}^2 = 1 - \frac{\sum(\mathrm{eKE}_i - y_i)^2}{\sum(\mathrm{eKE}_i - \frac{1}{N}\sum \mathrm{eKE}_i)^2} \quad \text{and} \quad y_i = a_2 R_i^2 + a_4 (R_i^2)^2. \tag{2.23}$$

### 2.5.3 Circularization of VMI Images

In the event of imperfect shielding in the field-free region of the VMI spectrometer, it is possible for slight angular deformations to appear in the accumulated images. These angular deformities are a greater issue for features with larger radii, and thus can have a strong impact on the resolution of higher-eKE features. This is not always necessary to correct for in cryo-SEVI spectra, where the focus is on features with low eKEs and smaller radii; however, if desired, a circularization algorithm may be employed. This algorithm and the accompanying software is described by Gascooke and coworkers,[192] and the general principles behind this method will be described in this section.

First, the accumulated image is converted from Cartesian coordinates to polar coordinates, yielding an image similar to that shown in Figure 2.16a. These polar coordinate plots make angular deformations particularly evident, as performing this transformation on a perfectly circular image would give perfectly vertical lines. An inverse Able transform centered around $r = 0$ is then performed on this to give an image resembling that shown in Figure 2.16b, which gives constant-angle line-outs that resemble a series of Gaussian-like peaks, each corresponding to a ring in the original image. Each individual feature $i$ is isolated and fit to the equation

$$I(r,\theta) = I_i(\theta) \exp\left[-\frac{(r - r_\theta)^2}{2\sigma_i^2}\right] \tag{2.24}$$

where $I_i(\theta)$ is related to the standard PAD of the transition and

$$r_\theta = r_i + \sum_{n=1}^{N} \left[A_n^{(i)} \sin n\theta + B_n^{(i)} \cos n\theta\right]. \tag{2.25}$$

The fit parameters are $\beta_i$ (obtained from the expression of $I_i(\theta)$[192]), $\sigma_i$, $r_i$, and the trigonometric coefficients. Typically $N = 3$ to 4 is sufficient to correct for the angular deformations observed in cryo-SEVI images.

The next step is to determine the radial dependence of the trigonometric coefficients, $A_n(r) = a_n r$ and $B_n(r) = b_n r$. Figure 2.16c shows the coefficients extracted from the sample

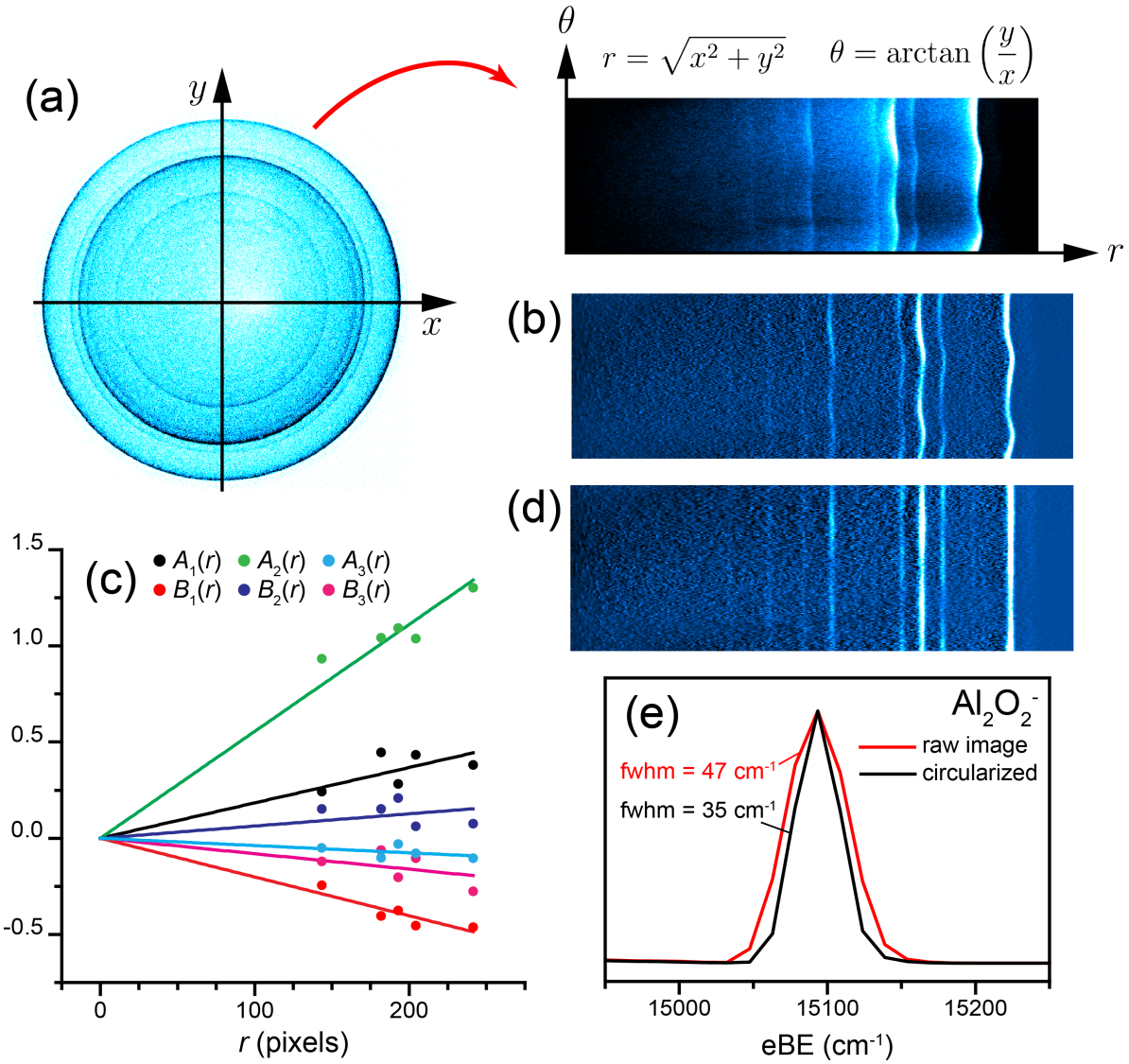


**Figure 2.16:** Demonstration of the application of the circularization algorithm to a VMI image showing detachment from $Al_2O_2^-$ at a photon energy of 16920 $cm^{-1}$. **(a)** Illustration of the conversion of the raw VMI image from Cartesian coordinates to polar coordinates. **(b)** Inverse-Abel transform of the uncorrected polar coordinate image, where the axis of symmetry was taken to be $r = 0$. This inverse transform is performed so that the features resemble Gaussian-like distributions centered around specific radii $r_i$. **(c)** Radial dependence of the trigonometric coefficients extracted from fitting the five intense features in the inverse-Abel transformed polar coordinate image. **(d)** Inverse-Abel transform of the corrected polar coordinate image. **(e)** Comparison of the spectra obtained from the raw (black) and circularized (red) images for a feature with an eKE of $\approx$ 1800 $cm^{-1}$.

data in Figure 2.16, along with linear fits extrapolated to $r = 0$. Once the $a_n$ and $b_n$ coefficients are obtained, the circularization algorithm can be performed on the uncorrected image. For each $(x, y)$ point in the image, the corresponding polar coordinate $(r, \theta)$ coordinate is determined, and the intensity at $(r, \theta)$ is shifted to $(r + \Delta r, \theta)$ where

$$\Delta r(r, \theta) = \sum_{n=1}^{N} \left( a_n r \sin n\theta + b_n r \cos n\theta \right). \tag{2.26}$$

The circularized image can then be processed using the same methods and energy calibration as the raw image.

The effectiveness of this transform in removing angular deformations is most easily observed in the inverse-Abel transformed polar coordinate plot of the circularized image, shown in Figure 2.16d. The straighter lines observed in the polar coordinate plot translates to an improvement in the resolution of the final spectrum, as illustrated in Figure 2.16e for the highest-eKE feature. Even greater reductions of peak widths can be obtained for higher eKEs, due to the relationship between the magnitude of the angular deformities and the radius in the uncorrected images.

# Chapter 3

# Metal Oxide Cluster Reactor Source

## 3.1 Introduction

In order to use cryo-SEVI to map out a neutral species' vibronic structure, one must have the capability to generate the corresponding anion in the gas phase. Small organic anions are relatively easy to generate using electron injection into a supersonic expansion, as described in Section 2.1.1; metal oxide clusters, which serve as tractable model systems for bulk catalytic reaction centers, are in general not able to be synthesized by such an approach. For this reason, a laser ablation ion source was incorporated into the cryo-SEVI project as described in the thesis of Jongjin Kim.[163]

In a laser ablation source, a laser is focused onto a solid target, ablating the material and generating a plasma just above the surface. A pulse of carrier gas is then passed through this plasma to entrain the species present, which are largely cations and free electrons. Collisions with the carrier gas result in recombination and formation of anions and clusters.[169] The pre-existing laser ablation ion source enabled application of the cryo-SEVI technique to metal oxide clusters, leading to a number of successful stories regarding the vibronic structure of these species.[34,151–155]

The next logical step after characterization of the unreacted cluster is to probe a reacted cluster, providing access to an alternative point along the neutral reaction coordinate. For an example reaction $M_xO_y + R \rightarrow$ products, detachment of the bare $M_xO_y^-$ anion provides access to the reactant well; detachment of the $(M_xO_y{\cdot}R)^-$ cluster could in principle provide access to the products, a reactive intermediate, or even potentially a transition state, depending on the anion geometry. Comparison between the bare and reacted spectra could then provide useful insight into the potential energy surface for the neutral reaction, moving further towards the goal of using gas phase clusters to understand bulk reactivity.

To expand the applicability of cryo-SEVI to systems of this nature, a modification of the laser ablation source has been designed, which enables production of reacted metal oxide clusters by introduction of reactant molecules ($H_2O$, $CO_2$, etc.) to the plasma entrainment prior to expansion of the ion packet into vacuum. This modification involved the construction

of two primary components, described in this chapter. Section 3.2 describes the mechanical changes made to the ablation stage. Section 3.3 describes the circuit constructed to provide the driving pulse for the solenoid valve through which the reactant is introduced.

## 3.2 Laser Ablation Reactor Source

The design of the modified ablation source is largely based off of that used in the group of Caroline Chick-Jarrold,[171] and these flow reactor sources are similar in concept to the Smalley reactor source.[170] A diagram of the old and new configurations is shown in Figure 3.1. In both designs, the second harmonic of an Nd:YAG laser ($\sim$ 3 mJ/pulse) impinges on a rotating and translating metal target, generating a plasma. The Even-Lavie valve pulses a carrier gas (He, pulse width $\sim$ 60 µs, backing pressure $\sim$ 100 psig) into the clustering channel, entraining the species in the plasma. While passing through the clustering channel, the ions and neutrals cool and condense, forming clusters. Typically, the surface oxide layer which develops as a result of storing the ablation targets in ambient conditions is sufficient to generate a wide range of $M_xO_y^-$. If a higher degree of oxidation is desired, the carrier gas may be seeded with $N_2O$ to introduce additional oxygen atoms into the plasma entrainment. In the old design used to generate bare metal oxides, these clusters immediately expand into vacuum.

In the new design, the clusters exit the growth channel and are passed through a reactant channel connected to a pulsed general valve backed by the desired reactant gas. Ideally, the reactant gas pulse would be timed so as to collide with the carrier gas pulse, resulting in fast flow conditions which ensure efficient mixing of the species present. To minimize back-flow of the reactant gas, a small 1 mm diameter slit separates the two channels. The total channel length in the ablation back plate was limited by the distance between the nozzle and the

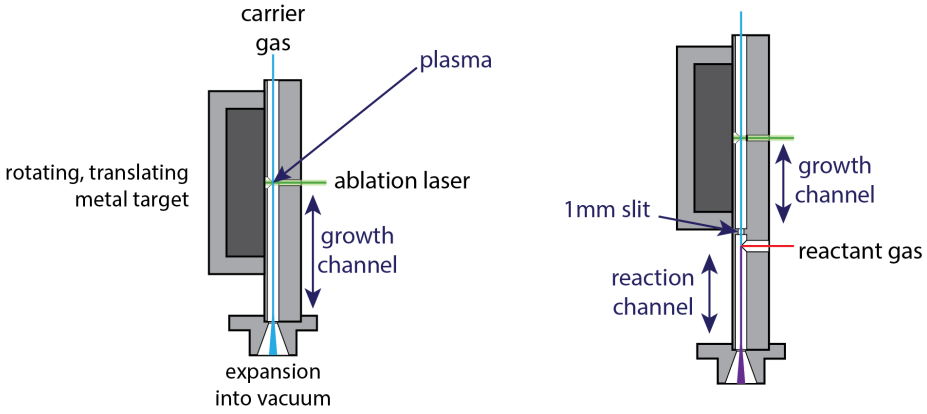


**Figure 3.1:** Schematic of the old (left) and new (right) laser ablation sources showing the metal target, channel plate, and nozzle. Targets are 1 inch in diameter and the drawings are to scale.

**Table 3.1:** Summary of the various channels used in the laser ablation reactor source showing their dimensions and their orientation relative to the direction of carrier gas flow (vertical in Fig. 3.1). The ∥ direction is defined by the direction of the carrier gas flow from the Even-Lavie valve (up/down in Figure 3.1).

| Channel | Direction | Length (mm) | Diameter (mm) |
|---|---|---|---|
| Laser | ⊥ | 4 | 1 |
| Growth | ∥ | 42 | 2 |
| Slit | ∥ | 1 | 1 |
| Reaction | ∥ | 20 | 2 |

skimmer in the ion source vacuum chamber; the length of the reaction channel can be altered using cylindrical spacers prior to the nozzle. The dimensions of the various channels in the aluminum plate are provide in Table 3.1.

To achieve fast flow conditions, the reactant valve should sit as close as possible to the reaction channel. However, given the spatial constraints of the existing source chamber, the gas line needed to be extended slightly such that the valve did not obstruct the laser path. The inlet used to introduce the reactant gas to the reaction channel terminates in a female 1/8" NPT connection. An NPT/Swagelok adapter is used to extend this line with 1/8" steel tubing. This tubing then connects to a "mini" ConFlat adapter which uses a copper gasket seal to connect to the reactant valve. In this configuration, it is found that the relative timing of the reactant valve pulse does not affect the yield or distribution of clusters formed; thus, it is expected that the reaction channel maintains a relatively constant pressure as a result of the extended inlet line, and fast flow conditions are not met.

Regardless, it is apparent that this configuration is capable of producing reacted metal oxide clusters. Figure 3.2 shows example mass spectra obtained for ablating a zirconium target with this new design. In this case, the reactant valve was backed by helium gas which

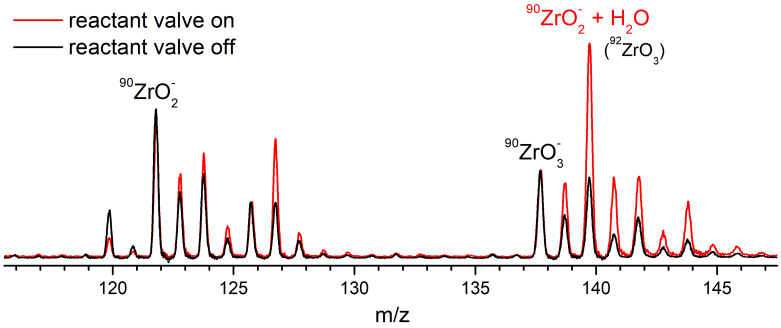


**Figure 3.2:** Mass spectra obtained using a zirconium ablation target in the cluster reactor source with the reactant valve turned off (black) and on (red) and backed by helium bubbled through room-temperature $H_2O$.

flowed through a bubbler filled with $H_2O$. A clear change in the distribution of clusters can be observed following introduction of the reactant gas, resulting in the formation of the $ZrO_2^-$ + $H_2O$ adduct. As the reaction conditions are expected to be quite energetic, it is difficult to draw any conclusions regarding the anion reaction from the valve on / valve off mass spectra, and it is expected that the anions probed (following cooling in the ion trap) will reflect the global minimum of the anion potential energy surface. This is indeed found to be the case, as described in Chapter 10 for the $TiO_2^-$ + $H_2O$ adduct.

## 3.3 General Valve Driver

In the interest of minimizing cost, a home-built pulsed valve driver is used to drive the general valve, and the circuit diagram for this is shown in Figure 3.3. This circuit takes a TTL pulse as input and the rising edge is used to trigger a typical multivibrator (CD4047), a solid state device which produces pulses of variable widths using an appropriately connected RC circuit. For the design used here, the tunability in pulse width is achieved by using a potentiometer as the resistor linking the R and C terminals of the multivibrator; pulse widths range from ≈100 to 700 μs. This pulse (which reads out at 0-5V) is then amplified to ∼24 V with an internal AC-DC voltage converter.

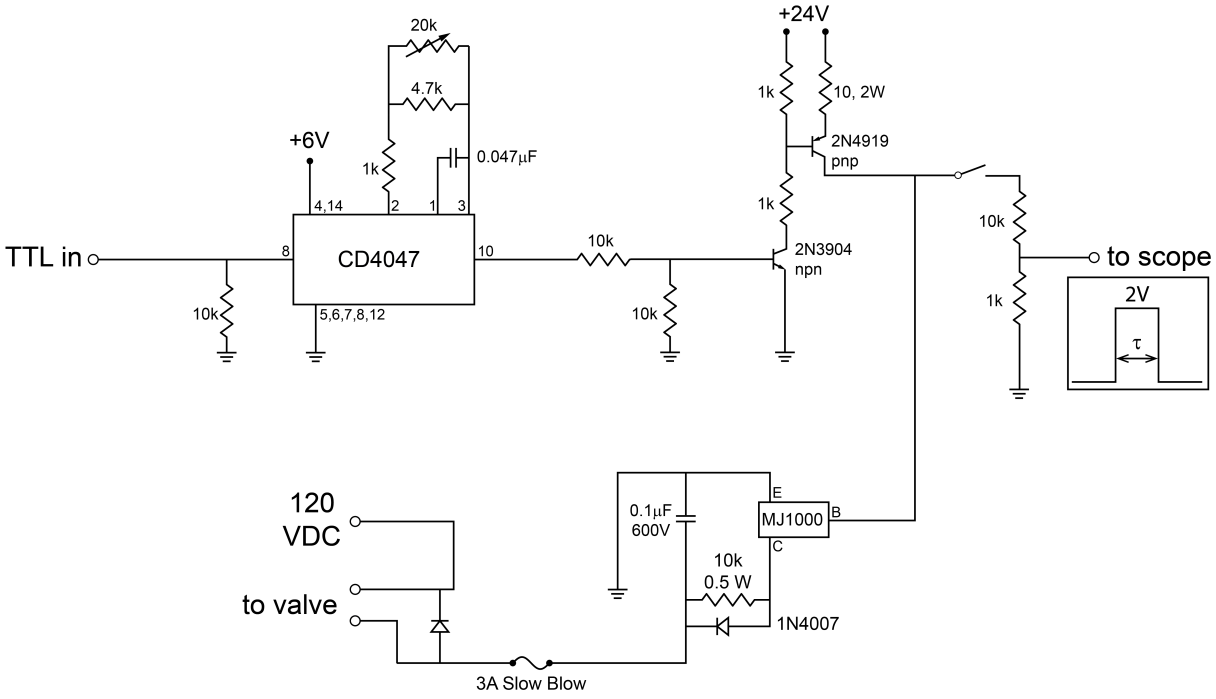


**Figure 3.3:** Circuit diagram for the home-built general valve driver.

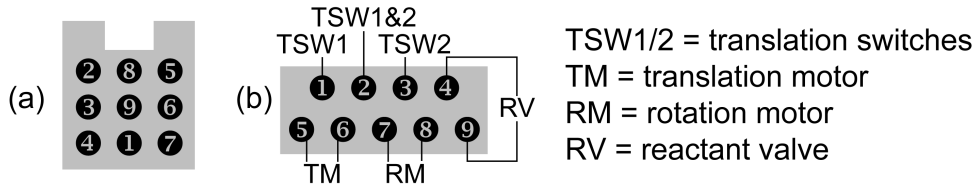


**Figure 3.4: (a)** Connectivity of the male leads (facing the source flange) for the exterior laser ablation controller connections. Numbers correspond to the experimental elements specified in panel (b). **(b)** Connectivity on the male 9-pin connector (facing the soldering joints) that connects the 9 electrical connections directly to the indicated components of the laser ablation setup.

The user has the option of reading the 0-24 V pulse on an oscilloscope by flipping a switch on the front of the box; when switched on, the signal passes through a voltage divider and is read out on a BNC cable. For the work presented in this thesis, the pulse width was read from the oscilloscope signal. An alternative way to do this would be to read the resistance across terminals 2 and 3 of the multivibrator, as there is a well-defined linear relationship between the pulse width $\tau$ and R (for the capacitances shown in Figure 3.3, $\tau \approx 0.12$R μs, with R in Ω). Designing a circuit to accomplish this was considered unnecessary at the time of construction.

Regardless of the readout switch setting, the 0-24 V pulse passes into a Darlington transistor and the final leg of the circuit, where an external high-voltage source is connected. The voltage necessary to power the valve is dependent on the desired pulse width; for shorter widths, a higher voltage threshold is required for the valve to start pulsing. The smallest pulse widths used here ($\tau \sim 60$ μs) required an external voltage of 120 VDC. The two output leads are interfaced with the valve by connecting them to the circuit box which controls the ablation translation and rotation motors, which then connects through the source flange via a 9-pin connector. The male leads which face to the atmosphere side of the source chamber are configured as shown in Figure 3.4a; these connect to a second 9-pin connector that is mounted to the ablation stage in vacuum. Figure 3.4b shows how the wires which directly connect to the indicated components are soldered to the rear of the male leads for this 9-pin connector.

# Part II

# Free Radicals

# Chapter 4

# α- and β-Furanyl

The content and figures of this chapter are reprinted or adapted with permission from J. A. DeVine, M. L. Weichman, S. J. Lyle, D. M. Neumark, "High-resolution photoelectron imaging of cryogenically-cooled α- and β-furanyl anions" *J. Mol. Spec.* **332**, 16 (2017).

## Abstract

Isomer-specific, high-resolution photoelectron spectra of α- and β-furanyl obtained via slow electron velocity-map imaging of cryogenically-cooled anions are reported. The spectra yield electron affinities of 1.8546(4) and 1.6566(4) eV for the α- and β-furanyl neutral radicals, respectively. New vibronic structure is resolved and assigned based on density functional theory and Franck-Condon simulations, providing several vibrational frequencies for the ground electronic state of both neutral isomers. Subtle differences in orbital hybridization resulting from varying proximity of the deprotonated carbon to the heteroatom are inferred from photoelectron angular distributions, and the $C_\beta$-H bond dissociation energy is estimated from a combination of experimental and theoretical results to be 119.9(2) kcal $mol^{-1}$.

## 4.1 Introduction

Furan ($C_4H_4O$) is a well-known aromatic heterocycle that plays a role in many chemical processes and applications. Substituted furans are widely used to construct intermediates in organic synthesis, providing a valuable route to the formation of carbon-carbon bonds.[193] A primary structural component of coal,[81] the high energy density of furan and its facile production from biomass have led to the use of furanic compounds as components of biofuel.[82,194,195] Central to the large-scale use of furan-based biofuels is an understanding of the thermochemistry of furan, and the major product channels of its thermal decomposition have been identified using flow reactors and reflected shock tubes.[196–198] Several proposed mechanisms for the pyrolysis of furan indicate formation of the furanyl radicals (Figure 4.1) through the reaction of furan with the primary products of its decomposition;[199–202] thus, characterization of these intrinsically reactive species could be of interest in further understanding the chemical processes involved in the combustion of furan-containing biofuels.

Characterization of the furanyl radicals has largely been accomplished through photoelectron spectroscopy (PES) of furanyl anions formed from nonspecific deprotonation of furan.[203,204] Due to the relative acidity of the α-carbon in furan and the consequent stability of the α-furanyl anion,[205] these experiments have been limited to the α-furanyl system. In this work, we obtain high resolution PE spectra of both the α- and β-furanyl radicals by slow electron velocity-map imaging of cryogenically-cooled furanyl anions (cryo-SEVI).

The photoelectron spectrum of the α-furanyl anion was first reported by Vogelhuber and coworkers,[203] providing the adiabatic electron affinity (EA) for neutral α-furanyl, three vibrational frequencies for the radical $\tilde{X}\ ^2A'$ ground state, and the term energy for the $\tilde{A}\ ^2A''$ excited state. This study also provided the first experimentally-derived measure of the $C_\alpha$-H bond dissociation enthalpy (BDE) of furan, giving a value of 119.9(2) kcal mol$^{-1}$. Photoelectron imaging experiments carried out by the Sanov group have provided the term energy for the $\tilde{B}\ ^2A''$ excited state of the α-furanyl radical, and comparison of the photoelectron angular distributions for this system and other aromatic heterocycles highlighted a connection between orbital hybridization and aromatic stabilization, with more fractional *p*-character in the highest-occupied molecular orbital (HOMO) of the anion corresponding to a greater degree of aromatic stabilization in the protonated parent molecule.[91,204] In all of these experiments, negligible contribution from the β-furanyl anion was observed, reflecting the relative stability of the α-furanyl anion.

Slow electron velocity-map imaging (SEVI) of negative ions is a variant of traditional PES

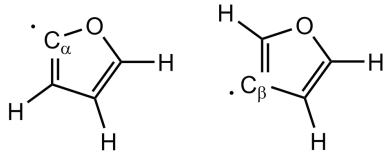


**Figure 4.1:** Molecular structures of (left) α- and (right) β-furanyl radicals.

which employs a velocity-map imaging (VMI) detection scheme and a tunable detachment laser to selectively detect slow photoelectrons in high resolution, thus providing a detailed probe of electronic and vibrational energies of the neutral species generated upon photodetachment.[157] Incorporation of a cryogenically-cooled ion trap into the SEVI apparatus results in efficient cooling of the anion internal degrees of freedom, reducing spectral congestion and providing narrow (2-4 $cm^{-1}$) spectral features.[19] Cryo-SEVI has been extremely successful in characterizing the vibronic structure of radicals with sub-meV resolution,[32,36,177] and the use of trimethylsilyl (TMS)-substituted molecular precursors has provided isomer-specific photoelectron spectra for systems such as the naphthyl and anthracenyl radicals.[35,43]

We present isomer-specific cryo-SEVI spectra of the two furanyl anions, and report electron affinities and ground-state vibrational frequencies for the corresponding radicals. This work is the first spectroscopic investigation of the β-furanyl neutral and anion, using an appropriate TMS-based precursor to generate the anion, and represents a considerable improvement in resolution upon the previously published α-furanyl spectra from the Lineberger and Sanov groups.[91,203,204] Additionally, the angular information provided by cryo-SEVI is used to discuss differences in orbital hybridization resulting from the proximity of the heteroatom to the deprotonated carbon in aromatic heterocyclic radicals, and the $C_\beta$-H bond energy of furan is estimated.

## 4.2 Methods

### 4.2.1 Experimental

The cryo-SEVI method is described in Chapter 2. Furanyl anions were generated by supersonic expansion of a neutral molecular precursor with trace $NF_3$ in helium through the filament ionizer described in Section 2.1.1. Injection of electrons from the ionizer resulted in dissociative electron attachment to $NF_3$ forming $F^-$, which then reacted with the molecular precursor to produce the desired anions. Use of furan as a precursor largely produced the α-furanyl anion, with little to no contribution from the β-isomer. To obtain the β-furanyl anion, the $NF_3$/He mixture was passed through a cartridge containing 3-(trimethylsilyl)furan held at 70 °C, which reacted with $F^-$ to selectively form the β-furanyl anion due to the strength of the fluorine-silicon bond.[167] Energy calibration of the SEVI spectrometer was carried out using images of the well-characterized detachment transitions of atomic $O^-$.[190]

The synthesis of 3-(trimethylsilyl)furan was carried out by Steven J. Lyle and was adapted from a previously published procedure.[206] 3-bromofuran (1 mL, 11.3 mmol) was added to a -78 °C solution of *n*-butyllithium (4.5 mL, 2.5 M, 11.3 mmol) in dry diethyl ether (80 mL) dropwise over 10 minutes. The reaction mixture was then stirred for 1 h. at -78 °C before trimethylsilylchloride (1.6 mL, 12.4 mmol) was added dropwise. The solution was allowed to warm to 25 °C and stirred for an additional 16 h. After quenching with saturated ammonium chloride (20 mL), the organic phase was separated, dried with anhydrous magnesium sulfate, and concentrated by rotary evaporation. 3-(trimethylsilyl)furan was isolated as a colorless

liquid by distillation (580 mg, 4.1 mmol, 36%). $^1$H-NMR (300 MHz, $CDCL_3$, δ): δ7.50 (s, 1H), 6.58 (s, 1H), 6.38 (s, 1H), 0.22 (s, 9H).

### 4.2.2 Theoretical

To assist in spectral assignments, geometrical optimizations and frequency calculations were carried out for the anion and neutral ground state of α- and β-furanyl at the B3LYP/6-311+G* level in Gaussian 09.[53] Optimized geometries, relative energies, and harmonic frequencies are provided in Tables 4.4-4.7.

The *ab initio* geometries, frequencies, and normal mode coordinates were then used to simulate the Franck-Condon profile for detachment from the two anion isomers. The Duschinsky transformation,[59]

$$\mathbf{Q}' = \mathbf{J}\mathbf{Q} + \mathbf{K}', \tag{4.1}$$

was used to relate the neutral ($\mathbf{Q}$) and anion ($\mathbf{Q}'$) normal coordinates, where $\mathbf{J}$ is the block-diagonal Duschinsky rotation matrix and $\mathbf{K}'$ expresses the difference in anion and neutral geometries in terms of the anion normal coordinates. The $\mathbf{J}$ and $\mathbf{K}'$ matrices were computed using FCFGauss,[207] and Pescal[58] took these as inputs to calculate Franck-Condon intensities using the Sharp and Rosenstock[208] method with corrections by Chen.[209] *Ab initio* harmonic frequencies were scaled to match the experimental frequencies, with scaling factors ranging from 0.975-0.999.

Absolute gas-phase enthalpies of the two anion isomers were obtained using the implementation of the Weizmann-1 theory in Gaussian 09,[210] replacing the coupled cluster calculations with Brunecker doubles to obtain the most accurate energies (WIBD).[211] Calculated enthalpies are reported in Table 4.9, and correspond to the total electronic energy of the species plus a thermal correction for a temperature of 273.15 K.

## 4.3 Results

The cryo-SEVI spectra of the α- and β-furanyl anions are presented in Figure 4.2. As in previous work, the blue traces correspond to overview spectra taken with high photon energies, and the black traces are high-resolution SEVI scans that are taken near-threshold and scaled to match overview intensities. In the spectra of both species, peak A corresponds to the vibrational origin of the $\tilde{X}\ ^2A' \leftarrow \tilde{X}\ ^1A'$ transition, yielding adiabatic electron affinities of 1.8546(4) and 1.6566(5) eV for the α- and β-furanyl radicals, respectively. Assignments of spectral features to vibrational transitions are presented in Tables 4.1 and 4.2, permitting extraction of several vibrational frequencies of the neutral radicals.

Density functional theory (DFT) calculations, key results of which are provided in Section 4.6, indicate that the α-furanyl anion is $\sim$ 0.2 eV more stable than the β-isomer, whereas the neutrals are within 20 meV of each other; thus, the 0.2 eV difference in EAs for the two radicals is largely a reflection of the relative stability of the α-furanyl anion. This stability also led to some contamination from the α-isomer in the spectrum of the β-furanyl anion; the

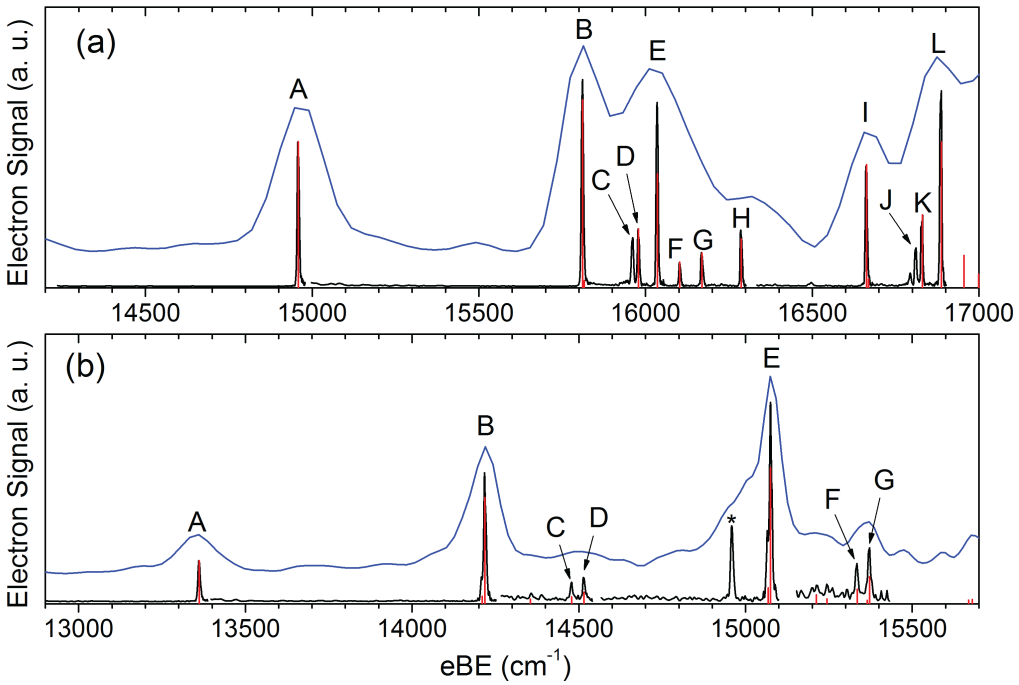


**Figure 4.2:** SEVI spectra of the (a) α- and (b) β-furanyl anions. The blue traces are low-resolution overview scans, and the black traces are high-resolution scans taken near-threshold and scaled to match the overview intensities. The stick spectra represent results of FC simulations (red).

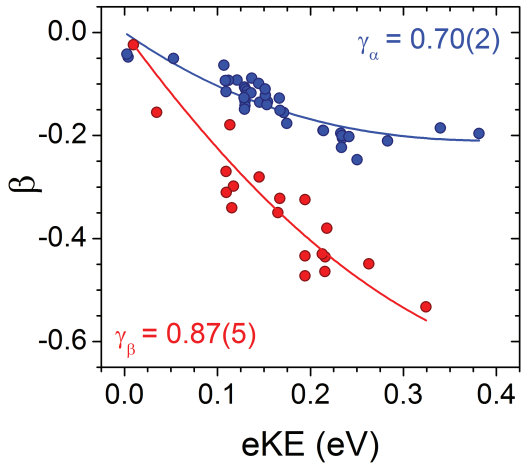


**Figure 4.3:** Experimental PADs and fits of the anisotropy parameters to the mixed-*sp* model (Equation 4.3) for (blue) α- and (red) β-furanyl. Errors in $\gamma$ correspond to one standard deviation from the regression results.

**Table 4.1:** Peak positions ($cm^{-1}$), shifts from the origin ($cm^{-1}$), and vibrational assignments for features observed in the $\tilde{X}\ ^2A' \leftarrow \tilde{X}\ ^1A'$ detachment transition of the α-furanyl anion. All peaks had a Gaussian full-width at half-maximum of 7-8 $cm^{-1}$.

| Peak | eBE | Shift | Assn. |
|---|---|---|---|
| A | 14958 | 0 | $0_0^0$ |
| B | 15810 | 852 | $13_0^1$ |
| C | 15961 | 1002 | $11_0^1$ |
| D | 15978 | 1020 | $10_0^1$ |
| E | 16035 | 1076 | $9_0^1$ |
| F | 16102 | 1144 | $8_0^1$ |
| G | 16169 | 1210 | $7_0^1$ |
| H | 16286 | 1328 | $6_0^1$ |
| I | 16662 | 1703 | $13_0^2$ |
| J | 16810 | 1852 | $11_0^1 13_0^1$ |
| K | 16828 | 1870 | $10_0^1 13_0^1$ |
| L | 16885 | 1927 | $9_0^1 13_0^1$ |

**Table 4.2:** Peak positions ($cm^{-1}$), shifts from the origin ($cm^{-1}$), and vibrational assignments for features observed in the $\tilde{X}\ ^2A' \leftarrow \tilde{X}\ ^1A'$ detachment transition of the β-furanyl anion. All peaks had a Gaussian full-width at half-maximum of 8-9 $cm^{-1}$.

| Peak | eBE | Shift | Assn. |
|---|---|---|---|
| A | 13361 | 0 | $0_0^0$ |
| B | 14218 | 857 | $12_0^1$ |
| C | 14478 | 1117 | $9_0^1$ |
| D | 14515 | 1154 | $8_0^1$ |
| E | 15075 | 1714 | $12_0^2$ |
| F | 15333 | 1972 | $9_0^1 12_0^1$ |
| G | 15371 | 2010 | $8_0^1 12_0^1$ |

intensity of the α-furanyl vibrational origin (indicated by an asterisk in Figure 4.2b) relative to features in the β-furanyl spectrum was found to be dependent on the amount of buffer gas used to cool the ions, suggesting that the ions isomerize with $H_2$ in the octupole trap.

In addition to transition energies, SEVI yields the photoelectron angular distribution (PAD) associated with a particular photodetachment transition. For detachment with a single linearly polarized photon, the PAD is given by[22]

$$\frac{d\sigma}{d\Omega} = \frac{\sigma_{tot}}{4\pi}\left[1 + \beta P_2(\cos\theta)\right], \tag{4.2}$$

where $\sigma_{tot}$ is the total detachment cross section, $P_2(x)$ is the second-order Legendre polynomial, $\theta$ is the angle of the outgoing electron's velocity vector with respect to the laser polarization axis, and $\beta$ is the anisotropy parameter, which ranges from -1 to +2 corresponding to perpendicular and parallel detachment, respectively. The anisotropy parameter reflects the symmetry and angular momentum of the orbital from which an electron is detached; detachment from *s*-like orbitals results in outgoing *p*-wave electrons and parallel PADs ($\beta > 0$), whereas detachment from *p*-like orbitals results in outgoing *s*- and *d*-wave electrons, generally yielding isotropic PADs ($\beta = 0$) or PADs with $\beta < 0$.[26]

The PADs of α- and β-furanyl are presented in Figure 4.3. Both isomers show negative anisotropies, though the energy dependence of $\beta$ is distinctly different between the two, with the β-isomer displaying more perpendicular PADs for moderate kinetic energies. This suggests a difference in the orbital hybridization between the two isomers, which will be discussed in detail in the following section.

## 4.4 Discussion

### 4.4.1 Spectral Assignments

The FC simulations for both isomers show generally excellent agreement with experiment, providing straightforward assignment of most observed vibronic features and yielding several vibrational frequencies, summarized in Table 4.3. As furanyl has $C_s$ symmetry, the FC-allowed vibrational modes all correspond to totally symmetric in-plane motions of the neutral radical, shown in Figure 4.4. The most significant geometry change upon photodetachment from the furanyl anion is an increase in the ring-angle centered on the deprotonated carbon due to removal of electron density from the lone pair orbital (Figure 4.5); as such, the most FC-active mode in both isomers ($\nu_{13}$ in α-furanyl, $\nu_{12}$ in β-furanyl) involves a large distortion of this angle. Of the seven frequencies obtained for the α-isomer, only three ($\nu_6$, $\nu_9$, and $\nu_{13}$) have been previously measured experimentally.[203]

Peaks C and J are absent in the FC simulation for α-furanyl based on the *ab initio* geometries, so their assignment requires further consideration. Each of these peaks lies $\sim 20$ cm$^{-1}$ below a transition involving $\nu_{10}$ ($10_0^1$ for C and $10_0^1 13_0^1$ for J); due to the $\sim 19$ cm$^{-1}$ difference in the *ab initio* harmonic frequencies for $\nu_{10}$ and $\nu_{11}$, we assign peaks C

**Table 4.3:** Experimental and calculated vibrational frequencies for the $\tilde{X}\ ^2A'$ state of α- and β-furanyl. Uncertainties represent one standard deviation of a Gaussian fit to the experimental peak.

| | | exp. | calc. |
|---|---|---|---|
| α | EA, eV | 1.8546 (4) | 1.8429 |
| | $\nu_6$, $cm^{-1}$ | 1328 (4) | 1362 |
| | $\nu_7$, $cm^{-1}$ | 1210 (5) | 1235 |
| | $\nu_8$, $cm^{-1}$ | 1144 (4) | 1170 |
| | $\nu_9$, $cm^{-1}$ | 1076 (4) | 1095 |
| | $\nu_{10}$, $cm^{-1}$ | 1020 (4) | 1022 |
| | $\nu_{11}$, $cm^{-1}$ | 1002 (4) | 1003 |
| | $\nu_{13}$, $cm^{-1}$ | 852 (4) | 868 |
| β | EA, eV | 1.6566 (4) | 1.6404 |
| | $\nu_8$, $cm^{-1}$ | 1154 (5) | 1174 |
| | $\nu_9$, $cm^{-1}$ | 1117 (5) | 1138 |
| | $\nu_{12}$, $cm^{-1}$ | 857 (5) | 867 |

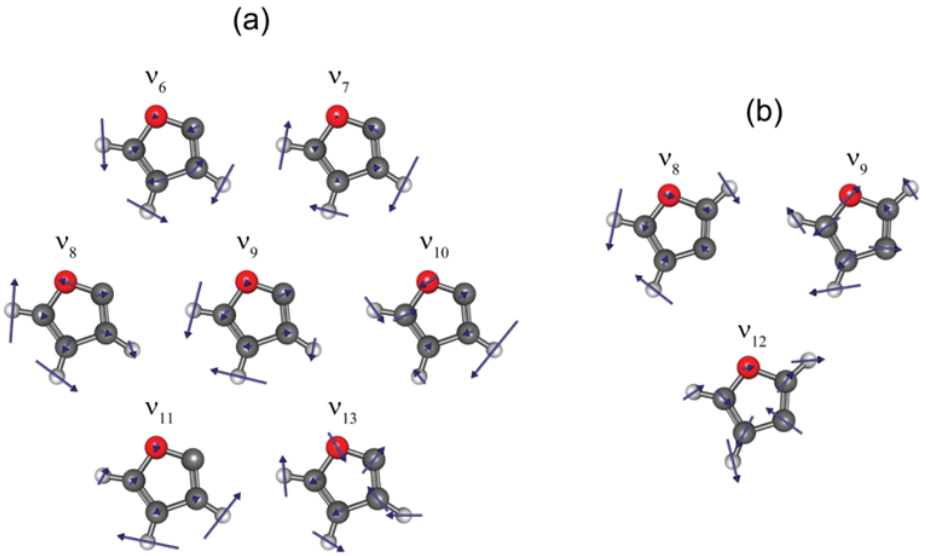


**Figure 4.4:** Normal modes for the (a) α- and (b) β-furanyl radicals that are active in the cryo-SEVI spectra.

and J to the $11_0^1$ and $11_0^113_0^1$ transitions, respectively. Modest changes in normal mode displacements, corresponding to changes in the neutral geometry relative to the anion, may result in increased FC-activity of $\nu_{11}$. The geometry displacement along $\nu_{11}$ was allowed to vary using the optimization feature of PESCAL, and this was found to result in the appearance of peaks C and J with appropriate intensity in the simulated spectrum, shown in Figure 4.6. The corresponding difference between the *ab initio* and optimized geometry has a norm of 0.086 Å, and the most significant geometry changes are a 0.019 Å decrease in the $C_\alpha$-$C_\beta$ bond length and a 0.019 Å increase in the distance between the oxygen and the protonated α-carbon. A summary of the geometry changes is presented in Table 4.8. The small changes required to fit the spectrum suggest the absence of peaks C and J from the *ab initio* FC simulations is indeed due to slight inaccuracies in the calculated geometry changes associated with photodetachment of the α-furanyl anion.

### 4.4.2 Photoelectron Angular Distributions

As indicated in Figure 4.3, the anisotropy parameters for the two furanyl isomers show distinct energy dependences. The HOMO of the furanyl anion is nominally $sp^2$ hybridized and primarily localized on a single carbon atom (Figure 4.5). Thus, to more quantitatively analyze the PADs provided by SEVI, we will employ the single-center mixed-*sp* model developed by Sanov and coworkers, which they successfully applied to the α-furanyl anion.[91,204] Previously, cryo-SEVI has been used to identify isomeric trends in the PADs of polycyclic aromatic hydrocarbons;[35,43] in a similar vein, we presently aim to use the isomer-specificity of our furanyl spectra to compare orbital hybridization for radical heterocycles with varying proximity between the radical carbon and the heteroatom.

In the mixed-*sp* model, the orbital from which an electron is detached is taken to be a single-center orbital comprised of *s*- and *p*-components, with fractional *p*-character $\gamma$. Since low kinetic energies ($< 0.5$ eV) are considered in this work, the relative scaling of the possible detachment channels is given by the Wigner threshold law,[21] permitting replacement of the radial dipole integrals in the Cooper-Zare formula with the $A$ and $B$ Hanstorp coefficients.[23] As was shown by Sanov and coworkers, the anisotropy parameter that arises from the mixed-

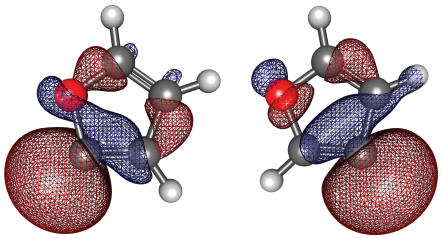

**Figure 4.5:** Highest-occupied molecular orbitals for the (left) α- and (right) β-furanyl anions.

*sp* model orbital can then be expressed as

$$\beta = \frac{2\left[\frac{B}{A}\left(\frac{1-\gamma}{\gamma}\right) - 2\right] A \cdot \mathrm{eKE} + 2(A \cdot \mathrm{eKE})^2}{1 + \frac{B}{A}\left(\frac{1-\gamma}{\gamma}\right) A \cdot \mathrm{eKE} + 2(A \cdot \mathrm{eKE})^2}, \tag{4.3}$$

where $A$ reflects the relative scaling of the $p \rightarrow d$ and $p \rightarrow s$ detachment channels, and $B$ represents the relative scaling of the $p \rightarrow s$ and $s \rightarrow p$ detachment channels.[24]

As was done in the treatment of the α-furanyl anion by Culberson and coworkers, we will take $B/A$ to be 8/3, which has been successful in describing detachment from mixed $2s2p$ orbitals.[27] Due to the relatively localized nature of the anion orbital on the deprotonated carbon, we will use $A = 0.75$ eV$^{-1}$, which corresponds to detachment from atomic $C^-$ and has been used previously to describe the PADs of aromatic radicals.[25,212] Thus we obtain a single-parameter expression for $\beta$, which can be fit to the experimental PADs to extract $\gamma$ for both isomers. We obtain values of 0.70 and 0.87 for α- and β-furanyl, respectively, demonstrating that the β-furanyl anion has more fractional *p*-character. This is consistent with the trends in PADs of deprotonated aromatic heterocycles, where less fractional *p*-character was observed for anions with closer proximity between the site of deprotonation and electron-withdrawing heteroatoms.[91] This proximity effect may also account for the higher electron affinity of the α-isomer, given that the anion HOMO for this isomer is more delocalized onto the heteroatom than in the β-isomer (see Fig. 4.5).

### 4.4.3 $C_\beta$-H Bond Dissociation Energy of Furan

The thermochemistry of furan has attracted considerable attention, in part due to its unusually strong C-H bonds.[213] Using a standard gas-phase acidity/electron affinity thermodynamic cycle (elaborated in the supplementary information), the C-H bond dissociation enthalpy (BDE) is given by

$$\mathrm{BDE(R\text{-}H)} = \Delta H^\circ_{acid}(\mathrm{RH}) + \mathrm{EA}(\mathrm{R}^-) - \mathrm{IE(H)}, \tag{4.4}$$

where $\Delta H^\circ_{acid}$(RH) is the gas-phase acidity of RH, EA($R^-$) is the electron affinity of the deprotonated neutral, and IE(H) is the ionization energy of hydrogen, which is well-known to be 313.6 kcal mol$^{-1}$.[214] Previously, using experimental values of the gas-phase acidity and electron affinity of α-furanyl, this equation was used to calculate the $C_\alpha$-H BDE of furan, giving a value of 119.8(2) kcal mol$^{-1}$.[203] Our measurement of the EA of β-furanyl motivates a similar calculation to obtain the $C_\beta$-H BDE of furan, but experimental gas-phase acidity data for the β-position of furan is not available, and previous theoretical calculations were not carried out at a very high level.[205] To estimate the $C_\beta$-H BDE, we will take an approach similar to that used in the estimation of the $C_2$-H BDE in oxazole;[91] specifically, we determine from *ab initio* calculations the expected difference in gas-phase acidities for the α- and β-positions of furan, and use this difference with the experimentally determined gas-phase

acidity for the α-carbon to yield a hybrid experimental-theoretical estimation of the gas-phase acidity of the β-carbon in furan. This will then be used with our experimental EA for β-furanyl to determine the $C_\beta$-H BDE of furan.

In terms of the absolute enthalpies, the gas-phase acidity for the α/β-carbon of furan is given by

$$\Delta H^\circ_{acid}(\alpha/\beta) = H^\circ(\alpha/\beta\text{-}C_4H_3O^-) + H^\circ(H) - H^\circ(\text{furan}). \quad (4.5)$$

Evidently, the difference in gas phase acidities is simply the difference in the absolute enthalpies of the anion isomers. From the enthalpies in Table 4.9, we find that the α-carbon of furan is around 4.6 kcal $mol^{-1}$ more acidic; using the gas-phase acidity reported by Grabowski and coworkers ($\Delta H^\circ_{acid}(\alpha)$ = 390.7 ± 0.2 kcal $mol^{-1}$),[215] this gives an estimate of $\Delta H^\circ_{acid}(\beta)$ = 395.3(2) kcal $mol^{-1}$. Substituting this into equation 4.4, we obtain the experimental-theoretical BDE of the $C_\beta$-H bond of furan to be 119.9(2) kcal $mol^{-1}$; our calculations indicate that the $C_\beta$-H bond is only stronger than the $C_\alpha$-H bond by 0.05 kcal $mol^{-1}$, which is smaller than the uncertainty imposed by the experimental determination of $\Delta H^\circ_{acid}(\alpha)$. This result is consistent with our earlier assertion that the differences in electron affinities between the two isomers is primarily a reflection of the energetic ordering of the anions, and that the radical isomers are equally stable. Additionally, the estimated gas-phase acidity explains the lack of formation of the β-furanyl anion from reaction of furan with fluoride anions that has prevented prior experimental observation of this isomer.

## 4.5 Conclusion

High-resolution photoelectron spectra of the cryo-cooled α- and β-furanyl anions have been obtained using slow photoelectron velocity-map imaging. In the case of the α-furanyl system, an order-of-magnitude improvement in resolution over previous PES investigations is achieved, resulting in newly resolved vibronic structure that permits extraction and refinement of several vibrational frequencies. The β-furanyl anion has been probed experimentally for the first time, providing its electron affinity, several vibrational frequencies, and an experimental-theoretical estimation of the $C_\beta$-H bond dissociation enthalpy of furan. The photoelectron angular distributions for the two isomers reflect differences in orbital hybridization that are related to the proximity of the site of deprotonation to the heteroatom, and these are used to explain the energetic ordering of the furanyl anions.

## 4.6 Supplementary Information

### 4.6.1 Adjustment of Normal Mode Displacements

To obtain a better match between Franck-Condon simulations and the SEVI spectrum of α-furanyl, displacement along the $\nu_{11}$ normal coordinate between the anion and neutral geometries was optimized using PESCAL.[58] The geometry of the anion was held fixed, and

the geometry of the neutral was varied to obtain the best match, with the consequent neutral geometry described in Table 4.8. Figure 4.6 shows the *ab initio* and optimized FC profiles, with an 8 $cm^{-1}$ Gaussian convolution.

### 4.6.2 Thermodynamic Computations

The C-H bond dissociation enthalpy (BDE) of furan can be calculated from the following thermodynamic cycle:[203]

| | | | |
|---|---|---|---|
| $C_4H_4O$ | $\rightarrow$ | $C_4H_3O^- + H^+$ | $\Delta H^\circ_{acid}$ |
| $H^+ + e^-$ | $\rightarrow$ | $C_4H_3O + e^-$ | -IE(H) |
| $C_4H_3O^-$ | $\rightarrow$ | $C_4H_3O + e^-$ | EA |
| $C_4H_4O$ | $\rightarrow$ | $C_4H_3O + H$ | BDE(C-H) |

### 4.6.3 Supplemental Figures and Tables

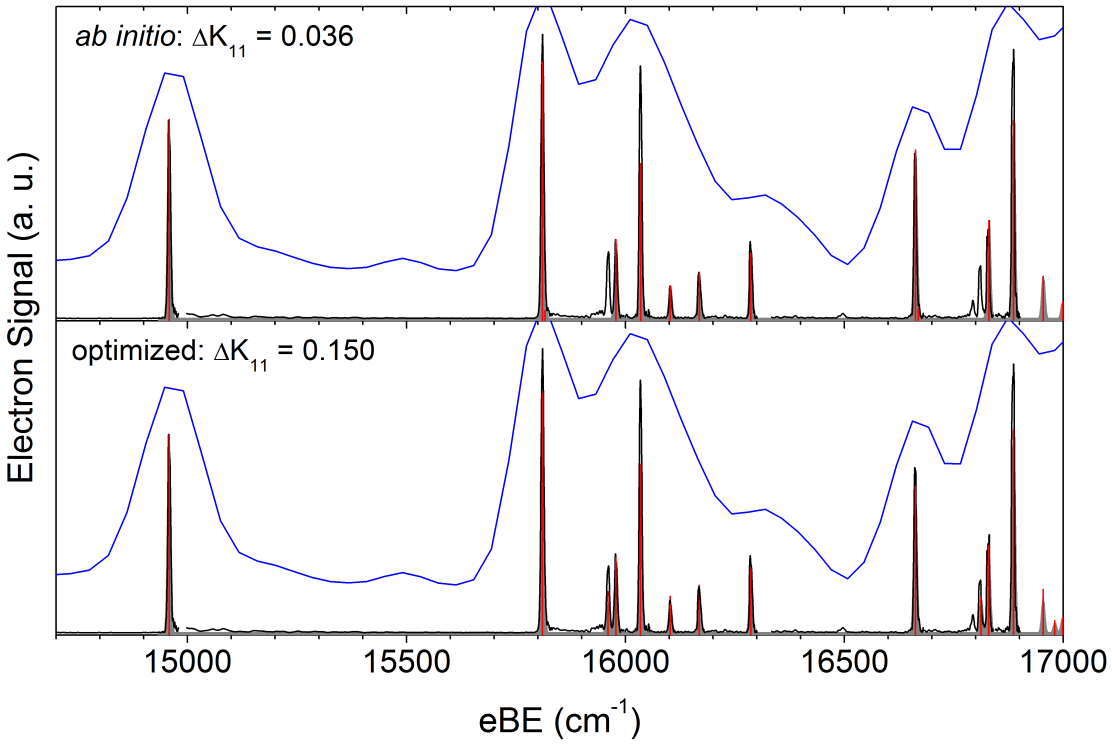


**Figure 4.6:** SEVI spectrum of α-furanyl with the *ab initio* (top) and optimized (bottom) Franck-Condon profiles shown as red sticks. The gray shaded curves correspond to an 8 $cm^{-1}$ Gaussian convolution of the stick spectra.

**Table 4.4:** Equilibrium geometries of α-$C_4H_3O^{-/0}$ calculated with B3LYP/6-311+G* and the resultant geometry change upon photodetachment. Bond lengths are in units of Å and angles are in degrees. Carbons 1 and 4 are adjacent to the heteroatom, whereas carbons 2 and 3 occupy the β-position in the furan ring.

| | $\tilde{X}\ ^1A'$ | $\tilde{X}\ ^2A'$ | change |
|---|---|---|---|
| O-$C_1$ | 1.433 | 1.329 | -0.104 |
| $C_1$-$C_2$ | 1.391 | 1.354 | -0.037 |
| $C_2$-$C_3$ | 1.440 | 1.446 | 0.006 |
| $C_3$-$C_4$ | 1.362 | 1.357 | -0.005 |
| $C_4$-O | 1.365 | 1.385 | 0.020 |
| $C_2$-H | 1.086 | 1.076 | -0.010 |
| $C_3$-H | 1.085 | 1.079 | -0.006 |
| $C_4$-H | 1.083 | 1.076 | -0.007 |
| ∠O-$C_1$-$C_2$ | 110.0 | 114.1 | 4.1 |
| ∠$C_1$-$C_2C_3$ | 105.4 | 103.4 | -2.0 |
| ∠$C_2$-$C_3C_4$ | 111.0 | 107.3 | -3.7 |
| ∠$C_3$-$C_4$-O | 103.2 | 109.6 | 6.4 |
| ∠$C_4$-O-$C_1$ | 110.4 | 105.7 | -4.7 |

**Table 4.5:** Equilibrium geometries of β-$C_4H_3O^{-/0}$ calculated with B3LYP/6-311+G* and the resultant geometry change upon photodetachment. Bond lengths are in units of Å and angles are in degrees.

| | $\tilde{X}\ ^1A'$ | $\tilde{X}\ ^2A'$ | change |
|---|---|---|---|
| O-$C_1$ | 1.429 | 1.376 | -0.053 |
| $C_1$-$C_2$ | 1.360 | 1.348 | -0.012 |
| $C_2$-$C_3$ | 1.465 | 1.423 | -0.042 |
| $C_3$-$C_4$ | 1.365 | 1.363 | -0.002 |
| $C_4$-O | 1.362 | 1.364 | 0.002 |
| $C_1$-H | 1.084 | 1.076 | -0.008 |
| $C_3$-H | 1.088 | 1.079 | -0.009 |
| $C_4$-H | 1.084 | 1.078 | -0.006 |
| ∠O-$C_1$-$C_2$ | 115.0 | 107.8 | -7.2 |
| ∠$C_1$-$C_2C_3$ | 100.6 | 109.8 | 9.2 |
| ∠$C_2$-$C_3C_4$ | 110.4 | 103.8 | -6.6 |
| ∠$C_3$-$C_4$-O | 110.5 | 111.4 | 0.9 |
| ∠$C_4$-O-$C_1$ | 103.5 | 107.2 | 3.7 |

**Table 4.6:** Relative energies (calculated with B3LYP/6-311+G*) in eV with zero-point corrections of the anion and neutral states of α- and β-furanyl.

| Isomer | $^1A'$ | $^2A'$ |
|---|---|---|
| α | 0.000 | 1.843 |
| β | 0.181 | 1.821 |

**Table 4.7:** Harmonic frequencies in $cm^{-1}$ calculated with B3LYP/6-311+G* for the ground anion and neutral states of α- and β-furanyl.

| | | α-$C_4H_3O$ | | β-$C_4H_3O$ | |
|---|---|---|---|---|---|
| Sym. | | anion | neutral | anion | neutral |
| $a'$ | $\nu_1$ | 3194.89 | 3288.04 | 3185.33 | 3296.77 |
| | $\nu_2$ | 3164.31 | 3271.94 | 3178.66 | 3274.60 |
| | $\nu_3$ | 3147.80 | 3236.72 | 3118.51 | 3252.06 |
| | $\nu_4$ | 1543.42 | 1572.54 | 1496.13 | 1545.81 |
| | $\nu_5$ | 1375.25 | 1455.87 | 1437.57 | 1491.58 |
| | $\nu_6$ | 1354.31 | 1362.32 | 1325.12 | 1376.59 |
| | $\nu_7$ | 1167.27 | 1235.42 | 1246.69 | 1243.64 |
| | $\nu_8$ | 1110.29 | 1169.64 | 1139.02 | 1174.12 |
| | $\nu_9$ | 1075.22 | 1095.01 | 1071.59 | 1138.21 |
| | $\nu_{10}$ | 984.45 | 1022.14 | 1032.47 | 1046.15 |
| | $\nu_{11}$ | 899.32 | 1003.13 | 913.81 | 1014.28 |
| | $\nu_{12}$ | 852.73 | 876.56 | 863.34 | 875.13 |
| | $\nu_{13}$ | 798.89 | 868.15 | 828.59 | 866.67 |
| $a$" | $\nu_{14}$ | 771.78 | 854.13 | 787.09 | 837.15 |
| | $\nu_{15}$ | 740.72 | 770.99 | 700.01 | 752.61 |
| | $\nu_{16}$ | 623.72 | 702.17 | 651.99 | 691.85 |
| | $\nu_{17}$ | 608.10 | 602.96 | 609.55 | 613.85 |
| | $\nu_{18}$ | 594.79 | 480.08 | 601.64 | 540.11 |

**Table 4.8:** Initial and final internal coordinates of the α-furanyl radical generated by the PESCAL Franck-Condon simulation and optimization software.[58] The most significantly changed parameters are bolded. Bond lengths are in units of Å, and angles are in degrees.

| | DFT | PESCAL | Change |
|---|---|---|---|
| O-$C_1$ | 1.329 | 1.331 | 0.002 |
| $C_1$-$C_2$ | 1.354 | 1.355 | 0.001 |
| $C_2$-$C_3$ | **1.446** | **1.427** | **-0.019** |
| $C_3$-$C_4$ | 1.357 | 1.361 | 0.004 |
| $C_4$-O | **1.385** | **1.404** | **0.019** |
| $C_1$-H | 1.076 | 1.077 | 0.001 |
| $C_3$-H | 1.079 | 1.083 | 0.004 |
| $C_4$-H | 1.076 | 1.076 | 0.0 |
| ∠O-$C_1$-$C_2$ | 114.1 | 114.2 | 0.1 |
| ∠$C_1$-$C_2C_3$ | 103.4 | 104.1 | 0.7 |
| ∠$C_2$-$C_3C_4$ | 107.3 | 107.6 | 0.3 |
| ∠$C_3$-$C_4$-O | 109.6 | 109.2 | -0.4 |
| ∠$C_4$-O-$C_1$ | 105.7 | 104.8 | -0.9 |

**Table 4.9:** Absolute enthalpies of the furanyl anions calculated with W1BD for a temperature of 298.15 K. These correspond to the sum of the total electronic energy and a thermal correction. All values are in units of Hartrees.

| | |
|---|---|
| α-$C_4H_3O^-$ | -229.414567 |
| β-$C_4H_3O^-$ | -229.407213 |

# Chapter 5

# *tert*-Butyl Peroxy

The content and figures of this chapter are reprinted or adapted with permission from J. A. DeVine, M. L. Weichman, M. C. Babin, D. M. Neumark, "Slow photoelectron velocity-map imaging of cold *tert*-butyl peroxide" *J. Chem. Phys.* **147**, 013915 (2017).

## Abstract

Photoelectron spectra of cryogenically cooled $\tilde{X}\ ^1A'$ *tert*-butyl peroxide anions are obtained using slow electron velocity-map imaging. The spectra show highly structured bands corresponding to detachment to the $\tilde{X}\ ^2A''$ and $\tilde{A}\ ^2A'$ electronic states of the neutral radical and represent a notable improvement in resolution over previous photoelectron spectra. We report an electron affinity of 1.1962(20) eV and a term energy $T_0(\tilde{A}\ ^2A')$ of 0.9602(24) eV for the *tert*-butyl peroxy radical. New vibrational structure is resolved, providing several frequencies for both neutral states. Additionally, the threshold behavior of the photodetachment cross section is investigated within the context of Dyson orbital calculations.

## 5.1 Introduction

Alkyl peroxy radicals (ROO) are important intermediates in atmospheric oxidation and combustion of organic compounds.[98,101,104,108,216] Atmospheric reactions of alkyl peroxy radicals with NO result in the formation of tropospheric ozone,[217,218] motivating a large body of work studying the kinetics of reactions of alkyl peroxy radicals with nitroxides.[219–221] In the absence of nitroxide pollutants, alkyl peroxy radicals can undergo self-reactions,[222–224] addition to other species,[225] and unimolecular decomposition.[226,227] Many of these processes also play a role in low-temperature combustion of hydrocarbons, where alkyl peroxy radicals are an important class of reactive intermediates that exhibit complex, temperature-dependent chemistry.[228–230] The interesting chemistry of alkyl peroxy radicals has motivated the experimental characterization of their energetics and molecular properties using infrared and electronic spectroscopy,[109,231–233] photoionization,[234] and negative ion photoelectron spectroscopy.[235–237] These species have also been investigated in electronic structure calculations.[238–242] Here, we present slow photoelectron velocity-map imaging (SEVI) spectra of cryogenically cooled *tert*-butyl peroxide ($tBuOO^-$) anions, yielding vibrational frequencies as well as the energies of the two lowest electronic states of the neutral *tert*-butyl peroxy radical (tBuOO).

Spectroscopic characterization of the tBuOO radical has been carried out via infrared (IR) absorption in the gas phase and in cryogenic rare gas matrices, yielding several vibrational frequencies ranging from $\sim$ 300 to 2000 $cm^{-1}$.[243,244] In these works, comparison of the frequency shifts upon isotopic substitution permitted vibrational assignments. More recently, near-IR cavity ringdown spectroscopy was used to obtain vibrationally resolved spectra of the $\tilde{A}\ ^2A' \leftarrow \tilde{X}\ ^2A''$ electronic transition, giving a term energy of 0.9618(19) eV for the $\tilde{A}\ ^2A'$ state of tBuOO as well as C-O-O bending and O-O stretching frequencies for this state.[245]

The vibrational and electronic structure of the tBuOO radical can also be characterized by negative ion photoelectron spectroscopy of the corresponding anion. This approach has been used previously by Clifford and co-workers[236] to obtain the photoelectron spectrum of the closed-shell $\tilde{X}\ ^1A'$ $tBuOO^-$ anion, probing the $\tilde{X}\ ^2A''$ and $\tilde{A}\ ^2A'$ electronic states of the neutral radical. These spectra gave an electron affinity (EA) of 1.196(11) eV for $\tilde{X}\ ^2A''$ tBuOO and the term energy of the excited state. Vibrational frequencies for both electronic states consistent with previous IR experiments were obtained, in addition to frequencies below 300 $cm^{-1}$ that were not previously reported.

Slow photoelectron velocity-map imaging (SEVI) is a variation of traditional photoelectron spectroscopy that uses a tunable detachment laser and a velocity-map imaging (VMI) detection scheme optimized for the detection of slow electrons to obtain photoelectron kinetic energy spectra with sub-meV resolution.[157] The resolution of this method is enhanced considerably by cryogenically cooling the anions prior to detachment (cryo-SEVI), resulting in narrower molecular rotational profiles and removal of spectral congestion arising from hot bands. In the current work, we report the cryo-SEVI spectra of the tBuOO system and obtain vibrational resolution for the $\tilde{X}\ ^2A'' \leftarrow \tilde{X}\ ^1A'$ and $\tilde{A}\ ^2A' \leftarrow \tilde{X}\ ^1A'$ electronic bands.

The presented spectra show an improvement in resolution over previous results, resolving new vibrational structure and refining previously observed peaks. The attainable resolution in this particular system is ultimately limited by the threshold behavior of the detachment cross section,[21] and this is discussed in the context of Dyson orbital calculations.

## 5.2 Experimental Methods

The cryo-SEVI method and apparatus are described in detail in Chapter 2. The $tBuOO^-$ anions are formed by flowing a precursor gas mixture containing trace *tert*-butyl hydroperoxide (tBuOOH) and $NF_3$ in He through the filament ionizer described in Section 2.1.1. Electrons from the ionizer are injected into the precursor gas, leading to dissociative electron attachment to $NF_3$ that generates fluoride anions. $F^-$ preferentially deprotonates tBuOOH at the hydroxyl site to form the $tBuOO^-$ anion. The VMI spectrometer was calibrated by obtaining images of well-known detachment transitions of atomic $O^-$ and $S^-$ at several photon energies.[190,246]

## 5.3 Calculations

All electronic structure calculations were carried out using version 4.4 of the Q-Chem software package.[247,248] Optimized geometries, harmonic frequencies, and normal mode displacements for the ground state of $tBuOO^-$ and the two lowest doublet states of tBuOO were determined at the B3LYP/6-311+G* level, which has previously been successful in predicting the SEVI spectra for detachment to neutral radical species.[32,36,249] The maximum-overlap method was employed to treat the excited $\tilde{A}\ ^2A'$ neutral state.[56]

Dyson orbitals for the $\tilde{X}\ ^2A''\leftarrow\tilde{X}\ ^1A'$ and $\tilde{A}\ ^2A'\leftarrow\tilde{X}\ ^1A'$ detachment transitions were calculated using EOM-IP-CCSD/6-311+G*, and these were used as input for the ezDyson program.[63] This software determines the contributions to the outgoing electron wavefunction from spherical waves of angular momentum $\ell \leq 5$ and uses these to calculate the detachment cross section and photoelectron angular distribution (PAD) as functions of eKE.[62]

Franck-Condon (FC) simulations for the $\tilde{X}\ ^2A''\leftarrow\tilde{X}\ ^1A'$ and $\tilde{A}\ ^2A'\leftarrow\tilde{X}\ ^1A'$ electronic bands were carried out using ezSpectrum.[57] The B3LYP/6-311+G* geometries, frequencies, and normal mode displacements were taken as input to calculate the Franck-Condon overlap of the anion and neutral vibrational wavefunctions within the harmonic approximation, with Duschinsky mixing included to account for differences in anion and neutral normal modes. The neutral frequencies were scaled by a factor of 0.964 (0.947) for the ground (excited) neutral state so that the $\nu_{13}$ ($\nu_{14}$) fundamental matched experiment, and the origin of each simulated spectrum was shifted to the appropriate experimental band origin.

In cases where there were discrepancies between the simulated FC profiles and the experimental spectra, small displacements along various normal modes were applied to the ground and excited state neutral geometries in order to see if these discrepancies could be reduced.

For a displacement of magnitude $\delta$ along normal mode $\nu_a$, the transformed B3LYP/6-311+G* geometry is given by

$$\vec{r}^{\,(i)} = \vec{r}_{eq}^{\,(i)} + \delta\vec{q}_a^{\,(i)}, \tag{5.1}$$

where $\vec{r}_{eq}^{\,(i)}$ and $\vec{r}^{\,(i)}$ are the equilibrium and shifted positions of the $i$th atom, respectively, and $\vec{q}_a^{\,(i)}$ is the displacement vector for the $i$th atom associated with mode $\nu_a$. Details of these calculations are provided in Section 5.7.1.

## 5.4 Results

Figure 5.1 shows the full cryo-SEVI spectrum of $tBuOO^-$. In this figure and those that follow, the blue traces are low-resolution overview scans taken at photon energies well above the electronic band of interest, resulting in values of eKE ranging from 2000 to 6000 $cm^{-1}$ for the band origins. Black traces are high-resolution SEVI scans taken near the detachment threshold for various peaks in the spectrum, yielding much slower electrons in the vicinity of these peaks.

Two distinct bands can be seen in Figure 5.1; expanded views of these two regions are shown in Figure 5.2 (eBE <16000 $cm^{-1}$) and Fig. 5.3 (eBE >16000 $cm^{-1}$). All features in Figure 5.1 show negative anisotropy parameters for the observed kinetic energies, as will be addressed in more detail in Section 5.5.2. The general structure of the two bands is similar, with both Figures 5.2 and 5.3 showing a dominant progression (X1-X4-X12-X18 and A1-A4-A7) modulated by one or more weaker, lower-frequency progressions. Similar structure was also observed by Clifford and coworkers,[236] albeit in lower resolution. From the previous photoelectron spectra of this system as well as the calculated energies, the lower-eBE region in Figure 5.2 is assigned to the $\tilde{X}\ ^2A''\leftarrow\tilde{X}\ ^1A'$ ground state band, and the higher-eBE region

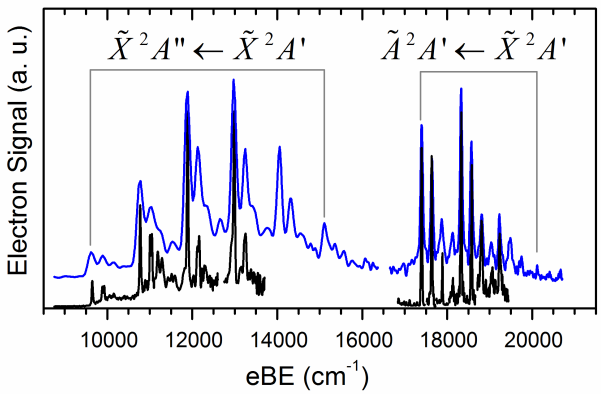


**Figure 5.1:** Cryo-SEVI spectrum of $tBuOO^-$ showing detachment to the $\tilde{X}\ ^2A''$ and $\tilde{A}\ ^2A'$ electronic states of the neutral radical. The blue traces are low-resolution overview spectra taken far above threshold, and the black traces are lower-eKE, high-resolution SEVI scans scaled to match overview intensities and spliced together.

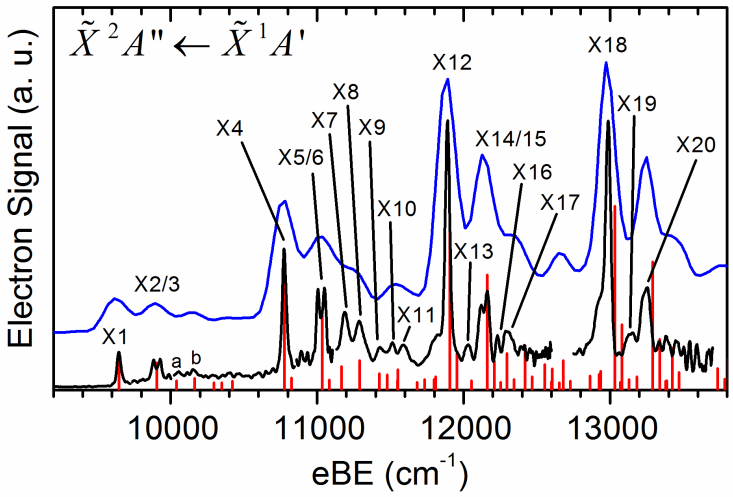


**Figure 5.2:** Cryo-SEVI spectrum of $tBuOO^-$ in the region of the $\tilde{X}\,^2A'' \leftarrow \tilde{X}\,^1A'$ electronic band. The blue trace is an overview spectrum taken with a photon energy of 17698 $cm^{-1}$, and the black traces are high-resolution scans taken close to threshold. A Franck-Condon calculation based on B3LYP/6-311+G* results is shown as the red stick spectrum.

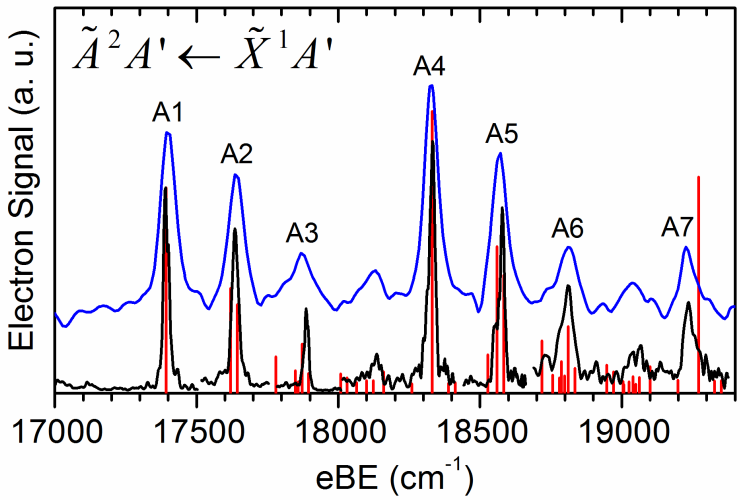


**Figure 5.3:** Cryo-SEVI spectrum of $tBuOO^-$ in the region of the $\tilde{A}\,^2A' \leftarrow \tilde{X}\,^1A'$ electronic band. The blue trace is an overview spectrum taken with a photon energy of 20814 $cm^{-1}$, and the black traces are high-resolution scans taken close to threshold. A Franck-Condon calculation based on B3LYP/6-311+G* results is shown as the red stick spectrum.

in Figure 5.3 is assigned to the $\tilde{A}\ ^2A' \leftarrow \tilde{X}\ ^1A'$ excited state band. Peak widths in the ground and excited state bands are $\sim 40$ cm$^{-1}$ and 20 cm$^{-1}$ respectively. The peaks are somewhat broader than usually obtained in cryo-SEVI experiments, particularly in the ground state band; this broadening reflects low detachment cross sections near threshold and is discussed in Section 5.5.2.

Due to the absence of vibrational hot bands resulting from the low temperature of cryo-SEVI, the first feature in each band (X1 in Figure 5.2, A1 in Figure 5.3) corresponds to the vibrational origin ($0_0^0$) transition to the relevant neutral electronic state, providing useful information on the electronic energetics of the neutral tBuOO radical. The position of peak X1 gives the electron affinity EA = 1.1962(20) eV for the neutral tBuOO radical, which represents an order-of-magnitude improvement in resolution over previous results.[236] The position of peak A1 relative to X1 provides a term energy of $T_0(\tilde{A}\ ^2A') = 0.9602(24)$ eV for the first neutral excited state, well within the error of the term energy measured using near-IR cavity ringdown spectroscopy.[245]

FC simulations for both electronic bands are shown as red stick spectra in Figures 5.2 and 5.3 and can be seen to provide good agreement with the observed structure. This agreement facilitates assignment of several vibrational features, summarized in Tables 5.1 and 5.2 for the ground and excited states, respectively. The calculated normal coordinates for active modes participating in the spectra are shown in Figure 5.4. Two peaks assigned in Table 5.1, a and b, are visible in the ground state band overview and line up quite well with simulated features but are just barely above the signal-to-noise level in the higher resolution traces.

## 5.5 Discussion

### 5.5.1 Spectral Assignments

Term values and vibrational frequencies extracted from the present results are summarized in Table 5.3 and compared to available literature data. Vibrational frequencies were determined by measuring peak displacements from the appropriate band origin. Error bars were obtained using standard error propagation formulas, taking the uncertainty in peak positions to be the width parameter obtained from a Gaussian fit to the experimental peak and taking the covariance between peak positions to be zero. Anharmonicity is expected to be non-negligible for the dominant progression in both electronic bands given the visible decrease in peak spacing in the main X1-X4-X12-X18 and A1-A4-A7 progressions.

The previously reported photoelectron spectrum[236] found $\nu_{13} = 1130(90)$ and $\nu_{21} = 245(90)$ cm$^{-1}$ for the FC-active ground state O-O stretching and C-O-O bending modes, respectively. Two frequencies were reported but not assigned for the excited state band: $\nu_r = 930(90)$ and $\nu_s = 240(90)$ cm$^{-1}$. In the present spectra, comparison to the FC simulations confirms the previous assignment of the $\nu_{13}$ progression in the ground state band and enables the assignment of the excited state $\nu_r$ progression as a similar O-O stretching mode ($\nu_{14}$, Figure 5.4). The experimental O-O stretching frequencies are found to be $\nu_{13} = 1129(20)$

**Table 5.1:** Peak positions, shifts from the origin, and assignments of vibrational features in the $\tilde{X}\ ^2A''\leftarrow\tilde{X}\ ^1A'$ electronic band of the $tBuOO^-$ cryo-SEVI spectrum. Uncertainties in peak positions correspond to the width parameter of a Gaussian fit to the experimental peak.

| Peak | eBE ($cm^{-1}$) | shift ($cm^{-1}$) | assn. |
|---|---|---|---|
| X1 | 9648 (16) | 0 | $0_0^0$ |
| X2 | 9884 (14) | 236 | $22_0^1$ |
| X3 | 9927 (13) | 279 | $21_0^1$ |
| a | 10054 (13) | 407 | $19_0^1$ |
| b | 10157 (16) | 510 | $21_0^2$ |
| X4 | 10776 (15) | 1129 | $13_0^1$ |
| X5 | 11007 (12) | 1360 | $13_0^122_0^1$ |
| X6 | 11048 (14) | 1401 | $13_0^121_0^1$ |
| X7 | 11189 (25) | 1542 | $13_0^119_0^1$ |
| X8 | 11289 (32) | 1642 | $13_0^121_0^2$ |
| X9 | 11435 (30) | 1788 | $13_0^119_0^121_0^1$ |
| X10 | 11512 (21) | 1865 | $13_0^117_0^1$ |
| X11 | 11590 (29) | 1943 | $13_0^121_0^3$ |
| X12 | 11890 (16) | 2243 | $13_0^2$ |
| X13 | 12030 (21) | 2382 | $12_0^113_0^1$ |
| X14 | 12119 (20) | 2472 | $13_0^222_0^1$ |
| X15 | 12164 (15) | 2517 | $13_0^221_0^1$ |
| X16 | 12230 (10) | 2583 | $12_0^113_0^121_0^1$ |
| X17 | 12305 (34) | 2657 | $13_0^219_0^1$ |
| X18 | 12986 (17) | 3339 | $13_0^3$ |
| X19 | 13145 (42) | 3498 | $12_0^113_0^2$ |
| X20 | 13243 (76) | 3596 | $13_0^321_0^1$ |

**Table 5.2:** Peak positions, shifts from the origin, and assignments of vibrational features in the $\tilde{A}\ ^2A' \leftarrow \tilde{X}\ ^1A'$ electronic band of the $tBuOO^-$ cryo-SEVI spectrum. Uncertainties in peak positions correspond to the width parameter of a Gaussian fit to the experimental peak.

| Peak | eBE ($cm^{-1}$) | shift ($cm^{-1}$) | assn. |
|---|---|---|---|
| A1 | 17392 (10) | 0 | $0_0^0$ |
| A2 | 17636 (11) | 244 | $x_0^1$ |
| A3 | 17888 (7) | 495 | $x_0^2$ |
| A4 | 18331 (10) | 939 | $14_0^1$ |
| A5 | 18577 (11) | 1184 | $14_0^1x_0^1$ |
| A6 | 18807 (23) | 1415 | $14_0^1x_0^2$ |
| A7 | 19238 (19) | 1846 | $14_0^2$ |

**Table 5.3:** Experimental and calculated molecular properties of the neutral tBuOO radical obtained in the present work, as well as comparison to available literature values. Reported vibrational frequencies correspond to the energy of the fundamental ($n = 1$) level relative to the neutral zero-point energy.

| State | Parameter | Expt. | Calc. | Lit. |
|---|---|---|---|---|
| $\tilde{X}\ ^2A''$ | EA, eV | 1.1962 (20) | 1.0274 | 1.196 (6)[236] |
| | $\nu_{22}$, $cm^{-1}$ | 236 (21) | 265 | 245 (90)[236] |
| | $\nu_{21}$, $cm^{-1}$ | 279 (21) | 267 | |
| | $\nu_{19}$, $cm^{-1}$ | 410 (29) | 406 | 403 (3)[244] |
| | $\nu_{17}$, $cm^{-1}$ | 740 (26) | 728 | 730 (2)[244] |
| | $\nu_{13}$, $cm^{-1}$ | 1129 (22) | 1171 | 1124 (2)[244] |
| | $\nu_{12}$, $cm^{-1}$ | 1254 (26) | 1221 | |
| $\tilde{A}\ ^2A'$ | $T_0$, eV | 0.9602 (24) | 0.9836 | 0.9618 (19)[245] |
| | $\nu_x$, $cm^{-1}$ | 244 (15) | 241/265 | 240 (90)[236] |
| | $\nu_{14}$, $cm^{-1}$ | 939 (14) | 992 | 938 (2)[245] |

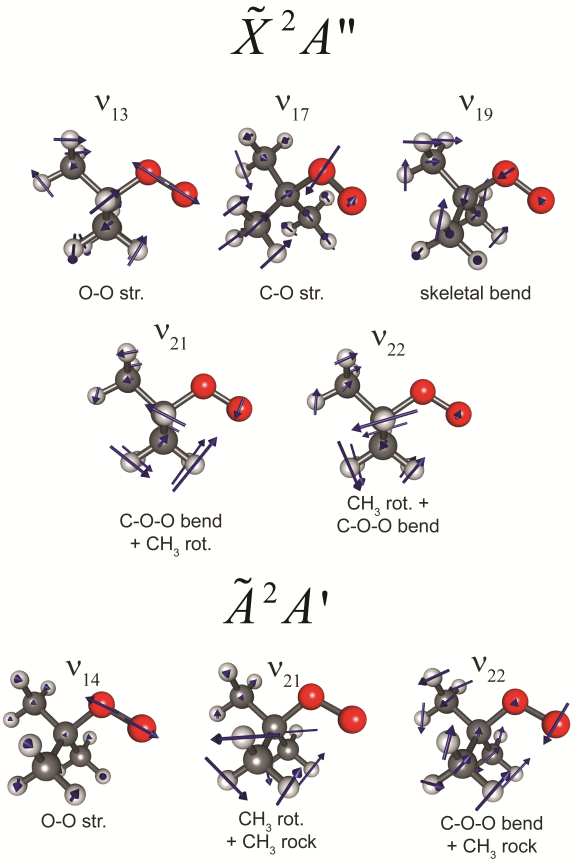


**Figure 5.4:** Franck-Condon active vibrational modes of the $\tilde{X}\,^2A''$ (top) and $\tilde{A}\,^2A'$ (bottom) electronic states of neutral tBuOO observed in the cryo-SEVI spectra. Brief descriptions of the molecular motions are included for clarity.

and $\nu_{14} = 939(14)$ cm$^{-1}$ for the ground and excited states, respectively, in agreement with O-O stretching frequencies observed in infrared experiments.[244,245]

The assignment of the lower-frequency progressions is slightly more challenging. Figure 5.2 demonstrates that peaks in the ground state band associated with the low-frequency $\nu_{21}$ mode reported in the previous work are closely spaced doublets with a $\sim 40$ cm$^{-1}$ splitting (peaks X2/3 and X5/6), whereas there is only a single peak in the simulations. In addition, several smaller peaks are seen and assigned to excitation of additional lower frequency modes, as indicated in Tables 5.1 and 5.3.

The simulated peak for the two doublets involves $\nu_{21}$, which is best described as $CH_3$ internal rotations with some C-O-O bending character (Figure 5.4). The C-O-O bending character results in a larger frequency than is typically expected for internal rotations. The other doublet component is likely due to vibrational mode $\nu_{22}$, which corresponds to a similar totally symmetric motion as $\nu_{21}$ (though with less C-O-O bending character), and is calculated to be only 2 cm$^{-1}$ lower in frequency. A reasonable explanation for the observed

splitting is that both vibrational modes are in fact FC-active, and the activity of $\nu_{22}$ is not captured in the FC simulations shown in Figure 5.2 due to slight inaccuracies in the B3LYP/6-311+G* optimized geometries resulting from treatment of the methyl groups.

To quantify the geometry displacement necessary to yield Franck-Condon activity in the $\nu_{22}$ mode, displacements along this normal coordinate as defined in Eq. 5.1 were applied to the calculated $\tilde{X}\ ^2A''$ neutral geometry, and the resultant geometries were used to generate the FC simulations shown in Figure 5.7. We find that displacements of magnitude $0.3 < \delta < 0.4$ along $\nu_{22}$ are sufficient to yield a doublet of peaks with approximately equal intensities. This geometry displacement corresponds to a slight rotation of the out-of-plane methyl groups as well as a $< 2^\circ$ increase in the C-O-O bond angle. Thus, the lower-frequency progression in the ground state band that was resolved in the previous photoelectron spectrum is actually a progression in two close-lying vibrational modes, with frequencies $\nu_{21} = 279(21)$ and $\nu_{22} = 236(21)$ cm$^{-1}$.

In the excited state band, the FC simulation predicts that two features with similar intensity should be present where peak A2 appears, but only one feature is observed. Although the simulated peaks involving single excitation of the $\nu_{22}$ and $\nu_{23}$ modes are 25 cm$^{-1}$ apart, the experimental peak A2 is only 20 cm$^{-1}$ wide (i.e., the same width as the band origin, A1), suggesting that most of its intensity comes from a single transition. Again, we attribute this discrepancy to the high sensitivity of the FC intensities to the geometries and normal modes used to calculate them.

Comparison to the simulated spectra indicates that peak A2 corresponds to either the $\nu_{21}$ or $\nu_{22}$ fundamental. As such, small displacements along these normal modes were carried out on the excited state geometry, and the resultant FC simulations are shown in Figures 5.8 and 5.9. A displacement of magnitude $0.2 < \delta < 0.3$ along $\nu_{21}$ results in the disappearance of this mode from the simulated spectrum and corresponds to a similar geometry displacement as for the ground state band, whereas a displacement of magnitude $0.1 < \delta < 0.2$ along $\nu_{22}$ is required for peak A2 to correspond to the $\nu_{21}$ fundamental. The displacement along the $\nu_{22}$ mode results in a slight rotation of the methyl groups, as well as a $3.2^\circ$ decrease in the C-O-O bond angle. As can be seen from Figures 5.8 and 5.9, elimination of either $\nu_{21}$ or $\nu_{22}$ from the spectrum results in similar agreement with the experimental results, preventing definitive assignment of the single-component low-frequency excited state progression. We thus refer to this unassigned frequency as $\nu_x$, and this notation is used in Tables 5.2 and 5.3 to emphasize that this frequency may correspond to either $\nu_{21}$ or $\nu_{22}$.

The FC-activity of O-O stretching modes can be understood from the localized nature of the detached anion orbitals. As can be seen in Figure 5.5, the Dyson orbitals for detachment to both the $\tilde{X}\ ^2A''$ and $\tilde{A}\ ^2A'$ neutral states appear to be antibonding orbitals localized on the O-O bond. Detachment to both of these states removes density from these orbitals, resulting in a decrease in the length of this bond. This geometry difference between anion and neutral provides FC activity to $\nu_{13}$ in the ground state band and $\nu_{14}$ in the excited state band. Similarly, the involvement of modes possessing some $CH_3$ rotation character in the ground state band is likely due to the removal of electron density that can interact with the out-of-plane methyl groups. For the excited state, the lower-frequency progression corresponds

to a C-O-O bending mode ($\nu_{21}$ or $\nu_{22}$), due to the removal of electron density within the symmetry plane upon detachment. The similar character of the two Dyson orbitals is likely the cause for the relatively small term energy of the $\tilde{A}\,^2A'$ neutral state of tBuOO, which is similar to those observed for the first excited states of other simple ROO radicals.[237,245]

### 5.5.2 Detachment Cross Sections

While the resolution of the photoelectron spectra presented here is improved compared to previous work on this system, the ultimate peak widths obtained are not as narrow as is often seen in cryo-SEVI experiments, particularly for the $\tilde{X}$ band. This highlights the effects of the Wigner threshold law[21] on our ability to obtain a high-resolution cryo-SEVI spectrum, which in turn hinges on our ability to obtain appreciable detachment signal for low eKEs. The Wigner threshold law states that the photodetachment cross section $\sigma$ near the threshold for a particular transition scales as

$$\sigma \propto (\text{eKE})^{\ell+1/2}, \tag{5.2}$$

where $\ell$ is the angular momentum of the outgoing electron. Therefore, detachment transitions resulting in photoelectrons with appreciable $s$-wave ($\ell = 0$) character can be observed at photon energies close to threshold, yielding low kinetic energies and the highest possible resolution. For photodetachment transitions dominated by higher values of $\ell$, the cross section drops more rapidly as the photon energy approaches the photodetachment threshold, essentially raising the minimum eKE at which there is sufficient SEVI signal to observe a particular transition and leading to decreased energy resolution.[32]

The factors determining which values of $\ell$ contribute to photodetachment have been discussed elsewhere[250] and can be quantitatively assessed for a particular system by performing

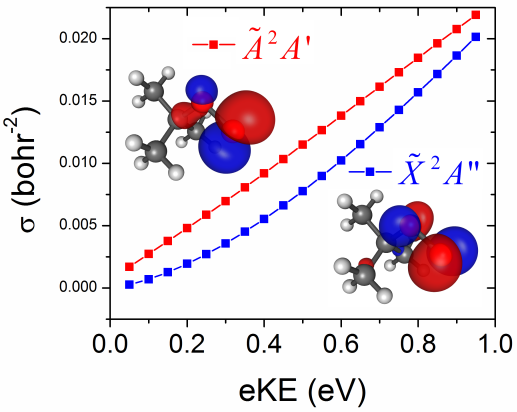


**Figure 5.5:** Calculated detachment cross sections for the $\tilde{X}\ ^2A''\leftarrow\tilde{X}\ ^1A'$ (blue) and $\tilde{A}\ ^2A'\leftarrow\tilde{X}\ ^1A'$ (red) electronic bands based on Dyson orbital calculations of $tBuOO^-$. The Dyson orbitals for both detachment transitions are also shown and are labeled with the corresponding neutral state.

a Dyson orbital analysis in which the photodetachment cross section is calculated as a function of eKE.[62,63] The results for photodetachment of $tBuOO^-$ to the $\tilde{X}$ and $\tilde{A}$ states are shown in Figure 5.5. Both cross sections decrease more rapidly than $\sqrt{\text{eKE}}$, indicating that partial waves with $\ell > 0$ contribute significantly to near-threshold photodetachment. This is confirmed by a partial wave decomposition analysis of the photoelectron wavefunctions for high-eKEs obtained in the Dyson orbital calculation, details of which are included in Section 5.7.2. As can be seen from Table 5.4, this analysis reveals that for an eKE of 1.05 eV, detachment to the $\tilde{X}\ ^2A''$ neutral state results in photoelectrons with larger contributions from $\ell > 0$ spherical waves than detachment to the $\tilde{A}\ ^2A'$ excited state, with calculated fractional $\ell > 0$ characters of 0.78 and 0.33 for detachment to the ground and excited states, respectively. As a result, the calculated cross section for photodetachment to the $\tilde{X}$ state falls off more rapidly than for the $\tilde{A}$ state, consistent with our ability to measure higher resolution SEVI spectra for the $\tilde{A}$ band.

Anisotropy parameters for both electronic bands were found to be negative for the observed electron kinetic energies, in agreement with the results of Dyson orbital calculations.[60] It should be noted that quantitative determination of the experimental PAD for the $\tilde{A}\ ^2A' \leftarrow \tilde{X}\ ^1A'$ electronic band was not feasible due to complications arising from reconstructing VMI images with high-eKE features that do not entirely fall on the phosphor screen. However, visual inspection of the VMI images indicates that the excited state band is more isotropic than the ground state band, which is another reflection of the finding that the $\tilde{A}\ ^2A' \leftarrow \tilde{X}\ ^1A'$ detachment transition yields photoelectrons with greater $s$-wave character than detachment to the neutral ground state.

## 5.6 Conclusion

Cryo-SEVI spectra of $tBuOO^-$ are presented, providing well-resolved vibronic structure of the two lowest electronic states of the neutral radical. These spectra yield several vibrational frequencies for both electronic states of the neutral, which are assigned by comparison to Franck-Condon simulations. The high resolution of the cryo-SEVI experiment reveals low-frequency vibrational modes not reported in IR experiments and new vibrational structure that was not observed in the previously reported anion photoelectron spectrum of $tBuOO^-$. The refined electron affinity and vibrational frequencies reported in this work are benchmarks that will assist in future studies of reactions involving the tBuOO radical and demonstrate the utility of cryo-SEVI as a spectroscopic probe for radical species.

## 5.7 Supporting Information

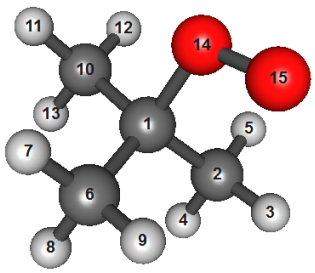


**Figure 5.6:** Atom labeling convention used to describe various geometrical parameters.

### 5.7.1 Effects of Geometry Displacements on FC Profiles

#### Ground State Band

As described in the main text, small displacements along the $\nu_{22}$ normal coordinate were applied to the ground state B3LYP/6-311+G* $\tilde{X}\ ^2A''$ neutral tBuOO geometry to determine the geometry change necessary to result in the appearance of the $\nu_{21}/\nu_{22}$ splitting observed experimentally. Experimental frequencies for $\nu_{21}$ and $\nu_{22}$ were used, and the other 37 frequencies were scaled as described in the text. Figure 5.7 demonstrates that a displacement of $\delta < 0.4$ is sufficient to account for the experimental structure. The primary geometry change is a rotation of the out-of-plane methyl groups, characterized by the $O_{14}$-$C_1$-$C_2$-$H_5$ torsion angle (see Figure 5.6); a displacement of magnitude $\delta = 0.4$ corresponds to a 7.9° increase in this angle, from 58.5° to 66.4°. To compare to the calculated anion-neutral change in this geometric parameter, the anion $O_{14}$-$C_1$-$C_2$-$H_5$ torsional angle was calculated to be 63.0°.

#### Excited State Band

A similar procedure was carried out for the excited state band to determine the necessary displacements along $\nu_{21}$ and $\nu_{22}$ to account for the clear single-component nature of peak A2. Figure 5.8 demonstrates that a displacement of magnitude $0.2 < \delta < 0.3$ is sufficient to remove the $\nu_{21}$ features from the FC profile. As in the ground state band, the primary geometry change involves the $O_{14}$-$C_1$-$C_2$-$H_5$ torsion angle; a displacement of magnitude $\delta = 0.3$ along $\nu_{21}$ corresponds to a 6.9° increase in this angle, from 55.6° to 62.5°.

To similarly determine whether the FC-active mode corresponds to $\nu_{21}$, this process was carried out for displacements along $\nu_{22}$, resulting in the FC simulations shown in Figure 5.9. A displacement of magnitude $\delta = 0.2$ corresponds to a decrease in the C-O-O angle from 112.6° to 109.4° (compared to 110.0° in the anion) and a slight increase in the torsional angle from 55.6° to 57.0°. It is clear that similarly small geometrical distortions are required to

$$\vec{r}^{(i)} = \vec{r}_{eq}^{(i)} + \delta\vec{q}_{22}^{(i)}$$

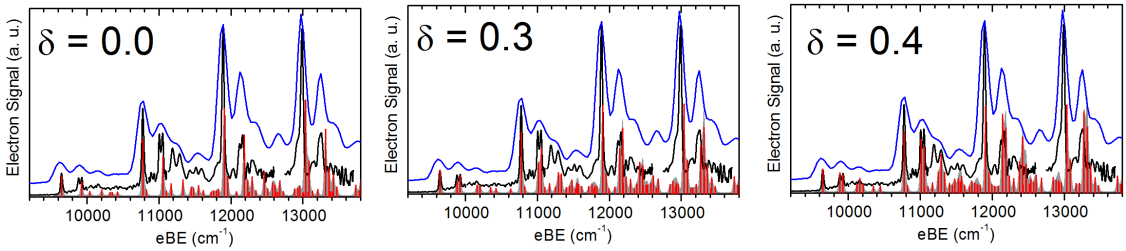


**Figure 5.7:** Franck-Condon simulations for detachment from the B3LYP/6-311+G* anion geometry to neutral geometries defined by the above equation, with the equilibrium positions taken from the $\tilde{X}\ ^2A''$ results. These results illustrate that a displacement of magnitude $0.3 < \delta < 0.4$ along $\nu_{22}$ is sufficient to explain the experimental observation of the FC-activity of this vibrational mode.

$$\vec{r}^{(i)} = \vec{r}_{eq}^{(i)} + \delta\vec{q}_{21}^{(i)}$$

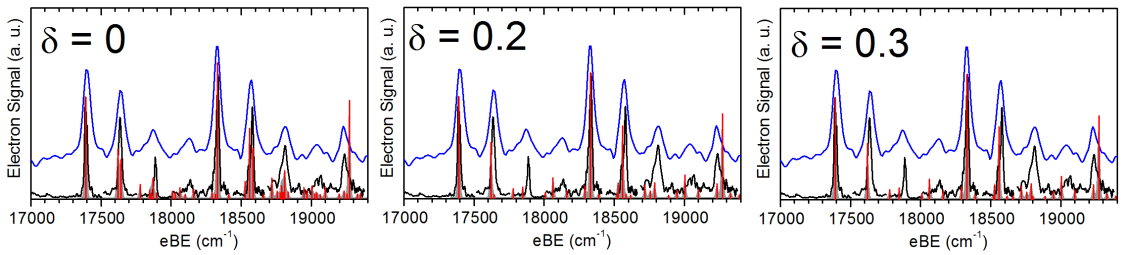


**Figure 5.8:** Franck-Condon simulations for detachment from the B3LYP/6-311+G* anion geometry to neutral geometries defined by the above equation, with the equilibrium positions taken from the $\tilde{A}\ ^2A'$ results.

$$\vec{r}^{(i)} = \vec{r}_{eq}^{(i)} + \delta\vec{q}_{22}^{(i)}$$

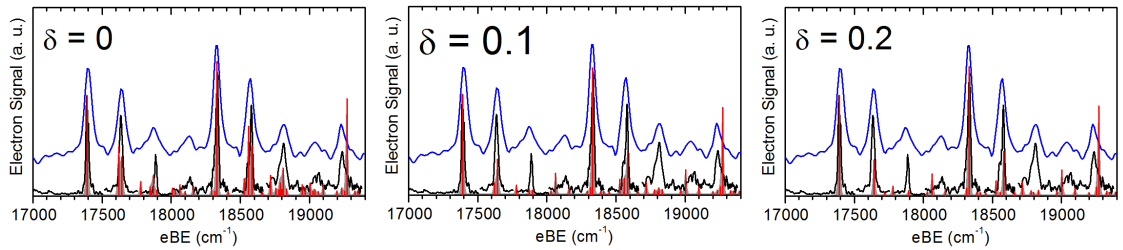


**Figure 5.9:** Franck-Condon simulations for detachment from the B3LYP/6-311+G* anion geometry to neutral geometries defined by the above equation, with the equilibrium positions taken from the $\tilde{A}\ ^2A'$ results.

eliminate the FC-activity in either $\nu_{21}$ or $\nu_{22}$, and thus assignment of features involving this mode is ambiguous.

### 5.7.2 Partial Wave Analysis from Dyson Orbital Calculations

The ezDyson software treats the wavefunction of the photodetached electron as a plane wave, which is then expanded as a sum of spherical waves with $\ell \leq 5$. In doing so, it obtains the $C_{k\ell m}$ parameters which describe the amplitude of each spherical wave (defined by $\ell$, $m$) that contributes to the wavefunction of a detached electron with wave vector $\vec{k}$.[63] We use these parameters to determine the partial wave character of the electrons detached to produce the two neutral states of tBuOO examined in this work. To get the best estimate of this partial wave character, we use the $C_{k\ell m}$ values obtained for the highest kinetic energies in the ezDyson calculations, which was 1.05 eV. Then, the partial wave characters are defined by

$$P_\ell = \sum_{m=-\ell}^{\ell} C^2_{k_{max}\ell m}, \tag{5.3}$$

where $k_{max}$ is the magnitude of the photoelectron wave vector, in atomic units, for an eKE of 1.05 eV. The fractional partial wave component is then given by

$$f_\ell = \frac{P_\ell}{\sum_{\ell=0}^{5} P_\ell}. \tag{5.4}$$

The results of this calculation for the $\tilde{X}\ ^2A''\leftarrow\tilde{X}\ ^1A'$ and $\tilde{A}\ ^2A'\leftarrow\tilde{X}\ ^1A'$ detachment transitions are provided in Table 5.4, and show that of the two, the $\tilde{X}\ ^2A''\leftarrow\tilde{X}\ ^1A'$ detachment transition produces photoelectrons with greater $\ell > 0$ character.

**Table 5.4:** Fractional partial wave decomposition (Eq. 5.4) for a photoelectron with eKE = 1.05 eV for detachment to the ground and excited neutral states of tBuOO.

| $\ell$ | $\tilde{X}\ ^2A''\leftarrow\tilde{X}\ ^1A'$ | $\tilde{A}\ ^2A'\leftarrow\tilde{X}\ ^1A'$ |
|---|---|---|
| 0 | 0.220 | 0.668 |
| 1 | 0.620 | 0.296 |
| 2 | 0.101 | 0.011 |
| 3 | 0.052 | 0.022 |
| 4 | 0.006 | 0.003 |
| 5 | 0.000 | 0.000 |

# Chapter 6

# *ortho*-, *meta*-, and *para*-Pyridyl

The content and figures of this chapter are reprinted or adapted with permission from J. A. DeVine, M. C. Babin, K. Blackford, D. M. Neumark, "High-resolution photoelectron spectroscopy of the pyridinide isomers" *J. Chem. Phys.* **151**, 064302 (2019).

## Abstract

Isomer-specific, high-resolution photoelectron spectra of cryogenically-cooled pyridinide anions obtained using slow photoelectron velocity-map imaging are presented. New vibrational structure in the detachment spectrum of *para*-pyridinide is resolved, and the spectra of *meta*- and *ortho*-pyridinide are reported for the first time. These spectra yield electron affinities of 1.4797(5), 1.4473(5), and 0.8669(7) eV for the *para*-, *meta*- and *ortho*-pyridyl radicals, respectively, as well as a number of vibrational frequencies for each neutral isomer. While most of the resolved structure in all three spectra is readily assigned by comparison to B3LYP/6-311+G* Franck-Condon simulations, the *para*-pyridinide spectrum shows newly-resolved fine structure attributed to anharmonic coupling within the vibrational manifold of the corresponding neutral radical. Isomeric trends in the photoelectron angular distributions are rationalized by approximating the detached anion orbitals as superpositions of $s$, $p$, and $d$-like hydrogenic orbitals, based on an application of Sanov's generalized mixing model [*J. Chem. Phys.* **141**, 124312 (2014)]. The presented experimental and theoretical results are used to address the relative energies of the anion and neutral isomers, as well as the site-specific bond dissociation energies of pyridine.

# 6.1 Introduction

Nitrogen-containing aromatic heterocycles such as pyridine ($C_5H_5N$) are common building blocks of coal and other high energy density materials.[80,81,251,252] Combustion of these species contributes to atmospheric $NO_x$ formation,[218] thus studies of the thermal decomposition of pyridine are important for understanding the environmental impact of such fuels.[253] The chemistry of pyridine and its derivatives are also of interest to astronomers, particularly following the observation of nitrogen-containing compounds in the atmosphere of Titan.[254,255] Mechanistic studies of the thermal decomposition of pyridine have established that the first step is hydrogen loss resulting in formation of the *o*-, *m*-, or *p*-pyridyl radical, shown in Figure 6.1.[256–260] Due to the prevalence of pyridine and the products of its decomposition in a wide range of chemical environments, spectroscopic characterization of the pyridyl radicals is of considerable interest. In this work, high-resolution anion photoelectron spectroscopy of cryogenically-cooled pyridinide anions is used to obtain isomer-specific spectra that reflect the vibronic structure of the neutral pyridyl radicals, providing quantitative and qualitative insight into these species.

Pyridyl radicals have been characterized using several methods aimed at understanding their inherent molecular properties as well as their reactivity and thermochemistry.[90,261–263] The H-loss channels that result from ultraviolet photodissociation of *m*- and *o*-pyridyl have been observed by Lucas and coworkers,[264,265] who used photolysis of 3- and 2-bromopyridine to generate the desired radical isomers. Korte *et al.*[266] used a similar method based on photolytic cleavage of a halogen-carbon bond to obtain a matrix infrared spectrum of the products, reporting several weak vibrational signatures attributed to the pyridyl radicals. Electron spin resonance spectroscopy, which is specifically sensitive to radical species, has been used to observe the pyridyl radicals in inert matrices[267–269] and in aqueous solution.[270]

Whereas free radicals are typically highly reactive species that can be difficult to isolate in a laboratory experiment, the corresponding anions are closed-shell and relatively long-lived in the gas phase, and can readily be mass-selected prior to spectroscopic investigation. Thus, a versatile approach to characterization of a neutral radical is anion photoelectron spectroscopy (PES) of the corresponding mass-selected anion.[271] PES of molecular anions can be used to simultaneously probe the electronic and vibrational structure of the corresponding neutrals,

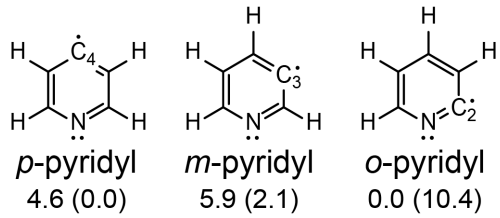


**Figure 6.1:** The three isomeric forms of the pyridyl radical. The zero-point corrected B3LYP/6-311+G* relative energies of the neutral (anion) isomers are provided in units of kcal $mol^{-1}$.

provided the spectral resolution is sufficient, and the photoelectron angular dependence can provide insight into the molecular orbital on the anion from which the electron is detached.[26] This strategy has been used previously by several groups to obtain detachment spectra of anions formed by deprotonation of pyridine, providing spectroscopic access to the *p*-pyridyl radical by photodetachment of the *p*-pyridinide anion.[25,91,272] In all of these studies, pyridinide anions were generated by gas phase deprotonation of pyridine, so only the *p*-pyridinide isomer was formed owing to the observed regioselectivity of this process.[273]

To date, the highest-resolution photoelectron spectrum of the *p*-pyridinide anion is that reported by Wren and coworkers,[272] who observed an isolated vibrational origin with 11 meV full-width at half-maximum (fwhm), followed by increasingly complex and partially-resolved vibrational structure. This work provided an electron affinity (EA) of 1.480(6) eV as well as two vibrational frequencies (600 ± 20 and 1010 ± 50 $cm^{-1}$) for the *p*-pyridyl radical. With experimental gas phase acidity measurements, this EA was used to obtain a bond dissociation enthalpy (BDE) of 110.4 ± 2.0 kcal $mol^{-1}$ for the $C_4$-H bond (see Fig. 6.1) of pyridine. Subsequent work using photoelectron imaging of the *p*-pyridinide anion was reported by Culberson and coworkers.[25] This spectrum did not show any vibrational structure, but the photoelectron angular distribution (PAD) was used as a test case for the mixed-*sp* model developed by Sanov,[24] which provides an intuitive framework for understanding how experimental PADs are related to the hybridization of anion orbitals. This model has been successfully used to assess the PADs for detachment from a number of organic anions.[91,249,274]

Slow electron velocity-map imaging (SEVI) is a variant of traditional anion PES wherein a velocity-map imaging (VMI) detection scheme and a tunable detachment laser are combined to obtain narrow windows of the photoelectron spectrum with sub-meV resolution, which are then concatenated to give a full high-resolution spectrum.[17,157] By cooling ions to internal temperatures of ∼10 K prior to detachment (cryo-SEVI), rotational broadening and spectral congestion are minimized, yielding transitions as narrow as 1.2 $cm^{-1}$ fwhm that reflect the vibronic structure of the corresponding neutral.[19,158] Cryo-SEVI has been highly successful in revealing subtleties in the vibronic structure of a number of aromatic radicals;[32,35,36,43,249] in cases where multiple radical isomers are possible, reaction of appropriate trimethylsilyl (TMS) substituted precursors with fluoride anions has enabled acquisition of isomer-specific spectra.[35,43,249]

Here, we use this approach to obtain cryo-SEVI spectra for the three anion isomers of deprotonated pyridine. These results represent the first reported photoelectron spectra of the *m*- and *o*-pyridinide anions, and provide a substantial improvement in resolution for the *p*-pyridinide detachment spectrum. Comparison of the spectra to B3LYP/6-311+G* calculations enables extraction of multiple vibrational frequencies and EAs for all three radical isomers. While the majority of features in all three spectra are well-described by harmonic Franck-Condon simulations, anharmonic mixing between vibrational levels of the *p*-pyridyl radical is proposed as the cause of ∼10 $cm^{-1}$ experimental peak splittings observed for several detachment transitions from the corresponding anion isomer. To describe the photoelectron angular distributions for all three anions in a unified framework, the mixed-*sp* model has been expanded to include a *d*-component following the generalized mixing model

developed by Sanov,[28] and the results of this treatment highlight isomeric trends in orbital hybridization for deprotonated pyridine. Finally, the experimental and theoretical results presented here are used to consider the origin of the relative isomeric stabilities for both charge states, and estimates of the C-H BDEs of pyridine are obtained using a combined experimental-theoretical approach.

## 6.2 Experimental Methods

The cryo-SEVI method is described in detail in Chapter 2. To generate pyridinide anions, a gas mixture consisting of trace $NF_3$ in He is passed over a temperature-controlled cartridge containing a molecular precursor. The precursor is entrained in the carrier gas, which then undergoes supersonic expansion through an Even-Lavie valve fitted with a circular filament ionizer.[164] Injection of electrons from the ionizer into the gas expansion results in dissociative electron attachment to $NF_3$ forming fluoride anions, which react with the molecular precursor to form the ion of interest. This method of ion generation is described in Section 2.1.1.

The use of pyridine as the molecular precursor resulted in formation of both *m*- and *p*-pyridinide, as shown in Figure 6.8. To obtain isomer-specific spectra, the valve cartridge was loaded with the appropriate isomer of trimethylsilyl(TMS)pyridine, which then reacted with $F^-$ in the pulsed gas expansion to produce the desired anion isomer and TMS fluoride.[167,205] 2-(TMS)pyridine was purchased from Sigma Aldrich and used as the precursor for generation of *o*-pyridinide. The precursors for *m*- and *p*-pyridinide were synthesized as described in Section 6.7.1. To prevent isomerization of the 4-(TMS)pyridine precursor, the Even-Lavie valve body was held at a temperature of 25 °C.

## 6.3 Computational Methods

With the exception of the thermochemical calculations detailed below, all computations were carried out at the B3LYP/6-311+G* level using QChem version 5.1.[55] Geometry optimizations for all three anion and neutral isomers were performed giving the results provided in Tables 6.6-6.8. Harmonic frequency calculations were also performed for all six species, and the resulting frequencies for all anion and neutral isomers are provided in Table 6.9.

The B3LYP/6-311+G* geometries, harmonic frequencies, and normal mode displacements were used as input for the ezSpectrum software package,[57] which calculates the Franck-Condon (FC) factors for detachment from the anion ground state to various vibrational levels of the neutral, including Duschinsky mixing to account for differences between anion and neutral normal modes. To provide a better match with experimental frequencies, the shifts from the origin were scaled by 0.975, 0.977, and 0.979 in the *p*-, *m*-, and *o*-pyridinide FC simulations, respectively. To further improve agreement with experiment for the *o*-pyridinide spectrum, small displacements along the $\nu_5$ mode were applied to the B3LYP/6-311+G* equilibrium geometry of *o*-pyridyl used to calculate the FC profile for this isomer, as de-

scribed in Section 6.5.1. A comparison of the B3LYP/6-311+G* equilibrium and shifted FC profiles is presented in Figure 6.9, and the neutral geometry used for the FC simulation which best matches experiment is summarized in Table 6.10.

To estimate gas-phase acidities for the three deprotonation sites of pyridine, thermochemical calculations were carried out using Gaussian 16.[54] Absolute enthalpies of pyridine and the three pyridinide anions at T = 298.15 K, as well as those of the neutral radicals, were calculated using the CBS-QB3 method.[275,276] Experimental-theoretical gas-phase acidities for the $C_3$ and $C_2$ positions are calculated using the experimental $\Delta H^{\circ}_{acid}(C_4)$ of the $C_4$ position, which is the only position for which an experimental measurement of this quantity is available. With the differences in absolute enthalpies defined as

$$\delta_n = H^{298}(n \text{ - pyridinide}) - H^{298}(4 \text{ - pyridinide}), \tag{6.1}$$

the acidities of the two carbon positions for which there are no experimental measurements of $\Delta H^{\circ}_{acid}$ are approximated as $\Delta H^{\circ}_{acid}(C_n) = \delta_n + \Delta H^{\circ}_{acid}(C_4)$. The calculated absolute enthalpies for all three anion and neutral isomers, as well as pyridine, are provided in Table 6.11.

## 6.4 Results

The TMS-substituted molecular precursors used for anion generation enabled acquisition of isomer-specific cryo-SEVI spectra of *p*-, *m*-, and *o*-pyridinide, shown in Figures 6.2, 6.3, and 6.4, respectively. In all cases, blue traces represent overview scans taken at relatively high photon energies, and black traces are low-eKE, high-resolution scans taken closer to threshold. The red stick spectra show the Franck-Condon simulations used for vibrational assignments and will be discussed in more detail in the following section.

The cryo-SEVI spectrum of *p*-pyridinide (Fig. 6.2) exhibits a number of well-resolved transitions (p1-p23) with typical peak widths of 8-10 $cm^{-1}$ fwhm. The binding energies of these features are summarized in Table 6.12. The spectrum in Figure 6.2 represents a substantial improvement over prior results, and the lowest eBE peak at p1 gives an EA of 1.4797(5) eV for the *p*-pyridyl radical. The vibrational progressions reported by Wren and coworkers[272] are observed here in higher resolution, giving refined frequencies of 603(5) $cm^{-1}$ (p1-p2-p10-p17) and 1020(6) $cm^{-1}$ (p1-p4, p2-p9, etc.). In addition to these previously-resolved progressions, new underlying vibrational structure is observed. As shown in Figure 6.5, high-resolution scans taken close to threshold show that feature p10 is a doublet of peaks (p10a/b) split by 9 $cm^{-1}$. Similar splittings are found for peaks p17, p22, and p23.

The cryo-SEVI spectrum of *m*-pyridinide (Figure 6.3) represents the first reported PE spectrum for this anion isomer, and shows vibrational structure similar to that observed for the *para* isomer. Features in the m1-m28 series (Table 6.13) have typical peak widths of 9-11 $cm^{-1}$ fwhm. The first peak occurs at a slightly lower eBE than is seen in the *p*-pyridinide spectrum, giving an EA of 1.4473(5) eV for the *m*-pyridyl radical. The vibrational structure in this spectrum shows a dominant progression (m1-m3-m8-m16-m25) with ∼650

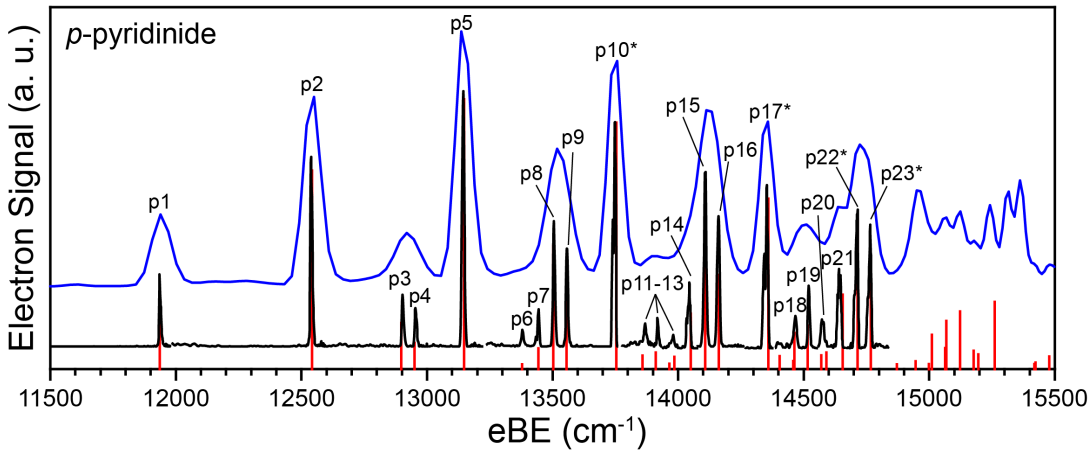


**Figure 6.2:** Cryo-SEVI spectrum of *p*-pyridinide. The blue trace corresponds to an overview spectrum taken with a photon energy of 15873 $cm^{-1}$, and the black traces are high-resolution scans taken near threshold. A Franck-Condon simulation based on B3LYP/6-311+G* results is shown as red sticks, where the shifts have been scaled by a factor of 0.975.

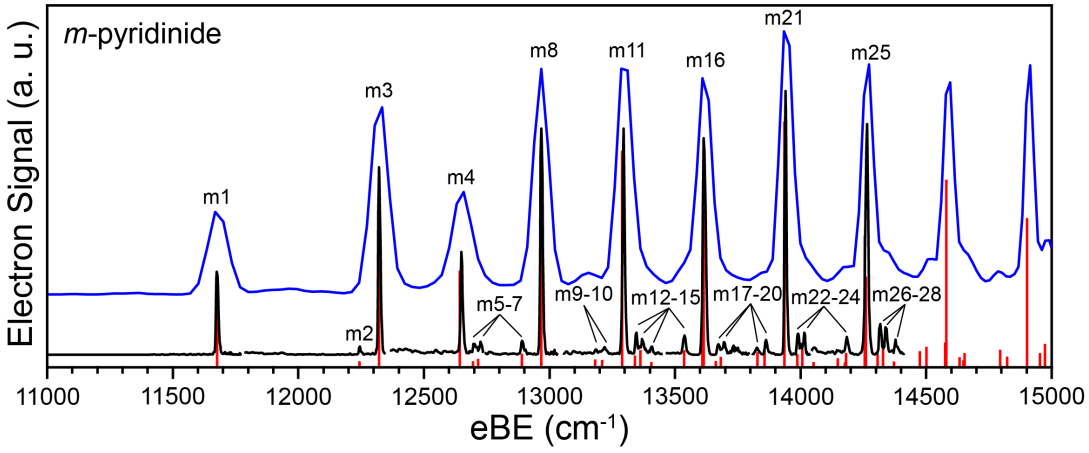


**Figure 6.3:** Cryo-SEVI spectrum of *m*-pyridinide. The blue trace corresponds to an overview spectrum taken with a photon energy of 15873 $cm^{-1}$, and the black traces are high-resolution scans taken near threshold. A Franck-Condon simulation based on B3LYP/6-311+G* results is shown as red sticks, where the shifts have been scaled by a factor of 0.977.

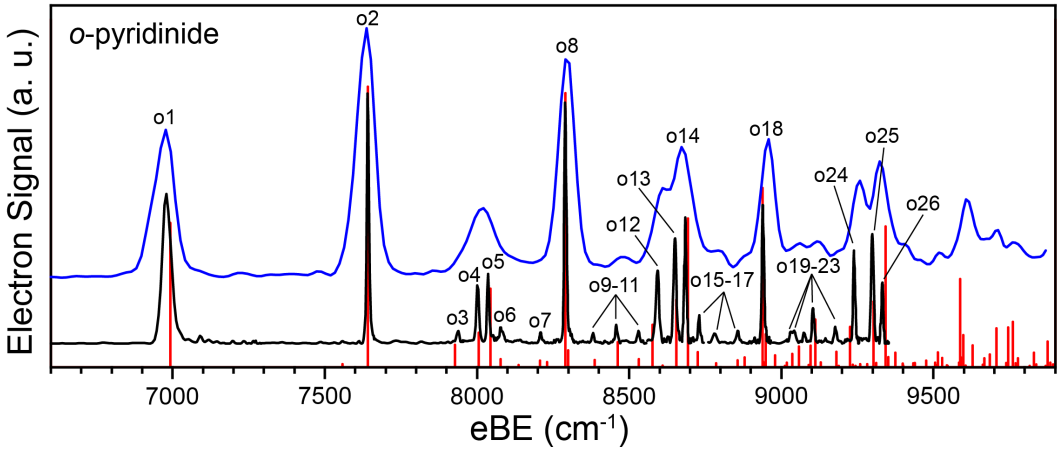


**Figure 6.4:** Cryo-SEVI spectrum of *o*-pyridinide. The blue trace corresponds to an overview spectrum taken with a photon energy of 11300 $cm^{-1}$, and the black traces are high-resolution scans taken near threshold. The Franck-Condon simulation based on the shifted neutral geometry is shown as a red stick spectrum, where the neutral frequencies have been scaled by a factor of 0.979.

$cm^{-1}$ splitting, and the remaining intense features observed in the overview spectrum (m4, m11, m21) correspond to a modulation of this progression by a mode with frequency 974(6) $cm^{-1}$. In addition, the high-resolution traces show a number of weak transitions that are obscured by more intense features in the overview spectrum.

The cryo-SEVI spectrum of the *o*-pyridinide isomer, shown in Figure 6.4, comprises a number of features (o1-o25) with similar resolution to that obtained for the other two anion isomers. The peak positions and widths are summarized in Table 6.14. As is the case for the other isomers, the cryo-SEVI spectrum of *o*-pyridinide is dominated by a single progression

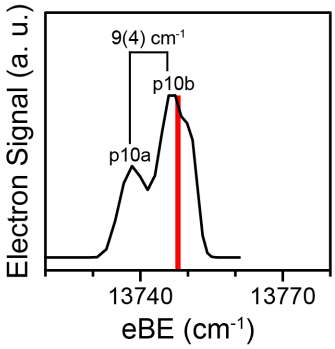


**Figure 6.5:** High-resolution scan showing the splitting of feature p10 in the cryo-SEVI spectrum of *p*-pyridinide. The red stick shows the $9_0^3$ transition of the *p*-pyridinide B3LYP/6-311+G* FC simulation.

(o1-o2-o8-o18), which is modulated by several less intense patterns. This dominant progression gives a harmonic frequency of 649(5) $cm^{-1}$ for the *o*-pyridyl radical. In addition, a closely-spaced doublet of peaks split by 10 $cm^{-1}$ (o19/o20) is resolved. This splitting may be seen more clearly in Figure 6.10.

The laser scheme used to obtain the high-resolution spectra of the *o*-pyridinide anion involves a single-pass Raman shifter cell, which extends the tuning range of the dye laser system to photon energies as low as ∼7300 $cm^{-1}$.[38] This is still several hundred $cm^{-1}$ above the photon energies that would be required to obtain optimal resolution for the vibrational origin (o1), and as a result this feature has a larger reported width (30 $cm^{-1}$ fwhm) than the higher-eBE features o2-o26 (7-10 $cm^{-1}$ fwhm). Thus, rather than using feature o1 to extract the electron affinity of the neutral radical, we take the EA to be given by the eBE of the first feature in the dominant progression (o2) minus the harmonic frequency of 649(5) $cm^{-1}$ extracted from the dominant progression, giving a final EA of 0.8669(7) eV for the *o*-pyridyl radical. This value of the EA is used to calculate the shifts of features o2-o26 in Table 6.14.

## 6.5 Discussion

### 6.5.1 Vibrational Assignments

#### *p*-pyridinide

The cryo-SEVI spectrum of *p*-pyridinide (Fig. 6.2) shows excellent agreement with the B3LYP/6-311+G* Franck-Condon simulation, providing vibrational assignments for the majority of observed features as transitions terminating in FC-allowed vibrational levels of *p*-pyridyl. These assignments are presented in Table 6.12. The dominant progression (p1-p2-p10-p17) is assigned to the $\nu_9$ mode, a ring distortion mode which heavily involves the radical-centered $C_3$-$C_4$-$C_3$ angle (see Fig. 6.11). The high degree of FC activity for this mode arises from the relatively large change in this geometrical parameter, which increases

**Table 6.1:** Molecular parameters of the *p*-pyridyl radical obtained from the cryo-SEVI spectra of the corresponding anion. Theoretical values obtained from a harmonic B3LYP/6-311+G* analysis are also provided.

| | SEVI | B3LYP |
|---|---|---|
| EA, eV | 1.4797 (5) | 1.4725 |
| $\nu_3$, $cm^{-1}$ | 1509 (4) | 1543 |
| $\nu_4$, $cm^{-1}$ | 1445 (5) | 1476 |
| $\nu_7$, $cm^{-1}$ | 1020 (6) | 1038 |
| $\nu_8$, $cm^{-1}$ | 969 (6) | 983 |
| $\nu_9$, $cm^{-1}$ | 603 (5) | 620 |

from 110.2 to 124.0° between the anion and neutral equilibrium geometries. Four other vibrational frequencies are extracted based on the positions of the corresponding vibrational fundamentals relative to the vibrational origin (p3-p7). These frequencies are summarized in Table 6.1, where they are compared to the calculated B3LYP/6-311+G* harmonic values.

The high-resolution scan for feature p10 (Figure 6.5) reveals that this peak in fact consists of two separate transitions (p10a/b), while only a single transition ($9_0^3$) is predicted in the FC simulation. Similar splittings are observed for features p17, p22, and p23. Given the relatively small magnitude of the observed splitting, a likely source of the unexplained features is a Fermi resonance between the $3\nu_9$ level (which plays a role in all FC transitions showing the $\sim$10 cm$^{-1}$ splitting) and some other totally-symmetric vibrational level. This level would then gain its observed FC-activity through anharmonic mixing with the $3\nu_9$ level. Coupling of this nature is particularly likely for levels that are close in energy, such as the Fermi resonance between the $1\nu_{39}$ and $1\nu_{59} + 1\nu_{61}$ vibrational levels of the 1-anthracenyl radical, which was found to result in the appearance of the $59_0^1 61_0^1$ detachment transition in the cryo-SEVI spectrum of the 1-anthracenyl anion.[43] In that case, the totally symmetric $1\nu_{39}$ vibrational state interacts with a totally-symmetric combination band of non-totally symmetric modes, resulting in an 8 cm$^{-1}$ splitting in the $\nu_{39}$ fundamental (as well as FC-predicted combination bands involving this mode).

Consideration of the harmonic frequencies of the *p*-pyridyl radical (Table 6.9) shows that the closest totally-symmetric combination band which could give rise to the 10 cm$^{-1}$ splitting is the $1\nu_8 + 2\nu_{16}$ level, whose calculated harmonic energy is 9 cm$^{-1}$ higher than that of $3\nu_9$. Thus, we tentatively assign the state which interacts with $3\nu_9$ to give rise to the splitting observed for features p10a/b (p17a/b, p22a/b, p23a/b) to the $8_0^1 16_0^2$ ($8_0^1 9_0^1 16_0^2$, $8_0^2 16_0^2$, $7_0^1 8_0^1 16_0^2$) transition. As each pair of states is strongly coupled, the neutral levels accessed in each transition likely corresponds to an admixture of the two vibrational levels. Keeping this in mind, we may treat the $\nu_9$ progression as an anharmonic series (Section 6.7.2 and Eq. 6.7), and this showed that p10b is most appropriate to assign as the FC-allowed detachment transition; similarly, p17b, p22b, and p23b are assigned to the FC-allowed $9_0^4$, $8_0^1 9_0^3$, and $7_0^1 9_0^3$ transitions, respectively, suggesting that peaks p10a, p17a, p22a, and p23a are best described as the $8_0^1 16_0^2$, $8_0^1 9_0^1 16_0^2$, $8_0^2 16_0^2$, and $7_0^1 8_0^1 16_0^2$ transitions, respectively.

### *m*-pyridinide

The B3LYP/6-311+G* FC simulation for detachment from *m*-pyridinide, shown as red sticks in Figure 6.3, accounts for all observed transitions in the cryo-SEVI spectrum for this isomer, allowing for assignment of peaks m1-m28 as detachment transitions terminating in totally symmetric vibrational levels of the *m*-pyridyl radical. These assignments are provided in Table 6.13. The dominant progression (m1-m3-m8-m16-m25) is attributed to the $\nu_{16}$ vibrational mode, a ring distortion that involves the $C_4$-$C_3$-$C_2$ bond angle centered on the deprotonated carbon atom. The second-most FC active mode which modulates the $\nu_{16}$ progression (m4, m11, m21) is identified as $\nu_{17}$, another ring-distortion mode that involves the $C_2$-N-$C_2$ and $C_3$-$C_4$-$C_3$ angles.

**Table 6.2:** Molecular parameters of the *m*-pyridyl radical obtained from the cryo-SEVI spectra of the corresponding anion. Theoretical values obtained from a harmonic B3LYP/6-311+G* analysis are also provided, as are available vibrational frequencies observed previously in an Ar matrix.

| | SEVI | B3LYP | matrix IR[266] |
|---|---|---|---|
| EA, eV | 1.4473 (5) | 1.4391 | |
| $\nu_6$, cm$^{-1}$ | 1509 (6) | 1543 | 1499.9 |
| $\nu_{12}$, cm$^{-1}$ | 1085 (6) | 1110 | 1084.9 |
| $\nu_{13}$, cm$^{-1}$ | 1050 (8) | 1065 | 1035.9 |
| $\nu_{14}$, cm$^{-1}$ | 1027 (8) | 1044 | |
| $\nu_{15}$, cm$^{-1}$ | 974 (6) | 990 | |
| $\nu_{16}$, cm$^{-1}$ | 646 (6) | 662 | 646.3 |
| $\nu_{17}$, cm$^{-1}$ | 568 (5) | 581 | 569.5 |

A total of 7 vibrational modes of *m*-pyridyl play a role in the spectrum; these are pictured in Figure 6.12, and their experimental frequencies are reported in Table 6.2. Several of the measured frequencies have been identified previously in the matrix-IR study of the products formed by photolysis of 3-iodopyridine,[266] and the reported IR frequencies are included in Table 6.2. As was the case for the *para* isomer, the strong involvement of ring-distortion modes involving the $C_4$-$C_3$-$C_2$ angle centered on the radical carbon can be attributed to the difference in equilibrium values between anion and neutral (110.8 and 123.8°, respectively).

### *o*-pyridinide

The experimental cryo-SEVI spectrum of *o*-pyridinide shows excellent agreement with the Franck-Condon simulation in Figure 6.4, enabling assignment of all resolved features (Table 6.14). The dominant progression (o1-o2-o8-o18) is assigned to the $\nu_{16}$ mode, an in-plane ring distortion which involves bending of the $C_2$-N-$C_2$ angle as well as stretching of the $C_2$-$C_3$ bonds (Figure 6.13). Other vibrational fundamentals (o3-o6, o9-o11) are also observed; while the eBEs of these fundamentals would typically be used to extract vibrational frequencies by calculating their shifts relative to the vibrational origin (o1), we have instead used the $16_0^1$ (o2) and $x_0^1 16_0^1$ (o7, o12, o13, o14, o15, o16, o19, o22, and o23) peaks to obtain the vibrational frequencies $\nu_x$ presented in Table 6.3, due to the narrower peak width obtained for feature o2 relative to o1. Ten vibrational frequencies for the *o*-pyridyl radical are extracted in this manner, with uncertainties ranging from 4 to 7 cm$^{-1}$. Two of these frequencies, $\nu_{13} = 1043(5)$ cm$^{-1}$ and $\nu_{17} = 568(5)$ cm$^{-1}$, were previously assigned in the matrix isolation study of Korte and coworkers,[266] who gave frequencies of 1044 and 565 cm$^{-1}$, respectively.

The FC simulation based on the B3LYP/6-311+G* equilibrium geometries (Fig. 6.9a) predicts that a relatively intense feature, corresponding to the $5_0^1$ transition, should appear

between features o12 ($15_0^1 16_0^1$) and o13 ($14_0^1 16_0^1$). This feature was not observed in the experimental spectrum. Such a discrepancy can result from slight inaccuracies in the calculated anion/neutral geometries, which then leads to over- or under-estimation of the displacement along particular vibrational modes corresponding to anomalously high or low FC intensities. To investigate this possibility in the *o*-pyridinide detachment spectrum, a number of FC simulations were performed for detachment from the B3LYP/6-311+G* equilibrium anion geometry to a neutral geometry defined by $\vec{r}^{(i)} = \vec{r}_{eq}^{(i)} + \xi \vec{q}_5^{(i)}$, where $\vec{r}_{eq}^{(i)}$ is the B3LYP/6-311+G* equilibrium position of atom $i$, $\vec{q}_5^{i}$ is the atomic displacement vector for atom $i$ associated with $\nu_5$, and $\xi$ defines the magnitude of the shift. This parameter was varied to yield shifted neutral geometries, which was used to calculate the Franck-Condon profile for detachment from the equilibrium anion geometry. This enabled determination of the magnitude of shift $\xi$ necessary to account for the absence of the $5_0^1$ transition in the experimental spectrum.

As shown in Figure 6.9, the FC intensity of this transition is approximately quadratic in $\xi$, reaching a minimum at a shift of $\xi = -0.0625$. The corresponding root-mean-square change in the neutral geometry, defined by $[\sum(\vec{r}^{(i)} - \vec{r}_{eq}^{(i)})]^{1/2}$, is only 0.062 Å, with the most substantial change corresponding to a 0.06 Å increase in the bond length between the nitrogen and the deprotonated carbon atom (see Table 6.10). Given the fairly small geometry adjustment required to bring the calculated intensity of the $\nu_5$ fundamental to near-zero, we take the absence of the transition in the cryo-SEVI spectrum to be a consequence of the true neutral geometry, which differs slightly from that predicted by B3LYP/6-311+G* calculations. The $\xi = -0.0625$ FC simulation is shown alongside the experimental results in

**Table 6.3:** Molecular parameters of the *o*-pyridyl radical obtained from the cryo-SEVI spectra of the corresponding anion. Theoretical values obtained from a harmonic B3LYP/6-311+G* analysis are also provided.

| | SEVI | B3LYP |
|---|---|---|
| EA, eV | 0.8669 (7) | 0.8236 |
| $\nu_6$, cm$^{-1}$ | 1536 (5) | 1572 |
| $\nu_7$, cm$^{-1}$ | 1463 (5) | 1502 |
| $\nu_8$, cm$^{-1}$ | 1390 (4) | 1424 |
| $\nu_{11}$, cm$^{-1}$ | 1140 (7) | 1169 |
| $\nu_{12}$, cm$^{-1}$ | 1088 (4) | 1108 |
| $\nu_{13}$, cm$^{-1}$ | 1043 (5) | 1074 |
| $\nu_{14}$, cm$^{-1}$ | 1010 (5) | 1035 |
| $\nu_{15}$, cm$^{-1}$ | 951 (6) | 956 |
| $\nu_{16}$, cm$^{-1}$ | 649 (5) | 663 |
| $\nu_{17}$, cm$^{-1}$ | 568 (5) | 578 |

Figure 6.4, and a comparison of this simulation to that obtained using the neutral equilibrium B3LYP/6-311+G* geometry is provided in Figure 6.9.

### 6.5.2 Photoelectron Angular Distributions

Figure 6.6 shows the eKE-dependence of the anisotropy parameters observed for detachment from the three pyridinide anions. It was found that for each isomer, all resolved features show similar anisotropies, indicating that each spectrum in Figs. 6.2, 6.3, and 6.4 involves a single electronic transition. The PADs for the three isomers are clearly different; the *para* and *meta* isomers show perpendicular detachment ($\beta < 0$), with the *para* isomer yielding slightly more negative values of $\beta$. The *ortho* isomer exhibits parallel detachment ($\beta > 0$) at low-eKEs that tends towards near-zero anisotropies as eKE increases.

The measured PADs reflect the angular momentum composition of the outgoing electron, which in turn is related to the anion orbital from which detachment occurs. For the pyridinide anions, the relevant orbitals are taken to be the highest-occupied molecular orbitals (HOMOs) shown in Figure 6.7. These orbitals show that as the site of deprotonation moves towards the heteroatom, the resultant anion HOMO becomes more delocalized, with more involvement of the heteroatom. In particular, the HOMO of the *ortho* isomer shows considerable electron density around the nitrogen atom, as well as distinct nodal structure along the $C_2$-N bond. Given the clear distinctions between the observed PADs, we aim to develop a conceptual framework that can connect these isomeric trends.

The anisotropy parameter for detachment from an anion orbital with well-defined angular momentum $l$ is described by the Cooper-Zare equation (Eq. 6.8).[22] For $l > 0$, the outgoing electron is a superposition of $l+1$ and $l-1$ partial waves; at low eKEs, the relative scaling of these detachment channels may be determined from the Wigner threshold law,[21] allowing for a direct expression of $\beta$ as a function of eKE (Section 6.7.3). For molecules, $l$ is not a good

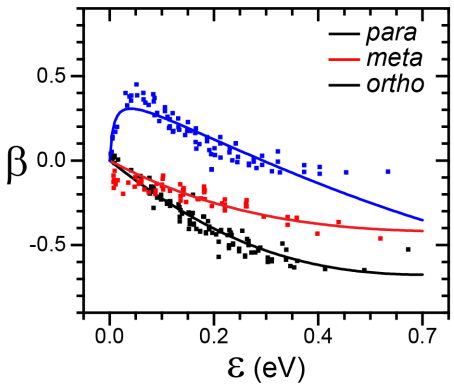


**Figure 6.6:** Anisotropy parameters observed for photodetachment from *p*- (black), *m*- (red), and *o*-pyridinide (blue) as a function of electron kinetic energy. The solid lines show the results of fitting the experimental PADs to the mixed-*spd* model.

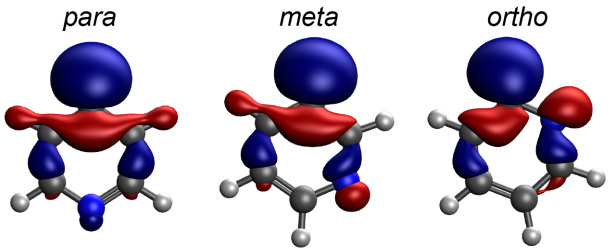


**Figure 6.7:** Highest-occupied molecular orbitals of the three pyridinide anions as determined at the B3LYP/6-311+G* level of theory.

quantum number, and such a single-$l$ treatment is unlikely to adequately describe observed angular distributions. Previously, the PAD for detachment from *p*-pyridinide has been modeled using the mixed-$sp$ formulation of Sanov and coworkers (Section 6.7.3),[24,25] where the detached anion orbital is assumed to be a combination of an $s$ ($|0\rangle$) and $p$ ($|1\rangle$) component with fractional $p$-character $\gamma_1$, i.e. $|\Psi_{MO}\rangle = \sqrt{1-\gamma_1}\,|0\rangle + \sqrt{\gamma_1}\,|1\rangle$. The basis functions are taken to be hydrogenic $s$ and $p$ orbitals (Eq. 6.11) defined by charge parameters $Z_0$ and $Z_1$, which fully determine the Hanstorp coefficients $A_1$ and $B_1$ (Eq. 6.12) describing the relative scaling of different detachment channels in the Wigner limit.[21,23] Here, $A_1$ describes the relative scaling between the $p \rightarrow d$ and $p \rightarrow s$ detachment channels, and $B_1$ quantifies the relative scaling for the $s \rightarrow p$ and $p \rightarrow s$ channels.

With these assumptions, an explicit expression for the eKE($\varepsilon$)-dependence of the anisotropy parameter may then be derived in terms of the fractional $p$-character $\gamma_1$ as well as the $A_1$ and $B_1$ coefficients (Eq. 6.13). For detachment from an orbital localized on a particular atomic center, the choice of $A_1$ and $B_1$ is fairly straightforward; in the treatment of *p*-pyridinide and other deprotonated aromatic anions,[91] the basis set parametrization was set to that typical for detachment from a $2s2p$ orbital centered on a carbon atom, $A_1 = 0.75$ eV$^{-1}$ and $B_1 = 8A_1/3$ (corresponding to $Z_0 = Z_1 = 0.885$).[27,212] Using these, Eq. 6.13 gives a single-parameter expression for $\beta(\varepsilon)$ that can be fit to experimental data to extract the fractional $p$-character of the detached orbital, giving a direct link between the experimental PAD and the orbital hybridization of the anion.[91,249]

The formulation of the mixed-$sp$ model has since been expanded to a generalized mixing model,[28] described in Section 6.7.3. In the generalized model, the detached MO is taken to be a linear combination of an arbitrary number of angular momentum components, $|\Psi_{MO}\rangle = \sum_l \sqrt{\gamma_l}\,|l\rangle$. This expansion of $|\Psi_{MO}\rangle$ in terms of an atomic orbital basis set is valid for any orbital so long as it is centered about a particular point in space; thus while these mixing models have typically been applied to orbitals which are primarily localized on a particular atom, a more delocalized orbital may also be treated so long as it is reasonably described by a single-center function. The resulting expression for the anisotropy parameter is given in Eq. 6.14.

For *p*-pyridinide, the C-centered $2s2p$ model is a logical choice for treating the anion HOMO, and the strong resemblance between the *m*- and *p*-pyridinide orbitals suggests that

**Table 6.4:** Fractional $s$, $p$, and $d$-character of the detached orbital of each of the three pyridinide anion isomers as determined by application of the mixed-*spd* model to the experimental results. Uncertainties correspond to the standard error obtained from a least-squares fitting of the experimental data, and $\gamma_0 = 1 - \gamma_1 - \gamma_2$.

| | $\gamma_0$ | $\gamma_1$ | $\gamma_2$ |
|---|---|---|---|
| *para* | 0.12 | 0.88 (3) | 0.00 (4) |
| *meta* | 0.22 | 0.71 (5) | 0.07 (6) |
| *ortho* | 0.30 | 0.03 (2) | 0.67 (12) |

this is also an appropriate starting point for describing the *meta* isomer. However, the *o*-pyridinide HOMO (Figure 6.7) is better described as being centered along the $C_2$-N bond, and this picture suggests that appreciable $d$-character should be accounted for in an adequate treatment of this isomer. Thus, to understand the PADs of all three pyridinide isomers within a single conceptual framework, we have developed a mixed-*spd* model for photoelectron angular distributions as determined by Sanov's general formula.

The mixed-*spd* basis set consists of the same $2s$ and $2p$ hydrogenic orbitals (parametrized by $Z_0$ and $Z_1$) as well as a $3d$ function (Eq. 6.15, with charge parameter $Z_2$), so that

$$|\Psi_{spd}\rangle = \sqrt{1-\gamma_1-\gamma_2}\,|0\rangle + \sqrt{\gamma_1}\,|1\rangle + \sqrt{\gamma_2}\,|2\rangle\,. \tag{6.2}$$

As described in Section 6.7.3, the introduction of an $l = 2$ contribution to the molecular orbital results in two new Hanstorp coefficients, $A_2$ and $B_2$, which are fully determined by the basis set parametrization in a similar manner as $A_1$ and $B_1$ (Eq. 6.16). Here, $A_2$ gives the relative scaling of the cross sections for the $d \rightarrow f$ and $d \rightarrow p$ detachment channels, and $B_2$ similarly quantifies the relationship between the $p \rightarrow d$ and $d \rightarrow p$ channels. In terms of the $p$- and $d$-character of the anion MO ($\gamma_1$ and $\gamma_2$, respectively), as well as the four Hanstorp coefficients, the mixed-*spd* application of the general model in Eq. 6.14 can be shown to reduce to

$$\beta_{spd}(\varepsilon) = \frac{2\left[\frac{B_1}{A_1}(1-\gamma_1-\gamma_2) - 2\gamma_1 + \frac{1}{5}\frac{A_1}{B_2}\gamma_2\right]A_2\varepsilon + 2\left(\gamma_1 - \frac{18}{5}\frac{A_2}{B_2}\gamma_2\right)A_1A_2\varepsilon^2 + \frac{12}{5}\frac{A_1}{B_2}\gamma_2A_2^3\varepsilon^3}{\frac{A_2}{A_1}\gamma_1 + \left[\frac{B_1}{A_1}(1-\gamma_1-\gamma_2) + 2\frac{A_1}{B_2}\gamma_2\right]A_2\varepsilon + 2\gamma_1A_1A_2\varepsilon^2 + 3\gamma_2\frac{A_1}{B_2}A_2^3\varepsilon^3}. \tag{6.3}$$

Here, we have neglected the phase shifts between outgoing $l+1$ and $l-1$ partial waves for simplicity.

To apply this model to the pyridinide anions, we must first determine an appropriate parametrization of the basis set defined by Eqs. 6.11 and 6.15. We fix $Z_0$ and $Z_1$ to the values presented above for the *para* isomer, $Z_0 = Z_1 = 0.885$. Based on the orbitals in Figure 6.7, the *ortho* isomer is expected to show the most appreciable $d$-character, and so the experimental PAD for this isomer was fit to Eq. 6.3 to determine an appropriate value of $Z_2$. This gives parameter values of $Z_2 = 1.45(8)$, $\gamma_1 = 0.03(2)$, and $\gamma_2 = 0.68(13)$ for

the *ortho* isomer. The extracted value of $Z_2$ as well as the previously set value of $Z_1$ gives Hanstorp coefficients of $A_2 = 0.5$ and $B_2 = 2.1$ eV$^{-1}$.

To treat the other two isomers, this value of $Z_2 = 1.45$ is fixed, and the fractional *p*- and *d*-characters are extracted by fitting Eq. 6.3 to the experimental PAD for the *meta* and *para* isomers. The results of this mixed-*spd* treatment are shown as solid lines in Figure 6.6, and the extracted fractional *s*-, *p*-, and *d*-characters are presented in Table 6.4 for all three isomers. These results agree well with the intuitive expectations given the appearance of the HOMOs in Figure 6.7. The *p*-pyridinide isomer shows zero fractional *d*-character, as expected for a PAD that is well-described by the mixed-*sp* model. The *m*-pyridinide isomer shows similar fractional character, with slightly more *s*-character and small nonzero *d*-character. The *o*-pyridinide isomer is roughly two-thirds *d*-character, with very little *p*-character. This trend suggests that, as the site of deprotonation moves towards the carbon atom, the fractional *d* character in the resultant anion HOMO increases. This is not a result of the involvement of atomic *d*-orbitals, but rather due to the increased delocalization of the orbital resulting from the involvement of N-centered *p*-like orbitals, leading to a greater number of angular nodes which are associated with higher angular momenta.

### 6.5.3 Bond-Dissociation Energies of Pyridine and Isomeric Stabilities

Previously, the measured gas-phase acidity of the $C_4$ position of the pyridine ring $\Delta H^\circ_{acid}(C_4) = 389.9 \pm 2.0$ kcal mol$^{-1}$ was used in conjunction with the experimental electron affinity of the *p*-pyridyl radical to calculate the bond dissociation enthalpy of the $C_4$-H bond of pyridine,[272]

$$\mathrm{BDE}(C_4\text{-H}) = \Delta H^\circ_{acid}(C_4) + \mathrm{EA}(C_4^\bullet) - \mathrm{IE}(H), \tag{6.4}$$

where IE(H) = 313.6 kcal mol$^{-1}$ is the ionization energy of atomic hydrogen. The measurement of the EAs for the other two radical isomers motivates a similar calculation for the $C_3$-H and $C_2$-H BDEs of pyridine. However, due to the relative stability of the *p*-pyridinide isomer, experimental measurements of $\Delta H^\circ_{acid}(C_3)$ and $\Delta H^\circ_{acid}(C_2)$ are not available. Thus, instead of using purely experimental results to calculate the *meta* and *ortho* analogs of Eq. 6.4, we employ a hybrid experimental-theoretical approach akin to that used previously to treat the oxazole[91] and furan[249] C-H bonds, as was discussed briefly in Section 6.3.

The CBS-QB3 method is a chemically-accurate procedure which can be used to calculate absolute enthalpies of molecular species. This was used to obtain the enthalpy change associated with heterolytic C-H bond cleavage, i.e. the gas-phase acidity,

$$\text{pyridine} \rightarrow \mathrm{H}^+ + n\text{ - pyridinide} \quad [\Delta H^\circ_{acid}(C_n)], \tag{6.5}$$

for all three anion isomers. For each carbon position on the pyridine ring, we first find $\delta_n$ (Eq. 6.1), which expresses the difference in gas-phase acidities as compared to the 4-position for which an experimental value is already available. The CBS-QB3 enthalpies of the pyridinide anions for T = 298 K (Table 6.11) give $\delta_2 = 9.9$ and $\delta_3 = 1.7$ kcal mol$^{-1}$.

Taking these differences to be accurate to within 2.0 kcal mol$^{-1}$ – the uncertainty on the experimental measurement of $\Delta H^{\circ}_{acid}(C_4)$ – we then estimate the gas-phase acidity of the $C_2$ and $C_3$ positions of pyridine as

$$\Delta H^{\circ}_{acid}(C_n) = \delta_n + \Delta H^{\circ}_{acid}(C_4), \tag{6.6}$$

giving $\Delta H^{\circ}_{acid}(C_3) = 391.6 \pm 2.0$ and $\Delta H^{\circ}_{acid}(C_2) = 399.8 \pm 2.0$ kcal mol$^{-1}$. Using the experimental EAs provided in Tables 6.1-6.3 as well as equations analogous to Eq. 6.4, we obtain enthalpies of BDE($C_3$-H) = 111.4 ± 2.0 and BDE($C_2$-H) = 106.2 ± 2.0 kcal mol$^{-1}$ for pyridine. The purely experimental value of BDE($C_4$-H) calculated using the cryo-SEVI value for the EA of *p*-pyridyl is identical to that reported previously, 110.4 ± 2.0 kcal mol$^{-1}$.

It should be noted that the measured EAs technically correspond to a temperature of 0 K, and thus should be corrected in order to be used alongside the T = 298 K quantities included in Eq. 6.4. The thermal correction, $[H^{298}(\text{neutral}) - H^{0}(\text{neutral})] - [H^{298}(\text{anion}) - H^{0}(\text{anion})]$, may be calculated from our absolute enthalpies in Table 6.11, and is found to be $< 0.2$ kcal mol$^{-1}$ for all three isomers. As this is substantially smaller than the uncertainty in the experimental gas phase acidity of the $C_4$ position, we have neglected this correction here.

Table 6.5 presents the experimental-theoretical values for BDE($C_n$-H) and $\Delta H^{\circ}_{acid}(C_n)$, the $\delta_n$ values used in calculation of $\Delta H^{\circ}_{acid}(C_n)$, and the experimental EAs for the pyridyl radicals obtained from the cryo-SEVI spectra. These thermodynamic quantities reflect the relative energies of the anion and neutral isomers, which are provided in Figure 6.1 for the B3LYP/6-311+G* level of theory. For the neutral radicals, the *m*- and *p*-pyridyl isomers are within 2.5 kcal mol$^{-1}$ of each other, resulting in similar BDEs for the $C_3$ and $C_4$ positions of pyridine. The corresponding anion isomers are similarly close in energy, resulting in similar gas-phase acidities for the $C_3$ and $C_4$ carbons of pyridine. This similarity is consistent with the observation that both anion isomers are formed by deprotonation of pyridine by $F^-$ (Figure 6.8). The small energy differences found in both charge states for these two isomers is the causeall difference in EAs (∼30 meV) determined for the *p*- and *m*-pyridyl radicals.

The *ortho* isomers of the anion and neutral have energies which deviate more substantially from the other two isomers. The *o*-pyridyl radical is more stable than the other two isomers

**Table 6.5:** Thermodynamic properties of the $C_n$ ring positions of pyridine ($n$ = 2, 3, 4) and the $x$-pyridyl radicals ($x$ = *p*, *m*, *o*). The gas phase acidity of the $C_4$ position of pyridine is obtained from previous measurements,[272] and values for the other two positions were obtained using the hybrid experimental-theoretical approach described in Section 6.5.3. BDEs are obtained for all carbon positions using Eq. 6.4.

| $x$ | $n$ | EA($x$-pyridyl) | $\Delta H^{\circ}_{acid}(C_{\circ})$n | BDE($C_n$-H) |
|---|---|---|---|---|
| *p* | 4 | 34.122 ± 0.012 | 389.9 ± 2.0 | 110.4 ± 2.0 |
| *m* | 3 | 33.375 ± 0.012 | 391.6 ± 2.0 | 111.4 ± 2.0 |
| *o* | 2 | 19.991 ± 0.016 | 399.8 ± 2.0 | 106.2 ± 2.0 |

by 5 kcal $mol^{-1}$, in agreement with the result that the $C_2$ position of pyridine has the weakest C-H bond. The stabilization of the *o*-pyridyl radical has previously been suggested to be a consequence of two-center three-electron (2c,3e) interactions between the unpaired electron and nitrogen lone pair for this radical isomer.[90] In contrast, the *o*-pyridinide anion is the highest-energy isomer for this charge state, lying several hundred meV above the other two anion isomers. This shift is attributed to destabilizing steric interactions resulting from repulsion of the C- and N-centered lone pairs. Thus, whereas the proximity between the site of deprotonation and the nitrogen lone pair results in stabilization of the neutral radical through (2c,3e) bonding, the addition of an extra electron results in destabilization due to repulsion between the adjacent lone pairs. These effects are reflected in the low EA of *o*-pyridyl, a consequence of the simultaneous stabilization of the neutral and destabilization of the anion.

## 6.6 Conclusion

High-resolution photoelectron spectra have been obtained for all three pyridinide anion isomers, yielding insight into the vibronic structure and energetics of the three pyridyl radicals. This work represents the first reported photoelectron spectra for the *m*- and *o*-pyridinide isomers, and provides a substantial improvement in resolution over prior results for *p*-pyridinide. The resultant spectra are found to be in good agreement with Franck-Condon simulations based on B3LYP/6-311+G* calculations, enabling extraction of a number of vibrational frequencies for each neutral isomer. In addition to resolving fine structure that would be obscured in a lower-resolution experiment, these results allow for observation of subtle vibrational effects such as anharmonic coupling between close-lying vibrational levels of the *p*-pyridyl radical.

The photoelectron angular distributions have been modelled using a three-component implementation of the generalized mixing model proposed by Sanov,[28] revealing chemically intuitive isomeric trends in the highest-occupied molecular orbitals of the pyridinide anions. Whereas the *p*-pyridinide PAD is found to be well-described by a HOMO consisting only of *s* and *p* components, the *o*-pyridinide PAD suggests substantially more *d*-character in the detached orbital. This analysis indicates that as the distance between the deprotonated carbon and the heteroatom is decreased, the angular momentum of the detached orbital is increased, which is related to the extent of delocalization of this MO. Finally, the measured electron affinities of each neutral radical were used with experimental and theoretical gas-phase acidities to obtain experimental-theoretical estimations of the C-H bond dissociation enthalpies of pyridine, and these energies are related to the relative stabilities of the anion and neutral isomers.

# 6.7 Supplementary Material

## 6.7.1 Synthesis of Pyridinide Precursors[a]

### 3-(trimethylsilyl)pyridine

Synthesis was adapted from that published by Cantat.[206] To a -78 °C solution of 3-bromopyridine (6.6 mL, 69 mmol) in dry diethyl ether (100 mL) was added *n*-butyllithium (45 mL, 1.6 M, 72 mmol) dropwise over 90 min. The reaction mixture was then stirred for 1 h. at -78 °C before trimethylsilylchloride (19.6 mL, 75.4 mmol) was added dropwise over 20 min. The solution was allowed to warm to 25 °C and stirred for an additional 18 h. After cooling to 0 °C, the reaction mixture was quenched with 150 mL $H_2O$. The aqueous layer was extracted with ether (3 x 50 mL), and the combined organics were washed with brine (1 x 50 mL), dried with anhydrous magnesium sulfate, and concentrated by rotary evaporation. 3-(trimethylsilyl)pyridine (4.9 g, 32 mmol, 47%) was isolated as a yellow oil by column chromatography on silica (eluent: 10/90 EtOAc/hexanes). $^1$H-NMR (300 MHz, $CDCl_3$): $\delta$ 8.64 (dd, J = 1.8, 1.0 Hz, 1H), 8.53 (dd, J = 4.9, 1.9 Hz, 1H), 7.74 (dt, J = 7.5, 1.9 Hz, 1H), 7.21 (ddd, J = 7.5, 4.9, 1.0 Hz, 1H), 0.26 (s, 9H).

### 4-(trimethylsilyl)pyridine

Synthesis was adapted from that published by Cantat.[206] 4-bromopyridine hydrochloride (5.0 g, 26 mmol) was added to an aqueous solution of 2M NaOH (200 mL). 300 mL $CH_2Cl_2$ was added, and the organic layer was separated, then extracted with DCM (2 x 100 mL). The combined organic layers were dried over anhydrous magnesium sulfate and concentrated by rotary evaporation. To a -78 °C solution of the resulting 4-bromopyridine (4.1 g, 26 mmol) in dry diethyl ether (40 mL) was added *n*-butyllithium (17 mL, 1.6 M, 27 mmol) dropwise over 35 min. The reaction mixture was then stirred for 1 h. at -78 °C before trimethylsilylchloride (3.6 mL, 28 mmol) was added dropwise over 10 min. The solution was allowed to warm to 25 °C and stirred for an additional 18 h. After cooling to 0 °C, the reaction mixture was quenched with 75 mL $H_2O$. The aqueous layer was extracted with ether (3 x 50 mL), and the combined organics were washed with brine (1 x 50 mL), dried with anhydrous magnesium sulfate, and concentrated by rotary evaporation. The resulting orange oil containing 4-(trimethylsilyl)pyridine was used crude. $^1$H-NMR (300 MHz, $CDCl_3$): $\delta$ 8.60–8.51 (m, 2H), 7.42–7.34 (m, 2H), 0.29 (s, 9H).

[a]Synthesis carried out by Katie Blackford.

### 6.7.2 Assignments of Peaks p10 and p17

From the p1-p2-p10a/b-p17a/b series of peaks, there are four possible candidates for the $9_0^n$ progression:

$$\begin{aligned}
&\text{aa} : \text{p1} - \text{p2} - \text{p10a} - \text{p17a}\\
&\text{ab} : \text{p1} - \text{p2} - \text{p10a} - \text{p17b}\\
&\text{ba} : \text{p1} - \text{p2} - \text{p10b} - \text{p17a}\\
&\text{bb} : \text{p1} - \text{p2} - \text{p10b} - \text{p17b}.
\end{aligned}$$

To determine which of these four candidates should be assigned as the FC-allowed progression, we fit the corresponding peak shifts (Table 6.12) to an anharmonic series,

$$\text{shift} = n\,\omega_e - n\,(n+1)\,\omega_e x_e,$$

and determined which series gave the best fit by considering the standard errors of the least-squares fitting parameters. The results are summarized in Eq. 6.7, and clearly suggest that the "bb" series corresponds to the FC-allowed $9_0^n$ progression.

$$\begin{array}{lll}
 & \omega_e & \omega_e x_e\\
\text{aa} & 603.7 \pm 1.6 & 0.53 \pm 0.46\\
\text{ab} & 600.1 \pm 3.6 & 1.01 \pm 1.06\\
\text{ba} & 606.0 \pm 2.5 & 0.97 \pm 0.72\\
\text{bb} & 602.5 \pm 0.3 & 0.58 \pm 0.08
\end{array} \tag{6.7}$$

### 6.7.3 Modelling Photoelectron Angular Distributions

#### Cooper-Zare and Hanstorp Formulations

The Cooper-Zare equation[22] provides the anisotropy parameters obtained for detachment from an orbital $\phi_l(r)$ with angular momentum $l$,

$$\beta_l = \frac{l(l-1)\chi_{l,l-1}^2 + (l+1)(l+2)\chi_{l,l+1}^2 - 6l(l+1)\chi_{l,l+1}\chi_{l,l-1}\cos\delta_{l+1,l-1}}{(2l+1)[l\chi_{l,l-1}^2 + (l+1)\chi_{l,l+1}^2]} \equiv \frac{N_l}{D_l}, \tag{6.8}$$

where $\delta_{l+1,l-2}$ describes the phase shift between the outgoing $l+1$ and $l-1$ partial waves, and the $\chi_{l,l\pm1}$ are the radial transition dipole matrix elements,

$$\chi_{l,l\pm1} = \int_0^\infty j_{l\pm1}(kr) r^3 \phi_l(r) dr.$$

Here, $j_\ell(kr)$ describes the $\ell$ partial wave contribution to the wavefunction of a photoelectron with eKE $= \varepsilon = k^2/2$ (in atomic units).

For $l = 0$, Eq. 6.8 reduces to +2, and thus the anisotropy parameter for detachment from a pure-$s$ orbital is independent of eKE. For $l > 0$, it is readily shown that Eq. 6.8 may be rearranged in terms of the ratio $\chi_{l,l+1}/\chi_{l,l-1}$, rather than the explicit matrix elements

themselves, by dividing the numerator and denominator by $\chi^2_{l,l-1}$. In the limit of low-eKE detachment, the relative scaling of the cross section for detachment of the $l \pm 1$ partial waves is taken to be given by the Wigner threshold law,[21]

$$\frac{\sigma_{l+1}}{\sigma_{l-1}} = \frac{\varepsilon^{l+3/2}}{\varepsilon^{1-1/2}} = \varepsilon^2.$$

As each cross section is proportional to the square of the appropriate transition dipole moment, the $\chi_{l,l+1}/\chi_{l,l-1}$ ratio is proportional to $\varepsilon$. The Hanstorp $A_l$ coefficient defines this proportionality,[23]

$$A_l\varepsilon = \frac{\chi_{l,l+1}}{\chi_{l,l-1}}\varepsilon. \tag{6.9}$$

Using this coefficient, Eq. 6.8 is simplified, giving

$$\beta_l = \frac{l(l-1) + (l+1)(l+2)A_l^2\varepsilon^2 - 6l(l+1)A_l\varepsilon\cos\delta_{l+1,l-1}}{(2l+1)[l + (l+1)A_l^2\varepsilon^2]} = \frac{N_l}{D_l}.$$

Thus, the Hanstorp coefficient provides a direct expression of the eKE-dependence of the anisotropy parameter.

In the mixing models described in the following sections, the detached orbital is better described as a combination of several $l$-components. For the purposes of these models, a similar Hanstorp-like coefficient is introduced, $B_l$, in cases where the anion MO includes $l$ and $l-1$ contributions. Whereas the $A_l$ coefficient describes the relative scaling of the $l \rightarrow l \pm 1$ detachment channels, $B_l$ describes the relative scaling of the $l-1 \rightarrow l$ and $l \rightarrow l-1$ detachment channels (e.g. $B_1$ concerns the $s \rightarrow p$ and $p \rightarrow s$ scaling). This coefficient is defined as

$$B_l\varepsilon = \frac{\chi^2_{l-1,l}}{\chi^2_{l,l-1}}\varepsilon. \tag{6.10}$$

### Mixed-*sp* Model for *p*-Pyridinide

In the mixed-*sp* model used previously by Sanov and others,[25,26,91,249] the detached orbital is modelled as a linear combination of an $s$- and a $p$-component,

$$|\Psi_{sp}\rangle = \sqrt{1-\gamma_1}\,|0\rangle + \sqrt{\gamma_1}\,|1\rangle \ .$$

For treatment of the $p$-pyridinide anion HOMO (and other $2s2p$ hybridized orbitals), the radial basis functions $\phi_l(r)$ used in evaluation of $\chi_{l,l\pm1}$ are taken to be atomic $2s$ and $2p$ orbitals,

$$\begin{aligned}\phi_0(r) &= \left(\frac{Z_0}{2}\right)^{3/2}(2 - Z_0 r)e^{-Z_0 r/2} \\ \phi_1(r) &= \frac{1}{\sqrt{3}}\left(\frac{Z_1}{2}\right)^{3/2} Z_1 r e^{-Z_1 r/2}.\end{aligned} \tag{6.11}$$

To evaluate expressions for the Hanstorp coefficients in terms of our basis set parametrization (defined by the charge parameters $Z_0$ and $Z_1$), the $j_\ell(kr)$ describing the outgoing electron are taken to be given by the spherical Bessel functions. In the low-eKE limit applicable to SEVI, we can approximate these by the first term of their McLaurin series expansion,

$$j_\ell(kr) \approx \frac{(kr)^\ell}{(2\ell+1)!}.$$

With this, the Hanstorp coefficients in Eqs. 6.9 and 6.10 may be evaluated in terms of the charge parameters used to describe the basis set,

$$A_1\varepsilon = \frac{\int_0^\infty j_2(kr)r^3\phi_1(r)dr}{\int_0^\infty j_0(kr)r^3\phi_1(r)dr} = \frac{16}{Z_1^2}\varepsilon \quad \text{and} \quad B_1\varepsilon = \frac{\left(\int_0^\infty j_1(kr)r^3\phi_0(r)dr\right)^2}{\left(\int_0^\infty j_0(kr)r^3\phi_1(r)dr\right)^2} = \frac{128Z_1^5}{3Z_0^7}\varepsilon. \quad (6.12)$$

In applying this model to the *p*-pyridinide anion, the value of $A_1$ associated with detachment from a carbanion was selected ($A_1 = 0.75$ eV$^{-1}$),[212] and the chosen $B_1 = 8A_1/3$ value is appropriate for treatment of $2s2p$ hybridized orbitals.[27] These give charge parameters of $Z_0 = Z_1 = 0.885$.

The eKE dependence of the anisotropy parameter is then derived as $\beta_{sp} = (N_0 + N_1)/(D_0 + D_1)$, where $N_l$ and $D_l$ are the numerator and denominator of the Cooper-Zare equation in Eq. 6.8. Using the Hanstorp coefficients, this is simplified by expressing each term in the numerator and denominator in terms of $\gamma_1$, $A_1$, $B_1$, and $\chi^2_{2,1}$; $\chi^2_{2,1}$ is then factored out of both numerator and denominator, giving the mixed-*sp* result,

$$\beta_{sp}(\varepsilon) = \frac{2\left[\frac{B_1}{A_1}(1-\gamma_1) - 2\gamma_1\right]A_1\varepsilon + 2\gamma_1 A_1^2\varepsilon^2}{\gamma_1 + \frac{B_1}{A_1}(1-\gamma_1)A_1\varepsilon + 2\gamma_1 A_1^2\varepsilon^2}. \quad (6.13)$$

**Generalized Mixing Model**

The generalized mixing model of Sanov and coworkers[28] is a generalization of the mixed-*sp* model where the detached orbital is taken to be a sum of an arbitrary number of angular momentum components. Noting that single-center atomic orbitals form a complete basis set, we take the detached orbital to be a linear combination of atomic orbitals,

$$|\Psi_{MO}\rangle = \sum_l \sqrt{\gamma_l}\,|l\rangle\ .$$

As in the mixed-*sp* case, the radial wavefunctions $\phi_l(r)$ are typically taken to be hydrogenic orbitals (parametrized by charge parameters $Z_l$) appropriate for the system under consideration. The choice of basis set parametrization is particularly straightforward for treatment of orbitals that are localized on a single atomic center, such as in the C-centered $2s2p$ case described above. Given the completeness of the hydrogenic eigenfunctions, even relatively

delocalized orbitals whose center of mass may not coincide with a particular atom can be described as above, although the appropriate parameters are not as readily assumed.

For detachment from an orbital of the form $|\Psi_{MO}\rangle$, the generalized mixing model shows that the anisotropy parameter is given by $\beta = (\sum N_l)/(\sum D_l)$,

$$\beta = \frac{\sum \gamma_l \left[ l(l-1)\chi^2_{l,l-1} + (l+1)(l+2)\chi^2_{l,l+1} - 6l(l+1)\chi_{l,l-1}\chi_{l,l+1}\cos\delta_{l+1,l-1} \right] /(2l+1)}{\sum \gamma_l \left[ l\chi^2_{l,l-1} + (k+1)\chi^2_{l,l+1} \right]}. \tag{6.14}$$

Further simplification of this expression requires definition of the number of terms included in the expansion of $|\Psi_{MO}\rangle$.

### Mixed-*spd* Model for Pyridinide Isomers

To model the PADs for detachment from all three pyridinide isomers, the mixed-*sp* model presented above was expanded to include a $3d$ atomic orbital in the basis set,

$$|\Psi_{spd}\rangle = \sqrt{1-\gamma_1-\gamma_2}\,|0\rangle + \sqrt{\gamma_1}\,|1\rangle + \sqrt{\gamma_2}\,|2\rangle \quad \text{and} \quad \phi_2(r) = \frac{4}{27\sqrt{10}}\left(\frac{Z_2}{3}\right)^{3/2}(Z_2 r)^2 e^{-Z_2 r/3}. \tag{6.15}$$

The $s$ and $p$ basis functions are taken to be identical to those used in the treatment of the pyridinide anion, using the same charge parameters $Z_0 = Z_1 = 0.885$.

Using this three-component basis set, Equation 6.14 can be evaluated in similar manner as that used to obtain Eq. 6.13. Introducing the Hanstorp coefficients $A_2$ and $B_2$ as defined by Eqs. 6.9 and 6.10, each term in the numerator and denominator may be expressed in terms of $\gamma_1$, $\gamma_2$, $A_1$, $B_1$, $A_2$, $B_2$, and $\chi^2_{1,2}$. Again, the remaining transition dipole term can be factored out of both numerator and denominator, giving

$$\beta_{spd}(\varepsilon) = \frac{2\left[\frac{B_1}{A_1}(1-\gamma_1-\gamma_2) - 2\gamma_1 + \frac{1}{5}\frac{A_1}{B_2}\gamma_2\right] A_2\varepsilon + 2\left(\gamma_1 - \frac{18}{5}\frac{A_2}{B_2}\gamma_2\right) A_1 A_2 \varepsilon^2 + \frac{12}{5}\frac{A_1}{B_2}\gamma_2 A_2^3\varepsilon^3}{\frac{A_2}{A_1}\gamma_1 + \left[\frac{B_1}{A_1}(1-\gamma_1-\gamma_2) + 2\frac{A_1}{B_2}\gamma_2\right] A_2\varepsilon + 2\gamma_1 A_1 A_2\varepsilon^2 + 3\gamma_2\frac{A_1}{B_2}A_2^3\varepsilon^3}.$$

The Hanstorp coefficients $A_2$ and $B_2$ are given in terms of the basis set parametrization,

$$A_2\varepsilon = \frac{\int_0^\infty j_3(kr) r^3 \phi_2(r) dr}{\int_0^\infty j_1(kr) r^3 \phi_2(r) dr} = \frac{144}{5Z_2^2}\varepsilon \quad \text{and} \quad B_2\varepsilon = \frac{\left(\int_0^\infty j_1(kr) r^3 \phi_2(r) dr\right)^2}{\left(\int_0^\infty j_2(kr) r^3 \phi_1(r) dr\right)^2} = \frac{512 Z_2^7}{3645 Z_1^9}\varepsilon. \tag{6.16}$$

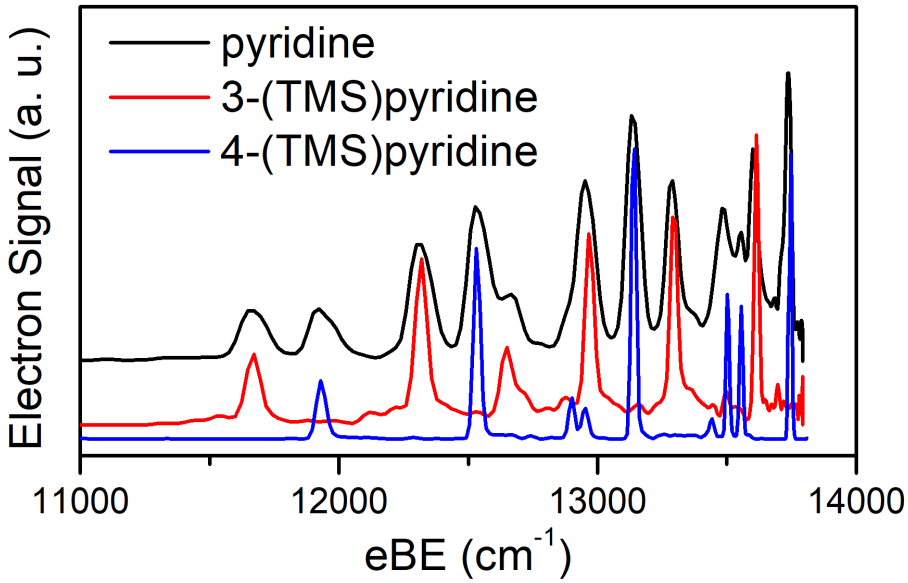


**Figure 6.8:** Photoelectron spectra at 1.71 eV for $m/z$ = 78 anions generated by reacting fluoride ions with (black) pyridine, (red) 3-(trimethylsilyl)pyridine, and (blue) 4-(trimethylsilyl)pyridine.

**Table 6.6:** Cartesian coordinates for the B3LYP/6-311+G* optimized geometries of *p*-pyridyl and *p*-pyridinide. The ZPE-corrected energies relative to the *p*-pyridinide anion are also provided.

| | *p*-pyridinide ($\tilde{X}\ ^1A_1$, 0.000 eV) | | | *p*-pyridyl ($\tilde{X}\ ^2A_1$, 1.473 eV) | | |
|---|---|---|---|---|---|---|
| N | -0.000048 | -1.395296 | 0.000000 | -0.000008 | -1.343856 | 0.000000 |
| C | -1.130163 | -0.669961 | 0.000000 | -1.143315 | -0.658313 | 0.000000 |
| H | -2.060000 | -1.249723 | 0.000000 | -2.059970 | -1.243937 | 0.000000 |
| C | 1.130111 | -0.670038 | 0.000000 | 1.143304 | -0.658327 | 0.000000 |
| H | 2.059913 | -1.249859 | 0.000000 | 2.059951 | -1.243964 | 0.000000 |
| C | -1.162952 | 0.725934 | 0.000000 | -1.210801 | 0.745338 | 0.000000 |
| H | -2.157002 | 1.188304 | 0.000000 | -2.167778 | 1.255929 | 0.000000 |
| C | 1.163004 | 0.725863 | 0.000000 | 1.210811 | 0.745328 | 0.000000 |
| H | 2.157093 | 1.188152 | 0.000000 | 2.167803 | 1.255891 | 0.000000 |
| C | 0.000056 | 1.536569 | 0.000000 | 0.000009 | 1.389819 | 0.000000 |

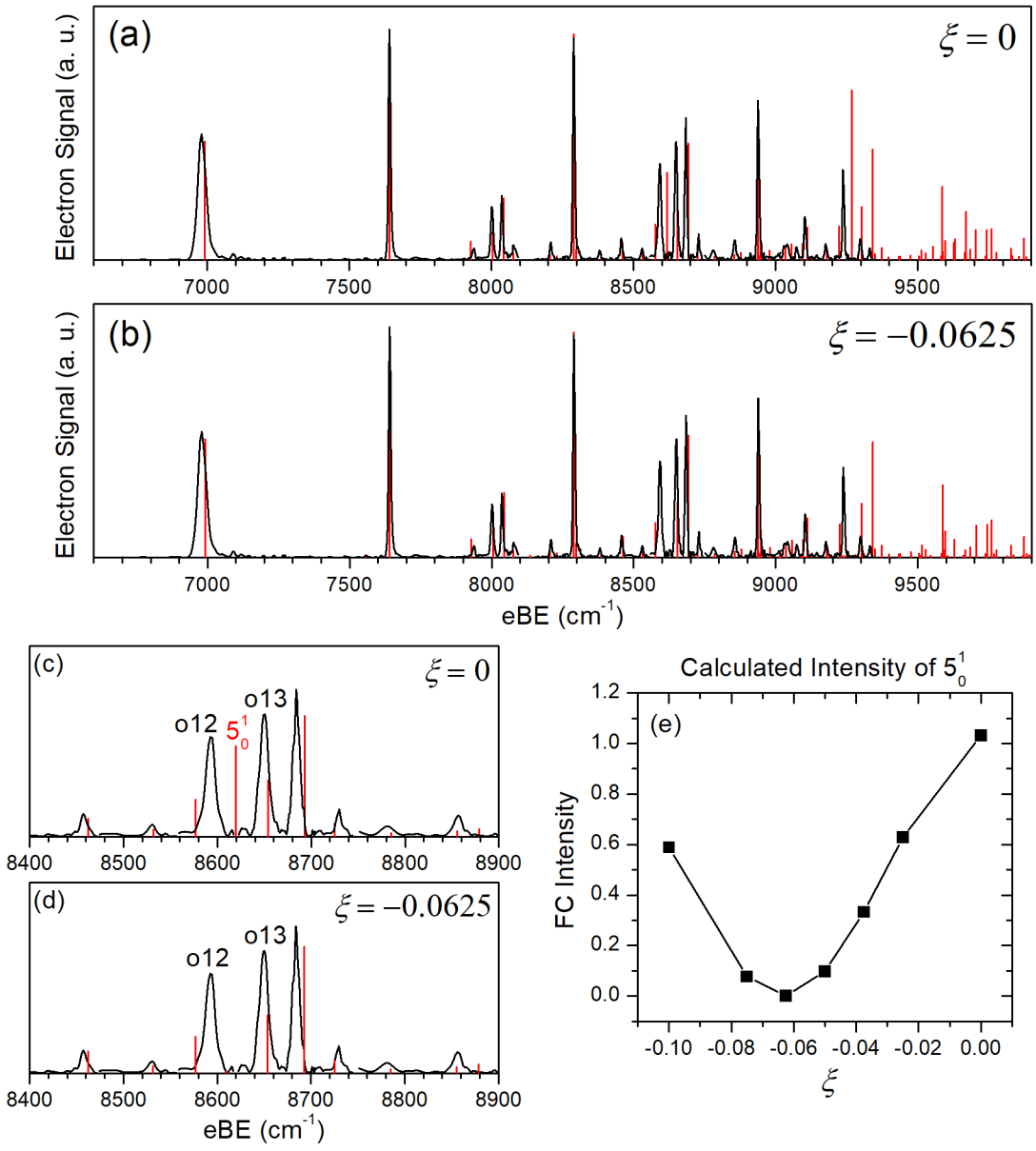


**Figure 6.9:** Dependence of the FC profile for detachment from *o*-pyridinide on displacement of the neutral geometry along $\nu_5$. In panels a-d, the red sticks represent the calculated FC profiles, and the black traces are the high-resolution cryo-SEVI traces. (a) Full FC profile using the equilibrium neutral geometry. (b) Full FC profile calculated after applying a $\delta = -0.0625$ magnitude shift along $\nu_5$ to the neutral. (c) $5^1_0$ region of the FC profile shown in panel a. (d) $5^1_0$ region of the FC profile shown in panel b. (e) Dependence of the calculated FC intensity on the magnitude of the shift applied to the neutral geometry.

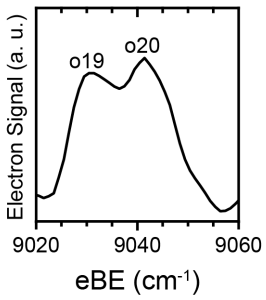


**Figure 6.10:** High-resolution scan for detachment from *o*-pyridinide using a photon energy of 9148 $cm^{-1}$, showing the 10 $cm^{-1}$ splitting of features o19/o20.

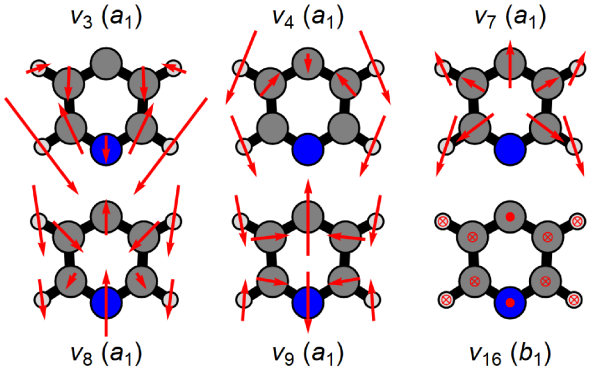


**Figure 6.11:** Vibrational modes of *p*-pyridyl involved in the cryo-SEVI spectrum of *p*-pyridinide. For $\nu_{16}$, the solid circles indicate atomic movement out of the molecular plane, and the crossed circles indicate movement into the plane.

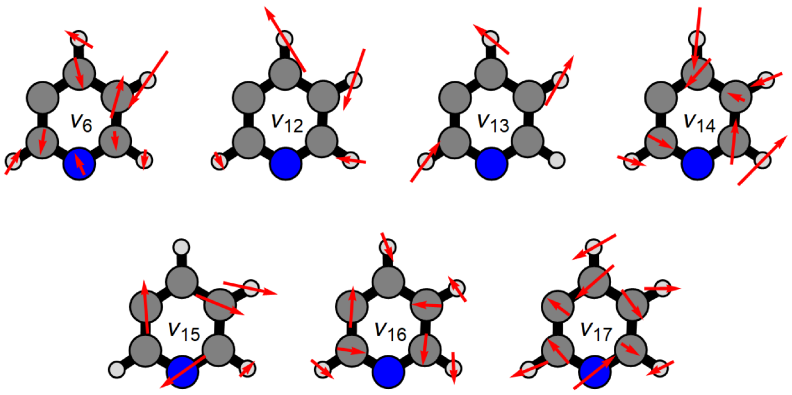


**Figure 6.12:** Vibrational modes of *m*-pyridyl involved in the cryo-SEVI spectrum of *m*-pyridinide.

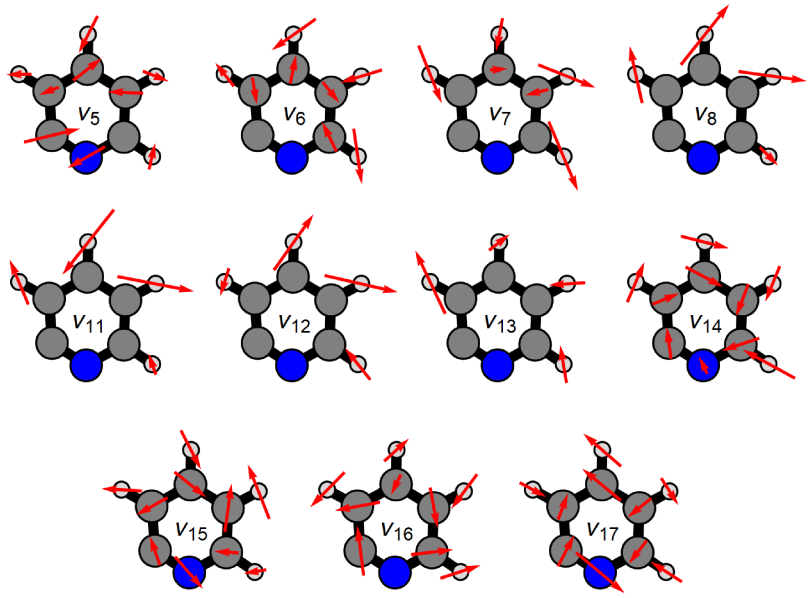


**Figure 6.13:** Vibrational modes of *o*-pyridyl involved in the discussion of the cryo-SEVI spectrum of *o*-pyridinide.

**Table 6.7:** Cartesian coordinates for the B3LYP/6-311+G* optimized geometries of *m*-pyridyl and *m*-pyridinide. The ZPE-corrected energies relative to the *p*-pyridinide anion are also provided.

| | *m*-pyridinide ($\tilde{X}\ ^1A'$, 0.090 eV) | | | *m*-pyridyl ($\tilde{X}\ ^2A'$, 1.529 eV) | | |
|---|---|---|---|---|---|---|
| N | 1.149210 | 0.791845 | 0.000000 | 1.169122 | 0.737125 | 0.000000 |
| C | -0.083525 | 1.315159 | 0.000000 | -0.050624 | 1.280253 | 0.000000 |
| H | -0.150403 | 2.405370 | 0.000000 | -0.082206 | 2.366701 | 0.000000 |
| C | 1.228055 | -0.559772 | 0.000000 | 1.272152 | -0.604069 | 0.000000 |
| H | 2.265078 | -0.913102 | 0.000000 | 2.273761 | -1.021505 | 0.000000 |
| C | -1.231546 | 0.526638 | 0.000000 | -1.234377 | 0.542418 | 0.000000 |
| H | -2.216789 | 0.999797 | 0.000000 | -2.198656 | 1.041300 | 0.000000 |
| C | -1.080729 | -0.867052 | 0.000000 | -1.141468 | -0.855133 | 0.000000 |
| H | -1.998574 | -1.467746 | 0.000000 | -2.029077 | -1.480531 | 0.000000 |
| C | 0.177113 | -1.509512 | 0.000000 | 0.129706 | -1.374442 | 0.000000 |

**Table 6.8:** Cartesian coordinates for the B3LYP/6-311+G* optimized geometries of *o*-pyridyl and *o*-pyridinide. The ZPE-corrected energies relative to the *p*-pyridinide anion are also provided.

| | *o*-pyridinide ($\tilde{X}\ ^1A'$, 0.450 eV) | | | *o*-pyridyl ($\tilde{X}\ ^2A'$, 1.274 eV) | | |
|---|---|---|---|---|---|---|
| N | 1.088158 | -0.942555 | 0.000000 | 1.058886 | -0.936056 | 0.000000 |
| C | 1.258417 | 0.386420 | 0.000000 | 1.289057 | 0.393317 | 0.000000 |
| H | 2.297368 | 0.736336 | 0.000000 | 2.325381 | 0.715876 | 0.000000 |
| C | -0.181710 | -1.502012 | 0.000000 | -0.153960 | -1.353841 | 0.000000 |
| C | 0.228224 | 1.326398 | 0.000000 | 0.235376 | 1.298022 | 0.000000 |
| H | 0.441985 | 2.394312 | 0.000000 | 0.433691 | 2.364149 | 0.000000 |
| C | -1.076539 | 0.826700 | 0.000000 | -1.076650 | 0.810668 | 0.000000 |
| H | -1.930355 | 1.510637 | 0.000000 | -1.916312 | 1.499961 | 0.000000 |
| C | -1.253611 | -0.554224 | 0.000000 | -1.300424 | -0.565374 | 0.000000 |
| H | -2.274788 | -0.943092 | 0.000000 | -2.297898 | -0.987801 | 0.000000 |

**Table 6.9:** Harmonic and anharmonic vibrational frequencies (in $cm^{-1}$) for the pyridyl and pyridinide isomers calculated at the B3LYP/6-311+G* level, as well as their symmetries within the appropriate molecular point ground ($C_{2v}$ for *para*, $C_s$ for *meta* and *ortho*).

| | *para* | | | *meta* | | | *ortho* | | |
|---|---|---|---|---|---|---|---|---|---|
| | | anion | neutral | | anion | neutral | | anion | neutral |
| $\nu_1$ | $a_1$ | 3047 | 3187 | $a'$ | 3089 | 3184 | $a'$ | 3167 | 3204 |
| $\nu_2$ | $a_1$ | 3010 | 3151 | $a'$ | 3060 | 3178 | $a'$ | 3120 | 3197 |
| $\nu_3$ | $a_1$ | 1567 | 1543 | $a'$ | 3034 | 3167 | $a'$ | 3097 | 3178 |
| $\nu_4$ | $a_1$ | 1463 | 1476 | $a'$ | 3005 | 3156 | $a'$ | 3068 | 3165 |
| $\nu_5$ | $a_1$ | 1237 | 1233 | $a'$ | 1573 | 1613 | $a'$ | 1607 | 1662 |
| $\nu_6$ | $a_1$ | 1104 | 1080 | $a'$ | 1528 | 1543 | $a'$ | 1592 | 1572 |
| $\nu_7$ | $a_1$ | 1013 | 1038 | $a'$ | 1458 | 1473 | $a'$ | 1468 | 1502 |
| $\nu_8$ | $a_1$ | 984 | 983 | $a'$ | 1396 | 1442 | $a'$ | 1426 | 1424 |
| $\nu_9$ | $a_1$ | 602 | 620 | $a'$ | 1348 | 1333 | $a'$ | 1289 | 1335 |
| $\nu_{10}$ | $a_2$ | 957 | 973 | $a'$ | 1230 | 1263 | $a'$ | 1170 | 1265 |
| $\nu_{11}$ | $a_2$ | 899 | 817 | $a'$ | 1208 | 1206 | $a'$ | 1159 | 1169 |
| $\nu_{12}$ | $a_2$ | 338 | 376 | $a'$ | 1094 | 1110 | $a'$ | 1083 | 1108 |
| $\nu_{13}$ | $b_1$ | 953 | 951 | $a'$ | 1070 | 1065 | $a'$ | 1075 | 1074 |
| $\nu_{14}$ | $b_1$ | 784 | 760 | $a'$ | 1039 | 1044 | $a'$ | 1029 | 1035 |
| $\nu_{15}$ | $b_1$ | 723 | 708 | $a'$ | 971 | 990 | $a'$ | 996 | 956 |
| $\nu_{16}$ | $b_1$ | 404 | 443 | $a'$ | 666 | 662 | $a'$ | 665 | 663 |
| $\nu_{17}$ | $b_2$ | 3040 | 3185 | $a'$ | 613 | 581 | $a'$ | 613 | 578 |
| $\nu_{18}$ | $b_2$ | 3013 | 3149 | $a''$ | 967 | 981 | $a''$ | 1012 | 993 |
| $\nu_{19}$ | $b_2$ | 1513 | 1619 | $a''$ | 928 | 939 | $a''$ | 975 | 961 |
| $\nu_{20}$ | $b_2$ | 1416 | 1413 | $a''$ | 898 | 916 | $a''$ | 883 | 885 |
| $\nu_{21}$ | $b_2$ | 1332 | 1322 | $a''$ | 759 | 779 | $a''$ | 777 | 749 |
| $\nu_{22}$ | $b_2$ | 1243 | 1269 | $a''$ | 727 | 684 | $a''$ | 710 | 703 |
| $\nu_{23}$ | $b_2$ | 1062 | 1076 | $a''$ | 390 | 421 | $a''$ | 374 | 425 |
| $\nu_{24}$ | $b_2$ | 685 | 647 | $a''$ | 336 | 389 | $a''$ | 352 | 385 |

**Table 6.10:** Comparison of geometric parameters of *o*-pyridyl based on application of shifts of magnitude $\xi$ along $\nu_5$, as well as the percent change induced by this shift. An *a* subscript denotes the atom on the same side of the ring as the deprotonated carbon atom ($C_{2a}$).

| $\xi$ | 0.0 | -0.0625 | % change |
|---|---|---|---|
| N-$C_{2a}$ | 1.28 | 1.34 | 4.7 |
| N-$C_{2b}$ | 1.35 | 1.33 | -1.5 |
| $C_{2a}$-$C_{3a}$ | 1.39 | 1.36 | -2.2 |
| $C_{2b}$-$C_{3b}$ | 1.39 | 1.37 | -1.4 |
| $C_{3a}$-$C_4$ | 1.39 | 1.37 | -1.4 |
| $C_{3b}$-$C_4$ | 1.4 | 1.44 | 2.9 |
| $C_{2b}$-H | 1.09 | 1.09 | 0 |
| $C_{3a}$-H | 1.08 | 1.08 | 0 |
| $C_{3b}$-H | 1.08 | 1.09 | 0.9 |
| $C_4$-H | 1.09 | 1.09 | 0 |
| $C_{2a}$-N-$C_{2b}$ | 118.8 | 117.7 | -0.9 |
| N-$C_{2a}$-$C_{3a}$ | 126.5 | 125 | -1.2 |
| N-$C_{2b}$-$C_{3b}$ | 120.8 | 122.7 | 1.6 |
| $C_{2a}$-$C_{3a}$-$C_4$ | 115.3 | 117.7 | 2.1 |
| $C_{2b}$-$C_{3b}$-$C_4$ | 119 | 118.4 | -0.5 |
| $C_{3a}$-$C_4$-$C_{3b}$ | 119.6 | 118.5 | -0.9 |

**Table 6.11:** Absolute enthalpies at T = 298 and 0 K for pyridine, the three pyridyl radicals, and the pyridinide anions, as determined using the CBS-QB3 procedure. Values are in units of Hartrees. For all enthalpy changes calculated from these results, the T = 298 K values were used unless otherwise specified.

| | $H$(298 K) | $H$(0 K) |
|---|---|---|
| *p*-pyridinide | -247.205004 | -247.210296 |
| *m*-pyridinide | -247.202289 | -247.207611 |
| *o*-pyridinide | -247.189189 | -247.194638 |
| *p*-pyridyl | -247.149234 | -247.154462 |
| *m*-pyridyl | -247.147209 | -247.152443 |
| *o*-pyridyl | -247.156388 | -247.161631 |
| pyridine | -247.825705 | -247.830959 |

**Table 6.12:** Peak positions ($cm^{-1}$), shifts from the origin ($cm^{-1}$), and vibrational assignments for features in the cryo-SEVI spectrum of *p*-pyridinide. The uncertainty in peak positions corresponds to the width parameter obtained from a Gaussian fit to the experimental peak.

| peak | eBE | shift | assn. |
|---|---|---|---|
| p1 | 11934 (4) | 0 | $0_0^0$ |
| p2 | 12537 (4) | 603 | $9_0^1$ |
| p3 | 12902 (4) | 967 | $8_0^1$ |
| p4 | 12953 (4) | 1019 | $7_0^1$ |
| p5 | 13142 (3) | 1207 | $9_0^2$ |
| p6 | 13380 (3) | 1445 | $4_0^1$ |
| p7 | 13443 (3) | 1509 | $3_0^1$ |
| p8 | 13504 (4) | 1570 | $8_0^1 9_0^1$ |
| p9 | 13556 (4) | 1622 | $7_0^1 9_0^1$ |
| p10a | 13738 (3) | 1804 | $8_0^1 16_0^2$ |
| p10b | 13747 (3) | 1813 | $9_0^3$ |
| p11 | 13868 (5) | 1933 | $8_0^2$ |
| p12 | 13918 (3) | 1983 | $7_0^1 8_0^1$ |
| p13 | 13980 (4) | 2045 | $4_0^1 9_0^1$ |
| p14 | 14044 (4) | 2110 | $3_0^1 9_0^1$ |
| p15 | 14107 (5) | 2173 | $8_0^1 9_0^2$ |
| p16 | 14160 (5) | 2225 | $7_0^1 9_0^2$ |
| p17a | 14341 (4) | 2407 | $8_0^1 9_0^1 16_0^2$ |
| p17b | 14353 (4) | 2419 | $9_0^4$ |
| p18 | 14466 (6) | 2531 | $8_0^2 9_0^1$ |
| p19 | 14520 (4) | 2585 | $7_0^1 8_0^1 9_0^1$ |
| p20 | 14574 (6) | 2640 | $7_0^2 9_0^1$ |
| p21 | 14642 (7) | 2707 | $3_0^1 9_0^2$ |
| p22a | 14702 (5) | 2768 | $8_0^2 16_0^2$ |
| p22b | 14713 (4) | 2778 | $8_0^1 9_0^3$ |
| p23a | 14754 (4) | 2820 | $7_0^1 8_0^1 16_0^2$ |
| p23b | 14765 (4) | 2830 | $7_0^1 9_0^3$ |

**Table 6.13:** Peak positions ($cm^{-1}$), shifts from the origin ($cm^{-1}$), and vibrational assignments for features in the cryo-SEVI spectrum of *m*-pyridinide. The uncertainty in peak positions corresponds to the width parameter obtained from a Gaussian fit to the experimental peak.

| peak | eBE | shift | assn. |
|---|---|---|---|
| m1 | 11673 (4) | 0 | $0_0^0$ |
| m2 | 12242 (3) | 568 | $17_0^1$ |
| m3 | 12320 (4) | 646 | $16_0^1$ |
| m4 | 12647 (4) | 974 | $15_0^1$ |
| m5 | 12700 (7) | 1027 | $14_0^1$ |
| m6 | 12724 (7) | 1050 | $13_0^1$ |
| m7 | 12889 (5) | 1216 | $16_0^1 17_0^1$ |
| m8 | 12966 (4) | 1292 | $16_0^2$ |
| m9 | 13183 (4) | 1509 | $6_0^1$ |
| m10 | 13216 (8) | 1543 | $15_0^1 17_0^1$ |
| m11 | 13293 (4) | 1619 | $15_0^1 16_0^1$ |
| m12 | 13343 (4) | 1670 | $14_0^1 16_0^1$ |
| m13 | 13368 (5) | 1695 | $13_0^1 16_0^1$ |
| m14 | 13405 (4) | 1731 | $12_0^1 16_0^1$ |
| m15 | 13535 (5) | 1862 | $16_0^2 17_0^1$ |
| m16 | 13614 (6) | 1940 | $16_0^3$ |
| m17 | 13671 (8) | 1998 | $14_0^1 15_0^1$ |
| m18 | 13694 (5) | 2021 | $13_0^1 15_0^1$ |
| m19 | 13825 (6) | 2151 | $6_0^1 16_0^1$ |
| m20 | 13861 (4) | 2188 | $15_0^1 16_0^1 17_0^1$ |
| m21 | 13938 (4) | 2265 | $15_0^1 16_0^2$ |
| m22 | 13988 (4) | 2315 | $14_0^1 16_0^2$ |
| m23 | 14013 (3) | 2340 | $13_0^1 16_0^2$ |
| m24 | 14183 (5) | 2510 | $16_0^3 17_0^1$ |
| m25 | 14262 (6) | 2589 | $16_0^4$ |
| m26 | 14316 (4) | 2642 | $14_0^1 15_0^1 16_0^1$ |
| m27 | 14339 (4) | 2665 | $13_0^1 15_0^1 16_0^1$ |
| m28 | 14377 (3) | 2704 | $12_0^1 15_0^1 16_0^1$ |

**Table 6.14:** Peak positions (in $cm^{-1}$) and vibrational assignments for features in the cryo-SEVI spectrum of *o*-pyridinide. The uncertainty in peak positions corresponds to the width parameter obtained from a Gaussian fit to the experimental peak. For transitions terminating in vibrationally excited neutral states, the eBE shifts relative to the EA extracted from the $\nu_{16}$ progression (EA = 6992 ± 6 $cm^{-1}$) are given in units of $cm^{-1}$.

| peak | eBE | shift | assn. |
|---|---|---|---|
| o1 | 6980 (13) | – | $0_0^0$ |
| o2 | 7641 (3) | 649 | $16_0^1$ |
| o3 | 7938 (4) | 945 | $15_0^1$ |
| o4 | 8002 (3) | 1010 | $14_0^1$ |
| o5 | 8037 (3) | 1044 | $13_0^1$ |
| o6 | 8079 (5) | 1086 | $12_0^1$ |
| o7 | 8209 (3) | 1216 | $16_0^1 17_0^1$ |
| o8 | 8290 (3) | 1298 | $16_0^2$ |
| o9 | 8381 (3) | 1389 | $8_0^1$ |
| o10 | 8457 (3) | 1465 | $7_0^1$ |
| o11 | 8530 (4) | 1538 | $6_0^1$ |
| o12 | 8593 (5) | 1600 | $15_0^1 16_0^1$ |
| o13 | 8651 (3) | 1659 | $14_0^1 16_0^1$ |
| o14 | 8684 (4) | 1692 | $13_0^1 16_0^1$ |
| o15 | 8729 (2) | 1737 | $12_0^1 16_0^1$ |
| o16 | 8781 (6) | 1789 | $11_0^1 16_0^1$ |
| o17 | 8857 (4) | 1864 | $16_0^2 17_0^1$ |
| o18 | 8939 (4) | 1947 | $16_0^3$ |
| o19 | 9031 (3) | 2039 | $8_0^1 16_0^1$ |
| o20 | 9041 (3) | 2049 | $13_0^1 14_0^1$ |
| o21 | 9075 (4) | 2082 | $13_0^2$ |
| o22 | 9104 (3) | 2112 | $7_0^1 16_0^1$ |
| o23 | 9177 (3) | 2185 | $6_0^1 16_0^1$ |
| o24 | 9239 (3) | 2246 | $15_0^1 16_0^2$ |
| o25 | 9299 (4) | 2306 | $14_0^1 16_0^2$ |
| o26 | 9332 (3) | 2339 | $13_0^1 16_0^2$ |

# Part III

# Vinylidene

# Chapter 7

# Vinylidene Excited State Bands

The content and figures of this chapter are reprinted or adapted with permission from J. A. DeVine, M. L. Weichman, X. Zhou, J. Ma, B. Jiang, H. Guo, D. M. Neumark, "Non-adiabatic effects on excited states of vinylidene observed with slow photoelectron velocity-map imaging" *J. Am. Chem. Soc.* **138**, 16417 (2016).

## Abstract

High-resolution slow photoelectron velocity-map imaging spectra of cryogenically cooled $\tilde{X}\ ^2B_2$ $H_2CC^-$ and $D_2CC^-$ in the region of the vinylidene triplet excited states are reported. Three electronic bands are observed and, with the assistance of electronic structure calculations and quantum dynamics on *ab initio*-based near-equilibrium potential energy surfaces, are assigned as detachment to the $\tilde{a}\ ^3B_2$ ($T_1$), $\tilde{b}\ ^3A_2$ ($T_2$), and $\tilde{A}\ ^1A_2$ ($S_1$) excited states of neutral vinylidene. This work provides the first experimental observation of the $\tilde{A}$ singlet excited state of $H_2CC$. While regular vibrational structure is observed for the $\tilde{a}$ and $\tilde{A}$ electronic bands, a number of irregular features are resolved in the vicinity of the $\tilde{b}$ band vibrational origin. High-level *ab initio* calculations suggest that this anomalous structure arises from a conical intersection between the $\tilde{a}$ and $\tilde{b}$ triplet states near the $\tilde{b}$ state minimum, which strongly perturbs the vibrational levels in the two electronic states through nonadiabatic coupling. Using the adiabatic electron affinity of $H_2CC$ obtained from the ground state spectrum discussed in Chapter 8, term energies for the excited neutral states of $H_2CC$ are found to be $T_0(\tilde{a}\ ^3B_2) = 2.0671(15)$, $T_0(\tilde{b}\ ^3A_2) = 2.7407(5)$, and $T_0(\tilde{A}\ ^1A_2) = 2.9939(5)$ eV.

## 7.1 Introduction

Vinylidene ($H_2CC$), a high energy isomer of acetylene (HCCH) and the simplest unsaturated carbene, is an important chemical species as a reactive intermediate in a variety of processes.[277–280] Of particular importance is the vinylidene-acetylene isomerization, which serves as a prototype for 1,2-hydrogen shift reactions widely seen in organic chemistry.[114] This isomerization, believed to proceed over a remarkably low barrier ($< 4$ kcal mol$^{-1}$ with respect to vinylidene) on the ground electronic ($\tilde{X}$) state,[119] is a benchmark unimolecular process in chemical physics and as such has been the focus of many experimental and theoretical studies.[48,116,121,122,124,125,281,282] Due to this low barrier, the spectroscopy of ground-state vinylidene is intimately connected to its possible isomerization to acetylene, and considerable effort has been devoted to detection of its spectroscopic signature among highly excited vibrational levels of HCCH.[283] Vinylidene can be probed more directly by photoelectron spectroscopy of the vinylidene anion ($H_2CC^-$), which has previously shown transitions to the neutral ground singlet state and low-lying triplet states with well-resolved vibrational structure.[126,284] The ground state features in these spectra were considerably broader than those of the excited states, possibly reflecting a lower barrier to isomerization in the ground state. Motivated by this earlier work, higher resolution experiments have been carried out using slow electron velocity-map imaging of cryogenically cooled vinylidene anions (cryo-SEVI). In this chapter, spectra for detachment to the two lowest triplet ($\tilde{a}\ ^3B_2$, $\tilde{b}\ ^3A_2$) states of vinylidene along with the first experimental observation of an excited singlet ($\tilde{A}\ ^1A_2$) state are reported.

The first experimental evidence for the observation of vinylidene was reported in 1980, when the $H_2CC$ species was identified as a possible carrier of a transient signal in the absorption spectrum of acetylene.[285] Vinylidene has since been proposed as a key intermediate in a number of photochemical reactions, highlighting its relevance to the study of reactive species.[286–288] Extensive studies of acetylene near the threshold of isomerization in its ground electronic state have been carried out by Field and co-workers,[289] whose results pointed to traces of vinylidene in the stimulated emission pumping spectra of acetylene and provided an estimate of $\sim 1.88$ eV for the energy of the $H_2CC$ minimum relative to HCCH on the neutral $\tilde{X}$ electronic surface. Vinylidene has also been found to be a relevant isomer of dicationic acetylene; experiments probing photofragmentation following double ionization of acetylene indicate that the $HCCH^{2+}$ dication proceeds through a vinylidene configuration prior to dissociation, with an isomerization lifetime of less than 60 fs.[290,291] Given the apparent importance of the transient vinylidene species, characterization of its vibronic properties is of great interest and can provide a more complete picture of the $C_2H_2$ system, especially when considered in the context of the long history of experimental investigations of acetylene.[292–298]

Fortunately, the vinylidene isomer constitutes the global minimum on the anionic electronic surface of $C_2H_2$, providing a straightforward route to formation of neutral $H_2CC$ by removal of an electron from the relatively stable vinylidene anion.[127,128,299,300] To date, the most quantitative data regarding excited states of vinylidene remain the vibrationally resolved anion photoelectron spectra reported by Ervin *et al.*, who observed detachment from

$H_2CC^-$ and its isotopologues to the three lowest electronic ($\tilde{X}\ ^1A_1$, $\tilde{a}\ ^3B_2$, and $\tilde{b}\ ^3A_2$) states of vinylidene.[126] Their results provided the adiabatic electron affinity (EA) of neutral vinylidene, as well as term energies of 2.065(6) and 2.75(2) eV for the two lowest triplet excited states. Several vibrational features were observed and assigned in the $\tilde{a}$ electronic band, but these spectra were limited to binding energies below $\sim$ 3.5 eV, preventing detachment to levels above the $\tilde{b}$ vibrational ground state. Peaks in the $\tilde{X}$ band were found to be broader than features arising from detachment to the excited triplet states, suggesting rapid ($<$ 200 fs) isomerization of the singlet state to an unresolved quasicontinuum of acetylene states. However, Coulomb explosion imaging experiments implied a much longer-lived vinylidene species.[127]

A great deal of theoretical work has also been carried out with the goal of elucidating the electronic structure of vinylidene and calculating its isomerization barrier in excited states. Schaefer and co-workers[301–303] have investigated low-lying triplet excited states of $H_2CC$, reporting energetic and structural information as well as demonstrating that the barrier for isomerization to acetylene on the $\tilde{a}$ electronic surface is $\sim$ 2 eV. An additional state, the $\tilde{A}$ singlet state, was calculated by Stanton and co-workers[304,305] to lie just above the $\tilde{a}$ and $\tilde{b}$ triplet states with a similarly high barrier, and $H_2CC$ was found to be the global minimum on this surface. Regardless of geometry, the energetic ordering of excited electronic states of the acetylene-vinylidene system is found to be $\tilde{a} < \tilde{b} < \tilde{A}$.[306,307] Recently, the photodetachment of $H_2CC^-$ has been investigated with a full-dimensional quantum method using highly accurate potential energy surfaces (PESs) for the anion and singlet neutral ground state,[48] which reproduced all experimentally observed features in the $\tilde{X}$ electronic band;[49] as of yet, such a theoretical treatment has not been used to investigate detachment to excited states of vinylidene.

This chapter presents high-resolution photoelectron spectra of $H_2CC^-$ and $D_2CC^-$ obtained using slow electron velocity-map imaging (SEVI), a variation of traditional photoelectron spectroscopy that employs a tunable detachment laser and velocity-map imaging (VMI) detection scheme to obtain sub-meV resolution for low kinetic energy electrons.[157] Cryogenic cooling of the ions prior to photodetachment (cryo-SEVI) enhances resolution for molecular systems and reduces spectral congestion. The reported spectra represent the first experimental observation of the lowest-lying singlet excited state of vinylidene, and partial rotational resolution is obtained for detachment to the $\tilde{b}\ ^3A_2$ and $\tilde{A}\ ^1A_2$ neutral states. Detachment to the lowest triplet $\tilde{a}\ ^3B_2$ state is observed with higher resolution than previous spectra. Due to the limited operating range of our detachment laser at the time of measurement, the discussion of the ground state band is postponed until Chapter 8.

The $\tilde{a}\ ^3B_2 \leftarrow \tilde{X}\ ^2B_2$, $\tilde{b}\ ^3A_2 \leftarrow \tilde{X}\ ^2B_2$, and $\tilde{A}\ ^1A_2 \leftarrow \tilde{X}\ ^2B_2$ electronic bands are analyzed with the assistance of high-level *ab initio* calculations and a full-dimensional quantum dynamics treatment analogous to that performed for photodetachment to the ground singlet state.[126] While the $\tilde{a}$ and $\tilde{A}$ electronic bands are relatively well-reproduced by theory, the $\tilde{b}$ band is visibly perturbed, with a collection of irregular features near the vibrational origin of this band. This anomalous structure is attributed to a conical intersection between the $\tilde{a}$ and $\tilde{b}$ triplet states that occurs near the $\tilde{b}$ state minimum.

## 7.2 Methods

### 7.2.1 Experimental

The cryo-SEVI method and apparatus are described in Chapter 2. Vinylidene ions were made by supersonic expansion of a gas mixture containing $N_2O$ and $C_2H_4$ or $C_2D_4$ in He through the filament ionizer described in Section 2.1.1. Upon injection of electrons from the ionizer, $N_2O$ undergoes dissociative electron attachment to form $O^-$, which then proceeds to react with $C_2H_4$ or $C_2D_4$ to form $H_2CC^-$ or $D_2CC^-$, respectively.[308] The energy calibration of the VMI for data presented in this chapter was carried out by obtaining images for the well-characterized detachment transitions of atomic $F^-$ at several photon energies.[188]

### 7.2.2 Theoretical[a]

High-level *ab initio* calculations for various $C_2H_2$ isomers were performed at the explicitly correlated internally contracted multireference configuration interaction (ic-MRCI-F12) level,[309] using reference wave functions generated from state-averaged complete active space self-consistent field (SA-CASSCF) calculations with the two lowest singlet ($\tilde{X}$, $\tilde{A}$) and two triplet ($\tilde{a}$, $\tilde{b}$) states equally weighted.[310,311] A full valence active space was used with 10 electrons in 10 active orbitals, i.e., CASSCF (10,10), excluding the $1s$ orbital of both carbon atoms. The correlation-consistent triple-$\zeta$ basis set optimized for the explicitly correlated approach (cc-pVTZ-F12)[312] was found to converge the vertical and adiabatic excitation energies. This computational procedure, referred to as ic-MRCI-F12/cc-pVTZ-F12 hereafter, was applied throughout the subsequent geometry optimization and construction of potential energy surfaces (PESs). All calculations were carried out using the MOLPRO electronic structure computational package.[313]

Semiglobal adiabatic PESs for the $\tilde{a}$, $\tilde{b}$, and $\tilde{A}$ states of the vinylidene isomer were constructed using the permutationally invariant polynomial neural network (PIP-NN) method.[314–316] In this method, the NN input layer consists of a number of PIPs which are conveniently obtained by symmetrizing monomials of transformed internuclear distances,[317]

$$G_l = \hat{S} \prod_{i<j}^{N} p_{ij}^{l_{ij}}, \tag{7.1}$$

where $\hat{S}$ is the symmetrization operator, which rigorously enforces the permutation symmetry in the system, and $p_{ij} = \exp(-\lambda r_{ij})$ where $r_{ij}$ is the internuclear distance between atoms $i$ and $j$ and $\lambda$ is a positive length parameter typically close to 1 $Å^{-1}$.[318] The sum of the order $l_{ij}$ in Eq. 7.1 represents the total degree of a monomial. In this $A_2B_2$ type molecule, 74 PIPs up to the fourth order were included, and the NNs were trained by the Levenberg-Marquardt

[a]The theoretical calculations described here were carried out by our collaborators Xueyao Zhou, Jianyi Ma, Bin Jiang, and Hua Guo.

algorithm with the root-mean-square error (RMSE) being used as the performance function,

$$\text{RMSE} = \sqrt{\frac{1}{N}\sum_{i=1}^{N}\left(E_t^i - E_f^i\right)^2}, \tag{7.2}$$

where $E_t^i$ and $E_f^i$ are the target and fitted energy of the $i^{\text{th}}$ point, and $N$ is the total number of points in the data set. Since the points are all chosen in the vinylidene well, the resulting PESs are not expected to be accurate elsewhere. The final PESs are the average of three best fits, with overall RMSEs of 1.45, 3.57, and 3.25 meV for the $\tilde{a}$, $\tilde{b}$, and $\tilde{A}$ states, respectively. These three PESs and the anion PES developed by Han and co-workers[49] were used for the subsequent quantum dynamics calculations of the photodetachment process. Contour plots of the resultant PESs are provided in Figure 7.6.

The full-dimensional quantum dynamical calculations were performed using the C+HCH (2+1) Radau-Jacobi coordinates,[319] denoted as $(r_0, r_1, r_2, \theta_1, \theta_2, \phi)$: $r_0$ is the distance between C and the center-of-mass of $CH_2$, $r_1$ and $r_2$ are two Radau radial coordinates for the HCH species, $\theta_1$ ($\theta_2$) is the angle between vectors $r_1$ ($r_2$) and $r_0$, and $\phi$ is the relative azimuthal angle between $r_1$ and $r_2$ in the body-fixed (BF) frame, which places the $z$ axis along $r_0$. The rotationless ($J = 0$) Hamiltonian in this coordinate system is given (in atomic units) by

$$\hat{H} = -\frac{1}{2\mu_0}\frac{\partial^2}{\partial r_0^2} + \sum_{i=1}^{2}\left(-\frac{1}{2\mu_i}\frac{\partial^2}{\partial r_i^2}\right) + \sum_{i=0}^{2}\frac{\hat{j}_i^2}{2\mu_i r_i^2} + V(r_0, r_1, r_2, \theta_1, \theta_2, \phi), \tag{7.3}$$

where $\mu_0 = m_C(m_C + 2m_H)/(2m_C + 2m_H)$, $\mu_1 = \mu_2 = m_H$, $\hat{j}_1$ ($\hat{j}_2$) is the angular momentum operator for $r_1$ ($r_2$), and $\hat{j}_0^2 = (\hat{j}_1 + \hat{j}_2)^2$. $V$ is the potential energy function described in terms of the Radau-Jacobi coordinates. The Hamiltonian was discretized using a mixed grid-basis representation;[320] radial coordinates were represented with the potential optimized discrete variable representation (POVDR),[321,322] while the angular coordinates were represented by basis functions. For the $D_2CC$ calculations, the H atoms were substituted by its heavier isotope.

The initial wave packet ($\Psi_i$) on a neutral PES was assumed, within the Condon approximation, to arise from a vertical transition from an eigenstate on the anion PES. The anion wave functions for the four lowest-lying rotationless vibrational levels were obtained by diagonalizing the same Hamiltonian in eq. 7.3 substituted by the anion PES using the Lanczos method.[323] The wave packet on the neutral state PES was propagated using the real Chebyshev propagator,[324]

$$\Psi_k = 2D\hat{H}_s\Psi_{k-1} - D^2\Psi_{k-2},\ k \geq 2, \tag{7.4}$$

with $\Psi_1 = D\hat{H}_s\Psi_0$ and $\Psi_0 = \Psi_i$. The Hamiltonian in eq. 7.4 was scaled to the spectral range of (-1,1) by $\hat{H}_s = (\hat{H} - H^+)/H^-$. The spectral medium, $H^+ = (H_{max} + H_{min})/2$, and half-width, $H^- = (H_{max} - H_{min})/2$, were determined by the spectral extrema. Dynamical parameters used are listed in Table 7.5.

Photoelectron spectra were obtained from the discrete cosine Fourier transform of the Chebyshev autocorrelation functions.[325] The eigenfunctions are assigned based on the nodal structure of the wave functions. However, it should be noted that, in the severe state mixing limit, the nodal structure of the eigenfunctions is not straightforward to interpret.

## 7.3 Results

### 7.3.1 Experimental

Figure 7.1 shows the excited state region of the vinylidene photoelectron spectrum, the focus of the present chapter. In this and the following figures, the green traces are low-resolution overview spectra taken with high photon energies, and the black traces represent the high-resolution SEVI scans taken closer to threshold and scaled to match the relative intensities in the overview spectra. Two regions of structure are observed, the first spanning eBE $\approx 20000 - 24000$ cm$^{-1}$ and the second more congested region above eBE = 25000 cm$^{-1}$. The lower-eBE region, shown in more detail in Figure 7.2a, exhibits regular vibrational structure in agreement with the reported $\tilde{a}$ band of the vinylidene anion photoelectron spectrum.[126]

The higher binding energy region, shown in Figure 7.2b for both $H_2CC^-$ and $D_2CC^-$, displays an intense peak (b1) at $\sim$ 26000 cm$^{-1}$ consistent with the reported binding energy of the $\tilde{b}$ band origin,[126] and, starting around 28000 cm$^{-1}$, three roughly evenly spaced features (A1-A3). The $25000 - 28000$ cm$^{-1}$ region of the spectrum displays a collection of

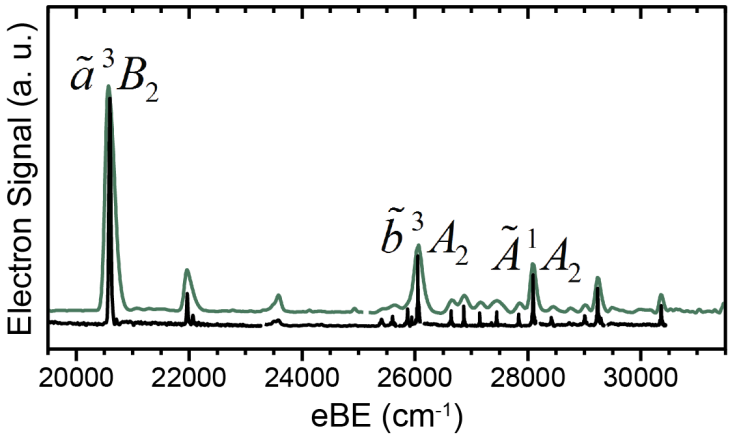


**Figure 7.1:** Anion photoelectron spectra showing detachment to the three lowest excited states of neutral $H_2CC$. The vibrational origin of each electronic band is labeled with the corresponding neutral state assignment. The green traces are overview spectra taken high above threshold, and the black traces correspond to composite higher-resolution, lower-eKE scans.

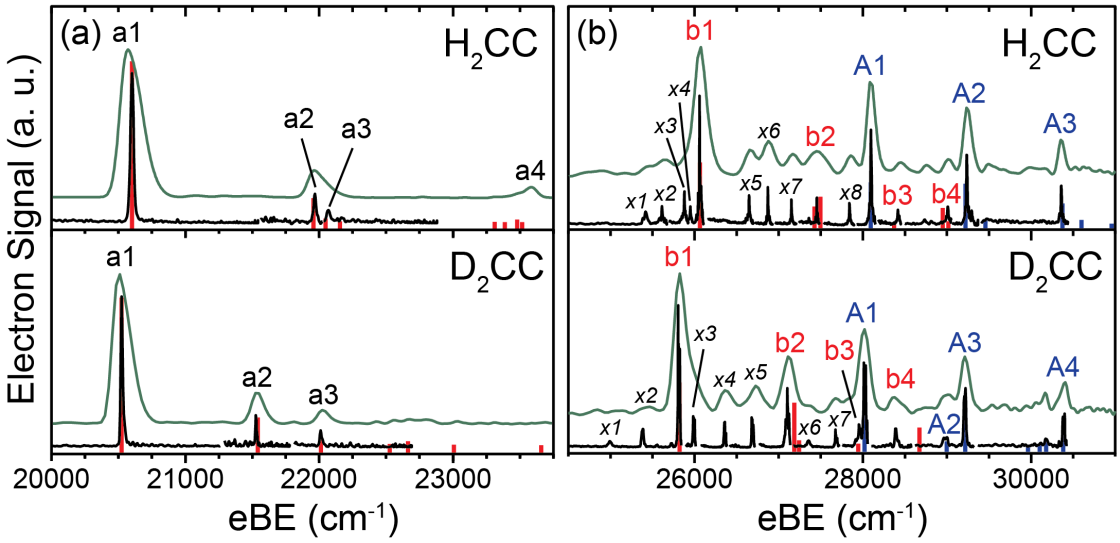


**Figure 7.2:** Cryo-SEVI spectra of $H_2CC^-$ (top) and $D_2CC^-$ (bottom). Green traces are low-resolution overview scans, and black traces are high-resolution SEVI scans. **(a)** Region assigned to the $\tilde{a}\ ^3B_2$ electronic band, with the red stick spectrum showing quantum dynamics calculations for the $\tilde{a}\ ^3B_2 \leftarrow \tilde{X}\ ^2B_2$ detachment transition. **(b)** Region assigned to the $\tilde{b}\ ^3A_2$ and $\tilde{A}\ ^1A_2$ electronic bands, with quantum dynamics simulations for the $\tilde{b}\ ^3A_2 \leftarrow \tilde{X}\ ^2B_2$ and $\tilde{A}\ ^1A_2 \leftarrow \tilde{X}\ ^2B_2$ shown as red and blue sticks, respectively.

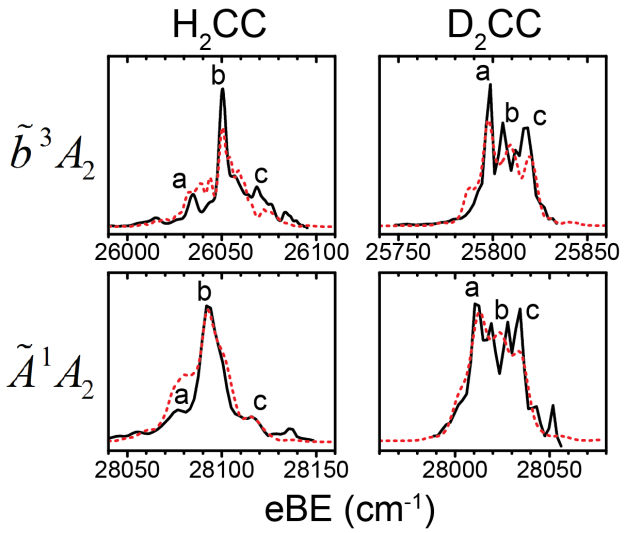


**Figure 7.3:** Rotational profiles of the $\tilde{b}$ (top) and $\tilde{A}$ (bottom) band origins in the cryo-SEVI spectra of $H_2CC^-$ (left) and $D_2CC^-$ (right). Experimental lineshapes are shown as solid black lines, and calculated contours are shown as red dashed lines.

relatively weak and irregularly spaced features (labeled x), some of which appear lower in binding energy than b1. We have previously shown that vibrational cooling is very efficient under the conditions used in the ion trap,[326] so these transitions are unlikely to correspond to vibrational hot bands and can be attributed to photodetachment from the ground vibrational state of the anion. This assignment is supported by the observation that the relative intensities of these features were insensitive to variations in the trap conditions. The irregular peaks are observed to shift upon deuteration, whereas the A1-A2-A3 progression does not shift substantially.

The resolution provided by cryo-SEVI is sufficient to partially resolve rotational contours for features in this region of the spectrum; representative profiles can be seen in Figure 7.3 for the band origins (b1 and A1) indicated in Figure 7.1. Rotational envelopes of other assigned features are shown in Figures 7.7 and 7.8.

In addition to detachment energies, SEVI yields the photoelectron angular distribution (PAD) associated with detachment to each neutral electronic state. For detachment with a single linearly polarized photon, the PAD is given by[22]

$$\frac{d\sigma}{d\Omega} = \frac{\sigma_{tot}}{4\pi}[1 + \beta P_2(\cos\theta)], \tag{7.5}$$

where $\sigma_{tot}$ is the total detachment cross section, $P_2(x)$ is the second-order Legendre polynomial, $\theta$ is the angle of the outgoing electron's velocity vector with respect to the laser polarization axis, and $\beta$ is the anisotropy parameter. The anisotropy parameter ranges from $-1$ to $+2$ corresponding to perpendicular and parallel polarization, respectively, and contains information regarding the shape of the anion orbital from which an electron is detached.

Consideration of the anisotropies of the different features in Figure 7.1 reveals two distinct trends for the spectral regions shown in Figures 7.2a and 7.2b. All peaks in Figure 7.2a have positive $\beta$ values close to $+2$, and determination of the anisotropy parameter for the $\tilde{a}$ band vibrational origin across spectra with varying photon energies show this to be true regardless of kinetic energy for eKE $< 0.5$ eV. This behavior is typical of detachment from $s$-like orbitals to form $p$-wave electrons with angular momentum $\ell = 1$. All features with eBE $> 25000$ cm$^{-1}$ show the same energy dependence of $\beta$, with $\beta \approx 0$ for low kinetic energies and $\beta < 0$ at moderate eKE, characteristic of detachment from $p$-like orbitals resulting in outgoing $s$- and $d$-wave electrons with $\ell = 0$ and 2, respectively.

According to the Wigner threshold law,[21] the cross section for photodetachment scales as $(\text{eKE})^{\ell+1/2}$; as we obtain our best resolution by detaching as close to threshold as possible, the SEVI method works best for detachment transitions that can produce outgoing $s$-wave electrons. As such, the resolution of the $\tilde{a}$ band in Figure 7.2a is more limited than the $\tilde{b}$ and $\tilde{A}$ bands in Figure 7.2b, and some of the weaker features present in the theoretical spectrum are below the detection limit for this experiment. Regardless, the resolution of the $\tilde{a}$ band is somewhat improved relative to the work of Ervin and co-workers; most peaks in this region are narrower than 20 cm$^{-1}$, which proves sufficient to resolve the C-C stretch fundamental (a3) that was assigned, but obscured by the nearby a2 feature, in the previous study.

### 7.3.2 Electronic Structure

Figure 7.4 shows the *ab initio* energetics of various stationary states of the HCCH-$H_2CC$ system on the $\tilde{X}$, $\tilde{a}$, $\tilde{b}$, and $\tilde{A}$ electronic surfaces; more detailed structural information can be obtained from Figure 7.9 and Tables 7.6 and 7.7. As in previous works, the energy ordering of the excited states is $\tilde{a} < \tilde{b} < \tilde{A}$ regardless of geometry, and barriers for isomerization to *trans*-acetylene in excited states are large with typical values around 2 eV. In the first triplet state, *cis*-HCCH is found to be the most stable isomer, followed by vinylidene and *trans*-HCCH, though energy differences between these isomers are relatively small. In the $\tilde{b}$ state, *trans*-HCCH is slightly lower in energy than vinylidene and *cis*-HCCH, again with relatively small ($\sim$ 0.2 eV) energy differences between the isomers. In the singlet $\tilde{A}$ state, vinylidene becomes the global minimum, lying 0.35 and 0.73 eV lower than *trans*- and *cis*-HCCH, respectively. The equilibrium geometries of $H_2CC$ in the $\tilde{b}$ and $\tilde{A}$ states are quite similar, with a somewhat elongated C-C bond relative to that of the $\tilde{X}$, $\tilde{a}$, and anion states. These results are in agreement with recent theoretical predictions.[303,304,306]

As a nonlinear tetratomic molecule with $C_{2v}$ symmetry, vinylidene has six vibrational modes: the symmetric C-H stretch ($\nu_1$, $a_1$); the C-C stretch ($\nu_2$, $a_1$); the $CH_2$ scissor mode ($\nu_3$, $a_1$); the out-of-plane wag ($\nu_4$, $b_1$); the antisymmetric C-H stretch ($\nu_5$, $b_2$); and the $CH_2$ rocking mode ($\nu_6$, $b_2$). Harmonic frequencies for the stationary states considered in this work and their corresponding zero-point energies (ZPEs) are listed in Tables 7.8-7.10. In the $\tilde{X}$

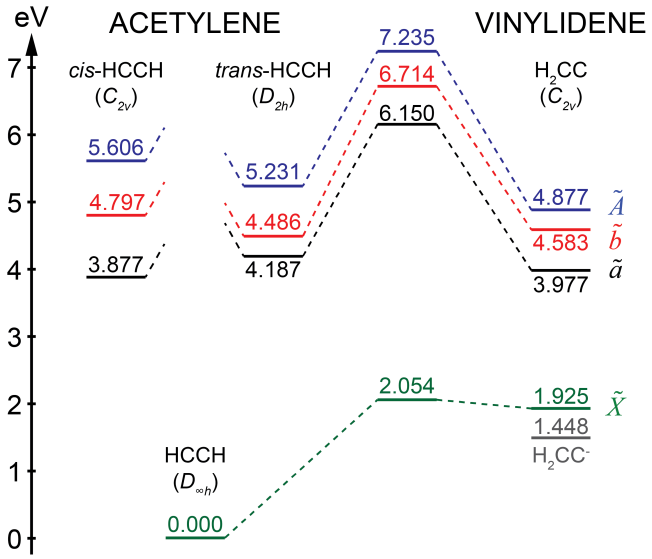


**Figure 7.4:** Energy level diagram for stationary points of the $\tilde{X}$ (green), $\tilde{a}$ (black), $\tilde{b}$ (red), and $\tilde{A}$ (blue) states of the acetylene-vinylidene system, along with the vinylidene anion (gray), which is taken from literature for comparison.[49] Other relative energies (in eV) were obtained at the ic-MRCI-F12/cc-pVTZ-F12 level in this work.

and $\tilde{a}$ states of vinylidene, $\nu_2$ is higher in frequency than $\nu_3$, whereas $\nu_2 < \nu_3$ in the $\tilde{b}$ and $\tilde{A}$ states; this is presumably due to the longer and therefore weaker C-C bond in the $\tilde{b}$ and $\tilde{A}$ states of vinylidene. It is also interesting to note that the $\nu_1$ and $\nu_2$ modes are strongly mixed in the $\tilde{a}$ state due to a 1:2 Fermi resonance. In the $\tilde{b}$ state, $\nu_1$ is strongly mixed with both $\nu_2$ and $\nu_3$, suggesting that there is Fermi coupling of the $1\nu_1$ state with the $2\nu_2$ and $2\nu_3$ levels. The ZPEs of $H_2CC$ in both singlet states are similar to that of the vinylidene anion, and lower than those of the two triplet states. With ZPE corrections, the adiabatic excitation energies for $\tilde{a}$, $\tilde{b}$, and $\tilde{A}$ $H_2CC$ are 2.091, 2.701, and 2.955 eV, respectively. The equilibrium geometries, energetics, and harmonic frequencies on all three PESs are in excellent agreement with *ab initio* values, demonstrating the high quality of the PIP-NN fits.

## 7.4 Discussion

### 7.4.1 Vibronic Assignments

The calculated spectra for photodetachment of $H_2CC^-$ and $D_2CC^-$ are shown as red and blue sticks superimposed on the experimental spectra in Figures 7.2a and 7.2b, and serve as a starting point for assignment of vibrational features. It should be noted that absolute peak positions in the calculated spectra depend sensitively on the energy difference between the anion and each neutral state, which is difficult to determine precisely at this level of theory. Indeed, the current calculation at the ic-MRCI-F12/cc-pVTZ-F12 level either overestimates by $\sim 30$ meV ($\tilde{a}$) or underestimates by $\sim 40$ meV ($\tilde{b}$ and $\tilde{A}$) the measured adiabatic excitation energies. As such, to facilitate comparison with experiment, we have artificially shifted the calculated band origin of each state to the corresponding experimental one, and focus our analysis on the relative peak positions for detachment to different vibrational levels.

Figure 7.2a shows that experimental peak positions and intensities for the $\tilde{a}\ ^3B_2 \leftarrow \tilde{X}\ ^2B_2$ electronic band are reproduced quite well by quantum dynamics calculations on the *ab initio* PES. The excellent agreement provides assignment of all resolved features. Peak positions and assignments for these features are presented in Table 7.1, along with the calculated frequencies. As discussed earlier, the improved resolution for this electronic band over previous work permits resolution of the close-lying a2 and a3 peaks that correspond to the $\nu_3$ fundamental and a Fermi resonance between the $2^1$ and $4^2$ levels, respectively.

In Figure 7.2b, peak b1 is assigned to the vibrational origin of the $\tilde{b}\ ^3A_2 \leftarrow \tilde{X}\ ^2B_2$ electronic band following the assignment of Ervin and co-workers.[126] Several other experimental peaks (b2-b4) roughly line up with the $\tilde{b}$ band quantum dynamics results, although most of the experimental peaks in Figure 7.2b between $25000 - 28000$ cm$^{-1}$ do not appear in the calculation. The origin of this discrepancy will be revisited below. At slightly higher eBEs, comparison of the $\tilde{A}\ ^1A_2 \leftarrow \tilde{X}\ ^2B_2$ calculated spectra (blue sticks) to experiment identifies peaks A1-A3 as arising from detachment to the $\tilde{A}$ singlet state, providing an explanation for the seemingly odd trend of the spectra in Figure 7.2b becoming more regular at higher binding energies. This electronic assignment is supported by the identical PADs observed for

all features in Figure 7.2b, as both the $\tilde{b}$ and $\tilde{A}$ states are formed by removal of an electron from the same $b_1$ anion orbital.

The quantum dynamics results allow assignment of peaks b1-b4 as well as the $\tilde{A}$ band; these are reported in Tables 7.2 and 7.3 for $H_2CC$ and $D_2CC$, respectively, along with experimental and theoretical peak positions. The most Franck-Condon (FC) active vibrational mode in both the $\tilde{b}$ and $\tilde{A}$ electronic states is $\nu_2$, presumably a consequence of the $\sim 0.1$ Å increase in the C-C bond length ($r_{CC}$) that occurs upon photodetachment to these neutral states. The assigned progressions in this mode all present some degree of anharmonicity; consideration of the A1-A2-A3 and A1-A3-A4 progressions in Tables 7.2 and 7.3 yields harmonic frequencies of 1158(10) and 1213(10) $cm^{-1}$ with anharmonicity constants of 8(4) and 9(4) $cm^{-1}$ for $H_2CC$ and $D_2CC$, respectively. While the $2_0^2$ transition in the $\tilde{b}$ band of $H_2CC^-$ is obscured by the $\nu_1$ fundamental, preventing calculation of an anharmonicity constant, similar values are found for the b1-b2-b4 progression in the $D_2CC^-$ spectrum.

The experimental binding energies of peaks a1, b1, and A1, along with the electron affinity of vinylidene reported in Chapter 8, yield term energies of $T_0(\tilde{a}\ ^3B_2) = 2.0671(15)$, $T_0(\tilde{b}\ ^3A_2) = 2.7408(5)$, and $T_0(\tilde{A}\ ^1A_2) = 2.9939(5)$ eV relative to the vibrational ground state of $\tilde{X}\ ^1A_1$ $H_2CC$, in good agreement with the *ab initio* results reported in this chapter. The term energy for the $\tilde{A}\ ^1A_2$ singlet state can be combined with the upper-bound for the energy of $\tilde{X}\ ^1A_1$ $H_2CC$ relative to HCCH ($\Delta E \approx 1.88$ eV)[289] to place $\tilde{A}\ ^1A_2$ $H_2CC$ at $\sim 4.38$ eV above the ground state of acetylene. As the adiabatic excitation of $\tilde{A}\ ^1A_u$ *trans*-HCCH is

**Table 7.1:** Peak positions ($cm^{-1}$), shifts from the origin and theoretical predictions ($cm^{-1}$), and assignments of features in the $\tilde{a}\ ^3B_2 \leftarrow \tilde{X}\ ^2B_2$ electronic band of the vinylidene photoelectron spectra. The $2_0^1$ and $4_0^2$ features form a strong Fermi resonance pair for peak a3 of $H_2CC$. Uncertainties in peak positions correspond to one standard deviation of a Gaussian fit to the experimental peak.

| peak | eBE | shift | theo. | assn. |
|---|---|---|---|---|
| | | $H_2CC$ | | |
| a1 | 20602 (12) | 0 | 0 | $0_0^0$ |
| a2 | 20602 (12) | 1366 | 1358 | $3_0^1$ |
| a3 | 22069 (12) | 1467 | 1439 | $2_0^1 \sim 4_0^2$ |
| a4 | 23553 (70) | 2951 | 2921 | $1_0^1$ |
| | | $D_2CC$ | | |
| a1 | 20525 (8) | 0 | 0 | $0_0^0$ |
| a2 | 21528 (5) | 1003 | 1002 | $3_0^1$ |
| a3 | 22016 (9) | 1491 | 1474 | $2_0^1$ |

**Table 7.2:** Peak positions ($cm^{-1}$), shifts from the origin and theoretical predictions ($cm^{-1}$), and assignments of features in the $\tilde{b}\,^3A_2 \leftarrow \tilde{X}\,^2B_2$ and $\tilde{A}\,^1A_2 \leftarrow \tilde{X}\,^2B_2$ electronic bands in the cryo-SEVI spectra of $H_2CC^-$. Uncertainties in peak positions, which are identical for all features in a given electronic band, correspond to one standard deviation of the Gaussian convolution used to calculated the rotational contour of the band origin.

| peak | eBE | shift | theo. | assn. |
|---|---|---|---|---|
| | $\tilde{b}\,^3A_2 \leftarrow \tilde{X}\,^2B_2$ | | | |
| b1 | 26035 (2) | 0 | 0 | $0_0^0$ |
| b2 | 27438 | 1403 | 1425 | $2_0^1$ |
| b3 | 28400 | 2365 | 2316 | $4_0^2$ |
| b4 | 28994 | 2958 | 2964 | $1_0^1$ |
| | $\tilde{A}\,^1A_2 \leftarrow \tilde{X}\,^2B_2$ | | | |
| A1 | 28077 (3) | 0 | 0 | $0_0^0$ |
| A2 | 29219 | 1142 | 1136 | $2_0^1$ |
| A3 | 30345 | 2267 | 2287 | $2_0^2$ |

**Table 7.3:** Peak positions ($cm^{-1}$), shifts from the origin and theoretical predictions ($cm^{-1}$), and assignments of features in the $\tilde{b}\,^3A_2 \leftarrow \tilde{X}\,^2B_2$ and $\tilde{A}\,^1A_2 \leftarrow \tilde{X}\,^2B_2$ electronic bands in the cryo-SEVI spectra of $D_2CC^-$. Uncertainties in peak positions, which are identical for all features in a given electronic band, correspond to one standard deviation of the Gaussian convolution used to calculated the rotational contour of the band origin.

| peak | eBE | shift | theo. | assn. |
|---|---|---|---|---|
| | $\tilde{b}\,^3A_2 \leftarrow \tilde{X}\,^2B_2$ | | | |
| b1 | 25797 (2) | 0 | 0 | $0_0^0$ |
| b2 | 27097 | 1301 | 1370 | $2_0^1$ |
| b3 | 27954 | 2157 | 2129 | $1_0^1$ |
| b4 | 28387 | 2590 | 2861 | $2_0^2$ |
| | $\tilde{A}\,^1A_2 \leftarrow \tilde{X}\,^2B_2$ | | | |
| A1 | 28012 (3) | 0 | 0 | $0_0^0$ |
| A2 | 28983 | 971 | 980 | $3_0^1$ |
| A3 | 29207 | 1195 | 1203 | $2_0^1$ |
| A4 | 30383 | 2371 | 2375 | $2_0^2$ |

known to be 5.219 eV,[298] our data thus confirm the predictions of Stanton and co-workers[48] that the global minimum on the first excited singlet surface of the acetylene-vinylidene system takes the vinylidene geometry.

### 7.4.2 Rotational Assignments

The resolution of the cryo-SEVI vinylidene spectra is sufficient to obtain partially resolved rotational envelopes for the vibrational origins of the $\tilde{b}$ and $\tilde{A}$ bands, as shown in Figure 7.3. Vinylidene is a near-prolate asymmetric top, with rotational constants $A > B \sim C$; the rotational energies for such a molecule can be approximated in terms of the quantum numbers $J$ and $K$ by[327]

$$E_{rot}(J,K) = \frac{1}{2}(B+C)J(J+1) + \left[A - \frac{1}{2}(B+C)\right]K^2. \tag{7.6}$$

Rotational constants for the ground state of vinylidene have been calculated previously from *ab initio* calculations.[118] For $H_2CC$, $A \approx 10$ cm$^{-1}$, whereas $B$ and $C$ are on the order of 1 cm$^{-1}$, so the resolution provided by SEVI is only sufficient to assign rotational branches corresponding to changes in $K$.

As was shown in our previous consideration of the partially resolved rotational profiles in the SEVI spectra of $CH_2CN^-$ and $CD_2CN^-$,[177] the selection rule for photodetachment requires that $\Delta K = K_{neutral} - K_{anion} = \pm 1$. Allowed values of $K_{anion}$ for $H_2CC^-$ ($D_2CC^-$), considering both *ortho* and *para* nuclear spin states, are governed by the requirement that the total internal wave function be antisymmetric (symmetric) with respect to hydrogen (deuterium) interchange.[328] In the $\tilde{X}\ ^2B_2$ anion state, we find that *o*-$H_2CC^-$ and *p*-$D_2CC^-$ are restricted to even values of $K_{anion}$, whereas *p*-$H_2CC^-$ and *o*-$D_2CC^-$ must have odd $K_{anion}$. Given the low internal temperatures typical of the cryo-SEVI experiment, we expect most of our anions to be in the $K = 0$ (*o*-$H_2CC^-$, *p*-$D_2CC^-$) or $K = 1$ (*p*-$H_2CC^-$, *o*-$D_2CC^-$) states, so the rotational contour will consist primarily of three branches, corresponding to the $1 \leftarrow 0$ and $0, 2 \leftarrow 1$ rotational transitions. The relative intensities of these branches are dictated by nuclear spin statistics directly analogous to those of $H_2$ ($D_2$); applied to $H_2CC^-$

**Table 7.4:** Assignments of rotational features for the vibrational origins of the $\tilde{b}$ and $\tilde{A}$ bands in the SEVI spectrum of vinylidene.

| feature | anion | | $K_{neutral} \leftarrow K_{anion}$ |
|---|---|---|---|
| a | *p*-$H_2CC^-$ | *o*-$D_2CC^-$ | $0 \leftarrow 1$ |
| b | *o*-$H_2CC^-$ | *p*-$D_2CC^-$ | $1 \leftarrow 0$ |
| c | *p*-$H_2CC^-$ | *o*-$D_2CC^-$ | $2 \leftarrow 1$ |

($D_2CC^-$), this results in a 3:1 (1:2) ratio of the $K = 0 : K = 1$ anion population. These considerations allow us to assign the labeled features in Figure 7.3 as presented in Table 7.4.

The PGOPHER software package was used to simulate and fit rotational envelopes with rotational constants from the ic-MRCI-F12/cc-pVTZ-F12 optimized geometries (Table 7.11).[329] This package calculates the rotational stick spectrum (with $-1 \leq \Delta J \leq +2$) for a vibrational transition at some temperature and convolutes it with a Gaussian profile with a variable width, which was used to obtain uncertainties in experimental peak positions. As the $\tilde{A}$ band shows more regularity in the spacing between and rotational contours of different vibrational features, the temperature, convolution width, and transition energy for the $\tilde{A}$ band origins were optimized simultaneously, giving ion temperatures of 13.4(1) and 14.2(2) K for $H_2CC^-$ and $D_2CC^-$, respectively, indicating that virtually all anions are in rotational levels with $J < 10$. These temperatures are in good agreement with ion temperatures extracted in previous cryo-SEVI experiments.[177,326] These temperatures were used for fitting the $\tilde{b}$ band origins, for which only the transition energies and convolution widths were varied. For the rest of the assigned features, only the transition energy was optimized, providing precise extraction of vibrational frequencies. Minor variations in rotational profiles were observed across the different features in both electronic bands (see Figures 7.7 and 7.8), likely due to threshold effects on the detachment cross section as well as the apparent anharmonicity of these excited states revealed in the $\nu_2$ progressions.

### 7.4.3 Non-Adiabaticity of Excited Vinylidene

We finally turn our attention to the eBE $= 25000 - 28000$ cm$^{-1}$ region of the cryo-SEVI spectra, which consists of the $\tilde{b}$ electronic band as well as a number of anomalous features. As mentioned earlier, the intensities of the unassigned peaks relative to assigned vibrational features are not temperature dependent, which suggests that they solely reflect the vibronic structure of neutral, rather than anionic, vinylidene. The shifts of several of these peaks relative to the $\tilde{b}$ band origin (Table 7.12) are smaller than the smallest harmonic frequency expected for vinylidene, indicating that they cannot correspond to detachment to nominally forbidden vibrational levels in the $\tilde{b}\,^3A_2$ state. Coupling to acetylene can in principle lead to perturbation of the photoelectron spectrum provided the barrier for isomerization to *trans*-HCCH is sufficiently low on the $\tilde{b}$ electronic surface, but the calculated barrier height of $> 2$ eV indicates that isomerization is unlikely to play a role for the detachment energies considered here.

It is conceivable, however, that the anomalous peaks stem from mixing with vibrational levels in other electronic states, due, for example, to nonadiabatic coupling between the $\tilde{a}$ and $\tilde{b}$ triplet states or spin-orbit coupling between the $\tilde{A}$ state and the lower-lying triplet states. As the spin-orbit coupling is typically quite small for hydrocarbons, the latter option is unlikely to play a role in the electronic structure of $H_2CC$.

Figure 7.5 shows one-dimensional potential energy curves calculated for the adiabatic and diabatic $\tilde{a}$, $\tilde{b}$, and $\tilde{A}$ states along the carbon-carbon bond length ($r_{CC}$) coordinate, with all other coordinates fixed at the vinylidene $\tilde{b}$ state equilibrium geometry. A conical

intersection between the $\tilde{a}$ and $\tilde{b}$ states is found $\sim 0.05$ eV above the $\tilde{b}$ state minimum; a two-dimensional depiction of the intersecting surfaces is shown in Figure 7.6. The binding energies of the anomalous features in Figure 7.2b suggest detachment to neutral states that are in the energetic vicinity (within 0.2 eV) of the $\tilde{b}$ state minimum, so the $\tilde{a} - \tilde{b}$ crossing is a compelling candidate as an explanation for the observed structure.

At such an intersection of electronic states, vibrational levels taken to belong to separate electronic states are no longer independent, and can mix with each other. The resultant vibronic levels typically show features of both electronic states and are often responsible for dynamical processes such as internal conversion.[330,331] In an optical excitation, such mixing results in intensity borrowing by "dark" levels from "bright" states, resulting in transitions to nominally forbidden levels. An example is the ultraviolet absorption spectrum of $SO_2$ in the Clements band, in which the unassignable spectrum is attributed to the strong mixing between dipole forbidden and dipole allowed states, also induced by a conical intersection. Indeed, recent theoretical studies showed the Clements band structure is not well-described by an adiabatic model, but consideration of nonadiabatic coupling successfully accounts for the observed features.[332,333]

In vinylidene, within the adiabatic picture, the vibrational origin and a few low-lying levels of the $\tilde{b}$ state have good FC overlap with the anion ground state, and thus appear in the calculated spectra in Figure 7.2b. High-lying vibrational levels of the $\tilde{a}$ state that lie near the $\tilde{b}$ state origin have poor FC overlap with the anion and hence do not appear in the calculated spectra. The observation of many more peaks in the experimental spectra than in the calculations suggests that the low-lying, FC-active vibrational levels of the $\tilde{b}$ state are

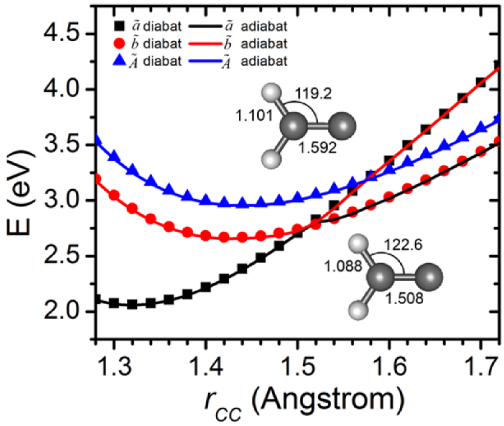


**Figure 7.5:** 1D potential energy curves of the adiabatic (lines) and diabatic (symbols) $\tilde{a}$ (black), $\tilde{b}$ (red), and $\tilde{A}$ (blue) states of vinylidene as functions of $r_{CC}$. Diabatic and adiabatic states are obtained from symmetry-controlled ab initio calculations and the PIP-NN-PESs, respectively. Energies are relative to the ground state of vinylidene, and structures of the two minimum crossing points obtained from the PESs are shown (bonds in Å, angles in degrees).

strongly mixed with high-lying vibrational levels of the $\tilde{a}$ state due to the conical intersection, leading to FC intensity-borrowing among these $\tilde{a}$ state levels. Although detachment to both the $\tilde{b}$ and $\tilde{a}$ states is allowed, their mixing via the conical intersection is likely to perturb the positions of the vibronic levels and alter their FC overlap with the anion ground state. In the limit of linear vibronic coupling, the two states are coupled by the $b_1$ out-of-plane vibration; however, a thorough treatment of the derivative coupling and conical intersection requires careful diabatization to allow full-dimensional quantum dynamics characterization of mode-specific nonadiabatic dynamics. While currently feasible for four-atom systems,[334] such a study is quite involved and beyond the scope of the current work.

In addition to the anomalous vibrational structure, the nonadiabaticity tied to the calculated intersection along the $r_{CC}$ coordinate is reflected in the observed rotational contours of features assigned to the $\tilde{b}$ and $\tilde{A}$ electronic bands. As seen in Figures 7.7 and 7.8, the rotational profiles show more variation across the different vibrational features in the $\tilde{b}$ electronic band. This enhanced perturbation for the $\tilde{b}$ state rotational profiles is attributed to the $\tilde{a} - \tilde{b}$ conical intersection near the $\tilde{b}$ state minimum.

There is also an intersystem crossing between the diabatic $\tilde{a}$ and $\tilde{A}$ states $\sim 0.25$ eV above the $\tilde{A}$ state minimum. This crossing lies among the higher vibrational levels we see detachment to in the $\tilde{A}$ state, but given the agreement with theory for this electronic band, this crossing does not significantly impact the observed structure and thus is likely a weaker interaction than the $\tilde{a} - \tilde{b}$ conical intersection.

The low rotational temperatures extracted from the present spectra suggest interesting implications for the future application of cryo-SEVI to the $\tilde{X}\ ^1A_1 \leftarrow \tilde{X}\ ^2B_2$ electronic band of the vinylidene spectrum. Ervin and co-workers[126] estimated a rotational temperature of 150 K from the width of the $\tilde{a}$ band origin in their photoelectron spectra, and used this temperature to extract lifetime-broadening of $< 200$ fs for the peaks in the $\tilde{X}$ band. This lifetime corresponds not to a relaxation into a continuum of states, but rather a quasicontinuum of acetylene states that were too dense to be resolved in their experiment. As pointed out by Fernando *et al.*,[288] rotational excitation can promote intramolecular vibrational relaxation (IVR) and increase the density of acetylene vibrational levels available for isomerization, in which case the lifetime for the isomerization of ground state vinylidene to HCCH should be strongly dependent on rotational temperature. Additionally, consideration of IVR of rovibrationally excited acetylene in its ground electronic state has shown that for the level of rotational excitation observed in the current work, the rate of IVR is significantly reduced, further decreasing the likelihood of lifetime-limited resolution.[335,336] Thus, application of the cryo-SEVI method to study the ground state band of vinylidene (Chapter 8) may reflect different dynamics than those observed in the previous photoelectron spectrum.

## 7.5 Conclusion

Newly resolved vibronic structure in the excited state region of the vinylidene photoelectron spectrum is presented, yielding new insight into this model system and demonstrating

that, in contrast to the ground state, electronically excited vinylidene is entirely decoupled from the acetylene isomer. The excited states of vinylidene prove to be spectroscopically interesting in their own right, and the reported spectra provide insight into possible spectroscopic manifestations of nonadiabatic effects in small molecules.

By photodetaching from cryogenically cooled vinylidene anions, well-resolved transitions to the $\tilde{a}\ ^3B_2$ and $\tilde{b}\ ^3A_2$ triplet states are seen, and the $\tilde{A}\ ^1A_2$ singlet state of $H_2CC$ is observed experimentally for the first time. Highly accurate potential energy surfaces based on *ab initio* calculations of the acetylene-vinylidene system have been developed and quantum dynamical calculations on the resultant adiabatic potential energy surfaces have successfully reproduced part of the experimental spectrum, helping to assign the vibrational features. In addition, irregular vibrational features near the $\tilde{b}\ ^3A_2 \leftarrow \tilde{X}\ ^2B_2$ origin are found to be a manifestation of the conical intersection between the $\tilde{a}$ and $\tilde{b}$ electronic states in the vicinity of the vinylidene $\tilde{b}\ ^3A_2$ minimum. These features are attributed to a mixing of vibronic states that arises from nonadiabatic coupling, though definitive assignment of the transitions is not attempted in this work.

## 7.6 Supporting Information

**Table 7.5:** Numerical parameters (in a. u.) used in wave packet calculations.

| | $H_2CC$ | $D_2CC$ |
|---|---|---|
| Grid/basis ranges and sizes | 10 PODVR for $r_1$ and $r_2$<br>15 PODVR for $r_0$ | 12 PODVR for $r_1$ and $r_2$<br>18 PODVR for $r_0$ |
| Largest values of $j_1$, $j_2$, and $m$ | 30, 30, 30 | 34, 34, 34 |
| Propagation steps | 20,000 | 20,000 |

**Table 7.6:** Geometries (in Å and degrees) and relative energies (in eV) of various HCCH/$H_2CC$ local minima in the four lowest neutral electronic states, obtained from *ab initio* (ic-MRCI-F12/cc-pVTZ-F12), PIP-NN PESs, and available theoretical and experimental data. The geometry and energy of the vinylidene anion are taken from previous theoretical work.[49]

| Species | State | $r_{C1C2}$ | $r_{C1H3}$ | $\alpha_{H3C1C2}$ | $E$ | |
|---|---|---|---|---|---|---|
| | | | | | This work | Refs |
| HCCH | $\tilde{X}$ | 1.206 | 1.063 | 180.0 | -1.925 | -1.955[a]<br>-1.951[b]<br>-1.862[c] |
| *trans*-HCCH | $\tilde{a}$ | 1.343 | 1.080 | 132.9 | 2.262 | 2.265[a] |
| | $\tilde{b}$ | 1.385 | 1.094 | 120.1 | 2.561 | 2.583[a] |
| | $\tilde{A}$ | 1.375 | 1.095 | 122.2 | 3.306 | 3.661[e] |
| *cis*-HCCH | $\tilde{a}$ | 1.335 | 1.090 | 128.0 | 1.952 | 1.945[a] |
| | $\tilde{b}$ | 1.358 | 1.094 | 130.4 | 2.872 | 2.883[a] |
| | $\tilde{A}$ | 1.344 | 1.097 | 132.1 | 3.681 | 4.039[e] |
| $H_2CC$ | $\tilde{X}$ | 1.302 | 1.086 | 120.0 | 0.000 | 0.000 |
| | | 1.300[b] | 1.087[b] | 120.1[b] | 0.000 | |
| | $\tilde{a}$ | 1.316 | 1.088 | 120.8 | 2.052 | 2.036[a] |
| | | 1.322[d] | 1.089[d] | 120.9[d] | 2.050[d] | 2.065(6)[f] |
| | | 1.346(40)[f] | 1.090(9)[f] | 118.9(27)[f] | | |
| | $\tilde{b}$ | 1.438 | 1.092 | 122.4 | 2.658 | 2.673[a] |
| | | 1.428[d] | 1.092[d] | 122.3[d] | 2.654[d] | 2.754(20)[f] |
| | $\tilde{A}$ | 1.441 | 1.093 | 122.2 | 2.952 | 3.109[f] |
| | | 1.441[d] | 1.093[d] | 122.2[d] | 2.952[d] | |
| | anion | 1.344[c] | 1.106[c] | 123.5[c] | -0.477[c] | -0.490(6)[f] |

[a] CCSD(T)/CBS//cc-pVTZ or cc-pCVTZ level[306]
[b] PIP-NN PES (CCSD(T)-F12a/cc-pCVTZ-F12)[48]
[c] PIP-NN PES (CCSD(T)-F12a/cc-pCVTZ-F12)[49]
[d] PIP-NN-PESs (CCSD(T)-F12a/cc-pCVTZ-F12) in this work
[e] EOM-CCSD/TZ2p[304]
[f] Experimental data including ZPEs[126]

**Table 7.7:** Geometries (in Å and degrees) and energies (in eV) of transition states linking *trans*-HCCH and $H_2CC$ in the $\tilde{X}$, $\tilde{a}$, $\tilde{b}$, and $\tilde{A}$ states and crossing points between $\tilde{a}$-$\tilde{b}$ and $\tilde{A}$-$\tilde{b}$ found using the presently reported PESs. Available data are also shown for comparison. All energies are relative to the $\tilde{X}$ state of vinylidene.

| | $r_{C1C2}$ | $r_{C1H3}$ | $r_{C1H4}$ | $\alpha_{H3C1C2}$ | $\alpha_{H4C1C2}$ | $\varphi_{H3C1C2H4}$ | $E$ (eV) | |
|---|---|---|---|---|---|---|---|---|
| | | | | | | | This work | Refs |
| TS($\tilde{X}$) | 1.277 | 1.084 | 1.361 | 174.3 | 55.8 | 180.0 | 0.129[a] | 0.097[b] |
| TS($\tilde{a}$) | 1.398 | 1.111 | 1.373 | 116.1 | 53.1 | 120.6 | 4.225 | 4.238[c] |
| TS($\tilde{b}$) | 1.447 | 1.117 | 1.281 | 135.2 | 61.3 | 180.0 | 4.789[a] | |
| TS($\tilde{A}$) | 1.402 | 1.109 | 1.279 | 129.8 | 60.4 | 147.3 | 5.310 | 5.441[d] |
| $\tilde{A}$-$\tilde{b}$ | 1.592 | 1.101 | – | 119.2 | – | 180 | 3.238 | – |
| $\tilde{a}$-$\tilde{b}$ | 1.508 | 1.088 | – | 122.6 | – | 180 | 2.749 | – |

[a] Optimized at the CASSCF/cc-pVTZ-F12 level with single point ic-MRCI-F12/cc-pVTZ-F12 calculations
[b] PIP-NN PES (CCSD(T)-F12a/cc-pCVTZ-F12)[48]
[c] CCSD(T)//CISD/TZ(2df,2pd)[283]
[d] EOM-CCSD/TZ2p[304]

**Table 7.8:** Harmonic frequencies ($cm^{-1}$) and ZPE ($cm^{-1}$) of HCCH in the ground electronic state ($\tilde{X}$), from *ab initio* (ic-MRCI-F12/cc-pVTZ-F12) and experimental values from Ref. [337].

| | *ab initio* | Exp. |
|---|---|---|
| CH sym. str. ($\nu_1$) | 3509 | 3497 |
| CC str. ($\nu_2$) | 2015 | 2011 |
| CH asym. str ($\nu_3$) | 3410 | 3415 |
| *trans*-bend ($\nu_4$) | 632[a] | 642[a] |
| *cis*-bend ($\nu_5$) | 747[a] | 747[a] |
| ZPE | 5846 | 5833 |

[a] Doubly degenerate mode

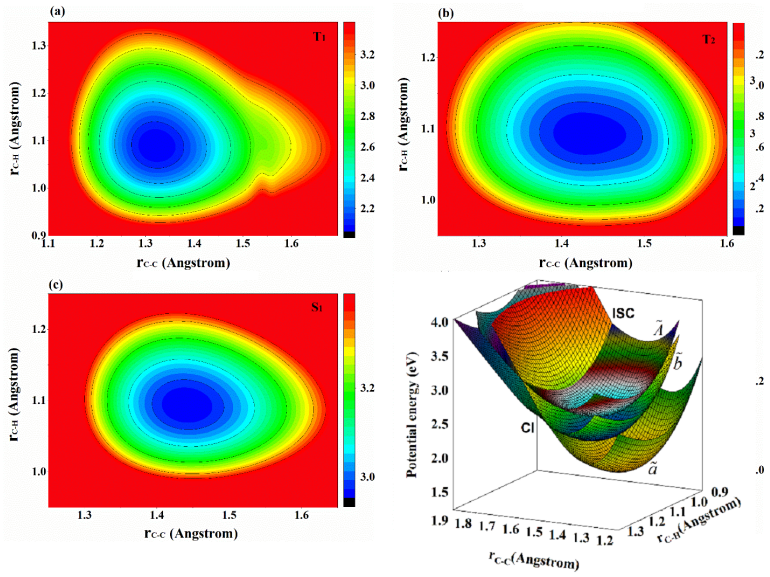


**Figure 7.6:** Contour plots of PIP-NN PESs for three low-lying excited states of vinylidene as functions of C-C distance ($r_{C-C}$) and C-H distance ($r_{C-H}$) with all other internal coordinates fixed at the equilibrium values of each state. (a) $\tilde{a}$ state; (b) $\tilde{b}$ state; (c) $\tilde{A}$ state. The conical intersection (CI) between $\tilde{a}$ and $\tilde{b}$, and the intersystem crossing (ISC) between $\tilde{b}$ and $\tilde{A}$ are presented in panel (d). The energies are relative to the ground state vinylidene (in eV).

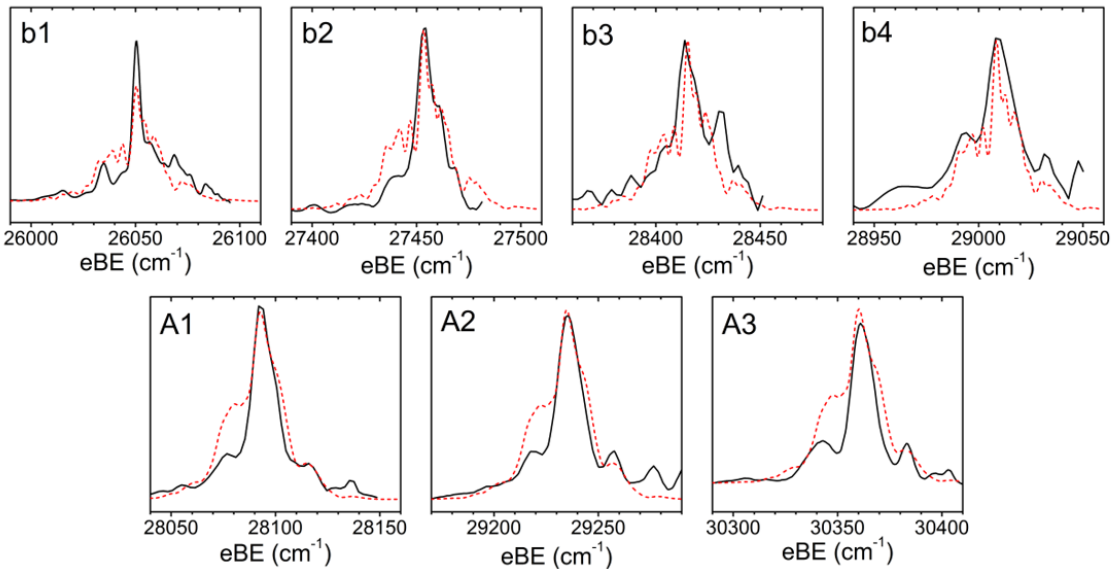


**Figure 7.7:** Rotational profiles for vibrational features in the $\tilde{b}$ (top) and $\tilde{A}$ (bottom) electronic bands of the photoelectron spectrum of $H_2CC^-$.

**Table 7.9:** *Ab initio* (ic-MRCI-F12/cc-pVTZ-F12) harmonic frequencies ($cm^{-1}$) and ZPE ($cm^{-1}$) of *cis*- and *trans*-HCCH in the three lowest excited electronic states.

| isomer | mode type (mode) | $\tilde{a}$ | $\tilde{b}$ | $\tilde{A}$ |
|---|---|---|---|---|
| | CH sym. str. ($\nu_1$) | 3214 | 3072 | 3051 |
| | sym. bend ($\nu_2$) | 743 | 802 | 795 |
| | CC str. ($\nu_3$) | 1523 | 1377 | 1409 |
| *trans* | out of plane ($\nu_4$) | 812 | 842 | 876 |
| | CH asym. str. ($\nu_5$) | 3203 | 3067 | 3034 |
| | asym. bend ($\nu_6$) | 1036 | 1115 | 1095 |
| | ZPE | 5266 | 5138 | 5130 |
| | CH sym. str. ($\nu_1$) | 3111 | 3052 | 2991 |
| | sym. bend ($\nu_2$) | 803 | 814 | 789 |
| | CC str. ($\nu_3$) | 1581 | 1485 | 1545 |
| *cis* | out of plane ($\nu_4$) | 743 | 1038 | 993 |
| | CH asym. str. ($\nu_5$) | 3082 | 3013 | 2940 |
| | asym. bend ($\nu_6$) | 1124 | 674 | 641 |
| | ZPE | 5222 | 5038 | 4949 |

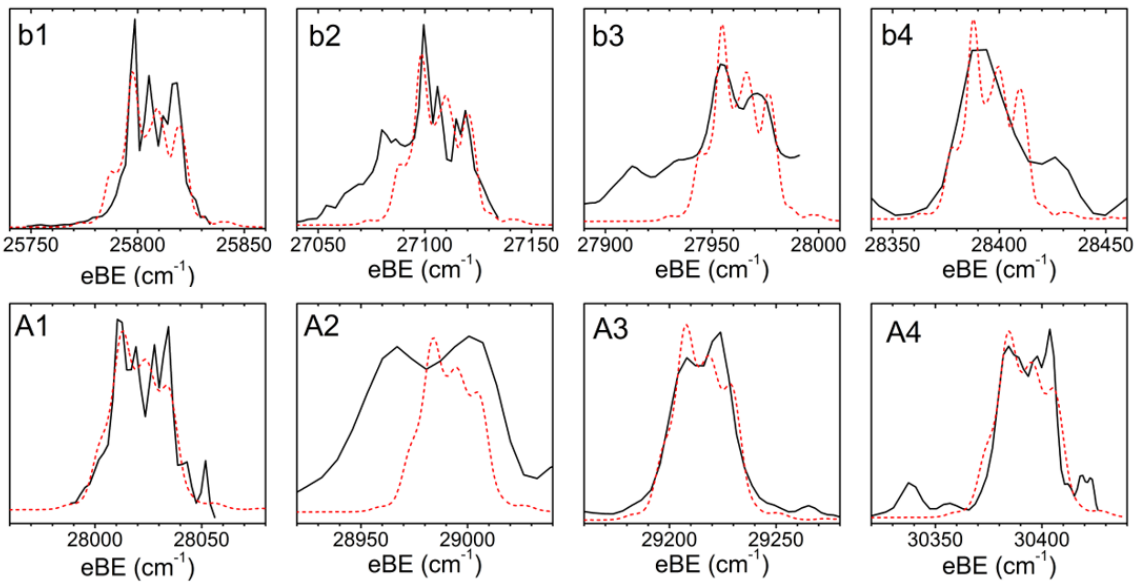


**Figure 7.8:** Rotational profiles for vibrational features in the $\tilde{b}$ (top) and $\tilde{A}$ (bottom) electronic bands of the photoelectron spectrum of $D_2CC^-$.

**Table 7.10:** Harmonic frequencies ($cm^{-1}$) and ZPE ($cm^{-1}$) of anionic and neutral vinylidene in the low-lying electronic states, from *ab initio* (ic-MRCI-F12/cc-pVTZ-F12) and PIP-NN PESs.

| | | $\tilde{X}$ | | | $\tilde{a}$ | | | $\tilde{b}$ | | $\tilde{A}$ | |
|---|---|---|---|---|---|---|---|---|---|---|---|
| charge state | mode type (mode) | *ab initio* | PES | Exp. | *ab initio* | PES | Exp. | *ab initio* | PES | *ab initio* | PES |
| neutral | CH sym. str. ($\nu_1$) | 3123 | 3122[a] | 3025(3)[c] | 3054 | 3054 | 2930(10)[c] | 3027 | 3032 | 3014 | 3007 |
| | CC str. ($\nu_2$) | 1666 | 1683[a] | 1635(10)[c] | 1561 | 1546 | 1530(70)[c] | 1174 | 1195 | 1161 | 1158 |
| | $CH_2$ scissor ($\nu_3$) | 1220 | 1221[a] | 1165(10)[c] | 1404 | 1405 | 1375(10)[c] | 1465 | 1452 | 1446 | 1442 |
| | out of plane ($\nu_4$) | 734 | 725[a] | | 765 | 757 | | 1314 | 1255 | 735 | 733 |
| | CH asym. str. ($\nu_5$) | 3217 | 3223[a] | | 3137 | 3137 | | 3111 | 3107 | 3094 | 3090 |
| | $CH_2$ rock ($\nu_6$) | 335 | 328[a] | | 1004 | 1000 | | 894 | 903 | 898 | 897 |
| | ZPE | 5147 | 5151[a] | | 5463 | 5449 | | 5492 | 5473 | 5174 | 5164 |
| anion | CH sym. str. ($\nu_1$) | 2858 | 2870[b] | | | | | | | | |
| | CC str. ($\nu_2$) | 1498 | 1505[b] | | | | | | | | |
| | $CH_2$ scissor ($\nu_3$) | 1337 | 1335[b] | | | | | | | | |
| | out of plane ($\nu_4$) | 765 | 776[b] | | | | | | | | |
| | CH asym. str. ($\nu_5$) | 2826 | 2840[b] | | | | | | | | |
| | $CH_2$ rock ($\nu_6$) | 881 | 875[b] | | | | | | | | |
| | ZPE | 5082 | 5101[b] | | | | | | | | |

[a] PIP-NN-PES (CCSD(T)-F12a/cc-pCVTZ-F12)[48]
[b] PIP-NN PES (CCSD(T)-F12a/cc-pCVTZ-F12)[49]
[c] Experimental frequencies from Ref.[126]

**Table 7.11:** Rotational constants (in $cm^{-1}$) used in simulation of the rotational profiles for the $\tilde{b}$ and $\tilde{A}$ vibrational origins in the $H_2CC^-$ and $D_2CC^-$ cryo-SEVI spectra. Constants were calculated from the ic-MRCI-F12/cc-pVTZ-F12 optimized geometries.

| | $H_2CC$ | | | $D_2CC$ | | |
|---|---|---|---|---|---|---|
| | $\tilde{X}\ ^2B_2$ | $\tilde{b}\ ^3A_2$ | $\tilde{A}\ ^1A_2$ | $\tilde{X}\ ^2B_2$ | $\tilde{b}\ ^3A_2$ | $\tilde{A}\ ^1A_2$ |
| $A$ | 9.92273 | 9.89502 | 9.83572 | 4.96518 | 4.95131 | 4.92164 |
| $B$ | 1.21658 | 1.08879 | 1.08681 | 1.02358 | 0.92770 | 0.92679 |
| $C$ | 1.08371 | 0.98086 | 0.97867 | 0.84864 | 0.78131 | 0.77993 |

**Table 7.12:** Peak positions and shifts from the $\tilde{b}$-band origin, in $cm^{-1}$, for the anomalous peaks observed in the $25000 - 28000$ $cm^{-1}$ region of the $H_2CC^-$ and $D_2CC^-$ cryo-SEVI spectra. Uncertainties in peak positions correspond to one standard deviation of a Gaussian fit to the experimental peak.

| $H_2CC^-$ | | | $D_2CC^-$ | | |
|---|---|---|---|---|---|
| peak | eBE | shift | peak | eBE | shift |
| x1 | 25406 (21) | -629 | x1 | 24986 (21) | -811 |
| x2 | 25601 (21) | -435 | x2 | 25375 (12) | -422 |
| x3 | 25870 (8) | -164 | x3 | 25985 (9) | 188 |
| x4 | 25941 (4) | -91 | x4 | 26353 (9) | 556 |
| x5 | 26642 (8) | 591 | x5 | 26683 (9) | 886 |
| x6 | 26866 (4) | 815 | x6 | 27352 (17) | 1556 |
| x7 | 27147 (5) | 1096 | x7 | 27680 (14) | 1884 |
| x8 | 27838 (6) | 1787 | | | |

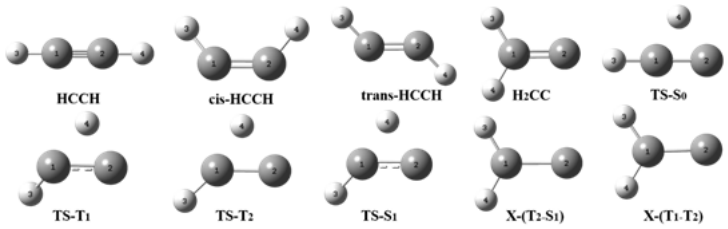


**Figure 7.9:** Structures of species listed in Tables 7.6-7.10.

# Chapter 8

# Vinylidene Ground State Band: Signatures of Isomerization

The content and figures of this chapter are reprinted or adapted with permission from J. A. DeVine, M. L. Weichman, B. Laws, J. Chang, M. C. Babin, G. Balerdi, C. Xie, C. L. Malbon, W. C. Lineberger, D. R. Yarkony, R. W. Field, S. T. Gibson, J. Ma, H. Guo, D. M. Neumark, "Encoding of vinylidene isomerization in its anion photoelectron spectrum" *Science* **358**, 336 (2017).

## Abstract

Vinylidene-acetylene isomerization is the prototypical example of a 1,2-hydrogen shift, one of the most important classes of isomerization reactions in organic chemistry. This reaction was investigated with quantum state specificity by high-resolution photoelectron spectroscopy of the vinylidene anions $H_2CC^-$ and $D_2CC^-$ and quantum dynamics calculations. Peaks in the photoelectron spectra are considerably narrower than in previous work and reveal subtleties in the isomerization dynamics of neutral vinylidene, as well as vibronic coupling with an excited state of vinylidene. Comparison with theory permits assignment of most spectral features to eigenstates dominated by vinylidene character. However, excitation of the $\nu_6$ in-plane rocking mode results in appreciable tunneling-facilitated mixing with highly vibrationally excited states of acetylene, leading to broadening and/or spectral fine structure that is largely suppressed for analogous vibrational levels of $D_2CC$.

## 8.1 Main Text

The 1,2-hydrogen shift is the simplest bond-breaking isomerization reaction in organic chemistry,[339] and the prototypical example of this process is the isomerization of vinylidene ($H_2CC$) to acetylene (HCCH). Vinylidene, the smallest unsaturated carbene,[340] has been implicated as a transient intermediate in many chemical processes,[277,279,280,285] but is of particular interest as a high-energy form of acetylene.[341] From the perspective of chemical physics, the $H_2CC \rightleftharpoons$HCCH isomerization (Fig. 8.1) is a benchmark unimolecular reaction; the small number of atoms allows application of sophisticated theoretical methods to describe the isomerization dynamics,[48,118,119,121,124,342] and the interplay between theory and experiment has provided a great deal of insight into this reaction.[283,289] The low barrier ($\sim$ 0.1 eV, see Figure 8.1) for vinylidene isomerization[119,124] is responsible for extensive tunneling interactions with acetylene states, and over the past several decades considerable effort has been invested in probing this isomerization from both sides of the barrier. On the acetylene side, Field and co-workers[289,343] have searched for spectroscopic signatures of vinylidene in highly vibrationally excited levels of HCCH, where the minimum energy isomerization path lies along the local-bending vibrational coordinates. Alternatively, the vinylidene well can be accessed directly by photodetachment of the vinylidene anion ($H_2CC^-$), and several research groups have used this approach to probe the spectroscopy and dynamics of neutral $H_2CC$.[126–128,178,299]

Previous photodetachment-based experiments have led to differing views regarding the timescale on which vinylidene isomerizes to acetylene. In an anion photoelectron spectroscopy study, Ervin *et al.*[126] observed that transitions to the $\tilde{X}\ ^1A_1$ state of $H_2CC$ were

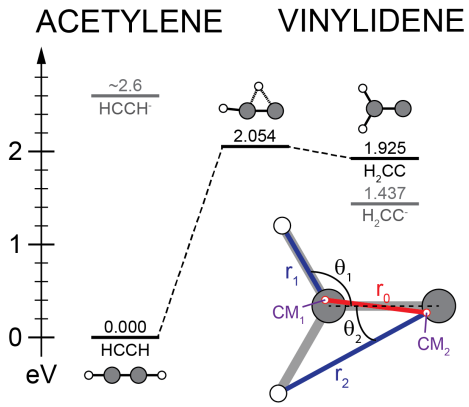


**Figure 8.1:** Energy diagram for the neutral vinylidene-acetylene isomerization. Energies (in eV, relative to HCCH) and geometries were obtained from [178]. Experimental energies for the anions of both isomers are shown in gray; the $H_2CC^-$ value was obtained from the present work, whereas the $HCCH^-$ value was estimated from electron scattering experiments.[338] The CH-CH Jacobi coordinate system used to describe the isomerization is shown as an inset.

considerably broader than those arising from detachment to the higher-lying $\tilde{a}\ ^3B_2$ state, for which the barrier to isomerization is significantly larger. The extra broadening of ground-state band features was attributed to isomerization on a sub-picosecond timescale. In contrast, later Coulomb explosion imaging (CEI) experiments by Vager[127] indicated that neutral $H_2CC$ formed by anion photodetachment is stable on at least a microsecond timescale. It should be noted that lifetime is an ill-defined concept in such a system, as both acetylene and vinylidene are bound species whose eigenstates cannot form a true continuum. However, individual eigenstates may have varying degrees of mixing between zeroth-order states of the two isomers, especially near and above the isomerization barrier. This mixing has been explored in quantum dynamical simulations of the anion photoelectron spectrum starting with work by Bowman,[124] who found the simulated spectrum to be dominated by sharp peaks associated with isolated vinylidene states.

The aim of the current work was to experimentally characterize individual vibrational eigenstates of vinylidene and to understand the vibrational mode dependence of mixing with acetylene. To this end, we measured photodetachment spectra of $H_2CC^-$ and $D_2CC^-$ anions at higher resolution than previous work[126] using two complementary experimental methods, high-resolution photoelectron imaging (HR-PEI)[344] and slow electron velocity-map imaging of cryogenically-cooled anions (cryo-SEVI).[19] The experiments are supplemented by full-dimensional quantum dynamics calculations on a highly accurate *ab initio*-based potential energy surface, carried out previously for the $H_2CC$-HCCH system[48,49] and expanded here by covering larger sections of configuration space in both isomeric regions.

The combination of experiment and theory shows that photodetachment directly accesses eigenstates that are mostly localized in the vinylidene well. The $H_2CC$ and $D_2CC$ isotopologues both undergo vibronic coupling to a high-lying vinylidene electronic state, which results in the appearance of nominally Franck-Condon (FC) forbidden transitions to neutral vibrational levels with excitation along non-totally-symmetric ($b_2$) modes. Most notable is the vibronic coupling-induced observation of features involving odd quanta of excitation in the in-plane rocking ($\nu_6$) mode, which, for the $H_2CC$ isotopologue, mixes strongly with the local-bending modes in the acetylene well. Isomerization is largely encoded in the spectra of vibrational states that involve excitation of this mode.

The experiments reported here used velocity-map imaging (VMI) detection schemes to measure the electron kinetic energy (eKE) distribution and photoelectron angular distribution (PAD) that result from electron photodetachment of mass-selected anions. The VMI spectrometer used in the HR-PEI measurements (Fig. 8.4) was optimized to provide 0.7 to 25 $cm^{-1}$ resolution over a wide range of eKE, so that a single photon energy ($h\nu$) could be used to obtain vibrationally-resolved spectra with reliable intensities and PADs. The cryo-SEVI spectrometer (Fig. 2.1) provided higher resolution (sub-meV) over a narrower range of eKEs, assisted by cooling the anions to $\sim$ 10 K prior to detachment to reduce spectral congestion arising from anion rotational and vibrational excitation. Together, the HR-PEI and cryo-SEVI techniques yield a more complete picture of the photoelectron eKE spectrum and PADs than when used separately.

The cryo-SEVI spectra of $H_2CC^-$ and $D_2CC^-$ (Fig. 8.2A) and the HR-PEI spectrum

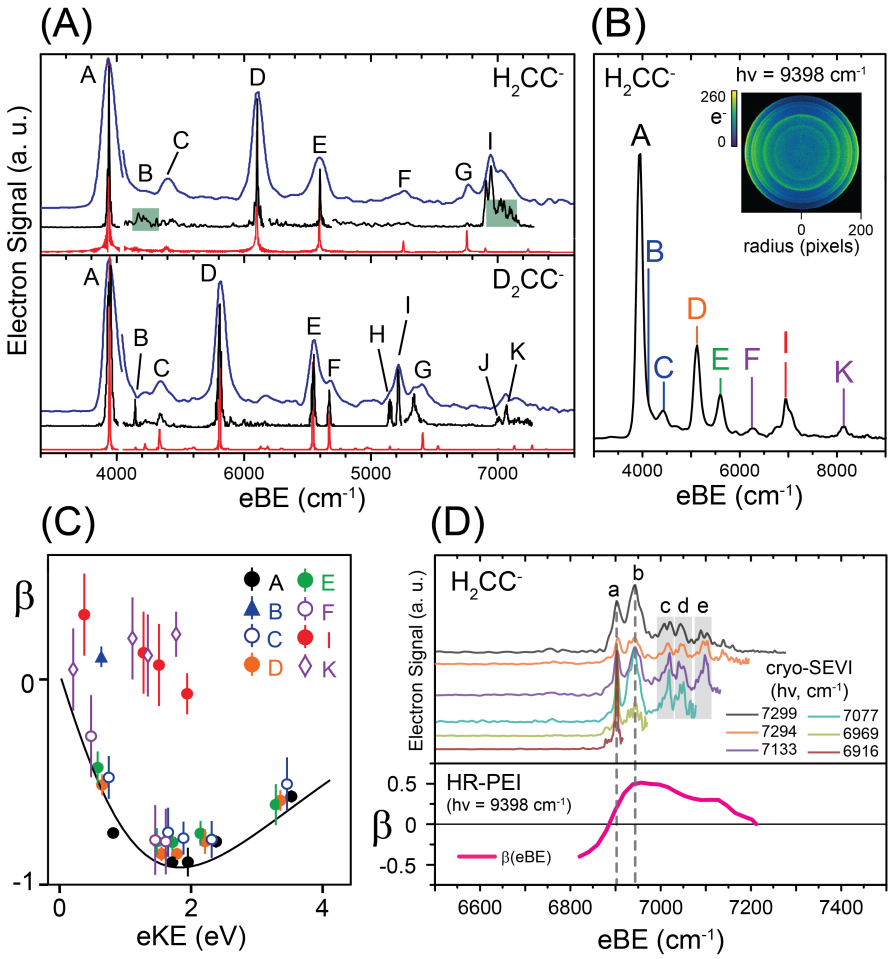


**Figure 8.2:** Vinylidene photoelectron spectra. **(A)** Cryo-SEVI spectra of $H_2CC^-$ (top) and $D_2CC^-$ (bottom), as well as theoretical results for both isotopologues (red). The blue traces represent overview spectra while the black traces are higher resolution composite spectra; see section 8.2.1 for more details. For clarity, all traces have been scaled by a factor of 2 following the break in the overview after peak A. **(B)** HR-PEI spectrum of $H_2CC^-$. The image used to construct the spectrum is shown as an inset. **(C)** PADs of various spectral features obtained from the HR-PEI $H_2CC^-$ spectrum. The solid line shows a Hanstorp *p*-orbital detachment fit to the anisotropy parameter of peak A.[23] Error bars correspond to one standard deviation of the anisotropy parameter obtained from the fitting process. **(D)** Region I of the $H_2CC^-$ photoelectron spectrum showing the underlying structure revealed by cryo-SEVI. The anisotropy parameter obtained from the HR-PEI spectrum is also shown to illustrate the variation in angular distribution across this region. Vertical dashed lines show how peaks a and b line up with the anisotropy parameter.

of $H_2CC^-$ (Fig. 8.2B) display photoelectron intensity versus electron binding energy (eBE), where eBE = $h\nu$ − eKE. All three spectra are dominated by the vibrational origin level (A) and show transitions to vibrational levels up to $\sim$ 4000 cm$^{-1}$ above the vinylidene vibrational ground state. PADs are readily obtained from photoelectron images (Section 8.2.2), an example of which is shown in Fig. 8.2B. For each peak, the PADs yield the anisotropy parameter ($\beta$), which by definition falls between -1 and 2; these limits correspond to perpendicular and parallel detachment, respectively.[22] Figure 8.2C shows $\beta$ for several peaks as a function of eKE, obtained from HR-PEI measurements at several photon energies. The PADs extracted from the cryo-SEVI spectra (Fig. 8.6) are in agreement with the HR-PEI results; with the exception of features B, I, and K, all peaks in the cryo-SEVI spectra of both isotopologues have $\beta < 0$ for eKEs below 1 eV, and peaks B, I, and K show distinctly positive $\beta$ at these kinetic energies.

The enhanced resolution of cryo-SEVI is evident in the considerably narrower linewidths in Figure 8.2A compared to previous photoelectron spectra;[126] a direct comparison may be seen in Fig. 8.5. The linewidths of the vibrational origins and most of the other peaks are $\sim$ 10 cm$^{-1}$ and $\sim$ 30 cm$^{-1}$ in the $H_2CC^-$ and $D_2CC^-$ spectra, respectively, suggesting that these features are predominantly transitions that terminate in single eigenstates. These linewidths are primarily determined by the underlying rotational contours (Fig. 8.8) and, as discussed previously[178] and in Section 8.2.3, reflect the differing nuclear spin statistics for H and D atoms. In contrast to the previously published spectrum, the majority of features do not display significant broadening relative to the previously observed excited state features.[178] However, there are several anomalously broadened and irregular regions (B, C, and I) in the $H_2CC^-$ cryo-SEVI spectrum, discussed in more detail below.

Comparison to the theoretical spectra in Fig. 8.2A (red traces) and Fig. 8.9 allows unambiguous assignment of nearly all experimentally observed peaks, as shown in Table 8.1. These assignments are particularly clear for $D_2CC$, where the discrepancies between theory and experiment are $<$ 10 cm$^{-1}$ for all features, excluding peak G. From the rotational contours of the $0_0^0$ bands, we obtain electron affinities (EAs) of 0.4866(8) and 0.488(2) eV for $H_2CC$ and $D_2CC$ respectively, as described in Section 8.2.3. These EAs lie within the error bars of the previously reported values[126] of 0.490(6) and 0.492(6) eV, respectively; they reflect our enhanced resolution and our ability to partially resolve the rotational structure of the band origins. Most of the remaining features in the two spectra can be attributed to FC-allowed transitions involving totally-symmetric ($a_1$) neutral vibrational levels, which, within the Born-Oppenheimer approximation, are the only transitions that can appear in the theoretical spectra for detachment from the anion vibrational ground state. Features B and I are nominally assigned to the FC-forbidden $6_0^1$ and mixed $5_0^1$ and $1_0^1 6_0^1$ transitions, both involving $b_2$-symmetric vibrational levels of neutral vinylidene.

These FC-forbidden transitions are attributed to Herzberg-Teller (HT) coupling to an excited electronic state with $B_2$ symmetry (Sections 8.2.2 and 8.2.3). The $\tilde{B}\ ^1B_2$ state has been predicted to lie about 4 eV above the $\tilde{X}\ ^1A_1$ state.[307] We have observed detachment to this state (Fig. 8.7), finding its term energy to be $T_0$ = 3.997(3) eV with respect to the $\tilde{X}\ ^1A_1$ state and its anisotropy parameter to be positive. The derivative coupling between the

**Table 8.1:** Peak positions ($cm^{-1}$), experimental and theoretical shifts from the vibrational origin ($cm^{-1}$), and assignments for the $H_2CC^-$ and $D_2CC^-$ ground state photoelectron spectra. Shifts were extracted from the cryo-SEVI scans, and HR-PEI peak positions for $H_2CC^-$ are shown for comparison. Cryo-SEVI peak positions were extracted from the high-resolution (black) traces in Figure 8.2A unless otherwise noted. Uncertainties in peak positions correspond to one-σ, obtained from a Gaussian fit to the experimental trace.

| | $H_2CC^-$ | | | | | $D_2CC^-$ | | | | |
|---|---|---|---|---|---|---|---|---|---|---|
| Peak | HR-PEI | eBE | Shift | Theo. | $H_2CC$% | eBE | Shift | Theo. | $D_2CC$% | Assn. |
| A | 3940 (60) | 3935 (7) | 0 | 0.0 | 100 | 3941 (17) | 0 | 0.0 | 100 | $0_0^0$ |
| B | – | 4190 (50)[a] | 255 | 283.2 | 84 | 4143 (3) | 202 | 203.9 | 100 | $6_0^1$ |
| C | 4400 (90) | 4402 (52)[b] | 470 | 454.1 | 58 | 4345 (18) | 404 | 396.8 | 98 | $6_0^2$ |
| D | 5120 (60) | 5103 (5) | 1168 | 1166.0 | 97 | 4809 (11) | 868 | 868.6 | 100 | $3_0^1$ |
| E | 5570 (50) | 5597 (4) | 1662 | 1659.6 | 97 | 5547 (10) | 1606 | 1601.8 | 99 | $2_0^1$ |
| F | 6250 (80) | 6240 (70)[b] | 2305 | 2322.6 | 96 | 5671 (8) | 1730 | 1730.0 | – | $3_0^2$ |
| G | 6740 (70) | 6780 (60)[b] | 2845 | 2822.0 | 97 | 6339 (18) | 2398 | 2468.0 | – | $2_0^1 3_0^1$ |
| H | – | – | – | 2967.7 | – | 6152 (12) | 2211 | 2206.7 | – | $1_0^1$ |
| I | 6950 (50) | 6943 (12)[c] | 3008 | 3013.7 | 82 | 6216 (7) | 2275 | 2276.9 | 99 | $5_0^1$ |
| – | – | – | – | 3117.6 | 68 | – | – | 2389.9 | 95 | $1_0^1 6_0^1$ |
| J | – | – | – | – | – | 7008 (14) | 3067 | 3059.7 | – | $1_0^1 3_0^1$ |
| K | 8130 (70) | 8125 (41)[b] | 4190 | 4218.4 | – | 7065 (12) | 3124 | 3125.5 | – | $3_0^1 5_0^1$ |

[a] Peak position obtained by fitting the highlighted region B in Figure 8.2A to a single Gaussian.

[b] These features did not maintain sufficient intensity near-threshold to appear in the cryo-SEVI scans, and thus the eBEs are obtained from the lower-resolution overview scans (blue traces) in Figure 8.2A.

[c] Reported position corresponds to feature b in Figure 8.2D.

$\tilde{X}\ ^1A_1$ and $\tilde{B}\ ^1B_2$ states has been calculated near the vinylidene minimum (Section 8.2.5), and the interaction between these states is found to be localized largely along the $\nu_6$ mode, with a minor contribution from the $\nu_5$ mode. Peaks B and I also exhibit positive anisotropy parameters (Fig. 8.2C), in contrast to all of the FC-allowed features, consistent with HT coupling between the two electronic states.[5] Moreover, as discussed in Section 8.2.3, the rotational selection rules for photodetachment differ for the FC-allowed ($\Delta K_a = \pm 1$) versus HT-allowed ($\Delta K_a = 0$) transitions, leading to the narrower rotational profiles of peaks B and I (7 and 16 $cm^{-1}$ fwhm, respectively) in the $D_2CC^-$ SEVI spectrum relative to the FC-allowed transitions.

Overall, the $D_2CC^-$ cryo-SEVI spectrum is what would be expected for a well-behaved, stable molecule, albeit one that exhibits HT coupling with an excited electronic state. The same is true for much of the $H_2CC^-$ spectrum, with the exception of features B, C, and I. Features B and C, assigned to the $6_0^1$ and $6_0^2$ transitions, appear in the cryo-SEVI spectrum as broad, weak features, even at high resolution (black trace, Figure 8.2A). The spectral broadening indicates participation of multiple eigenstates, each of which carries some vinylidene oscillator strength. Figure 8.2D shows that feature I, in the vicinity of the calculated $5_0^1$ and $1_0^1 6_0^1$ transitions, resolves into a cluster of five closely-spaced, narrow peaks (a-e, energies in Table 8.2). Comparison with the HR-PEI angular distribution reveals notable variation in the anisotropy parameter across this series of peaks, with a considerably lower $\beta$ value for peak 'a' than peaks 'b-e'. In addition, the intensity of peak 'a' decreases more slowly than the other features as the photon energy is lowered. Both observations indicate variation of the partial wave contributions to photodetachment across region I, suggesting that the electronic characters of the final eigenstates are highly variable.

To understand how the isomerization mechanism is encoded in the neutral eigenstates, and to gain additional insights into the experimental spectra, we turn to the calculated wavefunctions for the lowest two FC-allowed vibrational eigenstates populated by photodetachment of $H_2CC^-$ anions ($0^0$ and $6^2$) and an anharmonically-mixed eigenstate ($5^1$). Using the CH-CH Jacobi coordinates shown in the inset of Fig. 8.1, the wavefunctions are plotted in Fig. 8.3, superimposed on a contour plot of the potential energy surface. In the top and bottom panels, the distance between CH centers-of-mass ($r_0$) is constrained to either the vinylidene or acetylene equilibrium value, respectively, so that the bending wavefunctions are shown for both the vinylidene and acetylene wells. For the ground vinylidene state ($0^0$), there is very little acetylene character, indicating strong localization in the vinylidene well. However, excitation of the in-plane rocking mode of vinylidene ($6^2$) introduces appreciable acetylene character, featuring highly excited states in the local-bending coordinates (local-benders), evidenced by the large number of nodes along the angular coordinates $(\theta_1, \theta_2)$.[289]

The plots in Figs. 8.3 and 8.10 also show that the neutral $5^1$ state mixes with the $1^1 6^1$ state through an anharmonic interaction, giving region I its intensity through the $\nu_6$-dominated HT coupling. This interaction is enhanced by the energy-lowering of the $1^1 6^1$ state relative to the sum of the $\nu_1$ and $\nu_6$ fundamentals, due to the strong inter-mode anharmonicity ($x_{1,6}$) between the stretching and rocking modes. The other peaks in Feature I could be due to higher $b_2$ states such as $5^1 6^2$ and other nearby FC-allowed transitions.

Fig. 8.3 shows that this mixed $5^1 \sim 1^1 6^1$ state exhibits appreciable acetylene character along the local-bending coordinates, with similar nodal structure as is seen for the $6^2$ state. This result links the spectroscopy of vinylidene to its isomerization dynamics; the minimum energy isomerization pathway follows the rocking normal mode of vinylidene, which ultimately connects with the local-bending vibrational states of acetylene. Indeed, the acetylenic contributions to the $6^2$ and $5^1 \sim 1^1 6^1$ eigenfunctions involve strong admixtures of the local-bending excitation, which has been extensively probed by spectroscopic studies of highly excited acetylene.[289] For $D_2CC$, the extent of mixing with DCCD is negligible, presumably owing to the much narrower eigenfunctions resulting in suppressed tunneling. The wavefunctions for other $H_2CC$ and $D_2CC$ states can be found in Figs. 8.10-8.12.

Chemically, isomerization entails the breaking and formation of bonds within a molecule. To understand the dynamics of the 1,2-hydrogen shift in this system, one needs to quantum mechanically simulate transitions between various vibrational eigenstates that have different amplitudes of the zeroth-order vinylidene (1) and acetylene (2) basis states: $\Psi_n^{(neutral)} \approx c_n^{(1)}\psi_n^{(1)} + c_{nm}^{(2)}\psi_m^{(2)}$. The extent of mixing, which encodes the isomerization, depends on the energy difference between $\psi_n^{(1)}$ and $\psi_m^{(2)}$ as well as the strength of the interaction matrix element between the two. As mentioned above, the acetylene states involved in the mixing

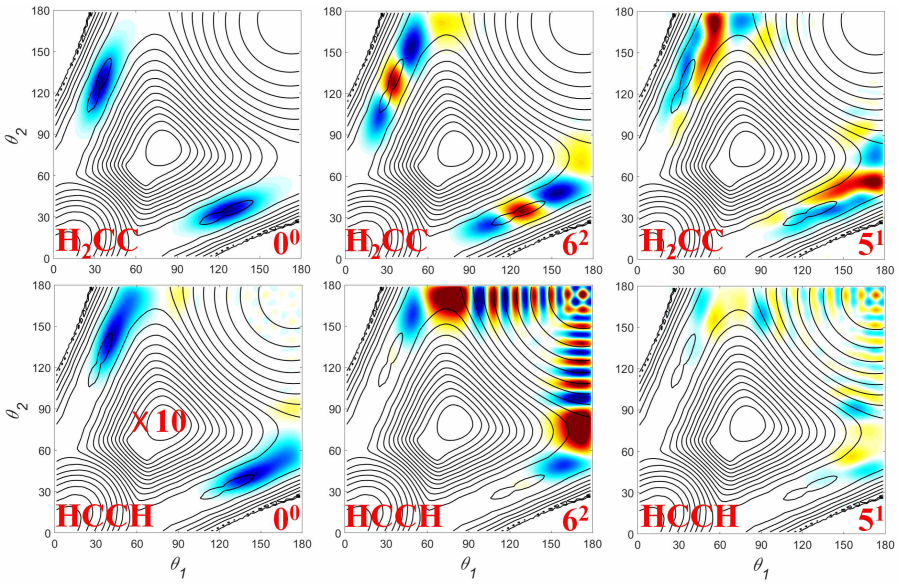


**Figure 8.3:** Calculated wavefunctions for neutral vibrational levels of $H_2CC$. Wavefunctions of the $0^0$, $6^2$, and $5^1$ states are shown along the $\theta_1$ and $\theta_2$ directions of the CH-CH Jacobi coordinates, with the coordinate $r_0$ taking the equilibrium value of $H_2CC$ (top) or HCCH (bottom) and the wavefunctions summed over the remaining coordinates. The acetylene component is dominated by local-bender states along the $\theta_1, \theta_2 \sim 180°$ axes. The two-dimensional potential energy surface is superimposed, in which the $\theta_1 = \theta_2 = 180°$ well corresponds to HCCH.

($\psi_n^{(2)}$) are mostly the local-benders, which have a much smaller density of states than the total density of acetylene vibrational states. The spectral intensity of a peak in the photoelectron spectrum is primarily determined by $I_n \approx \left|c_n^{(1)}\right|^2 \left|\langle\psi_n^{(1)}|\Psi^{(anion)}\rangle\right|^2$. The vinylidene weights, $\left|c_n^{(1)}\right|^2$, can be approximately extracted from the calculated $H_2CC$ and $D_2CC$ eigenfunctions and are listed in Table 8.1. For $H_2CC$, only those final states with $\nu_6$ excitation mix strongly with HCCH, whereas for $D_2CC$, the mixing with DCCD is much smaller due to the narrower wavefunctions.

The cryo-SEVI and HR-PEI spectra, with the supporting theoretical analysis, offer insights into the vinylidene-acetylene isomerization and its influence on the vinylidene photoelectron spectrum. Most neutral eigenstates formed via photodetachment are dominated by vinylidene character for both isotopologues, an observation consistent with the main conclusion of the CEI experiment[127] and the calculations by Bowman.[124] However, $H_2CC$ states in which the $\nu_6$ mode is excited show non-negligible acetylene character, which manifests as spectral broadening and/or fine structure for this isotopologue. Excitation of this mode can occur through FC-allowed transitions ($6^2$), vibronic coupling via an excited state of vinylidene ($6^1$), or anharmonic coupling between ground state vibrational levels ($5^1 \sim 1^1 6^1$). This spectroscopic result implies that in the range of excitation energies probed here, the isomerization of vinylidene to acetylene is highly state-specific and is promoted by excitation of the $\nu_6$ mode. Significantly less coupling to acetylene is observed for $D_2CC$, which suggests that isomerization of $D_2CC$ is considerably less facile even when the $\nu_6$ mode is excited. These insights provide a quantum mechanical foundation for understanding the 1,2-hydrogen shift reaction.

## 8.2 Supplementary Material

### 8.2.1 Experimental Methods

#### HR-PEI[a]

A schematic of the HR-PEI setup is shown in Figure 8.4, with the major components labeled. Further details of the apparatus have been provided in previous work.[344] Vinylidene anions are produced by passing ethylene gas through a pulsed valve, which then undergoes supersonic expansion into a high-voltage discharge. Negative ions are extracted, accelerated to 500 eV, and focused into an ion gating, bunching, and potential re-referencing unit.[345] The ions are separated by $m/z$ over a 2 m time-of-flight (TOF) region, and an electrostatic gate selects the mass packet of interest. This ion packet is directed to the interaction region of a VMI electrostatic lens, where it is crossed with a detachment laser beam.

[a]These experiments were carried out by Ben Laws and Stephen T. Gibson of Australian National University, Canberra.

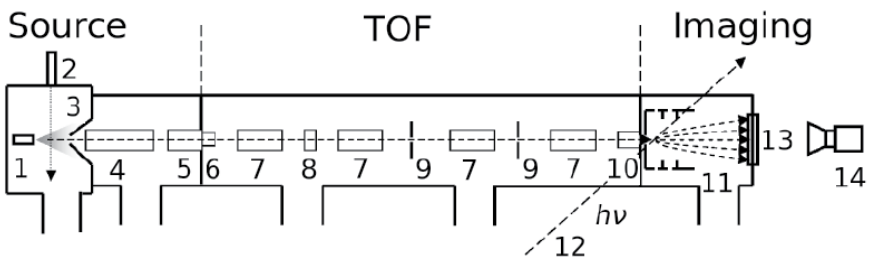


**Figure 8.4:** Schematic of the HR-PEI VMI spectrometer from the lab of Stephen Gibson.[344] Ions are formed by a pulsed supersonic jet and pulsed discharge source (1) coupled to an electron gun (2). The resultant ion beam is skimmed (3) and passes through ion electrostatic acceleration optics (4) which direct anions to the gating, potential re-referencing, and bunching unit (5). The time-of-flight (TOF) region contains a number of ion optics which serve to steer and focus the beam, including two sets of electrostatic ion-beam deflectors (6, 8), an ion-beam Einzel lens (7), and stainless steel apertures (9). A potential referencing switch, electrostatic ion-beam deflectors and potential barrier (10) direct the ions into the interaction region of a VMI lens (11), where they are photodetached by a vertically-polarized laser beam (12). The resultant photoelectrons are velocity-mapped onto a 75 mm multichannel plate and phosphor detector (13), which is photographed by a CCD camera (14) with each laser shot.

Several laser configurations were used to obtain the HR-PEI data presented in this work, employing a Continuum Powerlite 9010 Nd:YAG laser either alone or as a pump for a Sunlite EX optical parametric oscillator (OPO). The photoelectron spectrum in Figure 8.2B was measured using the fundamental output of the Nd:YAG laser (1064 nm). The anisotropy parameters in Figure 8.2C were determined using a number of photon energies; energies of 20247, 17271, 16155, 15649, and 15244 $cm^{-1}$ were obtained by using the third harmonic (355 nm) of the Nd:YAG laser to pump the OPO, and additional data points were obtained by directly using the third harmonic and fundamental output of the Nd:YAG laser (28169 and 9398 $cm^{-1}$, respectively).

The VMI lens is a modified version of the original concept of Eppink and Parker.[11] Photodetached electrons are velocity-mapped to a 75 mm diameter microchannel plate/phosphor screen detector (Burle). The MCP screen is gated to ensure that unwanted events from untargeted ions and neutral species are not detected. Images from the phosphor are captured by a 2048×2048 pixel monochrome CCD camera (PCO 2000), and each camera frame is transferred to a computer at the 10 Hz laser repetition rate. Camera frames are processed in real time to identify events, which are centroided and binned into a rectangular pixel-grid image. This image may be of arbitrary pixel number, with a larger image pixel number providing finer detail at the expense of greater statistical uncertainty in the individual pixel intensities. The accumulated image is circularized by an angular-dependent radial scaling determined through a comparison of adjacent radial intensity profiles.[192,346] In this work, the

radial correction to reduce image distortion is applied to the raw $(x, y)$-centroid data prior to forming the velocity-map image, eliminating any requirement for image pixel intensity interpolation.

The photoelectron velocity distribution is obtained from the velocity-mapped image by an inverse Abel transformation, which is based on the algorithm of Hansen and Law[347] and described in more detail on the PyAbel website.[346] For the low-distortion HR-PEI images, all quadrants are equivalent and may be combined to improve the statistical accuracy of the inverse Abel transform and, hence, the photoelectron spectrum and photoelectron angular distributions. Energy calibration is obtained using a single scaling factor (i.e., eKE = $aR^2$, where R is the radius in pixels), to align the origin peak with the known electron affinity of vinylidene.[126]

The relative kinetic energy resolution is approximately constant for VMI experiments. The HR-PEI spectrometer achieves sub-cm$^{-1}$ resolution for slow electrons detached from atomic species. In this study, a more quantitative comparison comes from a parallel measurement of the photoelectron spectrum of $O_2^-$, which has a similar electron affinity (3613 cm$^{-1}$) to vinylidene. A rotational model band decomposition gives a rotational linewidth of 10.1(1) cm$^{-1}$ for the $v' = 2$ transition, for detachment at 9398 cm$^{-1}$.

The experimental anisotropy parameters in Figure 8.2C are obtained by fitting Eq. 8.1, explained in more detail in Section 8.2.2, to radially-integrated transition intensities. For a single quadrant of a given image, the intensity variation is linear in $P_2(\cos\theta)$, with slope equal to $\beta\times$intercept. The most accurate anisotropy parameter determinations occur for the stronger transitions.

### Cryo-SEVI

The cryo-SEVI method is described in Chapter 2. The formation of gas-phase vinylidene anions is described in Chapter 7.

Several different laser schemes were used to obtain the data presented in this chapter. The overview spectra in Figure 8.2A (blue traces) were obtained using the fundamental output of an Nd:YAG laser (1064 nm, 9398 cm$^{-1}$). The higher-resolution scans (black traces) were taken using a home-built IR difference frequency generation (IR-DFG) setup,

**Table 8.2:** Binding energies, peak widths, and shifts from the origin of features a-e underlying region I in the cryo-SEVI spectrum of $H_2CC^-$.

| Peak | eBE (cm$^{-1}$) | fwhm (cm$^{-1}$) | shift from A (cm$^{-1}$) |
|---|---|---|---|
| a | 6904 | 16 | 2966 |
| b | 6943 | 35 | 3005 |
| c | 7018 | 11 | 3080 |
| d | 7045 | 32 | 3107 |
| e | 7097 | 19 | 3159 |

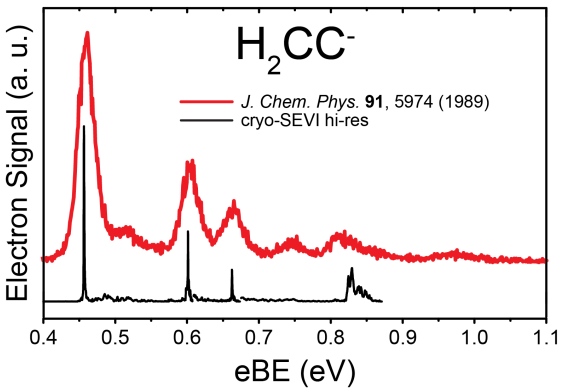


**Figure 8.5:** Comparison of the high-resolution cryo-SEVI spectrum of $H_2CC^-$ (black) with the anion photoelectron spectrum reported previously (red).[126]

covering the mid-IR (1.3-4 μm, 2500-7692 $cm^{-1}$), which is similar in design to the setup described by Lineberger and co-workers.[274] Further details of the IR-DFG setup can be found in the thesis of Marissa Weichman.[18] The IR laser wavelengths for the high resolution traces were chosen in order to maximize direct detachment; as will be discussed in the following chapter, there are narrow vibrational anion resonances in the vicinity of the origin band that undergo autodetachment,[128] leading to photoelectron spectra that vary strongly with photon energy. The photon energies used in Figure 8.2A do not access these resonances. To observe detachment to the $\tilde{B}\ ^1B_2$ electronic state, the third harmonic of an Nd:YAG laser (355 nm, 28169 $cm^{-1}$) was used to pump the tunable dye laser, the output of which was then frequency-doubled yielding tunable UV light (255-280 nm, 35714-39216 $cm^{-1}$).

The spectrometer is calibrated using SEVI images of the well-characterized photodetachment transitions of atomic anions. For the ground state electronic band, images of $O^-$[190] were obtained using the tunable red dye laser light aligned through the machine to be perfectly collinear with the DFG light. For detachment to the $\tilde{B}\ ^1B_2$ excited state, $Cl^-$ was used as a calibrant.[187] Figure 8.5 shows a direct comparison between the cryo-SEVI $H_2CC^-$ spectrum and the spectrum reported by Lineberger and co-workers,[126] showing the excellent agreement and improved resolution in the current results.

### 8.2.2 Photoelectron Angular Distributions and Vibronic Coupling

The photoelectron angular distribution (PAD) associated with each photodetachment feature can be extracted from a given VMI image, and is given by[22]

$$\frac{d\sigma}{d\Omega} = \frac{\sigma_{tot}}{4\pi}\left[1 + \beta P_2(\cos\theta)\right]. \tag{8.1}$$

Here, $\sigma_{tot}$ is the total detachment cross section for the transition in question, $P_2(x)$ is the second-order Legendre polynomial, $\theta$ is the angle of the photoelectron's velocity vector with

respect to the laser polarization axis, and $\beta$ is the anisotropy parameter, ranging from -1 (perpendicular detachment) to +2 (parallel detachment). The value of $\beta$ is directly related to the angular momentum of the outgoing photoelectron and thus reflects the electronic character of the detached anion molecular orbital.[23,250,344]

The MEVELER method used to reconstruct cryo-SEVI images[184] provides as output the projections of the reconstructed velocity-map image onto the zeroth- and second-order Legendre polynomials as a function of radial distance, or equivalently, eKE. The zeroth-order projection ($Q_0$) contains the photoelectron spectrum, whereas the second-order projection ($Q_2$) contains the angular information. Given these, the anisotropy parameter $\beta$ is given by

$$\beta = \frac{\int_{R_1}^{R_2} Q_2(R)dR}{\int_{R_1}^{R_2} Q_0(R)dR} \tag{8.2}$$

where $R_1$ and $R_2$ are limits set so that the integration is carried out over the peak of interest. Calculated $\beta$ values at several detachment energies for key features in the cryo-SEVI spectra of both isotopologues are presented in Figure 8.6. Alternatively, a plot of $\beta$ versus eBE for a single photon energy, such as that shown in Figure 8.2D, can be constructed by performing the integration on an interpolation of the (discrete) MEVELER output, with the limits of integration defined by the spacing between data points.

As can be seen in Figures 8.2C and 8.6, most features observed in the ground state band of both isotopologues have perpendicular ($\beta < 0$) anisotropies at moderate kinetic energies, and isotropic ($\beta \sim 0$) PADs for low eKEs. These features are well-reproduced by theory as shown for the $0_0$ detachment spectra in Figure 8.9. However, peak I in the spectra for both isotopologues, as well as peak B in the $D_2CC^-$ spectrum, show distinctly positive anisotropies. The shifts of peaks B and I from the vibrational origins are in excellent agreement with the values predicted by theory for detachment to the $6^1$ and $5^1$ neutral levels, respectively (see Table 8.1).

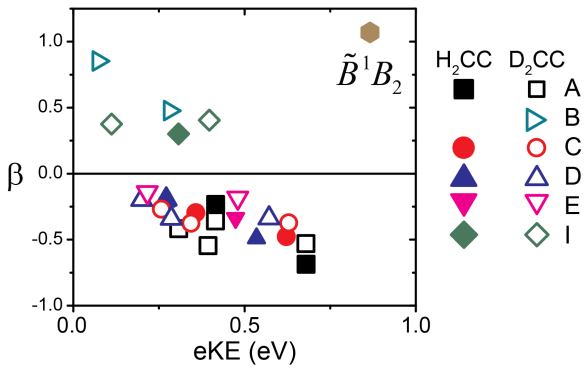


**Figure 8.6:** Photoelectron angular distributions of various features in the cryo-SEVI spectra of $H_2CC^-$ (solid markers) and $D_2CC^-$ (hollow markers), along with the $\beta$ value calculated for detachment to the $\tilde{B}\ ^1B_2$ neutral state of $H_2CC$.

The anomalous anisotropies of these regions are attributed to detachment to FC-forbidden $b_2$-symmetric vibrational levels activated through vibronic coupling. Let $|a\rangle$, $|b\rangle$ be two vibronic states with vibrational symmetries $\Gamma^{vib}_{a,b}$ and electronic symmetries $\Gamma^{elec}_{a,b}$. These states can couple provided

$$\Gamma^{vib}_a \otimes \Gamma^{vib}_b \otimes \Gamma^{elec}_a \otimes \Gamma^{elec}_b \supset \Gamma_{TS}, \tag{8.3}$$

where $\Gamma_{TS}$ is the totally symmetric representation in the relevant molecular point group.[40] If only one of these states has nonzero FC-overlap with the anion ground state (i.e. $\langle anion|a\rangle = 0, \langle anion|b\rangle \neq 0$), then the FC-forbidden transition can appear in the photoelectron spectrum through the borrowed FC-allowed character, and its detachment characteristics (in particular, the PAD) will match those of the FC-allowed transition.

Following the mixed-*sp* model developed by Sanov and co-workers,[26] detachment from the vibrational ground state of $\tilde{X}\ ^2B_2$ anionic vinylidene can only result in positive anisotropies if the neutral state has $B_2$ vibronic symmetry, suggesting that features B and I correspond to the $b_2$-symmetric $6^1$ and $5^1$ vibrational levels in $\tilde{X}\ ^1A_1$ vinylidene ($\Gamma^{vib}_{neutral} = b_2$, $\Gamma^{elec}_{neutral} = A_1$). As these transitions are FC-forbidden, there must be some coupling of these states to one or more FC-allowed ($\Gamma^{vib}_{neutral} = a_1$) states which satisfies Eq. 8.3. Thus, the state(s) giving FC-intensity to regions B and I must be totally symmetric vibrational levels in a $B_2$ electronic state.

The lowest singlet vinylidene electronic state satisfying this is the $\tilde{B}\ ^1B_2$ state, which we find to have a term energy of 3.9966(22) eV in agreement with previous theoretical calculations.[307] Detachment to this electronic state of $H_2CC$, shown in Figure 8.7, shows the same distinctly positive anisotropy observed for regions B and I in the ground state band, consistent with the assignment of the regions of anomalous anisotropies as arising from vibronic coupling to this excited state. This assignment is confirmed by the derivative coupling calculations that will be described in Section 8.2.5.

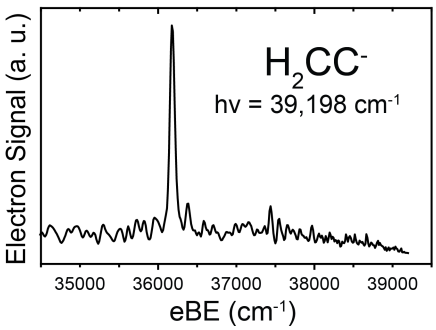


**Figure 8.7:** Photoelectron spectrum of $H_2CC^-$ obtained from the cryo-SEVI experiment showing detachment to the $\tilde{B}\ ^1B_2$ excited neutral state.

### 8.2.3 Rotational Contours

#### Linewidths and rotational selection rules

In contrast to the vinylidene photoelectron spectrum of Lineberger and co-workers,[126] the vinylidene ground state cryo-SEVI spectra do not show anomalous broadening (relative to the rotational temperatures extracted from excited state bands) for the majority of spectral features. Figure 8.8A compares the vibrational origins obtained for the $\tilde{X}\ ^1A_1 \leftarrow \tilde{X}\ ^2B_2$ band reported in the present work to those obtained for the $\tilde{A}\ ^1A_2 \leftarrow \tilde{X}\ ^2B_2$ transition discussed in Chapter 7. A more quantitative treatment of the rotational contours is provided in the following section; as can be seen, the rotational envelopes are qualitatively similar for both electronic bands represented in Figure 8.8A, and this similarity indicates that detachment from rotationally cold vinylidene anions to the neutral $\tilde{X}\ ^1A_1$ ground state does not result in features "broadened" by rapid isomerization to acetylene. Peak widths for other features in the ground state bands of both isotopologues are quite similar to the respective origins, with the exception of FC-forbidden features in the $D_2CC^-$ cryo-SEVI spectrum (B and I) that appear due to vibronic coupling and have substantially narrower widths (see Table 8.1). As shown below, this difference in lineshape is a result of different rotational selection rules for these transitions.

Let $\ell$ be the angular momentum of a photoelectron generated by detachment from an anion state with rovibronic symmetry $\Gamma_{rve}^{anion} = \Gamma_{rot}^{anion} \otimes \Gamma_{vib}^{anion} \otimes \Gamma_{elec}^{anion}$ to form a neutral state with symmetry $\Gamma_{rve}^{neutral}$. The general selection rule for this detachment transition is given by[348]

$$\Gamma_{rve}^{anion} \otimes \Gamma_{rve}^{neutral} \supset \begin{cases} \Gamma^*, & \ell \text{ even} \\ \Gamma_{TS}, & \ell \text{ odd} \end{cases} \tag{8.4}$$

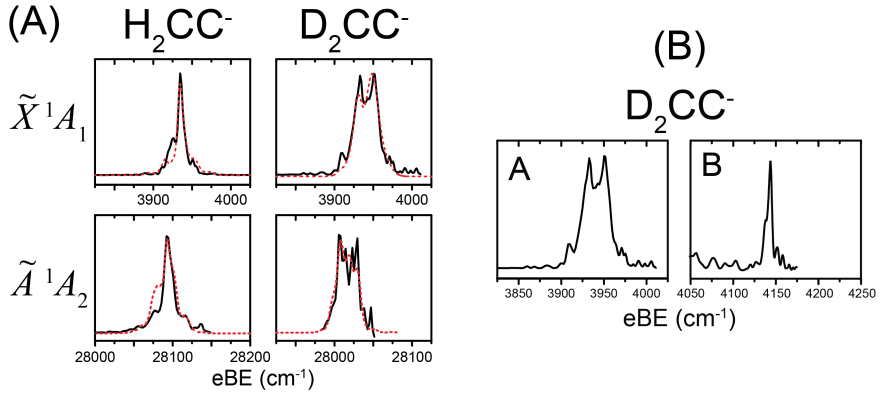


**Figure 8.8:** **(A)** Comparison of rotational contours for the band origins in the $\tilde{X}\ ^1A_1 \leftarrow \tilde{X}\ ^2B_2$ and $\tilde{A}\ ^1A_2 \leftarrow \tilde{X}\ ^2B_2$ electronic bands in the cryo-SEVI vinylidene spectra. The red traces show simulated rotational profiles for the $\tilde{A}\ ^1A_2$ electronic state. **(B)** Comparison of the lineshape of peak A ($0_0^0$) to peak B ($6_0^1$) in the cryo-SEVI spectrum of $D_2CC^-$.

where $\Gamma^*$ and $\Gamma_{TS}$ are the antisymmetric and totally symmetric representations, respectively, within the relevant molecular point group. In the case of vinylidene ($C_{2v}$), $\Gamma^*$ and $\Gamma_{TS}$ are $A_2$ and $A_1$, respectively. For Franck-Condon (FC) allowed detachment from vibrationally cold $\tilde{X}\ ^2B_2$ vinylidene anions (i.e. $\Gamma_{vib}^{neutral} = \Gamma_{vib}^{anion} = a_1$ and $\Gamma_{elec}^{neutral} = B_2$), this becomes

$$\Gamma_{rot}^{anion} \otimes \Gamma_{rot}^{neutral} \otimes \Gamma_{elec}^{neutral} \supset \begin{cases} B_1, & \ell \text{ even} \\ B_2, & \ell \text{ odd} \end{cases} \tag{8.5}$$

The symmetry of the rotational wavefunction of vinylidene (an asymmetric top) is classified by the parity (even, e, or odd, o) of the two quantum numbers $K_a$ and $K_c$. As addressed in the previous analysis of the vinylidene rotational contours,[178] the cryo-SEVI resolution is only sufficient to discern rotational branches corresponding to changes in $K_a$ due to the relative magnitudes of vinylidene's rotational constants; for $H_2CC$ ($D_2CC$), $A \sim 10$ (5) $cm^{-1}$, whereas $B, C \sim 1$ ($< 1$) $cm^{-1}$.[118,178] For even values of $K_a$, the rotational symmetry is either $A_1$ ($K_aK_c$ = ee) or $A_2$ (eo), and for odd $K_a$ the rotational symmetry is either $B_1$ (oo) or $B_2$ (oe).[328] For the FC-allowed features in the ground state band ($\Gamma_{elec}^{neutral} = A_1$), this results in the following possibilities for rotational transitions:

| even $\ell$ | odd $\ell$ |
|---|---|
| ee $\leftarrow$ oe | ee $\leftarrow$ oo |
| eo $\leftarrow$ oo | eo $\leftarrow$ oe |
| oe $\leftarrow$ ee | oe $\leftarrow$ eo |
| oo $\leftarrow$ eo | oo $\leftarrow$ ee |

Regardless of $\ell$, the selection rule requires that $K_a$ must change in parity (odd $\Delta K_a$) for FC-allowed transitions in the $\tilde{X}\ ^1A_1 \leftarrow \tilde{X}\ ^2B_2$ electronic band.

For a near-prolate rotor, $\Delta K_a = 0, \pm 1$ transitions are expected to dominate the rotational profile, depending on the specific electronic states involved. Thus, we take the rotational selection rule for FC-allowed transitions in the ground state band to be $\Delta K_a = \pm 1$. The low temperatures extracted from the previous vinylidene rotational contours suggests that the vast majority of anions will occupy the lowest rotational level allowed by their nuclear spin state (*ortho*, *o* or *para*, *p*); following the requirement that the total internal wavefunction must be antisymmetric (symmetric) with respect to hydrogen (deuterium) interchange, *o*-$H_2CC^-$ (*p*-$D_2CC^-$) is restricted to even $K_a$, whereas *p*-$H_2CC^-$ (*o*-$D_2CC^-$) is restricted to odd $K_a$. Thus, the majority of anions are in the $K_a = 0$ (*o*-$H_2CC^-$, *p*-$DDCC^-$) or $K_a = 1$ (*p*-$H_2CC^-$, *o*-$D_2CC^-$) states, and the rotational envelopes for FC-allowed transitions will be dominated by the $1 \leftarrow 0$ and $0, 2 \leftarrow 1$ transitions, which appear as three separate peaks spaced by $\sim 2A$. The relative intensities of these transitions are governed by nuclear spin statistics analogous to those of $H_2$ ($D_2$), which in the present case imply a 3:1 (1:2) ratio of the $K_a = 0 : K_a = 1$ population for $H_2CC^-$ ($D_2CC^-$). Since most of the $H_2CC^-$ anions are in their $K_a = 0$ level, the single $1 \leftarrow 0$ branch dominates, whereas for $D_2CC^-$ the $0 \leftarrow 1$ and $2 \leftarrow 1$ transitions are both prominent, resulting in a broader rotational profile for $D_2CC$ as observed in Figure 8.8A.

**Table 8.3:** Rotational constants (in $cm^{-1}$) for the anion and neutral ground states of $H_2CC$ and $D_2CC$. The constants for neutral $D_2CC$ were obtained using the equilibrium geometry for neutral $H_2CC$ reported in Ref. [48].

| | anion | | neutral | |
|---|---|---|---|---|
| | $H_2CC^{-178}$ | $D_2CC^{-178}$ | $H_2CC^{118}$ | $D_2CC$ |
| $A$ | 9.9227 | 4.9652 | 9.5318 | 4.7502 |
| $B$ | 1.2166 | 1.0236 | 1.3338 | 1.1221 |
| $C$ | 1.0837 | 0.8486 | 1.1573 | 0.9077 |

As discussed in the main text, several features (B and I) in the ground-state band of the $D_2CC^-$ spectrum are FC-forbidden but vibronically-allowed via coupling to the high-lying $\tilde{B}\ ^1B_2$ excited state. The rotational selection rules for these features are based on the borrowed $B_2$ electronic character of these vibrational levels, and so deviate from those described above. Detachment to a $B_2$ electronic state results in the following possibilities for rotational transitions:

| even $\ell$ | odd $\ell$ |
|---|---|
| ee $\leftarrow$ ee | ee $\leftarrow$ eo |
| eo $\leftarrow$ eo | eo $\leftarrow$ ee |
| oe $\leftarrow$ oe | oe $\leftarrow$ oo |
| oo $\leftarrow$ oo | oo $\leftarrow$ oe |

Thus, regardless of $\ell$, symmetry requires an even change in $K_a$, so $\Delta K_a = 0$ transitions dominate the rotational profile. From the above considerations of anion temperature and nuclear spin statistics, the two expected rotational transitions are $0 \leftarrow 0$ and $1 \leftarrow 1$, which have the same energy to within $< 1\ cm^{-1}$, resulting in a single rotational branch. For $D_2CC$, this is the source of the narrower observed peaks for transitions B and I. This difference is illustrated in Figure 8.8B, which shows peaks A and B from the $D_2CC^-$ cryo-SEVI spectrum.

### Rotational fits for the vibrational origins

A more quantitative analysis of the rotational lineshapes of peak A for both isotopologues was carried out by fitting the rotational contours using the PGOPHER software.[329] This program calculates the full rotational spectrum for excitation of a state characterized by rotational temperature $T$ to a final state with excitation energy $E$; in this case, the initial and final states are the anion and neutral vibrational ground states of vinylidene. The resultant stick spectrum is convoluted with a Gaussian function of width $w$. Rotational constants (see Table 8.3 for values used) and vibronic symmetries for both states are specified, as are the point group of the molecule and the statistical weighting of ee/eo versus oo/oe rotational levels.

The fit results are shown as red dashed lines in Figure 8.8. The agreement with experiment is generally good, particularly for the $H_2CC$ isotopologue, and gives a temperature of 17.0(6) K for $H_2CC^-$ in reasonable agreement with the results from a similar analysis of the excited state bands.[178] The excitation energy from the fitting procedure gives an electron affinity of 0.4866(8) eV for this isotopologue, where the uncertainty is given by the full-width at half-maximum (fwhm) of the Gaussian convolution.

For the deuterated isotopologue, the extracted excitation energy gives an electron affinity of 0.488(2) eV for $D_2CC$. The convolution width and ion temperature parameters yielded by the fitting procedure – 14(1) $cm^{-1}$ and 27(2) K, respectively – are larger than is typically expected for the cryo-SEVI technique. This suggests a minimal amount of broadening (<1 meV) relative to the excited state band; given the lack of acetylene character in the calculated wavefunction for the $0^0$ level of $D_2CC$, we take the source of this to be experimental in nature.

The most likely source of the relatively large fitted ion temperature is RF heating of ions in the ion trap, which leads to incomplete thermalization of the ions with the buffer gas.[174] This is particularly an issue when operating with a large amount of ions in the trap, leading to space-charge effects which push ions towards regions where the effective potential is nonzero. While efforts were taken to tune source conditions and ion optics such that the trap was not overloaded, this often introduced great instability in the ion signal and, due to time limits imposed by the expense of the deuterated precursor ($C_2D_4$), some compromise needed to be made – particularly for the high-resolution scans of peak A where detachment signal was at a minimum. Thus, it is entirely possible that the scans represented in the high-resolution peak A trace in Figure 8.2A correspond to detachment from ions that were not fully thermalized in the ion trap.

Working with large ion signals introduces the potential for too many detachment events with a single laser shot, leading to anomalous broadening of peaks in the spectrum due to the inability of the centroiding algorithm to discern overlapping electron events. However, this issue can always be mediated by decreasing the laser power, and so is not expected to contribute to the lineshape of the band origin in the $D_2CC^-$ cryo-SEVI spectra.

### 8.2.4 Quantum Dynamics Calculations[b]

The quantum dynamics calculations described here must treat both the acetylene and vinylidene isomers, and thus careful consideration is necessary to ensure an optimal coordinate system is used. The bond-length/bond-angle Hamiltonian has a complex kinetic energy operator, which is difficult to handle numerically. While preserving atomic permutation symmetry, the HH-CC Jacobi coordinates are optimal for neither acetylene nor vinylidene. The (2+1) Radau-Jacobi coordinates used in our previous work[49] are optimal for vinylidene, but not for acetylene, and cannot take advantage of the permutation symmetry in the system. Hence, the calculations reported here use the CH-CH Jacobi coordinate system, which preserves the CH-CH permutation symmetry. It is optimal for acetylene, but not quite so

[b]These calculations were carried out by Jing Chang, Changjian Xie, Jianyi Ma, and Hua Guo.

**Table 8.4:** Numerical parameters (in a.u.) used in wave packet calculations.

| | HC–CH | DC–CD |
|---|---|---|
| Grid/basis ranges and sizes | $r_1, r_2 \in (1.42, 5.78)$<br>$N_1 = N_2 = 26$<br>$r_0 \in (0.8, 3.2)$ $N_0 = 22$ | $r_1, r_2 \in (1, 42, 5.78)$<br>$N_1 = N_2 = 28$<br>$r_0 \in (1.35, 3.0)$ $N_0 = 35$ |
| Largest values of $j_1$, $j_2$, and $m$ | 38, 38, 38 | 42, 42, 42 |
| Propagation steps | 20,000 | 20,000 |

for vinylidene. As a result, a large basis/grid is still required to cover both isomers, which makes the computation quite demanding, especially for $D_2C_2$.

The CH-CH Jacobi coordinates are denoted as $(r_0, r_1, r_2, \theta_1, \theta_2, \phi)$. As shown in Figure 8.1, $r_0$ is the distance between the centers-of-mass of the two CH moieties, $r_1$ and $r_2$ are the two C-H bond lengths, $\theta_1$ ($\theta_2$) is the angle between vectors $\vec{r}_1$ ($\vec{r}_2$) and $\vec{r}_0$, and $\phi$ is the relative dihedral angle between the $\vec{r}_1$ and $\vec{r}_2$ vectors. The rotationless ($J = 0$) Hamiltonian in the diatom-diatom Jacobi coordinate system is given as follows ($\hbar = 1$):

$$\hat{H} = \sum_{i=0}^{2} \left( -\frac{1}{2\mu_i} \frac{\partial^2}{\partial r_i^2} \right) + \sum_{i=0}^{2} \frac{\hat{j}_i^2}{2\mu_i r_i^2} + V(r_0, r_1, r_2, \theta_1, \theta_2, \phi), \tag{8.6}$$

where $\mu_0 = (m_C + m_H)/2$, $\mu_1 = \mu_2 = m_H m_C/(m_H + m_C)$, $\hat{j}_1$ and $\hat{j}_2$ are the angular momentum operators for $r_1$ and $r_2$, respectively, and $\hat{j}_0^2 = \left(\hat{j}_1 + \hat{j}_2\right)^2$. $V$ is the potential energy function developed by Han, Li, and Guo.[48] The coordinates and Hamiltonian are defined analogously for $D_2C_2$ by replacing the H atoms in $H_2C_2$ with deuterium.

The Hamiltonian is discretized using a mixed grid-basis representation. The radial coordinates $r_1$ and $r_2$ are represented by DVR (discrete variable representation) grids and $r_0$ by PODVR (potential optimized DVR),[349] while the angular degrees of freedom are expressed in terms of associated Legendre functions. The real Chebyshev propagation is used to determine the energy levels and the wavefunctions:[324]

$$\Psi_k = 2\hat{H}_s \Psi_{k-1} - \Psi_{k-2}, \quad k \geq 3 \tag{8.7}$$

with $\Psi_1 = \hat{H}_s \Psi_0$ and $\Psi_0 = \Psi_i$. The Hamiltonian in Eq. 8.7 was scaled to the spectral range of $(-1, 1)$ via $\hat{H}_s = (\hat{H} - H^+)/H^-$. The spectral medium and half width ($H^{\pm} = (H_{max} \pm H_{min}/2)$ are determined by the spectral extrema, $H_{max}$ and $H_{min}$, which can be estimated easily from the discretized Hamiltonian. The initial wave packets ($\Psi_i$) on the neutral PES are anion vibrational eigenfunctions assuming photodetachment to be a vertical transition (Condon approximation). The anion wavefunctions are obtained by diagonalizing the Hamiltonian in Eq. 8.6 using the Lanczos method on the anion PES.[49] In order to preserve the CH−CH permutation symmetry, the initial wave packets were symmetrized by exchanging the $\vec{r}_1$ and $\vec{r}_2$ vectors.[320] A large basis set ($8 \times 10^8$ for $H_2CC$ and $2 \times 10^9$ for $D_2CC$)

and a relatively long propagation (20,000 Chebyshev steps) are used to obtain convergent energy levels for both isomers (with an uncertainty of 2.0 $cm^{-1}$). The parameters used in the calculations are listed in Table 8.4.

The energy spectrum is obtained from the discrete cosine Fourier transform of the Chebyshev autocorrelation functions, $C_k \equiv \langle \Psi_0 | \Psi_k \rangle$:[323]

$$S(E) = \frac{1}{\pi H^- \sin\vartheta} \sum_{k=0} (2 - \delta_{k,0}) \cos(k\vartheta) C_k, \tag{8.8}$$

where $\vartheta = \arccos(E_s)$ is the Chebyshev angle, $k$ is the Chebyshev order, and $E_s$ is the scaled total energy corresponding to $\hat{H}_s$. Once the eigenvalues are determined, the corresponding eigenfunctions can be regenerated by rerunning the same propagation. For each eigenfunction, the assignment of vibrational quanta is based on inspecting the nodal structure of the wavefunction. Finally, the HCCH (or DCCD) weight is determined approximately by integrating the squared wavefunction in the range where both $\theta_1$ and $\theta_2$ are larger than 85° or are less than 60°. The other details of the calculations can be found in our previous work.[49]

The calculated photoelectron spectra for detachment from the $5_1$ state of $H_2CC^-$ and $D_2CC^-$ are shown in Figure 8.9. Photodetachment of this $b_2$ state of the anion leads to excitation of several $b_2$ vibrational states of neutral vinylidene and their tentative assignments are given in the figure. It is clear that the $5^1$ and $1^16^1$ states are quite close in energy for both isotopologues, consistent with the resonance formed by these two states.

In Figure 8.11, the $0^0$, $6^2$, and $5^1$ wavefunctions of $D_2CC$ are plotted in both the $D_2CC$ and DCCD regions. Comparing with the analogous wavefunctions in Figure 8.3, it is clear that deuteration significantly reduces the mixing with DCCD (see the vinylidene weights in Table 8.1). This is not surprising as the wavefunctions of deuterated vinylidene are much narrower, thus it is more difficult to access the isomerization barrier. The extent of mixing

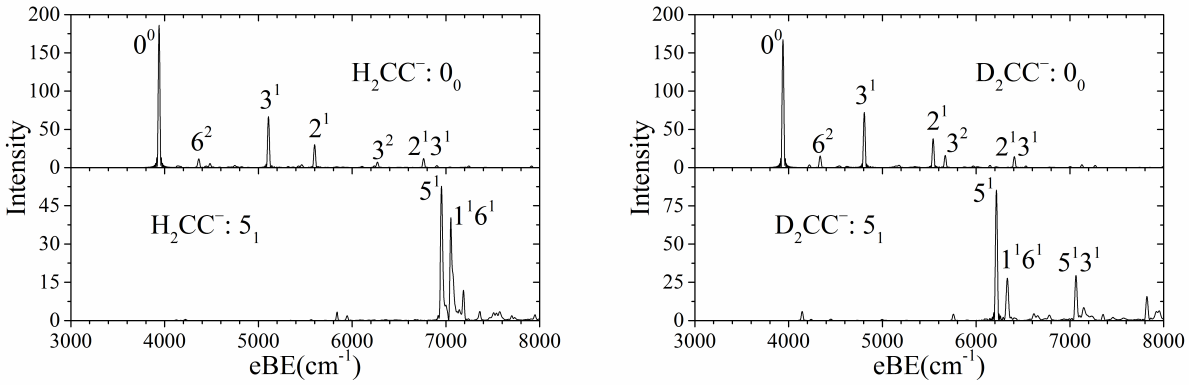


**Figure 8.9:** Calculated photoelectron spectra of the $0_0$ (top) and $5_1$ (bottom) states of $H_2CC^-$ (left) and $D_2CC^-$ (right).

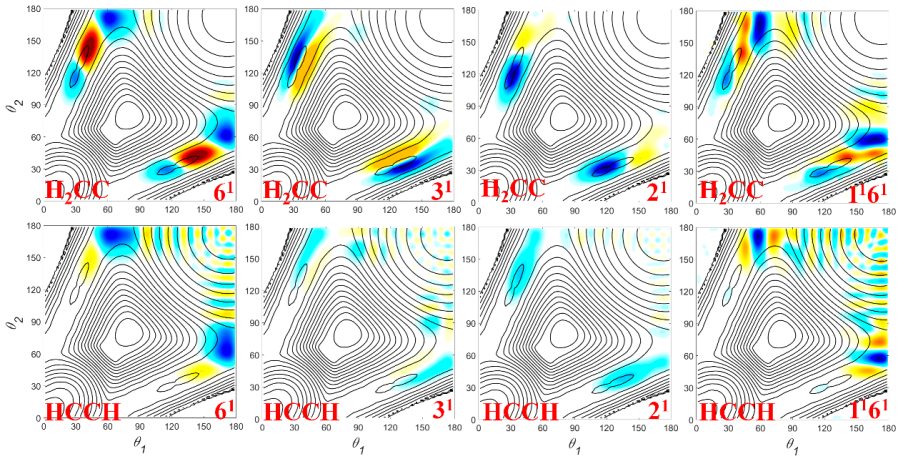


**Figure 8.10:** Wavefunctions of the $6^1$, $3^1$, $2^1$, and $1^16^1$ states of $H_2CC$.

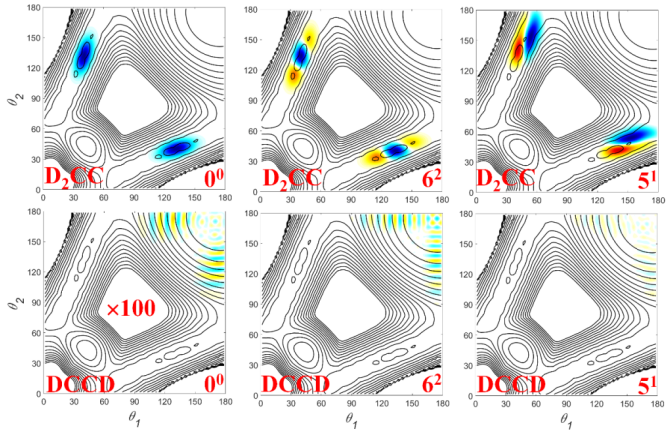


**Figure 8.11:** Wavefunctions of the $0^0$, $6^2$, and $5^1$ states of $D_2CC$.

is however expected to rise with energy, leading to more significant mixing between the two isomers for vibrationally excited $D_2CC$.

In Figures 8.10 and 8.12, the $6^1$, $3^1$, $2^1$, and $1^16^1$ wavefunctions of $H_2CC$ and $D_2CC$ are presented. The smaller acetylene component in the $D_2CC$ wavefunctions as compared to those of $H_2CC$ is quite apparent, consistent with the calculated vinylidene weights listed in Table 8.1. In addition, it is readily seen that the $1^16^1$ wavefunction of $H_2CC$ has a similar shape to that of the $5^1$ state, suggesting significant mixing due to accidental near-degeneracy of the two states. Indeed, the energy difference between the two states is quite small (104 $cm^{-1}$ for $H_2CC$). This near-degeneracy suggests a large intermodal anharmonicity ($x_{1,6}$) because the harmonic value of the $1^16^1$ state is 133 $cm^{-1}$ higher than its actual energy. Coupling between the in-plane rocking and stretching is plausible due to the low isomerization barrier and the resultant large anharmonicity along the isomerization minimum energy path.[48] The

mixing is much less severe for $D_2CC$, evidenced by the clear and regular nodal structures of the two wavefunctions. Finally, the acetylene states that mix with the vinylidene states are of the local bender nature, which possess large numbers of nodes along the two angular coordinates ($\theta_1$ and $\theta_2$), suggesting that only the highly excited local bending states of acetylene are involved in the mixing of the two isomers. This is consisted with previous theoretical analysis of the acetylene vibrational spectrum.[289,350,351]

### 8.2.5 Theoretical Treatment of Derivative Coupling[c]

In order to determine the derivative coupling between the ground and excited electronic states of vinylidene, *ab initio* calculations employing correlation-consistent polarized valence triple zeta (cc-pVTZ) basis sets on carbon and hydrogen with diffuse $s(0.044020)$, $p(0.035690)$, and $d(0.100000)$ functions added to carbon were performed. Molecular orbitals were optimized in a state-averaged multiconfiguration self-consistent field (SA-MCSCF) procedure averaging the four lowest states of a 2-orbital doubly-occupied space and a 7-orbital, 10-electron (all valence electron) active space. Energies and derivative couplings were computed at the multireference configuration single and double configuration interaction (MRSDCI) level, an expansion which adds to the SA-MCSCF reference space all single and double excitations out of that space. The MRSDCI expansion comprised 5,114,424 configuration state functions (CSFs). All calculations were performed using the COLUMBUS electronic structure suite.[352]

The derivative coupling vector, given by

$$f^{i,j}_{Q_\alpha}(\mathbf{R}) = \left\langle \Psi_i(\mathbf{r};\mathbf{R}) \left| \frac{\partial}{\partial Q_\alpha} \right| \Psi_j(\mathbf{r};\mathbf{R} \right\rangle_{\mathbf{r}}, \tag{8.9}$$

was evaluated using analytic gradient techniques.[353–355] Here, $\Psi_i$ and $\Psi_j$ are the electronic wavefunctions of adiabatic states $i$ and $j$, $\mathbf{R}$ and $\mathbf{r}$ represent nuclear and electronic coordinates, respectively, and $Q_\alpha$ the $\alpha$ internal coordinate. For the case at hand, where nuclear configurations with $C_{2v}$ symmetry are considered, $f^{i,j}_{Q_\alpha}(\mathbf{R})$ is nonzero provided the direct product of the irreducible representations carried by states $\Psi_i$ ($^1A_1$) and $\Psi_j$ ($^1B_2$) and nuclear coordinate $Q_\alpha$ is $A_1$. Thus, Eq. 8.9 is nonvanishing for $b_2$ vibrations, $Q_5$ (antisymmetric CH stretch) and $Q_6$ (in-plane rock) of $H_2CC$. When $\mathbf{f}^{i,j}$ is computed for vinylidene, $f^{i,j}_{Q_6} = -4.080516$ is nearly 30 times larger in magnitude than $f^{i,j}_{Q_6} = 0.14426998$ and composes almost 100% of the derivative coupling vector ($||\mathbf{f}^{i,j}|| = 4.08304976$); therefore, states $\Psi_i$ ($^1A_1$) and $\Psi_j$ ($^1B_2$) are strongly coupled by the in-plane rocking mode, $\nu_6$.

Figure 8.13A shows the derivative coupling vector $\mathbf{f}^{i,j}$. The top panel of Figure 8.13B is a plot of the $^1A_1$ and $^1B_2$ states and their mean energy along the $Q_6$ coordinate. The bottom panel plots the differences of states $^1A_1$ and $^1B_2$ from the mean energy.

[c]Derivative coupling calculations were carried out by Christopher Malbon and David R. Yarkony.

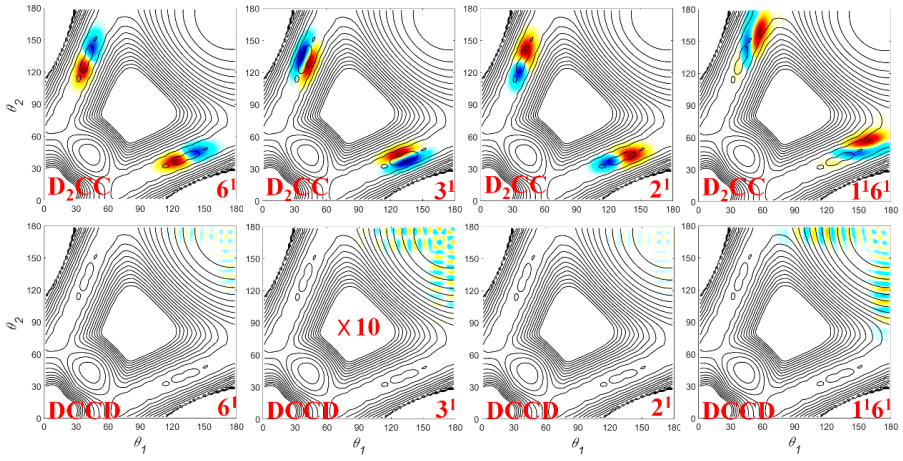


**Figure 8.12:** Wavefunctions of the $6^1$, $3^1$, $2^1$, and $1^16^1$ states of $D_2CC$.

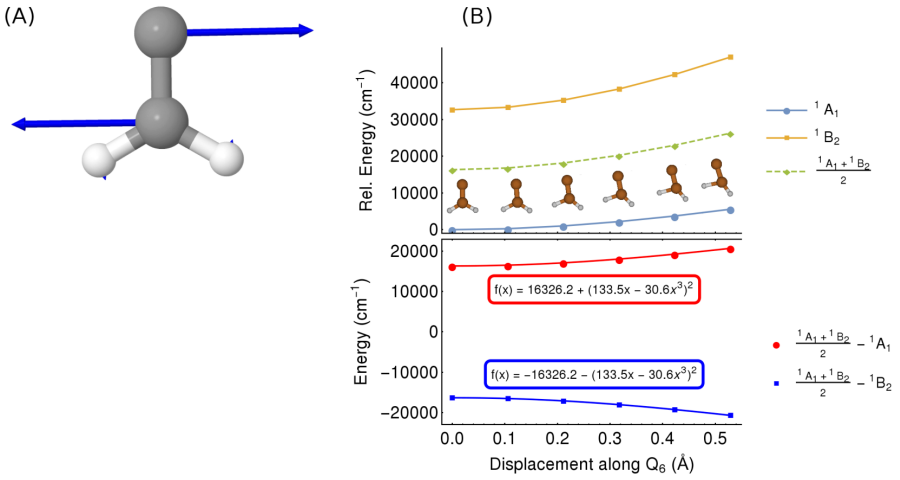


**Figure 8.13:** (A) Vector representation of the derivative coupling between $^1A_1$ and $^1B_2$. (B) (Top) plot of $^1A_1$ and $^1B_2$ state energies and their mean along the in-plane rocking mode, $Q_6$. (Bottom) plot of the deviation of each state from the mean energy. The $H_2CC \rightarrow HCCH$ transition state is located 0.913 Å along the $Q_6$ mode and features an electronic (ZPE-adjusted) barrier of 1639.5 (1005.8) $cm^{-1}$.

# Chapter 9

# Resonant Autodetachment from Vinylidene Anions

The content and figures of this chapter are reprinted or adapted with permission from J. A. DeVine, M. L. Weichman, C. Xie, M. C. Babin, M. A. Johnson, J. Ma, H. Guo, D. M. Neumark, "Autodetachment from vibrationally excited vinylidene anions" *J. Phys. Chem. Lett.* **9**, 1058 (2018).

## Abstract

Slow electron velocity-map imaging of the cryogenically-cooled $H_2CC^-$ anion reveals a strong dependence of its high-resolution photoelectron spectrum on detachment photon energy in two specific ranges, from $4000 - 4125$ cm$^{-1}$ and near 5020 cm$^{-1}$. This effect is attributed to vibrational excitation of the anion followed by autodetachment to $H_2CC + e^-$. In the lower energy range, the electron kinetic energy (eKE) distributions are dominated by two features that occur at constant eKEs of 114(3) and 151.9(14) cm$^{-1}$, rather than constant electron binding energies as is typically seen for direct detachment. These features are attributed to $\Delta J = \Delta K = 0$ autodetachment transitions from two vibrationally excited anion states. The higher-energy resonance autodetaches to neutral eigenstates with amplitude in the theoretically predicted shallow well lying along the vinylidene-acetylene isomerization coordinate. Calculations provide assignments of all autodetaching anion states and show that the observed autodetachment is facilitated by an intersection of the anion and neutral surfaces.

## 9.1 Main Text

Vinylidene ($H_2CC$) is the simplest unsaturated carbene,[340] a key reactive intermediate,[277,279,280] and a high-energy isomer of acetylene (HCCH).[118,119,121] The potential energy surface (PES) for the benchmark 1,2-hydrogen shift[114] from vinylidene to acetylene has a small barrier ($\sim 0.1$ eV),[124] allowing for tunneling-induced coupling between vinylidene and vibrationally excited acetylene. While HCCH does not support a bound anion,[338] vinylidene anions are relatively easy to generate in the gas phase, enabling experiments in which photodetachment of $H_2CC^-$ is used to characterize the neutral vinylidene isomer and the extent of its coupling to acetylene.[37,126–128,178,299] Most of this prior work has focused on direct photodetachment of $H_2CC^-$ to the neutral + electron continuum. In the current chapter, we consider autodetachment of the anion following vibrational excitation. Such an experiment explores novel aspects of coupling between anionic and neutral vinylidene and probes otherwise inaccessible regions of the $H_2CC$ PES. The experimental results are interpreted with the aid of quantum chemistry and dynamics calculations, a combined approach that has proved fruitful in gaining insights into complex molecular photodetachment processes.[37,356,357]

The photoelectron spectrum of the vinylidene anion was first measured by Lineberger and coworkers in 1983.[126,299] Vibrationally-resolved transitions to several electronic states of neutral vinylidene were observed, and comparison of linewidths between ground and excited state bands revealed that the ground state transitions were uniformly broader than those in the excited state spectra.[126] This broadening was attributed to detachment to a short-lived neutral vinylidene configuration that rapidly isomerized to acetylene on a sub-picosecond timescale. However, subsequent Coulomb explosion imaging (CEI) experiments[127] indicated that neutral $H_2CC$ formed by photodetachment is stable on a microsecond timescale, a result consistent with several theoretical studies of vinylidene isomerization dynamics.[121,122]

Recent work using slow electron velocity-map imaging of cryogenically-cooled anions (cryo-SEVI) at Berkeley and high-resolution photoelectron imaging at Australian National University[37,178] has yielded a series of high-resolution vinylidene photoelectron spectra covering electron binding energies (eBEs) from $\sim 0.5$ to 5 eV; these spectra include transitions to the singlet ground state and several electronically excited singlet and triplet states of neutral $H_2CC$. Detachment to the singlet ground state did not show the broadening reported by Ervin *et al.*[126] With the assistance of quantum dynamics calculations it was determined that coupling to acetylene only occurs for vinylidene vibrational levels with excitation along the $CH_2$ in-plane rocking mode ($\nu_6$). This work is consistent with the conclusion of the CEI experiments that neutral vinylidene is (for the most part) stable with respect to isomerization, though the state-specific information obtained from cryo-SEVI reveals that vinylidene-acetylene mixing is indeed promoted by excitation along $\nu_6$. The origin of the broadening in the earlier photoelectron spectrum[126] is unclear. It may reflect higher rotational and/or vibrational excitation of the anions in that experiment owing to warmer ion source temperatures; photodetachment could then produce internally excited $H_2CC$ that is more strongly coupled to acetylene.

In the process of acquiring the cryo-SEVI spectrum of $H_2CC^-$, it was observed that

the photoelectron kinetic energy (eKE) distribution depended nontrivially on photon energy ($h\nu$) over narrow energy regions near the adiabatic electron affinity (EA) of $H_2CC$, 0.4866(8) eV.[37] Such a result is not consistent with direct detachment to the neutral + electron continuum, Eq. 9.1, in which intensities are determined primarily by Franck-Condon (FC) factors involving the anion and neutral vibrational levels.

$$H_2CC^- + h\nu \rightarrow H_2CC + e^- \tag{9.1}$$

In direct detachment, the observed eKEs for each transition simply track the photon energy according to eKE = $h\nu$−eBE. The more complex photon energy dependence observed with cryo-SEVI is a signature of autodetachment, Eq. 9.2 and Fig. 9.1a, wherein an initially excited anion state subsequently detaches an electron via a nonadiabatic transition.[44–46]

$$H_2CC^- + h\nu \rightarrow H_2CC^{-*} \rightarrow H_2CC + e^- \tag{9.2}$$

In this process, the intermediate state can be a vibrationally excited anion in its ground electronic state,[358] or an electronically excited anion.[359–362] As illustrated in the energy diagram of Figure 9.1a, autodetachment occurs only when $h\nu$ is resonant with a transition in the anion, and can result in the observation of otherwise inaccessible neutral states and/or eKE distributions that deviate from a Franck-Condon profile.

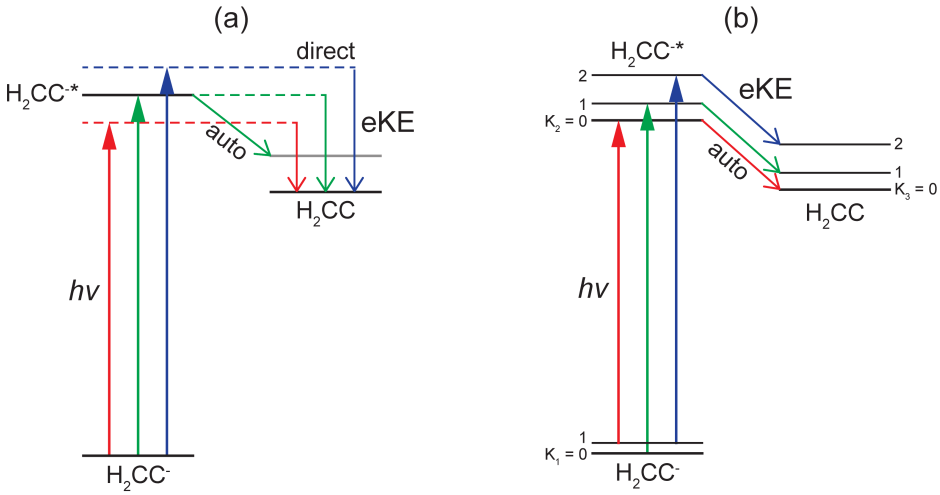


**Figure 9.1:** Schematic energy diagrams showing the detachment mechanisms used to describe the current results for detachment from vinylidene anions. **(a)** Direct detachment as well as autodetachment to a FC forbidden state (gray neutral energy level) neglecting the rotational manifolds of all three states. **(b)** Mechanism used to describe the constant-eKE autodetachment structure arising from $\Delta J_{2,3} = \Delta K_{2,3} = 0$ rotational transitions within a single vibrational resonance (see Eq. 9.3 for definition of notation). Direct photodetachment has been omitted from this panel for clarity.

Autodetachment from vibrationally excited vinylidene anions has been previously detected by Gerardi *et al.*,[128] who sought to measure the infrared spectrum of the vinylidene anion using predissociation spectroscopy of messenger-tagged $H_2CC^-$. In that work, autodetachment resonances of bare $H_2CC^-$ were reported for photon energies just above the EA of $H_2CC$, 0.4866(8) eV,[37] and the photon energies at which these transitions occurred were found to correspond to features in the predissociation spectrum of Ar-tagged $H_2CC^-$. This correspondence indicates that a vibrationally-mediated autodetachment process is in play, wherein the anion undergoes vibrational (rather than electronic) excitation and subsequently detaches to the neutral + free electron continuum.

The likelihood of an anion undergoing autodetachment is strongly dependent on the PESs of the relevant anion and neutral states.[45] There has been much effort to map out global PESs describing both isomers of the neutral vinylidene/acetylene system,[116,117,124] though a spectroscopically-accurate, full-dimensional PES has only become available somewhat recently.[48] The PES for anionic vinylidene has also been developed and successfully used to simulate the spectrum for direct detachment.[49] Interestingly, the neutral PES possesses a shallow intermediate well between the vinylidene and acetylene isomers that supports bound, delocalized vibrational levels.[49] Several eigenstates of neutral $H_2CC$ were found to be well-described as linear combinations of these intermediate-well states with the $\nu_6$ fundamental. These states have little or no FC overlap with the anion ground state, and are thus unlikely to be observed by direct photodetachment. However, the work presented herein shows that they are accessible via autodetachment.

Details of the cryo-SEVI method and apparatus are provided in Chapter 2. The experimental conditions used to obtain the data presented in this chapter are identical to those described in Chapters 7 and 8. Figures 9.2a and 9.2b show the complex structure observed in the $H_2CC^-$ cryo-SEVI spectra using photon energies ranging from 4000 to 4125 $cm^{-1}$ plotted vs. eBE and eKE, respectively. Individual scans are provided in Figures 9.4-9.5. This range of photon energies is sufficient to reach only the ground vibrational state of $H_2CC$ by direct detachment, and the trace at $h\nu = 4040$ $cm^{-1}$ in Fig. 9.2a was presented as the high-resolution scan of the vibrational origin in the previously reported cryo-SEVI spectrum of $H_2CC^-$.[37] Other spectra from $4000 - 4050$ $cm^{-1}$ are similarly dominated by a single peak at the vibrational origin, highlighted in gray in Fig. 9.2a, whose eBE is independent of photon energy as expected for direct detachment. In addition to this structure, there are two features that (in eBE) appear to pass through the vibrational origin as the photon energy is increased, in some cases dominating over the contributions from direct detachment. These shifting peaks are seen over two partially overlapping ranges of $h\nu$, $4000 - 4075$ $cm^{-1}$ and $4050 - 4100$ $cm^{-1}$. Figure 9.2b provides an alternate view of the same data, showing that many of the peaks appear at one of two values of constant eKE as the photon energy is varied, as indicated by the shaded regions A and B. This trend is shown more explicitly in Fig. 9.2c, in which the eKEs of major spectral features are plotted vs. photon energy and compared to the expected eKE for the vibrational origin (solid line) given the EA of $H_2CC$. Averaging the data in Figure 9.2c gives constant eKEs of 114(3) and 151.9(14) $cm^{-1}$ for features A and B, respectively.

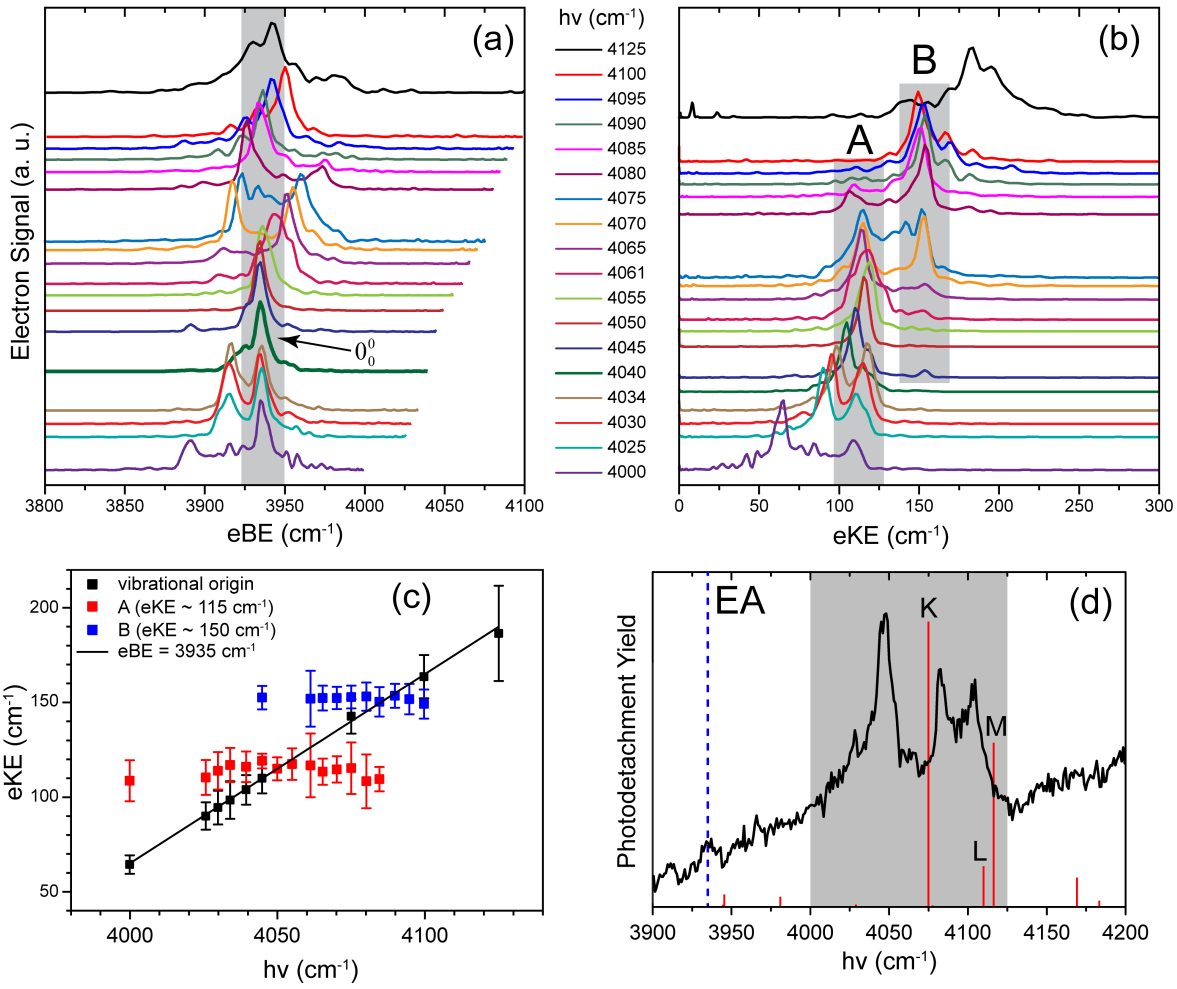


**Figure 9.2:** **(a)** $H_2CC^-$ cryo-SEVI data for photon energies ranging from $4000 - 4125$ $cm^{-1}$ plotted vs. electron binding energy (eBE). The position of the vibrational origin is highlighted in gray. Individual traces may be found in Figure 9.4. **(b)** The same cryo-SEVI data as in panel (a), plotted vs. electron kinetic energy (eKE). The constant-eKE features A and B are highlighted in gray. Individual traces are provided in Figure 9.5. **(c)** A summary of the eKEs of the major structure highlighted in panels (a) and (b), where error bars correspond to $2\sigma$ and $\sigma$ is the width parameter obtained from a Gaussian fit to the experimental feature. The solid line shows the expected eKE for detachment to the ground vibrational state of neutral $H_2CC$. **(d)** The relevant portion of the photodetachment spectrum previously measured by Gerardi *et al.* (black),[128] as well as the position of the EA of neutral $H_2CC$ (blue dashed line). The red sticks show the corresponding portion of the simulated infrared spectrum calculated in this work (red, arbitrarily scaled). See Section 9.2.2a and Table 9.2 for the details of the assignments of features K, L, and M.

The results in Figs. 9.2a-c indicate that there are significant contributions from processes other than direct photodetachment in the photoelectron spectrum of $H_2CC^-$ for this range of photon energies. Figure 9.2c shows that the spectral regions of the two constant eKE features are centered around 4050 and 4070 $cm^{-1}$; these energies line up reasonably well with two of the autodetachment peaks in the infrared photodetachment spectrum obtained by Gerardi *et al.,*[128] displayed in Fig. 9.2d. The peaks in that spectrum correspond to excitation of vibrationally excited states of $H_2CC^-$ that are embedded in the neutral continuum and decay by autodetachment, *i.e.* Eq. 9.2. We thus attribute the constant eKE features observed with cryo-SEVI to photoelectrons produced by the autodetachment transitions reported in the work of Gerardi *et al.* One must then elucidate the nature of the anion excitation, and formulate a mechanism for autodetachment that explains the constant eKE features.

To assign the anion excitations, we turn to the calculated infrared spectrum of the vinylidene anion, shown fully in the top panel of Figure 9.6. Details regarding the current theoretical work are provided in Sections 9.2.1-9.2.2. The portion of the theoretical spectrum that is relevant to the current discussion is shown in Figure 9.2d overlaid with the previously reported detachment spectrum.[128] Inspection of the relative oscillator strengths (which have been arbitrarily scaled in Figure 9.2d) reveals two vibrational transitions (K and M, Table 9.2) with elevated intensities. These transitions terminate in the $2_1 5_1$ and $1_1 2_1$ vibrational levels of the anion,[a] with calculated frequencies of 4075 and 4116 $cm^{-1}$, respectively. If the calculated frequencies are each red-shifted by 30-40 $cm^{-1}$, they line up well with the first two experimental peaks in Fig. 9.2d, suggesting that those peaks should be assigned as excitations to the $2_1 5_1$ and $1_1 2_1$ anion states. Given their energies, these levels can autodetach only to the $0^0$ level of neutral $H_2CC$.

In order to explain the constant eKE features, we consider the full autodetachment process as a vibrational excitation of the anion and subsequent relaxation to the neutral ground state, where each of these states has an associated rotational manifold. Using quantum numbers $J$ and $K$ to specify the rotational state of the near-prolate asymmetric top, the autodetachment process is expressed as

$$H_2CC^-(\mathbf{v}_1 = 0, J_1, K_1) + h\nu \rightarrow H_2CC^-(\mathbf{v}_2, J_2, K_2) \rightarrow H_2CC(\mathbf{v}_3 = 0, J_3, K_3) + e^-, \quad (9.3)$$

where $\mathbf{v}_i$ represents the full set of vibrational quantum numbers for state $i$. In this labelling convention, state 1 is the anion ground state, state 2 is the anion excited state, and state 3 is the final neutral state. The eKE depends only on the energy difference between states 2 and 3 and can be written as

$$\text{eKE} = E_{vib} - \text{EA} - \Delta E_{rot} \quad (9.4)$$

where $E_{vib}$ is the (rotationless) vibrational energy of the anion excited state, EA = 0.4866 eV is the neutral electron affinity,[37] and $\Delta E_{rot} = E_{rot,3} - E_{rot,2}$ is the change in rotational energy upon detachment.

[a]Here, we adopt a convention in which a vibrational state is represented by its normal-mode numerals with superscripts (subscripts) to denote the corresponding quantum numbers of the neutral (anion).

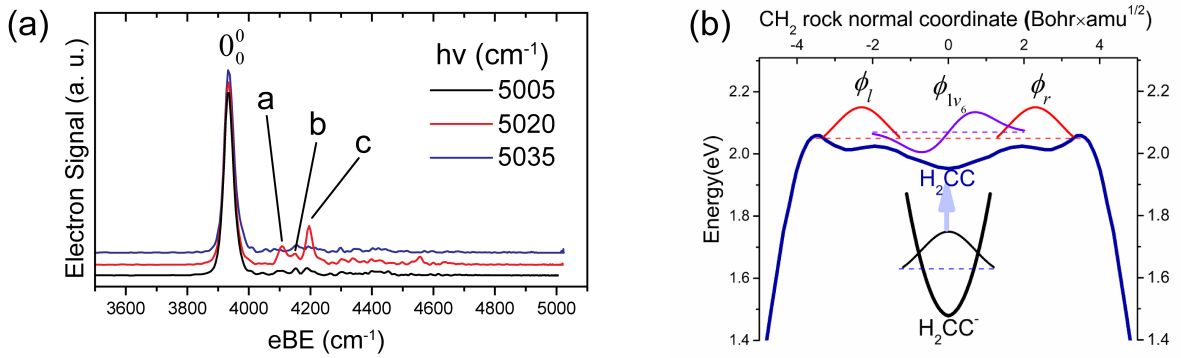


**Figure 9.3:** **(a)** $H_2CC^-$ cryo-SEVI scans showing the autodetachment structure observed for photon energies of $\sim 5020$ cm$^{-1}$. **(b)** Minimum energy path for the vinylidene-acetylene isomerization and the zeroth-order states in the vinylidene and intermediate wells. The anion potential and its ground vibrational state are also included for comparison.

Our experimental results show that as the detachment laser is tuned across the rotational manifold associated with each vibrational resonance, the eKE given by Eq. 9.4 remains constant. Vinylidene ions prepared by cryo-SEVI are rotationally cold, with rotational temperatures of around 17 K, as determined by fitting a rotational model to the lineshape of the experimental band origin.[37] At this temperature, the $K_1 = 1$ and 0 levels are populated in a 1:3 ratio according to nuclear spin statistics, and there is a small population ($\sim 2\%$) of anions with $K_1 > 1$. Hence, as discussed in more detail in Section 9.2.3, we expect a range of $K_2$ levels to be populated as we scan across each resonance. The eKE is constant under these circumstances if $\Delta E_{rot}$ is close to 0, which can be satisfied if (a) $\Delta J_{2,3} = \Delta K_{2,3} = 0$ and (b) the rotational constants of the vibrationally excited anion are similar to those of the $0^0$ neutral. Based on previous electronic structure calculations of the anion and neutral geometries,[37,118,178] the latter condition is satisfied insofar as rovibrational coupling is negligible, so we attribute the constant-eKE nature of detachment features A and B to $\Delta J = \Delta K = 0$ transitions between the excited anion and neutral ground vibrational states. This photophysical mechanism is illustrated schematically in Figure 9.1b for the $2_1 5_1$ resonance, for which $\Delta K_{1,2} = \pm 1$; the three transitions shown in Fig. 9.1b have different excitation energies but the electrons produced by autodetachment have the same eKE. As $\Delta E_{rot} \approx 0$, the energies of the autodetaching anion states ($E_{vib}$) in Eq. 9.4 are given by $E_{vib} = \text{EA} + \text{eKE}$, providing vibrational energies of 4039(7) and 4077(7) cm$^{-1}$ for the $2_1 5_1$ and $1_1 2_1$ anion states that autodetach to yield features A and B, respectively.

Increasing the photon energy past the range covered in Fig. 9.2 reveals an additional set of autodetaching resonances of the vinylidene anion over a narrower range of photon energies centered around 5020 cm$^{-1}$ (Figure 9.3a), resulting in the appearance of three features labelled a, b, and c. This photon energy is higher than those used in the work of Gerardi *et al.*, so these resonances are reported here for the first time. The oscillator strengths in the calculated anion infrared spectrum (Fig. 9.6) are quite small in the $h\nu \sim 5020$ cm$^{-1}$ vicinity,

**Table 9.1:** Binding energies and shifts from the vibrational origin for autodetachment features observed in the cryo-SEVI spectrum of $H_2CC^-$ obtained with a photon energy of 5020 $cm^{-1}$. Uncertainties correspond to one standard deviation of a Gaussian fit to the experimental peak. The neutral states involved in the autodetachment transitions are assigned (assn.) and the theoretical energies of these levels with respect to the vinylidene vibrational origin (theo.) are provided for comparison.

| Peak | eBE ($cm^{-1}$) | shift ($cm^{-1}$) | assn. | theo. ($cm^{-1}$)[49] |
|---|---|---|---|---|
| a | 4119(13) | 184 | $0^u$ | 183.9 |
| b | 4159(10) | 224 | $0^g$ | 208.8 |
| c | 4206(13) | 271 | $6^1$ | 283.2 |

but two transitions (P and Q) have elevated intensities relative to the other transitions in this region. These terminate in the $5_2$ and $1_15_1$ vibrational levels of the vinylidene anion (Table 9.2), with calculated excitation energies of 5066 and 5094 $cm^{-1}$, respectively. Of these two transitions, the $5_2$ feature (P) has higher intensity and is closer to the $\sim$ 5020 $cm^{-1}$ excitation energy estimated from experiment. Thus, the autodetachment transitions which give rise to peaks a, b, and c are assigned to detachment from the $5_2$ state of $H_2CC^-$ to three vibrational levels of neutral $H_2CC$.

The binding energies and assignments of these features in the $h\nu = 5020$ $cm^{-1}$ scan are summarized in Table 9.1; as discussed further in Section 9.2.2, the observed peak positions of a-c match well with the relative energies of the neutral eigenstates identified as possessing intermediate-well character ($0^u$, $0^g$, $6^1$).[49,b] The shape of the neutral PES giving rise to these states is shown in Figure 9.3b along the minimum energy path for isomerization. Thus, the autodetachment behavior observed in Figure 9.3a provides direct observation of the intermediate-well states described by Eq. 9.8, confirming the multi-well shape of the vinylidene/acetylene PES identified in previous work.[49]

The observation of autodetachment transitions requires coupling between the initial anion and final neutral + $e^-$ states which permits the conversion of nuclear kinetic energy (vibrational and rotational) into electronic energy (eKE). The interpretation of the constant eKE features in Fig. 9.2 in terms of $\Delta J = \Delta K = 0$ transitions implies that in the present case, the autodetachment transitions are purely driven by vibrational coupling of the anion and neutral electronic states through the nuclear kinetic energy operator. The electronic structure effects that favor such vibrationally-induced autodetachment from molecular anions have been explored extensively by Simons, who has used both perturbative and semiclassical approaches to derive explicit expressions for the state-to-state autodetachment rate.[45,363–365] These expressions show that autodetachment transitions are most likely to occur in regions

[b]The notation used to label the states containing intermediate-well character is borrowed from Ref. [49], where the $g$ and $u$ superscripts refer to symmetric and antisymmetric linear combinations of the left- (L) and right-well (R) localized vibrational states.

of nuclear configuration ($Q$) space where the anion and neutral PESs are close in energy, resulting in detachment of electrons with relatively low kinetic energies. In particular, if the anion and neutral PESs cross for some intermediate value $Q_0$, autodetachment (or the reverse process, resonant electron attachment[366]) is likely to occur between anion and neutral states provided that they have relatively large amplitudes in the vicinity of $Q_0$.

Further exploration of the anion and neutral PESs for the purposes of the current work has revealed such a crossing for the vinylidene system. This crossing seam is characterized in Section 9.2.2 and Figure 9.7. The minimum crossing point is very close to the neutral $H_2CC$ equilibrium and is merely 0.04 eV higher in energy. A first-principles characterization of the nonadiabatic autodetachment dynamics is beyond the scope of this work as it requires treatment of the derivative coupling between the two electronic states. However, the identification of such an anion/neutral surface crossing provides an explanation for the extensive involvement of vibrational autodetachment in the photoelectron spectrum of $H_2CC^-$ for photon energies near the neutral electron affinity.

To conclude, resonant autodetachment from vinylidene anions has been observed in two photon energy windows. All resonances reported here occur at energies sufficiently high that the anion excitation corresponds to a combination or overtone band, and the resultant eKEs indicate conversion of multiple quanta of vibrational excitation into electronic energy. Constant-eKE transitions were observed over a relatively wide range of photon energies, and were assigned as $\Delta J = \Delta K = 0$ detachment transitions from the $2_1 5_1$ and $1_1 2_1$ anion states to the $0^0$ neutral state. Additional anion resonances were seen over a narrower range of photon energies centered around 5020 $cm^{-1}$. These detachment transitions were identified as terminating in neutral vibrational levels with intermediate-well character, confirming the multi-well structure of the neutral $H_2CC$-HCCH isomerization PES. The nonadiabatic coupling between anion and neutral states that facilitates all of the observed autodetachment transitions is likely due to a crossing of these PESs, which has been reported here for the first time. This set of vinylidene cryo-SEVI data and the accompanying theoretical analysis reveal new subtleties in this benchmark system, highlighting the unexpected complexity of the tetraatomic $C_2H_2$ molecule.

## 9.2 Supporting Information

### 9.2.1 Theoretical Methods[c]

In the full-dimensional calculation of the vinylidene anion vibration, the rotationless ($J = 0$) Hamiltonian in the (2+1) Radau-Jacobi coordinates[319] (shown in Figure 9.8) is

[c]The theoretical treatments employed in the current chapter were carried out by Changjian Xie, Jianyi Ma, and Hua Guo.

written as ($\hbar = 1$ hereafter):

$$\hat{H} = -\sum_{i=0^2} \frac{1}{2\mu_i} \frac{\partial^2}{\partial r_i^2} + \sum_{i=0^2} \frac{\hat{j}_i^2}{2\mu_i r_i^2} + V(r_0, r_1, r_2, \theta_1, \theta_2, \phi) \tag{9.5}$$

where $r_0$ is the Jacobi radial coordinate, $r_1$ and $r_2$ are two Radau radial coordinates, $\mu_0$, $\mu_1$, and $\mu_2$ are the corresponding reduced masses, $\theta_1$ ($\theta_2$) is the angle between vectors $\vec{r}_1$ ($\vec{r}_2$) and $\vec{r}_0$, and $\phi$ is the relative azimuthal angle between $\vec{r}_1$ and $\vec{r}_2$ in the body-fixed frame. $\hat{j}_1$ and $\hat{j}_2$ are the angular momentum operators for $r_1$ and $r_2$, respectively, and $\hat{j}_0^2 = (\hat{j}_1 + \hat{j}_2)^2$. $V$ is the potential energy defined in Radau-Jacobi coordinates.

The Hamiltonian is discretized using a mixed grid-basis representation.[320] The radial coordinates $r_0$, $r_1$, and $r_2$ are represented by PODVR (potential optimized discrete variable representation),[349] while the angular coordinates are represented by basis functions. Energies of the vibrational states are obtained using the iterative Lanczos algorithm, and the corresponding wavefunctions can be recovered by additional iterations.[323] The numerical parameters in vibrational state calculations are listed in Table 9.3.

The infrared (IR) intensity for the transition $v' \leftarrow v$ can be computed by

$$I_{v' \leftarrow v} \propto |\langle \phi_{v'} | \mu | \phi_v \rangle|^2 \tag{9.6}$$

where $\phi_v$ and $\phi_{v'}$ are the initial and final vibrational states, and $\phi_v$ was selected as the ground vibrational state in our calculation. $\mu$ is the dipole moment of the system, which was obtained by the Taylor expansion at the equilibrium geometry defined in the Cartesian coordinates ($x_0$, $y_0$, $z_0$):

$$\mu = \mu_x \vec{i} + \mu_y \vec{j} + \mu_z \vec{k} \tag{9.7}$$

and

$$\begin{aligned} \mu_q = \; & \mu_{q,0} + \textstyle\sum_m (q_m - q_{m0}) \frac{\partial \mu_q}{\partial q_m}\Big|_{q_{m0}} + \frac{1}{2} \sum_m (q_m - q_{m0})^2 \frac{\partial^2 \mu_q}{\partial q_m^2}\Big|_{q_{m0}} \\ & + \textstyle\sum_{n \neq m} \sum_m (q_n - q_{n0})(q_m - q_{m0}) \frac{\partial^2 \mu_q}{\partial q_n \partial q_m}\Big|_{q_{n0}, q_{m0}} \end{aligned}$$

where $q = x, y, z$ denote the Cartesian coordinates, $m$ and $n$ are the atomic indices, and 0 denotes the anion equilibrium. The first and second order derivatives of dipole moments, which are necessary for two-quantum events, were numerically calculated at the UCCSD(T)-F12/cc-pVTZ-F12 level of theory[367] using a finite difference method. To obtain the IR intensities given by Eq. 9.6, one needs to compute the dipole moment function, which is obtained by transforming the Radau-Jacobi coordinates to the corresponding Cartesian coordinates, then finding out the Cartesian displacements with the Eckart condition,[368] and finally computing the dipole moment given by the above equation.

### 9.2.2 Theoretical Results

#### Infrared Spectrum of the Vinylidene Anion

The calculated IR spectrum of $H_2CC^-$ is displayed in the upper panel of Figure 9.6 and the vibrational band origins are listed in Table 9.2. The spectrum is dominated by two strong features at 2618.86 (D) and 2668.91 $cm^{-1}$ (E), which are assigned to the fundamentals of the C-H symmetric and antisymmetric stretches, namely the $1_1$ and $5_1$ states, respectively. These features are in good agreement with those observed by Gerardi *et al.* in Ar-tagged $H_2CC^-$, shown in the bottom panel of Fig. 9.6.[128] Near 4000 $cm^{-1}$, there are two features that are good candidates for vibrationally mediated autodetachment in this spectral region. They are features K and M in Figure 9.2d and Figure 9.6, which are assigned to the combination of the C-C stretch and C-H antisymmetric stretch, $2_1 5_1$ (4074.95 $cm^{-1}$), and the combination of the C-C stretch and C-H symmetric stretch, $1_1 2_1$ (4116.40 $cm^{-1}$), respectively. Their positions are also in good agreement with those reported by Gerardi *et al.*,[128] as shown in Figure 9.2d, but their oscillator strengths are much smaller than the C-H stretching fundamentals (D and E). Furthermore, two other bands (P and Q) are found near 5000 $cm^{-1}$, as shown in Figure 9.6, and they are candidates for vibrationally-mediated autodetachment in this spectral region. They are assigned to the first overtone of the antisymmetric C-H stretch, $5_2$ (5066.41 $cm^{-1}$), and combination of the symmetric and antisymmetric stretches, $1_1 5_1$ (5093.99 $cm^{-1}$), of the anion. The oscillator strengths are comparable to those near 4000 $cm^{-1}$, and they have not been reported in any previous experiment.

#### Intermediate-Well States of Neutral $H_2CC$

As shown in Figure 9.3b and described previously,[49] the intermediate well which lies along the isomerization coordinate on the neutral HCCH-$H_2CC$ PES is capable of supporting localized vibrational levels. Such a well has been identified in high-level *ab initio* calculations[282,369] and was included in the recent global PES.[49] As the isomerization PES is symmetric about the vinylidene minimum, there are two of these zeroth-order states to consider, denoted as $\phi_R$ and $\phi_L$, where the subscripts $R$ and $L$ denote the right and left wells, respectively, in Figure 9.3b. The terminal neutral eigenstates which give rise to features a, b, and c correspond to linear combinations of the left and right zeroth-order intermediate-well states, as well as the $6^1$ vibrational level of the vinylidene well, denoted as $\phi_{1v_6}$, which has roughly the same energy. Comparison of the energies for the different linear combinations identifies the neutral states for a, b, and c as the $0^u$, $0^g$, and $6^1$ states, respectively, whose vibrational eigenfunctions $\Phi$ are given by

$$\begin{aligned} \Phi[0^u] &= c_-^u(\phi_R - \phi_L) + c_6^u\phi_{1v_6} \\ \Phi[0^g] &= c_+^g(\phi_R + \phi_L) \\ \Phi[6^1] &= c_i^6(\phi_R - \phi_L) - c_6^6\phi_{1v_6} \end{aligned} \tag{9.8}$$

Although theoretical characterization of these states has been discussed in Ref. [49], no experimental evidence has been reported until now.

### Anion/Neutral Surface Crossing

The autodetachment process is not modelled directly in this work. However, we demonstrate its viability by locating the seam between the anion and neutral PESs. In Figure 9.7, the bending PES for the neutral is plotted with the other coordinates fixed at the $H_2CC$ equilibrium geometry. It can be clearly seen that the crossing seam is very close to the $H_2CC$ equilibrium, and nearly perpendicular to the antisymmetric bending coordinate $\theta_1 = -\theta_2 + 120°$. This implies that motion along the in-plane rocking ($\nu_6$) mode, which has been identified as the coupling mode to HCCH,[37] would strongly promote autodetachment. Energetically, it also permits the combination states of the anion near 4000 $cm^{-1}$ to couple with the ground state of $H_2CC$. A quantum mechanical characterization of the autodetaching dynamics would require *ab initio* determination of the derivative coupling between the anion and neutral + free electron states, which is beyond the scope of the current work.

## 9.2.3 Constant-eKE Autodetachment

This section considers the details of the autodetachment transitions involved in the complex structure of the vinylidene photoelectron spectrum observed for photon energies ranging from $4000 - 4125$ $cm^{-1}$. First, we consider the restrictions imposed on the anion excitation by standard spectroscopic selection rules as well as the initial anion states prepared in the cryo-SEVI experiment, concluding that a range of ($J_2$, $K_2$) rotational states are expected to be populated in the vibrationally excited anion state. We then discuss what conditions would give rise to constant-eKE autodetachment from this distribution of rotational states.

### Infrared Selection Rules for $H_2CC^-$

Vinylidene is a near-prolate asymmetric top, with a calculated asymmetry parameter of $\kappa = 0.891$ for the $0_0$ anion state.[178] Thus, the infrared selection rules governing the rotational transitions within a single vibrational excitation can be taken to be those of the prolate symmetric top,[327]

$$\begin{aligned} \parallel: &\quad K \neq 0 \implies \Delta K = 0; \Delta J = 0, \pm 1 \\ &\quad K = 0 \implies \Delta K = 0; \Delta J = \pm 1 \\ \perp: &\quad \Delta K = \pm 1; \Delta J = 0 \end{aligned} \tag{9.9}$$

where $\parallel$ and $\perp$ are used to denote the selection rules which pertain to parallel and perpendicular vibrational transitions, respectively.

As demonstrated by the rotational fits to the vibrational origin reported in the previous cryo-SEVI study, the majority of vinylidene anions prepared experimentally have $K_1 = 0$ or 1 in a 3:1 ratio as governed by nuclear spin statistics, and the extracted temperature of $\sim 15$ K implies that $J_1 < 20$ for the majority of the anions.[37] Even neglecting the contributions from anions with $K_1 > 1$, there is a wide range of rotational levels ($J_2$, $K_2$) that can be

populated within a given vibrational transition. Assuming an initial rotational spread of $K_1 \in \{0:1\}$ and $J_1 \in \{0:10\}$, the final rotational states obeying Eq. 9.9 correspond to $K_2 \in \{0:1\}$ and $J_2 \in \{0:11\}$ for a parallel vibrational excitation and $K_2 \in \{0:2\}$ and $J_2 \in \{0:10\}$ for a perpendicular transition. Using the rotational eigenvalues for the prolate symmetric top, defined in Eq. 9.10 in the following section, and approximating $A_2 = 10$ cm$^{-1}$ and $\tilde{B}_2 = 1$ cm$^{-1}$, this spread in rotational state covers roughly 150 cm$^{-1}$ in rotational energy, which adequately explains the relatively large range of photon energies over which the near-EA resonance behavior occurs. Additionally, a small population of anions are expected to have $K_1 > 1$, further increasing the possible range over which resonance behavior may be observed.

As described in the main text, two vibrational excitations are used to explain the two constant-eKE features observed in the cryo-SEVI spectra. The lower-eKE feature A is attributed to autodetachment from the $2_1 5_1$ state, which corresponds to a perpendicular excitation of the anion. Given the above considerations, a perpendicular vibrational excitation provides access to a wider range of $(J_2, K_2)$; this is likely what gives rise to the slightly larger window over which feature A is observed relative to the higher-eKE feature B, which arises from autodetachment following the parallel vibrational excitation of the anion to the $1_1 2_1$ state.

**Derivation of Conditions for Constant-eKE Autodetachment**

As shown in Eq. 9.4 of the main text, the change in rotational energy $\Delta E_{rot}$ between the excited anion (2) and neutral (3) states must be independent of the rotational state populated by photoexcitation $(J_2, K_2)$ for the eKEs to remain constant across a single vibrational resonance. The rotational eigenvalues of vinylidene can be approximated using those of the prolate symmetric top,[327]

$$E_{rot,i} = \tilde{B}_i J_i(J_i + 1) + (A_i - \tilde{B}_i)K_i^2 \tag{9.10}$$

where the rotational constants of state $i$ are given by $A_i$, $B_i$, and $C_i$, and $\tilde{B}_i = \frac{1}{2}(B_i + C_i)$. To determine the conditions which result in a rotational energy change $\Delta E_{rot} = E_{rot,3} - E_{rot,2}$ that is independent of $J_2$ and $K_2$, we then consider the change in rotational quantum numbers and constants that occur in the detachment transition,

$$\begin{array}{ll} A_2 = A_3 - \Delta A & J_3 = J_2 + \Delta J \\ \tilde{B}_2 = \tilde{B}_3 - \Delta\tilde{B} & K_3 = K_2 + \Delta K. \end{array} \tag{9.11}$$

These expressions and the neutral rotational constants $(A_3, B_3, C_3)$ calculated by Stanton and co-workers[118] are then used to obtain an expression for $\Delta E_{rot}$ in terms of these changes and the excited anion rotational state $(J_2, K_2)$, which is subsequently substituted into Eq. 9.4 for the eKE of the detached electron.

To obtain the conditions which ensure that this eKE is independent of the excited anion rotational state, we equate to zero the derivatives of this expression with respect to $J_2$ and

$K_2$ (neglecting that these are not continuous variables), yielding

$$\frac{d(\text{eKE})}{dJ_2} = 2\Delta\tilde{B}\ J_2 + 2.4911\Delta J + \Delta\tilde{B} = 0, \text{ and}$$

$$\frac{d(\text{eKE})}{dK_2} = 2(\Delta A - \Delta\tilde{B})K_2 + 16.5725\Delta K = 0.$$

Thus, vibrational autodetachment from a single anion excited state can result in constant-eKE features provided the detachment transition obeys $\Delta J = \Delta K = 0$ and the rotational constants of the vibrationally excited anion are similar to those of the neutral ground state (i.e. $\Delta A, \Delta\tilde{B} \approx 0$), as asserted in the main text. The second condition is expected to hold given the calculated rotational constants for anion and neutral vinylidene.[37,118,178] This detachment mechanism is described by the energy diagram in Figure 9.1b, showing transitions between the excited anion and ground state neutral rotational manifolds; direct detachment has been omitted from this figure for clarity.

### 9.2.4 Supplemental Figures and Tables

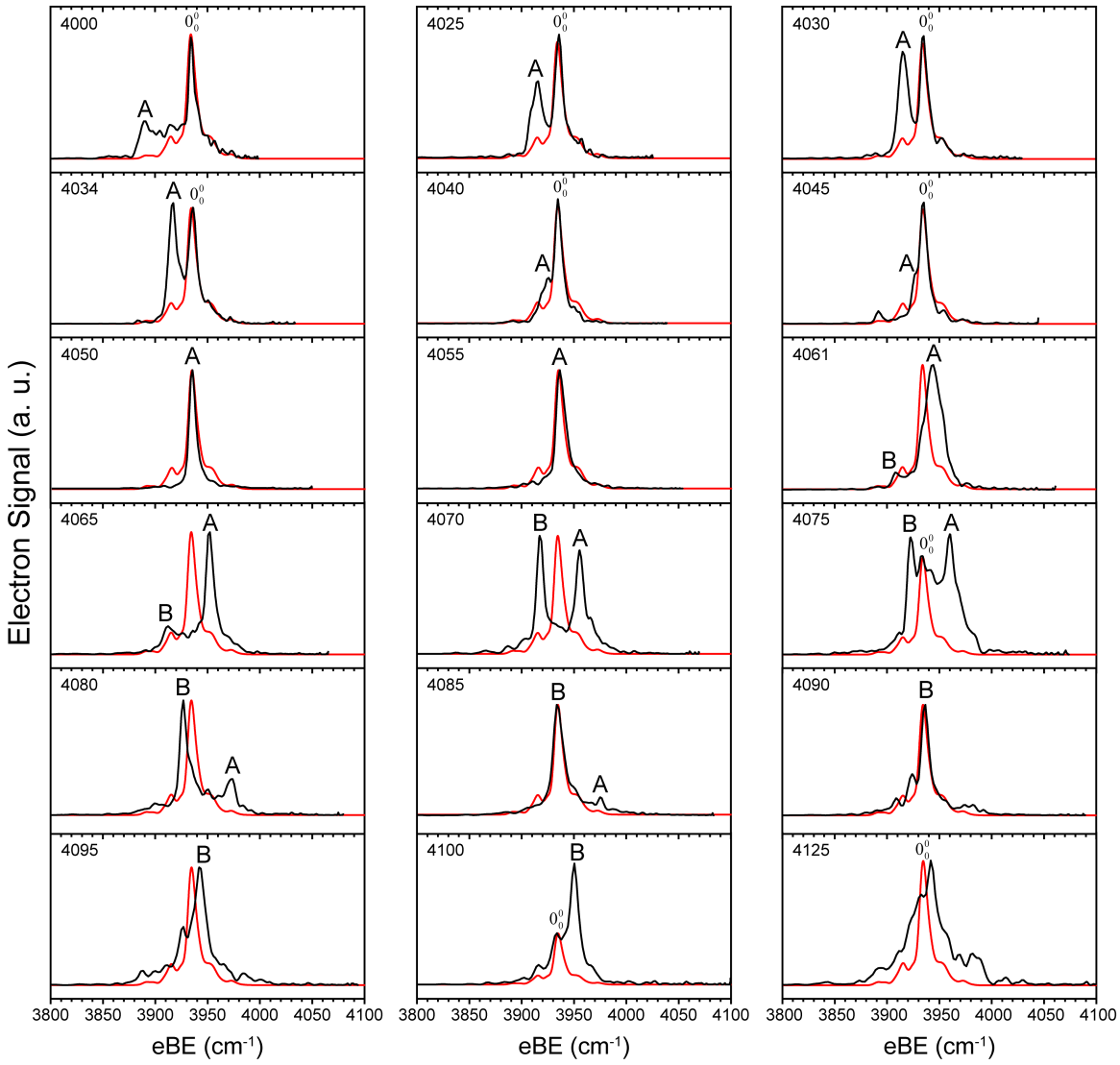


**Figure 9.4:** Cryo-SEVI scans showing the autodetachment structure observed for detachment energies ranging from 4000 to 4125 $cm^{-1}$ plotted versus eBE. The photon energy ($cm^{-1}$) for each scan is indicated in the top-left corner of the corresponding plot. The red trace in each plot shows the simulated rotational contour of the vibrational origin reported previously,[37] which corresponds to the expected lineshape for direct detachment and was obtained from fitting the lineshape of the $h\nu$ = 4040 $cm^{-1}$ scan to a rotational model.[329] This simulation gives an ion temperature of 17.0(6) K and is consistent with the rotational profiles observed for the relatively well-behaved vinylidene excited states.[178]

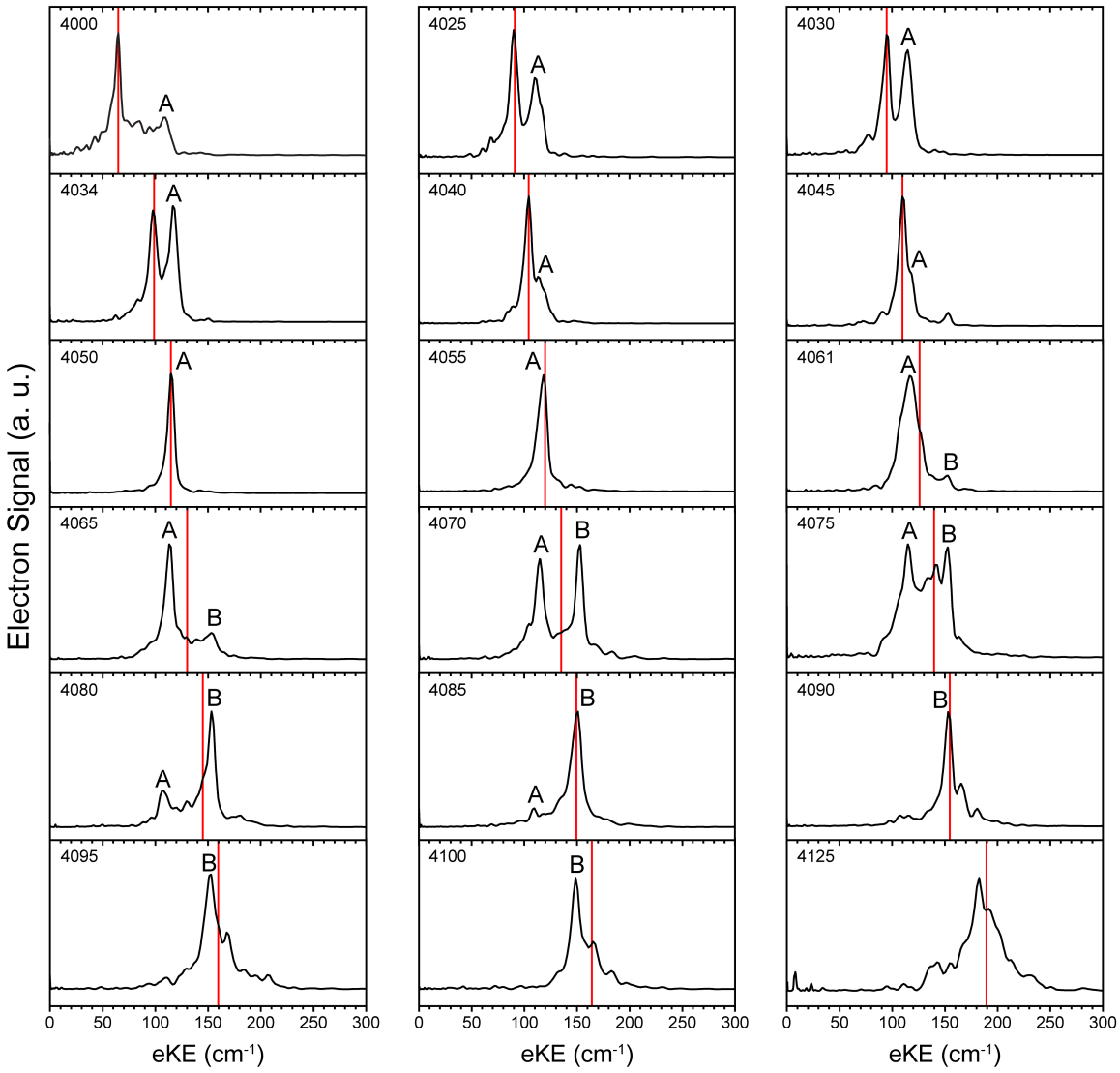


**Figure 9.5:** All cryo-SEVI scans presented in Figures 9.2 and 9.4, plotted versus eKE. The expected eKE for the center of the vibrational origin is indicated by the red vertical lines. The photon energy ($cm^{-1}$) for each scan is indicated in the top-left corner of the corresponding plot.

**Table 9.2:** Energies (in $cm^{-1}$) and assignments for the $H_2CC^-$ vibrational states in Figure 9.6. The vibrational modes are defined as follows: $\nu_1$, CH symmetric stretch; $\nu_2$, CC stretch; $\nu_3$, $CH_2$ scissors; $\nu_4$, out-of-plane bend; $\nu_5$, CH antisymmetric stretch; $\nu_6$, $CH_2$ in-plane rock.

| Label | Energy | Assignment |
|---|---|---|
| A | 2296.29 | $2_1 6_1$ |
| B | 2568.32 | $6_3$ |
| C | 2586.50 | $3_2$ |
| D | 2618.86 | $5_1$ |
| E | 2668.91 | $1_1$ |
| F | 2748.33 | $2_1 3_1$ |
| G | 2804.69 | $3_1 4_2$ |
| H | 2903.75 | $2_2$ |
| I | 3945.40 | $1_1 3_1$ |
| J | 3980.92 | $2_1 6_3$ |
| K | 4074.95 | $2_1 5_1$ |
| L | 4109.87 | $4_2 5_1$ |
| M | 4116.40 | $1_1 2_1$ |
| N | 4169.12 | $1_1 4_2$ |
| O | 4183.38 | $2_2 3_1$ |
| P | 5066.41 | $5_2$ |
| Q | 5093.99 | $1_1 5_1$ |
| R | 5326.96 | $1_2$ |

**Table 9.3:** Numerical parameters (in a.u.) used in vibrational calculations.

| |
|---|
| Grid/basis ranges and sizes |
| 4 POVDR for $r_1$ and $r_2$; 5 POVDR for $r_0$ |
| $j_{1max} = j_{2max} = m_{max} = 34$ |
| Lanczos steps: 3500 |

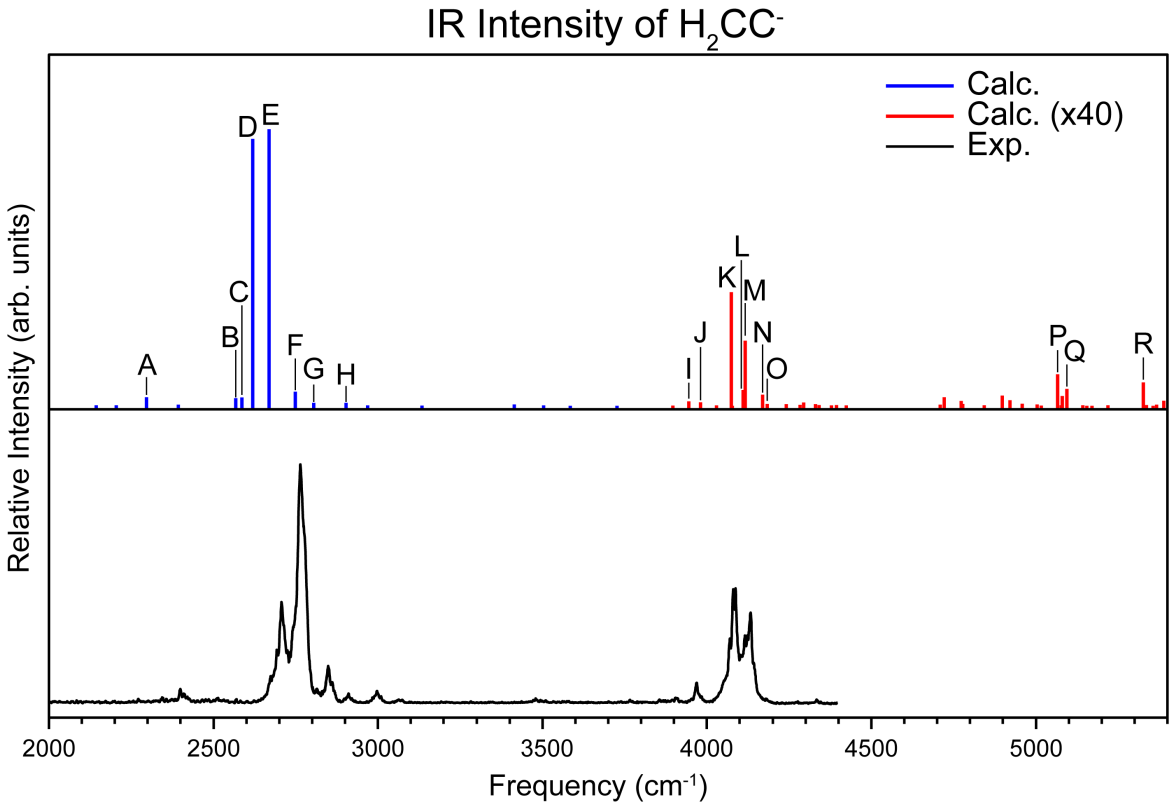


**Figure 9.6:** Comparison of calculated IR spectra of $H_2CC^-$ with the experimental IR spectrum of Gerardi *et al.* obtained from Ar-tagging experiments.[128] The strong peaks corresponding to specific vibrational excitations of the vinylidene anion are labelled A-R and their band origins are given in Table 9.2.

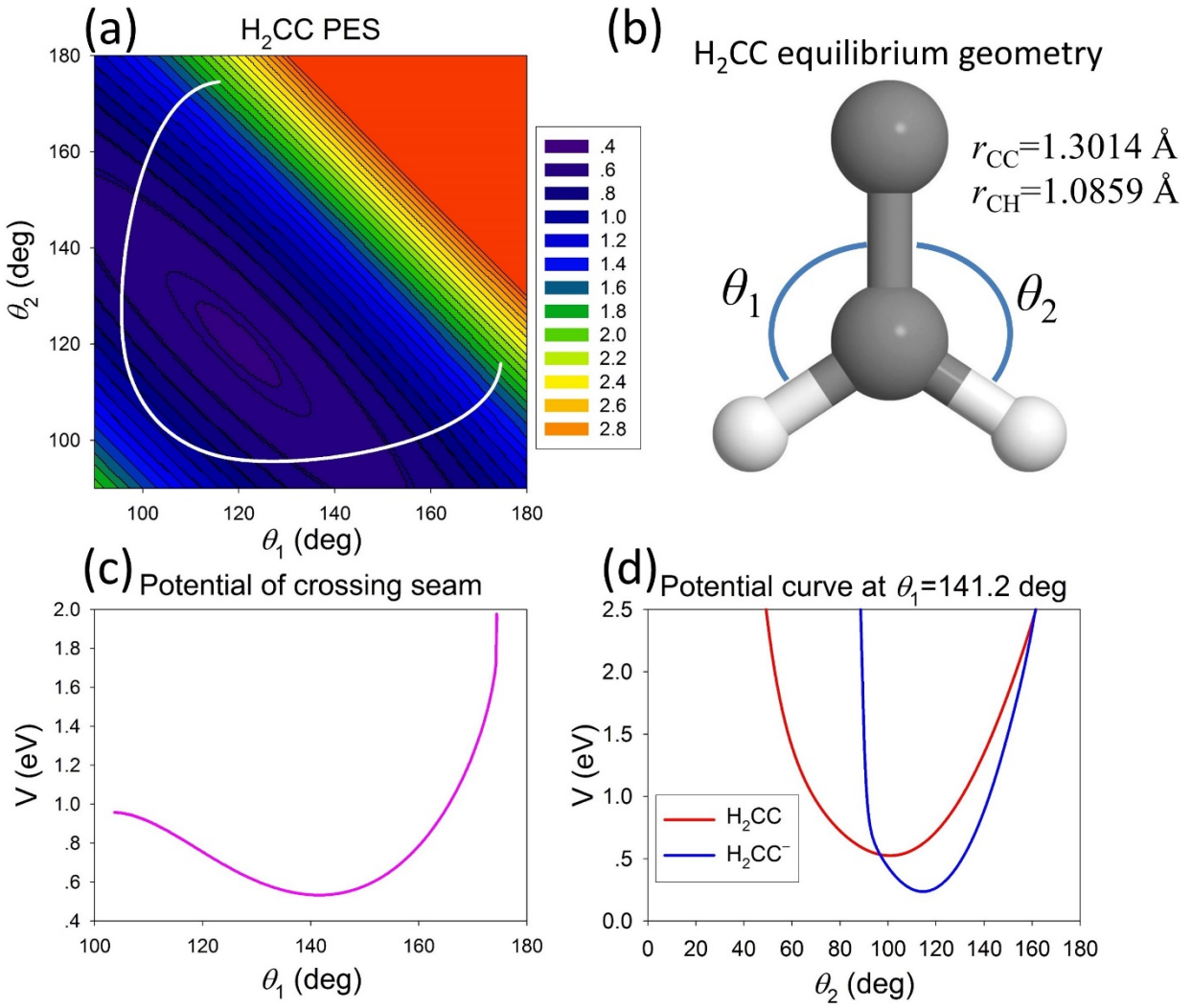


**Figure 9.7:** The crossing seam between the anion and neutral PESs. The $H_2CC$ PES near its equilibrium is plotted in the two bending angles (a) with the other coordinates fixed at the $H_2CC$ equilibrium geometry (b). The crossing seam is plotted as a white line superimposed on the contour plot. The dependence of the potential energy of the crossing seam on one bending angle is shown in (c), while the potential curves of the two states are shown in (d) as a function of the other bending angle.

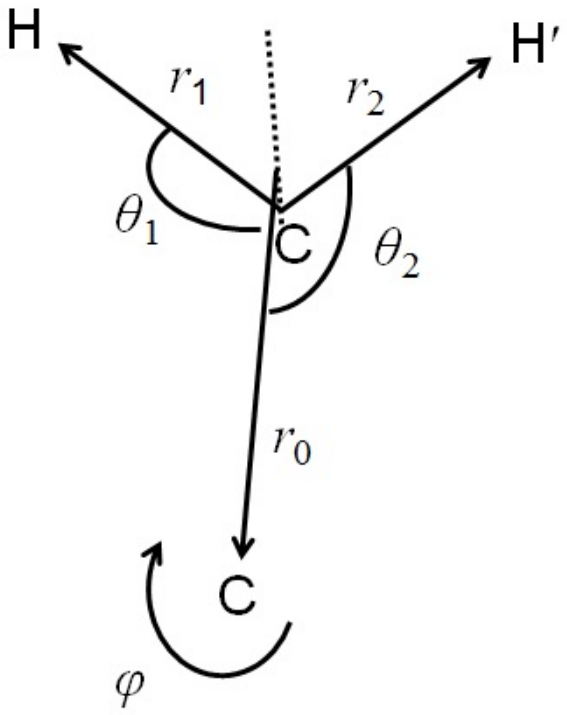


**Figure 9.8:** The Radau-Jacobi coordinates used in the theoretical calculations.

# Part IV

# Metal Oxide and Micro-Solvated Clusters

# Chapter 10

# Cryo-SEVI of the Dissociative $TiO_2^-$ + $H_2O$ Adduct

The content and figures of this chapter are reprinted or adapted with permission from J. A. DeVine, A. A. Taka, M. C. Babin, M. L. Weichman, H. P. Hratchian, D. M. Neumark, "High-resolution photoelectron spectroscopy of $TiO_3H_2^-$: Probing the $TiO_2^-$ + $H_2O$ dissociative adduct" *J. Chem. Phys.* **148**, 222810 (2018).

## Abstract

Slow electron velocity-map imaging spectroscopy of cryogenically-cooled $TiO_3H_2^-$ anions is used to probe the simplest titania/water reaction, $TiO_2^{0/-}$ + $H_2O$. The resultant spectra show vibrationally resolved structure assigned to detachment from the *cis*-dihydroxide $TiO(OH)_2^-$ geometry based on density functional theory calculations, demonstrating that for the reaction of the anionic $TiO_2^-$ monomer with a single water molecule, the dissociative adduct (where the water is split) is energetically preferred over a molecularly adsorbed geometry. This work represents a significant improvement in resolution over previous measurements, yielding an electron affinity of 1.2529(4) eV as well as several vibrational frequencies of neutral $TiO(OH)_2$. The energy resolution of the current results combined with photoelectron angular distributions reveals Herzberg-Teller coupling-induced transitions to Franck-Condon forbidden vibrational levels of the neutral ground state. A comparison to the previously measured spectrum of bare $TiO_2^-$ indicates that reaction with water stabilizes neutral $TiO_2$ more than the anion, providing insight into the fundamental chemical interactions between titania and water.

## 10.1 Introduction

Titania ($TiO_2$) is an inexpensive, extensively studied, and environmentally benign semiconducting material with widespread application in photovoltaics,[370–373] pollution management,[374] chemical sensing,[375,376] and heterogeneous catalysis.[377–379] The landmark discovery of photosensitization of water on a $TiO_2$ electrode[380] sparked a decades-long pursuit to harness the photocatalytic properties of $TiO_2$ as a practical means of solar-powered hydrogen fuel production.[381,382] However, the success of this endeavor has been limited in part by a lack of the mechanistic understanding necessary to design better catalysts.[383] Here, we present high-resolution photoelectron spectra of the $TiO_3H_2^-$ anion accompanied by theoretical analysis, in order to probe the nature of the interaction between $TiO_2^-$ and a single water molecule.

The most natural starting point for understanding water oxidation by $TiO_2$ is a consideration of how water adheres to bulk titania surfaces, an active and complex area of research.[384–386] The extent to which water dissociates on a $TiO_2$ surface is known to be dependent on surface structure,[387] with differing propensities for dissociative versus molecular adsorption for different crystal phases and planes[388–393] as well as a dependence on the extent of surface coverage by water.[394,395] While dissociation tends to play a minor role in water adsorption on stoichiometric $TiO_2$ surfaces, it is found to be strongly preferred at point defects such as steps,[396] edges,[397,398] and in particular, oxygen vacancies.[399–405] Thus, the conceptual key to understanding the surface chemistry of water on titania from a molecular level is the chemistry that occurs at these defect sites.

It is challenging to design a bulk experiment that is uniquely sensitive to the chemistry occurring at a specific surface defect. Defect sites typically make up a small fraction of total surface area, and are difficult to reproducibly generate. Gas phase metal oxide clusters have been shown to be useful model systems for gaining mechanistic insight into complex catalytic processes, as these species show structural motifs such as dangling moieties and undercoordinated atoms that mimic the geometries at common defect sites.[137–140,406] The control afforded by gas-phase experiments provides the ability to systematically manipulate reactivity-related factors such as particle size, charge, and stoichiometry. Fast-flow laser-ablation ion sources allow production of both bare and reacted clusters,[170] enabling the characterization of reactants, products, and potentially intermediates or transition states of model catalytic reactions using gas-phase spectroscopic techniques.[407,408] These species have the added benefit of being computationally tractable, enabling experimentalists and theorists to develop a clear, molecular-scale understanding of catalytic reaction mechanisms that is difficult to obtain from bulk experiments alone.

The experimental spectroscopic characterization of bare $(TiO_2)_n$ clusters constitutes a growing body of work,[147,409,410] including contributions from our laboratory.[34,151] Less work has been done to probe species formed from reaction of small $(TiO_2)_n$ clusters with a discrete number of water molecules, which can either adsorb molecularly or dissociatively as on the bulk surface. The hydration of cationic $TiO^+$ by up to 60 water molecules has been studied by mass spectrometry, though this measurement does not provide insight into the structure

of the resultant clusters.[411] These solvated cations have been structurally characterized using infrared action spectroscopy by Zheng and coworkers,[412] who have also performed anion photoelectron spectroscopy (PES) on the anionic $TiO_2^-(H_2O)_{0-7}$ clusters.[315] In both cases, their spectra indicated dissociative adsorption of water to form hydroxide species. Weichman and coworkers[356] have recently used infrared action spectroscopy to systematically characterize the anionic $(TiO_2)_n^-(D_2O)_m$ clusters for $n = 2-4$ and $m = 1-3$, finding that the dissociative geometries are preferred for these clusters as well.

A number of groups have used theoretical treatments – most commonly density functional theory (DFT) – to assess the extent to which $H_2O$ molecules dissociate on small $(TiO_2)_n$ clusters.[413–415] The most comprehensive work in this area has been carried out by Dixon and coworkers,[416,417] who used a hybrid genetic algorithm to determine the lowest-energy structures for $(TiO_2)_n(H_2O)_m$ ($n = 1-4$, $m = 1-2n$) clusters.[418] Geometry optimizations and single point calculations were carried out using both DFT and coupled cluster methods, yielding similar results for all model chemistries used. For the simplest stoichiometric $TiO_2$/water reaction, $TiO_2$ + $H_2O$, they found that the di-hydroxyl $TiO(OH)_2$ structure, in which the water is split, is preferred over molecular adsoprtion by over 40 kcal mol$^{-1}$. Of the two dissociatively adsorbed structures reported, the planar $C_{2v}$ *cis*-hydroxyl isomer was found to be more stable than the $C_s$ *trans*-OH isomer, though this energy difference was less than 3 kcal mol$^{-1}$.

The only experimental work on this system comes from the aforementioned anion PES study by Zheng and coworkers,[419] who reported the photodetachment spectrum for $TiO_3H_2^-$ formed by a laser ablation reactor source. This spectrum showed a single broad electronic band spanning $\sim$ 1 eV in electron binding energy (eBE), reflecting extended unresolved vibrational progressions. From this spectrum, they estimated an electron affinity (EA) of $1.15 \pm 0.08$ eV and a vertical detachment energy (VDE) of $1.51 \pm 0.08$ eV. By comparison to their photoelectron spectrum of bare $TiO_2^-$ and DFT calculations, the anion geometry was assigned to the $TiO(OH)_2^-$ dissociative adduct. Other than the general assignment based on the position of the detachment feature, little information regarding the structure of the $TiO_3H_2^{-/0}$ species can be gleaned from this work.

Slow electron velocity-map imaging of cryogenically-cooled anions (cryo-SEVI) is a high-resolution variation of traditional anion PES which provides vibrationally-resolved detachment spectra reflecting the geometric and vibronic structure of the anion and neutral. Previously, we have used cryo-SEVI to characterize the unreacted $TiO_2^-$ monomer;[34] here, we probe the $TiO_3H_2^-$ species, corresponding to a single $TiO_2^-$ reacted with one water molecule. These spectra represent a significant improvement in resolution compared to the work of Zheng and coworkers, showing extensive vibrational structure with typical peak widths of 10 cm$^{-1}$ full-width at half-maximum (fwhm). With the assistance of DFT calculations, we assign the anion structure to the dissociative di-hydroxide $TiO(OH)_2^-$ isomer identified as the lowest-energy neutral geometry by Dixon and coworkers. Several vibrational frequencies for the neutral $TiO(OH)_2$ species are extracted, as well as its EA. Comparison to the unreacted $TiO_2^-$ cryo-SEVI spectra elucidates the energetic effect of charge on the $TiO_2^{-/0}$ +

$H_2O$ reaction, highlighting the utility of small metal oxide clusters as tools for understanding catalytic reactions.

## 10.2 Experimental Methods

The cryo-SEVI technique and apparatus are described in Chapter 2. To generate $TiO_3H_2^-$ anions, the laser ablation reactor source described in Chapter 3 was used with a titanium target. Water was introduced through the pulsed General Valve (pulse width $\sim$ 160 μs) by bubbling He (15 psi backing pressure) through room temperature $H_2O$. The $m/z = 98$ mass peak was selected to acquire the cryo-SEVI spectra, and this peak should include some contribution from $^{50}TiO_3^-$ as well as the target $^{48}TiO_3H_2^-$ species. However, the electron affinity of $TiO_3$ is quite high[409] relative to the $< 2$ eV detachment energies used in this chapter, and thus does not contribute to the spectrum.

The detachment laser configurations available in the cryo-SEVI apparatus are described in detail in Section 2.4. In this chapter, the output of the dye laser was used without further modification for photon energies above $\sim$ 1.3 eV. Photon energies below 1.3 eV were generated using the Raman cell described in Section 2.4.2. Energy calibration was carried out by acquiring VMI images for detachment from $O^-$ and $Ni^-$ at several photon energies.[190,191]

## 10.3 Computational Methods[a]

Possible minimum-energy structures for both anionic and neutral $TiO_2$ + $H_2O$ were explored using a variety of DFT-based model chemistries. Preliminary results suggested meaningful differences between model chemistries. Therefore, initial benchmarking calculations were carried out to compare six DFT-based model chemistries with results of coupled-cluster singles and doubles (CCSD) calculations,[420,421] as summarized in Section 10.7.1. Based on comparisons of these CCSD results to DFT-predicted energetic ordering of candidate anion and neutral minimum energy structures as well as vertical and adiabatic detachment energies (Tables 10.3-10.4), the B3LYP/Def2TZVP model chemistry[422–426] was chosen and has been employed for the calculations described below.

Both doublet and quartet states were considered for anion candidates; singlet (closed-shell and open-shell) and triplet states were considered for neutral candidates. For all identified structures, doublet anions are more stable than quartet species and the closed-shell singlet state was found to be more stable than open-shell singlet or triplet states. Excited state calculations were carried out using the same model chemistry within the time-dependent DFT (TDDFT) formalism.[427–429] Analysis of these excited state calculations was facilitated by Martin's Natural Transition Orbital (NTO) model.[430]

[a]The electronic structure calculations described in this chapter were carried out by Ali Abou Taka and Hrant Hratchian.

All calculations were carried out using a local development version of the Gaussian suite of electronic structure programs.[54] Converged Kohn-Sham determinants were tested for stability.[427,431] Molecular geometries were optimized using standard methods[432] and reported potential energy minima were verified using analytical second-derivative calculations. Franck-Condon (FC) spectra were simulated using the implementation by Bloino, Barone, and coworkers.[433,434] Care was taken to determine appropriate scaling factors for the DFT force constants calculated for the lowest-energy neutral state (Table 10.5) such that simulated FC progressions aligned well with the experimental spectra. Further details of the FC simulations can be found in Section 10.7.2.

To describe the nature of the detached electron we have employed the Natural Ionization Orbital (NIO) model of Thompson, Harb, and Hratchian.[435] The NIO model provides a compact orbital representation of ionization processes by utilizing one-particle difference densities. Natural orbital analysis involving this difference density yields a simplified interpretation of electronic detachment processes. The NIO model has recently been shown to provide a convenient means to distinguish between one-electron transitions and those where the one-electron process is accompanied by excitation of a second electron into the virtual orbital space.[436] The current system is Koopmans-like, evidenced by the strong resemblance between the NIO and the canonical highest-occupied molecular orbital (HOMO) of the **1-1a** anion (Figure 10.6), and thus the detachment transitions considered here are one-electron transitions that can be equivalently described by considering the NIO or the anion HOMO. As such, the method of Liu and Ning[64] was applied to the HOMO of the lowest-energy anion to calculate the eKE-dependent PAD expected for removal of an electron from this orbital; results are shown as the solid lines in Fig. 10.2 and discussed further in Section 10.5.1.

## 10.4 Experimental Results

The cryo-SEVI spectrum for detachment from $TiO_3H_2^-$ is shown in Figure 10.1. In this figure, the blue trace corresponds to an overview scan taken with a relatively high detachment energy, and the black traces are higher-resolution SEVI scans taken with variable photon energies. The overview spectrum spans $10000-13500$ cm$^{-1}$ in eBE and exhibits considerable vibrational structure, revealing increasing spectral congestion as the eBE increases. Due to this increased complexity, our analysis will be focused on the first $\sim 2000$ cm$^{-1}$ of structure. In this region, the high-resolution scans reveal a number of transitions (A1-11, B1-11) with typical peak widths of $\sim 10$ cm$^{-1}$ fwhm, corresponding to detachment to different vibronic levels of the neutral $TiO_3H_2$ species. The sharp onset of structure at peak A1 gives an EA of 1.2519(4) eV for $TiO_3H_2$. The remainder of the spectrum is dominated by a $\sim 675$ cm$^{-1}$ progression (A1-3-7-11), modulated by several weaker patterns. Peak positions, widths, and shifts from the origin are summarized in Table 10.1.

The EA provided by cryo-SEVI is larger than the value of 1.15(8) eV reported by Zheng and coworkers.[315] This discrepancy is understandable given the lower resolution of their spectrum and the experimental conditions used to obtain it. In that work, the individ-

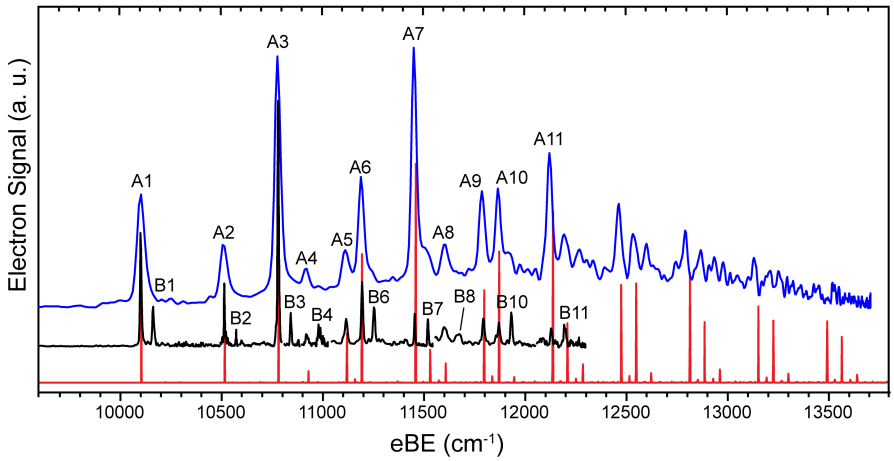


**Figure 10.1:** Cryo-SEVI spectrum of $TiO_3H_2^-$. The blue trace is an overview spectrum taken with a photon energy of 13721 $cm^{-1}$, and the black traces are high-resolution scans taken at variable photon energies. Black traces are scaled to match relative peak intensities observed in the overview as much as possible. The red stick spectrum shows the Franck-Condon simulation for detachment from the **1-1a** $C_{2v}$ *cis*-OH $TiO(OH)_2^-$ geometry using frequencies that have been scaled as described in Table 10.5.

ual transitions in the extended Franck-Condon progressions blend together to form a broad structureless feature, and the lack of a clear onset complicates extraction of the EA. Additionally, the ions probed in the previous work were not cooled prior to detachment, and given the relatively high temperatures typical of ions produced by laser ablation,[169] the resultant spectra likely contain contributions from hot bands that can lower the apparent electron binding energy relative to the true EA. Hot bands are effectively eliminated in the cryo-SEVI experiment, where ions are cooled to $\sim$ 10 K prior to detachment.[326]

Measurement of the PADs of features labeled in Figure 10.1 (Figure 10.7) reveals that all transitions fall into one of two groups with distinct angular distributions. These two groups are represented in Figure 10.2, which plots the anisotropy parameter ($\beta$) versus eKE for peaks A1-3 and B1-3. Features A1-3 show positive values of $\beta$, whereas features B1-3 show isotropic ($\beta \sim 0$) angular distributions. The remainder of features in Figure 10.1 all show PADs that are qualitatively similar to one of these two groups, and are labelled accordingly, where peaks labelled A correspond to parallel ($\beta > 0$) detachment transitions and peaks labelled B have isotropic ($\beta \sim 0$) PADs. The anisotropy parameters are summarized qualitatively in Table 10.1. Each B-series transition lies $\sim$ 60 $cm^{-1}$ above a peak in the A1-11 series, and has been numbered accordingly.

These two groups also show distinctly different dependencies of the photodetachment cross section on eKE. Far from threshold, the A1-11 series dominates the spectrum, as can be seen in the overview spectrum in Figure 10.1. As the photon energy is lowered, transitions in the B1-11 series become more apparent, resulting from the relative attenuation of the A1-

**Table 10.1:** Peak positions, shifts from the vibrational origin, qualitative anisotropy parameters (+ or 0), and vibrational assignments for features in the cryo-SEVI spectrum of $TiO_3H_2^-$. Uncertainties in peak positions correspond to one standard deviation ($\sigma$) obtained from a Gaussian fit to the highest-resolution scan of the experimental peak, which is related to the fwhm by fwhm $= 2\sqrt{2\ln 2}\sigma$.

| peak | eBE ($cm^{-1}$) | shift ($cm^{-1}$) | $\beta$ | assn. |
|---|---|---|---|---|
| A1 | 10106 (3) | 0 | + | $0_0^0$ |
| B1 | 10165 (3) | 60 | 0 | $8_0^1$ |
| A2 | 10519 (2) | 413 | + | $4_0^1$ |
| B2 | 10576 (2) | 471 | 0 | $4_0^1 8_0^1$ |
| A3 | 10784 (3) | 678 | + | $3_0^1$ |
| B3 | 10846 (3) | 741 | 0 | $3_0^1 8_0^1$ |
| A4 | 10926 (6) | 820 | + | $3_0^1 8_0^2$ |
| B4 | 10987 (7) | 881 | 0 | $3_0^1 8_0^3$ |
| A5 | 11121 (5) | 1016 | + | $2_0^1$ |
| A6 | 11199 (4) | 1093 | + | $3_0^1 4_0^1$ |
| B6 | 11258 (4) | 1152 | 0 | $3_0^1 4_0^1 8_0^1$ |
| A7 | 11459 (3) | 1354 | + | $3_0^2$ |
| B7 | 11524 (3) | 1418 | 0 | $3_0^2 8_0^1$ |
| A8 | 11607 (13) | 1501 | + | $3_0^2 8_0^2$ |
| B8 | 11673 (12) | 1568 | 0 | $3_0^2 8_0^3$ |
| A9 | 11798 (5) | 1692 | + | $2_0^1 3_0^1$ |
| A10 | 11874 (6) | 1769 | + | $3_0^2 4_0^1$ |
| B10 | 11936 (4) | 1831 | 0 | $3_0^2 4_0^1 8_0^1$ |
| A11 | 12133 (4) | 2027 | + | $3_0^3$ |
| B11 | 12200 (6) | 2095 | 0 | $3_0^3 8_0^1$ |

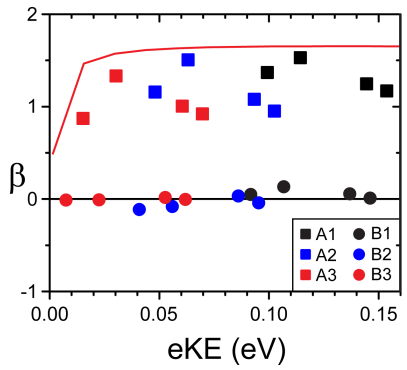


**Figure 10.2:** Anisotropy parameters of peaks A1-3 and B1-3 extracted from VMI images obtained at multiple photon energies, showing the distinctly different PADs for the two groups of features. The solid line shows the calculated anisotropy parameter expected for detachment from the **1-1a** anion HOMO found by DFT.[64]

11 peaks. This trend is illustrated in Figure 10.3, where peaks A1 and B1 are shown for several photon energies and the intensities are normalized to the peak intensity of B1. The relative scaling of detachment cross sections for low-eKE detachment is given by the Wigner threshold law,[21]

$$\sigma \propto (\text{eKE})^{\ell+1/2} \tag{10.1}$$

where $\sigma$ is the detachment cross section and $\ell$ is the angular momentum of the detached electron. According to this law, a sharper decrease in detachment signal as the photon energy is lowered reflects higher-$\ell$ detachment channels; it can therefore be inferred that transitions A1-11 correspond to higher-$\ell$ detachment than transitions B1-11.

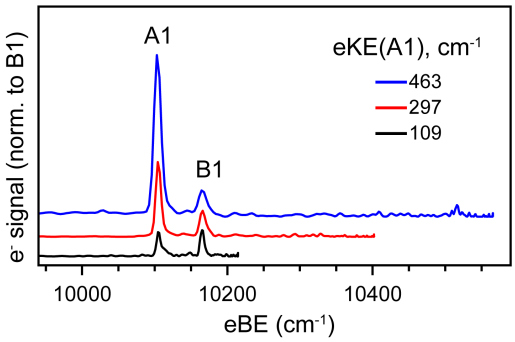


**Figure 10.3:** Detachment spectra of $TiO_3H_2^-$ at several photon energies illustrating the greater extent of signal attenuation for peak A1 versus peak B1 as eKE decreases. The intensity of each scan has been normalized to the intensity of peak B1. Photon energies used are 10568 (blue), 10297 (red), and 10215 $cm^{-1}$ (black).

## 10.5 Discussion

### 10.5.1 Structural Assignment of $TiO_3H_2^-$

Figure 10.4 shows optimized minimum-energy structures located on the anionic and neutral $TiO_3H_2$ potential energy surfaces, as well as zero-point corrected energies. Cartesian coordinates for these structures are provided in Sections 10.7.3-10.7.4. In agreement with previous work by Dixon and coworkers,[418] the $C_{2v}$ dissociative structure (**1-1a'**) is found to be the lowest-energy neutral geometry; likewise, the **1-1a** geometry is the lowest-energy anion isomer. Two additional minimum-energy structures, **1-1b** and **1-1e**, were found on the anion potential energy surface to lie 0.08 and 0.19 eV above **1-1a**, respectively, and differ from this isomer by rotation of the hydroxide groups. A local minimum corresponding to the *trans*-OH **1-1b'** geometry was discovered 0.11 eV above the neutral **1-1a'** structure, in reasonable agreement with the relative energy reported by Dixon. No neutral minimum corresponding to the **1-1e** isomer was identified. The lowest-energy molecularly adsorbed $TiO_3H_2$ adduct reported by Dixon was also identified as a local minimum for both anion (**1-1c**) and neutral (**1-1c'**), though these structures lie 2.34 and 3.13 eV above the anion and neutral global minima, respectively.

Given the relative energies of the anion geometries shown in Figure 10.4, the most likely structures contributing to the cryo-SEVI spectrum of $TiO_3H_2^-$ correspond to the dissociative

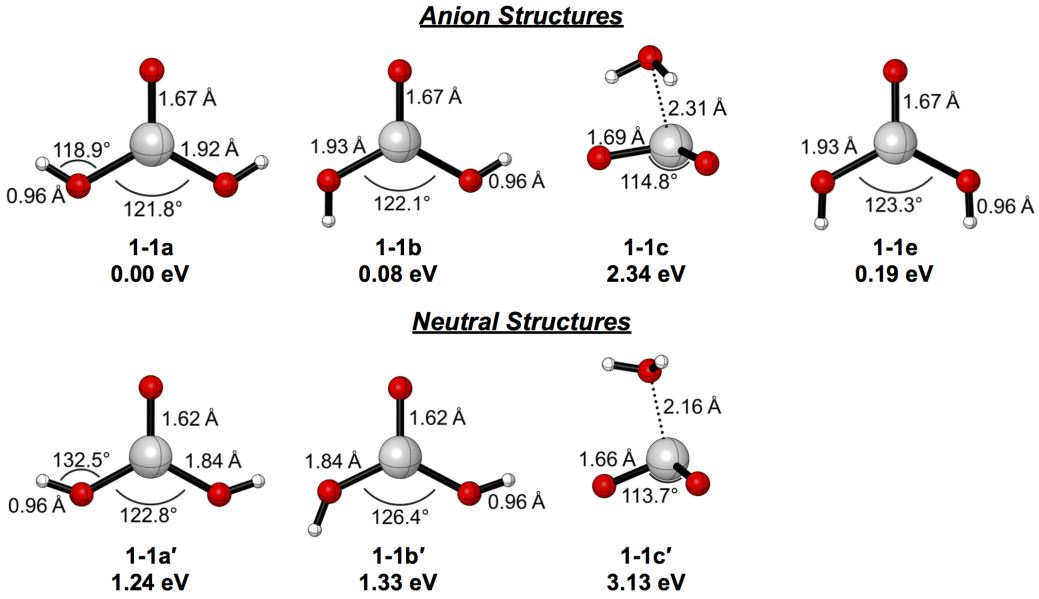


**Figure 10.4:** Optimized geometries of anionic and neutral $TiO_3H_2$ found with B3LYP/Def2TZVP. Energies are provided relative to the **1-1a** geometry of the anion and include zero-point corrections. Geometric parameters are also provided.

geometries **1-1a** and **1-1b**. The assignment of a dissociatively adsorbed anion geometry is consistent with the assessment of Zheng and coworkers.[315] Predicted adiabatic detachment energies (ADEs) for **1-1a** and **1-1b** are 1.23 and 1.26 eV, respectively, both in good agreement with the experimental electron affinity (1.25 eV). In both cases, NIO analysis clearly indicates that the detached electron resides in the anion HOMO, which strongly resembles the Ti $d_{z^2}$ orbital (see Figs. 10.5 and 10.8). Analysis of the NIO for either **1-1a** or **1-1b** gives an orbital angular momentum of $l = 2$, such that detachment from either of these orbitals would be expected to primarily yield outgoing $p$- ($\ell = 1$) and $f$-wave ($\ell = 3$) electrons. This high-$\ell$ detachment is consistent with the observed attenuation of signal near threshold for peaks A1-11.

Additionally, the eKE-dependence of the anisotropy parameter calculated[64] for detachment from the **1-1a** HOMO (Figure 10.2, solid lines) is in good agreement with the measured $\beta$ values for peaks A1-11, showing positive values in the eKE region of interest. Given the similarity between the **1-1a** and **1-1b** NIOs, detachment from the **1-1b** isomer is expected to yield a similar PAD. This agreement between experiment and theory further supports the conclusion that the global minimum of the $TiO_3H_2^-$ anion takes the dissociative $TiO(OH)_2^-$ di-hydroxide geometry, and that detachment from one of these isomers to the ground state of the corresponding neutral accounts for the most intense structure (A1-11).

To determine definitively which of these species is responsible for the experimentally observed detachment transitions, we consider the Franck-Condon profiles for detachment from both isomers, as the FC profile is highly sensitive to the anion and neutral geometries. Figures 10.9 and 10.10 show the experimental overview spectrum overlaid with FC simulations for detachment from the ground electronic state of the **1-1a** and **1-1b** anion, respectively, to the closed-shell singlet state of the corresponding neutral. To provide a better comparison to experiment, Figures 10.11 and 10.12 show FC profiles calculated using neutral vibrational frequencies that have been scaled as described in Table 10.5. Of these two isomeric candidates, the FC profile for detachment from the $\tilde{X}\ ^2A_1$ state of the **1-1a** anion (Figs. 10.9 and 10.11) provides better agreement with experiment than detachment from the $\tilde{X}\ ^2A'$

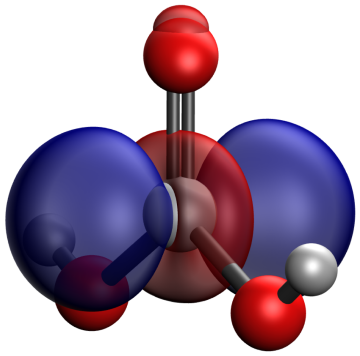

**Figure 10.5:** NIO describing the electron detachment from the **1-1a** anion to the ground electronic state of the corresponding **1-1a'** neutral species.

**1-1b** anion (Figs. 10.10 and 10.12). The calculation in Fig. 10.11 using scaled frequencies is shown in red in Fig. 10.1 and reproduces the dominant vibrational structure observed in the experimental spectrum. In particular, the first several intense features (A1-3) are reproduced in the FC simulation for **1-1a**, whereas the **1-1b** simulation shows extra structure between A1 and A3. Thus, we assign the **1-1a** *cis*-OH geometry as the lowest-energy isomer of $TiO_3H_2^-$, and the observed spectral features reflect the vibronic structure of the corresponding **1-1a'** neutral.

### 10.5.2 Vibrational Assignments

The agreement between the simulated and experimental spectra in Figure 10.1 enables straightforward assignment of the major structure (A1-11) as $\tilde{X}\ ^1A_1 \leftarrow \tilde{X}\ ^2A_1$ detachment transitions terminating in totally symmetric vibrational levels of the neutral ground state (Table 10.1). The less intense B1-11 series of peaks are not fully described by the FC simulation, and the previously described PADs indicate that these transitions do not have the same electronic character as A1-11. As such, we will first address the vibrational assignments of A1-11.

The dominant progression (A1-3-7-11) is assigned to the $\nu_3$ vibrational mode, which corresponds to a symmetric Ti-OH stretching motion (Figure 10.13). The shift of peak A3 from the vibrational origin (A1) gives a frequency of 678(5) $cm^{-1}$ for this mode. There is also significant participation of the $\nu_4$ totally-symmetric OH wagging mode in the spectrum (A2, A6, A10), as well as some activity in the $\nu_2$ terminal Ti=O stretch (A5, A9). The shifts of peaks A5 and A2 give neutral vibrational frequencies of 1016(8) and 413(3) $cm^{-1}$ for $\nu_2$ and $\nu_4$, respectively. Table 10.2 summarizes the energetic quantities for neutral $TiO(OH)_2$ extracted from experiment and compares them to the **1-1a'** B3LYP/Def2TZVP results, showing reasonably good agreement for these totally symmetric modes.

The Franck-Condon activity of different normal modes can be rationalized by considering the geometrical changes that occur upon photodetachment, which are summarized for the B3LYP/Def2TZVP **1-1a** $\tilde{X}\ ^2A_1$ anion and **1-1a'** $\tilde{X}\ ^1A_1$ neutral equilibrium geome-

**Table 10.2:** Electronic and vibrational energies for neutral **1-1a'** $TiO(OH)_2$ extracted from the $TiO_3H_2^-$ cryo-SEVI spectrum, and comparison to the (unscaled) results from B3LYP/Def2TZPV second-derivative calculations.

| | cryo-SEVI | B3LYP |
|---|---|---|
| EA, eV | 1.2529 (4) | 1.2341 |
| $\nu_2$, $cm^{-1}$ | 1016 (8) | 1062 |
| $\nu_3$, $cm^{-1}$ | 678 (5) | 683 |
| $\nu_4$, $cm^{-1}$ | 413 (3) | 485 |
| $\nu_8$, $cm^{-1}$ | 60 (4) | 16 |

tries in Table 10.6. The most significant change is a 13.6° increase in the H-O-Ti bond angle, which results in the FC activity of the $\nu_4$ OH-wagging mode. The involvement of the titanium-oxygen stretching modes $\nu_2$ and $\nu_3$ is a reflection of the change in bond lengths upon photodetachment for both the terminal Ti=O bond as well as the hydroxide Ti-O bonds. The hydroxide and terminal Ti-O bonds of the B3LYP geometries decrease by 0.08 and 0.05 Å, respectively, corresponding to modest 3-4% decreases in these bond lengths. These constitute the second- and third-largest fractional changes upon detachment for the five geometrical parameters summarized in Table 10.6.

While the above considerations fully assign peaks A1-11, the differing PADs and threshold behavior of peaks B1-11 indicate these transitions have different electronic character, ruling out assignment to Franck-Condon allowed transitions within the $\tilde{X}\ ^1A_1 \leftarrow \tilde{X}\ ^2A_1$ electronic band including vibrational hot bands. These transitions are also unlikely to correspond to detachment from an excited anion state, as a TDDFT calculation for the anion (Table 10.7) does not reveal an excited state with sufficiently low excitation energy to be populated in the cold trap. It is possible that peaks B1-11 arise from detachment to a separate electronic state of neutral $TiO(OH)_2$, and that the two groups of features correspond to overlapping electronic bands with the A1-B1 spacing providing the electronic term energy. However, this would require a neutral state with a term energy of around 60 $cm^{-1}$, and the present theoretical results do not provide evidence for such a state, with the lowest-energy neutral excited state of **1-1a'** lying 3.86 eV above the closed-shell singlet (Table 10.7).

Another possible assignment for peaks B1-11 is detachment from a different $TiO_3H_2^-$ geometry. In the current theoretical framework, the **1-1b** *trans*-OH $TiO(OH)_2^-$ dissociative adduct is expected to be only 0.08 eV higher than the *cis*-OH (**1-1a**) isomer. Given this low relative energy as well as its structural similarity to the global minimum, this geometry could interconvert with the slightly more stable **1-1a** geometry in the ion trap, resulting in contributions from multiple isomers in the cryo-SEVI spectrum. However, the barrier for conversion of the **1-1a** isomer to the **1-1b** geometry is estimated to be $\sim$ 1300 $cm^{-1}$ from constrained optimization and single point calculations (Figure 10.14), indicating that such interconversion is highly unlikely in the cold environment of the ion trap. Additionally, as discussed above, the NIOs for the **1-1a** and **1-1b** isomers are quite similar (Figures 10.5 and 10.8), with both orbitals dominated by Ti $d_{z^2}$ character. Thus, if detachment features from the **1-1b** geometry were observed, the transitions would not have PADs that deviate so significantly from the *cis*-OH detachment transitions, ruling out assignment of peaks B1-11 as detachment from the **1-1b** anion. A similar argument can be made to rule out detachment from the **1-1e** isomer, which also differs from **1-1a** only by rotation of the hydroxyl groups.

Given the above considerations, and the observation that each of the B1-11 features lies $\sim$ 60 $cm^{-1}$ above a transition in the A1-11 series, we conclude that these features correspond to detachment transitions terminating in $\tilde{X}\ ^1A_1$ vibrational levels with odd quanta of excitation along a low-frequency non-totally-symmetric mode. These FC-forbidden transitions obtain their oscillator strength and PADs through Herzberg-Teller (HT) coupling to an excited neutral electronic state.[40] The most likely vibrational assignment for peaks B1-11 involves the $b_1$-symmetric $\nu_8$ mode, which corresponds to the umbrella-like motion of

the Ti atom through the plane of the three oxygen atoms (Fig. 10.13) and has the lowest calculated frequency (Table 10.5) for the **1-1a'** neutral. Each B$i$ transition in the B1-11 series is thus assigned as terminating in the state corresponding to the A$i$ transition, plus a single quantum of excitation along $\nu_8$. With this assignment, the position of peak B1 relative to A1 gives a vibrational frequency of 60(4) cm$^{-1}$ for the $\nu_8$ umbrella mode of neutral $TiO(OH)_2$.

We now consider the symmetry requirements for the excited electronic state which gives rise to transitions B1-11 through Herzberg-Teller coupling. Consider a vibronic state $|a\rangle$ whose electronic and vibrational symmetries are $\Gamma^a_{elec}$ and $\Gamma^a_{vib}$, respectively. This state can undergo HT-coupling with another vibronic state, $|b\rangle$, with symmetries $\Gamma^b_{elec}$ and $\Gamma^b_{vib}$, provided

$$\Gamma^a_{elec} \otimes \Gamma^a_{vib} \otimes \Gamma^b_{elec} \otimes \Gamma^b_{vib} \supset \Gamma_{TS}, \tag{10.2}$$

where $\Gamma_{TS}$ is the totally symmetric representation within the relevant molecular point group. If state $b$ is FC-allowed for detachment from the anion in question (i.e., $\langle b|\Psi_{anion}\rangle \neq 0$), detachment to state $a$ will reflect the $b$-state electronic character, which will be observable in the PAD and threshold behavior.

In the current case, the observed HT-coupled levels correspond to states with odd quanta of excitation along the $b_1$-symmetric $\nu_8$ mode ($\Gamma^a_{vib} = b_1$) within the vibrational manifold of the ground neutral electronic state ($\Gamma^a_{elec} = A_1$). Within the $C_{2v}$ point group, these levels are Franck-Condon forbidden, and so can only be observed if they mix with some vibronic level $b$ that is not FC-forbidden, i.e., $\Gamma^b_{vib} = a_1$. Thus, the observed features must arise from HT-coupling with a $B_1$-symmetric electronic excited state. The lowest such singlet state identified from TDDFT (Table 10.7) is the relatively high-lying $\tilde{X}\ ^1B_1$ excited state, residing 4.45 eV above neutral $\tilde{X}\ ^1A_1$ **1-1a'**. Using the NTO model we determined this state would involve detachment from an orbital with angular momentum $l = 1$, resulting in outgoing $s-$ ($\ell = 0$) and $d$-wave ($\ell = 2$) electrons, in contrast to the $p$- and $f$-wave detachment expected from the **1-1a** NIO. Thus, the assignment of peaks B1-11 as arising from Herzberg-Teller coupling to this $^1B_1$ state is consistent with the observed relative attenuation of A1-11 versus B1-11 as photon energy is lowered.

### 10.5.3 Charge Effects on the $TiO_2$ + $H_2O$ Reaction

The cryo-SEVI spectrum of unreacted $TiO_2^-$ has been previously reported, giving an electron affinity of 1.5892(5) eV for the singlet ground state of $TiO_2$.[34] The electron affinity of the $TiO(OH)_2$ dissociative adduct is lower by roughly 0.3 eV, and this difference provides insight into the energetic effects of charge on the dissociation of $H_2O$ by $TiO_2$. The lower electron affinity for the reacted species implies that the neutral $TiO_2 + H_2O \rightarrow TiO(OH)_2$ reaction is more exothermic than the anionic counterpart – that is, reaction with water to form the dissociative $TiO(OH)_2$ adduct stabilizes neutral $TiO_2$ more than it does the anion. As a consequence, it can be inferred that neutral $TiO_2$, where the titanium center has a +4 oxidation state, is more reactive towards water than anionic $TiO_2^-$ where the Ti oxidation state is +3. The energies shown in Figure 10.4 indicate that the molecularly adsorbed **1-1c'**

geometry has an even lower EA (0.79 eV) than the dissociative structures. Given that all the geometries in Figure 10.4 involve binding interactions between the water oxygen and Ti, this charge effect likely derives from donation of electron density from the incoming water molecule to the metal center, which in turn is favored by a higher titanium oxidation state.

The enhanced reactivity towards water of neutral $TiO_2$ echoes the electrochemical mechanism of water splitting in photoelectrochemical cells (PECs) where titania is used as a photoanode.[383] In these systems, the generally understood mechanism is initiated by photoexcitation of titanium, resulting in the formation of an electron-hole pair. The electron is then transferred to the cathode, typically a metal, leaving behind a hole in the valence band of $TiO_2$. These holes participate in the oxidation half-reaction,

$$H_2O \rightarrow \tfrac{1}{2}O_2 + 2H^+ + 2e^-, \tag{10.3}$$

while the electrons at the cathode participate in the reduction half-reaction,

$$2H^+ + 2e^- \rightarrow H_2. \tag{10.4}$$

Within this mechanistic picture, the photosensitization of water by $TiO_2$ is a consequence of the ability of $TiO_2$ to donate a hole (or, equivalently, accept an electron). Direct parallels between the chemistry occurring in such PECs and the gas-phase $TiO_2^{-/0}$ reaction considered here are difficult to make, due to the fundamental differences in the electronic structures for these two systems and the increased complexity associated with the condensed phase. However, it is interesting to note that the reactivity of $TiO_2$ with water in the gas phase reflects, to some extent, the bulk electrochemical behavior - namely, the energetics of the $TiO_2$ / water reaction are directly related to the oxidation state of the Ti center, with a more positively-charged metal atom resulting in a more energetically favorable interaction with water.

## 10.6 Conclusion

Vibrationally-resolved photoelectron spectra of the $TiO_3H_2^-$ anion are obtained using slow electron velocity-map imaging of cryogenically-cooled anions, yielding spectra that reflect the vibronic structure of neutral $TiO_3H_2$. These results provide a significant improvement in resolution over prior work on this system, clearly resolving the onset of structure at the adiabatic detachment energy. A Franck-Condon simulation for detachment from the $C_{2v}$ **1-1a** $TiO(OH)_2^-$ *cis*-hydroxide geometry captures the dominant vibrational structure observed experimentally, enabling assignment of this geometry as the lowest-energy anion isomer in agreement with density functional theory calculations. In addition to transitions reproduced in the FC simulations, a series of features resulting from Herzberg-Teller coupling to an excited neutral electronic state is identified in the cryo-SEVI spectrum, evidenced by noticeable differences in the angular and energy dependence of the photodetachment cross sections.

The comparison of the current spectral results to the previously reported cryo-SEVI spectrum of unreacted $TiO_2^-$ provides insight into the reactivity of $TiO_2^{-/0}$ towards water. The lowered electron affinity of $TiO_3H_2$ relative to $TiO_2$ indicates that neutral $TiO_2$ is stabilized to a greater extent than anionic $TiO_2^-$ by reaction with water, suggesting that the reaction of $TiO_2$ with water is impeded by excess negative charge. This conclusion is consistent with the existing electrochemical understanding of photocatalytic water splitting by $TiO_2$ in photoelectrochemical cells, where the sensitization of water arises from the ability of $TiO_2$ to accept electron density. This work highlights the relevance of gas-phase studies of metal oxide cluster reactions to bulk catalytic reactions, as well as the utility of cryo-SEVI as a structural probe for such systems.

## 10.7 Supporting Information

### 10.7.1 Model Chemistry Benchmarking

Preliminary studies suggested meaningful functional and basis set dependencies in calculations of $TiO(OH)_2$ neutral and anion species. Using both B3LYP and ωB97XD[437] approximate density functionals, three basis/effective core potential (ECP) sets were considered: (1) the all-electron Def2TZVP basis set for all atoms; (2) the Stuttgard/Cologne ECP (designated DCP10MDF) with the corresponding valence electron basis set on Ti and the aug-cc-pVDZ all electron basis set for H and O centers,[438] and (3) the Stuttgard/Cologne ECP (designated ECP10MDF) with a modified form of the corresponding valence electron basis set that includes higher angular momentum functions for Ti and aug-cc-PVTZ to describe orbitals on H and O atoms.

Tables 10.3 and 10.4, below, give calculated adiabatic detachment energies (ADEs) and vertical detachment energies (VDEs) for the six functional/basis set combinations considered. For comparison, HF and CCSD results are also included. All CCSD and HF geometry optimization calculations converge to the expected planar $C_{2v}$ geometry (**1-1a**) for both anion and neutral. However, all geometry optimizations of neutral **1-1a'** using ωB97XD converged to non-planar structures. Similarly, the neutral **1-1a'** B3LYP/SC and B3LYP/SDD+TZ geometry optimizations converged to non-planar geometries. Optimization of the **1-1a** anion converged to the expected planar structure in all cases. Given these results, and the good agreement with CCSD for the ADE and VDE predictions, the B3LYP/Def2TZVP model chemistry was chosen for all calculations and results reported in this chapter.

### 10.7.2 Franck-Condon Simulations

Franck-Condon (FC) simulations were carried out for **1-1a** and **1-1b** using potentials derived from B3LYP/Def2TZVP calculations and are shown in Figures 10.9-10.10. All FC profiles have been manually shifted such that the vibrational origin occurs at the experimental value. To correct for expected systematic errors in the calculated force constants, the

neutral force constants were scaled to match experimentally derived values, resulting in the FC spectra shown in Figures 10.11-10.12. All vibrational frequencies and scaling factors for the **1-1a** and **1-1b** geometries are provided in Table 10.5.

### 10.7.3 Optimized Anion Geometries

The Cartesian coordinates for the optimized geometries of the doublet anion $TiO_3H_2^-$ species identified by B3LYP/Def2TZVP are provided below. The (non-ZPE corrected) energy in eV relative to the lowest-energy anion is also provided.

| **1-1a** | | | **E = 0.0000** |
|---|---|---|---|
| O | 0.00000000 | 1.68120500 | -0.88497500 |
| O | 0.00000000 | 0.00000000 | 1.72463800 |
| H | 0.00000000 | 2.49503300 | -0.37534700 |
| Ti | 0.00000000 | 0.00000000 | 0.05060000 |
| O | 0.00000000 | -1.68120500 | -0.88497500 |
| H | 0.00000000 | -2.49503300 | -0.37534700 |

| **1-1b** | | | **E = 0.0821** |
|---|---|---|---|
| O | 1.51464500 | -1.09805500 | 0.00023000 |
| O | 0.25786000 | 1.73467200 | -0.00004900 |
| H | 2.39847000 | -0.72256600 | 0.00032800 |
| Ti | -0.00213100 | 0.08177800 | -0.00000900 |
| O | -1.81952100 | -0.58020000 | -0.00017900 |
| H | -1.97545700 | -1.52788900 | -0.00015600 |

| **1-1c** | | | **E = 2.2700** |
|---|---|---|---|
| Ti | -0.49642100 | 0.35156400 | 0.00000000 |
| O | 0.38600900 | 0.58243000 | 1.42674100 |
| O | 0.38600900 | 0.58243000 | -1.42674100 |
| O | 0.38600900 | -1.78834700 | 0.00000000 |
| H | 0.82852900 | -1.37325500 | -0.77053300 |
| H | 0.82852900 | -1.37325500 | 0.77053300 |

| **1-1e** | | | **E = 0.2061** |
|---|---|---|---|
| O | -1.70048000 | -0.81281200 | 0.00000000 |
| O | -0.00001100 | 1.77743000 | 0.00000000 |
| H | -1.74529900 | -1.77146400 | 0.00000000 |
| Ti | 0.00000000 | 0.10583600 | 0.00000000 |
| O | 1.70049200 | -0.81280300 | 0.00000000 |
| H | 1.74529600 | -1.77145500 | 0.00000000 |

### 10.7.4 Optimized Neutral Geometries

The Cartesian coordinates for the optimized geometries of the closed-shell singlet neutral $TiO_3H_2^-$ species identified by B3LYP/Def2TZVP are provided below. The (non-ZPE corrected) energy in eV relative to the lowest-energy anion is also provided.

| **1-1a'** | | | **E = 1.1877** |
|---|---|---|---|
| O | 0.00000000 | 1.61434900 | -0.83227400 |
| O | 0.00000000 | 0.00000000 | 1.66500300 |
| H | 0.00000000 | 2.52311700 | -0.52046400 |
| Ti | 0.00000000 | 0.00000000 | 0.04715000 |
| O | 0.00000000 | -1.61434900 | -0.83227400 |
| H | 0.00000000 | -2.52311700 | -0.52046400 |

| **1-1b'** | | | **E = 1.2963** |
|---|---|---|---|
| O | 1.54294900 | -0.93583500 | 0.00023900 |
| O | 0.13579600 | 1.66575400 | -0.00008500 |
| H | 2.47500100 | -0.70256200 | 0.00032800 |
| Ti | 0.00026400 | 0.05346400 | 0.00000200 |
| O | -1.72162800 | -0.60533300 | -0.00017700 |
| H | -2.13774800 | -1.47034000 | -0.00018400 |

| **1-1c'** | | | **E = 3.0448** |
|---|---|---|---|
| Ti | -0.38212100 | 0.22987500 | 0.00000000 |
| O | 0.28113800 | 0.84520900 | 1.38618700 |
| O | 0.28113800 | 0.84520900 | -1.38618700 |
| O | 0.28113800 | -1.82563800 | 0.00000000 |
| H | 0.82968000 | -1.98774000 | -0.78012800 |
| H | 0.82968000 | -1.98774000 | 0.78012800 |

**Table 10.3:** Absolute energies including ZPE for optimized anion and neutral geometries of **1-1a** and ADEs using initial candidate model chemistries.

| | **Absolute Energy** ($E_h$) | | |
|---|---|---|---|
| **Model Chemistry** | **Anion** | **Neutral** | **ADE** (eV) |
| B3LYP/Def2TZVP | -1076.6312 | -1076.5858 | 1.23 |
| B3LYP/SC | -285.4334 | -285.3810 | 1.42 |
| B3LYP/SDD+TZ | -285.4891 | -285.4368 | 1.42 |
| ωB97XD/Def2TZVP | -1076.5214 | -1076.4824 | 1.06 |
| ωB97XD/SC | -285.3247 | -285.2800 | 1.22 |
| ωB97XD/SDD+TZ | -285.3771 | -285.3328 | 1.21 |
| HF/Def2TZVP | -1074.3943 | -1074.3467 | 1.30 |
| HF/SC | -283.7421 | -283.6372 | 1.46 |
| HF/SDD+TZ | -283.7421 | -283.6909 | 1.39 |
| CCSD/Def2TZVP | -1075.2521 | -1075.2104 | 1.13 |
| CCSD/SC | -284.4526 | -284.4032 | 1.34 |
| CCSD/SDD+TZ | -284.6343 | -284.5847 | 1.35 |

**Table 10.4:** Absolute energies including ZPE for anionic and neutral **1-1a** using the anion **1-1a** geometry, and the VDEs using initial candidate model chemistries.

| | **Absolute Energy** ($E_h$) | | |
|---|---|---|---|
| **Model Chemistry** | **Anion** | **Neutral** | **VDE** (eV) |
| B3LYP/Def2TZVP | -1076.6312 | -1076.5765 | 1.49 |
| B3LYP/SC | -285.4334 | -285.3720 | 1.67 |
| B3LYP/SDD+TZ | -285.4891 | -285.4278 | 1.67 |
| ωB97XD/Def2TZVP | -1076.5214 | -1076.4709 | 1.37 |
| ωB97XD/SC | -285.3247 | -285.2688 | 1.52 |
| ωB97XD/SDD+TZ | -285.3771 | -285.3217 | 1.51 |
| HF/Def2TZVP | -1074.3943 | -1074.3207 | 2.00 |
| HF/SC | -283.7421 | -283.6111 | 2.17 |
| HF/SDD+TZ | -283.7421 | -283.6655 | 2.09 |
| CCSD/Def2TZVP | -1075.2521 | -1075.1978 | 1.48 |
| CCSD/SC | -284.4526 | -284.3902 | 1.70 |
| CCSD/SDD+TZ | -284.6343 | | |

**Table 10.5:** Vibrational frequencies in $cm^{-1}$ for the lowest-energy anion and neutral states of **1-1a** $TiO_3H_2$ obtained at the B3LYP/Def2TZVP level. The scaling factors used to adjust neutral frequencies are also provided, where the frequencies $\nu_{fit}$ used to obtain Figures 10.11-10.12 are related to the frequencies $\nu_i$ in this table by $\nu_{fit} = (\text{scale factor}) * \nu_i$.

| | **1-1a** ($C_{2v}$) | | | | **1-1b** ($C_s$) | | | |
|---|---|---|---|---|---|---|---|---|
| mode | sym. | anion | neutral | scale factor | sym. | anion | neutral | scale factor |
| $\nu_1$ | $a_1$ | 3855.0 | 3866.9 | 1.000 | $a'$ | 3854.7 | 3877.6 | 1.000 |
| $\nu_2$ | $a_1$ | 941.2 | 1061.6 | 0.957 | $a'$ | 3850.0 | 3865.2 | 1.000 |
| $\nu_3$ | $a_1$ | 552.6 | 683.0 | 0.993 | $a'$ | 945.5 | 1058.8 | 0.960 |
| $\nu_4$ | $a_1$ | 502.4 | 484.9 | 0.852 | $a'$ | 649.9 | 786.7 | 1.000 |
| $\nu_5$ | $a_1$ | 166.3 | 194.1 | 1.000 | $a'$ | 543.9 | 684.4 | 0.991 |
| $\nu_6$ | $a_2$ | 334.6 | 509.4 | 1.000 | $a'$ | 496.6 | 506.1 | 1.000 |
| $\nu_7$ | $b_1$ | 334.7 | 528.6 | 1.000 | $a'$ | 471.9 | 335.3 | 1.237 |
| $\nu_8$ | $b_1$ | 68.2 | 16.2 | 3.750 | $a'$ | 225.5 | 252.7 | 1.000 |
| $\nu_9$ | $b_2$ | 3854.7 | 3863.8 | 1.000 | $a'$ | 155.1 | 177.3 | 1.000 |
| $\nu_{10}$ | $b_2$ | 661.4 | 790.06 | 1.000 | $a''$ | 338.7 | 522.1 | 1.000 |
| $\nu_{11}$ | $b_2$ | 489.4 | 489.5 | 1.000 | $a''$ | 281.7 | 453.5 | 1.000 |
| $\nu_{12}$ | $b_2$ | 205.2 | 225.9 | 1.000 | $a''$ | 102.8 | 56.4 | 1.071 |

**Table 10.6:** Structural parameters for the **1-1a** anion and neutral geometries obtained at the B3LYP/Def2TZVP level, as well as the percent changes in these parameters that occur upon photodetachment.

| | anion | neutral | % change |
|---|---|---|---|
| terminal Ti=O bond length, Å | 1.67 | 1.62 | -3.0 |
| hydroxyl Ti-O bond length, Å | 1.92 | 1.84 | -4.2 |
| O-H bond length, Å | 0.96 | 0.96 | 0.0 |
| O-Ti-O angle, deg. | 121.8 | 122.8 | +0.8 |
| H-O-Ti angle, deg. | 118.9 | 132.5 | +11.4 |

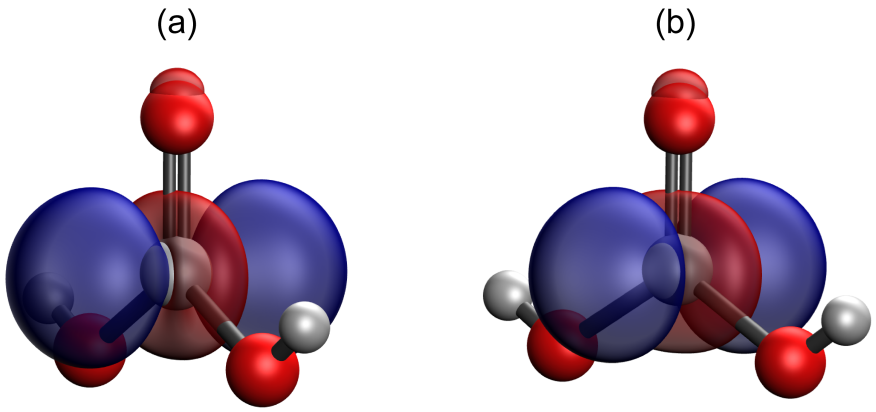


**Figure 10.6:** Orbitals used to describe the lowest-energy detachment transition of the **1-1a** anion: (a) NIO results; and (b) the canonical Kohn-Sham HOMO/Koopmans orbital.

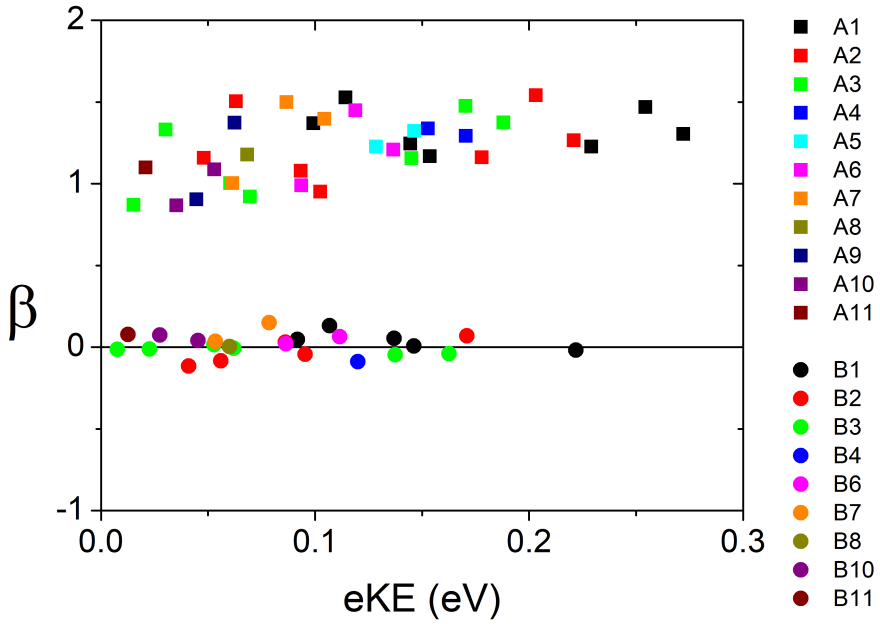


**Figure 10.7:** Photoelectron angular distributions for all labelled features in the cryo-SEVI spectrum of $TiO_3H_2^-$ demonstrating the distinct anisotropies observed for peaks A1-11 (squares) versus B1-11 (circles).

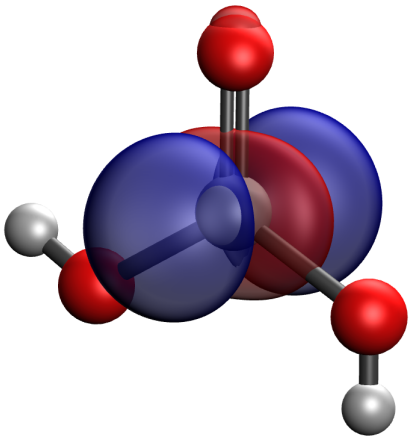

**Figure 10.8:** NIO for detachment from the **1-1b** anion.

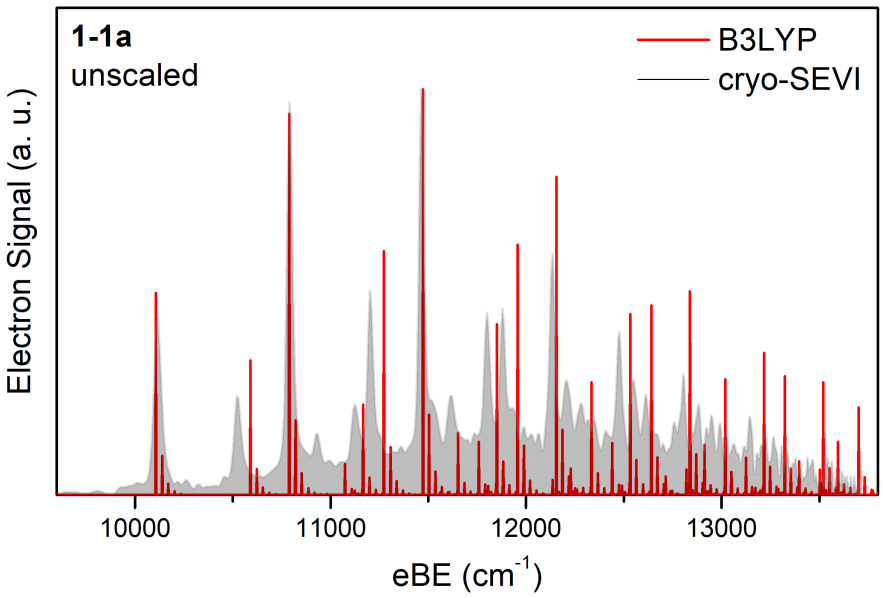


**Figure 10.9:** Franck-Condon simulation for detachment from the $\tilde{X}\ ^2A_1$ **1-1a** anion with unscaled frequencies (red) overlaid with the cryo-SEVI overview spectrum (gray).

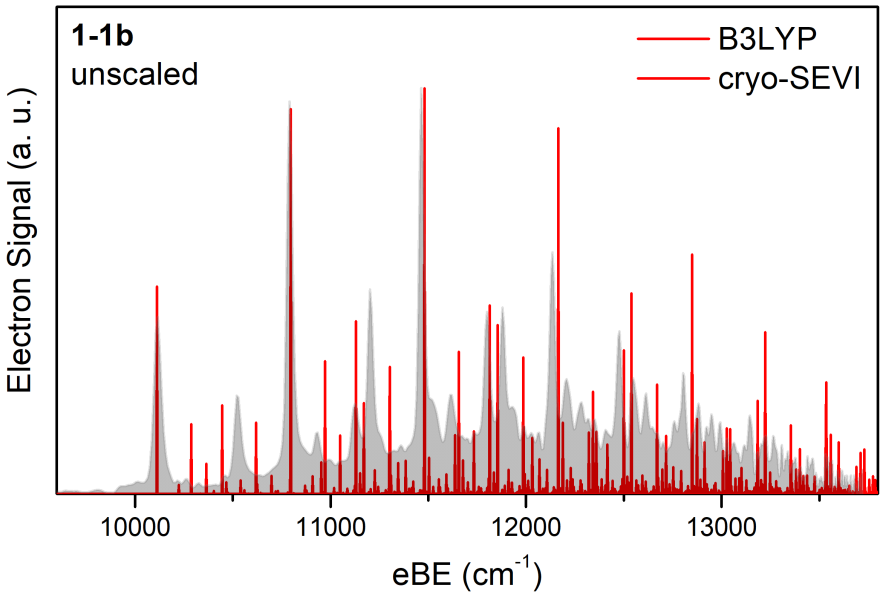


**Figure 10.10:** Franck-Condon simulation for detachment from the $\tilde{X}\ ^2A'$ **1-1b** anion with unscaled frequencies (red) overlaid with the cryo-SEVI overview spectrum (gray).

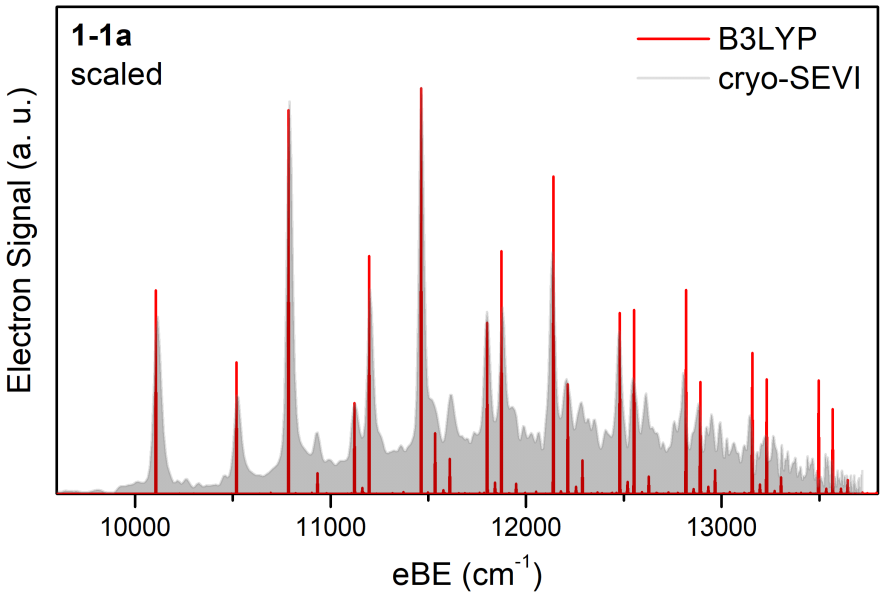


**Figure 10.11:** Franck-Condon simulation for detachment from the $\tilde{X}\ ^2A_1$ **1-1a** anion with scaled frequencies (red) overlaid with the cryo-SEVI overview spectrum (gray).

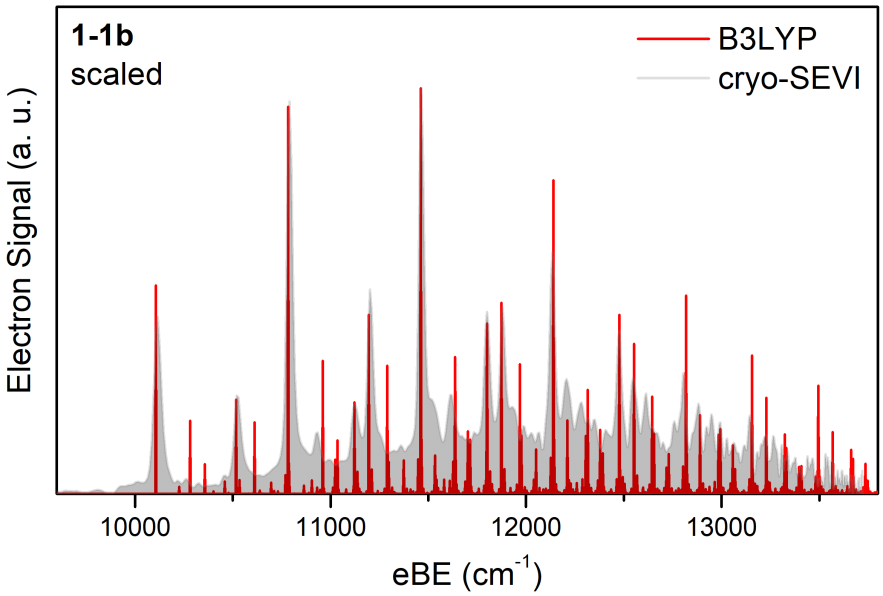


**Figure 10.12:** Franck-Condon simulation for detachment from the $\tilde{X}\ ^2A'$ **1-1b** anion with scaled frequencies (red) overlaid with the cryo-SEVI overview spectrum (gray).

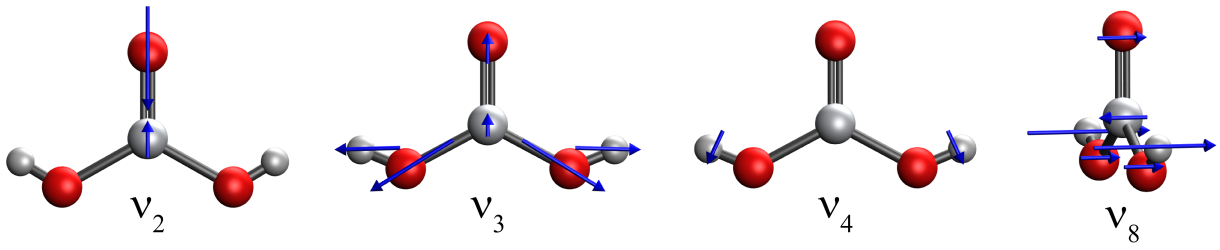


**Figure 10.13:** Vibrational modes of the **1-1a** $TiO_3H_2$ isomer that are active in the cryo-SEVI spectrum.

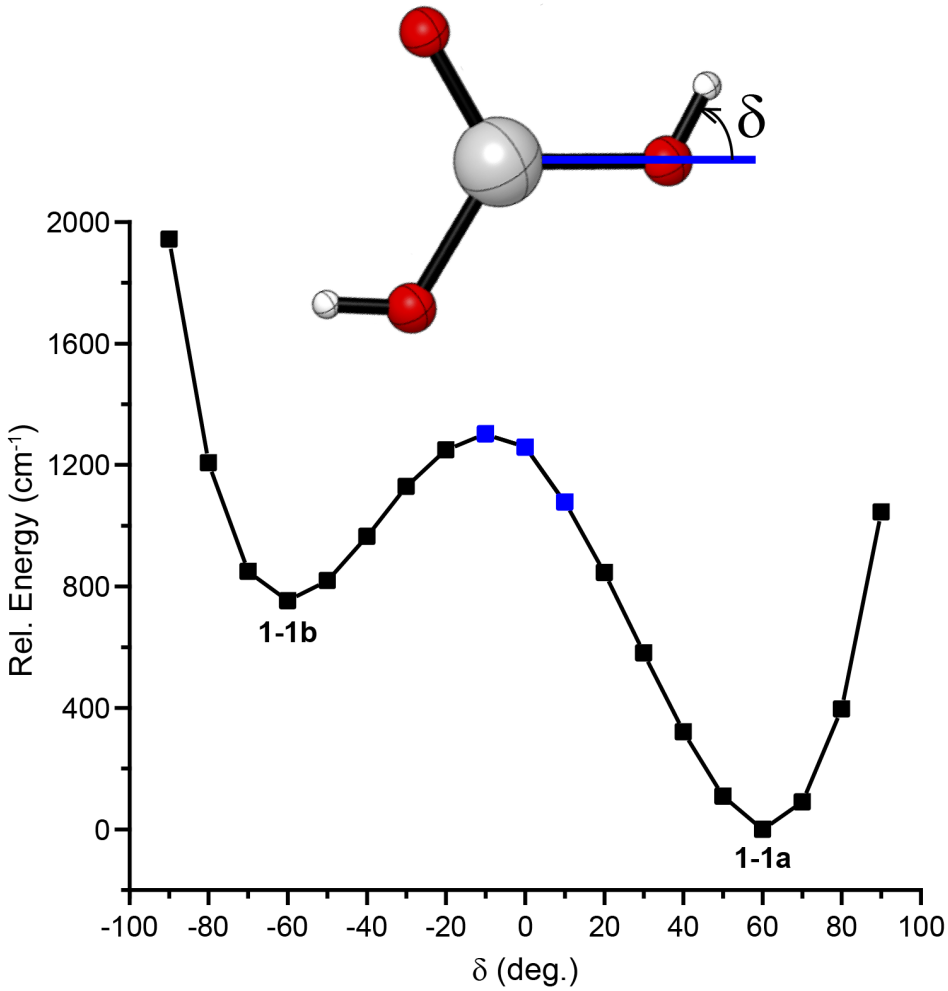


**Figure 10.14:** Scan of the anion potential energy surface along the angular coordinate $\delta$, defined in the top panel, which is used to distinguish between the *cis*- and *trans*-OH isomers **1-1a** and **1-1b**. These calculations were performed in Gaussian and carried out at the B3LYP/SDD+TZ level, as use of an ECP reduces computational expense. Points in black correspond to a constrained optimization where the value of $\delta$ was fixed and the other geometrical parameters were allowed to relax; for each of the $-10° \leq \delta \leq 10°$ data points, shown in blue, a single point calculation was carried out using the adjacent geometries with the $\delta$-angle fixed at the appropriate value. The resultant barrier height for the *trans*-to-*cis* rotation is 549 $cm^{-1}$, and that of the *cis*-to-*trans* rotation is 1302 $cm^{-1}$; these constitute upper bounds for the true barrier heights due to the inability to perform a constrained optimization for the $\delta \sim 0$ geometries.

**Table 10.7:** Ten lowest-energy electronic states of the **1-1a'** neutral $TiO(OH)_2$ species found using the B3LYP/Def2TZVP model chemistry. Excitation energies were obtained from a TDDFT calculation.

| State | Energy (eV) |
|---|---|
| $\tilde{X}\ ^1A_1$ | 0.00 |
| $\tilde{a}\ ^3A_1$ | 3.86 |
| $\tilde{b}\ ^3B_2$ | 4.02 |
| $\tilde{c}\ ^3B_1$ | 4.11 |
| $\tilde{A}\ ^1B_2$ | 4.20 |
| $\tilde{B}\ ^1A_1$ | 4.36 |
| $\tilde{d}\ ^3B_2$ | 4.42 |
| $\tilde{C}\ ^1B_1$ | 4.45 |
| $\tilde{D}\ ^1B_2$ | 4.55 |
| $\tilde{e}\ ^3B_1$ | 4.71 |

# Chapter 11

# Cryo-SEVI of $(AlO)_{2-3}^-$

The content and figures of this chapter are reprinted or adapted with permission from J. A. DeVine, M. C. Babin, D. M. Neumark, "Photoelectron spectra of $Al_2O_2^-$ and $Al_3O_3^-$ via slow electron velocity-map imaging" (2018).

## Abstract

High-resolution photoelectron spectra of cryogenically-cooled $Al_2O_2^-$ and $Al_3O_3^-$ cluster anions are obtained using slow electron velocity-map imaging. These spectra show vibrationally-resolved detachment from the ($\tilde{X}\ ^2B_{3u}$) ground state of $Al_2O_2^-$ to the $\tilde{X}\ ^1A_g$ and $\tilde{a}\ ^3B_{3u}$ neutral electronic states, giving an electron affinity of 1.87904(4) eV for neutral $Al_2O_2$ and a term energy of 0.4938(4) eV for the triplet excited state. Additionally, there is evidence for autodetachment from photoexcited anions as well as influences from vibronic coupling between excited states of the neutral $Al_2O_2$ cluster. Detachment from both the "kite" and "book" isomers of $Al_3O_3^-$ is observed, yielding electron affinities of 2.0626(4) and 2.792(3) eV for the corresponding neutral isomers. Experiments carried out at different anion temperatures suggest that the two anionic isomers are nearly isoenergetic but clearly identify the kite isomer as the global minimum structure, in contrast to prior studies. This finding is supported by density functional theory calculations, which show that the relative ordering of the anion isomers is sensitive to basis set size; calculations for the anion isomers at the B3LYP/aug-cc-pVQZ level find the kite isomer to lie 0.011 eV below the book isomer.

## 11.1 Introduction

Aluminum oxides are seen in a wide range of chemical environments and play important roles as ceramics,[439] components of atmospheric aerosols,[440] and catalytic supports.[441] Aluminum oxide nanoparticles have also been identified in dust particles surrounding brown dwarfs[442] and in supernova remnants.[443] Given the prevalence of these species in both bulk and nanoscale materials, there is considerable interest in understanding how their molecular properties scale with system size. This can be accomplished by investigating the spectroscopy and reactivity of size-selected aluminum oxide clusters.

Gas-phase metal oxide clusters involving a range of metallic centers have attracted much interest as model systems for reactive sites on bulk surfaces, and provide an avenue for understanding the development of chemical behavior with cluster size and stoichiometry.[137–139] In the case of aluminum oxides, oxygen-deficient systems ($Al_xO_y$ with $y < 3x/2$) are of particular interest, as these serve as models for oxygen vacancies on bulk $Al_xO_y$ surfaces that are susceptible to water adsorption.[444] In this work, we use high-resolution anion photoelectron spectroscopy to probe the anionic and neutral charge states of two oxygen-deficient aluminum oxide clusters, $Al_2O_2$ and $Al_3O_3$, providing a substantial improvement in resolution over prior work and revealing new energetic and spectroscopic subtleties of these systems.

Some of the smaller neutral aluminum oxides have been isolated in $N_2$ and Ar matrices, yielding vibrational frequencies and structural characterization of $Al_xO_y$ $(x, y = 1-2)$.[445–448] Neutral clusters over a wider size range have been characterized using infrared resonance-enhanced multiphoton ionization, the results of which suggest that clusters converge to a $\gamma$-$Al_2O_3$-like geometry over the $AlO{\cdot}(Al_2O_3)_{0-34}$ series.[449,450] Due to the important role that oxidation states play in the chemistry of aluminum oxides, ionic clusters are also of considerable interest, and infrared photodissociation experiments have yielded structural determination for both anionic and cationic $Al_xO_y$ clusters.[451–454] Anion photoelectron spectroscopy (PES) is another structurally-sensitive spectroscopic technique which, in contrast to infrared experiments, informs on both the anionic and neutral states of a given molecule, and has been used to characterize the structural and electronic properties of several aluminum oxide clusters.[455–457] These experiments combined with theoretical work[458] indicate that the most stable geometries of anionic and neutral $Al_xO_y$ typically contain 3- or 4-membered rings, with the cyclic Al-O-Al-O substructure being particularly prevalent.

The smallest cluster for which this cyclic moiety is present is $Al_2O_2$, which was suggested to contribute to the infrared spectrum of the products formed from reaction of Al atoms with oxygen in argon matrices.[446] The anion photoelectron spectrum of $Al_2O_2^-$ reported by Desai *et al.*[455] provided a more definitive observation of this cluster. This spectrum was consistent with detachment from the rhombic structure **2a** shown in Fig. 11.1. It showed partial vibrational resolution for detachment to the $\tilde{X}\ ^1A_g$ and $\tilde{a}\ ^3B_{3u}$ neutral electronic states, giving vibrational frequencies of 660(80) and 730(80) $cm^{-1}$ for the ground and excited neutral states, respectively. However, the authors noted that neither of these frequencies were consistent with the calculated values of totally symmetric modes and suggested that these instead correspond to averages of the frequencies of both $a_g$-symmetric modes in each state

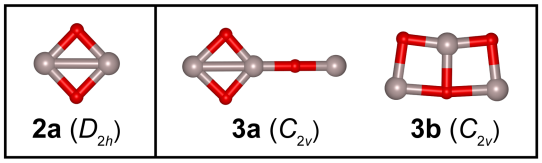


**Figure 11.1:** Isomers of (left) $Al_2O_2^{-/0}$ and (right) $Al_3O_3^{-/0}$ considered in the current work.

that could not be cleanly resolved.

The next-smallest cluster of the same stoichiometry, $Al_3O_3^-$, has received much attention since its photoelectron spectrum was first reported by Wu *et al.* in 1998.[456] These results showed two partially-resolved bands, $X'$ and $X$, with band $X'$ covering electron binding energies (eBEs) of $\sim 2.0 - 2.5$ eV and band $X$ spanning eBEs of $\sim 2.5 - 3.0$ eV. These two regions of structure were attributed to detachment from two distinct anion isomers, though structural assignments were not made in this initial work. Subsequent experimental[457] and theoretical studies[459–461] identified these isomers as the kite (**3a**) and book (**3b**) isomers pictured in Fig. 11.1, with bands $X'$ and $X$ assigned to detachment from anion isomers **3a** and **3b**, respectively. These structures can be understood as forming from the **2a** geometry by end-on (**3a**) or side-on (**3b**) addition of an AlO unit to the $Al_2O_2$ ring, resulting in the formation of additional Al-O bonds. In the photoelectron spectrum of Wu and coworkers, the partially resolved vibrational progressions in each band gave vibrational frequencies of 720(60) and 610(60) $cm^{-1}$ for the kite and book neutral isomers, respectively. A somewhat higher resolution photoelectron spectrum was reported by Meloni *et al.*,[457] who also saw detachment to an excited electronic state of isomer **3b**.

To determine which anion isomer contributing to the photoelectron spectrum corresponded to the lower-energy structure, Wu *et al.*[456] explored the effect of anion temperature on the relative intensities of each region of structure by varying the timing between the laser pulse and the carrier gas in their laser ablation ion source. In this analysis, a shorter time delay between ablation of the metal surface and injection of the carrier gas was assumed to result in the formation of warmer ions, as the ions in the plasma would have lower internal energies if allowed to collisionally cool for a longer duration before entrainment by the carrier gas. This study found that at shorter delays, the relative intensity of band $X'$ was enhanced, leading to the inference that isomer **3b** corresponds to the anion global minimum of $Al_3O_3^-$. This energy ordering was supported by density functional theory (DFT) and configuration interaction (QCISD) calculations,[460,461] though the calculated isomeric energies are typically small, with the kite anion isomer lying 30 and 200 meV higher in energy in the DFT and QCISD treatments, respectively.

Slow electron velocity-map imaging spectroscopy of cryogenically-cooled anions (cryo-SEVI) is a variant of anion PES wherein cold ions are detached with a tunable laser and the resultant electron kinetic energy distribution is analyzed by a velocity-map imaging (VMI) spectrometer that is optimized for the detection of slow electrons, yielding photoelectron spectra with sub-meV resolution.[157,158] In the current work, the photoelectron spectra of

$Al_2O_2^-$ and $Al_3O_3^-$ are revisited using cryo-SEVI, providing substantial improvements in resolution over previous work. In addition to well-resolved vibrational structure, the spectra of $Al_2O_2^-$ show evidence for autodetachment in the ground state singlet band and vibronic coupling between neutral excited states in the triplet band; these interpretations are supported by the measured photoelectron angular distributions across each band. Detachment from both isomers of $Al_3O_3^-$ is seen, despite the low ion temperatures associated with the cryo-SEVI experiment, reaffirming that the energy difference between anion isomers **3a** and **3b** is quite small. By explicitly varying the anion temperature and observing its effect on the photoelectron signals, we find the kite isomer **3a** to be the global minimum anion structure, in contrast to earlier work.[456,457,459–461] This conclusion is supported by new electronic structure calculations. Detachment from isomer **3a** is obtained in excellent resolution, yielding several vibrational frequencies for totally-symmetric modes of the neutral doublet ground state. Due to unusual threshold behavior, detachment from anion isomer **3b** was not obtained in as high resolution, though the current results do show considerably more vibrational structure than has been resolved previously.

## 11.2 Experimental Methods

The cryo-SEVI method and apparatus are described in detail in Chapter 2. $Al_xO_y^-$ cluster anions are generated in the standard laser ablation reactor source described in Chapter 2, using an Al target and He as the carrier gas. Accumulated images were circularized using the method described by Gascooke and coworkers[192] to correct for slight angular deformities resulting from imperfect shielding in the field-free region. Calibration of the VMI spectrometer was done by acquiring images for the well-characterized detachment transitions of atomic $O^-$, $S^-$, and $F^-$ at several photon energies.[188,190,246]

## 11.3 Computational Methods

To assign and interpret the cryo-SEVI spectra of $Al_2O_2^-$ and $Al_3O_3^-$, electronic structure calculations were performed using DFT as implemented in Gaussian 09.[53] For all systems, geometry optimizations and frequency calculations were carried out at the B3LYP/aug-cc-pVTZ level, using tight convergence criteria and an ultrafine integration grid with 99 radial points and 590 angular points. In light of previous work concerning the structural assignment of the $Al_2O_2^-$ and $Al_3O_3^-$ anions,[457,459–462] only geometries **2a**, **3a**, and **3b** shown in Figure 11.1 were considered.

Calculations were performed for the lowest-energy doublet anion state ($\tilde{X}\ ^2B_{3u}$) of the $Al_2O_2^-$ anion as well as the lowest-energy singlet ($\tilde{X}\ ^1A_g$) and triplet ($\tilde{a}\ ^3B_{3u}$) states of the corresponding neutral; the resultant geometries and relative energies are provided in Table 11.6 at the end of this chapter. For both isomers of $Al_3O_3$, the singlet anion and doublet neutral states were considered, and the resultant geometries and energies are provided in

Table 11.7. Calculated vibrational frequencies for both isomers of $Al_3O_3^{-/0}$ are provided in Table 11.8, and those of $Al_2O_2^{-/0}$ will be considered in more detail below. In addition, a time-dependent DFT (TDDFT) calculation was carried out to find excitations of the triplet state of $Al_2O_2$, the results of which are provided in Table 11.9.

The optimized geometries, normal modes, and harmonic frequencies obtained at the B3LYP/aug-cc-pVTZ level were used as input for the ezSpectrum software package[57] to calculate FC profiles for the $\tilde{X}\ ^1A_g \leftarrow \tilde{X}\ ^2B_{3u}$ and $\tilde{a}\ ^3B_{3u} \leftarrow \tilde{X}\ ^2B_{3u}$ detachment transitions of $Al_2O_2^-$ and the $\tilde{X}\ ^2A_1 \leftarrow \tilde{X}\ ^1A_1$ and $\tilde{X}\ ^2B_2 \leftarrow \tilde{X}\ ^1A_1$ detachment transitions of $Al_3O_3^-$ isomers **3a** and **3b**, respectively. All vibrational modes were treated as harmonic oscillators and Duschinsky mixing was used to account for differences between anion and neutral normal modes. To optimize the fit to experiment, the presented FC profiles for detachment from both isomers of $Al_3O_3^-$ use experimental frequencies for the FC-active modes of neutral isomers **3a** and **3b**.

Photodetachment cross sections and angular distributions based on the DFT anion molecular orbitals were calculated using the code of Liu and Ning.[64] This code models the outgoing electron (with momentum $k$) resulting from detachment from a specified anion orbital as a superposition of spherical waves with angular momenta $\ell < 6$. The expansion coefficients, $C_{k\ell m}$, describe the amplitude of each spherical wave component; from these, a fractional partial wave character, $f_\ell$, may be defined for a particular eKE as[60]

$$f_\ell = \frac{P_\ell}{\sum_{\ell=0}^{5} P_\ell} \quad \text{where} \quad P_\ell = \sum_{m=-\ell}^{\ell} C_{k\ell m}^2. \tag{11.1}$$

## 11.4 Experimental Results

### 11.4.1 $Al_2O_2$

The cryo-SEVI spectrum of $Al_2O_2^-$ is presented in Figure 11.2, covering the same two regions of structure observed previously.[455] Figure 11.2a shows the lower-eBE region of structure spanning eBEs of $\sim$ 14500 to 17500 cm$^{-1}$ and corresponding to the $\tilde{X}\ ^1A_g \leftarrow \tilde{X}\ ^2B_{3u}$ ground state band. The molecular orbital (MO) diagram of the $Al_2O_2^-$ anion obtained from DFT calculations is provided in Figure 11.3; the $\tilde{X}\ ^1A_g \leftarrow \tilde{X}\ ^2B_{3u}$ detachment transition corresponds to removal of an electron from the singly-occupied $5b_{3u}$ orbital. The higher-energy region of structure, shown in Figure 11.2b, spans eBEs from 18500 to 21000 cm$^{-1}$ and coincides with the previously reported $\tilde{a}\ ^3B_{3u} \leftarrow \tilde{X}\ ^2B_{3u}$ excited state band. This electronic transition corresponds to removal of an electron from the doubly-occupied $7a_g$ orbital in Fig. 11.3.

The singlet band (Fig. 11.2a) shows four well-defined features (X1-X4) that are observed over the entire range of photon energies used to produce the composite spectrum in Fig. 11.2a, and these are ascribed (as is typically the case in photoelectron spectra) to direct

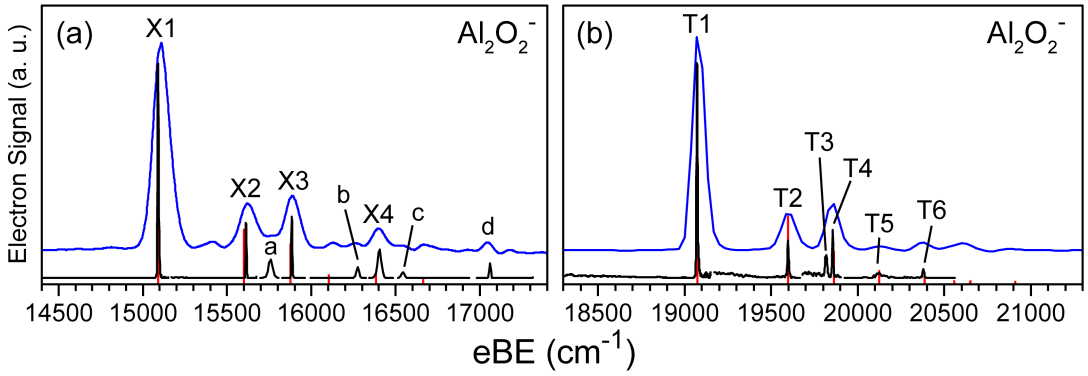


**Figure 11.2:** Cryo-SEVI spectra of $Al_2O_2^-$ showing detachment to the (a) singlet and (b) triplet states of neutral $Al_2O_2$. Blue traces are low-resolution overview scans taken with photon energies of 19154 and 23514 $cm^{-1}$ in panels (a) and (b), respectively. Black traces are high-resolution scans taken at variable photon energies, and the red stick spectra show the results of the FC simulations for detachment from the **2a** anion.

detachment transitions terminating in various vibrational levels of the $\tilde{X}\ ^1A_g$ ground state,

$$Al_2O_2^- + h\nu \rightarrow Al_2O_2 + e^-. \tag{11.2}$$

The binding energies of features X1-X4 are provided in Table 11.1. Peak X1 is assigned to the vibrational origin (the $0_0^0$ photodetachment transition), giving an electron affinity of EA = 1.8709(4) eV for the $Al_2O_2$ neutral cluster. For peaks X1-X3, sufficient intensity is maintained near-threshold to allow for low-eKE scans, resulting in peaks with $\sim$ 7 $cm^{-1}$ full-width at half-maximum (fwhm). Owing to the lower intensity of X4, its narrowest measurable peak width was 24 $cm^{-1}$ fwhm. Features X1-X4 show similar PADs (Fig. 11.4), with $\beta < 0$ over the range of photon energies used to construct Fig. 11.2a.

Peaks a-d in Fig. 11.2a exhibit notably different characteristics than peaks X1-X4. Figure 11.4 shows that the PADs of peaks a-d are characterized by positive values of $\beta$. Moreover, the relative intensities of peaks a-d demonstrate a complex dependence on photon energy. Figure 11.5 shows spectra taken at three different photon energies, illustrating the non-monotonic dependence of the intensity of peak a as a function of photon energy relative to those of two adjacent direct detachment features. At the lowest (15960 $cm^{-1}$) and highest (18866 $cm^{-1}$) photon energies shown, peak a is not observed. Between these energies, the intensity of peak a relative to X2 and X3 rises and falls (Figure 11.9), reaching a maximum intensity at around $h\nu$ = 16695 $cm^{-1}$. As can be seen in Fig. 11.9, similar behavior is observed for peak b, and both a and b are found to reach maximum intensities for photon energies which correspond to eKEs of around 900 $cm^{-1}$. Peaks c and d are less intense; hence, their dependence is more difficult to parse given the data shown in Fig. 11.9. However, we group them with peaks a and b based on their PADs.

The observed photon dependence suggests that transitions a-d result from autodetach-

**Table 11.1:** Peak positions (in $cm^{-1}$) for features observed in both electronic bands of the cryo-SEVI spectra of $Al_2O_2^-$. For each feature, the shift from the appropriate vibrational origin (X1 or T1) is provided in units of $cm^{-1}$. Vibrational assignments are provided for features attributed to direct detachment. Uncertainties in peak positions correspond to one standard deviation from a gaussian fit to the highest-resolution experimental trace for each feature.

| Peak | eBE | Shift | Assignment |
|---|---|---|---|
| | $\tilde{X}\ ^1A_g \leftarrow \tilde{X}\ ^2B_{3u}$ | | |
| X1 | 15090 (3) | 0 | $0_0^0$ |
| X2 | 15613 (3) | 523 | $2_0^1$ |
| a | 15753 (4) | 663 | |
| X3 | 15884 (3) | 794 | $1_0^1$ |
| b | 16276 (6) | 1186 | |
| X4 | 16405 (11) | 1315 | $1_0^1 2_0^1$ |
| c | 16544 (5) | 1454 | |
| d | 17062 (6) | 1971 | |
| | $\tilde{a}\ ^3B_{3u} \leftarrow \tilde{X}\ ^2B_{3u}$ | | |
| T1 | 19073 (3) | 0 | $0_0^0$ |
| T2 | 19599 (3) | 526 | $2_0^1$ |
| T3 | 19818 (6) | 745 | $5_0^1$ |
| T4 | 19856 (3) | 783 | $1_0^1$ |
| T5 | 20126 (20) | 1063 | $2_0^2$ |
| T6 | 20380 (4) | 1307 | $1_0^1 2_0^1$ |

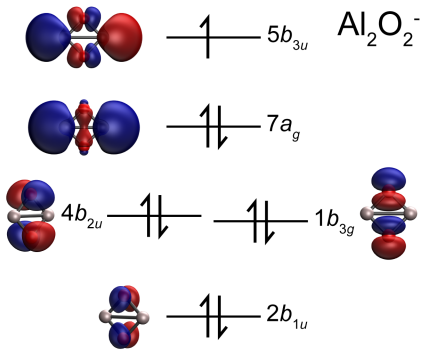


**Figure 11.3:** Molecular orbital diagram showing several of the highest-lying occupied orbitals of the $Al_2O_2^-$ anion as calculated at the B3LYP/aug-cc-pVTZ level.

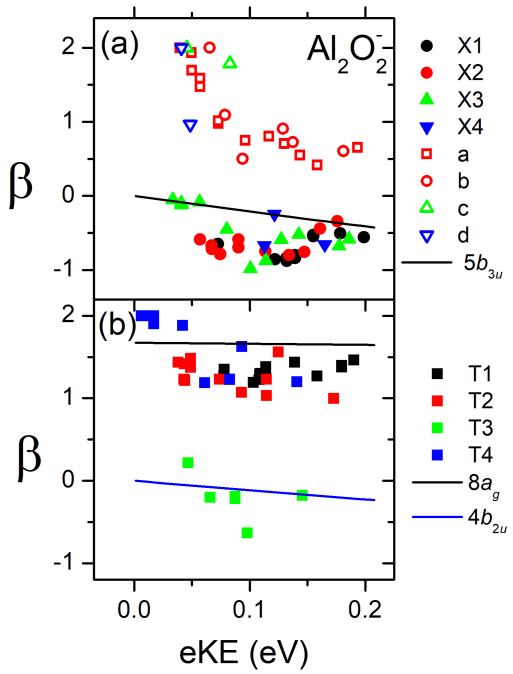


**Figure 11.4:** Anisotropy parameters for features observed in the (a) ground and (b) excited state bands of the $Al_2O_2^-$ cryo-SEVI spectrum. In both panels, the solid lines show the calculated anisotropy parameters for detachment from the indicated molecular orbitals of the $^2B_{3u}$ anion.

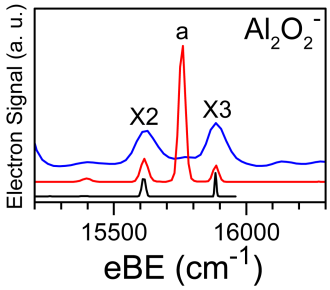


**Figure 11.5:** Cryo-SEVI scans taken at photon energies of 18866 $cm^{-1}$ (blue), 16695 $cm^{-1}$ (red), and 15960 $cm^{-1}$ (black), illustrating the non-monotonic dependence of the relative intensity of peak a in the detachment spectrum of $Al_2O_2^-$. All traces have been normalized to the peak intensity of feature X1.

ment,

$$Al_2O_2^- + h\nu \rightarrow Al_2O_2^{-*} \rightarrow Al_2O_2 + e^-, \tag{11.3}$$

where the incident photon induces a transition to an electronically excited state of the anion which can spontaneously eject an electron. This mechanism will be discussed in Section 11.5.1.

In the triplet band (Fig. 11.2b), the cryo-SEVI spectra again provide much clearer vibrational structure than was observed in prior work, showing a number of features (T1-T6) with typical peak widths of $\sim$ 8 $cm^{-1}$ fwhm. The electron binding energies of these features are provided in Table 11.1. The PADs of these features (Fig. 11.4b) show that with the exception of T3, all features exhibit positive anisotropies for the observed kinetic energies. All features (including T3) show straightforward dependences of their relative intensities on photon energy, and thus can be attributed to direct detachment transitions terminating in various vibrational levels of the triplet state of neutral $Al_2O_2$ (Eq. 11.2). The relative positions of the vibrational origin peaks, X1 and T1, give a term energy of 0.4938(4) eV for the $\tilde{a}\ ^3B_{3u}$ neutral state.

### 11.4.2 $Al_3O_3$

The full cryo-SEVI spectrum of $Al_3O_3^-$ is presented in Figure 11.6a, showing two regions of structure as in previous work.[456,457] The lower-eBE region, spanning eBEs of 16000 to 21000 $cm^{-1}$, was obtained in high resolution and is shown in more detail in Fig. 11.6b. This region was previously attributed to detachment from anion isomer **3a**. In this region, a number of vibronic transitions (A1-A16) are resolved, with typical peak widths of 8 $cm^{-1}$ fwhm. This electronic band shows a dominant progression with $\sim$ 760 $cm^{-1}$ spacing (A1-A4-A9-A15), in good agreement with the progression observed previously.[456,457] With the improvement in resolution afforded by cryo-SEVI, this progression is found to be modulated by several less intense patterns. All features show similar anisotropies, with $\beta > 0$ for all observed eKEs, and the PAD of feature A1 is provided in Figure 11.10a.

The higher-eBE region, spanning $\sim$ 22000 to 26000 $cm^{-1}$ of eBE and previously assigned as detachment from anion isomer **3b**, was not obtained in high resolution, due to the low-eKE noise at higher photon energies as well as the threshold behavior of features in this region. Figure 11.11 shows three scans taken at different photon energies; as can be seen, feature B1 does not become appreciably narrower with decreasing eKE, maintaining a peak width of 30 $cm^{-1}$ fwhm for eKEs of 600 $cm^{-1}$ and 300 $cm^{-1}$. Additionally, the two lower photon energies used in Fig. 11.11 result in non-negligible noise at low eKEs which overlaps with direct detachment features; this noise can also be seen in the high-eBE portion of the green trace in Fig. 11.6a. Regardless, the overview spectrum shown in Fig. 11.6a represents a significant improvement in resolution over previous results, showing the minor progressions which modulate the dominant structure resolved in prior experiments (B1-B4-B6).[456,457] As in the lower-eBE region, the sign of $\beta$ was found to be the same across the entire higher-eBE electronic band. The PAD for feature B1 is provided in Fig. 11.10a, showing perpendicular

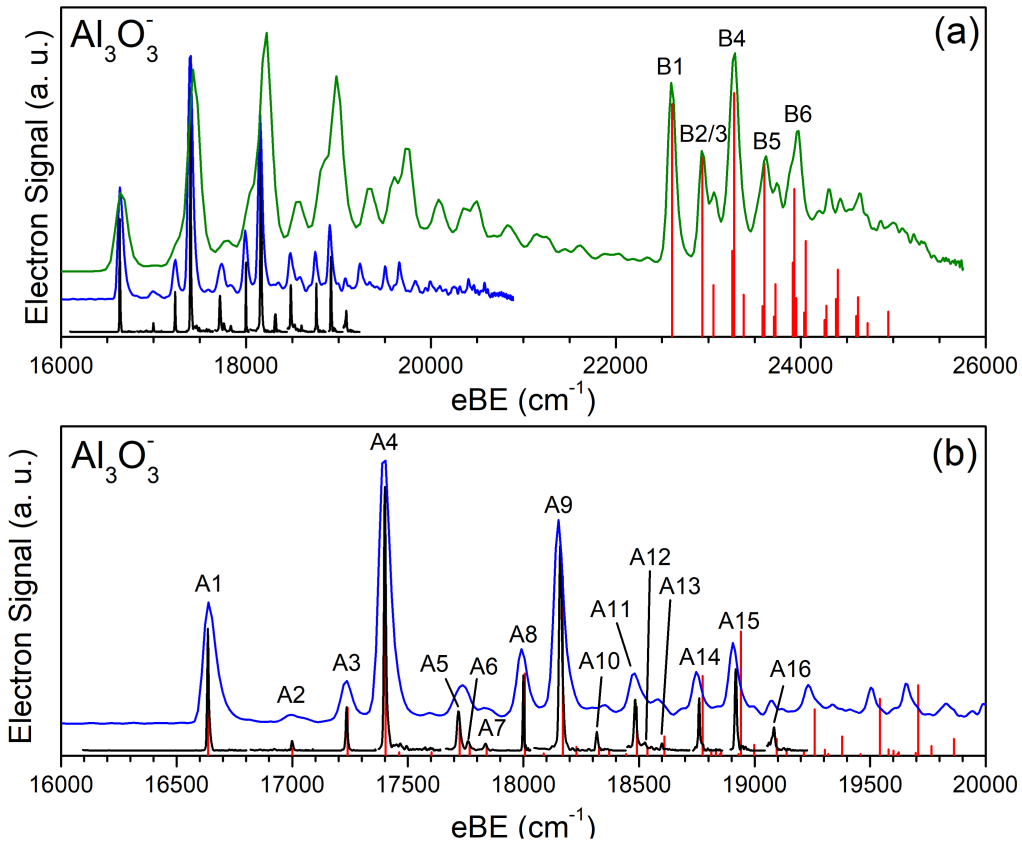


**Figure 11.6:** Cryo-SEVI spectra of $Al_3O_3^-$. **(a)** Full spectrum showing both regions of structure. The green and blue traces, taken with photon energies of 25757 and 20864 $cm^{-1}$, are lower-resolution overview scans for the higher-eBE and lower-eBE regions, respectively. The black traces are high-resolution scans taken with variable photon energies, and the red stick spectrum shows a Franck-Condon simulation for detachment from the **3b** anion isomer based on B3LYP/aug-cc-pVTZ results. **(b)** An expanded view of the lower-eBE region of structure, as well as a Franck-Condon simulation for detachment from the **3a** anion isomer shown as red sticks.

detachment ($\beta < 0$) for the photon energies used to construct Fig. 11.11. The peak positions of peaks B1-B6 and A1-A16 are summarized in Table 11.2.

To ascertain which of the two anion isomers corresponds to the global minimum of the anion, a temperature-dependence study was carried out on $Al_3O_3^-$. Ion temperature can be quantitatively controlled in the cryo-SEVI experiment by changing the temperature of the octupole trap; increasing the trap temperature gave the results shown in Figure 11.7 for detachment from $Al_3O_3^-$. In addition to increased peak widths leading to greater spectral congestion (as expected for detachment from rovibrationally hot ions), a clear enhancement of the higher-eBE region is observed as temperature is increased from 5 to 250 K. To quantify this enhancement, the integrated intensities for the two spectral regions were calculated, giving the fractional contribution to the total electron signal from each region of structure. This analysis shows that the higher-eBE region accounts for 31%, 44%, and 56% of the total electron signal in the T = 5, 175, and 250 K scans. This demonstrates that, in contrast to previous findings,[456] the isomer giving rise to transitions A1-A16 is the lowest-energy anion isomer. The structural assignment of the anions giving rise to each region of structure will be discussed in Section 11.5.2.

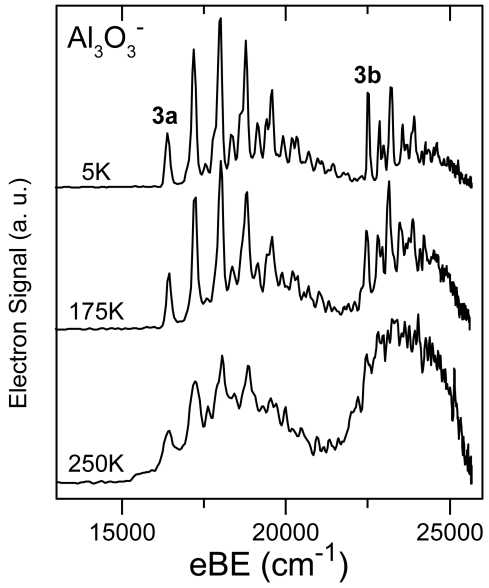


**Figure 11.7:** Detachment spectra of $Al_3O_3^-$ taken with a photon energy of 25663 $cm^{-1}$ at a number of trap temperatures.

**Table 11.2:** Peak positions (in $cm^{-1}$) and vibrational assignments for features observed in the cryo-SEVI spectra of $Al_3O_3^-$. For each feature, the shift from the appropriate vibrational origin (A1 or B1) is also provided in units of $cm^{-1}$, as is the sign of the anisotropy parameter $\beta$. Uncertainties in peak positions correspond to one standard deviation from a Gaussian fit to the highest-resolution experimental trace for each feature.

| Peak | eBE | Shift | Assignment | $\beta$ |
|---|---|---|---|---|
| A1 | 16636 (3) | 0 | $0_0^0$ | + |
| A2 | 16999 (3) | 264 | $5_0^1$ | + |
| A3 | 17235 (4) | 599 | $4_0^1$ | + |
| A4 | 17401 (4) | 765 | $3_0^1$ | + |
| A5 | 17719 (6) | 1084 | $1_0^1$ | + |
| A6 | 17762 (6) | 1126 | $3_0^1 5_0^1$ | + |
| A7 | 17836 (5) | 1200 | $4_0^2$ | + |
| A8 | 18000 (2) | 1364 | $3_0^1 4_0^1$ | + |
| A9 | 18161 (5) | 1525 | $3_0^2$ | + |
| A10 | 18318 (4) | 1682 | $1_0^1 4_0^1$ | + |
| A11 | 18484 (5) | 1848 | $1_0^1 3_0^1$ | + |
| A12 | 18525 (4) | 1889 | $3_0^2 5_0^1$ | + |
| A13 | 18599 (3) | 1963 | $3_0^1 4_0^2$ | + |
| A14 | 18760 (3) | 2124 | $3_0^2 4_0^1$ | + |
| A15 | 18918 (4) | 2283 | $3_0^3$ | + |
| A16 | 19082 (6) | 2446 | $1_0^1 3_0^1 4_0^1$ | + |
| B1 | 22607 (44) | 0 | $0_0^0$ | - |
| B2 | 22933 (38) | 326 | $5_0^1$ | - |
| B3 | 23062 (66) | 454 | $4_0^1$ | - |
| B4 | 23278 (59) | 671 | $2_0^1$ | - |
| B5 | 23619 (95) | 1012 | $2_0^1 5_0^1$ | - |
| B6 | 23951 (88) | 1344 | $2_0^2$ | - |

## 11.5 Discussion

### 11.5.1 $Al_2O_2$

#### Ground State Band

The calculated FC profile for the $\tilde{X}\ ^1A_g \leftarrow \tilde{X}\ ^2B_{3u}$ detachment transition of $Al_2O_2^-$, shown as red sticks in Figure 11.2a, provides excellent agreement for features X1-X4, yielding assignments for all four peaks attributed to direct detachment. These assignments are provided in Table 11.1. All of these transitions correspond to FC-allowed detachment transitions terminating in totally-symmetric ($a_g$) vibrational levels, yielding vibrational frequencies for both $a_g$-symmetric modes (Fig. 11.12) of the $\tilde{X}\ ^1A_g$ singlet state. These values are provided and compared to calculated values in Table 11.3. Transitions a-d are absent from the FC simulations, supporting our prior assertion that these do not arise from FC-allowed direct detachment.

The photoelectron angular distributions are an indication of the angular momentum composition of the outgoing electron, which in turn reflects the orbital from which the detached electron originated.[26] The calculated PAD for removal of an electron from the $5b_{3u}$ anion MO (Fig. 11.3) is shown as a solid black line in Fig. 11.4a, and agrees qualitatively with the anisotropies of features X1-X4, showing perpendicular detachment ($\beta < 0$) over the relevant range of eKEs. However, these PADs differ substantially from the anisotropies of features a-d, which exhibit predominantly parallel detachment ($\beta > 0$). This further emphasizes that these transitions have different electronic character than X1-X4.

The photon dependence of the relative intensities of transitions a-d (Figures 11.5 and 11.9) are a hallmark of autodetachment, wherein the incident photon results in an excitation of the anion rather than a direct transition to the neutral + free electron continuum (Eq. 11.2).

**Table 11.3:** Calculated and experimental values (in $cm^{-1}$) of the vibrational frequencies of anionic and neutral $Al_2O_2$, as well as their symmetries within the $D_{2h}$ point group.

| | | $\tilde{X}\ ^2B_{3u}$ | $\tilde{X}\ ^1A_g$ | | $\tilde{a}\ ^3B_{3u}$ | |
|---|---|---|---|---|---|---|
| mode | sym. | theo. | theo. | exp. | theo. | exp. |
| $\nu_1$ | $a_g$ | 736 | 787 | 794 (4) | 770 | 783 (4) |
| $\nu_2$ | $a_g$ | 476 | 504 | 523 (4) | 509 | 526 (5) |
| $\nu_3$ | $b_{1g}$ | 566 | 617 | 663 (5)[a] | 608 | |
| $\nu_4$ | $b_{1u}$ | 236 | 289 | | 261 | |
| $\nu_5$ | $b_{2u}$ | 683 | 751 | | 722 | 745 (7) |
| $\nu_6$ | $b_{3u}$ | 506 | 544 | | 720 | |

[a] This value assumes that the autodetachment transitions a-d terminate in vibrational states with odd quanta of excitation along $\nu_3$.

This initially excited anion state then detaches via a nonadiabatic transition as described in Eq. 11.3. The entire physical process leading to the observation of features a-d thus involves three states, denoted $\Psi_1^\alpha$, $\Psi_2^\alpha$, and $\Psi_3^\alpha$, where $\Psi_i^\alpha$ represents the vibronic wavefunction of the initial anion (1), excited anion (2), and final neutral state (3) participating in autodetachment transition $\alpha$ (a, b, c, d). Given the low temperatures of ions probed with cryo-SEVI,[326] $\Psi_1^\alpha$ is taken to correspond to the vibrational ground state ($0^0$) of the ground anion electronic state ($^2B_{3u}$) for all four transitions. In the following discussion, we will consider possible assignments for the $\Psi_2^\alpha$ and $\Psi_3^\alpha$ states involved in transitions a-d.

Transitions a, b, c, and d each lie $\sim 660$ cm$^{-1}$ above a FC-allowed transition (X1, X2, X3, and X4, respectively), suggesting that the final states $\Psi_3^\alpha$ differ from the neutral levels involved in X1-X4 by a single quantum of excitation in a vibrational mode with a frequency of $\sim 660$ cm$^{-1}$. As $Al_2O_2$ only possesses two totally-symmetric modes (Fig. 11.12), both of which participate in the FC-allowed transitions X1-X4, this third mode must be non-totally-symmetric within the $D_{2h}$ point group. Given the calculated frequencies in Table 11.3 for the singlet state of $Al_2O_2$, the $b_{1g}$-symmetric $\nu_3$ mode is the most likely candidate. If this is the case, then the neutral levels $\Psi_3^\alpha$ involved in transitions a, b, c, and d correspond to the $3^1$, $2^1 3^1$, $1^1 3^1$, and $1^1 2^1 3^1$ vibrational levels, respectively, of the $\tilde{X}\ ^1A_g$ neutral, giving a frequency of 663(5) cm$^{-1}$ for $\nu_3$ (Table 11.3).

The photon energy at which the lowest-energy autodetachment transition reaches its maximum intensity (Figure 11.9) suggests that the autodetaching anion state has an excitation energy of around 2.0 eV. According to the MRMP2 treatment of the $Al_2O_2^-$ anion carried out by Sarker and coworkers,[462] the three lowest-energy anion excited states lie in this region, suggesting that the $^2A_g$ (1.81 eV), $^2B_{2u}$ (2.08 eV), and $^2B_{1u}$ (2.10 eV) states are candidates for $\Psi_2^\alpha$. The $^2A_g$ excitation, formed by excitation of an electron from the $7a_g$ orbital to the $5b_{3u}$ orbital in Fig. 11.3, is the only candidate for which symmetry permits a nonzero oscillator strength for photoexcitation of the $\tilde{X}\ ^2B_{3u}$ anion ground state, suggesting that this is the state from which autodetachment occurs. In this case, autodetachment to the closed-shell singlet would involve a two-electron transition, with one electron moving from the $5b_{3u}$ orbital to the $7a_g$ orbital resulting in ejection of the other $5b_{3u}$ electron. This sort of two-electron mechanism is indicative of electronically-driven autodetachment, where the coupling to the continuum state occurs via electron correlation terms in the Hamiltonian. Similar mechanisms can be used to understand autodetachment from a variety of other systems, such as the metastable $5d6s6d$ state of the $Ba^-$ atomic anion[51] as well as autoionization of the $^{1,3}\Delta_u$ Rydberg states of $N_2$.[50] In both of these cases, the ejection of an electron occurs simultaneously with relaxation of an electron in a higher-lying orbital, and the loss in internal electronic energy is converted into the kinetic energy of the outgoing electron.

### Excited State Band

Good agreement between the reported FC simulations and experiment is also found for the $\tilde{a}\ ^3B_{3u} \leftarrow \tilde{X}\ ^2B_{3u}$ electronic band of $Al_2O_2^-$ shown in Fig. 11.2b, providing assignment of all features – with the exception of T3 – to FC-allowed transitions. Again, frequencies for

both $a_g$-symmetric vibrational modes are extracted, and are provided in Table 11.3 alongside the B3LYP/aug-cc-pVTZ results. The PADs of these features are in good agreement with the calculated results for detachment from the $7a_g$ orbital in Fig. 11.3, as shown by the solid black line in Fig. 11.4b.

Transition T3 is notably absent from the FC simulation for the triplet band of the $Al_2O_2^-$ cryo-SEVI spectrum. This transition lies only $\sim 40$ cm$^{-1}$ below the $\nu_1$ fundamental (T4), suggesting that it involves excitation of either $\nu_5$ or $\nu_6$ (Fig. 11.12) which have calculated frequencies lying $\sim 50$ cm$^{-1}$ below that of $\nu_1$ at the B3LYP/aug-cc-pVTZ level of theory (see Table 11.3). As their calculated values are within several cm$^{-1}$ of each other (722 and 720 cm$^{-1}$ for $\nu_5$ and $\nu_6$, respectively), further consideration is needed to definitively determine which mode participates in the cryo-SEVI spectrum. These modes have symmetries of $b_{2u}$ and $b_{3u}$, respectively, and thus their involvement in the photoelectron spectrum can only occur through vibronic coupling with a Franck-Condon allowed vibrational level (such as the vibrational ground state) within another electronic state.

For vibronic coupling to occur between two states $a$ and $b$, the direct product of their overall vibronic symmetries, $(\Gamma^a_{elec} \otimes \Gamma^a_{vib}) \otimes (\Gamma^b_{elec} \otimes \Gamma^b_{vib})$ where $\Gamma^x_{elec}$ and $\Gamma^x_{vib}$ are the electronic and vibrational symmetries of state $x$, must contain the totally symmetric representation within the relevant molecular point group.[40] In the current case, this gives two possibilities for electronic symmetries of the state coupled to the $\tilde{a}\ ^3B_{3u}$ triplet which could give rise to T3 in the spectrum. If T3 corresponds to the $5_0^1$ transition, then this excited state must have $B_{1g}$ symmetry, whereas the $6_0^1$ transition would require coupling to an $A_g$-symmetric state. The MRMP2 calculations carried out by Sarker and coworkers[462] found that the lowest-lying triplet $A_g$ and $B_{1g}$ states lie 6.75 and 3.23 eV, respectively, above the $\tilde{a}\ ^3B_{3u}$ triplet. Given that the extent of vibronic coupling decreases with increasing energy separation, we assign peak T3 as the $5_0^1$ transition, which appears through Herzberg-Teller coupling to the excited $^3B_{1g}$ state.

The observation of FC-forbidden levels through Herzberg-Teller coupling has been seen in a number of cryo-SEVI spectra, where the PAD is often a key indicator of vibronic coupling.[32,34,37,38] The assignment of T3 as arising through this coupling mechanism suggests that the electronic character of this transition – reflected in its PAD – should match that expected for detachment to the excited $^3B_{1g}$ neutral state. A TDDFT calculation was performed at the B3LYP/aug-cc-pVTZ level to identify the orbital transition giving rise to the lowest-energy state of this symmetry (Table 11.9), finding that this $^3B_{1g}$ state can be formed from the anion ground state by removal of an electron from the $4b_{2u}$ orbital shown in Figure 11.3. The calculated PAD for detachment from this orbital yields the solid blue line shown in Fig. 11.4b, demonstrating perpendicular detachment over the relevant eKE range. This agrees with the observed PAD for feature T3, confirming our assignment of this transition as arising from vibronic coupling to the $^3B_{1g}$ state.

### 11.5.2 $Al_3O_3$

**Lower-eBE Region**

The lower-eBE region of the $Al_3O_3^-$ photoelectron spectrum was obtained in high resolution, as shown in Fig. 11.6b. This region of structure was previously attributed to detachment from anion isomer **3a**, and a FC simulation for detachment from this structure (shown as red sticks in Fig. 11.6b) indeed provides good agreement with the experimental spectrum. Additionally, the position of feature A1 gives an EA of 2.0626(5) eV, in excellent agreement with the B3LYP/aug-cc-pVTZ value of 2.078 eV for neutral isomer **3a**. Thus, as in prior works, this region of the $Al_3O_3^-$ spectrum is attributed to detachment from the **3a** "kite" anion. This isomer can be understood as derived from the **2a** rhombic structure of $Al_2O_2^-$, where the added AlO unit connects end-on by the O to one of the ring Al atoms forming the "tail" of the kite.

The good agreement between the cryo-SEVI spectrum and the calculated FC profile for the kite anion isomer provides assignment of all resolved peaks (A1-A16) as FC-allowed detachment to totally-symmetric vibrational levels of the neutral. The dominant structure (A1-A4-A9-A15) is assigned as a progression along $\nu_3$, which corresponds to a totally-symmetric (in $C_{2v}$) distortion of the rhombic substructure of the kite isomer (Fig. 11.13). The shift of peak A4 relative to A1 gives a frequency of 765(5) $cm^{-1}$ for this mode, which is consistent with the $\sim 770$ $cm^{-1}$ progression observed previously.[456,457] In addition to this dominant progression, several other, less intense patterns are resolved, enabling extraction of frequencies for $\nu_2$, $\nu_4$, and $\nu_5$; these values are provided in Table 11.4 and compared to the B3LYP/aug-cc-pVTZ results.

The particularly high FC activity of the $\nu_3$ mode may be understood by considering the highest-occupied molecular orbital (HOMO) for the kite anion. As can be seen in Figure 11.8, the anion HOMO for isomer **3a** is an orbital with $a_1$-symmetry primarily localized on the ring Al atom that does not bond to the "tail" of the kite, and possesses some antibonding character resulting in longer Al-O bond lengths for that part of the anion geometry. These

**Table 11.4:** Calculated and experimental values (in $cm^{-1}$) of the vibrational frequencies of both neutral isomers of $Al_3O_3$ probed in the current work. For both isomers, all extracted frequencies correspond to totally symmetric ($a_1$) modes within the $C_{2v}$ point group.

| | **3a**, $\tilde{X}\ ^2A_1$ | | **3b**, $\tilde{X}\ ^2B_2$ | |
|---|---|---|---|---|
| mode | theo. | exp. | theo. | exp. |
| $\nu_1$ | 1073 | 1084 (7) | 726 | |
| $\nu_2$ | 802 | | 644 | 670 (70) |
| $\nu_3$ | 746 | 765 (5) | 573 | |
| $\nu_4$ | 586 | 599 (5) | 432 | 450 (80) |
| $\nu_5$ | 343 | 364 (5) | 246 | 330 (60) |

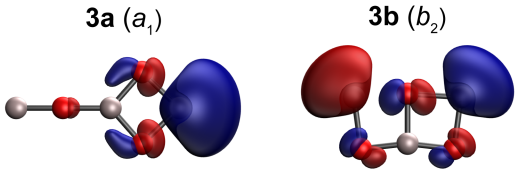


**Figure 11.8:** Highest-occupied molecular orbitals for the **3a** (left) and **3b** (right) isomers of the $Al_3O_3^-$ anion, as well as their symmetries within the $C_{2v}$ point group.

Al-O bond lengths decrease by 0.1 Å following detachment from the anion to the neutral ground state (1.86 and 1.76 Å for anionic and neutral **3a**, respectively), owing to the removal of an electron from this orbital.

The calculated PAD for detachment from this orbital was also found to be consistent with the observed anisotropies of features A1-A16 (Fig. 11.10a). A partial wave analysis of the PAD calculation (Table 11.10) demonstrates that at low eKEs, *s*-wave detachment dominates, resulting in near-isotropic detachment. At higher eKEs ($\sim$ 2 eV), *p*-wave detachment dominates, giving the parallel detachment ($\beta > 0$) observed experimentally for features A1-A16. The high-eKE partial wave analysis agrees with the expected PAD based on the mixed-*sp* model,[26] which considers the molecular orbital as containing primarily *s*- and *p*-character resulting in various contributions of outgoing *s*-, *p*-, and *d*-wave electrons. For detachment from an $a_1$-symmetric molecular orbital at moderate eKEs, parallel detachment is expected, corresponding to positive $\beta$-parameters associated with predominantly *p*-wave detachment.

### Higher-eBE Region

Due to low-eKE noise present for detachment with higher photon energies than those used in Fig. 11.6b and the threshold behavior demonstrated in Fig. 11.11, as well as increasing spectral congestion at higher binding energies, the higher-eBE region of structure of the $Al_3O_3^-$ photoelectron spectrum was not obtained in as high resolution as the lower-eBE region. Regardless, the overview spectrum in Fig. 11.6a (where the low-eKE noise does not overlap with the dominant vibrational structure) shows substantial improvement in resolution for this region of the spectrum, and provides excellent agreement with the FC profile for detachment from anion isomer **3b**. The first intense feature in this part of the spectrum (B1) gives an EA of 2.792(3) eV, which is in reasonable agreement with the B3LYP/aug-cc-pVTZ value of 2.589 eV for neutral isomer **3b**. Thus, we attribute peaks B1-B6 as arising from anion isomer **3b**, as in prior work. This structure can be understood as the result of side-on addition of an AlO unit to the rhombic **2a** geometry of $Al_2O_2^-$, resulting in a bicyclic structure with two additional Al-O bonds.

The agreement between the calculated FC profile in Fig. 11.6a and the experimental spectrum provides vibrational assignments of peaks B1-B6 as FC-allowed transitions terminating in totally-symmetric vibrational levels of neutral isomer **3b**. The dominant progression re-

solved in prior work,[456,457] B1-B4-B6, is assigned as a progression along the $\nu_2$ mode (Fig. 11.13), which corresponds to the stretching motion of the Al-O bonds forming the "page" edges of the book geometry. The B1-B4 peak spacing gives a frequency of 760(70) $cm^{-1}$ for this mode; while this is closer to the calculated value of the $\nu_1$ frequency for this neutral state, $\nu_1$ was found to have very little FC activity in the simulations of Fig. 11.6a. The $\nu_4$ and $\nu_5$ fundamentals are also observed, giving the frequencies provided in Table 11.4.

As was the case for the lower-eBE region of structure, the dominant progression in the detachment spectrum of isomer **3b** can be understood by considering the anion HOMO from which an electron is removed to form the doublet neutral (Fig. 11.8). While slightly more delocalized than the HOMO for anion isomer **3a**, the corner Al atoms on the "pages" of the book possess significantly more electron density than the other atoms, and again there is some Al-O antibonding character. Removal of an electron from this $b_2$-symmetric orbital results in a decrease in the Al-O bond length on the outer edge of the "pages", from 1.87 Å in the anion to 1.80 Å in the neutral. This geometry change results in particularly high FC activity of the $\nu_2$ mode pictured in Fig. 11.13.

The experimental PADs of features B1-B6 are consistent with this structural assignment (Fig. 11.10a). The partial wave analysis in Table 11.10 shows that at low eKEs, *s*-wave detachment dominates, and the *d*-wave contribution increases as eKE increases. This is again consistent with the mixed-*sp* model of photoelectron angular distributions,[26] which dictates that detachment from a $b_2$-symmetric orbital should primarily result in perpendicular detachment corresponding to outgoing electrons with even $\ell$ to give negative $\beta$ parameters.

From the partial wave analysis for the two isomers, it would be expected that B1-B6 would be able to be observed in higher resolution than is ultimately achieved, as isomer **3b** should undergo predominantly *s*-wave detachment at lower eKEs, with a larger $f_0$ at an eKE of 0.001 eV than the **3a** isomer ($f_0$ = 0.868 and 0.993 for **3a** and **3b**, respectively). However, while features B1-B6 do maintain intensity near threshold, the features do not become appreciably narrower, with nearly identical peak widths of $\sim$ 30 $cm^{-1}$ fwhm at eKEs of $\sim$ 600 and 300 $cm^{-1}$ (Fig. 11.11). The cause of the limited attainable resolution for detachment from the book isomer is somewhat unclear given the current results, though some speculation is possible.

One possibility is that the book isomer may be able to isomerize to the lower-lying kite isomer, resulting in a short-lived neutral which couples to the dense manifold of **3a** vibrational states, resulting in broadening of the cryo-SEVI peaks. To consider this possibility, a transition state calculation was performed in the neutral doublet surface of $Al_3O_3$ to identify a saddle point which connects isomers **3a** and **3b**. From this, the HPC algorithm[463,464] was used to calculate the intrinsic reaction path, giving the potential energy curve provided in Fig. 11.14. These calculations show that the saddle point for the book/kite isomerization of neutral $Al_3O_3$ lies much closer in geometry and energy to the book isomer, with the transition state lying 110 meV above isomer **3b**. This could potentially result in a relatively short-lived neutral isomer **3b** that is capable of isomerization to isomer **3a** following its formation by photodetachment from the corresponding $Al_3O_3^-$ anion isomer, leading to contributions from a range of neutral levels in the observed detachment transitions. It should be emphasized

that this is a highly speculative argument; a full theoretical treatment aimed at determining the relationship between isomerization and the observed near-threshold behavior is beyond the scope of the current work.

### $Al_3O_3^{-/0}$ Energetics

Previous theoretical work on the $Al_3O_3^-$ anionic cluster have suggested that both isomers, **3a** and **3b** in Fig. 11.1, contribute to the photoelectron spectrum and are quite close in energy.[457,460,461] In the work of Martinez and coworkers,[460] the book was found to lie 30 meV lower than the kite isomer at the B3LYP/6-311+G(2d) level, and the energy difference increased to 200 meV with a QCISD treatment. While these energies were not corrected for zero-point energies (ZPEs), the frequencies of both isomers published in a subsequent paper[461] show that accounting for ZPEs does not result in a different energetic ordering, though it does decrease the energy difference to 21 meV at the B3LYP/6-311+G(2d) level. The energy ordering was found to switch for the neutral cluster, with the kite lying $\sim 0.5$ eV below the book. DFT calculations were also reported by Meloni and coworkers,[457] who again found that isomer **3b** was lower in energy, giving a ZPE-corrected energy of 51 meV for isomer **3a** at the B3LYP/cc-pVTZ level.

The assignment of isomer **3b** as the global anion minimum was consistent with the temperature-dependence of the photoelectron spectrum determined by Wu *et al.*,[456] whose results suggested that increasing the temperature increased the intensity of the region attributed to detachment from anion isomer **3a**. However, the spectra shown in Figure 11.7 directly contradict this finding, showing that increasing ion temperature results in an enhancement of signal in the higher-eBE region attributed to detachment from anion isomer **3b**. This disagreement stems from the method used to control ion temperature in the current experiments versus the analysis of Wu *et al.*, who assumed a straightforward relationship between the timing of the laser pulse relative to the carrier gas in their laser ablation source and the resultant ion temperature. In cryo-SEVI, ion temperature can be controlled directly by adjusting the cryostat connected to the ion trap, changing the temperature to which trapped ions thermalize through collisions with the buffer gas. Thus, the results in Figure 11.7 can be taken to represent the true temperature-dependence of the $Al_3O_3^-$ photoelectron spectrum.

In the current work, the same functional used in previous DFT treatments (B3LYP) was used with the aug-cc-pVTZ basis set. The B3LYP/aug-cc-pVTZ method gives a different

**Table 11.5:** Relative zero-point corrected energies of the $Al_3O_3^-$ isomers, in eV, calculated using the B3LYP functional with the indicated basis sets.

| | aug-cc-pVDZ | aug-cc-pVTZ | aug-cc-pVQZ |
|---|---|---|---|
| **3a** | 0.138 | 0.000 | 0.000 |
| **3b** | 0.000 | 0.005 | 0.011 |

isomeric energy ordering, with isomer **3a** lying only 5 meV lower when accounting for zero-point effects. This result illustrates that this system, specifically the relative energies of the $Al_3O_3^-$ anion isomers, is highly sensitive to basis set choice. In particular, prior treatments used basis sets without diffuse functions, which is a key component of successful quantum chemical calculations on molecular anions, where the excess charge can result in relatively diffuse molecular orbitals. To further explore the basis set dependence of the isomeric energies, additional geometry optimizations and frequency calculations were carried out using the B3LYP functional with the aug-cc-pVDZ and aug-cc-pVQZ basis sets, giving the zero-point corrected energies shown in Table 11.5. While the aug-cc-pVDZ results agree with prior work that anion isomer **3b** is lower in energy, isomer **3a** becomes increasingly stable with the use of larger basis sets. Thus, given the temperature dependence observed in Figure 11.7, it is clear that anion isomer **3a** is, in fact, the global minimum structure for the $Al_3O_3^-$ cluster. It should be noted that the structural assignments based on FC profiles and electron affinities agree with prior results; the current assessment of the $Al_3O_3^-$ photoelectron spectrum only differs in the assignment of which isomer is more stable.

Given the small energy difference between anions **3a** and **3b** implied by the experimental observation of both isomers despite low ion temperatures, the difference between the electron affinities of neutral isomers **3a** and **3b** can be taken as largely arising due to the relative stability of neutral isomer **3a**, giving an upper bound of 0.729 eV for the energy of neutral isomer **3b** relative to **3a**. This is in fair agreement with the calculated value of 0.506 eV for this energy difference at the B3LYP/aug-cc-pVTZ level. Thus, the current work enables structural assignment of two charge states of $Al_3O_3$, with isomer **3a** being the lowest-energy structure for both anion and neutral. Further, the potential for isomerization explored in the previous section and Fig. 11.14 demonstrate that the neutral book isomer is quite close in geometry to the book/kite transition state, which may result in relatively facile isomerization following photodetachment to form neutral isomer **3b**.

## 11.6 Conclusions

High-resolution anion photoelectron spectra of two aluminum suboxide clusters, $Al_2O_2^-$ and $Al_3O_3^-$, are obtained using slow electron velocity-map imaging of cryogenically-cooled anions. In both cases, the resultant spectra show improved resolution over prior results, and the observed vibrational structure is consistent with FC simulations based on B3LYP/aug-cc-pVTZ calculations, yielding a number of vibrational frequencies for neutral $Al_2O_2$ and $Al_3O_3$.

The $Al_2O_2^-$ anion is assigned, as in prior studies, to the $D_{2h}$ rhombic geometry, which has been identified as a structural motif in larger aluminum oxide clusters. Detachment to two states of neutral $Al_2O_2$ is observed in high resolution. The ground state band, which corresponds to detachment to form a closed-shell singlet, shows several transitions that are attributed to autodetachment, and tentative assignments of the anion excitation and final neutral states are provided. The triplet band of the cryo-SEVI spectrum shows evidence for

Herzberg-Teller coupling between excited triplet states of the neutral cluster resulting in the appearance of nominally FC-forbidden levels.

As in previously reported photoelectron spectra, the cryo-SEVI spectra of $Al_3O_3^-$ show evidence of two coexisting anion isomers, identified as the kite and book geometries. While the observation of both isomers under the cold conditions of the cryo-SEVI experiment reaffirms the previously noted small energy differences between these two isomers, a controlled temperature study as well as B3LYP/aug-cc-pVTZ calculations establish the kite isomer as the global minimum of the anion. This is in contrast to previous experimental and theoretical work which found that the book isomer was lower in energy. The cause of the experimental discrepancy is attributed to the indirect method used to control ion temperature in previous experiments. The theoretical discrepancy likely arises due to the use of non-augmented basis sets in prior work, highlighting the importance of careful consideration of the theoretical treatments of gas phase metal oxide clusters, particularly in cases where multiple low-lying isomers are expected.

## 11.7 Supplementary Figures and Tables

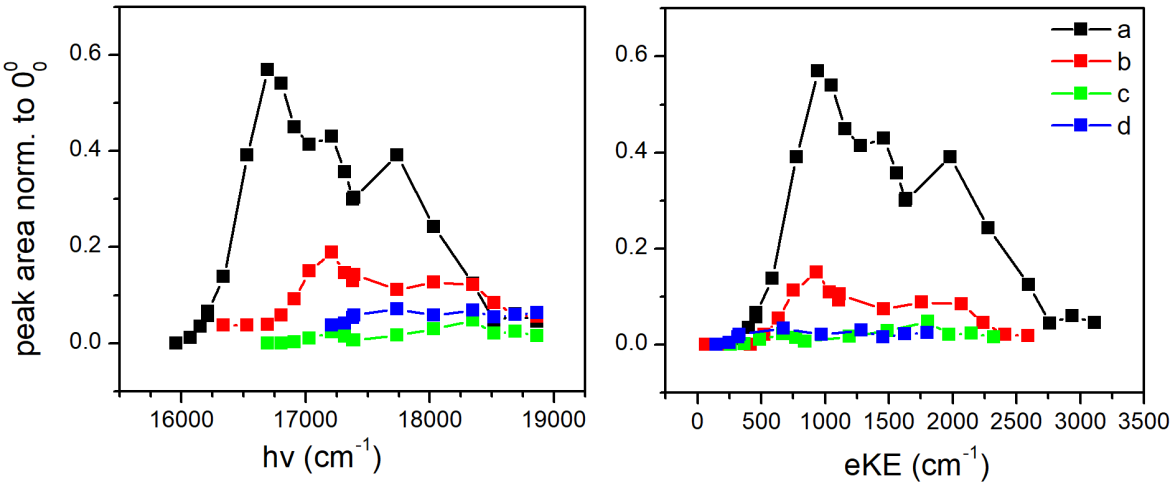


**Figure 11.9:** Peak areas of features a-d in the cryo-SEVI spectrum of $Al_2O_2^-$ normalized to the area of peak X1 as a function of (a) photon energy and (b) eKE.

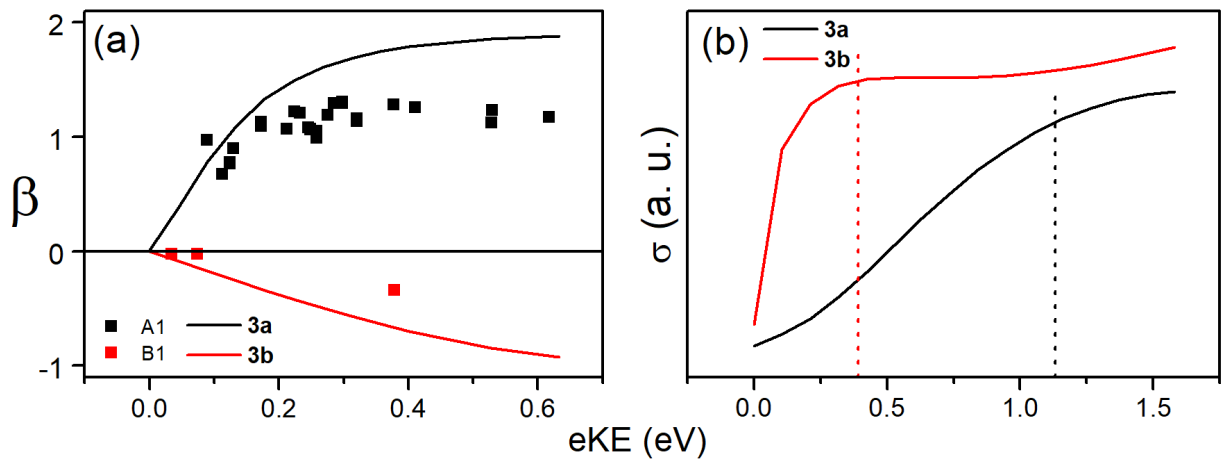


**Figure 11.10:** Results of the application of the code of Liu and Ning[64] to detachment from the HOMOs of the two different isomers of $Al_3O_3^-$. **(a)** Calculated anisotropy parameters for low-eKE detachment from the book and kite anion HOMOs are shown as solid red and black lines, respectively, and compared to the experimental PADs for the $0_0^0$ transition attributed to each (A1 and B1 for kite and book, respectively). **(b)** Calculated total detachment cross sections for the book (red) and kite (black) anion isomers. The dashed vertical lines show the eKEs of peaks A1 and B1 (black and red, respectively) at the photon energy used to acquire the green trace in Figure 11.6.

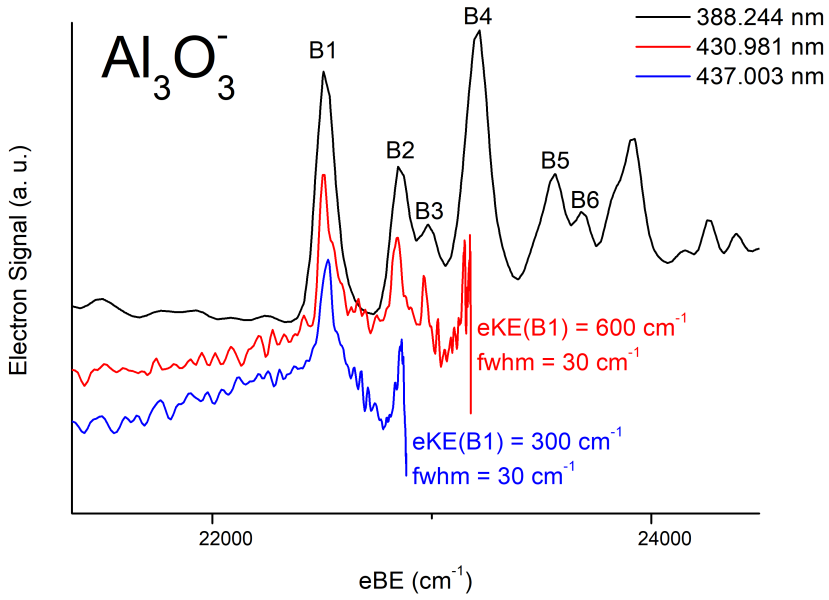


**Figure 11.11:** Three cryo-SEVI scans of $Al_3O_3^-$ focusing on the higher-eBE region of the photoelectron spectrum. The eKEs and peak widths for the vibrational origin in the two lower-energy scans are provided, demonstrating that decreasing the photon energy does not result in narrower features.

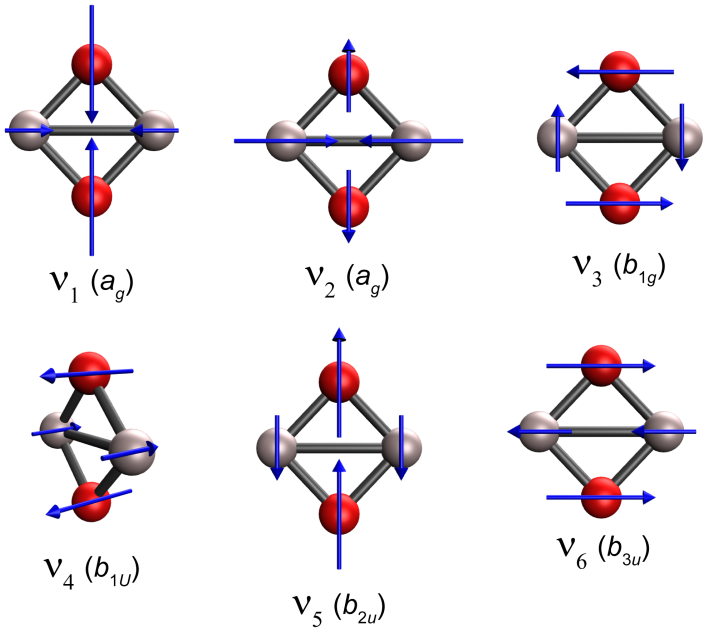


**Figure 11.12:** Vibrational modes of $Al_2O_2$, as well as their symmetries within the $D_{2h}$ point group.

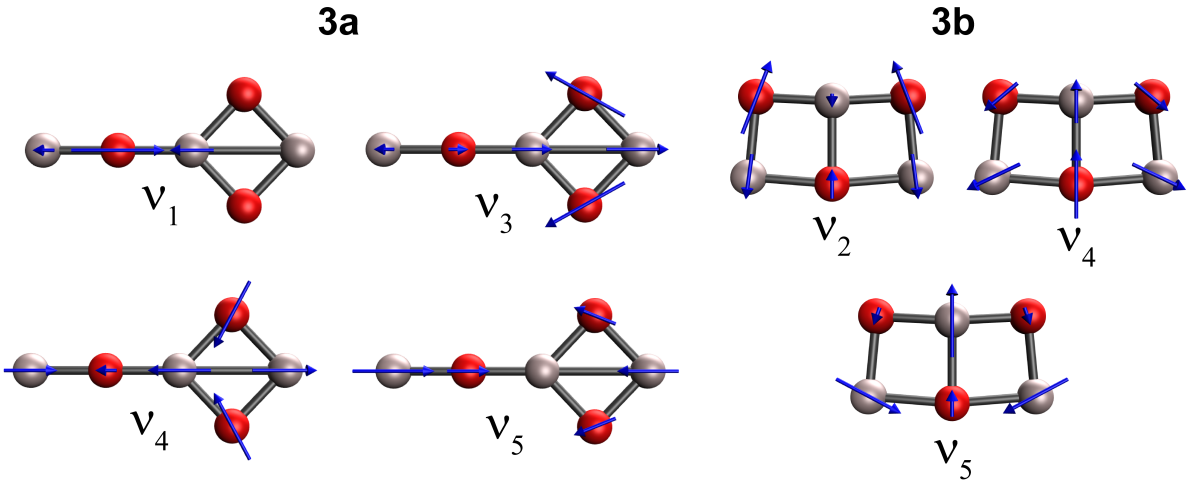


**Figure 11.13:** Vibrational frequencies of the neutral $Al_3O_3$ **3a** (left) and **3b** (right) isomers invoked in the vibrational assignments of the $Al_3O_3^-$ cryo-SEVI spectrum. All modes have $a_1$ symmetry within the $C_{2v}$ point group.

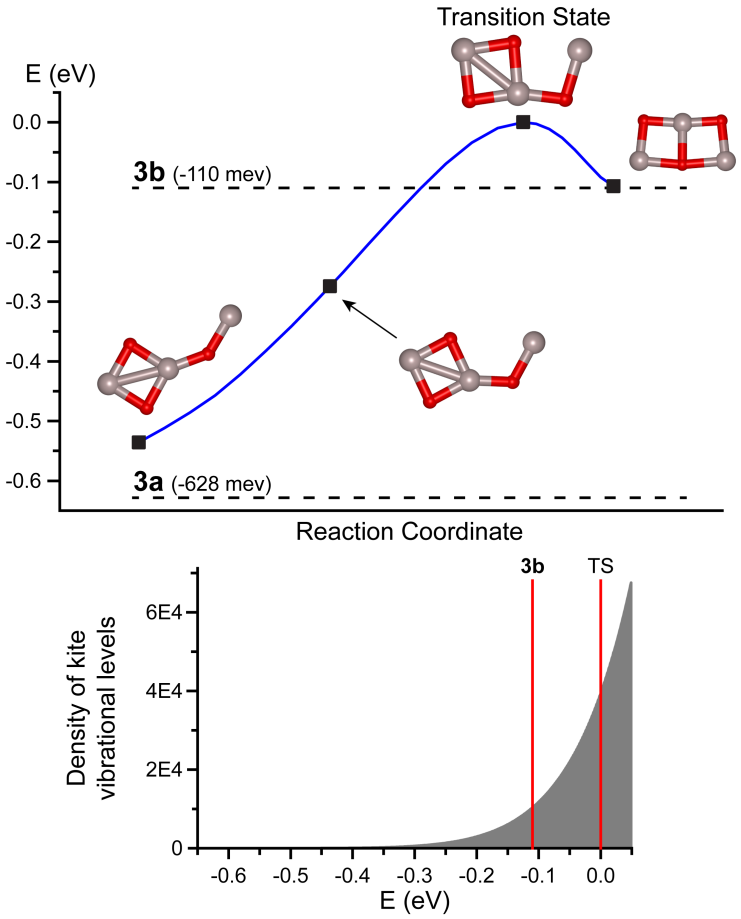


**Figure 11.14:** The top panel shows the intrinsic reaction coordinate path calculated for the book/kite isomerization of neutral $Al_3O_3$. The transition state geometry is pictured, as are several intermediate geometries. The dashed lines show the (non-ZPE corrected) energies of neutral isomers **3a** and **3b** relative to the transition state. The bottom panel shows the density of **3a** vibrational states using the same energy scale. Vertical lines are used to indicate the energies of the neutral **3b** isomer and the transition state.

**Table 11.6:** Cartesian coordinates (in Å) and relative energies (in eV) for the anion and neutral states of $Al_2O_2$ involved in this work calculated at the B3LYP/aug-cc-pVTZ level. Energies are relative to the anion ground state and are zero-point corrected.

| $\tilde{X}\ ^2B_{3u}$ (**2a** anion, $D_{2h}$) | | | **E = 0.000** |
|---|---|---|---|
| Al | 1.246489 | 0.000000 | 0.000000 |
| O | 0.000000 | 1.276998 | 0.000000 |
| O | 0.000000 | -1.276998 | 0.000000 |
| Al | -1.246489 | 0.000000 | 0.000000 |

| $\tilde{X}\ ^1A_g$ (**2a** neutral, $D_{2h}$) | | | **E = 2.189** |
|---|---|---|---|
| Al | 1.213801 | 0.000000 | 0.000000 |
| O | 0.000000 | 1.273649 | 0.000000 |
| O | 0.000000 | -1.273649 | 0.000000 |
| Al | -1.213801 | 0.000000 | 0.000000 |

| $\tilde{a}\ ^3B_{3u}$ (**2a** neutral, $D_{2h}$) | | | **E = 2.447** |
|---|---|---|---|
| Al | 1.211351 | 0.000000 | 0.000000 |
| O | 0.000000 | 1.279760 | 0.000000 |
| O | 0.000000 | -1.279760 | 0.000000 |
| Al | -1.211351 | 0.000000 | 0.000000 |

**Table 11.7:** Cartesian coordinates (in Å) and relative energies (in eV) for the lowest-energy anion and neutral states of the book and kite isomers of $Al_3O_3$, calculated at the B3LYP/aug-cc-pVTZ level. Energies are relative to the lowest-energy anion state and are zero-point corrected.

$\tilde{X}\ ^1A_1$ (**3a** anion, $C_{2v}$) **E = 0.000**

| | | | |
|---|---|---|---|
| Al | 0.000000 | 0.000000 | -0.122474 |
| Al | 0.000000 | 0.000000 | -2.600977 |
| O | 0.000000 | 1.285031 | -1.258241 |
| O | 0.000000 | -1.285031 | -1.258241 |
| O | 0.000000 | 0.000000 | 1.602762 |
| Al | 0.000000 | 0.000000 | 3.285740 |

$\tilde{X}\ ^1A_1$ (**3b** anion, $C_{2v}$) **E = 0.005**

| | | | |
|---|---|---|---|
| Al | 0.000000 | 0.000000 | 0.868074 |
| Al | 0.000000 | 1.930638 | -0.798390 |
| Al | 0.000000 | -1.930638 | -0.798390 |
| O | 0.000000 | 1.684254 | 1.051909 |
| O | 0.000000 | 0.000000 | -0.919668 |
| O | 0.000000 | -1.684254 | 1.051909 |

$\tilde{X}\ ^2A_1$ (**3a** neutral, $C_{2v}$) **E = 2.078**

| | | | |
|---|---|---|---|
| Al | 0.000000 | 0.000000 | -0.110949 |
| Al | 0.000000 | 0.000000 | -2.524745 |
| O | 0.000000 | 1.272736 | -1.312032 |
| O | 0.000000 | -1.272736 | -1.312032 |
| O | 0.000000 | 0.000000 | 1.570316 |
| Al | 0.000000 | 0.000000 | 3.284154 |

$\tilde{X}\ ^2B_2$ (**3b** neutral, $C_{2v}$) **E = 2.584**

| | | | |
|---|---|---|---|
| Al | 0.000000 | 0.000000 | 0.916806 |
| Al | 0.000000 | 1.866137 | -0.786967 |
| Al | 0.000000 | -1.866137 | -0.786967 |
| O | 0.000000 | 1.693535 | 1.004235 |
| O | 0.000000 | 0.000000 | -0.940637 |
| O | 0.000000 | -1.693535 | 1.004235 |

**Table 11.8:** B3LYP/aug-cc-pVTZ harmonic frequencies (in $cm^{-1}$) for the anionic and neutral states of both isomers of $Al_3O_3$. The symmetries of each mode within the $C_{2v}$ point group are also provided.

| | | **3a** | | **3b** | |
|---|---|---|---|---|---|
| | | $\tilde{X}\ ^1A_1$ | $\tilde{X}\ ^2A_1$ | $\tilde{X}\ ^1A_1$ | $\tilde{X}\ ^2B_2$ |
| $\nu_1$ | $a_1$ | 1051 | 1073 | 739 | 726 |
| $\nu_2$ | $a_1$ | 843 | 802 | 682 | 644 |
| $\nu_3$ | $a_1$ | 594 | 746 | 540 | 573 |
| $\nu_4$ | $a_1$ | 544 | 586 | 414 | 432 |
| $\nu_5$ | $a_1$ | 325 | 343 | 208 | 246 |
| $\nu_6$ | $b_1$ | 335 | 360 | 163 | 174 |
| $\nu_7$ | $b_1$ | 151 | 175 | 329 | 331 |
| $\nu_8$ | $b_1$ | 57 | 64 | 107 | 102 |
| $\nu_9$ | $b_2$ | 819 | 765 | 994 | 979 |
| $\nu_{10}$ | $b_2$ | 491 | 640 | 578 | 577 |
| $\nu_{11}$ | $b_2$ | 234 | 240 | 461 | 561 |
| $\nu_{12}$ | $b_2$ | 50 | 57 | 361 | 307 |

**Table 11.9:** Results of the TDDFT calculation performed on the $^3B_{3u}$ electronic state of the $Al_2O_2$ neutral cluster, calculated at the B3LYP/aug-cc-pVTZ level. For each of the three states, the excitation energy (in eV, relative to the closed-shell singlet) and orbital occupation are provided. The excitation energies (in eV) calculated at the MRMP2 level by Sarker and coworkers[462] are also provided for comparison.

| State | Orbital Occupation | TDDFT | MRMP2[462] |
|---|---|---|---|
| $^3B_{1g}$ | $...(2b_{1u})^2(4b_{2u})^1(1b_{3g})^2(7a_g)^2(5b_{3u})^1$ | 2.64 | 3.72 |
| $^3A_u$ | $...(2b_{1u})^2(4b_{2u})^2(1b_{3g})^1(7a_g)^2(5b_{3u})^1$ | 2.71 | 2.78 |
| $^3B_{2g}$ | $...(2b_{1u})^1(4b_{2u})^2(1b_{3g})^2(7a_g)^2(5b_{3u})^1$ | 3.62 | 2.09 |

**Table 11.10:** Partial wave analysis extracted from the PAD calculations for the $Al_3O_3^-$ anion HOMOs. The fractional character $f_\ell$ represents the fraction of the outgoing electron with angular momentum $\ell$, and is calculated as described in Eq. 11.1. For each eKE, the dominant contributions are shown in bold.

| Isomer | eKE (eV) | $f_0$ | $f_1$ | $f_2$ | $f_3$ | $f_4$ | $f_5$ |
|---|---|---|---|---|---|---|---|
| **3a** | 0.001 | **0.868** | 0.128 | 0.003 | 0 | 0 | 0 |
| **3b** | 0.001 | **0.993** | 0.005 | 0.001 | 0 | 0 | 0 |
| **3a** | 0.633 | 0.009 | **0.75** | 0.105 | 0.07 | 0.046 | 0.02 |
| **3b** | 0.633 | **0.448** | 0.074 | **0.434** | 0.023 | 0.02 | 0.001 |
| **3a** | 2.001 | 0.062 | **0.691** | 0.055 | 0.073 | 0.056 | 0.063 |
| **3b** | 2.001 | 0.099 | 0.073 | **0.658** | 0.06 | 0.101 | 0.007 |

# Chapter 12

# IR Spectra of $CH_3CO_2^- \cdot (H_2O)_{0-2}$


## Abstract

Infrared photodissociation spectroscopy of $D_2$-tagged anions is used to obtain the vibrational spectra of microsolvated acetate anions, $CH_3CO_2^-(H_2O)_n$ ($n = 0 - 2$), in two spectral regions encompassing the CC/CO stretch ($\sim 800 - 1800$ cm$^{-1}$) and CH/OH stretch ($\sim 2500 - 4000$ cm$^{-1}$) fundamentals. These results are analyzed by comparison to anharmonic spectra from MP2 calculations as well as molecular dynamics simulations. In agreement with prior work, we find that the first water molecule adds to the acetate anion by donating two hydrogen bonds, yielding a $C_s$ symmetric structure involving a six-membered H-bonded ring with OHO angles of $\sim 145°$. Two nearly degenerate binding motifs which differ in energy by 0.8 kJ/mol are identified for the $n = 2$ cluster, where the lowest-energy geometry shows two ion-water hydrogen bonding interactions. While the higher-energy geometry has three ion-water hydrogen bonds, we propose that the relative stabilities are primarily determined by the number of nearly linear hydrogen bonding interactions, with the lower- and higher-energy structures having two and one such bonds. The molecular dynamics simulations indicate that this lower-energy structure with fewer ion-water interactions is more dynamically stable, and an analysis of the spectra in terms of generalized normal modes provides assignment of all observed transitions to this geometry.

# 12.1 Introduction

The carboxylic acid group (-$CO_2H$) is a common substructure found in biomolecules such as amino and fatty acids. The local solvation environment can play a key role in determining the chemical and biological behavior of such molecules due to its effects on the protonation state of the acid group. At a typical *in vivo* pH ($\sim 7$), carboxylic acids are found primarily in the deprotonated $RCO_2^-$ state,[465] and so the geometry of the solvation shell surrounding carboxylate anions can be important for biomolecular interactions and protein structures.[466–470] Of the simple carboxylate ions, acetate (R = $CH_3$) is the smallest which possesses a hydrophobic group, providing the simplest model for the types of mixed hydration interactions prevalent in biomolecules where relatively extensive hydrophobic regions are interspersed with polar functional groups. In this work, the evolution of a solvation shell around the acetate anion is considered by using infrared (IR) action spectroscopy[471] as a structural probe of $CH_3CO_2^-(H_2O)_n$ clusters ($n = 0-2$), providing insight into the structures and dynamics involved in microhydration of a simple carboxylate anion.

The bulk solvation of the first three homologous carboxylate anions $RCO_2^-$ (R = H, $CH_3$, $CH_2CH_3$) has been investigated using IR spectroscopy of aqueous sodium carboxylate solutions,[472] where HDO was used as a probe of the local solvation environment. This work found that interaction of the solvent molecules with the carboxylate group imposes an asymmetric electronic distribution, where the extent of asymmetry is dependent on the electron-donating ability of the substituent group R. While this work demonstrated that larger hydrophobic groups result in a more asymmetric ion-water interaction, it is limited in its ability to determine the structural motifs present in the first solvation shell. One experimental approach to the structural characterization of microsolvated conjugate base anions is gas-phase spectroscopy of size-selected clusters, which allows for stepwise addition of solvent molecules to ions which are prevalent in aqueous media.[473] Anion photoelectron spectra have been obtained for several microsolvated acetate ($Ac^-$) clusters by Wang and coworkers;[474] however, vibrationally resolved spectra have not yet been reported, and thus structural information on these clusters is limited.

IR spectroscopy is well-known as a useful tool for the determination of molecular structure, though traditional IR methods such as absorption spectroscopy are not easily applied to gas-phase ions, where number densities are substantial lower than in experiments on neutral gases or aqueous solutions. A powerful alternative for obtaining the vibrational spectra of gas-phase ions is infrared action spectroscopy, where absorption of an IR photon is accompanied by a secondary process such as photofragmentation, loss of a weakly bound messenger tag, or electron ejection.[475–485] Product formation and/or reactant depletion are then monitored as a function of frequency using standard mass spectrometric methods, yielding a measurement of the IR absorption spectrum of the parent ion. Such methods have been used previously to probe the development of the first solvation shell around numerous conjugate bases prevalent in aqueous environments.[473,486–490]

Infrared action spectroscopy based upon electron ejection and subsequent capture by a scavenger ($SF_6$) has been used to probe the vibrational spectrum of $Ac^-$ in the $700 - 1700$

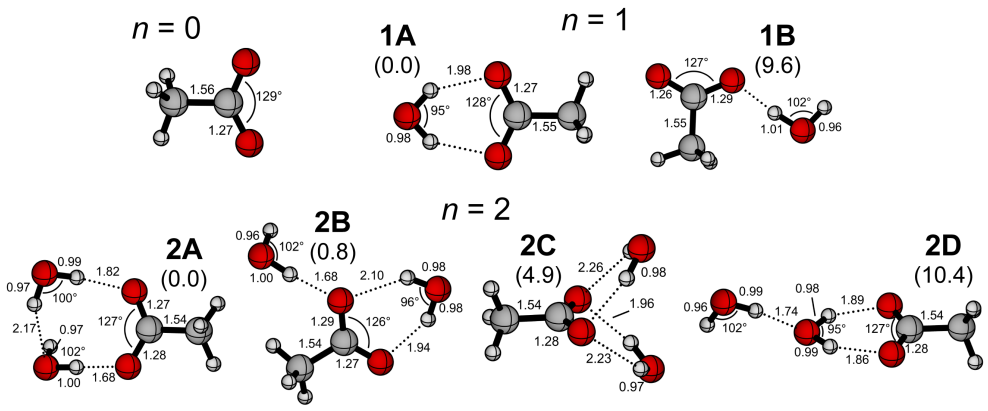


**Figure 12.1:** Cluster geometries identified at the MP2/aug-cc-pVDZ level for the $Ac^-(H_2O)_n$ cluster anions. Zero-point corrected relative energies obtained from the CCSD(T)/aug-cc-pVTZ calculations are provided in units of kJ/mol, and bond lengths are provided in Å.

$cm^{-1}$ frequency range, which includes the CC and CO stretching fundamentals.[491] This spectrum showed three features at 835, 1305, and 1590 $cm^{-1}$, with widths of $\sim 50-100$ $cm^{-1}$ full-width at half-maximum (FWHM). These relatively large widths are likely due to the temperature of the ions probed in this experiment, which was estimated to be $\sim 293$ K. IR action spectroscopies based on messenger-tagging require cooling of the ions ($T < 50$ K) in order for the weakly-bound tagged clusters to remain intact between formation and spectral interrogation.[492–494] The inherent low temperature of these experiments assists in structural assignment of the probed ions, particularly in cases where multiple low-energy isomers exist. This approach was used by Johnson and coworkers to characterize the monohydrate acetate anion, $Ac^-(H_2O)$,[482,495] where loss of an Ar tag to obtain the vibrational spectrum in the CH/OH stretching region ($\sim 2800-3800$ $cm^{-1}$). These results showed that the first water molecule forms two hydrogen bonds with the acetate anion as shown in Figure 12.1 (structure **1A**; OHO bond angles of $\sim 145°$). Particularly in the OH stretching region, a harmonic analysis was not found to adequately describe the observed spectrum, and an adiabatic model was introduced to describe coupling between the OH stretching mdoes and a low-frequency intermolecular (IM) rocking mode.

In the current work, infrared photodissociation (IRPD) spectroscopy is used to characterize the first steps in the formation of a solvation shell around $Ac^-$, the simplest carboxylate acid that possesses a hydrophobic group. Spectra for $D_2$-tagged $Ac^-$, $Ac^-(H_2O)$, and $Ac^-(H_2O)_2$ are presented which cover the CC/CO stretching ($800-1800$ $cm^{-1}$) and CH/OH stretching ($2500-4000$ $cm^{-1}$) spectral regions. For the two smaller clusters, the observed spectra are well-described by anharmonic frequencies and intensities obtained from MP2/aug-cc-pVDZ calculations, and this analysis confirms that the $n = 1$ cluster indeed assumes the **1A** geometry provided in Figure 12.1. Two nearly degenerate structural isomers are identified as potential candidates for the dihydrate, though molecular dynamics

simulations indicate that the dominant geometry contibuting to the observed spectrum is likely that proposed by Wang and coworkers (**2A** in Fig. 12.1),[474] where the second water disrupts the $n = 1$ hydrogen bonding motif to form a cluster that possesses near-linear ion-water hydrogen bonds as well as a water-water interaction. The apparent stability of this geometry relative to a low-lying isomer (**2B** in Fig. 12.1) with three hydrogen bonds, only one of which is near-linear, indicates that the geometry of the ion-water interactions is slightly more important than the total number of ion-water hydrogen bonds in determining relative stability. These results are compared to those found for several other ions with similar substructures, as well as the aqueous IR spectrum of $Ac^-$.[496]

## 12.2 Experimental Methods

IRPD experiments are performed using a cryogenic ion trap tandem mass spectrometer described previously.[488,497] In brief, microhydrated acetate anions, $Ac^-(H_2O)_n$, are continuously generated in a modified Z-spray ionization source using a 10 mM aqueous solution of sodium acetate in pure distilled water. Negative ions pass through a 4-mm diameter skimmer and are collimated in a radiofrequency (RF) decapole ion guide. The ions are then mass-selected with a quadrupole mass-filter, deflected 90° by an electrostatic quadrupole deflector, and focused into a cryogenic RF ring-electrode ion trap.[488]

The trap is held at 20 K and continuously filled with a $D_2$/He buffer gas mixture; a 5% $D_2$ gas mixture was used to tag the $Ac^-$ anion, whereas a 25% mixture was used for tagging the $Ac^-(H_2O)$ and $Ac^-(H_2O)_2$ clusters. The mass distributions of ions obtained with and without $D_2$ in the trap are provided in Figure 12.9. During their residence time in the trap, collisions with the buffer gas cool the ions' internal degrees of freedom to $\sim 20$ K and typically avoid the production of kinetically trapped species, although there are exceptions.[498] At sufficiently low ion-trap temperatures, ion-messenger complexes with $D_2$ are formed via three-body collisions.[493]

The ions are accumulated in the trap either for 100 ms or 200 ms, depending on the IR laser used, then extracted and focused both temporally and spatially into the extraction region of an orthogonal time-of-flight (TOF) mass spectrometer. Here, the ions are irradiated with a counter-propagating pulse of IR light generated either by the Fritz-Haber Institute Free Electron laser (FHI FEL)[499] or a table-top OPO/OPA laser system.[500] For the lower-energy spectral range (800-1800 $cm^{-1}$), the FHI FEL was used to generate light with spectral resolution $\Delta\lambda \approxeq 0.5\%$ FWHM and pulse energies of $2-6$ mJ with 5 Hz repetition rate. The OPO/OPA laser, operating at 10 Hz, provided access to frequencies ranging from $2500-3800$ $cm^{-1}$ with pulse energies of $2-8$ mJ. In both energy regions, care was taken to minimize multi-photon excitation.

Following interaction with IR radiation, all parent and photofragment ions are accelerated towards a microchannel plate detector and monitored as a function of irradiated wavelength. IRPD scans are recorded by averaging over 100 time-of-flight mass spectra per wavelength step (4 $cm^{-1}$ for the FHI FEL and 3 $cm^{-1}$ for the OPO/OPA system). Typically, at least

three scans are summed to obtain the final IRPD spectrum. The IRPD cross section, $\sigma_{\mathrm{IRPD}}$, is obtainted as described previously.[501,502]

## 12.3 Computational Methods

### 12.3.1 Electronic Structure and Frequency Calculations

Optimized geometries as well as harmonic and anharmonic vibrational frequencies and intensities for the bare and $D_2$-tagged $Ac^-(H_2O)_n$ ($n = 0-2$) anionic clusters were obtained at the MP2/aug-cc-pVDZ level of theory using the program package Gaussian 16.[54] A single structure was assumed for the $n = 0$ cluster. For clusters with 1 and 2 water molecules, several isomers were considered, and each final geometry was confirmed as a local minimum through a harmonic frequency analysis. These were then re-optimized to include a $D_2$ tag; the resultant cartesian coordinates for the low-energy $D_2$-tagged structures of each stoichiometry are provided in Tables 12.5-12.7. The MP2 harmonic spectra are provided in Figures 12.10-12.12, where they are compared to experimental results. Anharmonic frequency calculations were performed for the $D_2$-tagged ions using second-order vibrational perturbation theory (VPT2). For the low-energy isomers of each cluster, harmonic and anharmonic vibrational frequencies and fundamental intensities are presented in Tables 12.8-12.12.

To obtain more reliable energies, CCSD(T) single-point calculations were performed on each of the MP2/aug-cc-pVDZ optimized geometries for the $D_2$-tagged $n = 0-2$ clusters, as well as the $D_2$ and $H_2O$ molecules. The CCSD(T)/aug-cc-pVDZ and CCSD(T)/aug-cc-pVTZ energies were corrected using the MP2/aug-cc-pVDZ zero-point energies, yielding the relative energies, $D_2$ binding energies, and water binding energies provided in Tables 12.13-12.15. Unless otherwise indicated, all energies quoted in the following sections are derived from the CCSD(T)/aug-cc-pVTZ zero-point corrected energies.

### 12.3.2 Molecular Dynamics Simulations

To consider the dynamical nature of the hydrogen bonding interactions involved in the $n = 2$ cluster, Born-Oppenheimer molecular dynamics (BOMD) trajectories were obtained starting from each of the two lowest-energy isomers of the $n = 2$ cluster (**2A** and **2B**) using QChem version 5.1.[55] For each isomer, 10 trajectories were calcualted using the $\omega$B97X-D/6-31+G* method. The Nosè-Hoover thermostat was used to maintain a constant temperature of 150 K throughout the simulation. Initial velocities were sampled from a Boltzmann velocity distribution, and initial geometries were taken to be the MP2/aug-cc-pVDZ optimized structures shown in Figure 12.1. Dynamics were propagated for 20,000 steps with a 20 au ($\sim$ 0.5 fs) time step, providing trajectories which span roughly 10 ps in time.

The spectral density and IR spectra were then obtained from the Fourier transform of the nucelar velocity and dipole-dipole autocorrelation functions, respectively. For trajectories where the initial water binding motif was preserved for the full dynamical time frame (all 10

runs for **2A**; runs 1, 2, and 6 for **2B**), the $500-5000$ cm$^{-1}$ region of the IR and vibrational spectra were normalized, and the normalized average of these traces give the **2A** and **2B** BOMD spectra shown in Figure 12.13. To assign regions of relatively high intensity in the calculated IR spectrum to nuclear motion, an analysis tool was developed which calculates the generalized normal mode dominating the spectral density tensor at a specified frequency, using the method described previously by Mathias and Baer.[503]

# 12.4 Results

## 12.4.1 IRPD Spectra

The IRPD spectra of the $D_2$-tagged $Ac^-(H_2O)_n$ ($n = 0, 1, 2$) cluster anions obtained by monitoring the $D_2$ loss channel are shown in Figure 12.2 for the CC/CO stretching (800-1800 cm$^{-1}$) and CH/OH stretching (2600-3800 cm$^{-1}$) spectral regions. As noted above, the CH/OH stretching region of the Ar-tagged monohydrate cluster has been previously observed by Johnson and coworkers;[482,495] this spectrum is shown alongside the current results in Figure 12.14.

In the CC/CO stretching region, the spectrum for $D_2$-tagged $Ac^-$ shows the three intense features ($a_4$, $a_5$, $a_6$) observed previously in the IR multiple photon electron detachment spectrum recorded for the bare acetate ion.[491] These each have $\sim 10$ cm$^{-1}$ FWHM, giving a considerable improvement in resolution over the previously measured frequencies. Peaks are observed at similar positions in the $n = 1$ spectrum ($b_9$, $b_{10}$, $b_{11}$), and addition of the first water molecule resutls in the appearance of two new spectral features, $b_8$ and $b_{12}$. The $n = 2$ spectrum shows considerably more structure; the $800-1000$ cm$^{-1}$ region where transition $a_6$ is found for the $n = 0$ anion shows a triplet of peaks ($c_{12}$, $c_{13}$, $c_{14}$), and there may be additional weak features nearby that cannot be discerned here. In addition to intense features which roughly line up with the $1300-1500$ cm$^{-1}$ transitions observed for the $n = 0$ and $n = 1$ spectra ($c_8$, $c_9$, $c_{10}$), a new intense feature ($c_{11}$) is found at $\sim 1300$ cm$^{-1}$. Peak positions for the labelled features in Figure 12.2 are provided in Tables 12.1, 12.2, 12.3 for the $n = 0$, 1, and 2 clusters, respectively.

The higher-energy region of the $n = 0$ spectrum shows three overlapping transitions ($a_1$, $a_2$, $a_3$) at around $\sim 2800-3000$ cm$^{-1}$, which appear slightly broadened relative to the lower-frequency features. This region of the $n = 1$ spectrum is similar, showing three peaks resembling those observed previously[482] ($b_4 - b_6$) as well as a fourth weaker signal ($b_7$). In the OH stretching region at frequencies above $\sim 3000$ cm$^{-1}$, the $n = 1$ spectrum shows a broad transition with partially resolved structure ($b_1$, $b_2$, $b_3$), corresponding to the progression previously resolved by Johnson and coworkers.[482,495] The CH and OH stretching regions of the $n = 2$ spectrum are not as clearly separated, showing a low-intensity shoulder ($c_7$) at the red edge of four broad overlapping peaks ($c_3 - c_6$) followed by two relatively narrow transitions between $\sim 3500-3700$ cm$^{-1}$ ($c_1$, $c_2$).

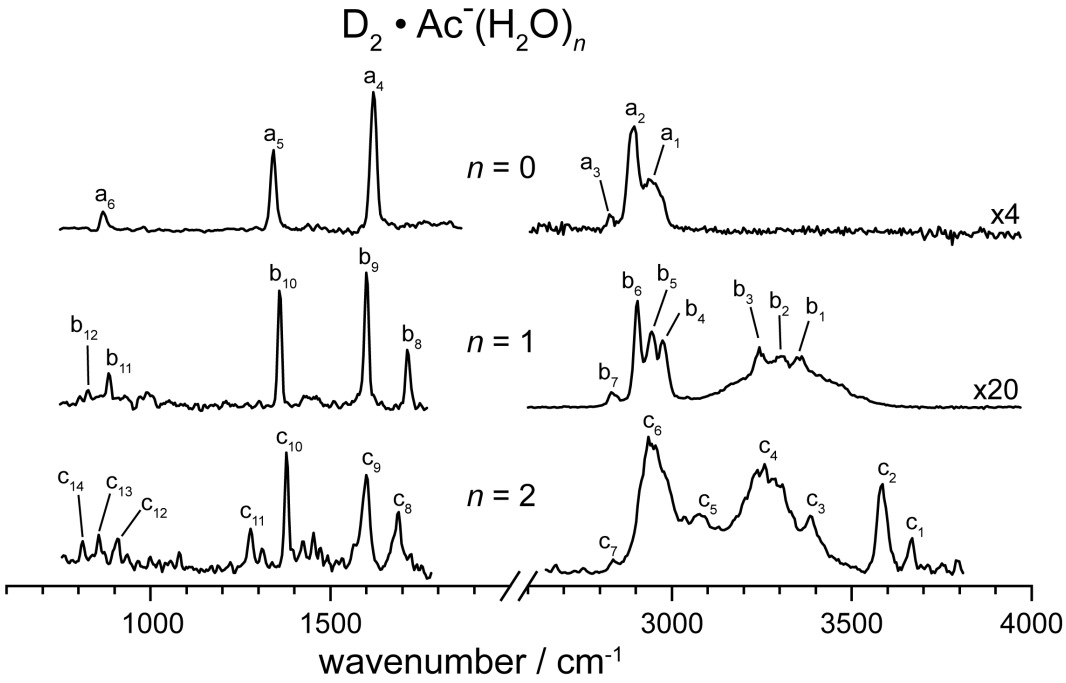


**Figure 12.2:** IRPD spectra of $D_2$-tagged $Ac^-(H_2O)_n$ cluster anions. For the $n = 0$ and 1 clusters, the higher-frequency region has been vertically scaled by the indicated factor for clarity.

**Table 12.1:** Peak positions, widths ($cm^{-1}$), and assignments for features in the IRPD spectrum of the $D_2$-tagged acetate anion. The corresponding VPT2 energies ($cm^{-1}$) are also provided.

| peak | $cm^{-1}$ | FWHM | VPT2 | desc. |
|---|---|---|---|---|
| $a_1$ | 2945 | 63 | 2984; 2980 | CH str. |
| $a_2$ | 2891 | 33 | 2940 | $D_2$ str. |
| $a_3$ | 2831 | 26 | 2916 | CH str. |
| $a_4$ | 1620 | 20 | 1595 | antisym. CO str. |
| $a_5$ | 1341 | 18 | 1350 | sym. CO str. |
| $a_6$ | 870 | 18 | 859 | CC str. |

**Table 12.2:** Peak positions, widths ($cm^{-1}$), and assignmens for features in the IRPD spectrum of the $D_2$-tagged $Ac^-(H_2O)$ anion. The corresponding VPT2 energies ($cm^{-1}$) are also provided, where the anharmonic energies corresponding to peaks $b_1$, $b_2$, and $b_3$ were obtained using Eq. 12.1. The variable $m$ is used to indicate that the resolution of the current results does not provide definitive assignment of these peaks.

| peak | $cm^{-1}$ | FWHM | VPT2 | desc. |
|---|---|---|---|---|
| $b_1$ | 3358 | 38 | $3651 + 73m$ | OH str. + $(m+2)$ IM rock |
| $b_2$ | 3299 | 55 | $3578 + 73m$ | OH str. + $(m+1)$ IM rock |
| $b_3$ | 3244 | 32 | $3505 + 73m$ | OH str. + $m$ IM rock |
| $b_4$ | 2977 | 31 | 3000 | antisym. CH str. |
| $b_5$ | 2942 | 31 | 2992 | antisym. CH str. |
| $b_6$ | 2904 | 22 | 2923 | sym. CH str. |
| $b_7$ | 2838 | 24 | 2814 | HOH bend OT |
| $b_8$ | 1715 | 14 | 1701 | HOH bend |
| $b_9$ | 1600 | 13 | 1581 | antisym. CO str. |
| $b_{10}$ | 1359 | 13 | 1377 | sym. CO str. |
| $b_{11}$ | 885 | 12 | 879 | CC str. |
| $b_{12}$ | 827 | 11 | 824 | $H_2O$ wag |

**Table 12.3:** Peak positions, widths ($cm^{-1}$), and assignments for observed features in the IRPD spectrum of the $D_2$-tagged $Ac^-(H_2O)_2$ anion. Assignments for peaks $c_1$ through $c_6$ are based on generalized motions obtained from the BOMD trajectories, where HD and HA are used to indicate the water which acts as a donor or acceptor in the water-water hydrogen bond.

| peak | $cm^{-1}$ | FWHM | desc. |
|---|---|---|---|
| $c_1$ | 3665 | 19 | free OH str. |
| $c_2$ | 3585 | 32 | HD-HA OH str. |
| $c_3$ | 3396 | 69 | ion-HD OH str./wag |
| $c_4$ | 3260 | 149 | ion-HD OH str./wag |
| $c_5$ | 3062 | 147 | both ion-water OH str./wag |
| $c_6$ | 2945 | 82 | ion-HA OH str./wag |
| $c_7$ | 2840 | 30 | CH str. |
| $c_8$ | 1686 | 32 | water bends |
| $c_9$ | 1599 | 25 | antisym. CO str. |
| $c_{10}$ | 1379 | 14 | sym. CO str. |
| $c_{11}$ | 1220 | 13 | $CH_3$ inv. |
| $c_{12}$ | 906 | 19 | CC str. |
| $c_{13}$ | 857 | 16 | $H_2O$ wag |
| $c_{14}$ | 812 | 15 | $H_2O$ wag |

### 12.4.2 Cluster Geometries

Figure 12.1 shows the low-energy isomers identified as local minima at the MP2/aug-cc-pVDZ level of theory for $Ac^-(H_2O)_n$ ($n = 0 - 2$), and Figure 12.3 shows the corresponding $D_2$-tagged geometries. Previous work studying the $n = 1$ anion[474,482,495] found that addition of the first water molecule to the acetate anion (**0**) forms a symmetric hydrogen-bonded structure (**1A**, $C_s$ symmetry) with OHO bond angles of $\sim 145°$, which is confirmed to be the lowest-energy geometry for this cluster by our calculated energies. The $D_2$ tag is not found to substantially break the symmetry of the hydrogen bonds. Additionally, a low-lying isomer possessing only one near-linear hydrogen bond is identified (**1B**, OHO bond angle of 174°); the relative energy corrected for the harmonic zero-point energy places this structure 9.6 kJ/mol above the **1A** global minimum. For the $D_2$-tagged ions, this energetic ordering is maintained, with **1B** $\cdot$ $D_2$ lying 9.3 kJ/mol above **1A** $\cdot$ $D_2$.

For the $n = 2$ cluster stoichiometry, four local minima were identified. The anion photoelectron spectrum of the $Ac^-(H_2O)_2$ cluster[474] was previously analyzed assuming an anion geometry similar to **2A**, where the second water molecule inserts into one of the ion-water H-bonds of **1A** to form two new hydrogen bonds, one with the H-atom of the first water (water-water) and the other with the acetate O atom (ion-water). For the sake of discussion, the two water molecules will be distinguished by their donor/acceptor role in the water-water hydrogen bond, with one water being the donor (HD) and one being the acceptor (HA), so that HA has one OH bond which does not participate in any intermolecular interactions (free OH). Both ion-water hydrogen bonds are found to be near-linear, with OHO bond angles of $\sim 175°$, whereas the water-water H-bond forms an OHO bond angle of $\sim 145°$.

The calculations reported here yield a nearly degenerate geometry for the $n = 2$ cluster (**2B**), where the second water adds to the **1A** geometry to form a near-linear ion-water H-bond with one of the acetate O atoms; in further discussions of this geometry, the water from the **1A** geometry will thus be referred to as the double hydrogen bonding water (DHB),

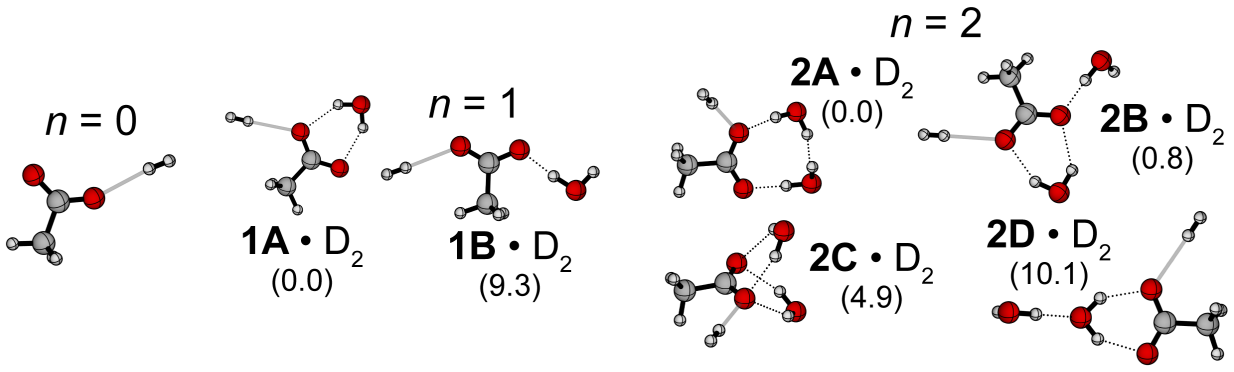


**Figure 12.3:** MP2/aug-cc-pVDZ geometries of the $D_2$-tagged $Ac^-(H_2O)_n$ cluster anions. Zero-point corrected relative energies obtained from the CCSD(T)/aug-cc-pVTZ calculations are provided in units of kJ/mol.

whereas the second water forms only a single hydrogen bond (SHB) with the ion. This isomer lies 0.8 kJ/mol above the **2A** isomer both with and without the $D_2$ tag. This small relative energy indicates the possibility of interconversion between the two lowest-energy isomers, which will be discussed in more detail below. Two other isomers, **2C** and **2D**, are also identified as local minima, and lie 4.9 and 10.4 kJ/mol, respectively, above the **2A** isomer; the $D_2$ tag does not substantially change the relative energies of these binding motifs.

### 12.4.3 BOMD Simulations

Given the similar energies for the two lowest-lying isomers of the $n = 2$ clusters shown in Figs. 12.1 and 12.3, it is possible that some interconversion between the two binding motifs may occur, and this would impact the resultant spectra. This possibility was explored by performing 10 molecular dynamics simulations starting from geometries **2A** and **2B** in Fig. 12.1, with a total of 20 trajectories carried out to observe the structural changes over 10 ps. To analyze these trajectories for interconversion between the different water binding motifs, the hydrogen-oxygen separations may be plotted as a function of time, using the labelling convention provided in Figure 12.4. The most useful metric for distinguishing between the **2A** and **2B** binding motifs is the water-water O-H separation which defines the presence or absence of a water-water hydrogen bonding interaction. Figure 12.4a shows all four such parameters as functions of time for a typical trajectory starting from the **2A** geometry, and Fig. 12.4b illustrates the behavior that is observed when the **2B** binding motif is preserved over the 10 ps run time. In Fig. 12.4b, we see that the absence of water-water hydrogen bonding interactions leads to larger fluctuations in the corresponding water-water separations for the **2B** isomer.

Figures 12.15-12.18 provide a full summary of the O-H separations and energies for all 20 trajectories. The only notable geometry change found in the 10 trajectories initiated in the **2A** potential well (Figs. 12.15 and 12.16) is a reversal of the donor/acceptor roles in the water-water hydrogen bond; this type of donor-acceptor switching has been noted previously for the dihydrate of the iodide anion,[504] though the current spectroscopic results do not enable distinguishing between these two configurations.

While all 10 trajectories initialed in the **2A** minimum showed persistence of this binding motif throughout the entire dynamical run time, several trajectories starting from the **2B** geometry show substantial changes during the 10 ps of simualtion. Of the 10 trajectories represented in Figures 12.17-12.18, only 3 show persistence of the **2B** binding motif. The remaining 7 trajectories indicate conversion to the **2A** isomer after varying amounts of time, ranging from 1.1 to 8.1 ps (average time of conversion was found to be $\sim$ 1.5 ps); an example of such behavior is illustrated in the hydrogen bonding plot of Figure 12.4c. Interestingly, a single trajectory which showed this **2B**-to-**2A** conversion shows evidence for further isomerization to **2D** (see trajectory B-4 in Fig. 12.17).

To summarize these results, all of the trajectories starting from the **2A** isomer show that this binding motif persists for the full 10 ps of simulation, though the water/water hydrogen bond is not strictly static, with 9 of the 10 trajectories showing some reversal of

the donor/acceptor role of the two waters. Of the 10 trajectories initiated with the **2B** binding motif, 7 show isomerization to form the **2A** isomer after some period of time. Of the 17 trajectories where the **2A** isomer is present – either through isomerization from **2B**, or from the initial geometry – only a single trajectory shows conversion to another isomer, and this isomer is the high-energy **2D** structure. While it is possible that the presence of the $D_2$ tag may impact the propensity for interconversion, these results, as well as the fact that the relative energies are not changed by the $D_2$ tag, indicate that the $n = 2$ cluster probed experimentally tends towards the **2A** $\cdot$ $D_2$ geometry.

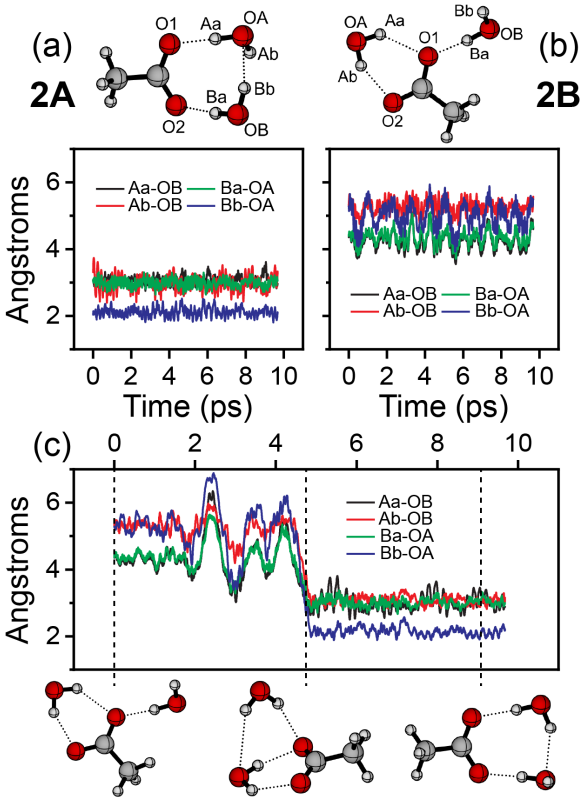


**Figure 12.4:** Typical water-water hydrogen bonding plots for BOMD trajectories starting from the **2A** (a) or **2B** (b) geometry, where the initial binding motif persists for the entire 10 ps run time. **(c)** Water-water O-H separations for a trajectory starting at the **2B** geometry which shows conversion to the **2A** binding motif, as well as snapshots of the molecular geometry before, during, and after the conformational change.

## 12.5 Spectral Assignments

### 12.5.1 $n = 0$ and 1

Figures 12.5 and 12.6 compare the IRPD spectra obtained for the $D_2$-tagged $Ac^-$ and $Ac^-(H_2O)$ anions in both spectral regions and compare these results to the VPT2 anharmonic spectra obtained from the MP2/aug-cc-pVDZ optimized geometries shown in Figure 12.3. In the lower-frequency region of the $n = 0$ spectrum, the VPT2 results for **0** $\cdot$ $D_2$ in Fig. 12.5 reproduce all three intense transitions, identifying peaks $a_6$, $a_5$, and $a_4$ as the CC stretching, symmetric CO stretching, and antisymmetric CO stretching fundamentals for the acetate anion. These acetate-specific features are also present in the simulations for both $n = 1$ isomers represented in Fig. 12.6, giving assignments for peaks $b_{11}$ (CC stretch), $b_{10}$ (symmetric CO stretch), and $b_9$ (antisymmetric CO stretch).

While the acetate-centered vibrations are similar in the spectra of **1A** $\cdot$ $D_2$ and **1B** $\cdot$ $D_2$, the different water binding motifs give distinctive spectral signals corresponding to water-centered vibrational modes. Both isomers show the water bending fundamental at around $\sim 1700$ cm$^{-1}$, corresponding to peak $b_8$ in the experimental spectrum. The predicted intensity of this feature varies considerably between the two structures, with the **1A** $\cdot$ $D_2$ simulation better reproducing the high intensity observed in the experiment. Thus, we take this structure to be the primary contributor to the experimental results for the $n = 1$ cluster, in agreement with previous work on this system as well as the calculated isomeric energies. An additional water-specific feature is tentatively identified in the CC stretching portion of this spectrum ($b_{12}$), where the **1A** $\cdot$ $D_2$ harmonic simulation shows a fundamental transition corresponding to a water wagging mode involving motion of the shared hydrogen atoms out of the plane formed by the hydrogen-bonded substructures.

In the higher-frequency region, the experimental spectrum for the $n = 0$ ion (Fig. 12.5) shows three broad overlapping features ($a_1$, $a_2$, $a_3$ with FWHMs of 63, 33, and 26 cm$^{-1}$, respectively), whose intensities are well-reproduced by a 15 cm$^{-1}$ FWHM convolution of the anharmonic stick spectrum. This choice of width is congruent with the relatively narrow features observed in the lower-energy spectral region for this cluster. From the position of the fundamental transitions in the theoretical spectrum, we assign $a_2$ and $a_3$ to the $D_2$ stretch and symmetric CH stretching modes, respectively. The broader feature in this region ($a_1$) likely encompasses the two antisymmetric CH stretching fundamentals. The anharmonic simulation and convolution suggests that the observed broadening of these features relative to transitions observed in the lower-energy region of the spectrum likely arises from numerous low-intensity combination bands (shown as red sticks in Fig. 12.5) involving the low-frequency $D_2$ wagging and $CH_3$ internal rotation modes.

For the $n = 1$ cluster anion, the CH and OH stretching regions were analyzed previously by Johnson and coworkers,[482,495] who used Ar as a messenger tag. In the CH stretching region, the Ar-tagged experiment (Fig. 12.14) showed three transitions, giving vibrational frequencies of 2912, 2953, and 2980 cm$^{-1}$ for the CH stretching modes of this cluster. These three transitions are also identified in the current results as peaks $b_6$, $b_5$, and $b_4$, and the

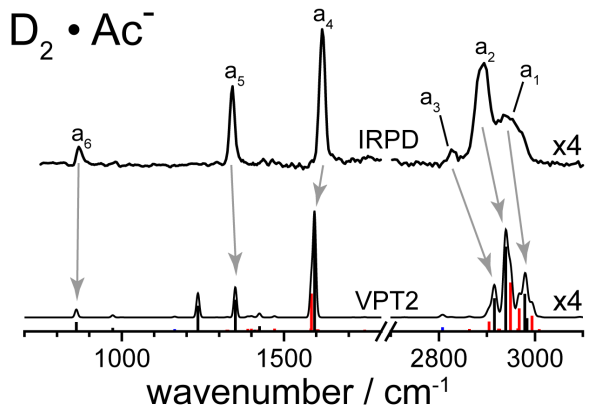


**Figure 12.5:** Comparison of the IRPD spectrum of the $D_2$-tagged acetate ion (top) with the simulated spectrum obtained from a VPT2 treatment of the MP2/aug-cc-pVDZ optimized geometry (bottom). The stick spectrum shows fundamental transitions, overtones, and combination bands as black, blue, and red sticks, respectively, and the solid black trace shows a convolution of this spectrum with a 15 $cm^{-1}$ FWHM Gaussian lineshape. The $2700 - 3100$ $cm^{-1}$ regions of both spectra have been vertically scaled by the indicated factors for clarity.

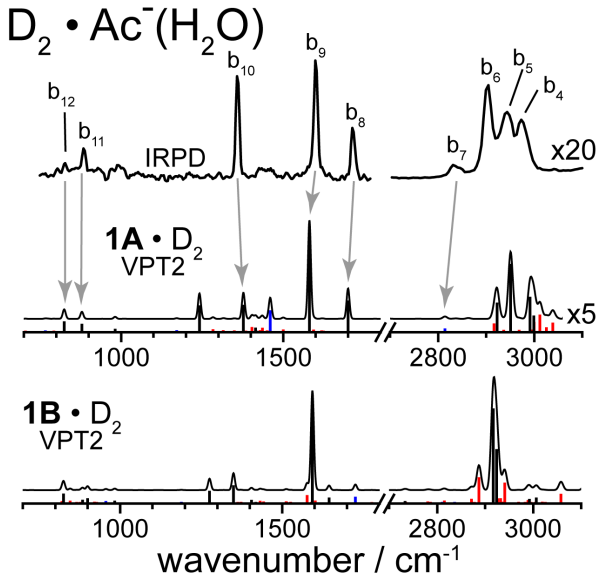


**Figure 12.6:** Comparison of the IRPD spectrum of $D_2$-tagged $Ac^-(H_2O)$ (top) to the VPT2 simulations obtained for the two $D_2$-tagged isomers identified in MP2/aug-cc-pVDZ calculations (bottom). The stick spectra show fundamental transitions, overtones, and combination bands as black, blue, and red sticks, respectively, and the solid black traces show a convolution of each spectrum with a 15 $cm^{-1}$ FWHM Gaussian lineshape. The $2700 - 3100$ $cm^{-1}$ regions of the experimental and **1A** $\cdot$ $D_2$ spectra have been vertically scaled by the indicated factors for clarity.

extracted CH stretching frequencies of 2904, 2942, and 2977 $cm^{-1}$ are in reasonable agreement with the previous results as well as the VPT2 frequencies of **1A** · $D_2$ (see Table 12.2). Peak $b_6$, corresponding to the symmetric CH stretching fundamental, is slightly more intense than was observed in the Ar-tagging experiment; given the calculated $D_2$ stretching frequency (2951 $cm^{-1}$) and intensity, it is likely that the $D_2$ stretch fundamental also contributes to this peak. In addition to the CH stretching features, the current results probe slightly lower frequencies, revealing an additional weak transition at 2838 $cm^{-1}$ ($b_7$) which lines up relatively well with the water bending overtone (OT) in the **1A** · $D_2$ spectrum.

The OH stretching region of the IRPD spectrum of the $n = 1$ cluster shown in Fig. 12.2 represents a lower-resolution measurement of the spectrum considered previously by Johnson and coworkers.[482] To analyze this portion of the Ar-tagging spectrum, an adiabatic model was developed that involves coupling of OH stretching modes with a low-frequency IM rocking motion, splitting the OH stretch fundamental into a collection of vibrational transitions associated with varying degrees of excitation of the low-frequency IM mode. This model was found to agree well with the spectrum observed in Ar tagging experiments for the monohydrate of the acetate and nitromethane anions,[495] and a similar treatment was used to consider the IRMPD spectrum of the $NO_3^-(H_2O)$ ion.[505]

The equations which give the predicted frequencies and intensities of transitions in the OH stretching region based on the adiabatic model are provided in Section 12.8.1, and Figure 12.19 shows the spectrum obtained using the anharmonic force constants from our VPT2 calculations of the **1A** · $D_2$ ion. While the simulated spectrum is slightly blue-shifted relative to experiment, the general pattern agrees relatively well, demonstrating that transitions $b_1 - b_3$ correspond to a partially-resolved progression involving combination bands of an OH stretching mode with the low-frequency IM rock as indicated in Table 12.2. The spacing between these peaks shows that the frequency of the IM mode is $\sim 60$ $cm^{-1}$, in reasonable agreement with the VPT2 value of $\sim 70$ $cm^{-1}$.

### 12.5.2 $n = 2$

Figure 12.7 compares the lower-frequency region of the IRPD spectrum of the $n = 2$ cluster to the VPT2 simulations for the two lowest-energy isomers identified in the MP2 calculations. Similar agreement is found for isomers **2A** · $D_2$ and **2B** · $D_2$, and comparison to these results as well as the $n = 0$ and 1 spectra allows for assignment of both CO stretching fundamentals ($c_9$ and $c_{10}$) as well as the water bending mode ($c_8$), as summarized in Table 12.3. Both VPT2 spectra show a relatively intense feature at $\sim 1300$ $cm^{-1}$ that corresponds to a $CH_3$ inversion mode, providing assignment of peak $c_{11}$. The positions of peaks $c_8 - c_{11}$ are in good agreement with the VPT2 frequencies of both isomers (Tables 12.11 and 12.12), and thus do not provide a clear answer as to whether one or both geometries contribute to the spectrum.

The three transitions observed below $\sim 1000$ $cm^{-1}$ – $c_{12}$, $c_{13}$, and $c_{14}$ at 906, 857, and 812 $cm^{-1}$, respectively – are more difficult to assign given the results shown in Fig. 12.7. Based on the assignments made for the $n = 0$ and 1 spectra, we expect that this portion

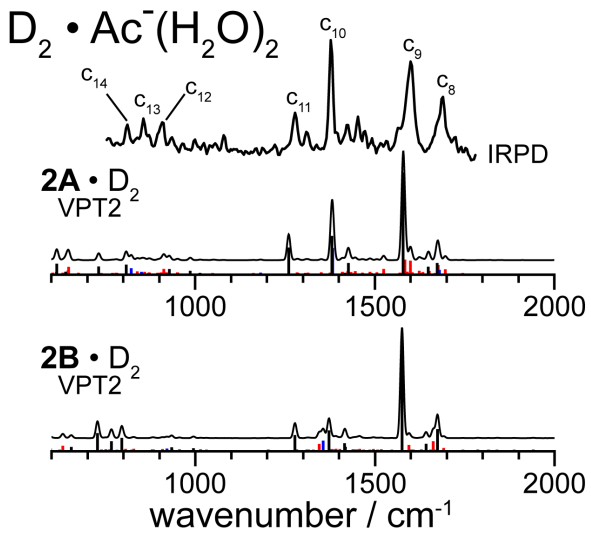


**Figure 12.7:** Comparison of the low-frequency region of the IRPD spectrum of $D_2$-tagged $Ac^-(H_2O)_2$ (top) to the VPT2 simulations for the two lowest-energy $D_2$-tagged isomers, **2A** $\cdot$ $D_2$ and **2B** $\cdot$ $D_2$ (bottom). The stick spectra show fundamental transitions, overtones, and combination bands as black, blue, and red sticks, respectively, and the solid black traces show a convolution of each spectrum with a 15 $cm^{-1}$ FWHM Gaussian lineshape.

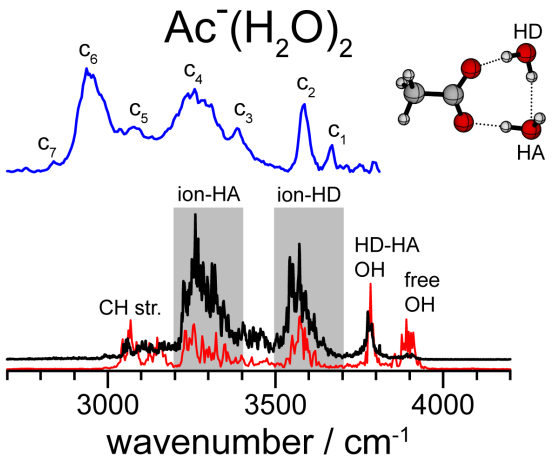


**Figure 12.8:** CH/OH stretching region of the IRPD spectrum of $D_2$-tagged $Ac^-(H_2O)_2$ (blue) compared to the **2A** BOMD IR spectrum (black), where the corresponding vibrational density of states is also provided.

of the $n = 2$ spectrum should show the CC stretch fundamental (analogous to $a_6$ and $b_{11}$) as well as one or more modes involving an $H_2O$ wagging motion (analogous to $b_{12}$). While the intensities of features in this portion of the **2A** $\cdot$ $D_2$ spectrum are substantially lower than expected based on experiment, the VPT2 frequencies in Table 12.11 show that the CC stretching frequency (928 $cm^{-1}$) as well as those of two $H_2O$ wagging modes (808 and 731 $cm^{-1}$) provide reasonable agreement with experimental results. The VPT2 results for isomer **2B** $\cdot$ $D_2$ show a triplet of water wagging fundamentals at 796, 772, and 720 $cm^{-1}$, which roughly reproduce the relative intensities of features $c_{12} - c_{14}$, though the calculated frequencies do not match as well with experiment. Thus, we base our assignments on the **2A** $\cdot$ $D_2$ anharmonic frequencies, and assign peaks $c_{12}$ and $c_{13}/c_{14}$ as the CC stretching and $H_2O$ wagging fundamentals.

The CH/OH stretching region of the VPT2 spectra obtained for both low-lying $n = 2$ isomers (Fig. 12.20) do not provide good agreement with the IRPD spectra. Instead, we consider the infrared absorption spectra calculated from BOMD trajectories where the initial binding motif is preserved over the 10 ps dynamical time frame (Fig. 12.13). Given the relatively low spectral intensity found for isomer **2B** in this frequency range, as well as its tendency to convert to the lower-energy isomer, we consider **2A** to be the primary contributor to the CH/OH stretching region of the IRPD spectrum.

Figure 12.8 compares the infrared absorption (black) and vibrational density of states (red) for the **2A** BOMD trajectories in this spectral region to experimental results, showing that the general shape of the spectrum is reproduced by theory. To assign the features labelled in Fig. 12.2 to nuclear motions, we consider the generalized normal coordinates calculated from our BOMD trajectories[503] and determine the dominant nuclear motion contributing to the spectral density at each frequency of interest. Doing so, we may then match the frequencies (or ranges of frequencies) where the IR absorption curve roughly corresponds to the labelled features in Fig. 12.2.

The highest-frequency feature, $c_1$, most likely corresponds to the free OH stretch associated with the HA water molecule, which dominates the spectral density at 3905 $cm^{-1}$ in the BOMD simulations; similarly, $c_2$ corresponds to a stretching motion of the water-water hydrogen bond, which is the dominant contributor to the spectral density at 3785 $cm^{-1}$. The corresponding nuclear motions are illustrated in Figure 12.21. The ability to attribute each of these experimental features to a single frequency in the simulated spectrum is consistent with the narrower peak widths obtained for $c_1$ and $c_2$ relative to peaks $c_3 - c_6$, which are associated with ion-water hydrogen bonding interactions.

The $\sim 3200 - 3700$ $cm^{-1}$ region of the simulated spectrum which shows vibrational signatures of ion-water interactions may be loosely separated into three sections, where the dominant contributing normal mode involves the ion-HA hydrogen bond ($\sim 3200 - 3400$ $cm^{-1}$), the ion-HD hydrogen bond ($\sim 3500 - 3700$ $cm^{-1}$), and an intermediate region where motion of both hydrogen bonds contributes to the spectrum ($\sim 3400 - 3500$). The first two regions are found to have relatively higher absorption intensity, and thus we assign peaks $c_6$ and $c_3/c_4$ to the OH stretching motion associated with the ion-HA and ion-HD hydrogen bonding interactions, respectively. It should be noted that over the indicated frequency

ranges, the contributing nuclear motions also showed substantial OH wagging character, suggesting a similar coupling between OH stretching and IM motions as was found for the $n = 1$ clsuter. The lower-intensity feature $c_5$ is then assigned to the simultaneous distortion of both ion-water hydrogen bonds.

In contrast to the other two clusters, the higher-frequency region of the $n = 2$ spectrum is almost entirely found to consist of vibrational signatures of OH stretching motions. This is consistent with the low intensity of the CH stretching reigon in the BOMD spectrum ($\sim 2900 - 3200$ cm$^{-1}$). Based on the spectrum in Figure 12.8, the weak feature $c_7$ at the lower-frequency edge of peak $c_6$ is assigned as a CH stretching mode (see Fig. 12.21); this likely corresponds to the low-frequency end of the CH stretching region, given the absence of structure at lower frequencies in the IRPD results. Thus, the separation of the CH and OH stretching regions would seem to be considerably larger in the simulated spectrum as compared to experiment, which could be a result of the relatively high frequencies predicted for the OH vibrational signatures.

## 12.6 Discussion

The apparatus used for the current results did not provide sufficient signal for the $Ac^-(H_2O)_3$ ion to obtain satisfactory spectra for clusters with more than 2 water molecules. When source conditions were optimized for the $n = 3$ peak of the mass distribution ($m/z$ = 113 for the untagged cluster), the optimum ion signal was found to be several orders of magnitude lower than the maximum intensities obtainable for $n \leq 2$ (see Fig. 12.9b). This is interesting considering the similarity in solvent structure for the microhydrated acetate and nitromethane anions, the latter of which has been observed in clusters with up to $n = 4$ water molecules.[506] The cause of this difficulty is unclear given the current results; one possible non-experimental cause is that replacement of the carbon atom with a nitrogen results in stronger ion-water hydrogen bonding. However, this is purely speculative, as the inability to form larger clusters in the current work could also be a function of experimental parameters involved in ion generation and trapping.

For the acetate anion, each oxygen atom is capable of forming up to three hydrogen bonds, indicating that the first solvation shell of bulk solvated $Ac^-$ consists of six water molecules. The CO stretching frequencies in Table 12.4 show that as the extent of hydration increases, the symmetric and antisymmetric stretches become more blue- and red-shifted, respectively. This is consistent with the values observed for an aqueous solution of sodium acetate, where the symmetric and antisymmetric CO stretch frequencies were found to be 1413 and 1556 cm$^{-1}$, respectively.[496] Assuming that this trend remains approximately linear as more molecules are added, these values suggest that the bulk CO stretch frequencies should be reached at $n \sim 5$, indicating that the frequency shifts observed for the bulk solution are largely due to interactions within the first solvation shell.

As noted above, IR studies in the CH/OH stretching region of microhydrated nitromethane anions, $CH_3NO_2^-(H_2O)_n$, have shown that the binding motifs of the adsorbed water

**Table 12.4:** Vibrational frequencies (in $cm^{-1}$) extracted from the IRPD spectra of the $D_2$-tagged $Ac^-(H_2O)_n$ clusters. OH stretching frequencies correspond to those involved with ion-water interactions and are provided as a range due to the relatively broad spectral signatures found for these motions.

| | $n = 0$ | $n = 1$ | $n = 2$ |
|---|---|---|---|
| CC str. | 870 | 885 | 906 |
| sym. CO str. | 1341 | 1359 | 1379 |
| antisym. CO str. | 1620 | 1600 | 1599 |
| CH str. | 2831, 2945 | 2904, 2942, 2977 | 2840 |
| $H_2O$ wag | – | 827 | 857, 812 |
| HOH bend | – | 1715 | 1686 |
| ion-water OH str. | – | 3000-3600 | 2800-3500 |

are similar to those shown in Figures 12.1 and 12.3.[482,506] As such, similar structural signatures and spectroscopic trends may be identified in the $CH_3CO_2^-(H_2O)_n$ spectra reported here. The average CH stretching frequency obtained from Table 12.4 (2888, 2919 $cm^{-1}$ for $n = 0, 1$) appears to increase with increasing $n$, keeping in mind that the higher-frequency CH stretching fundamentals for the $n = 2$ cluster are likely obscured by the features attributed to OH stretching motions. This trend of increasing CH stretching frequency is also found in the $CH_3NO_2^-(H_2O)_n$ series. In both cases, the increasing frequency is an indicator of increasing polarization of the excess charge away from the CH bonds as water molecules are added, due to the delocalization of this charge throughout the hydrogen bonding network. Additionally, the nitromethane spectra show that as $n$ increases, the CH and OH stretching regions move closer together, due to the aforementioned blue-shifting of the CH stretches as well as the spreading out of the OH stretch fundamentals over a broader range of frequencies. This trend is more pronounced in the acetate data, where only the lowest-frequency CH stretch is able to be observed for the $n = 2$ cluster due to the broad OH stretching region.

The spectra presented here may also be compared to those obtained for the microhydrated bicarbonate anion, which can be thought of as a carboxylate where R = OH, to elucidate the impact of the hydrophobicity of the R group on the hydration of $RCO_2^-$ anions. Infrared multi-photon dissociation (IRMPD) spectroscopy has been used to characterize $HCO_3^-(H_2O)_n$ clusters for up to $n = 10$ in the $\sim 600 - 1800$ $cm^{-1}$ region,[489] giving spectral signatures which may be compared to those identified in the CC/CO stretching regions of the $Ac^-(H_2O)_n$ spectra. The binding geometry for the addition of the first two water molecules is similar between the two ions, though two low-lying isomers (at +3.4 and +10.8 kJ/mol) were identified wherein the water forms a hydrogen bond with the OH group of bicarbonate. The reported water bending frequency for the monohydrate is slightly higher in the current results (1715 $cm^{-1}$ for R = $CH_3$ versus 1706 $cm^{-1}$ for R = OH), indicating that the water which binds to the carboxylate group of acetate is more structurally restricted. This may be a consequence of differences in charge delocalization between the two ions, as the $CH_3$

group is less likely to pull excess charge away from the $CO_2$ group.

## 12.7 Conclusion

Vibrational spectra of the acetate anion complexed with up to two water molecules have been obtained using infrared action spectroscopy of messenger-tagged ions. Frequencies of $\sim 800 - 1800$ cm$^{-1}$ were probed using IR light from the FHI FEL, providing spectroscopic access to the CC/CO stretching region of the $Ac^-(H_2O)_n$ spectra, whereas the $2500 - 3800$ cm$^{-1}$ spectral region was accessed using a table-top OPO. In the lower-frequency region, a clear evolution of vibrational signatures is identified, with the addition of $H_2O$ resulting in the appearance of features associated with the water bending mode as well as a rocking motion of the complexed water(s). While the $Ac^-$ and $Ac^-(H_2O)$ spectra are well-reproduced by harmonic calculations based on MP2/aug-cc-pVDZ geometries, BOMD simulations provide a better agreement with the observed spectrum for the $n = 2$ cluster, particularly in the higher-frequency region of the spectrum where contributions from OH and CH stretching modes are expected to dominate. The current results indicate that the **2A** binding motif is the dominant contributor to the observed spectra, and spectral signatures associated with ion-water and water-water hydrogen bonding interactions are able to be distinguished. These results are compared to vibrational spectra of ions with similar substructures as well as the bulk spectrum of aqueous acetate, providing insight into the solvation of this simple carboxylate anion.

## 12.8 Supporting Information

### 12.8.1 Results of the Adiabatic Mixing Model for $n = 1$

A full derivation of the results of the adiabatic model describing mixing between the intermolecular rocking mode ($\omega_R$) of the **1A** anion and its OH stretching modes ($\omega_A$ and $\omega_S$) is provided elsewhere.[495] The equations resulting from this model are used here to simulate the spectrum shown in Figure 12.19, using VPT2 results for the quadratic ($\omega_A$ = 3630.3 cm$^{-1}$, $\omega_S$ = 3617.6 cm$^{-1}$, $\omega_R$ = 72.9 cm$^{-1}$) reduced force constants as well as the cubic force constant coupling the three modes ($\lambda$ = -262.8 cm$^{-1}$). The energies of the vibrational transitions accompanying excitation of one quantum of OH stretch are given by

$$E(n_R) = \omega_L - \frac{\lambda^2}{8\omega_R} + \omega_R n_R \quad \text{where} \quad \omega_L^2 = \frac{\omega_A^2 + \omega_S^2}{2}, \tag{12.1}$$

and the corresponding intensities are given by

$$I(n_R) = \frac{e^{-\Delta q^2/2}(\Delta q)^{2n_R}}{2^{n_R} n_R!} \quad \text{with} \quad \Delta q = \frac{\lambda}{2\omega_R}. \tag{12.2}$$

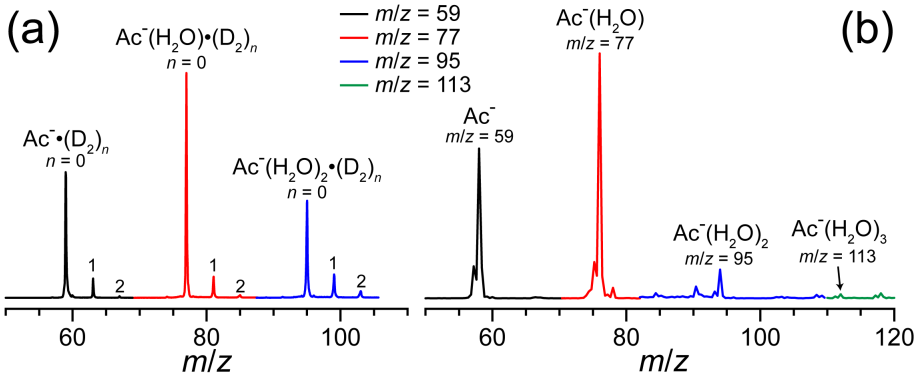


**Figure 12.9:** Mass spectra obtained with (a) and without (b) $D_2$ in the trap. The different colored traces were obtained using source conditions optimized for the indicated mass peak.

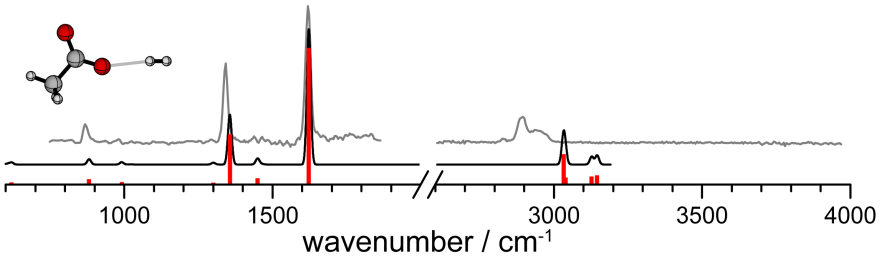


**Figure 12.10:** Harmonic MP2/aug-cc-pVDZ infrared spectrum for the $D_2$-tagged acetate anion. The black trace represents a convolution of the red stick spectrum with a 15 $cm^{-1}$ FWHM Gaussian lineshape, and experimental results are shown in gray.

**Table 12.5:** Cartesian coordinates (in Å) for the MP2/aug-cc-pVDZ optimized geometry of the $D_2$-tagged acetate anion.

| **0** | X | Y | Z |
|---|---|---|---|
| C | -0.091217 | -0.167193 | 0.000075 |
| O | -0.419461 | -1.394151 | -0.000040 |
| O | 1.077392 | 0.340779 | 0.000142 |
| C | -1.253734 | 0.865088 | -0.000037 |
| H | -2.235417 | 0.365721 | 0.001164 |
| H | -1.167767 | 1.513432 | -0.889005 |
| H | -1.166398 | 1.515372 | 0.887372 |
| D | 3.308591 | 0.374685 | -0.000252 |
| D | 4.067248 | 0.470393 | -0.000315 |

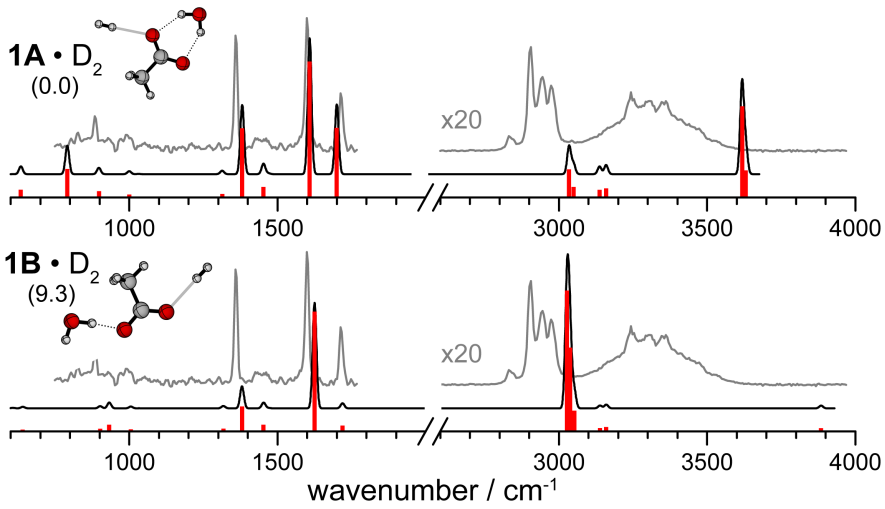


**Figure 12.11:** Harmonic MP2/aug-cc-pVDZ infrared spectra for the $D_2$-tagged $Ac^-(H_2O)$ isomers identified in the current work. The black traces represent convolutions of the red stick spectra with a 15 $cm^{-1}$ FWHM Gaussian lineshape, and experimental results are shown in gray. For both isomers, the relative (zero-point corrected) energies at the CCSD(T)/aug-cc-PVDZ level are provided in units of kJ/mol.

**Table 12.6:** Cartesian coordinates (Å) for the MP2/aug-cc-pVDZ optimized geometries of the $D_2$-tagged $Ac^-(H_2O)$ anion.

| **1A** | X | Y | Z | **1B** | X | Y | Z |
|---|---|---|---|---|---|---|---|
| C | -0.498236 | -0.241688 | -0.000028 | C | -0.662011 | -0.262295 | -0.000146 |
| O | 0.224078 | -1.289570 | -0.000041 | O | 0.424487 | -0.944103 | -0.000138 |
| O | -0.106288 | 0.973622 | -0.000057 | O | -1.842594 | -0.713580 | 0.000205 |
| C | -2.029495 | -0.445106 | 0.000047 | C | -0.476726 | 1.272121 | -0.000375 |
| H | -2.289313 | -1.514075 | -0.000042 | H | 0.106342 | 1.573786 | 0.885700 |
| H | -2.464199 | 0.043794 | -0.887747 | H | -1.447952 | 1.789057 | -0.000587 |
| H | -2.464075 | 0.043602 | 0.888010 | H | 0.106628 | 1.573515 | -0.886349 |
| H | 2.079956 | -0.592789 | 0.000039 | H | 1.879354 | -0.167454 | 0.000022 |
| O | 2.635111 | 0.214991 | 0.000047 | O | 2.809229 | 0.221931 | 0.000194 |
| H | 1.881607 | 0.841244 | -0.000011 | H | 3.359937 | -0.569793 | 0.001209 |
| D | -1.565817 | 2.751719 | 0.000010 | D | -3.814248 | 0.431949 | 0.000427 |
| D | -2.034982 | 3.354928 | 0.000036 | D | -4.486608 | 0.796000 | 0.000624 |

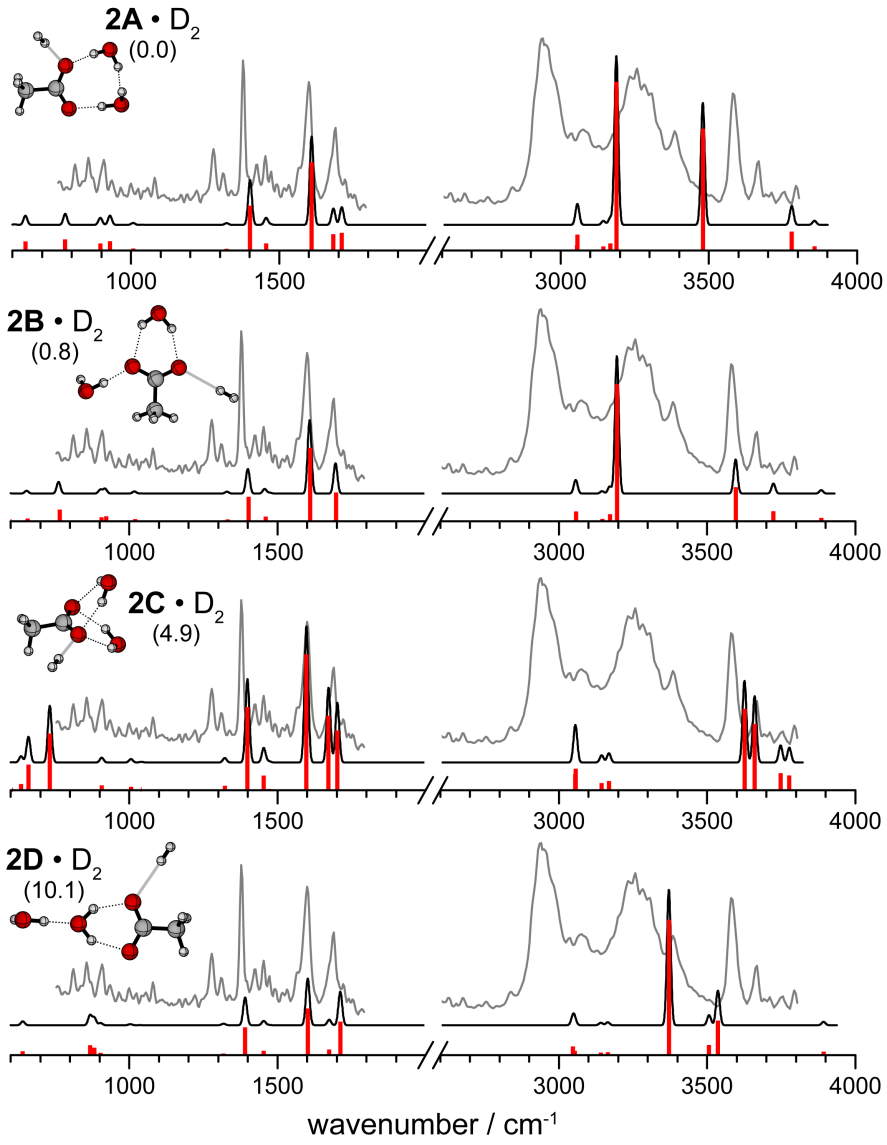


**Figure 12.12:** Harmonic MP2/aug-cc-pVDZ infrared spectra for the $D_2$-tagged $Ac^-(H_2O)_2$ isomers identified in the current work. The black traces represent convolutions of the red stick spectra with a 15 $cm^{-1}$ FWHM Gaussian lineshape, and experimental results are shown in gray. Relative isomeric energies at the CCSD(T)/aug-cc-pVDZ level including zero-point corrections are provided in units of kJ/mol.

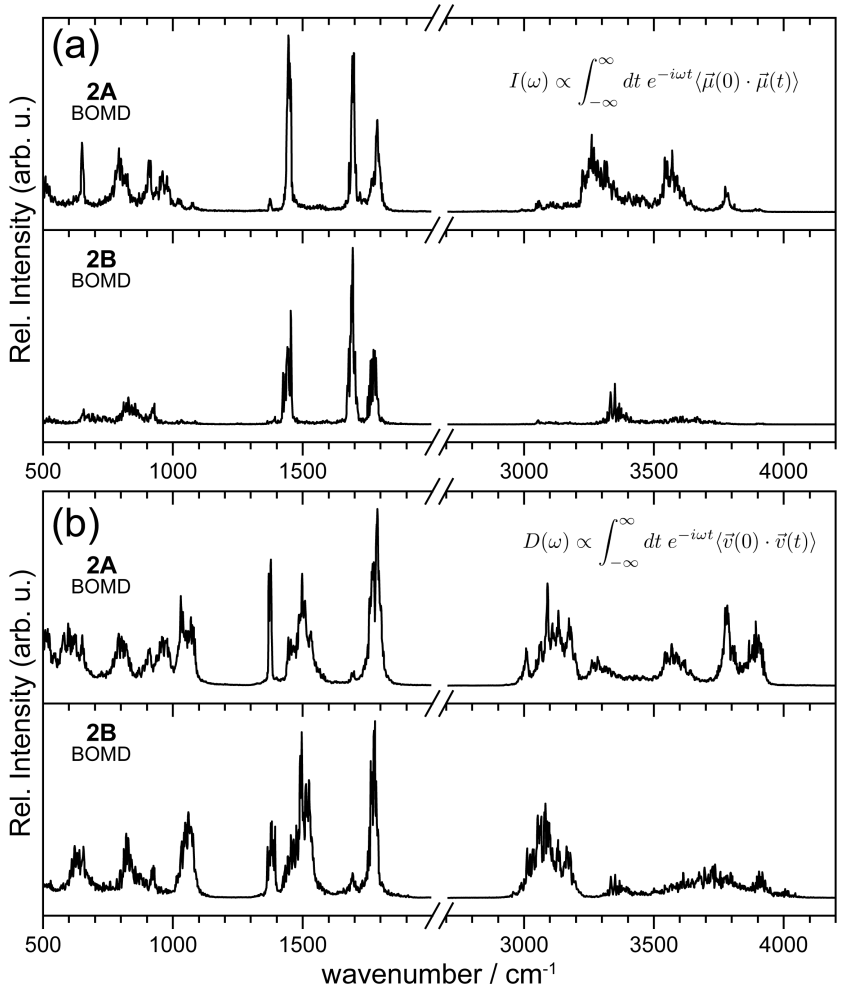


**Figure 12.13:** Average (a) infrared absorption and (b) vibrational spectrum from BOMD simulations A1-A10 and B1, B2, B6, where each spectrum is obtained from the molecular dynamics trajectories by the indicated Fourier transform.

**Table 12.7:** Cartesian coordinates (Å) for the MP2/aug-cc-pVDZ optimized geometry of the $D_2$-tagged $Ac^-(H_2O)_2$ anion.

| **2A** | X | Y | Z | **2B** | X | Y | Z |
|---|---|---|---|---|---|---|---|
| O | -0.37343 | -1.30772 | -0.27757 | C | -0.24567 | 0.54340 | 0.05307 |
| C | -1.00205 | -0.21666 | -0.08259 | O | 0.39673 | -0.56268 | 0.15557 |
| O | -0.50971 | 0.89394 | 0.30243 | O | -1.49982 | 0.67164 | -0.08542 |
| C | -2.51781 | -0.22820 | -0.34792 | C | 0.58990 | 1.83126 | 0.14663 |
| H | -2.88264 | -1.24949 | -0.52968 | H | 1.59265 | 1.68328 | -0.28117 |
| H | -3.04912 | 0.22033 | 0.50670 | H | 0.71275 | 2.08691 | 1.21286 |
| H | -2.72762 | 0.39797 | -1.23092 | H | 0.07318 | 2.66518 | -0.35084 |
| H | 1.24982 | -1.29666 | 0.22478 | H | -1.08460 | -2.05185 | 0.11034 |
| O | 2.19217 | -1.26068 | 0.55859 | O | -2.05324 | -2.10983 | 0.01478 |
| H | 2.12054 | -0.59076 | 1.25186 | H | -2.20827 | -1.14422 | -0.05912 |
| H | 1.12749 | 1.36086 | -0.35225 | H | 2.08073 | -0.61174 | 0.04998 |
| O | 2.04341 | 1.49462 | -0.69115 | O | 3.06576 | -0.70130 | -0.09394 |
| H | 2.39506 | 0.59491 | -0.59323 | H | 3.10827 | -1.30138 | -0.84805 |
| D | -1.75714 | 2.14730 | 1.82696 | D | -2.62234 | 2.69361 | -0.42184 |
| D | -2.17680 | 2.52332 | 2.34047 | D | -2.99312 | 3.34964 | -0.53833 |

| **2C** | X | Y | Z | **2D** | X | Y | Z |
|---|---|---|---|---|---|---|---|
| O | 0.02211 | -0.31214 | -1.26300 | O | 0.81230 | -1.33150 | -0.05739 |
| C | -0.71907 | -0.11578 | -0.24721 | C | 1.44269 | -0.22673 | 0.00996 |
| O | -0.32435 | 0.16642 | 0.93671 | O | 0.95194 | 0.94929 | -0.08748 |
| C | -2.24178 | -0.21132 | -0.44448 | C | 2.96536 | -0.29741 | 0.23482 |
| H | -2.48982 | -0.51816 | -1.47076 | H | 3.30942 | -1.33994 | 0.29766 |
| H | -2.66075 | -0.93161 | 0.27625 | H | 3.48233 | 0.21763 | -0.59150 |
| H | -2.69559 | 0.77013 | -0.23070 | H | 3.22207 | 0.23622 | 1.16474 |
| H | 1.32376 | -1.22535 | 1.04974 | H | -0.97585 | -0.80641 | -0.32823 |
| O | 1.81682 | -1.79992 | 0.43734 | O | -1.58350 | -0.04157 | -0.45505 |
| H | 1.44825 | -1.44151 | -0.39428 | H | -0.88535 | 0.64516 | -0.34686 |
| H | 1.41190 | 1.41808 | -0.92154 | H | -4.56201 | 0.15447 | -0.45855 |
| O | 1.54797 | 2.02364 | -0.17390 | O | -4.15968 | 0.12653 | 0.41739 |
| H | 1.01591 | 1.53647 | 0.48792 | H | -3.19511 | 0.06470 | 0.20005 |
| D | -1.80806 | 0.76299 | 2.64477 | D | 2.28168 | 2.85870 | 0.01285 |
| D | -2.27805 | 0.96282 | 3.21161 | D | 2.70594 | 3.49237 | 0.04139 |

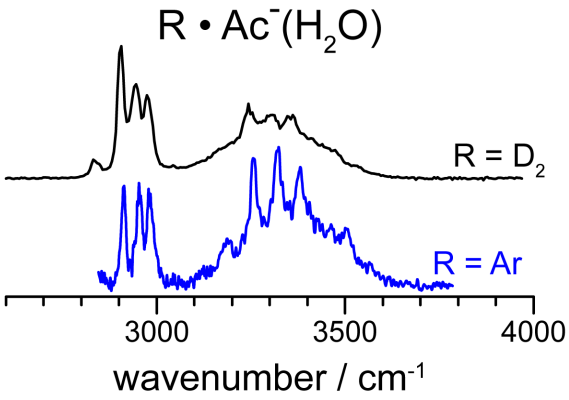


**Figure 12.14:** Infrared photodissociation spectra for tagged $Ac^-(H_2O)$ anions using a $D_2$ (black) or Ar (blue) tagging molecule. Results for Ar were previously reported by Johnson and coworkers.[482]

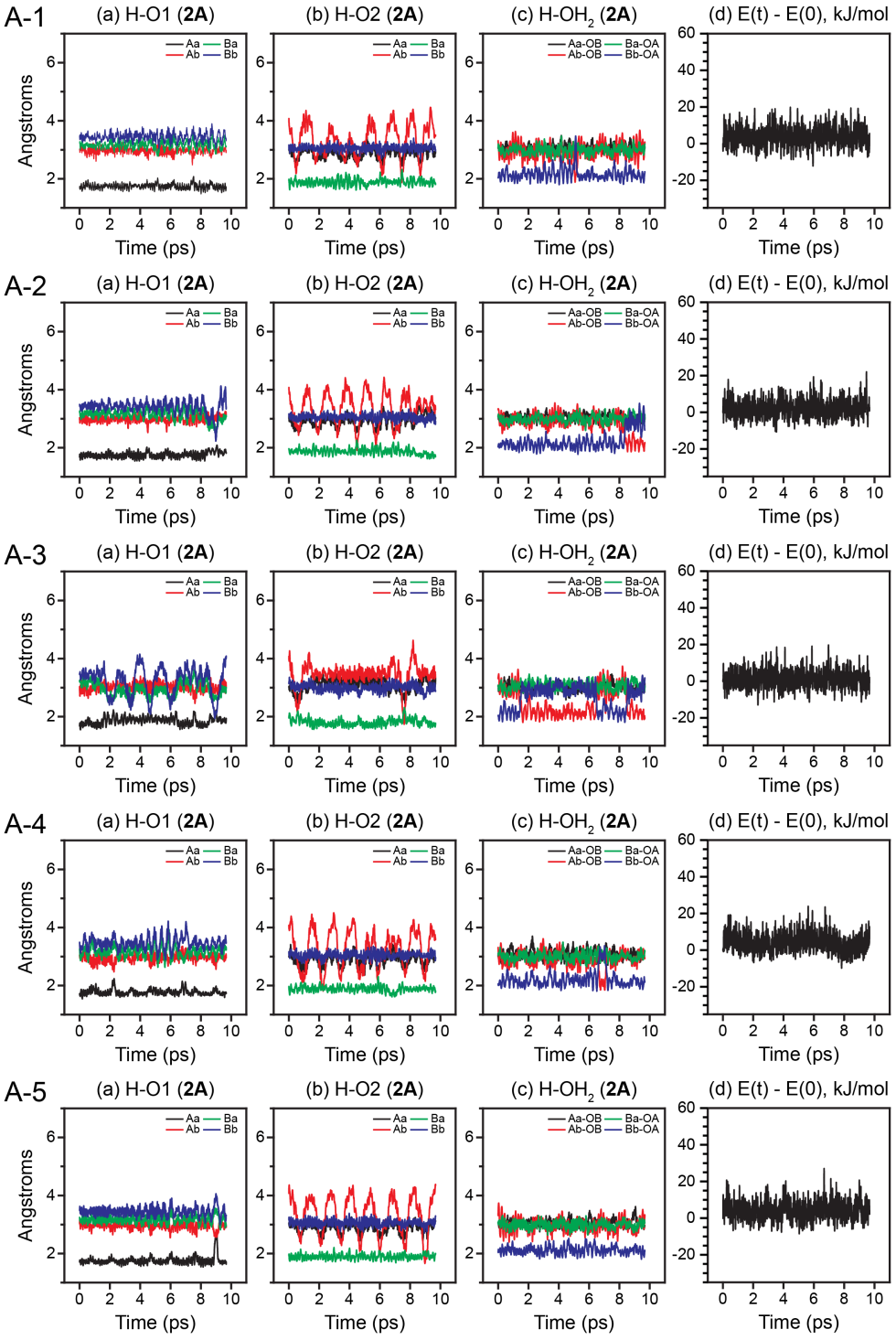


**Figure 12.15:** Summary of BOMD trajectories 1-5 initiated in the **2A** potential well. Each row shows the results of a single trajectory. For each row, panels (a), (b), and (c) are hydrogen bonding plots showing how the ion-water and water-water OH separations change over the 10 ps run time, and panel (d) shows the corresponding energy.

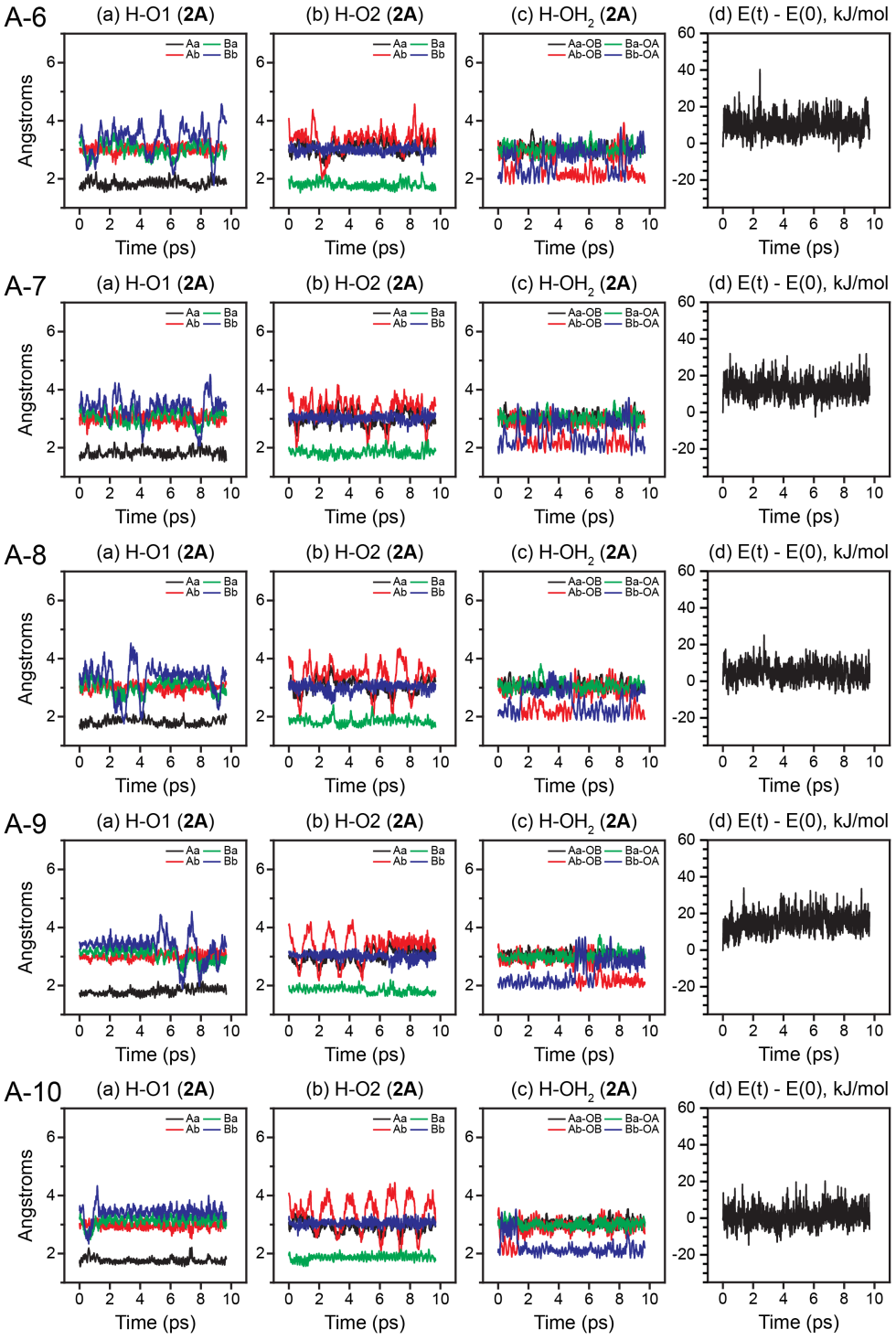


**Figure 12.16:** Summary of BOMD trajectories 6-10 initiated in the **2A** potential well. Each row shows the results of a single trajectory. For each row, panels (a), (b), and (c) are hydrogen bonding plots showing how the ion-water and water-water OH separations change over the 10 ps run time, and panel (d) shows the corresponding energy.

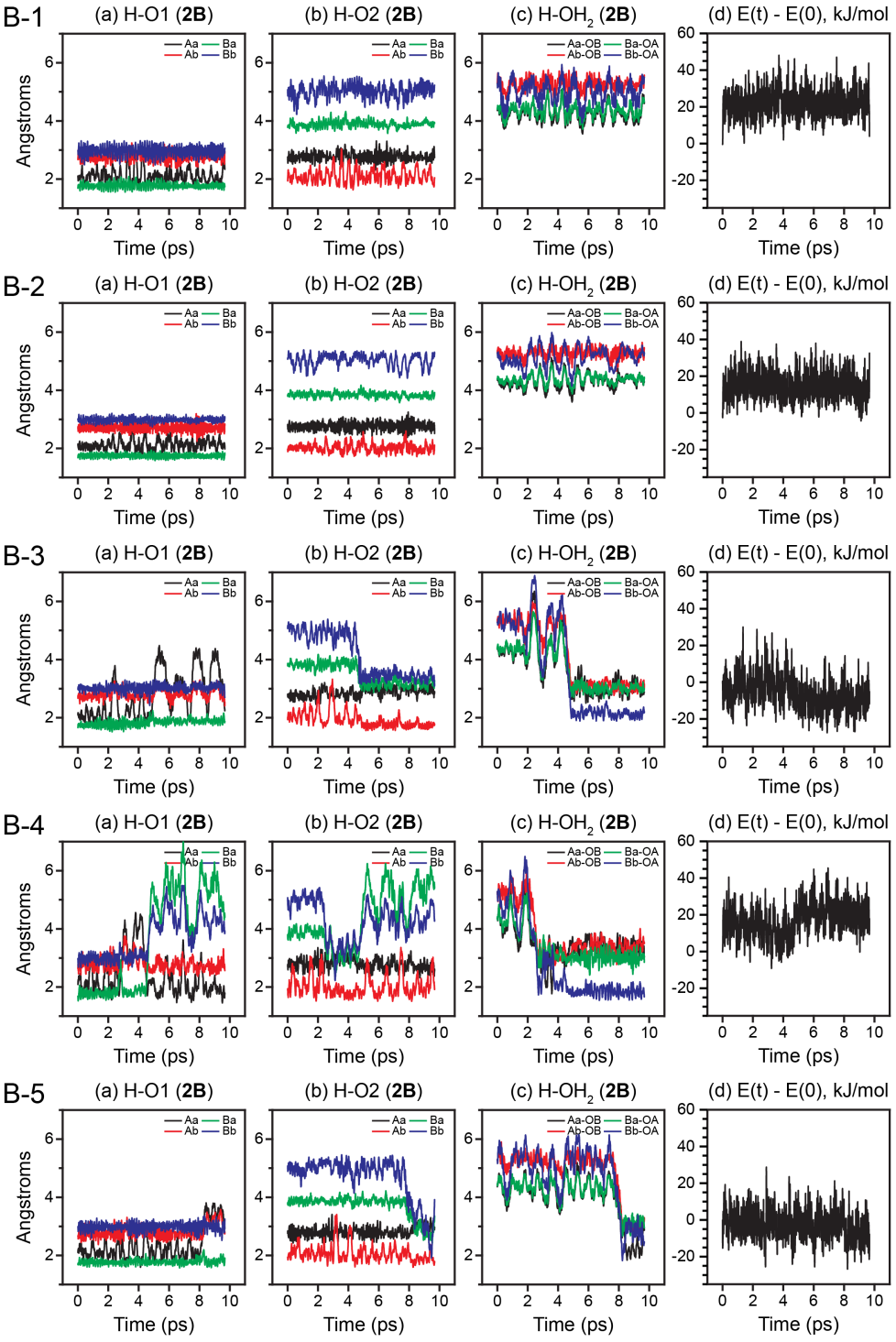


**Figure 12.17:** Summary of BOMD trajectories 1-5 initiated in the **2B** potential well. Each row shows the results of a single trajectory. For each row, panels (a), (b), and (c) are hydrogen bonding plots showing how the ion-water and water-water OH separations change over the 10 ps run time, and panel (d) shows the corresponding energy.

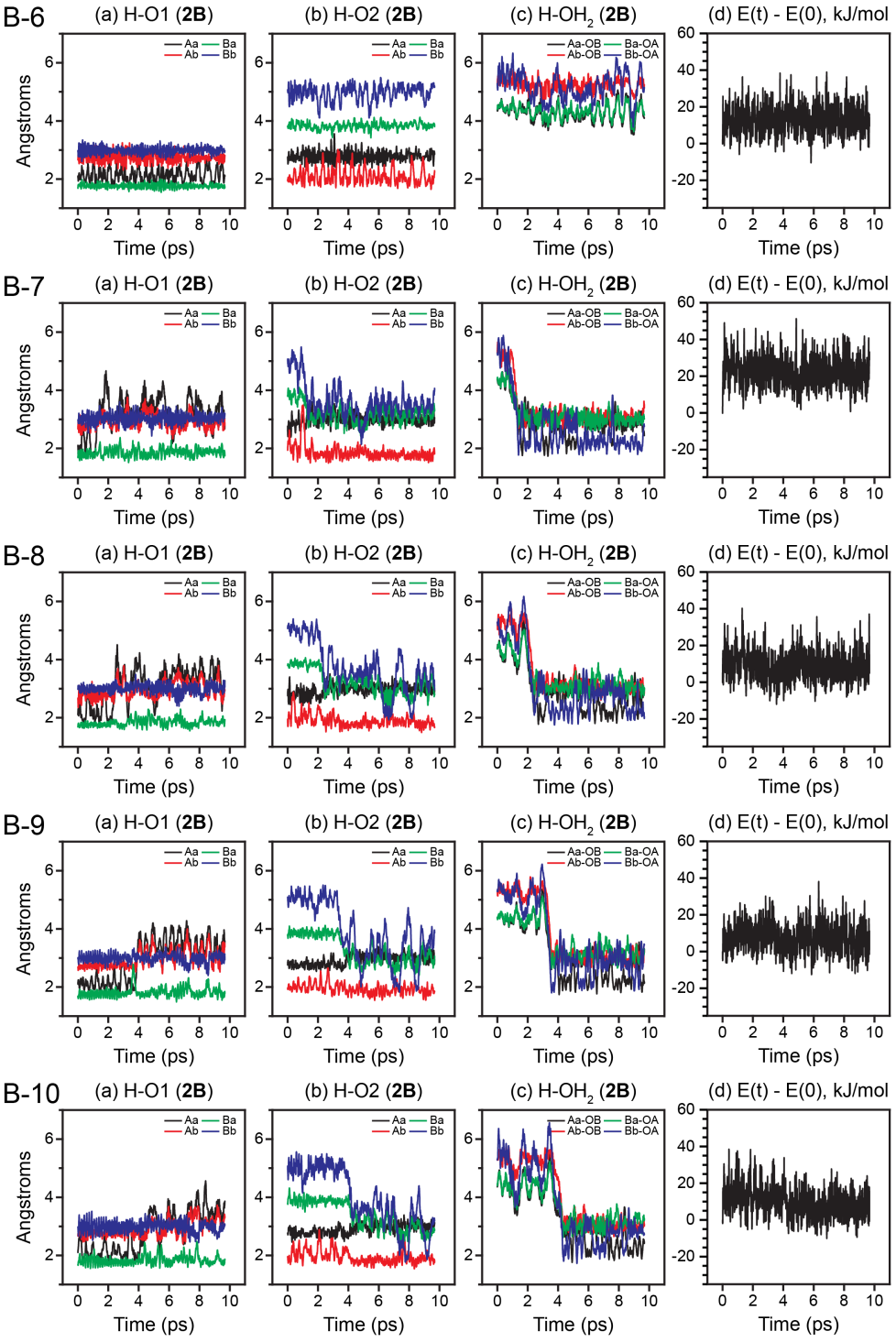


**Figure 12.18:** Summary of BOMD trajectories 6-10 initiated in the **2B** potential well. Each row shows the results of a single trajectory. For each row, panels (a), (b), and (c) are hydrogen bonding plots showing how the ion-water and water-water OH separations change over the 10 ps run time, and panel (d) shows the corresponding energy.

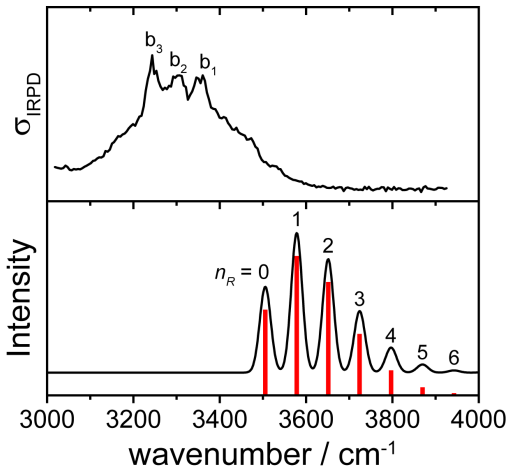


**Figure 12.19:** OH stretching region of the IRPD spectrum of the $n = 1$ cluster (top) compared to the predicted spectrum (bottom) based on the equations provided in Section 12.8.1. The red stick spectrum shows the intensities and energies of the vibrational transitions associated with the OH stretch fundamental using parameters obtained from VPT2 calculations, and the black trace shows a convolution of this spectrum with a 30 $cm^{-1}$ FWHM Gaussian lineshape.

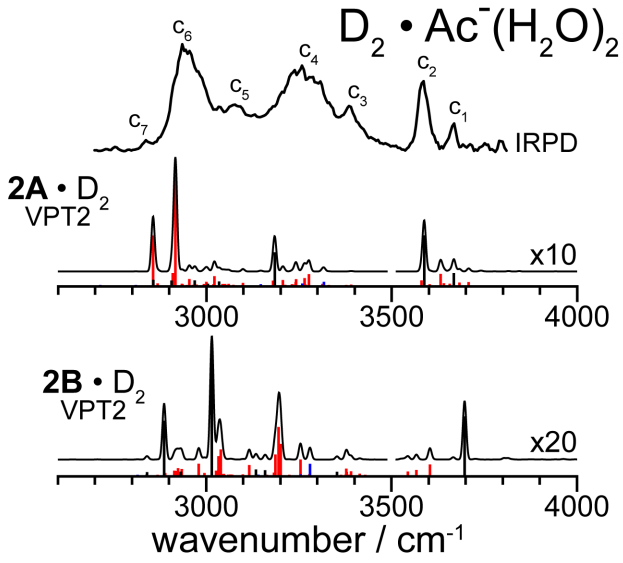


**Figure 12.20:** CH/OH stretching region of the IRPD spectrum of the $n = 2$ cluster (top) compared to the VPT2 results for the two lowest-lying $D_2$-tagged anion isomers (bottom).

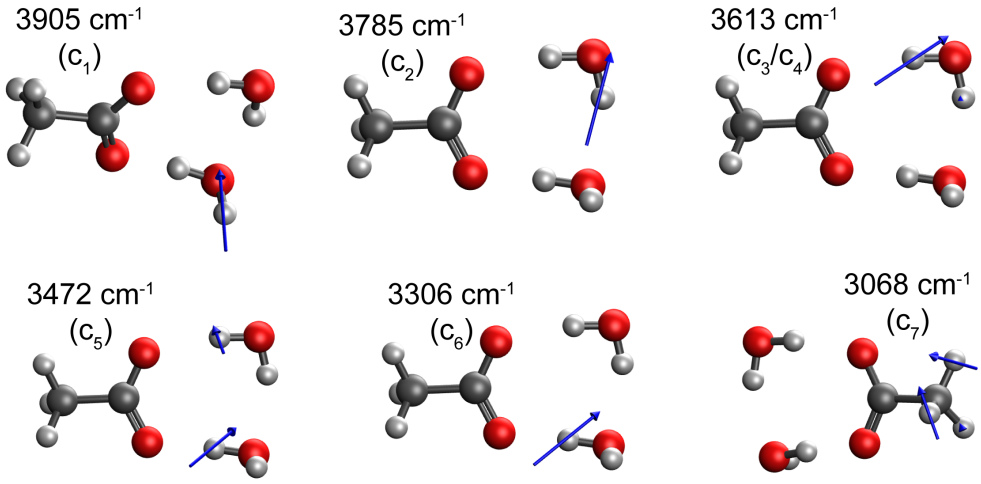


**Figure 12.21:** Generalized normal modes obtained from the BOMD simulations of isomer **2A** used to assign the indicated spectral transitions of the IRPD spectrum. For each illustrated motion, the corresponding frequency is provided.

**Table 12.8:** Vibrational frequencies (in $cm^{-1}$) of the $\mathbf{0} \cdot D_2$ ion calculated using a harmonic and a VPT2 analysis of the MP2/aug-cc-pVDZ optimized geometry. Symmetries are determined relative to the $C_s$ symmetry of the untagged acetate anion. Harmonic and anharmonic intensities are also provided in units of km $mol^{-1}$.

| | MP2 | | VPT2 | | |
|---|---|---|---|---|---|
| Mode | Freq. | Int. | Freq. | Int. | Description |
| $\nu_1$ | 3146 | 50 | 2984 | 15 | $a'$ antisym. CH str. |
| $\nu_2$ | 3127 | 43 | 2980 | 46 | $a''$ antisym. CH str. |
| $\nu_3$ | 3039 | 37 | 2916 | 40 | sym. CH str. |
| $\nu_4$ | 3033 | 163 | 2940 | 106 | $D_2$ str. |
| $\nu_5$ | 1622 | 934 | 1595 | 521 | antisym. CO str. |
| $\nu_6$ | 1466 | 3 | 1410 | 1 | $a''$ $CH_3$ bend |
| $\nu_7$ | 1450 | 34 | 1425 | 19 | $a'$ $CH_3$ bend |
| $\nu_8$ | 1356 | 271 | 1350 | 153 | sym. CO str. |
| $\nu_9$ | 1301 | 10 | 1235 | 123 | $CH_3$ inv. |
| $\nu_{10}$ | 1023 | 0 | 998 | 1 | $a''$ $CH_3$ rock |
| $\nu_{11}$ | 991 | 13 | 972 | 11 | $a'$ $CH_3$ rock |
| $\nu_{12}$ | 881 | 29 | 859 | 40 | CC str. |
| $\nu_{13}$ | 619 | 12 | 620 | 8 | $CO_2$ bend |
| $\nu_{14}$ | 606 | 5 | 586 | 3 | $a''$ $CO_2$ rock |
| $\nu_{15}$ | 436 | 3 | 437 | 3 | $a'$ $CO_2$ rock |
| $\nu_{16}$ | 397 | 1 | 271 | 0 | $D_2$ str. + rot. |
| $\nu_{17}$ | 381 | 1 | 273 | 0 | $D_2$ str. + rot. |
| $\nu_{18}$ | 178 | 12 | 145 | 11 | $D_2$ translation |
| $\nu_{19}$ | 34 | 1 | -19 | 1 | $CH_3$ rot. |
| $\nu_{20}$ | 23 | 1 | 3 | 0 | $CH_3$ rot. |
| $\nu_{21}$ | 17 | 3 | 17 | 2 | $D_2$ wag |

**Table 12.9:** Vibrational frequencies (in $cm^{-1}$) of the **1A** $\cdot$ $D_2$ ion calculated using a harmonic and a VPT2 analysis of the MP2/aug-cc-pVDZ optimized geometry. IM = intermolecular. Harmonic and anharmonic intensities are also provided in units of km $mol^{-1}$.

| | MP2 | | VPT2 | | |
|---|---|---|---|---|---|
| Mode | Freq. | Int. | Freq. | Int. | Description |
| $\nu_1$ | 3630 | 113 | 3328 | 68 | antisym. OH str. |
| $\nu_2$ | 3618 | 381 | 3186 | 108 | sym. OH str. |
| $\nu_3$ | 3159 | 38 | 3000 | 16 | antisym. CH str. |
| $\nu_4$ | 3137 | 32 | 2992 | 36 | antisym. CH str. |
| $\nu_5$ | 3049 | 44 | 2923 | 30 | sym. CH str. |
| $\nu_6$ | 3034 | 118 | 2951 | 71 | $D_2$ str. |
| $\nu_7$ | 1700 | 292 | 1701 | 161 | $H_2O$ bend |
| $\nu_8$ | 1608 | 569 | 1581 | 523 | antisym. CO str. |
| $\nu_9$ | 1469 | 4 | 1417 | 1 | $CH_3$ bend |
| $\nu_{10}$ | 1453 | 44 | 1415 | 17 | $CH_3$ bend |
| $\nu_{11}$ | 1381 | 289 | 1377 | 138 | sym. CO str. |
| $\nu_{12}$ | 1313 | 14 | 1242 | 135 | $CH_3$ inv. |
| $\nu_{13}$ | 1031 | 1 | 1008 | 1 | $CH_3$ rock |
| $\nu_{14}$ | 1000 | 12 | 981 | 11 | $CH_3$ rock |
| $\nu_{15}$ | 898 | 26 | 879 | 37 | CC str. |
| $\nu_{16}$ | 791 | 119 | 824 | 50 | sym. $H_2O$ wag |
| $\nu_{17}$ | 635 | 33 | 636 | 13 | $CO_2$ bend |
| $\nu_{18}$ | 606 | 0 | 587 | 0 | $CO_2$ rock |
| $\nu_{19}$ | 474 | 0 | 398 | 0 | antisym. $H_2O$ wag |
| $\nu_{20}$ | 449 | 2 | 447 | 0 | $CO_2$ rock |
| $\nu_{21}$ | 386 | 0 | 285 | 0 | $D_2$ str. + rot. |
| $\nu_{22}$ | 378 | 2 | 301 | 7 | $D_2$ str. + rot. |
| $\nu_{23}$ | 350 | 83 | 335 | 60 | $H_2O$ rock |
| $\nu_{24}$ | 204 | 18 | 200 | 16 | IM stretch |
| $\nu_{25}$ | 166 | 6 | 152 | 2 | $D_2$ translation |
| $\nu_{26}$ | 73 | 2 | 65 | 0 | IM rock |
| $\nu_{27}$ | 48 | 1 | 32 | 2 | $CH_3$ rot. |
| $\nu_{28}$ | 45 | 1 | 24 | 1 | IM wag |
| $\nu_{29}$ | 31 | 0 | 12 | 1 | $CH_3$ rot. |
| $\nu_{30}$ | 20 | 1 | 43 | 1 | $CH_3$ rot. |

**Table 12.10:** Vibrational frequencies (in $cm^{-1}$) of the **1B** · $D_2$ ion calculated using a harmonic and a VPT2 analysis of the MP2/aug-cc-pVDZ optimized geometry. IM = intermolecular, $OH_D$ refers to the OH bond of water which interacts with the ion. Harmonic and anharmonic intensities are also provided in units of km $mol^{-1}$.

| | MP2 | | VPT2 | | |
|---|---|---|---|---|---|
| Mode | Freq. | Int. | Freq. | Int. | Description |
| $\nu_1$ | 3884 | 25 | 3694 | 13 | free OH str. |
| $\nu_2$ | 3160 | 34 | 3007 | 42 | antisym. CH str. |
| $\nu_3$ | 3139 | 26 | 2992 | 30 | antisym. CH str. |
| $\nu_4$ | 3051 | 165 | 2924 | 482 | $OH_D$ str. + sym. CH str. |
| $\nu_5$ | 3037 | 664 | 2733 | 10 | $OH_D$ str. + sym. CH str. |
| $\nu_6$ | 3027 | 1117 | 2917 | 851 | $OH_D$ str. + $D_2$ str. |
| $\nu_7$ | 1719 | 46 | 1645 | 41 | $H_2O$ bend |
| $\nu_8$ | 1625 | 951 | 1594 | 901 | antisym. CO str. |
| $\nu_9$ | 1470 | 3 | 1419 | 2 | $CH_3$ bend |
| $\nu_{10}$ | 1453 | 52 | 1406 | 21 | $CH_3$ bend |
| $\nu_{11}$ | 1380 | 198 | 1350 | 153 | sym. CO str. |
| $\nu_{12}$ | 1317 | 21 | 1276 | 103 | $CH_3$ inv. |
| $\nu_{13}$ | 1033 | 1 | 1006 | 1 | $CH_3$ rock |
| $\nu_{14}$ | 1005 | 16 | 983 | 14 | $CH_3$ rock |
| $\nu_{15}$ | 933 | 52 | 899 | 35 | OH wag |
| $\nu_{16}$ | 902 | 20 | 884 | 22 | CC str. |
| $\nu_{17}$ | 641 | 14 | 635 | 10 | $CO_2$ bend |
| $\nu_{18}$ | 608 | 5 | 596 | 3 | $CO_2$ rock |
| $\nu_{19}$ | 524 | 69 | 825 | 78 | $H_2O$ wag |
| $\nu_{20}$ | 437 | 5 | 104 | 2 | $CO_2$ rock |
| $\nu_{21}$ | 389 | 1 | 289 | 0 | $D_2$ str. + rot. |
| $\nu_{22}$ | 386 | 1 | 297 | 0 | $D_2$ rot. |
| $\nu_{23}$ | 248 | 60 | 240 | 62 | IM stretch |
| $\nu_{24}$ | 166 | 8 | 132 | 8 | $D_2$ translation |
| $\nu_{25}$ | 86 | 61 | -47 | 1420 | $CH_3$ rot. |
| $\nu_{26}$ | 72 | 5 | 76 | 7 | IM wag |
| $\nu_{27}$ | 55 | 20 | 23 | 372 | $CH_3$ rot. |
| $\nu_{28}$ | 36 | 0 | 3 | 0 | $D_2$ translation |
| $\nu_{29}$ | 34 | 15 | -78 | 3528 | IM wag |
| $\nu_{30}$ | 18 | 0 | -22 | 277 | IM wag |

**Table 12.11:** Vibrational frequencies (in $cm^{-1}$) of the **2A** · $D_2$ ion calculated using a harmonic and a VPT2 analysis of the MP2/aug-cc-pVDZ optimized geometry. IM = intermolecular. Harmonic and anharmonic intensities are also provided in units of km $mol^{-1}$.

| | MP2 | | VPT2 | | |
|---|---|---|---|---|---|
| Mode | Freq. | Int. | Freq. | Int. | Description |
| $\nu_1$ | 3856 | 27 | 3668 | 15 | HA free OH str. |
| $\nu_2$ | 3779 | 124 | 3588 | 63 | HD free OH str. |
| $\nu_3$ | 3479 | 802 | 3186 | 415 | HD bound OH str. |
| $\nu_4$ | 3188 | 1111 | 2857 | 68 | HA bound OH str. |
| $\nu_5$ | 3167 | 46 | 3005 | 17 | CH str. |
| $\nu_6$ | 3144 | 26 | 3035 | 46 | CH str. |
| $\nu_7$ | 3057 | 104 | 2969 | 60 | $D_2$ str. |
| $\nu_8$ | 3056 | 34 | 2907 | 57 | CH str. |
| $\nu_9$ | 1711 | 116 | 1675 | 44 | sym. $H_2O$ bend |
| $\nu_{10}$ | 1683 | 107 | 1650 | 28 | asym. $H_2O$ bend |
| $\nu_{11}$ | 1609 | 581 | 1580 | 436 | asym. CO str. |
| $\nu_{12}$ | 1470 | 5 | 1417 | 2 | $CH_3$ bend |
| $\nu_{13}$ | 1455 | 46 | 1427 | 44 | $CH_3$ bend |
| $\nu_{14}$ | 1402 | 295 | 1381 | 161 | sym. CO str. |
| $\nu_{15}$ | 1322 | 12 | 1261 | 111 | $CH_3$ inv. |
| $\nu_{16}$ | 1038 | 1 | 1014 | 2 | $CH_3$ rock |
| $\nu_{17}$ | 1007 | 13 | 987 | 11 | $CH_3$ rock |
| $\nu_{18}$ | 929 | 61 | 928 | 18 | CC str. |
| $\nu_{19}$ | 897 | 46 | 808 | 38 | $H_2O$ wag |
| $\nu_{20}$ | 778 | 72 | 731 | 29 | $H_2O$ wag |
| $\nu_{21}$ | 644 | 60 | 639 | 6 | $CO_2$ bend |
| $\nu_{22}$ | 607 | 3 | 581 | 3 | $CO_2$ rock |
| $\nu_{23}$ | 567 | 23 | 457 | 8 | $H_2O$ rock |
| $\nu_{24}$ | 485 | 42 | 337 | 14 | $H_2O$ rock |
| $\nu_{25}$ | 467 | 20 | 370 | 4 | IM rock |
| $\nu_{26}$ | 449 | 21 | 615 | 41 | IM rock |
| $\nu_{27}$ | 357 | 1 | 253 | 0 | $D_2$ str. + rot. |
| $\nu_{28}$ | 350 | 0 | 244 | 0 | $D_2$ str. + rot. |
| $\nu_{29}$ | 234 | 38 | 391 | 229 | IM stretch |
| $\nu_{30}$ | 220 | 103 | -16 | 3 | IM stretch |
| $\nu_{31}$ | 186 | 13 | 143 | 12 | IM wag |
| $\nu_{32}$ | 161 | 7 | 156 | 10 | $D_2$ translation |
| $\nu_{33}$ | 116 | 16 | 56 | 12 | IM wag |
| $\nu_{34}$ | 74 | 3 | 72 | 9 | IM wag |
| $\nu_{35}$ | 63 | 1 | 46 | 1 | $D_2$ wag + $CH_3$ rot. |
| $\nu_{36}$ | 41 | 0 | 50 | 1 | $D_2$ wag + $CH_3$ rot. |
| $\nu_{37}$ | 26 | 1 | 13 | 11 | $CH_3$ rot. |
| $\nu_{38}$ | 24 | 3 | 44 | 13 | $CH_3$ rot. |
| $\nu_{39}$ | 13 | 1 | -10 | 7 | IM wag |

**Table 12.12:** Vibrational frequencies (in $cm^{-1}$) of the **2B** · $D_2$ ion calculated using a harmonic and a VPT2 analysis of the MP2/aug-cc-pVDZ optimized geometry. IM = intermolecular, non-HB is used to indicate the OH bond which does not participate in the hydrogen bonding framework, SHB refers to the water which shares in a single hydrogen bond, DHB refers to the water which forms two hydrogen bonds with the anion. Harmonic and anharmonic intensities are also provided in units of km $mol^{-1}$.

| | MP2 | | VPT2 | | |
|---|---|---|---|---|---|
| Mode | Freq. | Int. | Freq. | Int. | Description |
| $\nu_1$ | 3885 | 35 | 3695 | 22 | non-HB OH str. |
| $\nu_2$ | 3719 | 106 | 3347 | 5 | DHB OH str. |
| $\nu_3$ | 3602 | 338 | 3165 | 41 | DHB OH str. |
| $\nu_4$ | 3197 | 1397 | 2887 | 544 | SHB OH str. |
| $\nu_5$ | 3171 | 69 | 3015 | 803 | CH str. |
| $\nu_6$ | 3146 | 24 | 2932 | 27 | CH str. |
| $\nu_7$ | 3057 | 91 | 2837 | 21 | CH + $D_2$ str. |
| $\nu_8$ | 3056 | 48 | 3136 | 34 | CH + $D_2$ str. |
| $\nu_9$ | 1696 | 297 | 1673 | 142 | DHB HOH bend |
| $\nu_{10}$ | 1694 | 11 | 1646 | 33 | SHB HOH bend |
| $\nu_{11}$ | 1608 | 746 | 1579 | 710 | asym. CO str. |
| $\nu_{12}$ | 1474 | 9 | 1419 | 22 | $CH_3$ bend |
| $\nu_{13}$ | 1457 | 47 | 1417 | 32 | $CH_3$ bend |
| $\nu_{14}$ | 1400 | 250 | 1374 | 131 | sym. CO str. |
| $\nu_{15}$ | 1329 | 20 | 1279 | 99 | $CH_3$ inv. |
| $\nu_{16}$ | 1039 | 2 | 1015 | 2 | $CH_3$ rock |
| $\nu_{17}$ | 1017 | 22 | 995 | 10 | $CH_3$ rock |
| $\nu_{18}$ | 918 | 49 | 930 | 16 | CC str. |
| $\nu_{19}$ | 903 | 42 | 796 | 73 | SHB OH wag |
| $\nu_{20}$ | 761 | 119 | 772 | 53 | DHB OH wag |
| $\nu_{21}$ | 654 | 28 | 655 | 19 | $CO_2$ bend |
| $\nu_{22}$ | 598 | 3 | 590 | 9 | $CO_2$ wag |
| $\nu_{23}$ | 478 | 49 | 720 | 108 | $H_2O$ wag |
| $\nu_{24}$ | 455 | 20 | 199 | 1 | $H_2O$ rock |
| $\nu_{25}$ | 439 | 2 | 352 | 7 | $CO_2$ rock |
| $\nu_{26}$ | 359 | 0 | 267 | 0 | $H_2O$ rock |
| $\nu_{27}$ | 356 | 1 | 254 | 0 | $D_2$ str. + rot. |
| $\nu_{28}$ | 333 | 117 | 312 | 75 | $D_2$ str. + rot. |
| $\nu_{29}$ | 224 | 8 | 213 | 15 | IM wag |
| $\nu_{30}$ | 196 | 16 | 185 | 12 | IM str. |
| $\nu_{31}$ | 157 | 3 | 124 | 0 | IM str. |
| $\nu_{32}$ | 110 | 81 | -42 | 110 | IM wag |
| $\nu_{33}$ | 92 | 0 | 75 | 0 | IM wag |
| $\nu_{34}$ | 55 | 3 | 48 | 12 | IM rock |
| $\nu_{35}$ | 49 | 2 | 33 | 30 | $CH_3$ rot. |
| $\nu_{36}$ | 47 | 3 | 35 | 20 | $CH_3$ rot. |
| $\nu_{37}$ | 40 | 3 | 26 | 19 | $CH_3$ rot. |
| $\nu_{38}$ | 37 | 1 | 30 | 22 | $D_2$ wag |
| $\nu_{39}$ | 20 | 0 | 6 | 1 | $D_2$ wag |

**Table 12.13:** Relative isomeric energies in kJ/mol for the MP2-optimized bare and $D_2$-tagged $Ac^-(H_2O)_{1-2}$ clusters as obtained from varying levels of theory.

| | MP2 | CCSD(T) | | | MP2 | CCSD(T) | |
|---|---|---|---|---|---|---|---|
| | DZ | DZ | TZ | | DZ | DZ | TZ |
| **1A** | 0.0 | 0.0 | 0.0 | **1A** · $D_2$ | 0.0 | 0.0 | 0.0 |
| **1B** | 7.9 | 8.9 | 9.6 | **1B** · $D_2$ | 7.8 | 8.9 | 9.3 |
| **2A** | 0.0 | 0.0 | 0.0 | **2A** · $D_2$ | 0.0 | 0.0 | 0.0 |
| **2B** | 0.1 | 0.1 | 0.8 | **2B** · $D_2$ | 0.3 | 0.4 | 0.8 |
| **2C** | 3.9 | 2.9 | 4.9 | **2C** · $D_2$ | 3.7 | 2.8 | 4.9 |
| **2D** | 9.4 | 10.0 | 10.4 | **2D** · $D_2$ | 9.2 | 9.9 | 10.1 |

**Table 12.14:** $D_2$ binding energies of the MP2-optimized $Ac^-(H_2O)_{0-2}$ ions.

| | MP2 | CCSD(T) | |
|---|---|---|---|
| | DZ | DZ | TZ |
| **0** | -6.7 | -7.0 | -7.1 |
| **1A** | -5.3 | -5.8 | -5.3 |
| **1B** | -5.4 | -5.8 | -5.6 |
| **2A** | -4.5 | -5.0 | -4.5 |
| **2B** | -4.4 | -4.8 | -4.4 |
| **2C** | -4.7 | -5.2 | -4.4 |
| **2D** | -4.7 | -5.1 | -4.8 |

**Table 12.15:** Water binding energies of the MP2-optimized $Ac^-(H_2O)_{1-2}$ clusters. For the $n = 2$ clusters, energies are calcualted relative to the **1A** isomer.

| | MP2 | CCSD(T) | | | MP2 | CCSD(T) | |
|---|---|---|---|---|---|---|---|
| | DZ | DZ | TZ | | DZ | DZ | TZ |
| **1A** | -72.4 | -78.5 | -79.9 | **1A** · $D_2$ | -71.0 | -77.3 | -77.9 |
| **1B** | -64.5 | -69.5 | -70.1 | **1B** · $D_2$ | -63.2 | -68.4 | -68.7 |
| **2A** | -56.6 | -62.0 | -63.1 | **2A** · $D_2$ | -55.8 | -61.3 | -62.2 |
| **2B** | -56.5 | -61.9 | -62.3 | **2B** · $D_2$ | -55.5 | -60.9 | -61.4 |
| **2C** | -52.8 | -59.1 | -58.2 | **2C** · $D_2$ | -52.1 | -58.5 | -57.3 |
| **2D** | -47.2 | -52.1 | -52.7 | **2D** · $D_2$ | -46.6 | -51.4 | -52.1 |

# Part V

# Appendix

There are no surprising facts, only models that are surprised by facts; and if a model is surprised by the facts, it is no credit to that model.

Eliezer Yudkowsky
c. 2008

# Bibliography

[1]D. W. Turner, "Molecular photoelectron spectroscopy", *Phil. Trans. Roy. Soc. Long. A* **268**, 7 (1970).

[2]B. Brehm, M. A. Gusinow, and J. L. Hall, "Electron affinity of helium via laser photodetachment of its negative ion", *Phys. Rev. Lett.* **19**, 737 (1967).

[3]A. Kasdan, E. Herbst, and W. C. Lineberger, "Laser photoelectron spectrometry of $CH^-$", *Chem. Phys. Lett.* **31**, 78 (1975).

[4]F. Breyer, P. Frey, and H. Hotop, "High resolution photoelectron spectrometry of negative ions: Rotational transitions in laser-photodetachment of $OH^-$, $SH^-$, $SD^-$", *Z. Phys. A* **300**, 7 (1981).

[5]K. M. Ervin and W. C. Lineberger, "Photoelectron-spectra of $C_2^-$ and $C_2H$", *J. Phys. Chem.* **95**, 1167 (1991).

[6]A. A. Bengali, S. M. Casey, C. L. Cheng, J. P. Dick, P. T. Fenn, P. W. Villalta, and D. G. Leopold, "Negative-ion photoelectron spectroscopy of coordinatively unsaturated group-VI metal-carbonyls- $Cr(CO)_3$, $Mo(CO)_3$, and $W(CO)_3$", *J. Am. Chem. Soc.* **114**, 5257 (1992).

[7]J. C. Rienstra-Kiracofe, G. S. Tschumper, H. F. Schaefer, S. Nandi, and G. B. Ellison, "Atomic and molecular electron affinities: Photoelectron experiments and theoretical computations", *Chem. Rev.* **102**, 231 (2002).

[8]L. A. Posey, M. J. Deluca, and M. A. Johnson, "Demonstration of a pulsed photoelectron spectrometer on mass-selected negative ions: $O^-$, $O_2^-$, and $O_4^-$", *Chem. Phys. Lett.* **131**, 170 (1996).

[9]R. B. Metz, A. Weaver, S. E. Bradforth, T. N. Kitsopoulos, and D. M. Neumark, "Probing the transition state with negative ion photodetachment: The Cl + HCl and Br + HBr reactions", *J. Phys. Chem.* **94**, 1377 (1990).

[10]H. Handschuh, G. Ganteför, and W. Eberhardt, "Vibrational spectroscopy of clusters using a magnetic bottle electron spectrometer", *Rev. Sci. Instrum.* **66**, 3838 (1995).

[11]A. T.J. B. Eppink and D. H. Parker, "Velocity map imaging of ions and electrons using electrostatic lenses: Application in photoelectron and photofragment ion imaging of molecular oxygen", *Rev. Sci. Instrum.* **68**, 3477 (1997).

[12]D. W. Chandler and P. L. Houston, "Two-dimensional imaging of state-selected photodissociation products detected by multiphoton ionization", *J. Chem. Phys.* **87**, 1445 (1987).

[13]H. Helm, N. Bjerre, M. J. Dyer, D. L. Huestis, and M. Saeed, "Images of photoelectrons formed in intense laser fields", *Phys. Rev. Lett.* **70**, 3221 (1993).

[14]B. Baguenard, J. C. Pinare, C. Bordas, and M. Broyer, "Photoelectron imaging spectroscopy of small tungsten clusters: Direct observation of thermionic emission", *Phys. Rev. A* **63**, 023204 (2001).

[15]E. Surber and A. Sanov, "Photoelectron imaging spectroscopy of molecular and cluster anions: $CS_2^-$ and $OCS^-(H_2O)_{1,2}$", *J. Chem. Phys.* **116**, 5921 (2002).

[16]R. Mabbs, E. R. Grumbling, K. Pichugin, and A. Sanov, "Photoelectron imaging: An experimental window into electronic structure", *Chem. Soc. Rev.* **39** (2009).

[17]A. Osterwalder, M. J. Nee, J. Zhou, and D. M. Neumark, "High resolution photodetachment spectroscopy of negative ions via slow photoelectron imaging", *J. Chem. Phys.* **121**, 6317 (2004).

[18]M. L. Weichman, "Slow photoelectron velocity-map imaging and infrared photodissociation of cryo-cooled molecular and cluster anions", PhD thesis (University of California, Berkeley, 2017).

[19]C. Hock, J. B. Kim, M. L. Weichman, T. I. Yacovitch, and D. M. Neumark, "Slow photoelectron velocity-map imaging spectroscopy of cold negative ions", *J. Chem. Phys.* **137**, 244201 (2012).

[20]E. B. Wilson, J. C. Decius, and P. C. Cross, *Molecular vibrations: The theory of infrared and Raman vibrational spectra* (Dover Publications, New York, 1980).

[21]E. P. Wigner, "On the behavior of cross sections near thresholds", *Phys. Rev.* **73**, 1002 (1948).

[22]J. Cooper and R. N. Zare, "Angular distribution of photoelectrons", *J. Chem. Phys.* **48**, 942 (1968).

[23]D. Hanstorp, C. Bengtsson, and D. J. Larson, "Angular distributions in photodetachment from $O^-$", *Phys. Rev. A* **40**, 670 (1989).

[24]E. R. Grumbling and A. Sanov, "Photoelectron angular distributions in negative ion photodetachment from mixed *sp* states", *J. Chem. Phys.* **135**, 164302 (2011).

[25]L. M. Culberson, C. C. Blackstone, and A. Sanov, "Photoelectron angular distributions of pyridinide: A benchmark application of the mixed *sp* model to a truly polyatomic anion", *J. Phys. Chem. A* **117**, 11760 (2013).

[26]A. Sanov, "Laboratory-frame photoelectron angular distributions in anion photodetachment: Insight into electronic structure and intermolecular interactions", *Annu. Rev. Phys. Chem.* **65**, 341 (2014).

[27]A. Sanov, E. R. Grumbling, D. J. Goebbert, and L. M. Culberson, "Photodetachment anisotropy for mixed *sp* states: 8/3 and other fractions", *J. Chem. Phys.* **138**, 054311 (2013).

[28]D. Khuseynov, C. C. Blackstone, L. M. Culberson, and A. Sanov, "Photoelectron angular distributions for states of any mixed character: An experiment-friendly model for atomic, molecular, and cluster anions", *J. Chem. Phys.* **141**, 124312 (2014).

[29]J. Zhou, E. Garand, and D. M. Neumark, "Slow electron velocity-map imaging spectroscopy of the $C_4H^-$ and $C_4D^-$ anions", *J. Chem. Phys.* **127**, 154320 (2007).

[30]E. Garand, T. I. Yacovitch, and D. M. Neumark, "Slow photoelectron imaging spectroscopy of $CCO^-$ and $CCS^-$", *J. Chem. Phys.* **129**, 074312 (2008).

[31]T. I. Yacovitch, J. B. Kim, E. Garand, D. G. van der Poll, and D. M. Neumark, "Slow photoelectron velocity-map imaging spectroscopy of the *n*-methylvinoxide anion", *J. Chem. Phys.* **134**, 132307 (2011).

[32]J. B. Kim, M. L. Weichman, T. I. Yacovitch, C. Shih, and D. M. Neumark, "Slow photoelectron velocity map imaging spectroscopy of the $C_9H_7$ (indenyl) and $C_{13}H_9$ (fluorenyl) anions", *J. Chem. Phys.* **139**, 104301 (2013).

[33]M. L. Weichman, J. B. Kim, and D. M. Neumark, "Vibrational fine structure of $C_5$ via anion slow photoelectron velocity-map imaging", *J. Chem. Phys.* **139**, 144314 (2013).

[34]J. B. Kim, M. L. Weichman, and D. M. Neumark, "High-resolution anion photoelectron spectra of $TiO_2^-$, $ZrO_2^-$, and $HfO_2^-$ obtained by slow electron velocity-map imaging", *Phys. Chem. Chem. Phys.* **15**, 20973 (2013).

[35]M. L. Weichman, J. B. Kim, J. A. DeVine, D. S. Levine, and D. M. Neumark, "Vibrational and electronic structure of the α and β naphthyl radicals via slow photoelectron velocity map imaging", *J. Am. Chem. Soc.* **137**, 1420 (2015).

[36]M. L. Weichman, J. B. Kim, and D. M. Neumark, "Slow photoelectron velocity map imaging spectroscopy of the ortho hydroxyphenoxide anion", *J. Phys. Chem. A* **119**, 6140 (2015).

[37]J. A. DeVine, M. L. Weichman, B. Laws, J. Chang, M. C. Babin, G. Balerdi, C. Xie, C. L. Malbon, W. C. Lineberger, D. R. Yarkony, R. W. Field, S. T. Gibson, J. Ma, H. Guo, and D. M. Neumark, "Encoding of vinylidene isomerization in its anion photoelectron spectrum", *Science* **358**, 336 (2017).

[38]J. A. DeVine, A. A. Taka, M. C. Babin, M. L. Weichman, H. P. Hratchian, and D. M. Neumark, "High-resolution photoelectron spectroscopy of $TiO_3H_2^-$: Probing the $TiO_2^-$ + $H_2O$ dissociative adduct", *J. Chem. Phys.* **148**, 222810 (2018).

[39]H. Sponer and E. Teller, "Electronic spectra of polyatomic molecules", *Rev. Mod. Phys.* **13**, 75 (1941).

[40]G. Herzberg, *Electronic Spectra of Polyatomic Molecules*, Vol. 3, Molecular Spectra and Molecular Structure (D. Van Nostrand Company, Inc., Princeton, NJ, 1945).

[41]G. Orlandi and W. Siebrand, "Theory of vibronic intensity borrowing. Comparison of Herzberg-Teller and Born-Oppenheimer coupling", *J. Chem. Phys.* **58**, 4513 (1973).

[42]C. Cohen-Tannoudji, B. Diu, and F. Laloë, *Quantum Mechanics*, Vol. 2 (Wiley-VCH, 1977).

[43]M. L. Weichman, J. A. DeVine, D. S. Levine, J. B. Kim, and D. M. Neumark, "Isomer specific vibronic structure of the 9-, 1-, and 2-anthracenyl radicals via slow photoelectron velocity map imaging", *Proc. Natl. Acad. Sci. U. S. A.* **113**, 1698 (2016).

[44]R. S. Berry, "Ionization of molecules at low energies", *J. Chem. Phys.* **45**, 1228 (1966).

[45]J. Simons, "Propensity rules for vibration-induced electron detachment of anions", *J. Am. Chem. Soc.* **103**, 3971 (1981).

[46]C. L. Adams, H. Schneider, and J. M. Weber, "Vibrational autodetachment - intramolecular vibrational relaxation translated into electronic motion", *J. Phys. Chem. A* **114**, 4017 (2010).

[47]J. A. DeVine, M. L. Weichman, C. Xie, M. C. Babin, M. A. Johnson, J. Ma, H. Guo, and D. M. Neumark, "Autodetachment from vibrationally excited vinylidene anions", *J. Phys. Chem. Lett.* **9**, 1058 (2018).

[48]H. Han, A. Li, and H. Guo, "Toward spectroscopically accurate global ab initio potential energy surface for the acetylene vinylidene isomerization", *J. Chem. Phys.* **141**, 244312 (2014).

[49]L. Guo, H. Han, J. Ma, and H. Guo, "Quantum dynamics of vinylidene photodetachment on an accurate global acetylene vinylidene potential energy surface", *J. Phys. Chem. A* **119**, 8488 (2015).

[50]C. Duzy and R. S. Berry, "Autoionization of $N_2$", *J. Chem. Phys.* **64**, 2431 (1976).

[51]S. M. O'Malley and D. R. Beck, "Autodetachment lifetime calculations of long-lived metastable states of $Ba^-$ and $Eu^-$", *J. Phys. B: At. Mol. Opt. Phys.* **38**, 2645 (2005).

[52]N. Mardirossian and M. Head-Gordon, "Thirty years of density functional theory in computational chemistry: An overview and extensive assessment of 200 density functionals", *Mol. Phys.* **115**, 2315 (2017).

[53]M. J. Frisch, G. W. Trucks, H. B. Schlegel, G. E. Scuseria, M. A. Robb, J. R. Cheeseman, G. Scalmani, V. Barone, B. Mennucci, G. A. Petersson, H. Nakatsuji, M. Caricato, X. Li, H. P. Hratchian, A. F. Izmaylov, J. Bloino, G. Zheng, J. L. Sonnenberg, M. Hada, M. Ehara, K. Toyota, R. Fukuda, J. Hasegawa, M. Ishida, T. Nakajima, Y. Honda, O. Kitao, H. Nakai, T. Vreven, J. A. Montgomery, J. E. Peralta, F. Ogliaro, M. Bearpark, J. J. Heyd, E. Brothers, K. N. Kudin, V. N. Staroverov, R. Kobayashi, J. Normand, K. Raghavachari, A. Rendell, J. C. Burant, S. S. Iyengar, J. Tomasi, M. Cossi, N. Rega, J. M. Millam, M. Klene, J. E. Knox, J. B. Cross, V. Bakken, C. Adamo, J. Jaramillo, R. Gomperts, R. E. Stratmann, O. Yazyev, A. J. Austin, R. Cammi, C. Pomelli, J. W. Ochterski, R. L. Martin, K. Morokuma, V. G. Zakrzewski, G. A. Voth, P. Salvador, J. J. Dannenberg, S. Dapprich,

A. D. Daniels, O. Farkas, J. B. Foresman, J. V. Ortiz, J. Cioslowski, and D. J. Fox, *Gaussian 09, revision c.01*, Computer Program, 2009.

[54]M. J. Frisch, G. W. Trucks, H. B. Schlegel, G. E. Scuseria, M. A. Robb, J. R. Cheeseman, G. Scalmani, V. Barone, G. A. Petersson, H. Nakatsuji, X. Li, M. Caricato, A. V. Marenich, J. Bloino, B. G. Janesko, R. Gomperts, B. Mennucci, H. P. Hratchian, J. V. Ortiz, A. F. Izmaylov, J. L. Sonnenberg, D. Williams-Young, F. Ding, F. Lipparini, F. Egidi, J. Goings, B. Peng, A. Petrone, T. Henderson, D. Ranasinghe, V. G. Zakrzewski, J. Gao, N. Rega, G. Zheng, W. Liang, M. Hada, M. Ehara, K. Toyota, R. Fukuda, J. Hasegawa, M. Ishida, T. Nakajima, Y. Honda, O. Kitao, H. Nakai, T. Vreven, K. Throssell, J. A. Montgomery Jr., J. E. Peralta, F. Ogliaro, M. J. Bearpark, J. J. Heyd, E. N. Brothers, K. N. Kudin, V. N. Staroverov, T. A. Keith, R. Kobayashi, J. Normand, K. Raghavachari, A. P. Rendell, J. C. Burant, S. S. Iyengar, J. Tomasi, M. Cossi, J. M. Millam, M. Klene, C. Adamo, R. Cammi, J. W. Ochterski, R. L. Martin, K. Morokuma, O. Farkas, J. B. Foresman, and D. J. Fox, *Gaussian development version*, Wallingford, CT, 2016.

[55]Y. H. Shao, Z. T. Gan, E. Epifanovsky, A. T. B. Gilbert, M. Wormit, J. Kussmann, A. W. Lange, A. Behn, J. Deng, X. T. Feng, D. Ghosh, M. Goldey, P. R. Horn, L. D. Jacobson, I. Kaliman, R. Z. Khaliullin, T. Kus, A. Landau, J. Liu, E. I. Proynov, Y. M. Rhee, R. M. Richard, M. A. Rohrdanz, R. P. Steele, E. J. Sundstrom, H. L. Woodcock, P. M. Zimmerman, D. Zuev, B. Albrecht, E. Alguire, B. Austin, G. J. O. Beran, Y. A. Bernard, E. Berquist, K. Brandhorst, K. B. Bravaya, S. T. Brown, D. Casanova, C. M. Chang, Y. Q. Chen, S. H. Chien, K. D. Closser, D. L. Crittenden, M. Diedenhofen, R. A. DiStasio, H. Do, A. D. Dutoi, R. G. Edgar, S. Fatehi, L. Fusti-Molnar, A. Ghysels, A. Golubeva-Zadorozhnaya, J. Gomes, M. W. D. Hanson-Heine, P. H. P. Harbach, A. W. Hauser, E. G. Hohenstein, Z. C. Holden, T. C. Jagau, H. J. Ji, B. Kaduk, K. Khistyaev, J. Kim, J. Kim, R. A. King, P. Klunzinger, D. Kosenkov, T. Kowalczyk, C. M. Krauter, K. U. Lao, A. D. Laurent, K. V. Lawler, S. V. Levchenko, C. Y. Lin, F. Liu, E. Livshits, R. C. Lochan, A. Luenser, P. Manohar, S. F. Manzer, S. P. Mao, N. Mardirossian, A. V. Marenich, S. A. Maurer, N. J. Mayhall, E. Neuscamman, C. M. Oana, R. Olivares-Amaya, D. P. O'Neill, J. A. Parkhill, T. M. Perrine, R. Peverati, A. Prociuk, D. R. Rehn, E. Rosta, N. J. Russ, S. M. Sharada, S. Sharma, D. W. Small, A. Sodt, T. Stein, D. Stuck, Y. C. Su, A. J. W. Thom, T. Tsuchimochi, V. Vanovschi, L. Vogt, O. Vydrov, T. Wang, M. A. Watson, J. Wenzel, A. White, C. F. Williams, J. Yang, S. Yeganeh, S. R. Yost, Z. Q. You, I. Y. Zhang, X. Zhang, Y. Zhao, B. R. Brooks, G. K. L. Chan, D. M. Chipman, C. J. Cramer, W. A. Goddard, M. S. Gordon, W. J. Hehre, A. Klamt, H. F. Schaefer, M. W. Schmidt, C. D. Sherrill, D. G. Truhlar, A. Warshel, X. Xu, A. Aspuru-Guzik, R. Baer, A. T. Bell, N. A. Besley, J. D. Chai, A. Dreuw, B. D. Dunietz, T. R. Furlani, S. R. Gwaltney, C. P. Hsu, Y. S. Jung, J. Kong, D. S. Lambrecht, W. Z. Liang, C. Ochsenfeld, V. A. Rassolov, L. V. Slipchenko, J. E. Subotnik, T. Van Voorhis, J. M. Herbert, A. I. Krylov, P. M. W. Gill, and M. Head-Gordon, "Advances in molecular quantum chemistry contained in the Q-Chem 4 program package", *Mol. Phys.* **113**, 184 (2015).

[56]A. T. B. Gilbert, N. A. Besley, and P. M. W. Gill, "Self consistent field calculations of excited states using the maximum overlap method (MOM)", *J. Phys. Chem. A* **112**, 13164 (2008).

[57]V. A. Mozhayskiy and A. I. Krylov, *ezSpectrum 3.0*, `http://iopenshell.usc.edu/downloads/`, Los Angeles.

[58]K. M. Ervin, PESCAL, `http://wolfweb.unr.edu/~ervin/pes`, 2010.

[59]F. Duschinsky, "The importance of the electron spectrum in multi atomic molecules. Concerning the Franck Condon principle", *Acta Physicochim. URS* **7**, 551 (1937).

[60]J. A. DeVine, M. L. Weichman, M. C. Babin, and D. M. Neumark, "Slow photoelectron velocity map imaging of cold *tert*-butyl peroxide", *J. Chem. Phys.* **147**, 013915 (2017).

[61]C. M. Oana and A. I. Krylov, "Dyson orbitals for ionization from the ground and electronically excited states within equation-of-motion coupled-cluster formalism: Theory, implementation, and examples", *J. Chem. Phys.* **127**, 234106 (2007).

[62]C. M. Oana and A. I. Krylov, "Cross sections and photoelectron angular distributions in photodetachment from negative ions using equation of motion coupled cluster Dyson orbitals", *J. Chem. Phys.* **131**, 124114 (2009).

[63]S. Gozem and A. I. Krylov, *ezDyson 3.0*, `http://iopenshell.usc.edu/downloads/`, Los Angeles.

[64]Y. Liu and C. Ning, "Calculation of photodetachment cross sections and photoelectron angular distributions of negative ions using density functional theory", *J. Chem. Phys.* **143**, 144310 (2015).

[65]M. Gomberg, "Organic radicals", *Chem. Rev.* **1**, 91 (1924).

[66]C. Wentrup, "From reactive intermediates to stable compounds", *Science* **295**, 1846 (2002).

[67]M. Yan, J. C. Lo, J. T. Edwards, and P. S. Baran, "Radicals: Reactive intermediates with translational potential", *J. Am. Chem. Soc.* **138**, 12692 (2016).

[68]C. P. Constantinides, P. A. Koutentis, H. Krassos, J. M. Rawson, and A. J. Tasiopoulos, "Characterization and magnetic properties of a 'super stable' radical 1,3-diphenyl-7-trifluoromethyl-1,4-dihydro-1,2,4-benzotriazin-4-yl", *J. Org. Chem.* **76**, 2798 (2011).

[69]F. D. Vleeschouwer, A. Chankisjijev, W. Yang, P. G. P, and F. D. Proft, "Pushing the boundaries of intrinsically stable radicals: Inverse design using the thiadiazinyl radical as a template", *J. Org. Chem.* **78**, 3151 (2013).

[70]Y. Imada, H. Nakano, K. Furukawa, R. Kishi, M. Nakano, H. Maruyama, M. Nakamoto, A. Sekiguchi, M. Ogawa, T. Ohta, and Y. Yamamoto, "Isolation of hypervalent group-16 radicals and their application in organic-radical batteries", *J. Am. Chem. Soc.* **138**, 479 (2016).

[71]D. J. Hart, "Free-radical carbon-carbon bond formation in organic synthesis", *Science* **223**, 993 (1984).

[72]K. Matyjaszewski and J. Xia, "Atom transfer radical polymerization", *Chem. Rev.* **101**, 2921 (2001).

[73]S. W. M. Crossley, C. Obradors, R. M. Martinez, and R. A. Shenvi, "Mn-, Fe-, and Co-catalyzed radical hydrofunctionalizations of olefins", *Chem. Rev.* **116**, 8912 (2016).

[74]F. Khelifa, S. Erchov, Y. Habibi, R. Snyders, and P. Dubois, "Free-radical-induced grafting from plasma polymer surfaces", *Chem. Rev.* **116**, 3975 (2016).

[75]N. A. Romero and D. A. Nicewicz, "Organic photoredox catalysis", *Chem. Rev.* **116**, 10075 (1026).

[76]J. A. Imlay and S. Linn, "DNA damage and oxygen radical toxicity", *Science* **240**, 1302 (1988).

[77]K. C. Clemitshaw and J. R. Sodeau, "Atmospheric chemistry at 4.2 K: A matrix isolation study of the reaction between $CF_3O_3$ Radicals and NO", *J. Phys. Chem.* **91**, 3650 (1987).

[78]S. Aloisio and J. S. Francisco, "Radical-water complexes in Earth's atmosphere", *Acc. Chem. Res.* **33**, 825 (2000).

[79]A. M. Scheer, C. Mukarakate, D. J. Robichaud, G. B. Ellison, and M. R. Nimols, "Radical chemistry in the thermal decomposition of anisole and deuterated anisoles: An investigation of aromatic growth", *J. Phys. Chem. A* **114**, 9043 (2010).

[80]S. Wallace, K. D. Bartle, and D. L. Perry, "Quantification of nitrogen functional groups in coal and coal derived products", *Fuel* **68**, 1450 (1989).

[81]K. L. Smith, L. D. Smoot, T. H. Fletcher, and R. J. Pugmire, *The structure and reaction processes of coal*, The Plenum Chemical Engineering Series (Springer, 1994).

[82]J. P. Lange, E. van der Heide, J. van Buijtenen, and R. Price, "Furfural: A promising platform for lignocellulosic biofuels", *Chem. Sus. Chem.* **5**, 150 (2012).

[83]S. O. Baek, R. A. Field, M. E. Goldstone, P. W. Kirk, J. N. Lester, and R. Perry, "A review of atmospheric polycyclic aromatic hydrocarbons: Sources, fate and behavior", *Water Air Soil Pollut.* **60**, 279 (1991).

[84]A. Lakhani, "Polycyclic aromatic hydrocarbons: Sources, importance and fate in the atmospheric environment", *Curr. Org. Chem.* **22**, 1050 (2018).

[85]J. L. Puget and A. Léger, "A new component of the interstellar matter: Small grains and large aromatic molecules", *Annu. Rev. Astron. Astrophys.* **27**, 161 (1989).

[86]L. J. Allamandola, A. G.G. M. Tielens, and J. R. Barker, "Interstellar polycyclic aromatic hydrocarbons: The infrared emission bands, the excitation/emission mechanism, and the astrophysical implications", *Astrophys. J. Suppl. Ser.* **71**, 733 (1989).

[87]A. G.G. M. Tielens, "Interstellar polycyclic aromatic hydrocarbon molecules", *Annu. Rev. Astron. Astrophys.* **46**, 289 (2008).

[88]A. Ali, E. C. Sittler, D. Chornay, B. R. Rowe, and C. Puzzarini, "Organic chemistry in Titan's upper atmosphere and its astrbiological consequences. I. Views towards Cassini plasma spectrometer (CAPS) and ion neutral mass spectrometer (INMS) experiments in space", *Planet. Space Sci.* **109**, 46 (2015).

[89]T. W. Schmidt, "The electronic spectroscopy of resonance-stabilised hydrocarbon radicals", *Int. Rev. Phys. Chem.* **35**, 209 (2016).

[90]C. Sah, L. Jacob, M. Saraswat, and S. Venkataramani, "Does a nitrogen lone pair lead to two centered-three electron (2c-3e) interactions in pyridyl radical isomers?", *J. Phys. Chem. A* **121**, 3781 (2017).

[91]L. M. Culberson, C. C. Blackstone, A. A. Wallace, and A. Sanov, "Aromatic stabilization and hybridization trends in photoelectron imaging of heterocyclic radicals and anions", *J. Phys. Chem. A* **119**, 9770 (2015).

[92]K. U. Ingold, "Peroxy radicals", *Acc. Chem. Res.* **2**, 1 (1969).

[93]R. Atkinson, "Atmospheric chemistry of VOCs and $NO_x$", *Atmospheric Environ.* **34**, 2063 (2000).

[94]P. S. Monks, "Gas-phase radical chemistry in the troposphere", *Chem. Soc. Rev.* **34**, 376 (2005).

[95]J. D. Crounse, L. B. Nielsen, S. Jorgensen, H. G. Kjaergaard, and P. O. Wennberg, "Autoxidation of organic compounds in the atmosphere", *J. Phys. Chem. Lett.* **4**, 3513 (2013).

[96]T. Jokinen, M. Sipila, S. Richters, V. Kerminen, P. Paasonen, F. Stratmann, D. Worsnop, M. Kulmala, M. Ehn, H. Herrmann, and T. Berndt, "Rapid autoxidation forms highly oxidized $RO_2$ radicals in the atmosphere", *Angew. Chem. Int. Edit.* **53**, 14596 (2014).

[97]L. Batt, "Reactions of alkoxy and peroxy radicals", *Int. Rev. Phys. Chem.* **6**, 53 (1987).

[98]G. S. Tyndall, R. A. Cox, C. Granier, R. Lesclaux, G. K. Moortgat, M. J. Pilling, A. R. Ravishankara, and T. J. Wallington, "Atmospheric chemistry of small organic peroxy radicals", *J. Geophys. Res.* **106**, 12157 (2001).

[99]K. E. Kautzman, J. D. Surratt, M. N. Chan, A. W. H. Chan, S. P. Hersey, P. S. Chhabra, N. F. Dalleska, P. O. Wennberg, R. C. Flagan, and J. H. Seinfeld, "Chemical composition of gas- and aerosol-phase products from photooxidation of naphthalene", *J. Phys. Chem. A* **114**, 913 (2010).

[100]J. J. Orlando and G. S. Tyndall, "Laboratory studies of organic peroxy radical chemistry: An overview with emphasis on recent issues of atmospheric significance", *Chem. Soc. Rev.* **41**, 6294 (2012).

[101]P. D. Lightfoot, R. A. Cox, J. N. Crowley, M. Destriau, G. D. Hayman, M. E. Jenkin, G. K. Moortgat, and F. Zabel, "Organic peroxy radicals: kinetics, spectroscopy and tropospheric chemistry", *Atmos. Environ.* **26A**, 1805 (1992).

[102]D. J. Jacob, "Heterogeneous chemistry and tropospheric ozone", *Atmospheric Environ.* **34**, 2131 (2000).

[103]Y. Sadanaga, J. Matsumoto, and Y. Kajii, "Photochemical reactions in the urban air: Recent understandings of radical chemistry", *J. Photochem. Photobiol.* **4**, 85 (2003).

[104]D. R. Glowacki and M. J. Pilling, "Unimolecular reactions of peroxy radicals in atmospheric chemistry and combustion", *Chem. Phys. Chem.* **11**, 3836 (2010).

[105]S. S. Brown and J. Stutz, "Nighttime radical observations and chemistry", *Chem. Soc. Rev.* **41**, 6405 (2012).

[106]P. J. Ziemann and R. Atkinson, "Kinetics, products, and mechanisms of secondary organic aerosol formation", *Chem. Soc. Rev.* **41**, 6582 (2012).

[107]F. Bianchi, T. Kurten, M. Riva, C. Mohr, M. P. Rissanen, P. Roldin, T. Berndt, J. D. Crounse, P. O. Wennberg, T. F. Mentel, J. Wildt, H. Junninen, T. Jokinen, M. Kulmala, D. R. Worsnop, J. A. Thornton, N. Donahue, H. G. Kjaergaard, and M. Ehn, "Highly oxygenated organic molecules (HOM) from gas-phase autoxidation involving peroxy radicals: A key contributor to atmospheric aerosol", *Chem. Rev.* **119**, 3472 (2019).

[108]T. J. Wallington, P. Dagaut, and M. J. Kurylo, "Ultraviolet absorption cross sections and reaction kinetics and mechanisms for peroxy radicals in the gas phase", *Chem. Rev.* **92**, 667 (1992).

[109]E. N. Sharp, P. Rupper, and T. A. Miller, "The structure and spectra of organic peroxy radicals", *Phys. Chem. Chem. Phys.* **10**, 3955 (2008).

[110]A. T. Maccarone, B. B. Kirk, C. S. Hansen, T. M. Griffiths, S. Olsen, A. J. Trevitt, and S. J. Blanksby, "Direct observation of photodissociation products from phenylperoxyl radicals isolated in the gas phase", *J. Am. Chem. Soc.* **135**, 9010 (2013).

[111]A. J. Kalafut-Pettibone, J. P. Klems, D. R. Burgess, and W. S. McGivern, "Alkylperoxy radical photochemistry in organic aerosol formation processes", *J. Phys. Chem. A* **117**, 14141 (2013).

[112]B. Nichols, E. N. Sullivan, M. Ryazanov, C. M. Hong, and D. M. Neumark, "Investigation of the two- and three-fragment photodissociation of the *tert*-butyl peroxy radical at 248 nm", *J. Chem. Phys.* **147**, 134304 (2017).

[113]E. N. Sullivan, B. Nichols, and D. M. Neumark, "Photodissociation dynamics of the simplest alkyl peroxy radicals, $CH_3OO$ and $C_2H_5OO$, at 248 nm", *J. Chem. Phys.* **148**, 044309 (2018).

[114]H. F. Schaefer, "1,2 hydrogen shift: Common vehicle for the disappearance of evanescent molecular species", *Acc. Chem. Res.* **12**, 288 (1979).

[115]N. Y. Chang, M. Y. Shen, and C. H. Yu, "Extended ab initio studies of the vinylidene-acetylene rearrangement", *J. Chem. Phys.* **106**, 3237 (1997).

[116]R. Schork and H. Koppel, "Ab initio quantum dynamical study of the vinylidene acetylene isomerization", *Theo. Chem. Acc.* **100**, 204 (1998).

[117]S. L. Zou and J. M. Bowman, "A new ab initio potential energy surface describing acetylene/vinylidene isomerization", *Chem. Phys. Lett.* **368**, 421 (2003).

[118]H. Lee, J. H. Baraban, R. W. Fied, and J. F. Stanton, "High accuracy estimates for the vinylidene acetylene isomerization energy and the ground state rotational constants of :C=$CH_2$", *J. Phys. Chem. A* **117**, 11679 (2013).

[119]T. Carrington, L. M. Hubbard, H. F. Schaefer, and W. H. Miller, "Vinylidene potential energy surface and unimolecular reaction dynamics", *J. Chem. Phys.* **80**, 4347 (1984).

[120]T. C. Germann and W. H. Miller, "Quantum mechanical calculation of resonance tunneling in acetylene isomerization via the vinylidene intermediate", *J. Chem. Phys.* **109**, 94 (1998).

[121]R. L. Hayes, E. Fattal, N. Govind, and E. A. Carter, "Long live vinylidene! A new view of the $H_2C$=C: $\rightarrow$ HC$\equiv$CH rearrangement from ab initio molecular dynamics", *J. Am. Chem. Soc.* **123**, 641 (2001).

[122]R. Schork and H. Koppel, "Barrier recrossing in the vinylidene acetylene isomerization reaction: a five dimensional ab initio quantum dynamical investigation", *J. Chem. Phys.* **115**, 7907 (2001).

[123]M. Bittner and H. Koppel, "Reaction path description of the vinylidene-acetylene isomerization", *Phys. Chem. Chem. Phys.* **5**, 4604 (2003).

[124]S. L. Zou, J. M. Bowman, and A. Brown, "Full dimensionality quantum calculations of acetylene vinylidene isomerization", *J. Chem. Phys.* **118**, 10012 (2003).

[125]Y. Ren, B. Li, and W. Bian, "Full dimensional quantum dynamics study of vinylidene acetylene isomerization: A scheme using the normal mode Hamiltonian", *Phys. Chem. Chem. Phys.* **13**, 2052 (2011).

[126]K. M. Ervin, J. Ho, and W. C. Lineberger, "A study of the singlet and triplet states of vinylidene by photoelectron spectroscopy of $H_2C$=$C^-$, $D_2C$=$C^-$, and HDC=$C^-$. Vinylidene acetylene isomerization", *J. Chem. Phys.* **91**, 5974 (1989).

[127]J. Levin, H. Feldman, A. Baer, D. Ben-Hamu, O. Heber, D. Zajfman, and Z. Vager, "Study of unimolecular reactions by Coulomb explosion imaging: The nondecaying vinylidene", *Phys. Rev. Lett.* **81**, 3347 (1998).

[128]H. K. Gerardi, K. J. Breen, T. L. Guasco, G. H. Weddle, G. H. Gardenier, J. E. Laaser, and M. A. Johnson, "Survey of Ar tagged predissociation and vibrationally mediated photodetachment spectroscopies of the vinylidene anion, $C_2H_2$", *J. Phys. Chem. A* **114**, 1592 (2010).

[129]Y. J. Xu, Y. F. Zhang, and J. Q. Li, "Investigating the role of cationic vacancy on the MgO (001) defect surface: Embedded cluster models study", *Chem. Phys.* **315**, 267 (2005).

[130]A. Baraldi, "Structure and chemical reactivity of transition metal surfaces as probed by synchrotron radiation core level photoelectron spectroscopy", *J. Phys. Condens. Matter* **20**, 093001 (2008).

[131]T. Konig, G. H. Simon, H. P. Rust, G. Pacchioni, M. Heyde, and H. J. Freund, "Measuring the charge state of point defects on MgO/Ag(001)", *J. Am. Chem. Soc.* **131**, 17544 (2009).

[132]U. Diebold, S. C. Li, and M. Schmid, "Oxide surface science", *Annu. Rev. Phys. Chem.* **61**.

[133]S. Benedetti, N. Nilius, P. Myrach, I. Valenti, H. J. Freund, and S. Valeri, "Spontaneous oxidation of Mg atoms at defect sites in an MgO surface", *J. Phys. Chem. C* **115**, 3684 (2011).

[134]K. A. Zemski, D. R. Justes, and A. W. Castleman, "Studies of metal oxide clusters: Elucidating reactive sites responsible for the activity of transition metal oxide catalysts", *J. Phys. Chem. B* **106**, 6136 (2002).

[135]D. K. Bohme and H. Schwarz, "Gas-phase catalysis by atomic and cluster metal ions: The ultimate single-site catalysts", *Angew. Chem. Int. Ed.* **44**, 2336 (2005).

[136]G. E. Johnson, R. Mitric, V. Bonacic-Koutecky, and A. W. Castleman, "Clusters as model systems for investigating nanoscale oxidation catalysis", *Chem. Phys. Lett.* **475**, 1 (2009).

[137]H.-J. Zhai and L.-S. Wang, "Probing the electronic structure of early transition metal oxide clusters: Molecular models towards mechanistic insights into oxide surfaces and catalysis", *Chem. Phys. Lett.* **500**, 185 (2010).

[138]A. W. Castleman, "Cluster structure and reactions: Gaining insights into catalytic processes", *Catal. Lett.* **141**, 1243 (2011).

[139]S. M. Lang and T. M. Bernhardt, "Gas phase metal cluster model systems for heterogeneous catalysis", *Phys. Chem. Chem. Phys.* **14**, 9255 (2012).

[140]M. Anpo, T. Shima, S. Kodama, and Y. Kubokawa, "Photocatalytic hydrogenation of $CH_3CCH$ with $H_2O$ on small-particle $TiO_2$: Size quantization effects and reaction intermediates", *J. Phys. Chem.* **91**, 4305 (1987).

[141]C. Burgel, N. M. Reilly, G. E. Johnson, R. Mitric, M. L. Kimble, A. W. Castleman, and V. Bonacic-Koutecky, "Influence of charge state on the mechanism of CO oxidation on gold clusters", *J. Am. Chem. Soc.* **130**, 1694 (2008).

[142]G. E. Johnson, J. U. Reveles, N. M. Reilly, E. C. Tyo, S. N. Khanna, and A. W. Castleman, "Influence of stoichiometry and charge state on the structure and reactivity of cobalt oxide clusters with CO", *J. Phys. Chem. A* **112**, 11330 (2008).

[143]G. E. Johnson, N. M. Reilly, and A. W. Castleman, "Effect of charge state and stoichiometry on the structure and reactivity of nickel oxide clusters with CO", *Int. J. Mass Spectrom.* **280**, 93 (2009).

[144]J. U. Reveles, G. E. Johnson, S. N. Khanna, and A. W. Castleman, "Reactivity trends in the oxidation of CO by anionic transition metal oxide clusters", *J. Phys. Chem. C* **114**, 5438 (2010).

[145]L. S. Wang, X. Li, and H. F. Zhang, "Probing the electronic structure of iron clusters using photoelectron spectroscopy", *Chem. Phys.* **262**, 53 (2000).

[146]A. Pramann, K. Koyasu, A. Nakajima, and K. Kaya, "Photoelectron spectroscopy of cobalt oxide cluster anions", *J. Phys. Chem. A* **106**, 4891 (2002).

[147]H.-J. Zhai and L.-S. Wang, "Probing the electronic structure and band gap evolution of titanium oxide clusters $(TiO_2)_n^-$ $(n = 1 - 10)$ using photoelectron spectroscopy", *J. Am. Chem. Soc.* **129**, 3022 (2007).

[148]S. G. Li, H. J. Zhai, L. S. Wang, and D. A. Dixon, "Structural and electronic properties of reduced transition metal oxide clusters, $M_3O_8$ and $M_3O_8^-$ (M = Cr, W), from photoelectron spectroscopy and quantum chemical calculations", *J. Phys. Chem. A* **113**, 11273 (2009).

[149]J. E. Mann, S. E. Waller, D. W. Rothgeb, and C. C. Jarrold, "Study of $Nb_2O_y$ $(y = 2-5)$ anion and neutral clusters using anion photoelectron spectroscopy and density functional theory calculations", *J. Chem. Phys.* **135**, 104317 (2011).

[150]X. L. Xu, B. Yang, Z. Y. Wei, G. J. Cao, H. G. Xu, and W. J. Zheng, "Structural and bonding properties of $Cu_3O_3^-$ and $Cu_3O_4^-$ clusters: Anion photoelectron spectroscopy and density functional calculations", *Phys. Chem. Chem. Phys.* **20**, 20622 (2018).

[151]J. B. Kim, M. L. Weichman, and D. M. Neumark, "Structural isomers of $Ti_2O_4$ and $Zr_2O_4$ anions identified by slow photoelectron velocity-map imaging spectroscopy", *J. Am. Chem. Soc.* **136**, 7159 (2014).

[152]J. B. Kim, M. L. Weichman, and D. M. Neumark, "Slow photoelectron velocity-map imaging spectroscopy of the $Fe_3O^-$ and $Co_3O^-$ anions", *J. Chem. Phys.* **141**, 174307 (2014).

[153]J. B. Kim, M. L. Weichman, and D. M. Neumark, "Vibronic structure of $VO_2$ probed by slow photoelectron velocity-map imaging spectroscopy", *J. Chem. Phys.* **140**, 034307 (2014).

[154]J. B. Kim, M. L. Weichman, and D. M. Neumark, "Low-lying states of FeO and $FeO^-$ by slow photoelectron spectroscopy", *Mol. Phys.* **113**, 2105 (2015).

[155]M. L. Weichman, J. A. DeVine, and D. M. Neumark, "High-resolution photoelectron imaging spectroscopy of cryogenically cooled $Fe_4O^-$ and $Fe_5O^-$", *J. Chem. Phys.* **145**, 054302 (2016).

[156]M. L. Weichman, B. Vlaisavljevich, J. A. DeVine, N. S. Shuman, S. G. Ard, T. Shiozaki, D. M. Neumark, and A. A. Viggiano, "Electronic structure of SmO and $SmO^-$ via slow photoelectron velocity-map imaging spectroscopy and CASPT2 calculations", *J. Chem. Phys.* **147**, 234311 (2017).

[157]D. M. Neumark, "Slow electron velocity map imaging of negative ions: applications to spectroscopy and dynamics", *J. Phys. Chem. A* **112**, 13287 (2008).

[158]M. L. Weichman and D. M. Neumark, "Slow photoelectron velocity-map imaging of cryogenically-cooled anions", *Annu. Rev. Phys. Chem.* **69**, 4 (2018).

[159]M. J. Nee, "Chemical dynamics and structure studied with slow electron velocity-map imaging spectroscopy and infrared dissociation", PhD thesis (University of California, Berkeley, 2005).

[160]J. Zhou, "Slow electron velocity-map imaging spectroscopy of small radicals and infrared multiphoton dissociation study of solvated systems", PhD thesis (University of California, Berkeley, 2007).

[161]E. Garand, "Slow photoelectron imaging and infrared dissociation spectroscopy of ionic clusters", PhD thesis (University of California, Berkeley, 2010).

[162]T. Yacovitch, "Slow photoelectron velocity-map imaging of transient species and infrared multiple photon dissociation of atmospherically relevant anion clusters", PhD thesis (University of California, Berkeley, 2012).

[163]J. B. Kim, "Slow photoelectron imaging spectroscopy of cryogenically-cooled anions", PhD thesis (University of California, Berkeley, 2014).

[164]U. Even, J. Jortner, D. Noy, N. Lavie, and C. Cossart-Magos, "Cooling of large molecules below 1 K and He clusters formation", *J. Chem. Phys.* **112**, 8068 (2000).

[165]J. Simons, "Molecular anions", *J. Phys. Chem. A* **112**, 6401 (2008).

[166]R. M. Reese and V. H. Dibeler, "Ionization and dissociation of nitrogren trifluoride by electron impact", *J. Chem. Phys.* **24**, 1175 (1956).

[167]C. H. DePuy, V. M. Bierbaum, L. A. Flippin, J. J. Grabowski, G. K. King, R. J. Schmitt, and S. A. Sullivan, "Gas phase reactions of anions with substituted silanes", *J. Am. Chem. Soc.* **102**, 5012 (1980).

[168]E. L. Chaney and L. G. Christophorou, "Electron attachment to $N_2O$", *J. Chem. Phys.* **51**, 883 (1989).

[169]M. A. Duncan, "Laser vaporization cluster sources", *Rev. Sci. Instrum.* **83**, 041101 (2012).

[170]M. E. Geusic, M. D. Morse, S. C. O'Brien, and R. E. Smalley, "Surface reactions of metal clusters II: The fast flow cluster reactor", *Rev. Sci. Instrum.* **56**, 2123 (1985).

[171]J. A. Felton, M. Ray, S. E. Waller, J. O. Kafader, and C. C. Jarrold, "$Ce_xO_y^-$ $(x = 2-3)$ + $D_2O$ reactions: Stoichiometric cluster formation from deuteroxide decomposition and anti-Arrhenius behavior", *J. Phys. Chem. A* **118**, 9960 (2014).

[172]W. Paul, "Electromagnetic traps for charged and neutral particles", Rev. Mod. Phys. **62**, 531 (1990).

[173]D. Gerlich, "Inhomogeneous RF-fields - a versatile tool for the study of processes with slow ions", *Adv. Chem. Phys.* **82**, 1 (1992).

[174]R. Wester, "Radiofrequency multipole traps: tools for spectroscopy and dynamics of cold molecular anions", *J. Phys. B: At. Mol. Opt. Phys.* **42**, 153001 (2009).

[175]W. C. Campbell and J. M. Doyle, "Cooling, Trap Loading, and Beam Production Using a Cryogenic Helium Buffer Gas", in *Cold Molecules: Theory, Experiment, Applications*, edited by R. V. Krems, W. C. Stwalley, and B. Friedrich (CRC Press, Boca Raton, FL, 2009) Chap. 13, pp. 473–508.

[176]R. D. Levine, "State-changing collisions: Molecular energy transfer", in *Molecular Reaction Dynamics* (Cambridge University Press, 2009) Chap. 9, pp. 356–393.

[177]M. L. Weichman, J. B. Kim, and D. M. Neumark, "Rovibronic structure in slow photoelectron velocity map imaging spectroscopy of $CH_2CN$ and $CD_2CN$", *J. Chem. Phys.* **140**, 104305 (2014).

[178]J. A. DeVine, M. L. Weichman, X. Zhou, J. Ma, B. Jiang, H. Guo, and D. M. Neumark, "Non adiabatic effects on excited states of vinylidene observed with slow photoelectron velocity map imaging", *J. Am. Chem. Soc.* **138**, 16417 (2016).

[179]W. C. Wiley and I. H. Mclaren, "Time-of-flight mass spectrometer with improved resolution", *Rev. Sci. Instrum.* **26**, 1150 (1955).

[180]B. P. Stoicheff, "High resolution Raman spectroscopy of gases. IX. Spectra of $H_2$, HD, and $D_2$", *Can. J. Phys.* **35**, 730 (1957).

[181]T. M. James, M. Schlosser, S. Fischer, M. Sturm, B. Bornschein, R. J. Lewis, and H. H. Telle, "Accurate depolarization ratio measurements for all diatomic hydrogen isotopologues", *J. Raman. Spectrosc.* **44**, 857 (2013).

[182]B. E. Grossmann, U. N. Singh, N. S. Higdon, L. J. Cotnoir, T. D. Wilkerson, and E. V. Browell, "Raman shifted dye laser for water vapor DIAL measurements", *Appl. Opt.* **26**, 1617 (1987).

[183]M. B. Doyle, C. Abeyasera, and A. G. Suits, *NuACQ*, `http://faculty.missouri.edu/suitsa/NuAqc.html`, 2012.

[184]B. Dick, "Inverting ion images without abel inversion: maximum entropy reconstruction of velocity maps", *Phys. Chem. Chem. Phys.* **16**, 570 (2014).

[185]B. Dick, "MELEXIR: Maximum entropy Legendre expanded image reconstruction. A fast and efficient method for the analysis of velocity map imaging or photoelectron imaging data", *Phys. Chem. Chem. Phys.* **21**, 19499 (2019).

[186]V. Dribinski, A. Ossadtchi, V. A. Mandelshtam, and H. Reisler, "Reconstruction of Abel-transformable images: The Gaussian basis-set expansion Abel transform method", *Rev. Sci. Instrum.* **73**, 2634 (2002).

[187]U. Berzinsh, M. Gustafsson, D. Hanstorp, A. Klinkmuller, U. Ljungblad, and A. M. Martenssonpendrill, "Isotope shift in the electron-affinity of chlorine", *Phys. Rev. A* **51**, 231 (1995).

[188]C. Blondel, C. Delsart, and F. Goldfarb, "Electron spectrometer at the μeV level and the electron affinities of Si and F", *J. Phys. B: At., Mol. Opt. Phys.* **34**, L281 (2001).

[189]F. Breyer, P. Frey, and H. Hotop, "High resolution photoelectron spectrometry of negative ions: Fine-structure transitions in $O^-$ and $S^-$ photodetachment", *Z. Phys.* **286**, 133 (1978).

[190]C. Blondel, W. Chaibi, C. Delsart, C. Drag, F. Goldfarb, and S. Kroger, "The electron affinities of O, Si, and S revisited with the photodetachment microscope", *Eur. Phys. J. D* **33**, 335 (2005).

[191]M. Scheer, C. A. Brodie, R. C. Bilodeau, and H. K. Haugen, "Laser spectroscopic measurements of binding energies and fine-structure splittings of $Co^-$, $Ni^-$, $Rh^-$, and $Pd^-$", *Phys. Rev. A* **58**, 2051 (1998).

[192]J. R. Gascooke, S. T. Gibson, and W. D. Lawrence, "A 'circularisation' method to repair deformations and determine the center of velocity map images", *J. Chem. Phys.* **147**, 013924 (2017).

[193]B. H. Lipshutz, "5 membered heteroaromatic rings as intermediates in organic synthesis", *Chem. Rev.* **86**, 795 (1986).

[194]M. Mascal and E. B. Nikitin, "Direct, high yield conversion of cellulose into biofuel", *Angew. Chem. Int. Ed.* **47**, 7924 (2008).

[195]M. S. Mettler, S. H. Mushrif, A. D. Paulsen, A. D. Javadekar, D. G. Vlachos, and P. J. Dauenhauer, "Revealing pyrolysis chemistry for biofuels production: Conversion of cellulose to furans and small oxygenates", *Energ. Environ. Sci.* **5**, 5414 (2012).

[196]O. S. L. Bruinsma, P. J. J. Tromp, H. J.J. D. Nolting, and J. A. Moulijn, "Gas phase pyrolysis of coal related aromatic compounds in a coiled tube flow reactor 2. Heterocyclic compounds, their benzo and dibenzo derivatives", *Fuel* **67**, 334 (1988).

[197]D. Fulle, A. Dib, J. H. Kiefer, Q. Zhang, J. Yao, and R. D. Kern, "Pyrolysis of furan at low pressures: Vibrational relaxation, unimolecular dissociation, and incubation times", *J. Phys. Chem. A* **102**, 7480 (1998).

[198]M. A. Grela, V. T. Amorebieta, and A. J. Colussi, "Very low pressure pyrolysis of furan, 2-methylfuran, and 2,5-dimethylfuran the stability of the furan ring", *J. Phys. Chem.* **89**, 38 (1985).

[199]A. Lifshitz, M. Bidani, and S. Bidani, "Thermal reactions of cyclic ethers at high temperatures 3. Pyrolysis of furan behind reflected shocks", *J. Phys. Chem.* **90**, 5373 (1986).

[200]A. Lifshitz, C. Tamburu, and R. Shashua, "Thermal decomposition of 2,5 dimethylfuran. Experimental results and computer modeling", *J. Phys. Chem. A* **102**, 10655 (1998).

[201]P. P. Organ and J. C. Mackie, "Kinetics of pyrolysis of furan", *J. Chem. Soc. Faraday Trans.* **87**, 815 (1991).

[202]K. Sendt, G. B. Bacskay, and J. C. Mackie, "Pyrolysis of furan: Ab initio quantum chemical and kinetic modeling studies", *J. Phys. Chem. A* **104**, 1861 (2000).

[203]K. M. Vogelhuber, S. W. Wren, L. Sheps, and W. C. Lineberger, "The CH bond dissociation energy of furan: Photoelectron spectroscopy of the furanide anion", *J. Chem. Phys.* **134**, 064302 (2011).

[204]L. M. Culberson and A. Sanov, "Electronic states of thiophenyl and furanyl radicals and dissociation energy of thiophene via photoelectron imaging of negative ions", *J. Chem. Phys.* **134**, 204306 (2011).

[205]C. H. DePuy, S. R. Kass, and G. P. Bean, "Formation and reactions of heteroaromatic anions in the gas phase", *J. Org. Chem.* **53**, 4427 (1988).

[206]R. Liska, "New photocleavable structures I: Synthesis of hydroxyalkylphenone analogues electron rich heterocycles", *Heterocycles* **55**, 1475 (2001).

[207]K. M. Ervin, *FCFGAUSS: Gaussian 03 output conversion program*, `http://wolfweb.unr.edu/~ervin/pes`, 2004.

[208]T. E. Sharp and H. M. Rosenstock, "Franck Condon factors for polyatomic molecules", *J. Chem. Phys.* **41**, 3453 (1964).

[209]P. Chen, "Supersonic Jets of Organic Radicals", in *Unimolecular and Bimolecular Ion-Molecule Reaction Dynamics*, edited by C. Y. Ng, T. Baer, and I. Powis (John Wiley, Cambridge, U. K., 1994), pp. 371–397.

[210]J. M. L. Martin and G. de Oliveira, "Towards standard methods for benchmark quality ab initio thermochemistry: W1 and W2 theory", *J. Chem. Phys.* **111**, 1843 (1999).

[211]E. C. Barnes, G. A. Petersson, J. A. Montgomery, M. J. Frisch, and J. M. L. Martin, "Unrestricted coupled cluster and Brueckner doubles variations of W1 theory", *J. Chem. Theor. Comput.* **5**, 2687 (2009).

[212]J. L. Hall and M. W. Siegel, "Angular dependence of laser photodetachment of negative ions of carbon oxygen and hydrogen", *J. Chem. Phys.* **48**, 943 (1968).

[213]J. M. Simmie and H. J. Curran, "Formation enthalpies and bond dissociation energies of alkylfurans. The strongest CX bonds known?", *J. Phys. Chem. A* **113**, 5128 (2009).

[214]S. G. Lias, "Ionization energy evaluation", in *NIST Chemistry WebBook, NIST Standard Reference Database*, Vol. 69, edited by P. J. Linstrom and W. G. Mallard (National Institute of Standards and Technology, Gaithersburg, MD, 2010).

[215]E. P. Clifford, P. G. Wenthold, W. C. Lineberger, G. B. Ellison, C. X. Wang, J. J. Grabowski, F. Vila, and K. D. Jordan, "Properties of tetramethyleneethane (TME) as revealed by ion chemistry and ion photoelectron spectroscopy", *J. Chem. Soc. Perk. T. 2* **5**, 1015 (1998).

[216]S. W. Benson, "Effects of resonance and structure on the thermochemistry of organic peroxy radicals and the kinetics of combustion reactions", *J. Am. Chem. Soc.* **87**, 972 (1964).

[217]F. Kirchner and W. R. Stockwell, "Effect of peroxy radical reactions on the predicted concentrations of ozone, nitrogenous compounds, and radicals", *J. Geophys. Res. Atmos.* **101**, 21007 (1996).

[218]B. J. Finlayson-Pitts and J. N. Pitts, "Tropospheric air pollution: Ozone, airborne toxics, polycyclic aromatic hydrocarbons, and particles", *Science* **276**, 1045 (1997).

[219]J.-H. Xing and A. Miyoshi, "Rate constants for the reactions of a series of alkylperoxy radicals with NO", *J. Phys. Chem. A* **109**, 4095 (2005).

[220]S. Goldstein and A. Samuni, "Kinetics and mechanism of peroxyl radical reactions with nitroxides", *J. Phys. Chem. A* **111**, 1066 (2007).

[221]K. McKee, M. A. Blitz, and M. J. Pilling, "Temperature and pressure studies of the reactions of $CH_3O_2$, $HO_2$, and 1,2 $C_4H_9O_2$ with $NO_2$", *J. Phys. Chem. A* **120**, 1408 (2016).

[222]J. R. Thomas, "Self reactions of *tert* butylperoxy radicals", *J. Am. Chem. Soc.* **87**, 3935 (1965).

[223]A. Tomas and R. Lesclaux, "Self reaction kinetics of the $(CH_3)_2CHC(O)O_2$ and $(CH_3)_3CC(O)O_2$ acylperoxy radicals between 275 and 363 K", *Chem. Phys. Lett.* **319**, 521 (2000).

[224]R. Lee, G. Grynova, K. U. Ingold, and M. L. Coote, "Why are *sec*-alkylperoxyl bimolecular self reactions orders of magnitude faster than the analogous reactions of tert alkylperoxyls? The unanticipated role of CH hydrogen bond donation", *Phys. Chem. Chem. Phys.* **18**, 23673 (2016).

[225]M. S. Stark, "Addition of peroxyl radicals to alkenes and the reaction of oxygen with alkyl radicals", *J. Am. Chem. Soc.* **122**, 4162 (2000).

[226]A. Tomas, E. Villenave, and R. Lesclaux, "Kinetics of the $(CH_3)_2CHCO$ and $(CH_3)_3CCO$ radical decomposition: Temperature and pressure dependences", *Phys. Chem. Chem. Phys.* **2**, 1165 (2000).

[227]A. Miyoshi, "Systematic computational study on the unimolecular reactions of alkylperoxy ($RO_2$), hydroperoxyalkyl (QOOH), and hydroperoxyalkylperoxy ($O_2$QOOH) radicals", *J. Phys. Chem. A* **115**, 3301 (2011).

[228]J. Zádor, C. A. Taatjes, and R. X. Fernandes, "Kinetics of elementary reactions in low temperature autoignition chemistry", *Prog. Energ. Combust.* **37**, 371 (2011).

[229]O. Welz, J. Zádor, J. D. Savee, L. Sheps, D. L. Osborn, and C. A. Taatjes, "Low temperature combustion chemistry of *n*-butanol: Principal oxidation pathways of hydroxybutyl radicals", *J. Phys. Chem. A* **117**, 11983 (2013).

[230]J. D. Savee, E. Papajak, B. Rotavera, H. Huang, A. J. Eskola, O. Welz, L. Sheps, C. A. Taatjes, and D. L. Osborn, "Direct observation and kinetics of a hydroperoxyalkyl radical (QOOH)", *Science* **347**, 643 (2015).

[231]H. E. Hunziker and H. R. Wendt, "Electronic absorption spectra of organic peroxyl radicals in near infrared", *J. Chem. Phys.* **64**, 3488 (1976).

[232]M. B. Pushkarsky, S. J. Zalyubovsky, and T. A. Miller, "Detection and characterization of alkyl peroxy radicals using cavity ringdown spectroscopy", *J. Chem. Phys.* **112**, 10695 (2000).

[233]P. Ase, W. Bock, and A. Snelson, "Alkyperoxy and alkyl radicals. 1. Infrared spectra of $CH_3O_2$ and $CH_3O_4CH_3$ and the ultraviolet photolysis of $CH_3O_2$ in argon + oxygen matrices", *J. Phys. Chem.* **90**, 2099 (1986).

[234]G. Meloni, P. Zou, S. J. Klippenstein, M. Ahmed, S. R. Leone, C. A. Taatjes, and D. L. Osborn, "Energy resolved photoionization of alkylperoxy radicals and the stability of their cations", *J. Am. Chem. Soc.* **128**, 13559 (2006).

[235]J. M. Oakes, L. B. Harding, and G. B. Ellison, "The photoelectron spectroscopy of $HO_2$", *J. Chem. Phys.* **112**, 10695 (1985).

[236]E. P. Clifford, P. G. Wenthold, R. Gareyev, W. C. Lineberger, C. H. DePuy, V. M. Bierbaum, and G. B. Ellison, "Photoelectron spectroscopy, gas phase acidity, and thermochemistry of *tert*-butyl hydroperoxide: Mechanisms for the rearrangement of peroxyl radicals", *J. Chem. Phys.* **109**, 10293 (1998).

[237]S. J. Blanksby, T. M. Ramond, G. E. Davico, M. R. Nimlos, S. Kato, V. M. Bierbaum, and G. B. Ellison, "Heat of formation of the hydroperoxyl radical HOO via negative ion studies", *J. Am. Chem. Soc.* **123**, 9585 (2001).

[238]M. Krauss and R. Osman, "Absorption spectra of ethynyl, ethenyl, and phenyl peroxyl radicals", *J. Phys. Chem.* **99**, 11387 (1995).

[239]J. L. Weisman and M. Head-Gordon, "Origin of substituent effects in the absorption spectra of peroxy radicals: Time dependent density functional theory calculations", *J. Am. Chem. Soc.* **123**, 11686 (2001).

[240]A. F. Gao, X. Sun, X. L. Liang, X. F. Fang, Z. Y. Zhu, and Y. P. Me, "The alkyl peroxyl radicals and their anions: structures and electron affinities", *J. Mol. Struct.* **862**, 105 (2008).

[241]W. Xu and G. Lu, "Structures, electron affinities, and harmonic vibrational frequencies of the simplest alkyl peroxyl radicals and their anions", *J. Phys. Chem. A* **112**, 6999 (2008).

[242]J. Agarwal, A. C. Simmonett, and H. F. Schaefer, "Fundamental vibrational frequencies and spectroscopic constants for the methylperoxyl radical, $CH_3O_2$, and related isotopologues ($CH_3OO$) $C^{13}$, ($CH_3OO$) $O^{18}$ $O^{18}$, and $CD_3OO$", *Mol. Phys.* **110**, 2419 (2012).

[243]D. A. Parkes and R. J. Donovan, "Infrared absorption spectrum of *t*-butylperoxy radicals in the gas phase", *Chem. Phys. Lett.* **36**, 211 (1975).

[244]G. Chettur and A. Snelson, "Alkylperoxy and alkyl radicals. 5. Infrared spectra and ultraviolet photolysis of *t*-$C_4H_9O_2$ radicals in argon plus oxygen matrices", *J. Phys. Chem.* **91**, 5873 (1987).

[245]B. G. Glover and T. A. Miller, "Near IR cavity ringdown spectroscopy and kinetics of the isomers and conformers of the butyl peroxy radical", *J. Phys. Chem. A* **109**, 11191 (2005).

[246]C. Blondel, W. Chaibi, C. Delsart, and C. Drag, "The fine structure of S and $S^-$ measured with the photodetachment microscope", *J. Phys. B: At. Mol. Opt. Phys.* **39**, 1409 (2006).

[247]Y. Shao, L. F. Molnar, Y. Jung, J. Kussmann, C. Ochsenfeld, S. T. Brown, A. T. Gilbert, L. V. Slipchenko, S. V. Levchenko, D. P. O'Neill, R. A. D. Jr, R. C. Lochan, T. Wang, G. J. Beran, N. A. Besley, J. M. Herbert, C. Y. Lin, T. V. Voorhis, S. H. Chien, A. Sodt, R. P. Steele, V. A. Rassolov, P. E. Maslen, P. P. Korambath, R. D. Adamson, B. Austin, J. Baker, E. F. C. Byrd, H. Dachsel, R. J. Doerksen, A. Dreuw, B. D. Dunietz, A. D. Dutoi, T. R. Furlani, S. R. Gwaltney, A. Heyden, S. Hirata, C.-P. Hsu, G. Kedziora, R. Z. Khalliulin, P. Klunzinger, A. M. Lee, M. S. Lee, W. Liang, I. Lotan, N. Nair, B. Peters, E. I. Proynov, P. A. Pieniazek, Y. M. Rhee, J. Ritchie, E. Rosta, C. D. Sherrill, A. C. Simmonett, J. E. Subotnik, H. L. W. III, W. Zhang, A. T. Bell, A. K. Chakraborty, D. M. Chipman, F. J. Keil, A. Warshel, W. J. Hehre, H. F. S. III, J. Kong, A. I. Krylov, P. M. W. Gilla, and M. Head-Gordon, "Advances in methods and algorithms in a modern quantum chemistry program package", *Phys. Chem. Chem. Phys.* **8**, 3172 (2008).

[248]A. I. Krylov and P. M. W. Gill, "Q Chem: An engine for innovation", *Comput. Mol. Sci.* **3**, 317 (2013).

[249]J. A. DeVine, M. L. Weichman, S. J. Lyle, and D. M. Neumark, "High resolution photoelectron imaging of cryogenically cooled α and β furanyl anions", *J. Mol. Spec.* **332**, 16 (2017).

[250]K. J. Reed, A. H. Zimmerman, H. C. Andersen, and J. I. Brauman, "Cross sections for photodetachment of electrons from negative ions near threshold", *J. Chem. Phys.* **64**, 1368 (1975).

[251]J. R. Kershaw, "Fluorescence spectroscopic analysis of coal-derived liquids: Determination of polycyclic aromatic hydrocarbon systems and identification of basic nitrogen heterocycles", *Fuel* **62**, 1430 (1983).

[252]L. E. Fried, M. R. Manaa, P. F. Pagoria, and R. L. Simpson, "Design and synthesis of energetic materials", *Annu. Rev. Mat. Res.* **31**, 291 (2001).

[253]A. E. Axworthy, V. H. Dayan, and G. B. Martin, "Reactions of fuel-nitrogen compounds under conditions of inert pyrolysis", *Fuel* **57**, 29 (1978).

[254]Z.-C. Wang, C. A. Cole, N. J. Demarais, T. P. Snow, and V. M. Bierbaum, "Reactions of azine anions with nitrogen and oxygen atoms: Implications for Titan's upper atmosphere and interstellar chemistry", *J. Am. Chem. Soc.* **137**, 10700 (2015).

[255]J. C. Loison, E. Hebrard, M. Dobrijevic, K. M. Hickson, F. Daralp, V. Hue, G. Gronoff, O. Venot, and Y. Benilan, "The neutral photochemistry of nitriles, amines and imines in the atmosphere of Titan", *Icarus* **247**, 218 (2015).

[256]T. J. Houser, M. E. McCarville, and T. Biftu, "Kinetics of the thermal decomposition of pyridine in a flow system", *Int. J. Chem. Kinet.* **12**, 555 (1980).

[257]J. Jones, G. B. Bacskay, J. C. Mackie, and A. Doughty, "Ab initio studies of the thermal decomposition of azaaromatics: Free radical versus intramolecular mechanism", *J. Chem. Soc. Faraday Trans.* **91**, 1587 (1995).

[258]J. H. Kiefer, Q. Zhang, R. D. Kern, J. Yao, and B. Jursic, "Pyrolyses of aromatic azines: Pyrazine, pyrimidine, and pyridine", *J. Phys. Chem. A* **101**, 7061 (1997).

[259]N. R. Hore and D. K. Russell, "Radical pathways in the thermal decomposition of pyridine and diazines: A laser pyrolysis and semi-empirical study", *J. Chem. Soc., Perkin Trans.* **2**, 269 (1998).

[260]R. Liu, T. T.-S. Huang, J. Tittle, and D. Xia, "A theoretical investigation of the decomposition mechanism of pyridyl radicals", *J. Phys. Chem. A* **104**, 8368 (2000).

[261]X. L. Cheng, Y. Y. Zhao, and Z. Y. Zhou, "Theoretical studies on *p*-pyridyl radical decomposition reactions", *J. Mol. Struc.* **678**, 17 (2004).

[262]X. Cheng, L. Niu, Y. Zhao, and Z. Zhou, "Vibrational analysis for multi-channel decomposition reactions of *o*-pyridyl radical based on DFT methods", *Spectrochim. Acta A* **60**, 907 (2004).

[263]X. Cheng, "Reaction mechanism of decomposition system of *m*-pyridyl radical: A theoretical investigation", *J. Mol. Struc.* **731**, 89 (2005).

[264]M. Lucas, J. Minor, J. Zhang, and C. Brazier, "Ultraviolet photodissociation dynamics of the *o*-pyridyl radical", *J. Phys. Chem. A* **117**, 12138 (2013).

[265]M. Lucas, J. Minor, J. Zhang, and C. Brazier, "H-atom dissociation channels in ultraviolet photochemistry of *m*-pyridyl radical", *Chin. J. Chem. Phys.* **27**, 621 (2014).

[266]A. Korte, A. Mardyukov, and W. Sander, "Pyridyl- and pyridylperoxy radicals – a matrix isolation study", *Aust. J. Chem.* **67**, 1324 (2014).

[267]P. H. Kasai and D. McLeod, "Generation of pyridyl radicals by dissociative electron capture in argon matrices", *J. Am. Chem. Soc.* **92**, 6085 (1970).

[268]J. E. Bennett and B. Mile, "Electron spin resonance spectra of some sigma-type aromatic radicals", *J. Phys. Chem.* **75**, 3432 (1971).

[269]P. H. Kasai and D. McLeod, "Electron spin resonance study of heterocycles. I. Pyridyl radicals", *J. Am. Chem. Soc.* **94**, 720 (1972).

[270]H. Zemel and R. W. Fessenden, "Electron spin resonance studies of phenyl and pyridyl radicals in aqueous solution", *J. Phys. Chem.* **79**, 1419 (1975).

[271]P. G. Wenthold and W. C. Lineberger, "Negative ion photoelectron spectroscopy studies of organic reactive intermediates", *Acc. Chem. Res.* **32**, 597 (1999).

[272]S. W. Wren, K. M. Vogelhuber, J. M. Garver, S. Kato, L. Sheps, V. M. Bierbaum, and W. C. Lineberger, "C-H bond strengths and acidities in aromatic systems: Effects of nitrogen incorporation into mono-, di-, and triazines", *J. Am. Chem. Soc.* **134**, 6584 (2012).

[273]B. S. Schafman and P. G. Wenthold, "Regioselectivity of pyridine deprotonation in the gas phase", *J. Org. Chem.* **72**, 1645 (2007).

[274]A. M. Oliveira, Y. J. Lu, J. H. Lehman, P. B. Changala, J. H. Baraban, J. F. Stanton, and W. C. Lineberger, "Photoelectron spectroscopy of the methide anion: Electron affinities of $CH_3$ and $CD_3$ and inversion splittings of $CH_3^-$ and $CD_3^-$", *J. Am. Chem. Soc.* **137**, 12939 (2015).

[275]J. A. Montgomery, M. J. Frisch, and J. W. Ochterski, "A complete basis set model chemistry. VII. Use of the minimum population localization method", *J. Chem. Phys.* **112**, 6532 (2000).

[276]G. P. F. Wood and L. Radom, "A restricted-open-shell complete-basis-set model chemistry", *J. Chem. Phys.* **125**, 094106 (2006).

[277]P. S. Skell, J. E. Villaume, and F. A. Fagone, "Formation of vinylidene intermediates in reaction of diatomic carbon with propylene", *J. Am. Chem. Soc.* **94**, 7866 (1972).

[278]G. H. Hatzikos and R. I. Masel, "Structure sensitivity of ethylene adsorption on Pt(100): Evidence for vinylidene formation on (1x1) Pt(100)", *Surf. Sci.* **185**, 479 (1987).

[279]M. M. Hills, J. E. Parmeter, and W. H. Weinberg, "Chemisorption and reaction of ethylene on chemically modified Ru(001) surfaces", *J. Am. Chem. Soc.* **109**, 4224 (1987).

[280]M. Ahmed, D. S. Peterka, and A. G. Suits, "The photodissociation of the vinyl radical ($C_2H_2$) at 243nm studied by velocity map imaging", *J. Chem. Phys.* **110**, 4248 (1999).

[281]R. P. Duran, V. T. Amorebieta, and A. J. Colussi, "Pyrolysis of acetylene a thermal source of vinylidene", *J. Am. Chem. Soc.* **109**, 3154 (1987).

[282]S. Joseph and A. J. C. Varandas, "Accurate MRCI and CC study of the most relevant stationary points and other topographical attributes for the ground state $C_2H_2$ potential energy surface", *J. Phys. Chem. A* **114**, 13277 (2010).

[283]J. K. Lundberg, R. W. Field, C. D. Sherrill, E. T. Seidl, Y. Xie, and H. F. Schaefer, "Acetylene: Synergy between theory and experiment", *J. Chem. Phys.* **98**, 8384 (1993).

[284]J. F. Stanton and J. Gauss, "Vibrational structure in the vinylidene anion photoelectron spectrum: Closing the gap between theory and experiment", *J. Chem. Phys.* **110**, 6079 (1999).

[285]A. H. Laufer, "An excited state of acetylene photochemical and spectroscopic evidence", *J. Chem. Phys.* **73**, 49 (1980).

[286]A. H. Laufer, "The formation of the vinylidene radical as an intermediate in the combination of triplet methylene", *J. Chem. Phys.* **76**, 945 (1982).

[287]C. Chen, B. Braams, D. Y. Lee, J. M. Bowman, P. L. Houston, and D. Stranges, "Evidence for vinylidene production in the photodissociation of the allyl radical", *J. Phys. Chem. Lett.* **1**, 1875–1880 (2010).

[288]R. Fernando, C. Qu, J. M. Bowman, R. W. Field, and A. G. Suits, "Does infrared multiphoton dissociation of vinyl chloride yield cold vinylidene?", *J. Phys. Chem. Lett.* **6**, 2457 (2015).

[289]M. P. Jacobson and R. W. Field, "Acetylene at the threshold of isomerization", *J. Phys. Chem. A* **104**, 3073 (2000).

[290]R. Thissen, J. Delwiche, J. M. Robbe, D. Duflot, J. P. Flament, and J. H. D. Eland, "Dissociations of the ethyne dication $C_2H_2^{2+}$", *J. Chem. Phys.* **99**, 6590 (1993).

[291]T. Osipov, C. L. Cocke, M. H. Prior, A. Landers, T. Weber, O. Jagutzki, L. Schmidt, H. Schmidt-Bocking, and R. Dorner, "Photoelectron photoion momentum spectroscopy as a clock for chemical rearrangements: isomerization of the di cation of acetylene to the vinylidene configuration", *Phys. Rev. Lett.* **90**, 233002 (2003).

[292]G. W. King and C. K. Ingold, "The bent excited state of acetylene", *Nature* **169**, 1101 (1952).

[293]C. K. Ingold and G. W. King, "Excited states of acetylene. 1. Possibilities of interaction between sigma bond hybridisation and pi electron excitation with resulting changes of shape during transitions", *J. Chem. Soc.*, 2702 (1953).

[294]C. K. Ingold and G. W. King, "Excited states of acetylene 2. Experimental methods of recording the near ultra violet absorption spectra of acetylenes", *J. Chem. Soc.*, 2704 (1953).

[295]E. N. Lassettre, A. Skerbele, and M. A. Dillon, "Electron impact spectra of ethane and other saturated hydrocarbons", *J. Chem. Phys.* **49**, 2382 (1968).

[296]C. S. Burton and H. E. Hunziker, "Triplet state of acetylene biacetyl emission from mercury photosensitized reaction", *J. Chem. Phys.* **57**, 339 (1972).

[297]H. R. Wendt, H. Hippler, and H. E. Hunziker, "Triplet acetylene: Near infrared electronic absorption spectrum of the *cis* isomer, and formation from methylene", *J. Chem. Phys.* **70**, 4044 (1979).

[298]J. K. G. Watson, M. Herman, J. C. Vancraen, and R. Colin, "The $\tilde{A}$-$\tilde{X}$ band system of acetylene: Analysis of long wavelength bands, and vibration rotation constants for the levels $n\nu_4''$ $(n = 0 - 4)$, $n\nu_3'$ $(n = 0 - 3)$, and $\nu_2' + n\nu_3'$ $(n = 0 - 2)$", *J. Mol. Spec.* **95**, 101 (1982).

[299]S. M. Burnett, A. E. Stevens, C. S. Feigerle, and W. C. Lineberger, "Observation of $X\ ^1A_1$ vinylidene by photoelectron spectroscopy of the $C_2H_2$ ion", *Chem. Phys. Lett.* **100**, 124 (1983).

[300]D. Sulzle and H. Schwarz, "The generation and identification of triplet vinylidene, $H_2C{=}C$, by neutralization reionization mass spectrometry", *Chem. Phys. Lett.* **156**, 397 (1989).

[301]M. P. Conrad and H. F. Schaefer, "Absence of an energetically viable pathway for triplet 1,2 hydrogen shifts: a theoretical study of vinylidene acetylene isomerization", *J. Am. Chem. Soc.* **100**, 7820 (1978).

[302]C. E. Dykstra and H. F. Schaefer, "Vinylidene acetylene rearrangement: self consistent electron pairs study of a model unimolecular reaction", *J. Am. Chem. Soc.* **100**, 1378 (1978).

[303]G. Vacek, J. R. Thomas, B. J. Deleeuw, Y. Yamaguchi, and H. F. Schaefer, "Isomerization reactions on the lowest potential energy hypersurface of triplet vinylidene and triplet acetylene", *J. Chem. Phys.* **98**, 4766 (1993).

[304]J. F. Stanton, C. M. Huang, and P. G. Szalay, "Stationary points on the S1 potential energy surface of $C_2H_2$", *J. Chem. Phys.* **101**, 356 (1994).

[305]J. F. Stanton and J. Gauss, "Some predictions relevant to future spectroscopic observation of S1 vinylidene", *J. Chem. Phys.* **101**, 3001 (1994).

[306]C. D. Sherrill, E. F. C. Byrd, and M. Head-Gordon, "Complete basis set extrapolations for low lying triplet electronic states of acetylene and vinylidene", *J. Chem. Phys.* **113**, 1447 (2000).

[307]S. Boye-Peronne, D. Gauyacq, and J. Lievin, "Theoretical description of electronically excited vinylidene up to 10 eV: First high level ab initio study of singlet valence and Rydberg states", *J. Chem. Phys.* **141**, 174317 (2014).

[308]J. H. J. Dawson and K. R. Jennings, "Production of gas phase radical anions by reaction of O ions with organic substrates", *J. Chem. Soc., Faraday Trans. 2* **72**, 700 (1976).

[309]T. Shiozaki, G. Knizia, and H.-J. Werner, "Explicitly correlated multireference configuration interaction: MRCI-F12", *J. Chem. Phys.* **134** (2011).

[310]P. J. Knowles and H. J. Werner, "An efficient 2nd order MC-SCF method for long configuration expansions", *Chem. Phys. Lett.* **115**, 259 (1985).

[311]H. J. Werner and P. J. Knowles, "A 2nd-order multiconfiguration SCF procedure with optimum convergence", *J. Chem. Phys.* **82**, 5053 (1985).

[312]K. A. Peterson, T. B. Adler, and H.-J. Werner, "Systematically convergent basis sets for explicitly correlated wavefunctions: The atoms H, He, B Ne, and Al Ar", *J. Chem. Phys.* **128**, 084102 (2008).

[313]H.-J. Werner, P. J. Knowles, G. Knizia, F. R. Manby, and M. Schuetz, "Molpro: A general purpose quantum chemistry program package", *Wiley Interdiscip. Rev. Comput. Mol.* **2**, 242 (2012).

[314]B. Jiang and H. Guo, "Permutation invariant polynomial neural network approach to fitting potential energy surfaces", *J. Chem. Phys.* **139**, 054112 (2013).

[315]J. Li, B. Jiang, and H. Guo, "Permutation invariant polynomial neural network approach to fitting potential energy surfaces. ii. four atom systems", *J. Chem. Phys.* **139**, 204103 (2013).

[316]B. Jiang, J. Li, and H. Guo, "Potential energy surfaces from high fidelity fitting of ab initio points: The permutation invariant polynomial neural network approach", *Int. Rev. Phys. Chem.* **35**, 479 (2016).

[317]Z. Xie and J. M. Bowman, "Permutationally invariant polynomial basis for molecular energy surface fitting via monomial symmetrization", *J. Chem. Theo. Comp.* **6**, 26 (2010).

[318]B. J. Braams and J. M. Bowman, "Permutationally invariant potential energy surfaces in high dimensionality", *Int. Rev. Phys. Chem.* **28**, 577 (2009).

[319]H. G. Yu and J. T. Muckerman, "A general variational algorithm to calculate vibrational energy levels of tetraatomic molecules", *J. Mol. Spec.* **214**, 11 (2002).

[320]R. Chen, G. Ma, and H. Guo, "Six dimensional quantum calculations of highly excited vibrational energy levels of hydrogen peroxide and its deuterated isotopomers", *J. Chem. Phys.* **114**, 4763 (2001).

[321]J. Echave and D. C. Clary, "Potential optimized discrete variable representation", *Chem. Phys. Lett.* **190**, 225 (1992).

[322]H. Wei and T. Carrington, "The discrete variable representation of a triatomic hamiltonian in bond length bond angle coordinates", *J. Chem. Phys.* **97**, 3029 (1992).

[323]H. Guo, "Recursive solutions to large eigenproblems in molecular spectroscopy and reaction dynamics", *Rev. Comput. Chem.* **25**, 285 (2007).

[324]R. Chen and H. Guo, "The Chebyshev propagator for quantum systems", *Comput. Phys. Commun.* **119**, 19 (1999).

[325]H. Guo, "A time independent theory of photodissociation based on polynomial propagation", *J. Chem. Phys.* **108**, 2466 (1998).

[326]J. B. Kim, C. Hock, T. I. Yacovitch, and D. M. Neumark, "Slow photoelectron velocity map imaging spectroscopy of cold thiozonide ($S_3^-$)", *J. Phys. Chem. A* **117**, 8126 (2013).

[327]G. Herzberg, *Infrared and Raman Spectra of Polyatomic Molecules*, Vol. 2, Molecular Spectra and Molecular Structure (D. Van Nostrand Company, Inc., Princeton, NJ, 1945).

[328]P. R. Bunker and P. Jensen, *Molecular symmetry and spectroscopy*, 2nd ed. (NRC Research Press, Ottawa, 2006).

[329]C. M. Western, "PGOPHER: A program for simulating rotational, vibrational, and electronic spectra", *J. Quant. Spectrosc. Rad.* **186**, 221 (2017).

[330]M. Bixon and J. Jortner, "Intramolecular radiationless transitions", *J. Chem. Phys.* **48**, 715 (1998).

[331]R. Schneider and W. Domcke, "S1-S2 conical intersection and ultrafast S2-S1 internal conversion in pyrazine", *Chem. Phys. Lett.* **150**, 235 (1988).

[332]C. Xie, X. Hu, L. Zhou, D. Xie, and H. Guo, "Ab initio determination of potential energy surfaces for the first two UV absorption bands of $SO_2$", *J. Chem. Phys.* **139** (2013).

[333]C. Leveque, A. Komainda, R. Taieb, and H. Koeppel, "Ab initio quantum study of the photodynamics and absorption spectrum for the coupled $^1A_2$ and $^1B_1$ states of $SO_2$", *J. Chem. Phys.* **138** (2013).

[334]H. Guo and D. R. Yarkony, "Accurate nonadiabatic dynamics", *Phys. Chem. Chem. Phys.* **18**, 26335 (2016).

[335]D. S. Perry, A. Miller, B. Amyay, A. Fayt, and M. Herman, "Vibration rotation alchemy in acetylene , ($^{12}C_2H_2$), $\tilde{X}\ ^1\Sigma_g^+$ at low vibrational excitation: From high resolution spectroscopy to fast intramolecular dynamics", *Mol. Phys.* **108**, 1115 (2010).

[336]D. S. Perry, J. Martens, B. Amyay, and M. Herman, "Hierarchies of intramolecular vibration rotation dynamical processes in acetylene up to 13,000 $cm^{-1}$", *Mol. Phys.* **110**, 2687 (2012).

[337]G. Strey and I. M. Mills, "Anharmonic force field of acetylene", *J. Mol. Spec.* **59**, 103 (1976).

[338]R. Dressler and M. Allan, "A dissociative electron-attachment, electron transmission, and electron energy-loss study of the temporary negative-ion of acetylene", *J. Chem. Phys.* **87**, 4510 (1987).

[339]Y. Yamamoto, S. I. Murahashi, and I. Moritani, "Direct and sensitized photodecompositions of 1-phenyldiazoethane: the spin state in the 1,2-hydrogen migration to the carbene center", *Tetrahedron* **31**, 2663 (1975).

[340]P. J. Stang, "Unsaturated carbenes", *Chem. Rev.* **78**, 383 (1978).

[341]J. Zador, M. D. Fellows, and J. A. Miller, "Initiation reactions in acetylene pyrolysis", *J. Phys. Chem. A* **121**, 4203 (2017).

[342]Y. Ren and W. Bian, "Mode-specific tunneling splittings for a sequential double-hydrogen transfer case: An accurate quantum mechanical scheme", *J. Phys. Chem. Lett.* **6**, 1824 (2015).

[343]M. P. Jacobson, J. P. O'Brien, and R. W. Field, "Anomalously slow intramolecular vibrational redistribution in the acetylene $X\ ^1\Sigma_g^+$ state above 10000 $cm^{-1}$ of internal energy", *J. Chem. Phys.* **109**, 3831 (1998).

[344]S. J. Cavanagh, S. T. Gibson, M. N. Gale, C. J. Dedman, E. H. Roberts, and B. R. Lewis, "High-resolution velocity-map imaging photoelectron spectroscopy of the O(-) photodetachment fine-structure transitions", *Phys. Rev. A* **76**, 052708 (2007).

[345]C. J. Dedman, E. H. Roberts, S. T. Gibson, and B. R. Lewis, "Fast 1 kV MOSFET switch", *Rev. Sci. Instrum.* **72**, 3718 (2001).

[346]D. D. Hickstein, R. Yurchak, D. Das, C.-Y. Shih, and S. T. Gibson, *PyAbel (v0.7): A Python package for Abel transforms*, `https://github.com/PyAbel/PyAbel`, 2016.

[347]E. W. Hansen and P.-L. Law, "Recursive methods for computing the Abel transform and its inverse", *J. Opt. Soc. Am.* **2**, 510 (1985).

[348]R. Signorell and F. Merkt, "General symmetry selection rules for the photoionization of polyatomic molecules", *Mol. Phys.* **92**, 793 (1997).

[349]J. C. Light and T. Carrington, "Discrete-variable representations and their utilization", *Adv. Chem. Phys.* **114**, 263 (2000).

[350]M. P. Jacobson, C. Jung, H. S. Taylor, and R. W. Field, "State-by-state assignment of the bending spectrum of acetylene at 15000 $cm^{-1}$: A case study of quantum-classical correspondence", *J. Chem. Phys.* **111**, 600 (1999).

[351]D. Xu, R. Chen, and H Guo, "Probing highly excited vibrational eigenfunctions using a modified single Lanczos method: Application to acetylene (HCCH)", *J. Chem. Phys.* **118**, 7273 (2003).

[352]H. Lischka, T. Muller, P. G. Szalay, I. Shavitt, R. M. Pitzer, and R. Shepard, "Columbus-a program system for advanced multireference theory calculations", *Comput. Mol. Sci.* **1**, 191 (2011).

[353]B. H. Lengsfield and D. R. Yarkony, "Advances in Chemical Physics: State-Selected and State-To-State Ion-Molecule Reaction Dynamics, Part 2, Theory", in, Vol. 82 (John Wiley & Sons, Inc., 1992), pp. 1–71.

[354]H. Lischka, M. Dallos, P. G. Szalay, D. R. Yarkony, and R. Shepard, "Analytic evaluation of nonadiabatic coupling terms at the MR-CI level. I. Formalism", *J. Chem. Phys.* **120**, 7322 (2004).

[355]H. Lischka, M. Dallos, P. G. Szalay, D. R. Yarkony, and R. Shepard, "Analytic evaluation of nonadiabatic coupling terms at the MR-CI level. II. Minima on the crossing seam: Formaldehyde and the photodimerization of ethylene", *J. Chem. Phys.* **120**, 7330 (2004).

[356]M. L. Weichman, S. Debnath, J. T. Kelly, S. Gewinner, W. Schollkopf, D. M. Neumark, and K. R. Asmis, "Dissociative water adsorption on gas-phase titanium dioxide cluster anions probed with vibrational action spectroscopy", *Top. Catal.* **61**, 92 (2017).

[357]R. E. Continetti and H. Guo, "Dynamics of transient species in polyatomic photodetachment", *Chem. Soc. Rev.* **46**, 7650 (2017).

[358]D. M. Neumark, K. R. Lykke, T. Andersen, and W. C. Lineberger, "Infrared spectrum and autodetachment dynamics of $NH^-$", *J. Chem. Phys.* **83**, 4364 (1985).

[359]R. F. Foster, W. Tumas, and J. I. Brauman, "Unimolecular decomposition and vibrationally induced electron autodetachment of acetone enolate ion", *J. Chem. Phys.* **79**, 4644 (1983).

[360]T. Andersen, K. R. Lykke, D. M. Neumark, and W. C. Lineberger, "Autodetachment study of the electronic spectroscopy of $FeO^-$", *J. Chem. Phys.* **86**, 1858 (1987).

[361]K. R. Lykke, D. M. Neumark, T. Andersen, V. J. Trapa, and W. C. Lineberger, "Autodetachment spectroscopy and dynamics of $CH_2CN^-$ and $CD_2CN^-$", *J. Chem. Phys.* **87**, 6842 (1987).

[362]J. Lyle, O. Wedig, S. Gulania, A. I. Krylov, and R. Mabbs, "Channel branching ratios in $CH_2CN^-$ photodetachment: Rotational structure and vibrational energy redistribution in autodetachment", *J. Chem. Phys.* **147**, 234309 (2017).

[363]J. Simons, "Semiquantum expressions for electronically nonadiabatic electron ejection rates", *J. Phys. Chem. A* **102**, 6035 (1998).

[364]J. Simons, "Time-domain and tunneling pictures of nonadiabatic induced electron ejection in molecular anions", *J. Phys. Chem. A* **103**, 9408 (1999).

[365]J. Simons, "An analytical model for vibrational non-Born-Oppenheimer induced electron ejection in molecular anions", *J. Chem. Phys.* **117**, 9124 (2002).

[366]S. Matejcik, A. Kiendler, P. Stampfli, A. Stamatovic, and T. D. Mark, "Vibrationally resolved electron attachment to oxygen clusters", *Phys. Rev. Lett.* **77**, 3771 (1996).

[367]G. Knizia, T. B. Adler, and H. J. Werner, "Simplified CCSD(T)-F12 methods: Theory and benchmarks", *J. Chem. Phys.* **130**, 054104 (2009).

[368]C. Eckart, "Some studies concerning rotating axes and polyatomic molecules", *Phys. Rev. Lett.* **47**, 552 (1935).

[369]S. Boye-Peronne, D. Gauyacq, and J. Lievin, "Vinylidene-acetylene cation isomerization investigated by large scale ab initio calculations", *J. Chem. Phys.* **124**, 214305 (2006).

[370]A. J. Bard, "Photoelectrochemistry and heterogeneous photocatalysis at semiconductors", *J. Photochem.* **10**, 59 (1979).

[371]B. O'Regan and M. Gratzel, "A low-cost, high-efficiency solar-cell based on dye-sensitized colloidal $TiO_2$ films", *Nature* **353**, 737 (1991).

[372]G. Phani, G. Tulloch, D. Vittorio, and I. Skryabin, "Titania solar cells: New photovoltaic technology", *Renew. Energ.* **22**, 303 (2001).

[373]M. Gratzel, "Photoelectrochemical cells", *Nature* **414**, 338 (2001).

[374]M. R. Hoffmann, S. T. Martin, W. Y. Choi, and D. W. Bahnemann, "Environmental applications of semiconductor photocatalysis", *Chem. Rev.* **95**, 69 (1995).

[375]K. Satake, A. Katayama, H. Ohkoshi, T. Nakahara, and T. Takeuchi, "Titania $NO_x$ sensors for exhaust monitoring", *Sensor. Actuat. B* **20**, 111 (1994).

[376]G. K. Mor, O. K. Varghese, M. Paulose, and C. A. Grimes, "A self-cleaning, room-temperature titania-nanotube hydrogen gas sensor", *Sens. Lett.* **1**, 42 (2003).

[377]A. L. Linsebigler, G. Lu, and J. T. Yates, "Photocatalysis on $TiO_2$ surfaces: principles, mechanisms, and selected results", *Chem. Rev.* **95**, 735 (1995).

[378]K. Hashimoto, H. Irie, and A. Fujishima, "$TiO_2$ photocatalysis: A historical overview and future prospects", *Jpn. J. Appl. Phys.* **44**, 8269 (2005).

[379]S. N. Habisreutinger, L. Schmidt-Mende, and J. K. Stolarczyk, "Photocatalytic reduction of $CO_2$ on $TiO_2$ and other semiconductors", *Angew. Chem. Int. Edit.* **52**, 7372 (2013).

[380]A. Fujishima and K. Honda, "Electrochemical photolysis of water at a semiconductor electrode", *Nature* **238**, 37 (1972).

[381]A. J. Bard, "Design of semiconductor photoelectrochemical systems for solar energy conversion", *J. Phys. Chem.* **86**, 172 (1982).

[382]M. Ni, M. K. H. Leung, D. Y. C. Leung, and K. Sumathy, "A review and recent developments in photocatalytic water-splitting using $TiO_2$ for hydrogen production", *Renew. Sust. Energ. Rev.* **11**, 401–425 (2007).

[383]J. Schneider, M. Matsuoka, M. Takeuchi, J. Zhang, Y. Horiuchi, M. Anpo, and D. W. Bahnemann, "Understanding $TiO_2$ photocatalysis: Mechanisms and materials", *Chem. Rev.* **114**, 9919 (2014).

[384]M. A. Henderson, "The interaction of water with solid surfaces: Fundamental aspects revisited", *Surf. Sci. Rep.* **46**, 1 (2002).

[385]U. Diebold, "A controversial benchmark system for water-oxide interfaces: $H_2O/TiO_2(110)$", *J. Chem. Phys.* **147**, 040901 (2017).

[386]R. Mu, Z.-j. Zhao, Z. Dohnalek, and J. Gong, "Structural motifs of water on metal oxide surfaces", *Chem. Soc. Rev.* **46**, 1785 (2017).

[387]M. A. Henderson, "The influence of oxide surface-structure on adsorbate chemistry - desorption of water from the smooth, the macrofaceted and the ion sputtered surfaces of $TiO_2(100)$", *Surf. Sci.* **319**, 315 (1994).

[388]T. Bredow and K. Jug, "Theoretical investigation of water adsorption at rutile and anatase surfaces", *Surf. Sci.* **327**, 398 (1995).

[389]M. A. Henderson, "Structural sensitivity in the dissociation of water on $TiO_2$ single-crystal surfaces", *Langmuir* **12**, 5093 (1996).

[390]D. Brinkley, M. Dietrich, T. Engel, P. Farrall, G. Gantner, A. Schafer, and A. Szuchmacher, "A modulated molecular beam study of the extent of $H_2O$ dissociation on $TiO_2(110)$", *Surf. Sci.* **395**, 292 (1998).

[391]G. S. Herman, Z. Dohnalek, N. Ruzycki, and U. Diebold, "Experimental investigation of the interaction of water and methanol with anatase-$TiO_2(101)$", *J. Phys. Chem. B* **107**, 2788 (2003).

[392]M. Takeuchi, G. Martra, S. Coluccia, and M. Anpo, "Investigations of the structure of $H_2O$ clusters adsorbed on $TiO_2$ surfaces by near-infrared absorption spectroscopy", *J. Phys. Chem. B* **109**, 7387 (2005).

[393]S. J. Tan, H. Feng, Y. F. Ji, Y. Wang, J. Zhao, A. D. Zhao, B. Wang, Y. Luo, J. L. Yang, and J. G. Hou, "Observation of photocatalytic dissociation of water on terminal Ti Sites of $TiO_2(110)$ (1 x 1) surface", *J. Am. Chem. Soc.* **134**, 9978 (2012).

[394]L. E. Walle, A. Borg, E. M. J. Johansson, S. Plogmaker, H. Rensmo, P. Uvdal, and A. Sandell, "Mixed dissociative and molecular water adsorption on anatase $TiO_2(101)$", *J. Phys. Chem. C* **115**, 9545 (2011).

[395]Z. H. Geng, X. Chen, W. S. Yang, Q. Guo, C. B. Xu, D. X. Dai, and X. M. Yang, "Highly efficient water dissociation on anatase $TiO_2(101)$", *J. Phys. Chem. C* **120**, 26807 (2016).

[396]H. H. Kristoffersen, J. O. Hansen, U. Martinez, Y. Y. Wei, J. Matthiesen, R. Streber, R. Bechstein, E. Laegsgaard, F. Besenbacher, and B. Hammer, "Role of steps in the dissociative adsorption of water on rutile $TiO_2$(110)", *Phys. Rev. Lett.* **110**, 146101 (2013).

[397]P. C. Redfern, P. Zapol, L. A. Curtiss, T. Rajh, and M. C. Thurnauer, "Computational studies of catechol and water interactions with titanium oxide nanoparticles", *J. Phys. Chem. B* **107**, 11419 (2003).

[398]T. Zheng, C. Wu, M. Chen, Y. Zhang, and P. T. Cummings, "A DFT study of water adsorption on rutile $TiO_2$ (110) surface: The effects of surface steps", *J. Chem. Phys.* **145**, 044702 (2016).

[399]R. L. Kurtz, R. Stockbauer, T. E. Madey, E. Roman, and J. L. D. Segovia, "Synchrotron radiation studies of $H_2O$ adsorption on $TiO_2$ (110)", *Surf. Sci.* **218**, 178 (1989).

[400]M. B. Hugenschmidt, L. Gamble, and C. T. Campbell, "The interaction of $H_2O$ with a $TiO_2$(110) surface", *Surf. Sci.* **302**, 329 (1994).

[401]L.-Q. Wang, K. F. Ferris, P. X. Skiba, A. N. Shultz, D. R. Baer, and M. H. Engelhard, "Interactions of liquid and vapor water with stoichiometric and defective $TiO_2$(100) surfaces", *Surf. Sci.* **440**, 60 (1999).

[402]R. Schaub, P. Thostrup, N. Lopez, E. Laegsgaard, I. Stensgaard, J. K. Norskov, and F. Besenbacher, "Oxygen vacancies as active sites for water dissociation on rutile $TiO_2$(110)", *Phys. Rev. Lett.* **87**, 266104 (2001).

[403]S. Wendt, R. Schaub, J. Matthiesen, E. K. Vestergaard, E. Wahlstrom, M. D. Rasmussen, P. Thostrup, L. M. Molina, E. Laegsgaard, I. Stensgaard, B. Hammer, and F. Besenbacher, "Oxygen vacancies on $TiO_2$(110) and their interaction with $H_2O$ and $O_2^-$: A combined high-resolution STM and DFT study", *Surf. Sci.* **598**, 226 (2005).

[404]O. Bikondoa, C. L. Pang, R. Ithnin, C. A. Muryn, H. Onishi, and G. Thornton, "Direct visualization of defect-mediated dissociation of water on $TiO_2$(110)", *Nat. Mater.* **5**, 189 (2006).

[405]Z. Zhang, O. Bondarchuk, B. D. Kay, J. M. White, and Z. Dohnalek, "Imaging water dissociation on $TiO_2$(110): Evidence for inequivalent geminate OH groups", *J. Phys. Chem. B* **110**, 21840 (2006).

[406]E. Berardo and M. A. Zwijnenburg, "Modeling the water splitting activity of a $TiO_2$ rutile nanoparticle", *J. Phys. Chem. C* **119**, 13384 (2015).

[407]R. O. Ramabhadran, J. E. Mann, S. E. Waller, D. W. Rothgeb, C. C. Jarrold, and K. Raghavachari, "New insights on photocatalytic $H_2$ liberation from water using transition-metal oxides: Lessons from cluster models of molybdenum and tungsten oxides", *J. Am. Chem. Soc.* **135**, 17039 (2013).

[408]M. R. Fagiani, X. Song, S. Debnath, S. Gewinner, W. Scholkopf, K. R. Asmis, F. A. Bischoff, F. Muller, and J. Sauer, "Dissociative water adsorption by $Al_3O_4^+$ in the gas phase", *J. Phys. Chem. Lett.* **8**, 1272 (2017).

[409]H. Wu and L.-S. Wang, "Electronic structure of titanium oxide clusters: $TiO_y$ ($y = 1-3$) and $(TiO_2)_n$ ($n = 1-4$)", *J. Chem. Phys.* **107**, 8221 (1997).

[410]M. L. Weichman, X. Song, M. R. Fagiani, S. Debnath, S. Gewinner, W. Schollkopf, D. M. Neumark, and K. R. Asmis, "Gas phase vibrational spectroscopy of cold $(TiO_2)_n^-$ ($n = 3-8$) clusters", *J. Chem. Phys.* **144**, 124308 (2016).

[411]H. Deng, K. P. Kerns, B. C. Guo, R. C. Bell, and A. W. Castleman, "The formation of $[TiO(H_2O)_n]^+$ cluster ions", *Croat. Chem. Acta* **71**, 1105 (1998).

[412]H.-G. Xu, Z.-N. Li, X.-Y. Kong, S.-G. He, and W.-J. Zheng, "Interaction of $TiO^+$ with water: Infrared photodissociation spectroscopy and density functional calculations", *Phys. Chem. Chem. Phys.* **15**, 17126 (2013).

[413]L. B. Pandey and C. M. Aikens, "Theoretical investigation of the electrochemical mechanism of water splitting on a titanium oxide cluster model", *J. Phys. Chem. A* **116**, 526 (2012).

[414]H. Du, A. D. Sarkar, H. Li, Q. Sun, Y. Jia, and R.-Q. Zhang, "Size dependent catalytic effect of $TiO_2$ clusters in water dissociation", *J. Mol. Catal. A* **366**, 163 (2013).

[415]F. Rodriguez-Hernandez, D. C. Tranca, B. M. Szyja, R. A. v. Santen, A. Martinez-Mesa, L. Uranga-Pina, and G. Seifert, "Water splitting on $TiO_2$-based electrochemical cells: A small cluster study", *J. Phys. Chem. C* **120**, 437 (2016).

[416]T.-H. Wang, Z. Fang, N. W. Gist, S. Li, and D. A. Dixon, "Computational study of the hydrolysis reactions of the ground and first excited triplet states of small $TiO_2$ nanoclusters", *J. Phys. Chem. C* **115**, 9344 (2011).

[417]Z. Fang, M. D. Outlaw, K. K. Smith, N. W. Gist, S. Li, D. A. Dixon, and J. L. Gole, "Computational study of the hydrolysis reactions of small $MO_2$ (M = Zr and Hf) nanoclusters with water", *J. Phys. Chem. C* **116**, 8475 (2012).

[418]M. Chen, T. P. Straatsma, and D. A. Dixon, "Molecular and dissociative adsorption of water on $(TiO_2)_n$ clusters, $n = 1-4$", *J. Phys. Chem. A* **119**, 11406 (2015).

[419]R.-Z. Li, H.-G. Xu, G.-J. Cao, X.-L. Xu, and W.-J. Zheng, "Interaction of $TiO_2^-$ with water: Photoelectron spectroscopy and density functional calculations", *J. Chem. Phys.* **139**, 184303 (2013).

[420]G. D. Purvis and R. J. Bartlett, "A full coupled-cluster singles and doubles model - the inclusion of disconnected triples", *J. Chem. Phys.* **76**, 1910 (1982).

[421]G. E. Scuseria, C. L. Janssen, and H. F. Schaefer, "An efficient reformulation of the closed-shell coupled cluster single and double excitation (CCSD) equations", *J. Chem. Phys.* **89**, 7382 (1988).

[422]S. H. Vosko, L. Wilk, and M. Nusair, "Accurate spin-dependent electron liquid correlation energies for local spin-density calculations - a critical analysis", *Can. J. Phys.* **58**, 1200 (1980).

[423]C. T. Lee, W. T. Yang, and R. G. Parr, "Development of the Colle-Salvetti correlation-energy formula into a functional of the electron-density", *Phys. Rev. B* **37**, 785 (1988).

[424]A. D. Becke, "Density-functional thermochemistry. 3. The role of exact exchange", *J. Chem. Phys.* **98**, 5648 (1993).

[425]P. J. Stephens, F. J. Devlin, C. F. Chabalowski, and M. J. Frisch, "Ab-initio calculation of vibrational absorption and circular-dichroism spectra using density-functional force-fields", *J. Phys. Chem.* **98**, 11623 (1994).

[426]F. Weigend and R. Ahlrichs, "Balanced basis sets of split valence, triple zeta valence and quadruple zeta valence quality for H to Rn: Design and assessment of accuracy", *Phys. Chem. Chem. Phys.* **7**, 3297 (2005).

[427]R. Bauernschmitt and R. Ahlrichs, "Stability analysis for solutions of the closed shell Kohn-Sham equation", *J. Chem. Phys.* **104**, 9047 (1996).

[428]M. E. Casida, C. Jamorski, K. C. Casida, and D. R. Salahub, "Molecular excitation energies to high-lying bound states from time-dependent density-functional response theory: Characterization and correction of the time-dependent local density approximation ionization threshold", *J. Chem. Phys.* **108**, 4439 (1998).

[429]R. E. Stratmann, G. E. Scuseria, and M. J. Frisch, "An efficient implementation of time-dependent density-functional theory for the calculation of excitation energies of large molecules", *J. Chem. Phys.* **109**, 8218 (1998).

[430]R. L. Martin, "Natural transition orbitals", *J. Chem. Phys.* **118**, 4775 (2003).

[431]R. Seeger and J. A. Pople, "Self-consistent molecular-orbital methods. 18. Constraints and stability in Hartree-Fock theory", *J. Chem. Phys.* **66**, 3045 (1977).

[432]H. P. Hratchian and H. B. Schlegel, "Finding Minima, Transition States, and Following Reaction Pathways on Ab Initio Potential Energy Surfaces", in *Theory and applications of computational chemistry: The first forty years*, edited by C. E. Dykstra, G. Frenking, K. S. Kim, and G. E. Scuseria (Elsevier, Amsterdam, 2005), p. 195.

[433]F. Santoro, R. Improta, A. Lami, J. Bloino, and V. Barone, "Effective method to compute Franck-Condon integrals for optical spectra of large molecules in solution", *J. Chem. Phys.* **126**, 084509 (2007).

[434]F. Santoro, A. Lami, R. Improta, and V. Barone, "Effective method to compute vibrationally resolved optical spectra of large molecules at finite temperature in the gas phase and in solution", *J. Chem. Phys.* **126**, 184102 (2007).

[435]L. M. Thompson, H. Harb, and H. P. Hratchian, "Natural ionization orbitals for interpreting electron detachment processes", *J. Chem. Phys.* **144**, 204117 (2016).

[436]L. M. Thompson, C. C. Jarrold, and H. P. Hratchian, "Explaining the $MoVO_4^-$ photoelectron spectrum: Rationalization of geometric and electronic structure", *J. Chem. Phys.* **146**, 104301 (2017).

[437]J.-D. Chai and M. Head-Gordon, "Long-range corrected hybrid density functionals with damped atom-atom disperson corrections", *Phys. Chem. Chem. Phys.* **10**, 6615 (2008).

[438]M. Dolg, U. Wedig, H. Stoll, and H. Preuss, "Energy-adjusted ab initio pseudopotentials for the first row transition elements", *J. Chem. Phys.* **86**, 866 (1987).

[439]P. Boch and T. Chartier, "Alumina, Mullite and Spinel, Zirconia", in *Ceramic Materials: Processes, Properties and Applications* (Wiley, Hoboken, 2010).

[440]P. Warneck, "The atmospheric aerosol", in *Chemistry of the natural atmosphere*, Vol. 71, 2nd (Elsevier, Amsterdam, 1999).

[441]M. Trueba and S. P. Trasatti, "$\gamma$-alumina as a support for catalysts: A review of fundamental aspects", *Eur. J. Inorg. Chem.* **17**, 3393 (2005).

[442]C. Helling and P. Woitke, "Dust in brown dwarfs. V. Growth and evaporation of dirty dust grains", *Astron. Astrophys.* **455**, 325 (2006).

[443]C. Biscaro and I. Cherchneff, "Molecules and dust in Cassiopeia A. I. Synthesis in the supernova phase and processing by the reverse shock in the clumpy remnant", *Astron. Astrophys.* **564**, A25 (2014).

[444]G. E. Brown, V. Henrich, W. Casey, D. Clark, C. Eggleston, A. Felmy, D. W. Goodman, M. Gratzel, G. Maciel, M. I. McCarthy, K. H. Nealson, D. A. Sverjensky, M. F. Toney, and J. M. Zachara, "Metal oxide surfaces and their interactions with aqueous solutions and microbial organisms", *Chem. Rev.* **99**, 77 (1999).

[445]D. M. Makowiecki, J. Denis A. Lynch, and K. D. Carlson, "Infrared spectra of the aluminum family suboxides", *J. Phys. Chem.* **75**, 1963 (1971).

[446]L. V. Serebrennikov, S. B. Osin, and A. A. Maltsev, "Infrared spectra of the products of reaction of aluminum, gallium, indium, and thallium with oxygen in an argon matrix: Estimation of the fundamentals, $\nu_3$, in cyclic superoxides of group III metals", *J. Mol. Spec.* **81**, 25 (1982).

[447]S. M. Sonchik, L. Andrews, and K. D. Carson, "Matrix reactions of molecular oxygen and ozone with aluminum atoms", *J. Phys. Chem.* **87**, 2004 (1983).

[448]L. Andrews, T. R. Burkholder, and J. T. Yustein, "Reactions of pulsed-laser evaporated aluminum atoms with oxygen. Infrared spectra of the reaction products in solid argon", *J. Phys. Chem.* **96**, 10182 (1992).

[449]D. van Heijnsbergen, K. Demyk, M. A. Duncan, G. Meijer, and G. von Helden, "Structure determination of gas phase aluminum oxide clusters", *Phys. Chem. Chem. Phys.* **5**, 2515 (2003).

[450]K. Demyk, D. van Heijnsbergen, G. von Helden, and G. Meijer, "Experimental study of gas phase titanium and aluminum oxide clusters", *Astron. Astrophys.* **420**, 547 (2004).

[451]M. Sierka, J. Dobler, J. Sauer, G. Santambrogio, M. Brummer, L. Woste, E. Janssens, G. Meijer, and K. R. Asmis, "Unexpected structures of aluminum oxide clusters in the gas phase", *Angew. Chem. Int. Ed.* **46**, 3372 (2007).

[452]G. Santambrogio, E. Janssens, S. Li, T. Siebert, G. Meijer, K. R. Asmis, J. Dobler, M. Sierka, and J. Sauer, "Identification of conical structures in small aluminum oxide clusters: Infrared spectroscopy of $(Al_2O_3)_{1-4}(AlO)^+$", *J. Am. Chem. Soc.* **130**, 15143 (2008).

[453]X. Song, M. R. Fagiani, S. Gewinner, W. Schollkopf, K. R. Asmis, F. A. Bischoff, F. Berger, and J. Sauer, "Gas phase structures and charge localization in small aluminum oxide anions: Infrared photodissociation spectroscopy and electronic structure calculations", *J. Chem. Phys.* **144**, 244305 (2016).

[454]X. Song, M. R. Fagiani, S. Gewinner, W. Schollkopf, K. R. Asmis, F. A. Bischoff, F. Berger, and J. Sauer, "Gas-phase vibrational spectroscopy of the aluminum oxide anions $(Al_2O_3)_{1-6}AlO_2^-$, journal = *chem. phys. chem.*, volume = 18, pages = 868, year = 2017, type = Journal Article",

[455]S. R. Desai, H. Wu, and C. M. Rohlfing, "A study of the structure and bonding of small aluminum oxide clusters by photoelectron spectroscopy: $Al_xO_y^-$ $(x = 1-2,\ y = 1-5)$", *J. Chem. Phys.* **106**, 1309 (1997).

[456]H. Wu, X. Li, X.-B. Wang, C.-F. Ding, and L.-S. Wang, "$Al_3O_y$ $(y = 0-5)$ clusters: Sequential oxidation, metal-to-oxide transformation, and photoisomerization", *J. Chem. Phys.* **109**, 449 (1998).

[457]G. Meloni, M. J. Ferguson, and D. M. Neumark, "Negative ion photodetachment spectroscopy of the $Al_3O_2$, $Al_3O_3$, $Al_4O_x$, $Al_5O_x$ $(x = 3-5)$, $Al_6O_5$, and $Al_7O_5$ clusters", *Phys. Chem. Chem. Phys.* **5**, 4073 (2003).

[458]A. B. C. Patzer, C. Chang, E. Sedlmayr, and D. Sulzle, "A density functional study of small $Al_xO_y$ $(x, y = 1-4)$ clusters and their thermodynamic properties", *Eur. Phys. J. D* **32**, 329 (2005).

[459]T. K. Ghanty and E. R. Davidson, "Theoretical interpretation of the photoelectron spectra of $Al_3O_2^-$ and $Al_3O_3^-$", *J. Phys. Chem. A* **103**, 8985 (1999).

[460]A. Martinez, F. J. Tenorio, and J. V. Ortiz, "Electronic structure of $Al_3O_n$ and $Al_3O_n^-$ $(n = 1-3)$", *J. Phys. Chem. A* **105**, 8787 (2001).

[461]A. Martinez, L. E. Sansores, R. Salcedo, F. J. Tenorio, and J. V. Ortiz, "$Al_3O_n$ and $Al_3O_n^-$ $(n = 1-3)$ clusters: Structures, photoelectron spectra, harmonic vibrational frequencies, and atomic charges", *J. Phys. Chem. A* **106**, 10630 (2002).

[462]M. I. M. Sarker, C.-S. Kim, and C. H. Choi, "Ground and excited states of $Al_2O_2$ and its anion", *Chem. Phys. Lett.* **411**, 297 (2005).

[463]H. P. Hratchian and H. B. Schlegel, "Accurate reaction paths using a Hessian based predictor-corrector integrator", *J. Chem. Phys.* **120**, 9918 (2005).

[464]H. P. Hratchian and H. B. Schlegel, "Using Hessian updating to increase the efficiency of a Hessian based predictor-corrector reaction path following method", *J. Chem. Theory Comput.* **1**, 61 (2005).

[465]J. J. Max and C. Chapados, "Infrared spectroscopy of aqueous carboxylic acids: Comparison between different acids and their salts", *J. Phys. Chem. A* **108**, 3324 (2004).

[466]J. L. Cornette, K. B. Cease, H. Margalit, J. L. Spouge, J. A. Berzofsky, and C. Delisi, "Hydrophobicity scales and computational techniques for detecting ampipathic structures in proteins", *J. Mol. Bio.* **195**, 659 (1987).

[467]H. Cid, M. Bunster, M. Canales, and F. Gazitua, "Hydrophobicity and structural classes in proteins", *Protein Eng.* **5**, 373 (1992).

[468]J. L. Finney and A. K. Soper, "Solvent structure and perturbations in solutions of chemical and biological importance", *Chem. Soc. Rev.* **23**, 1 (1994).

[469]M. Ide, Y. Maeda, and H. Kitano, "Effect of hydrophobicity of amino acids on the structure of water", *J. Phys. Chem. B* **101**, 7022 (1997).

[470]F. Franks, "Protein stability: The value of 'old literature'", *Biophys. Chem.* **96**, 117 (2002).

[471]H. Schwarz and K. R. Asmis, "Identification of active sites and structural characterization of reactive ionic intermediates by cryogenic ion trap vibrational spectroscopy", *Chem. Eur. J.* **25**, 2112 (2019).

[472]E. Gojlo, M. Smiechowski, A. Panuszko, and J. Stangret, "Hydration of carboxylate anions: Infrared spectroscopy of aqueous solutions", *J. Phys. Chem. B* **113**, 8128 (2009).

[473]K. R. Asmis and D. M. Neumark, "Vibrational spectroscopy of microhydrated conjugate base anions", *Acc. Chem. Res.* **45**, 43 (2012).

[474]X. B. Wang, B. Jagoda-Cwiklik, C. X. Chi, X. P. Xing, M. F. Zhou, P. Jungwirth, and L. S. Wang, "Microsolvation of the acetate anion $[CH_3CO_3^-(H_2O)_n$, $n = 1-3]$: A photoelectron spectroscopy and ab initio computational study", *Chem. Phys. Lett.* **477**, 41 (2009).

[475]A. S. Sudbo, P. A. Schulz, Y. R. Shen, and Y. T. Lee, "Molecular-Beam Studies of Laser-Induced Multiphoton Dissociation", in *Multiple-Photon Excitation and Dissociation of Polyatomic Molecules*, edited by C. D. Cantrell (Springer, 1986), p. 95.

[476]E. J. Bieske and J. P. Maier, "Spectroscopy studies of ionic complexes and clusters", *Chem. Rev.* **93**, 2603 (1993).

[477]J. M. Lisy, "Spectroscopy and structure of solvated alkali-metal ions", *Int. Rev. Phys. Chem.* **16**, 267 (1997).

[478]T. Ebata, A. Fujii, and N. Mikami, "Vibrational spectroscopy of small-sized hydrogen-bonded clusters and their ions", *Int. Rev. Phys. Chem.* **17**, 331 (1998).

[479]P. Ayotte, J. Kim, J. A. Kelly, S. B. Nielsen, and M. A. Johnson, "Photoactivation of the $Cl^-$ + $CH_3Br$ SN2 reaction via rotationally resolved C-H stretch excitation of the $Cl{\cdot}CH_3Br$ entrance channel complex", *J. Am. Chem. Soc.* **121**, 6950 (1999).

[480]E. J. Bieske and O. Dopfer, "High-resolution spectroscopy of cluster ions", *Chem. Rev.* **100**, 3693 (2000).

[481]M. A. Duncan, "Intrared spectroscopy to probe structure and dynamics in metal ion-molecule complexes", *Int. Rev. Phys. Chem.* **22**, 407 (2003).

[482]W. H. Robertson and M. A. Johnson, "Molecular aspects of halide ion hydration: The cluster approach", *Annu. Rev. Phys. Chem.* **54**, 173 (2003).

[483]J. Oomens, B. G. Sartakov, G. Meijer, and G. V. Helden, "Gas-phse infrared multiple photon dissociation spectroscopy of mass-selected molecular ions", *Int. J. Mass Spectrom.* **254**, 1 (2006).

[484]K. R. Asmis, A. Fielicke, G. von Helden, and G. Meijer, "Vibrational spectroscopy of gas-phase clusters and complexes", in *Atomic Clusters: From Gas Phase to Deposited*, edited by D. P. Woodruff (Elsevier, 2007), p. 327.

[485]K. R. Asmis, D. M. Neumark, and J. M. Bowman, "Gas Phase Vibrational Spectroscopy of Strong Hydrogen Bonds", in *Hydrogen-Transfer Reactions*, edited by J. T. Hynes, J. P. Klinman, H. Limbach, and R. L. Schowen (Wiley, 2007), p. 53.

[486]J. Zhou, G. Santambrogio, M. Brummer, D. T. Moore, G. Meijer, D. M. Neumark, and K. R. Asmis, "Infrared spectroscopy of hydrated sulfate dianions", *J. Chem. Phys.* **125**, 111102 (2006).

[487]Y. Miller, G. M. Chaban, J. Zhou, K. R. Asmis, D. M. Neumark, and R. B. Gerber, "Vibrational spectroscopy of $(SO_4^{2-})\cdot(H_2O)_n$ clusters, $n = 1-5$: Harmonic and anharmonic calculations and experiment", *J. Chem. Phys.* **127**, 094305 (2007).

[488]D. J. Goebbert, E. Garand, T. Wende, R. Bergmann, G. Meijer, K. R. Asmis, and D. M. Neumark, "Infrared spectroscopy of the microhydrated nitrate ions $NO_3^-(H_2O)_{1-6}$", *J. Phys. Chem. A* **113**, 7584 (2009).

[489]E. Garand, T. Wende, D. J. Goebbert, R. Bergmann, G. Meijer, D. M. Neumark, and K. R. Asmis, "Infrared spectroscopy of hydrated bicarbonate anion clusters: $HCO_3^-(H_2O)_{1-10}$", *J. Am. Chem. Soc.* **132**, 849 (2010).

[490]T. I. Yacovitch, T. Wende, L. Jiang, N. Heine, G. Meijer, D. M. Neumark, and K. R. Asmis, "Infrared spectroscopy of hydrated bisulfate anion clusters: $HSO_4^-(H_2O)_{(1-16)}$", *J. Phys. Chem. Lett.* **2**, 2135 (2011).

[491]J. D. Steill and J. Oomens, "Action spectroscopy of gas-phase carboxylate anions by multiple photon IR electron detachment/attachment", *J. Phys. Chem. A* **113**, 4941 (2009).

[492]M. Okumura, L. I. Yeh, and Y. T. Lee, "The vibrational predissociation spectroscopy of hydrogen cluster ions", *J. Chem. Phys.* **83**, 3705 (1985).

[493]M. Brummer, C. Kaposta, G. Santambrogio, and K. R. Asmis, "Formation and photodepletion of cluster ion-messenger atom complexes in a cold ion trap: Infrared spectroscopy of $VO^+$, $VO_2^+$, and $VO_3$", *J. Chem. Phys.* **119**, 12700 (2003).

[494]A. B. Wolk, C. M. Leavitt, E. Garand, and M. A. Johnson, "Cryogenic ion chemistry and spectroscopy", *Acc. Chem. Res.* **47**, 202 (2014).

[495]E. M. Myshakin, K. D. Jordan, E. L. Sibert, and M. A. Johnson, "Large anharmonic effects in the infrared spectrum of the symmetrical $CH_3NO_2^-(H_2O)$ and $CH_3CO_2^-(H_2O)$ complexes", *J. Chem. Phys.* **119**, 10138 (2003).

[496]K. Ito and H. J. Bernstein, "The vibrational spectra of the formate, acetate, and oxalate ions", *Can. J. Chem.* **34**, 170 (1956).

[497]D. J. Goebbert, G. Meijer, and K. R. Asmis, "10K ring electrode trap - tandem mass spectrometer for infrared spectroscopy of mass selected ions", *AIP Conf. Proc.* **1104**, 22 (2009).

[498]T. K. Esser, H. Knorke, F. Siro-Brigiano, D. R. Galimberti, K. R. Asmis, M. P. Gaigeot, and M. J. Lisy, "Influence of argon and $D_2$ tagging on the hydrogen bond network in $Cs^+(H_2O)_3$: Kinetic trapping below 40 K", *Phys. Chem. Chem. Phys.* **20**, 28476 (2018).

[499]W. Schollkopf, S. Gewinner, H. Junkes, A. Paarmann, G. von Helden, H. Bluem, and A. M. M. Todd, "The new IR and THz FEL Facility at the Fritz Haber Institute in Berlin", *Proc. SPIE* **9512**, WEB04 (2015).

[500]N. Dietl, T. Wende, K. Chen, L. Jiang, M. Schlangen, X. H. Zhang, K. R. Asmis, and H. Schwarz, "Structure and chemistry of the heteronuclear oxo-cluster $[VPO_4]^{\cdot+}$: A model system for the gas-phase oxidation of small hydrocarbons", *J. Am. Chem. Soc.* **135**, 3711 (2013).

[501]N. Heine and K. R. Asmis, "Cryogenic ion trap vibrational spectroscopy of hydrogen-bonded clusters relevant to atmospheric chemistry", *Int. Rev. Phys. Chem.* **34**, 1 (2015).

[502]N. Heine and K. R. Asmis, "Cryogenic ion trap vibrational spectroscopy of hydrogen-bonded clusters relevant to atmospheric chemistry (vol 34, pg 1, 2015)", *Int. Rev. Phys. Chem.* **35**, 507 (2016).

[503]G. Mathias and M. D. Baer, "Generalized normal coordinates for the vibrational analysis of molecular dynamics simulations", *J. Chem. Theory Comput.* **7**, 2028 (2011).

[504]N. Yang, C. H. Duong, P. J. Kelleher, and M. A. Johnson, "Unmasking rare, large-amplitude motions in $D_2$-tagged $I^-(H_2O)_2$ isotopomers with two-color, infrared-infrared vibrational predissociation spectroscopy", *J. Phys. Chem. Lett.* **9**, 3744 (2018).

[505]N. Heine, E. G. Kratz, R. Bergmann, D. P. Schofield, K. R. Asmis, K. D. Jordan, and A. B. McCoy, "Vibrational spectroscopy of the water-nitrate complex in the O-H stretching region", *J. Phys. Chem. A* **118**, 8188 (2014).

[506]J. C. Marcum and J. M. Weber, "Microhydration of nitromethane anions from both a solute and solvent perspective", *J. Phys. Chem. A* **114**, 8933 (2010).

# Index of Abbreviations Used

| | |
|---|---|
| **(2c-3e)** | two-center, three-electron |
| **ADE** | adiabatic detachment energy |
| **BBO** | β-barium borate |
| **BDE** | bond dissociation enthalpy |
| **BF** | body-fixed |
| **BOMD** | Born-Oppenheimer molecular dynamics |
| **CASSCF** | complete active space self-consistent field |
| **CCD** | charge-coupled device |
| **CCSD** | coupled clusters singles and doubles |
| **CEI** | Coulomb explosion imaging |
| **CI** | conical intersection |
| **cryo-SEVI** | slow electron velocity-map imaging of cryogenically-cooled ions |
| **cw** | continuous wave |
| **DC** | direct current |
| **DFG** | difference frequency generation |
| **DFT** | density functional theory |
| **EA** | electron affinity |
| **eBE** | electron binding energy |
| **ECP** | effective core potential |
| **eKE** | electron kinetic energy |
| **EL** | Even-Lavie |
| **EOM-CC** | equation-of-motion coupled cluster |
| **FC** | Franck-Condon |
| **fwhm** | full-width at half-maximum |
| **HF** | Hartree-Fock |
| **HOMO** | highest-occupied molecular orbital |
| **HR** | high-reflecting |
| **HR-PEI** | high-resolution photoelectron imaging |
| **HT** | Herzberg-Teller |
| **ic-MRCI-F12** | internally contracted multireference configuration interaction |
| **IR** | infrared |
| **IRMPD** | infrared multi-photon photodissociation |
| **IRPD** | infrared photodissociation |

| | |
|---|---|
| **ISC** | intersystem crossing |
| **IVR** | intramolecular vibrational relaxation |
| **MCP** | microchannel plate |
| **MEVELER** | maximum entropy velocity Legendre reconstruction |
| **MEVIR** | maximum entropy velocity reconstruction |
| **MO** | molecular orbital |
| **MOM** | maximum overlap method |
| **MRMP2** | multireference second-order Moller-Plesset perturbation theory |
| **Nd:YAG** | neodymium-doped yttrium-aluminum-garnet |
| **NIO** | natural ionization orbital |
| **NMR** | nuclear magnetic resonance |
| **NN** | neural network |
| **NTO** | natural transition orbital |
| **OPO** | optical parametric oscillator |
| **OT** | overtone |
| **PAD** | photoelectron angular distribution |
| **PEC** | photoelectrical chemical cell |
| **PES** | photoelectron spectroscopy *or* potential energy surface |
| **PIP** | permutationally invariant polynomial |
| **PAH** | polycyclic aromatic hydrocarbon |
| **POVDR** | potential optimized discrete variable representation |
| **QCISD** | quantum configuration interaction (singles and doublets) |
| **QY** | quantum yield |
| **RF** | radiofrequency |
| **RMSE** | root-mean-square error |
| **SEVI** | slow electron velocity-map imaging |
| **SHG** | second harmonic generation |
| **tBuOO** | *tert*-butyl peroxy |
| **TDDFT** | time-dependent density functional theory |
| **TFP** | thin film polarizer |
| **TMP** | turbomolecular pump |
| **TMS** | trimethyl silyl |
| **TOF** | time-of-flight |
| **VCI** | vibrational configuration interaction |
| **VDE** | vertical detachment energy |
| **VMI** | velocity-map imaging |
| **VPT2** | second-order vibrational perturbation theory |
| **WKB** | Wentzel-Kramers-Brillouin |
| **WM** | Wiley-McLaren |
| **ZPE** | zero-point energy |

# Publications from Graduate Work

1. **J. A. DeVine**, S. Debnath, Y. Li, L. M. McCaslin, W. Schöllkopf, S. Gewinner, D. M. Neumark, K. R. Asmis, "Infrared photodissociation spectroscopy of $D_2$-tagged $CH_3CO_2^-(H_2O)_{0-2}$ anions" *Mol. Phys.*, in preparation.

2. M. C. Babin, **J. A. DeVine**, M. DeWitt, J. F. Stanton, D. M. Neumark, "High resolution photoelectron spectroscopy of cryogenically-cooled $NO_3^-$" *J. Phys. Chem. Lett.*, accepted for publication (2019).

3. **J. A. DeVine**, M. C. Babin, K. Blackford, D. M. Neumark, "High-resolution photoelectron spectroscopy of the pyridinide isomers" *J. Chem. Phys.* **151**, 064302 (2019).

4. **J. A. DeVine**, M. C. Babin, D. M. Neumark, "Photoelectron spectra of $Al_2O_2^-$ and $Al_3O_3^-$ via slow electron velocity-map imaging" *Faraday Discuss.* **217**, 235 (2019).

5. M. C. Babin, **J. A. DeVine**, M. L. Weichman, D. M. Neumark, "Slow photoelectron velocity-map imaging of cold $C_7^-$ and $C_9^-$" *J. Chem. Phys.* **149**, 174306 (2018).

6. **J. A. DeVine**, A. A. Taka, M. C. Babin, M. L. Weichman, H. P. Hratchian, D. M. Neumark, "High-resolution photoelectron spectroscopy of $TiO_3H_2^-$: Probing the $TiO_2^-$ + $H_2O$ dissociative adduct" *J. Chem. Phys.* **148**, 222810 (2018).

7. **J. A. DeVine**, M. L. Weichman, C. Xie, M. C. Babin, M. A. Johnson, J. Ma, H. Guo, D. M. Neumark, "Autodetachment from vibrationally excited vinylidene anions" *J. Phys. Chem. Lett.* **9**, 1058 (2018).

8. M. L. Weichman, B. Vlaisavljevich, **J. A. DeVine**, N. S. Shuman, S. G. Ard, T. Shiozaki, D. M. Neumark, A. A. Viggiano, "Electronic structure of SmO and $SmO^-$ via slow photoelectron velocity-map imaging spectroscopy and spin-orbit CASPT2 calculations" *J. Chem. Phys.* **147**, 234311 (2017).

9. **J. A. DeVine**,* M. L. Weichman,* B. Laws, J. Chang, M. C. Babin, G. Balerdi, C. Xie, C. L. Malbon, W. C. Lineberger, D. R. Yarkony, R. W. Field, S. T. Gibson, J. Ma, H. Guo, D. M. Neumark, "Encoding of vinylidene isomerization in its anion photoelectron spectrum" *Science* **358**, 336 (2017). (**equal authorship*)

10. M. L. Weichman, **J. A. DeVine**, M. C. Babin, J. Li, L. Guo, J. Ma, H. Guo, D. M. Neumark, "Feshbach resonances in the exit channel of the F + $CH_3OH \rightarrow HF + CH_3O$ reaction observed using transition-state spectroscopy" *Nat. Chem.* **9**, 950 (2017).

11. **J. A. DeVine**, M. L. Weichman, M. C. Babin, D. M. Neumark, "Slow photoelectron velocity-map imaging of cold *tert*-butyl peroxide" *J. Chem. Phys.* **147**, 013915 (2017).

12. **J. A. DeVine**, M. L. Weichman, S. J. Lyle, D. M. Neumark, "High-resolution photoelectron imaging of cryogenically cooled α- and β-furanyl anions" *J. Mol. Spec.* **332**, 16 (2017).

13. **J. A. DeVine**, M. L. Weichman, X. Zhou, J. Ma, B. Jiang, H. Guo, D. M. Neumark, "Non-adiabatic effects on excited states of vinylidene observed with slow photoelectron velocity-map imaging" *J. Am. Chem. Soc.* **138**, 16417 (2016).

14. M. L. Weichman, **J. A. DeVine**, D. M. Neumark, "High-resolution photoelectron imaging spectroscopy of cryogenically-cooled $Fe_4O^-$ and $Fe_5O^-$" *J. Chem. Phys.* **145**, 054302 (2016).

15. M. L. Weichman, **J. A. DeVine**, D. S. Levine, J. B. Kim, D. M. Neumark, "Isomer-specific vibronic structure of the 9-, 1-, and 2-anthracenyl radicals via slow photoelectron velocity-map imaging" *Proc. Natl. Acad. Sci. USA* **113**, 1698 (2016).

16. M. L. Weichman, J. B. Kim, **J. A. DeVine**, D. S. Levine, D. M. Neumark, "Vibrational and electronic structure of the α- and β-naphthyl radicals via slow photoelectron velocity-map imaging" *J. Am. Chem. Soc.* **137**, 1420 (2015).